AFRL-SN-HS-TR- 2002-002

PROCEEDINGS OF THE 2001 ANTENNA APPLICATIONS SYMPOSIUM –VOLUME II

Daniel H. Schaubert, et al
Electrical and Computer Engineering Department
University of Massachusetts
Amherst MA 01002

Electromagnetics Laboratory
University of Illinois
Urbana-Champaign

FINAL REPORT : September 19 – 21 2001

AIR FORCE RESEARCH LABORATORY
Sensors Directorate
Electromagnetics Technology Division
80 Scott Dr
Hanscom AFB MA 01731-2909

TITLE OF REPORT:

2001 Antenna Applications Symposium Volume II

PUBLICATION REVIEW

This report has been reviewed and is approved for publication.

APPROVED:

Livio D. Poles
Antenna Technology Branch
Electromagnetics Technology Division

FOR THE DIRECTOR

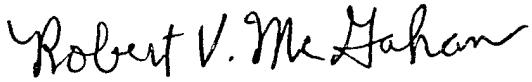

Robert V. McGahan,
Division Technical Advisor
Electromagnetics Technology Division

REPORT DOCUMENTATION PAGE

Form Approved
OMB No. 0704-0188

1. REPORT DATE *(DD-MM-YYYY)*	2. REPORT TYPE	3. DATES COVERED *(From - To)*
11 February 2002	Final	19-21 September 2001

4. TITLE AND SUBTITLE
PROCEEDINGS OF THE 2001 ANTENNA APPLICATION SYMPOSIUM

5a. CONTRACT NUMBER
GS01K99BKM0012

5b. GRANT NUMBER
TASK ORDER NUMBER
R15701321

5c. PROGRAM ELEMENT NUMBER

6. AUTHOR(S)
Daniel H. Schaubert et, al

5d. PROJECT NUMBER

5e. TASK NUMBER

5f. WORK UNIT NUMBER

7. PERFORMING ORGANIZATION NAME(S) AND ADDRESS(ES)
Air Force Research Laboratory
80 Scott Rd
Electromagnetics Technology Division
Sensors Directorate
Hanscom AFB, MA 01731

8. PERFORMING ORGANIZATION REPORT NUMBER
Volume I

9. SPONSORING/MONITORING AGENCY NAME(S) AND ADDRESS(ES)
Air Force Research Laboratory
80 Scott Rd
Electromagnetics Technology Division
Sensors Directorate
Hanscom AFB, MA 01731

10. SPONSOR/MONITOR'S ACRONYM(S)

11. SPONSOR/MONITOR'S REPORT
AFRL-SN-HS-TR-2002-002

12. DISTRIBUTION/AVAILABILITY STATEMENT
Approved for Public Release; Distribution Unlimited.

13. SUPPLEMENTARY NOTES
SNHA Project Engineer
Volume I consists of Pages 1-249, Volume II consists of Pages 250-587

14. ABSTRACT
The proceedings of the 2001 Antenna Applications Symposium is a collection of state-of-the-art papers relating to phased array antennas, Reconfigurable Antennas, Microstrip Antennas, Fractal Antennas.

15. SUBJECT TERMS
Antennas, Phased Array, Reconfigurable, Fractal Antennas, Digital Beamforming, Mictrostrip Antennas

16. SECURITY CLASSIFICATION OF:			17. LIMITATION OF ABSTRACT	18. NUMBER OF PAGES	19a. NAME OF RESPONSIBLE PERSON
a. REPORT	b. ABSTRACT	c. THIS PAGE			Livio D. Poles
U	U	U	SAR	249	19b. TELEPHONE NUMBER *(Include area code)* 781-377-4087

THURSDAY, SEPTEMBER 20, 2001
MORNING

ARRAYS I

THURSDAY, SEPTEMBER 20, 2001
AFTERNOON

ARRAYS II

FRIDAY, SEPTEMBER 21, 2001
MORNING

APERTURES

Identifiers for Proceedings of Symposia

The USAF Antenna Research and Development Program

Year	Symp. No.	Identifier
1951	First	
1952	Second	C054 520
1953	Third	AD63794
1954	Fourth	AD63139
1955	Fifth	AD90397
1956	Sixth	AD114702
1957	Seventh	AD138500
1958	Eighth	AD301151
1959	Ninth	AD314721
1960	Tenth	AD244388 (Vol. 1) AD319613 (Vol. 2)
1961	Eleventh	AD669109 (Vol. 1) AD326549 (Vol. 2)
1962	Twelfth	AD287185 (Vol. 1) AD334484 (Vol. 2)
1963	Thirteenth	AD421483
1964	Fourteenth	AD609104
1965	Fifteenth	AD474238L
1966	Sixteenth	AD800524L
1967	Seventeenth	AD822894L
1968	Eighteenth	AD846427L
1969	Nineteenth	AD860812L
1970	Twentieth	AD875973L
1971	Twenty-First	AD888641L
1972	Twenty-Second	AD904360L
1973	Twenty-Third	AD914238L

Antenna Applications Symposium

		TR#	ADA#
1977	First	None	955413
1978	Second	None	955416
1979	Third	_____	077167
1980	Fourth	_____	205907
1981	Fifth	_____	205816
1982	Sixth	_____	129356
1983	Seventh	_____	142003; 142754
1984	Eighth	85-14	153257; 153258
1985	Ninth	85-242	166754; 165535
1986	Tenth	87-10	181537; 181536
1987	Eleventh	88-160	206705; 206704
1988	Twelfth	89-121	213815; 211396
1989	Thirteenth	90-42	226022; 226021
1990	Fourteenth	91-156	237056; 237057
1991	Fifteenth	92-42	253681; 253682
1992	Sixteenth	93-119	268167; 266916
1993	Seventeenth	94-20	277202; 277203
1994	Eighteenth	95-47	293258; 293259
1995	Nineteenth	96-100	309715; 309723
1996	Twentieth	97-189	341737
1997	Twenty First	1998-143	
1998	Twenty Second	1999-86	
1999	Twenty Third	2000-008 (I), (II)	

SOME NOTABLE FIRSTS IN ARRAY ANTENNA HISTORY

Helmut E. Schrank, Consultant, Hunt Valley, MD
(Retired from Westinghouse Electric Corp., Baltimore, MD)

1. ABSTRACT

This paper briefly describes some of the significant array antenna developments known to the author from his studies and experiences over the past 58 years. Others may recall additional milestones and their contributions to this historical review are most welcome.

Antenna technology began in the late 1880's with the Hertzian experiments to verify Maxwell's (then controversial) theory of EM (electromagnetic) waves. Hertz was the first to use wire loop, dipole, and parabolic cylinder reflector antennas. Most early antennas for "wireless telegraphy" (radio) communication were made of wires in various forms, and were mostly omnidirectional.

Array antennas began in 1926 with the invention of the Yagi-Uda three element endfire array in Japan. Phased arrays, capable of non-mechanical beam steering, began in the mid-1930's with the MUSA (Multiple Unit Steerable Antenna) system used by AT&T for trans-Atlantic circuits. Other "firsts" are discussed below.

Hopefully, our looking back at these past achievements will challenge and inspire our younger engineers to make even greater "firsts" in this Third Millennium.

2. ANTENNA and ARRAY PROGRESS

A brief annotated chronological list of major milestones in the history of array antennas. Some of these items will be expanded in following sections.

1886-'88 FIRST ANTENNAS
Heinrich Hertz – Karlsruhe, Germany
Experiments to verify Maxwell's EM theory. Used resonant loop, dipoles, and parabolic reflectors.

1895 FIRST WIRELESS TELEGRAPHY (RADIO)
Guglielmo Marconi – Bologona, Italy
Demonstrated wireless communication using EM ("Hertzian") waves. Used omnidirectional wire antenna.

1926 FIRST ARRAY ANTENNA
Hidetsugu Yagi and Shintaro Uda – Sendai, Japan
Three-element endfire array, unidirectional beam.

1937 FIRST PHASED ARRAY
AT&T/BTL engineers – New York, USA
MUSA array of rhombics to reduce signal fading in trans-Atlantic telephone link.

1941 FIRST U.S. MILITARY RADAR DETECTION OF ENEMY ACTION IN WW2
U.S. Army Signal Corp. operators – Oahu, Hawaii
SCR-270 radar using dipole array

1940's FIRST ELECTRONIC AZIMUTH SCAN
Bell Telephone Labs engineers – New Jersey, USA
Using polyrod array, motor driven phasers, Navy radar.

1940's FIRST ELECTRONIC ELEVATION SCAN
Hughes Aircraft Co. engineers – California, USA
Freq. scanned elevation stabilization, Navy radar.

1946 FIRST RADAR ECHO FROM THE MOON
U.S. Army Signal Corp. engineers – Ft. Monmouth, USA
Modified SCR-270 radar, dipole array.

1960 FIRST SWITCHED-BEAM SPHERICAL ARRAY
JHU/APL and Westinghouse engineers – Maryland, USA
U.S. Navy SPG-59 TYPHON experimental radar system.

1960's FIRST MULTIFUNCTION PHASED ARRAY
Texas Instruments (now Raytheon) engineers – Texas, USA
MERA planar array, USAF experimental radar.

1967 FIRST EXPERIMENTAL ULTRALOW SIDELOBE ARRAY
Westinghouse engineers (Phil Hacker) – Baltimore, USA

1970's FIRST AFFORDABLE MULTIFUNCTION ARRAY
Westinghouse engineers (B. Sichelstiel) – Baltimore, USA
EAR planar array, U.S.A.F. experimental radar.

1970's FIRST PRODUCTION ULTRALOW SIDELOBE PHASED ARRAY
Westinghouse (now Northrop Grumman) engineers – Baltimore, USA
USAF AWACS surveillance radar.

3. The YAGI-UDA ARRAY

In 1926 Professors Yagi and Uda invented the well-known and widely used endfire array consisting of one driven dipole element and two (or more) parallel parasitic rods of different lengths to produce a unidirectional beam. It had moderate gain and a narrow bandwidth, but its use in Japan was limited to communication with off-shore islands. However, it found wide applications by the U.K. and U.S. military forces in WW2 for communication, radar, and other systems. Later, the Yagi principle led to the ubiquitous TV receiver antennas throughout Europe and the U.S.

As Gentei Sato points out in his article "A Secret Story About the Yagi Antenna" [1], the Japanese were surprised to discover the use of Yagi antennas by U.K. forces after the battle of Singapore. Later they learned that the Yagi antenna was a key component of the atom bombs dropped on Hiroshima and Nagasaki to end the Pacific War.

Much R&D has been done since WW2 to improve Yagi performance. See the June 1991 issue of the IEEE Antennas and Propagation Magazine.

4. THE MUSA PHASED ARRAY

In the 1930's, before submarine cables were laid, the AT&T Company used a short-wave radio link across the Atlantic for its commercial telephone circuits to and from Europe. To reduce signal fading caused by instability of the ionosphere, Bell Laboratories developed a phased array of receiving antennas. This antenna system was called MUSA, for Multiple Unit Steerable Antenna [2].

The antenna consisted of a linear array of sixteen rhombic elements, phased to produce a near-endfire pattern. In Figure 1, a simplified four element array is shown, with each element connected to the central receiver by individual transmission lines. The 16-element array was two miles long, and was aligned in the direction of the incoming wavefront. The resulting pattern (shown in Figure 2) has much higher directivity in the vertical plane, and therefore, reduces fading caused by interference between waves arriving from different vertical angles. To

control the vertical angle of the array pattern, mechanically-driven condenser phase shifters were used.

Although most modern phased arrays are designed for radar applications, it is interesting to note that the first phased array was used for communication.

5. THE SCR-270 RADAR ARRAY

The SCR-270 [3] radar was one of the first to see service in WW2. It was developer for the U.S. Army Signal Corp. in Ft. Monmouth, NJ and manufactured by Westinghouse in Baltimore, MD. Its antenna was a planar array of 32 dipoles in front of a wire mesh groundplane, mounted to a vertical tower. As seen in Figure 3, the horizontally oriented dipoles were arranged in four bays of eight dipoles each. It produced a beam narrower in azimuth than in elevation (approx. 7 by 17 degrees) normal to the array plane. The entire antenna and tower rotated mechanically for azimuth scanning. The radar measured range and azimuth direction of target echoes. It operated at a frequency of 106 MHz.

An earlier version (SCR-270-B) was operational on Oahu, Hawaii on Dec. 7, 1941 when Pearl Harbor was bombed by Japanese aircraft. Echoes from the oncoming raid were detected at a range of 137 miles north of the Opala radar site. When this was reported to superior officers by the radar operator, the report was dismissed with the assumption that a group of U.S. B-17 aircraft was on its way from the U.S. West Coast.

This detection was the first use of radar by the U.S. military forces in warfare, a truly historic event. In 1946 a modified SCR-270 radar was used to detect the first echoes from the Moon, another historic event.

6. EARLY SHIPBORNE RADAR PHASED ARRAYS

Early radars for Navy ships had antennas designed to scan in azimuth only to detect other surface vessels. Most of these radars used parabolic reflector antennas, and were scanned mechanically. The inertia of these antennas limited how fast they could be scanned.

For rapid azimuth scanning, one of the first non-mechanically scanned phased array antennas was invented at Bell Telephone Laboratories in the late 1940's. It was known as the Polyrod Array [4] because it was a planar array of dielectric rods made of polystyrene, fed from open-ended rectangular waveguides. Motor-driven rotating phase shifters were used to rapidly scan the antenna beam over an azimuth sector, for an experimental fire control radar. (See Figure 4).

Another early shipborne phased array antenna was developed at the Hughes Aircraft Company. It was a vertical array of radiating elements fed by serpentine waveguides to rapidly scan the beam in elevation without moving the entire antenna. Its purpose was to stabilize the beam for horizon scan in rough seas. The means used to keep the antenna beam on the horizon while the ship

rolled and pitched was to vary the radar frequency, which resulted in phase shifts to the radiators. This was one of the first applications of frequency scanning.

7. A SPHERICAL ARRAY FOR THE TYPHON SYSTEM RADAR

In the late 1950's, the U.S. Navy sponsored a study and experimental development program known as TYPHON. This ambitious program was to design a shipborne radar system capable of defending against aircraft and/or missile threats. The new multifunction radar was required to not only search for threatening targets, but to also do target tracking and missile guidance. These requirements called for an agile-beam antenna, capable of rapidly dealing with more than one target. The TYPHON weapon system was designated AN/SPG-59, and a prototype radar was built and installed on the USS Norton Sound for system evaluation tests at sea. The radar performed but did not meet all system requirements, so the program was terminated. Later the AEGIS system was developed by RCA to replace TYPHON. [5]

The TYPHON antennas consisted of a spherical array for transmitting and three Luneburg lens antennas for receiving. (See Figure 5). This innovative arrangement was conceived by system engineers at the Johns Hopkins University Applied Physics Laboratory (JHU/APL) and built at Westinghouse Electric Corporation (now Northrop Grumman) in Baltimore. The antennas formed almost 3000 discrete beams in space covering about 3Π steradians. Beam switching was used rather than beam scanning.

The spherical transmit array (Figure 6) consisted of 3240 dielectric-filled circular waveguide radiating elements, designed to radiate circular polarization. These elements were fed by semi-rigid coax cables as shown in Figure 7. Almost 900 elements were activated to form each beam in space. Elaborate switching was required to connect the 900 TWT power amplifiers to the designated beam group. Similar switching was required between the outputs of the so-called "Computing Lens" to the inputs of the TWT amplifiers. (See Figure 8). The Computing Lens was completely surrounded by a metal shell containing 3612 circular waveguide radiators. The Computing Lens and the transmit array were approximately four feet in diameter.

Although this system failed to provide the necessary performance requirements, the unique spherical phased array antenna provided a challenging opportunity in both design and construction techniques, to say the least. It represents and interesting chapter in the history of phased array antenna technology.

8. MULTIFUNCTION AIRBORNE PHASED ARRAYS

The USAF Avionics Laboratory (WPAFB) sponsored two significant array antenna development programs in the 1960's and 1970's. The purpose of

both programs was to develop solid-state electronically scanned antennas for future airborne radar applications.

The first of these programs was conducted by the Texas Instruments Company in the mid 1960's, and was called Molecular Electronics for Radar Applications (MERA). The MERA antenna (built in 1967) was a planar array of X-band radiators with a hexagonal aperture shape. It was designed for a multi-purpose radar capable of ground mapping, air-to-ground ranging, terrain follow, and terrain avoidance. Although these functions were successfully achieved, the antenna was very heavy and excessively costly, mainly due to the electronic phase control modules behind each radiating element.

The second program was conducted by Westinghouse Electric Corp. Systems Development Division in Baltimore, from 1974 through 1979. It was call the Electronically Agile Radar (EAR). The EAR antenna was a planar array of 1800 elements forming a circular aperture about a meter in diameter. (See Figure 9). It too (as did MERA) operated in the X-band and provided multi-function radar capability. The radiating elements were especially developed by two suppliers (Raytheon and Microwave Application Group) to include a 6-bit digital ferrite phase shifter and control circuit integral with the dielectric filled circular waveguide radiator. This array was designed to scan its main beam to +/- 60 ° off normal in any direction. Sidelobes were low and did not deteriorate with scan angle, although the main beam gain followed the unavoidable cosine loss factor. Three experimental antennas were built and two were flight-tested.

The main achievements of this program were not only its excellent multifunction performance, but also its low weight, long MTBF period and its affordability. The mass-produced phase-shifter/radiator elements cost approximately $300 each. This was an order of magnitude lower than previous similar components.

The EAR technology was directly applied to the design of the radar antenna for the B-1B aircraft. Figure 10 shows a partially assembled array.

9. THE AWACS ULTRALOW SIDELOBE PHASED ARRAY

In the late 1960's and early 1970's, Westinghouse developed the surveillance radar for the USAF AWACS System (Airborne Warning and Control System, AN/APY-1). [6] This system required an antenna with special characteristics to enable the radar to detect and track large numbers of aircraft from its flight altitude of approximately 30,000 ft. Most of the aircraft targets would be at lower altitude so the antenna had to illuminate 360 ° of azimuth airspace from the horizon and downward in elevation. Echoes from low-flying targets competed with stronger echoes from the ground, known as "ground clutter". To minimize ground clutter, the antenna had to have its minor lobes ("sidelobes") suppressed to levels never before achieved. Most antenna experts at

that time believed –40 dB sidelobes to be the lowest achievable. Had this been true, AWACS would not have been successful. What was required was an antenna with sidelobes one or more orders of magnitude lower than –40 dB. [7]

Westinghouse engineer, Phil Hacker, investigated slotted waveguide arrays to achieve the required performance. An experimental waveguide array with narrow-wall slots was designed to form an ultralow (less than –40 dB) sidelobe pattern. It was recognized that mutual coupling between slots caused both amplitude and phase errors in the radiation from each slot. To get a desired low-sidelobe distribution, it was necessary to take mutual couplings into account. A computer-aided design program (CAD) was devised by Phil Hacker and Richard McComas to do just that, and applied to design an 8-waveguide resonant array. (See Figure 11). Slots were machined to close tolerances by a numerically controlled milling machine. The resulting pattern came within 1 or 2 dB of the theoretical, down to levels below –50 dB.

This breakthrough in antenna technology can be attributed, not only to smart engineering, but also to the developments of accurate computer-controlled machining techniques and of precision microwave measuring facilities such as the network analyzer and other test range equipment. Design, production, and testing improvements were all necessary to achieve "impossible" results.
The AWACS antenna (shown in Figure 12) is a planar array of slotted S-band rectangular waveguides, forming an oval-shaped aperture which produces a main beam approximately 1 ° in azimuth by 5 ° in elevation. This beam is scanned in azimuth by mechanical rotation of the radome-enclosed antenna, and is scanned in elevation by electronically controlled phase shifters. It achieved a beam efficiency of better than 99.5%, which means that less than 0.5% of all the power radiated is in all minor lobes.

This achievement constitutes a notable advance in the history of array antenna technology. When the antenna experts said "it couldn't be done", Phil Hacker and Dick McComas (and many others at Westinghouse) showed it could indeed be accomplished. Because the AWACS program was classified, the successful "breakthrough" could not be publicized for years, and it took a while for the radar antenna community to appreciate what had been achieved.

10. ACKNOWLEDGEMENTS

The author appreciates the help of Ross Stone, Editor in Chief of the IEEE Antennas and Propagation Magazine, the assistance of the Historical Electronics Museum staff, and the encouragement of Prof. Dan Schaubert of the University of Massachusetts/Amherst. Also, sincere thanks to Arthur Schrank for his invaluable help in producing this paper.

11. REFERENCES

[1] G. Sato, "A Secret Story About the Yagi Antenna", IEEE Antennas & Propagation Magazine, June 1991, pp7-18.

[2] F. A. Polkinghorn, "A MUSA Receiving System", BSTJ, April 1940 and Proc. IRE, April 1940.

[3] M. Skolnik, "Introduction to Radar Systems", pp. 11, 604, McGraw-Hill, 1962.

[4] Bell Laboratories Staff, "Radar Systems and Components"' Polyrod Fire Control Array, pp. 824-825, 843-845, D. Van Nostrand, 1949.

[5] B. D. Inman, "From TYPHON to AEGIS", Naval Engineers Journal, May 1988, pp. 62-72.

[6] M. Skolnik, "Radar Handbook" (2nd Ed.), pp. 7.72-7.73, McGraw-Hill, 1990.

[7] E. Brookner, Ed. "Aspects of Modern Radar", Chap 6 (Schrank), pp. 337-340, Artech House, 1988.

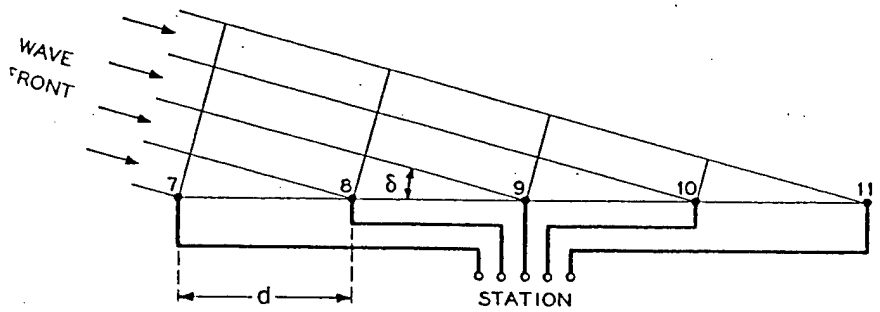

Figure 1. Partial MUSA array (from Polkinghorn)

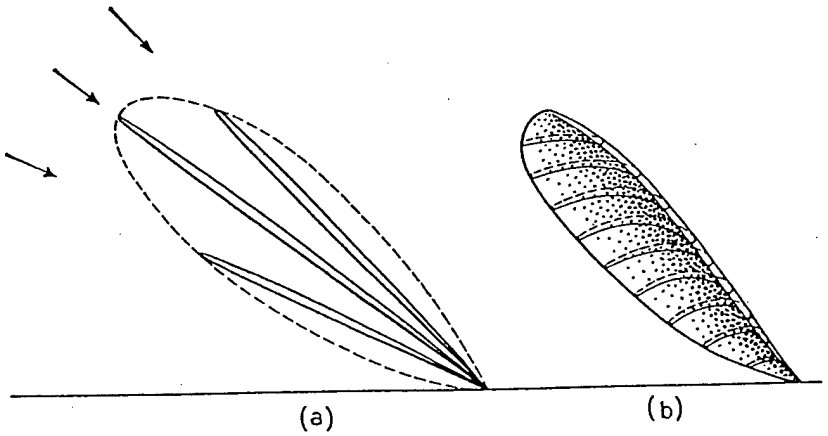

Figure 2. MUSA antenna pattern (from Pokinghorn)

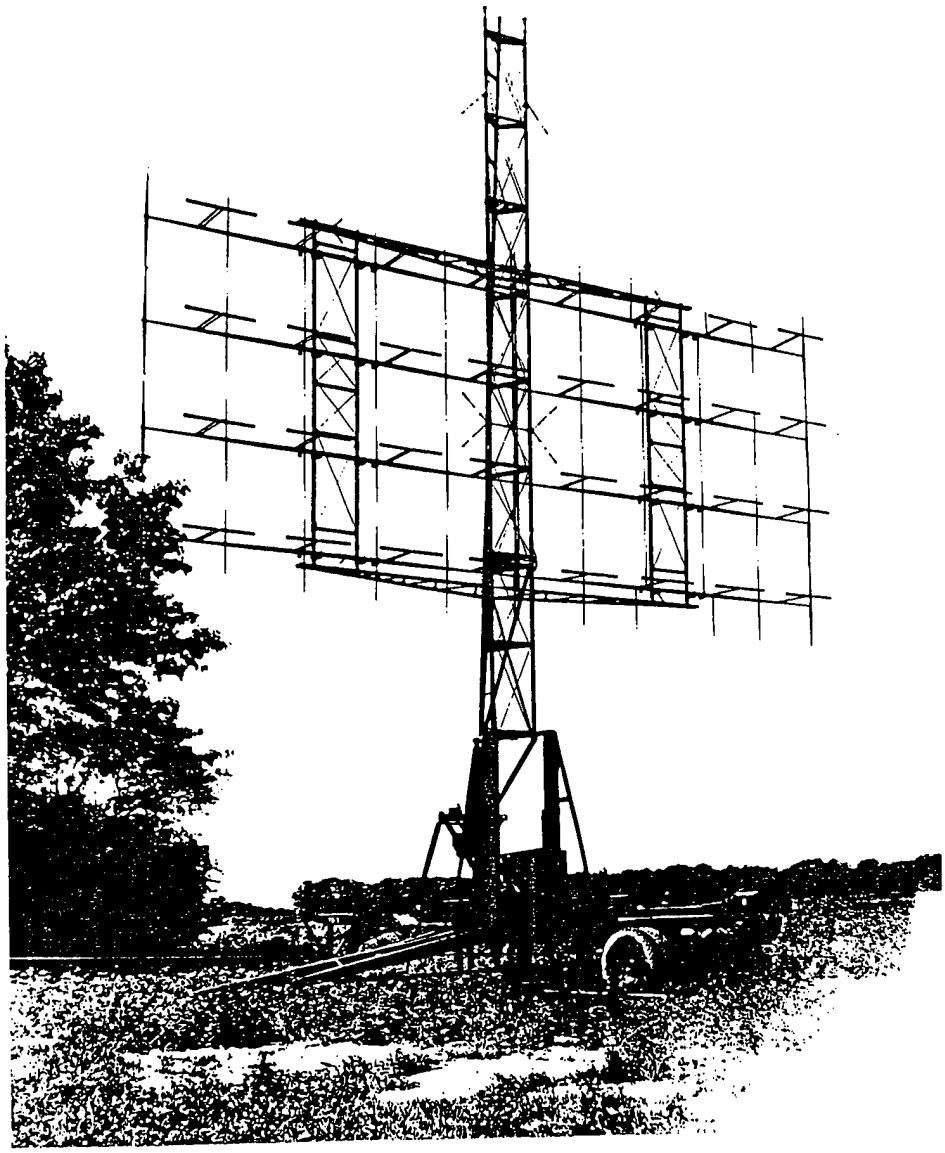

Figure 3. SCR-270 dipole array (courtesy of Historical Electronics Museum, Baltimore, MD).

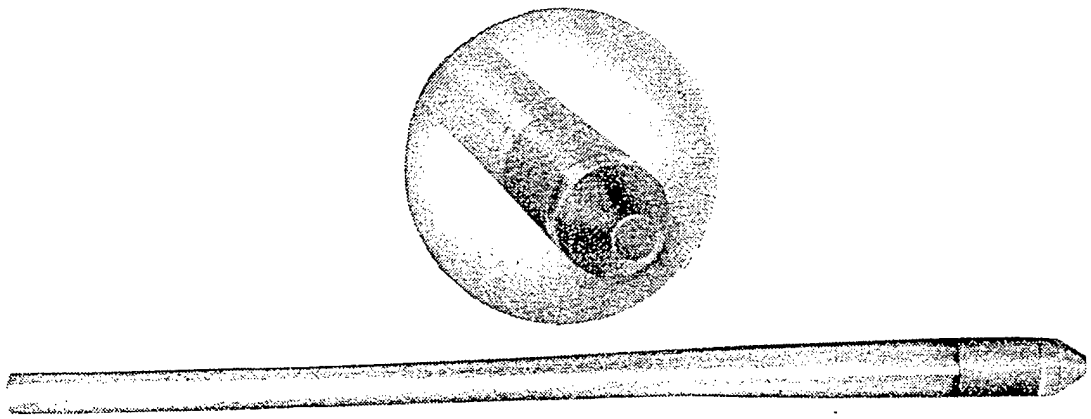

Fig. 38—A Polyrod.

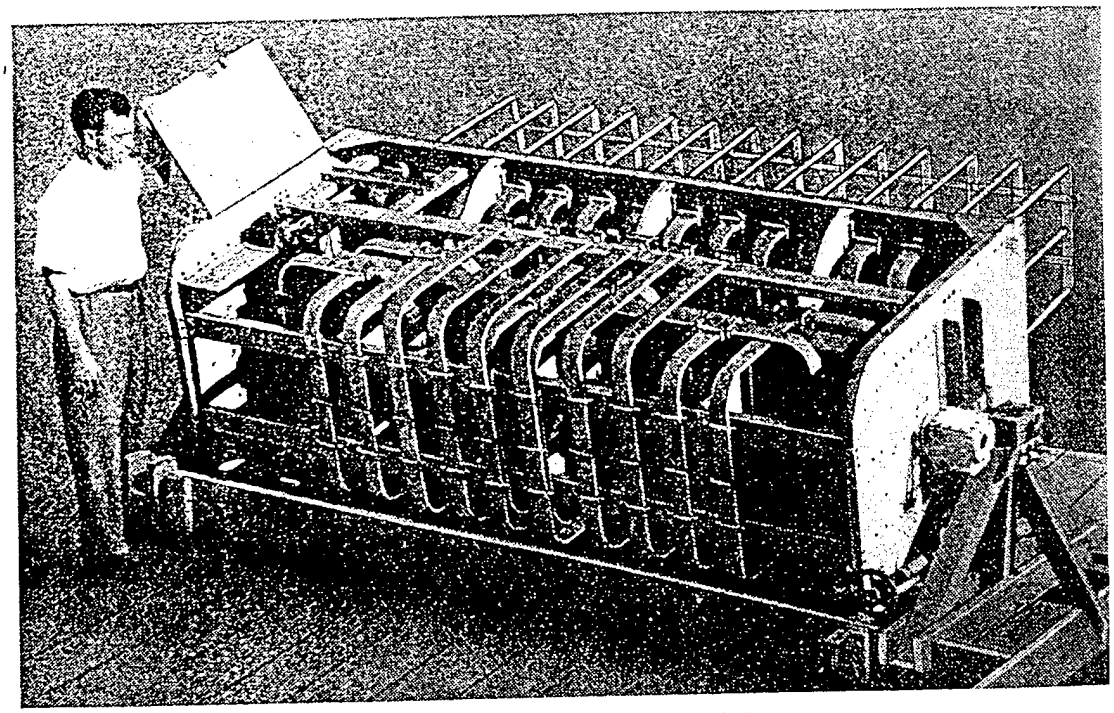

Fig. 39.—Experimental Polyrod Array.

Figure 4. Polyrod phased array (from BTL Radar Systems and Components).

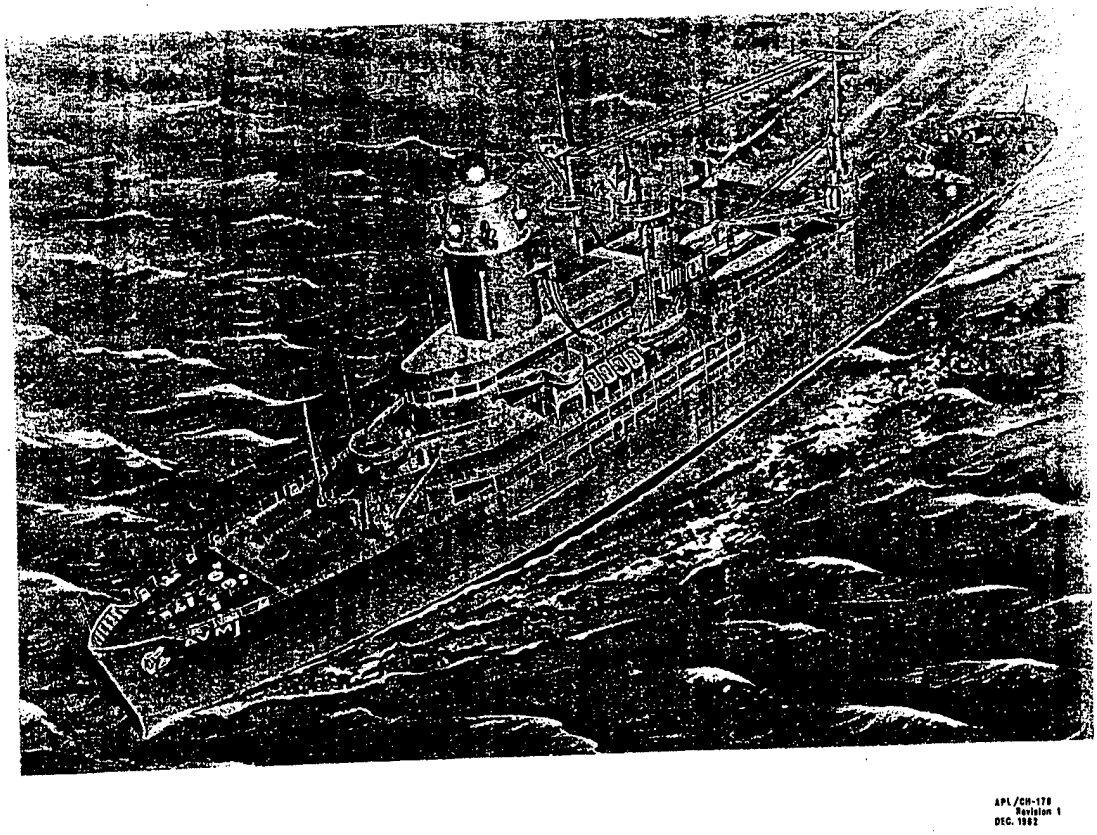

Figure 5. Typhon radar system ship installation (courtesy of JHU/APL).

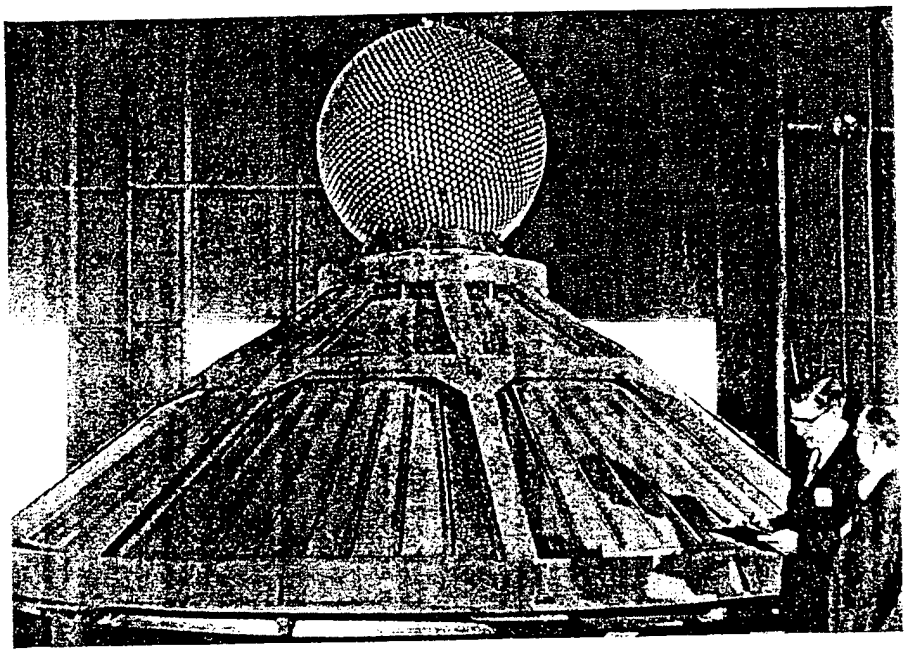

Figure 6. Spherical phased array for transmitting.

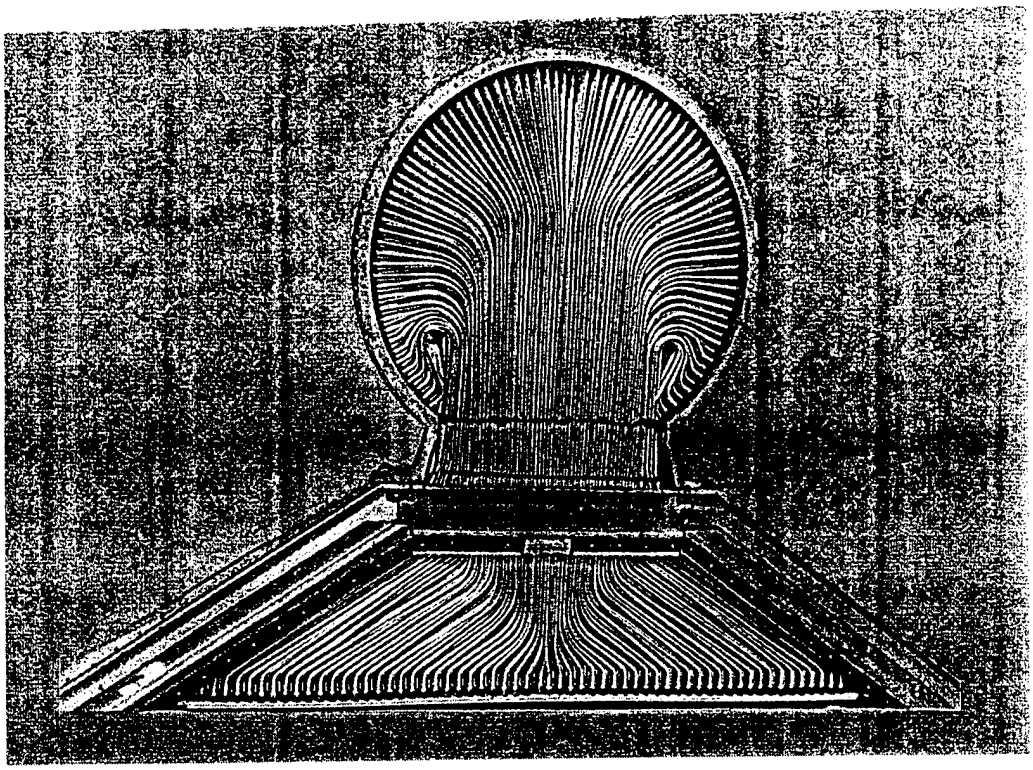

Figure 7. Half of spherical array showing semi-rigid coaxial cables (courtesy of Westinghouse).

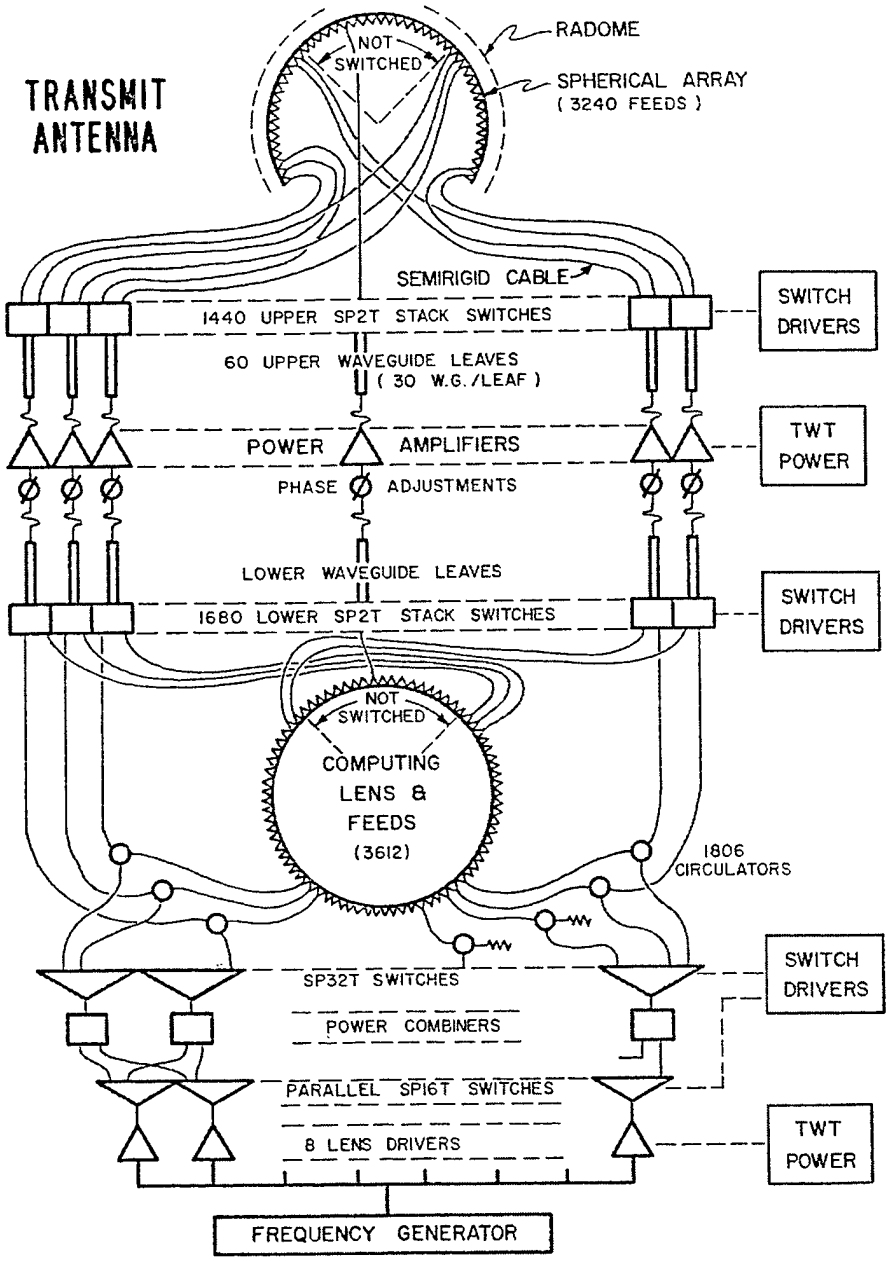

Figure 8. Transmit array diaram

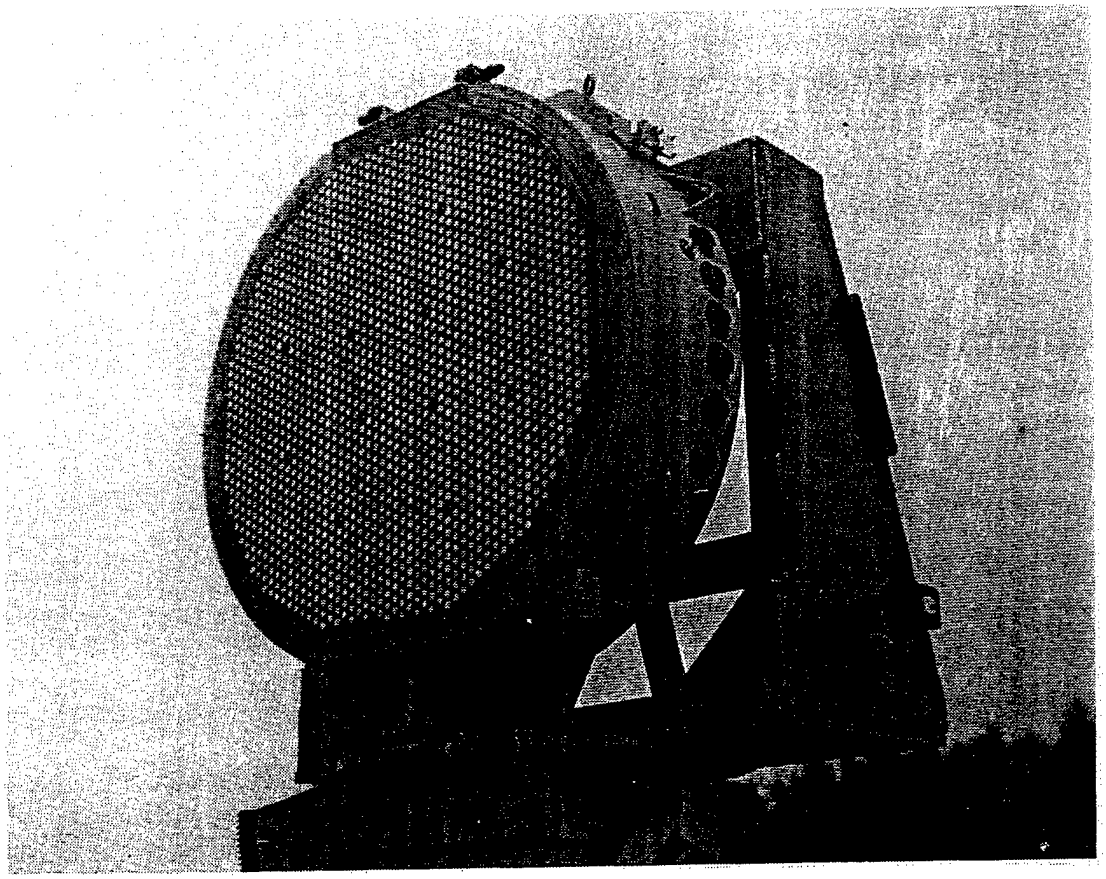

Figure 9. Electronically Agile Radar (EAR) phased array.

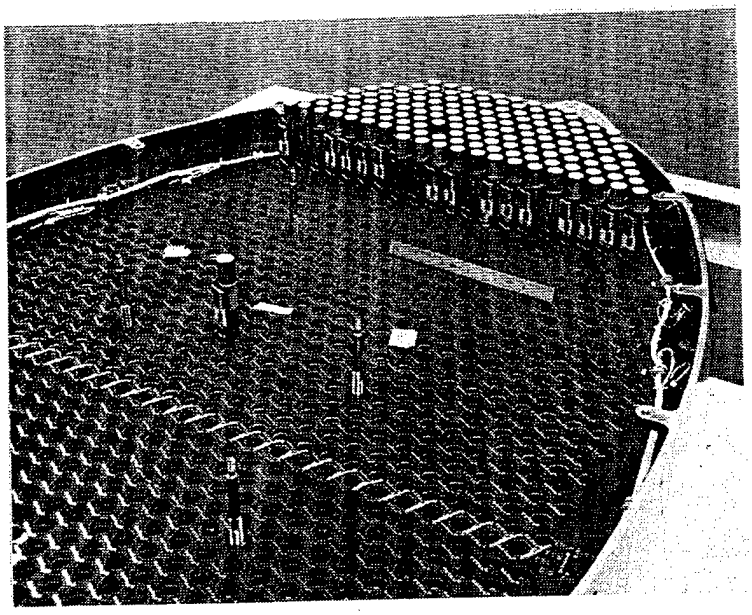

Figure 10. Partially assembled EAR-type array.

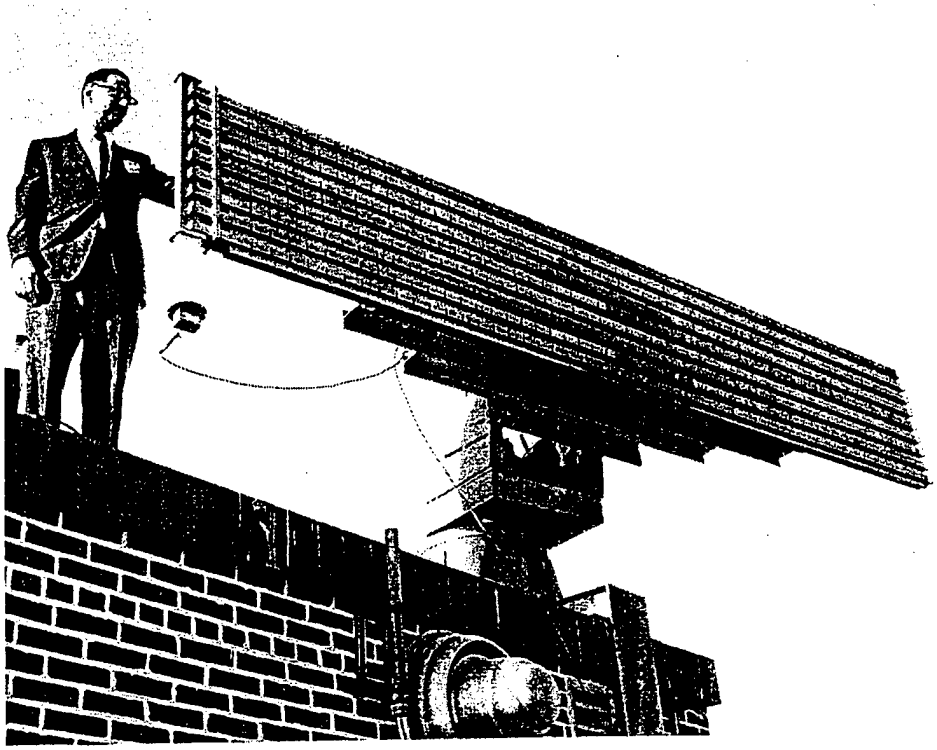

Figure 11. Phil Hacker with experimental ultralow sidelobe array

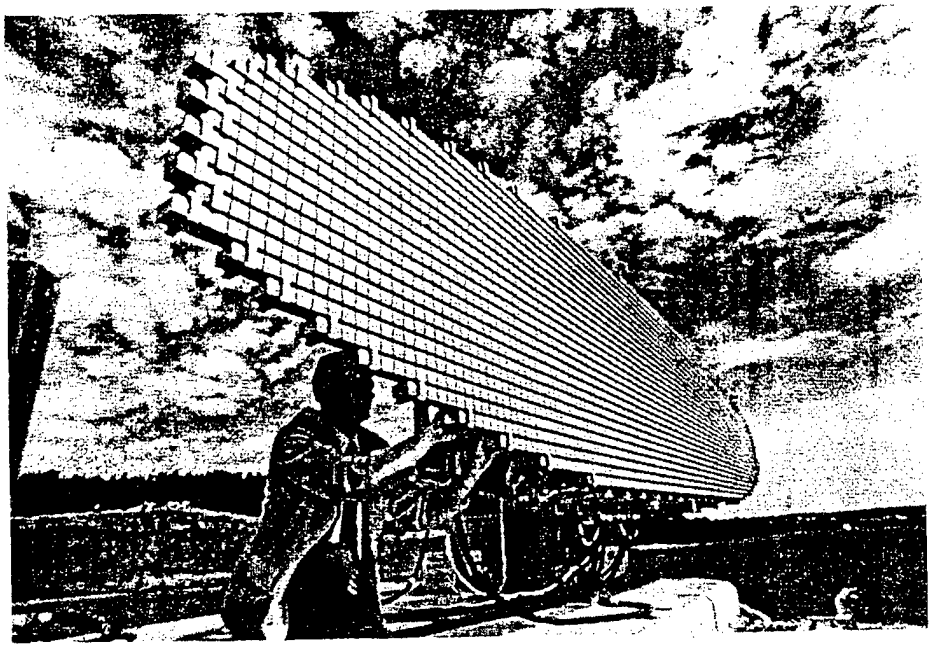

Figure 12. AWACS ultralow sidelobe phased array antenna.

PREDICTED PERFORMANCE OF SMALL ARRAYS OF DIELECTRIC-FREE TAPERED SLOT ANTENNAS

A. Boryssenko and D. H. Schaubert
Antenna Laboratory
University of Massachusetts
Amherst, MA 01003

Abstract: A rigorous time-domain integral equation simulation has been developed to predict the performance of small arrays of dielectric-free tapered slot antennas. Broadband data are obtained with moderate computer resources. By studying the input impedances of all array elements, some insights into truncation effects are obtained. Linear arrays that are five to ten elements in extent exhibit oscillations of the impedance that may be associated with energy diffracted from the edges of the array. Single elements seem to possess a critical frequency above which the impedance is nearly real and nearly constant. Linear arrays exhibit similar behavior with all array elements having approximately the same impedance, i.e., truncation effects are not important in this frequency range. Planar arrays do not exhibit this desirable effect.

1. Background

Tapered slot antennas, also known as Vivaldi or notch antennas, are appearing in many antenna arrays. Design of a wideband scanning array requires extensive numerical simulation and the relationships between performance and various design parameters is still not adequately understood. Nonetheless, antenna engineers with experience in the operation of tapered slot antenna (TSA) arrays and access to the correct simulation tools are successfully designing arrays with two or more octaves of bandwidth. Recently a significant limitation to the design of practical TSA arrays has emerged; truncation effects in arrays of small to moderate size are far more important for wideband TSA arrays than for narrowband arrays of traditional elements [1]. Hence, every element of the array behaves differently (impedance and radiation pattern). Existing electromagnetic simulation programs cannot evaluate moderate-size arrays of stripline-fed TSA's efficiently to predict their performance over wide bandwidths and wide scan ranges. Furthermore, many potential applications require lower cost array fabrication than is possible with etched and bonded stripline structures that have dominated TSA designs. Dielectric-free TSA's comprised of a thin sheet of metal cut or stamped in the shape shown in Figure 1 are attractive for these low-cost

applications. An additional benefit of eliminating the dielectric substrate with two metallic ground planes is the removal of some anomalous resonances that usually appear at the upper end of the frequency band of stripline-fed antennas [2]. Dielectric-free TSA arrays have been shown to posses excellent wideband characteristics, similar to those obtained with stripline-fed designs [3].

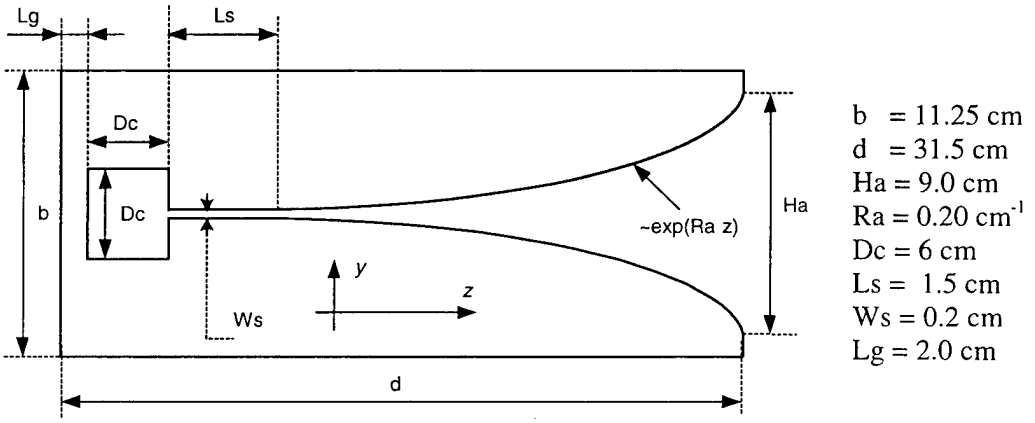

Figure 1. Configuration of single dielectric-free Vivaldi tapered slot antenna element with geometrical parameters for array simulations.

The purpose of this paper is (1) to introduce a new simulation tool that has been developed to analyze small arrays of dielectric-free TSA's and (2) to demonstrate some of the truncation effects that occur in these arrays. A 3x3 array of TSA's is depicted in Figure 2. The configuration is formed by repeating the slot pattern in both transversal directions, i.e. first along the y-axis to form a single sheet and then a number of sheets are spaced parallel to each other.

Analysis of finite phased arrays generally proceeds along one of three paths:

1) A brute force technique using the element-by-element method. This works pretty well for electrically small problems or approximately with a very limited number of modes per array element for moderate size arrays. Often there are severe limitations for larger arrays due to computational requirements, for example, [4].
2) A windowing technique using the results of infinite array analysis with a "windowed" amplitude excitation, e.g., [5]. This approach is only approximate and seems best suited for arrays of elements that satisfy the minimum scattering criterion [6]. It seems not to work for TSA arrays.

3) Various asymptotic techniques [7,8] have been developed for some specific array configurations but they have limited accuracy and/or are not generally applicable.

The element complexity and strong mutual coupling between the array elements in Figure 2 necessitates a rigorous analysis that efficiently produces wideband results. The elements in a 5:1 bandwidth array are separated by only 1/10 wavelength at the lower frequencies, but a practical array can be twenty or more wavelengths across at the upper frequencies. A single element of the array is typically about 1/4 wavelength long at the lower frequencies and more than one wavelength long at the upper frequencies. An accurate analysis of the currents flowing on the metallic fins requires a fine computational mesh for frequency-domain or time-domain analysis. A typical Method of Moments mesh is illustrated in Figure 3.

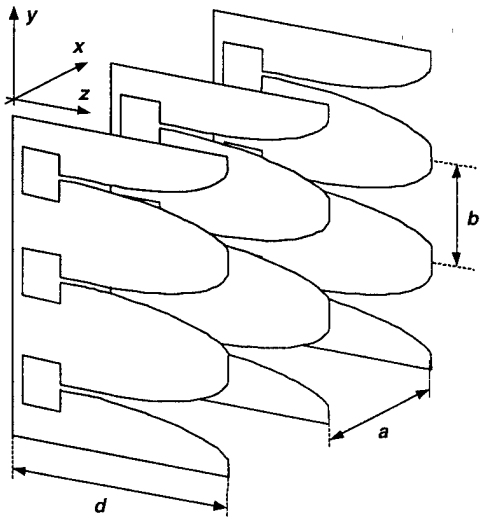

Figure 2.
3x3 single-polarized array composed of dielectric-free Vivaldi antennas to be simulated with d=31.5 cm, a=b=11.25 cm for operation to about 1.33 GHz where first grating lobe appears.

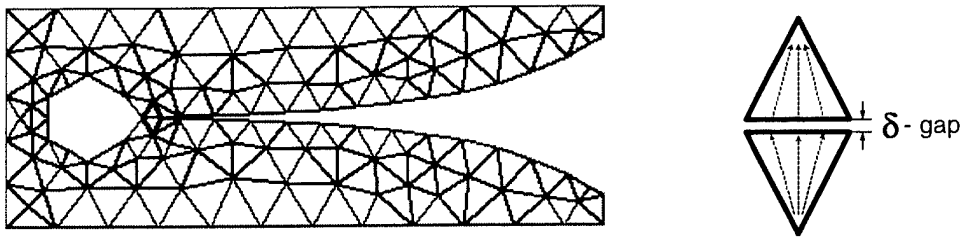

Figure 3. Triangular mesh for Vivaldi slot antenna with RWG feed mode.

A brute force element-by-element approach has been chosen by the authors for this study to treat accurately the edge effects in finite phased arrays of the type in Figure 2. At the same time, we were not able to use existing numerical techniques of computational electromagnetics like frequency domain MoM and FDTD. Available versions of these numerical codes have strong requirements on computer resources and limitations on the problem size when used on readily accessible computer platforms. We developed and tested recently a time-domain integral equation (TDIE) analysis based on the mixed potential formulation for the electric field integral equation. This time-domain numerical technique uses time stepping to compute the surface transient current and charge distributions over the 3-D perfect electric conductor (PEC) surfaces of the antenna. After Fourier transformation, the performance of the array can be predicted in the frequency domain in traditional terms such as active scan impedance, return losses, etc.

The formulation of the TDIE analysis is rigorous and efficient for numerical implementation on readily available workstations. Preliminary versions of the simulation utilizing a mixed Matlab-Fortran code can compute the impedance of all elements of a 5x5 array, 25 elements total, over three or four octaves of frequency in about 2 hours using a PC configuration with 933 MHz Pentium-III processor and 256 MB RAM.

The rest of the paper is organized in the following order. The next section presents the principal points of the TDIE simulation technique and discusses effective computational realization for broadband dielectric-free TSA single-polarized arrays. Section 3 describes application of this technique to linear TSA arrays starting from a single TSA element and considering in detail 5x1 and 10x1 array cases. Section 4 includes similar results for planar arrays of 3x3 and 5x5 elements. Several observations about the behavior of TSA elements in a small array are discussed in sections 3 and 4.

2. Method of numerical analysis

In this section, we present our recently developed numerical simulation technique for finite phased array explorations dealing with mutual coupling and edge effects. After review of several existing computational electromagnetics techniques that could be applicable to finite phased array problems like that in Figure 2, the time-domain integral equation method was chosen as the basic concept to be realized. The time-domain integral equation (TDIE) technique is preferred to finite-difference time-domain (FDTD) because:

1) Considerable memory saving is achievable with surface discretization in TDIE instead of volume meshing in FDTD.
2) The radiation condition is automatically included in the formulation while FDTD requires specific radiation boundary conditions like ABC or PML.
3) TDIE does not experience grid dispersion errors like FDTD, which affect the accuracy of large array simulations.

The TDIE method we have developed can be used with readily available PCs or workstations to analyze small to moderate size arrays of dielectric-free TSA's. By comparison, FDTD can treat small arrays of very general geometry [9] and material, or infinite arrays by using periodic boundary conditions [10].

The TDIE method is closely related to existing time-domain MoM solutions that use the Marching-on-in-Time (MoT) technique [11,12,13]. The MoM-MoT formulation starts from the boundary condition on the PEC antenna surface that requires zero magnitude of the total tangential electrical field composed of incident, *(i)*, and scattered, *(s)*, fields.

$$\vec{E}^i + \vec{E}^s = 0 \tag{1}$$

Then the scattered field is expressed via the magnetic vector potential and electric scalar potential

$$\vec{E}^s(\vec{r},\mathrm{t}) = -\frac{\partial}{\partial t}\vec{A}(\vec{r},t) - \nabla\Phi(\vec{r},\mathrm{t}) \tag{2}$$

$$\vec{A}(\vec{r},t) = \mu_0 \cdot \int_S \frac{\vec{I}(s',\tau)}{4\pi R} ds' \tag{3}$$

$$\Phi(\vec{r},t) = 1/\varepsilon_0 \cdot \int_S \frac{q(s',\tau)}{4\pi R} ds' \tag{4}$$

The current density, I, and the charge density, q, are connected through the continuity equation:

$$\frac{\partial}{\partial t} q(s',t) + \nabla \cdot \vec{I}(s',t) = 0 \tag{5}$$

In (2)-(5), $\tau = t - R/c$ is retarded time, $R = |\vec{r} - \vec{r}'|$ is the distance from the source to the observer, c is the free-space light velocity; ε_0, μ_0 are the fundamental electric and magnetic constants, respectively.

Next, the system (1)-(5) is discretized in a manner similar to [13]. This discretization provides a finite difference approximation to derivatives and a summation approximation to integrals. An appropriate testing procedure must be applied to enforce equation (1). These topics are treated in detail in the references. However, some points should be emphasized because they affect the numerical stability and accuracy of computed data. Many MoM-MoT solvers suffer from numerical instability in late time and are useful mainly for electrically small problems due to the large computer resources required. The analytical formulation, numerical algorithm and code implementation of our TDIE substantially overcome these limitations.

A key point here is numerical solution of the coupled system of first-order differential equations (2) and (5) with integral representations for the scalar and magnetic potentials, equations (3) and (4). The system (1)-(5) is commonly transformed to a single operator equation involving only the unknown current [11,12,13], where numerical differentiations and integrations must be performed on the integral kernel with unavoidable loss in accuracy. A coupled system of first order differential equations, analogous to the telegrapher equations, is presumably more accurate for solution with finite difference and sum approximation than an equivalent second-order equation [14]. The idea to solve (1)-(5) numerically through a system of integrodifferential equations leads to the published works [12,15] where the simplest case of a PEC square plate scattering with rectangular uniform meshing is treated. We developed further this approach to be applicable to arbitrary PEC 3-D bodies with surface triangular meshing and RWG current modes [16] as shown in Figure 3 for a typical Vivaldi element. The time dependence of the current and charge representations employs simple pulse functions. Also, the RWG mode with delta-gap excitation is used for the feed mode across the slot, as depicted in Figure 3.

Computationally the effectiveness of matrix operations in the MoM-MoT scheme depends on how topological parameters of the mesh are related to electrical unknowns through the mesh description in the connection matrices. To this end, some algorithm optimization can be done regarding a tradeoff of RAM usage and CPU time. We found that a sparse matrix representation is effective in updating computations at each time step because it provides optimal distribution of RAM and CPU resources. The pre-computed and stored connection matrices are a part of the output data given from a special automated mesh/mode generator based on geometrical triangulation with the Delanay-Voronoy technique.

Inaccuracies in the numerically computed integrals (3) and (4) and finite difference approximations in (2) and (5) have a strong negative effect on the

stability of numerical computations in MoM-MoT schemes [15,17]. These effects should be minimized by:

1) Accurate evaluation of the integrals in (3) and (4) using analytical techniques [18] with separated spatial and temporal basis functions.
2) Leapfrog sampling for current/charge in time-space that gives more accurate nested central difference approximations for derivatives [13,14].
3) Low-frequency adaptive filtering [15,17] in MoM-MoT for stabilization the late time transient responses.
4) Prony extrapolation technique [19] for weaker late-time stability requirements permits increasing the time step and minimizing CPU time.

Figure 4 reflects the major functional blocks of the code that was first realized in Matlab. After validation of the method, some of the slower numerical procedures were transformed to faster compiled Fortran modules. Currently we have a mixed Matlab-Fortran code because Matlab is still attractive for further code development. Also we prefer Fortran 90 that supports after compilation very effective code for massive matrix summation and multiplication.

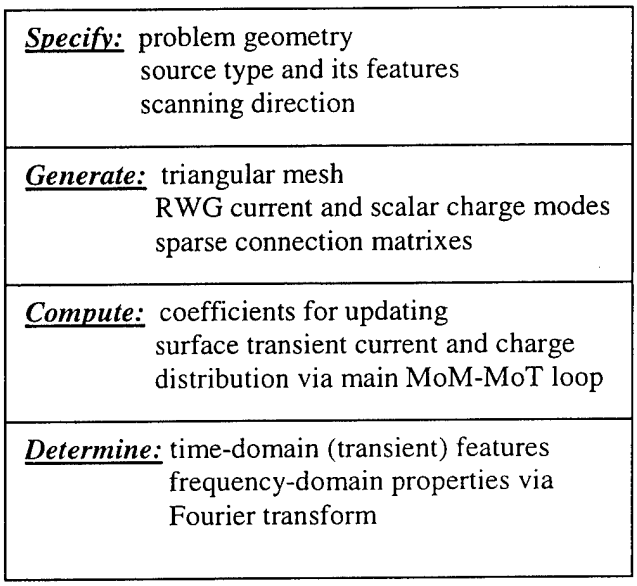

Figure 4.
Major functional blocks of the developed TDIE numerical solver for analysis of finite broadband phased arrays.

The code has been validated by comparisons for several different structures such as square plate scattering, flat dipoles, bow-tie antennas, round and square loops, etc, computed by our TDIE code and other available methods, including

frequency-domain MoM and FDTD. Very good agreement has been obtained for all cases including simple phased arrays of flat dipoles, bow-tie arrays, etc.

Another important point for the MoM-MoT scheme is the choice of source signal waveform. The Gaussian pulse is commonly used in time-domain simulations [13]. Unfortunately, we found during our computations that application of this pulse has a numerical effect similar to DC offset for PEC structures with a closed path for current in close proximity to the source region, like around the resonator cavity of the Vivaldi element in Figure 1. We exploit the Rayleigh pulse, which does not have DC spectral component. Figure 5 shows a Rayleigh pulse and a Gaussian pulse with similar spectrum coverage, but a significant DC component.

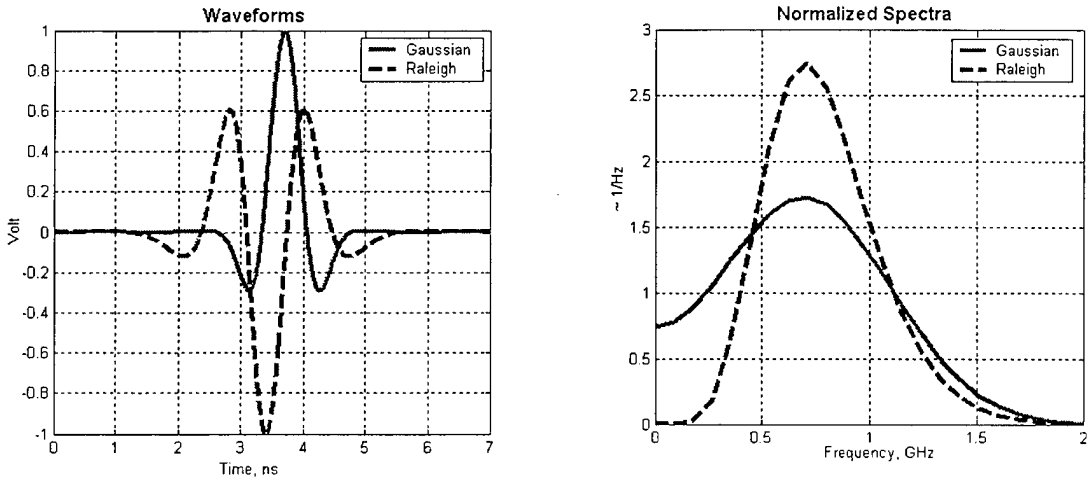

Figure 5. Gaussian and Rayleigh 1-Volt peak pulses and their spectra.

The developed code permits arbitrary beam position by introducing successive time delays between elements in the array at their feed points and amplitude weighting of the array can be easy implemented. Also a forward radiation transformation can be applied to compute at the post-processing stage any component of transient radiated fields at any spatial near- or far-range observation point.

3. Simulation of linear arrays

Truncation effects cause elements near the edge of a phased array to behave differently than those in the central region. These effects are the result of mutual

coupling between array elements, which are different for central elements that are completely surrounded by neighboring active elements, than for edge elements that do not have as many neighboring elements. Wideband TSA arrays are particularly susceptible to truncation effects at lower frequencies, because the spacing between elements is of the order of 1/10 wavelength. We have begun to explore truncation effects in TSA arrays by considering linear arrays and small planar arrays.

We present first the limiting case of a single TSA element. The basic mesh in Figure 6a yields good results for the antenna element in Figure 1. Alternative meshes with slightly different cavity shapes and greater number of modes for the unknown current and charge yield similar results, with some small differences due to the cavity shapes (Figure 7). Note the resonance peak near 0.6 GHz for all three cases. Also, note that the input impedance is nearly real and relatively constant above about 1.0 GHz. The mesh of Figure 6a will be used in the array simulations that follow.

Figure 8 shows a 5x1 linear array of dielectric-free elements like that in Fig. 6a. The array is scanned to 45 degrees by delaying the excitations of elements 2, 3, 4, and 5. That is, the beam points in the E-plane toward element #5. Figure 9 shows the Rayleigh pulse applied to the antennas and the transient current at the feed point of element #1. The current amplitude decays in late time, demonstrating the stability that is typical of the TDIE method. Normalized magnitudes of the spectra for both signals are depicted at the bottom of figure 9.

Figure 10 shows the input resistance and reactance of all five elements for the cases of broadside and 45 degrees in the E-plane.

As expected, the element impedances differ, depending on location in the array. For broadside radiation, #1 and #5 are identical, as are #2 and #4. For scanning away from broadside, the impedances of all elements differ.

The data for broadside illustrate several features:

1. The resonance peak that was observed near 0.6 GHz for a single element (Fig. 7) is evident for elements #1 and #5, but the peak values are somewhat diminished.
2. Elements #2, #3 and #4 display a resonance at somewhat higher frequencies.
3. The input resistances in the frequency range 0.3-0.5 GHz are larger than for the single element. The central elements (#2, #3, #4) have higher resistance at the lower frequencies than the outer elements (#1 and #5).

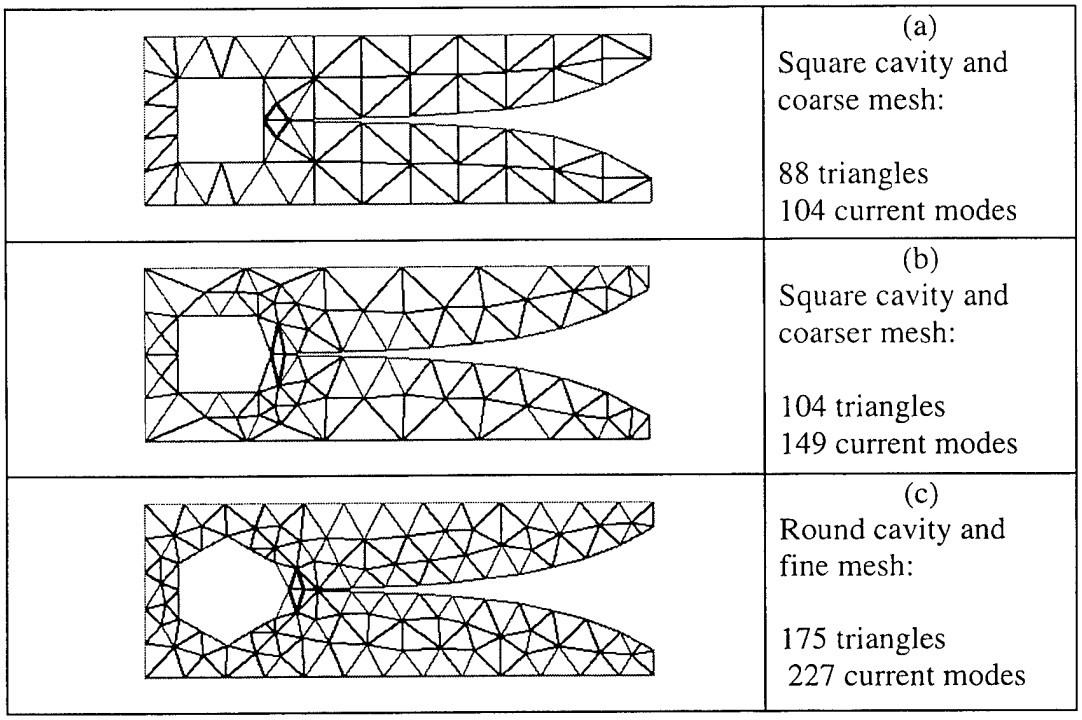

Figure 6. Vivaldi element with different cavity shapes and triangular meshing.

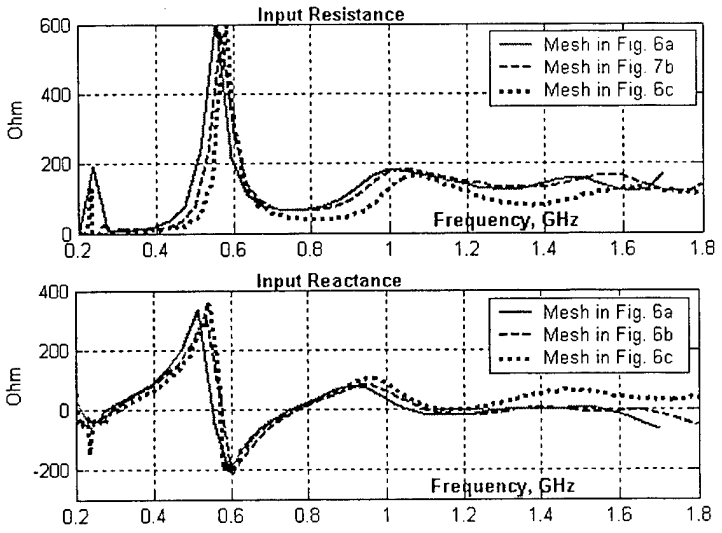

Figure 7. Computed input impedance for the fin elements in Figure 6 with different mesh and shape of resonator cavity.

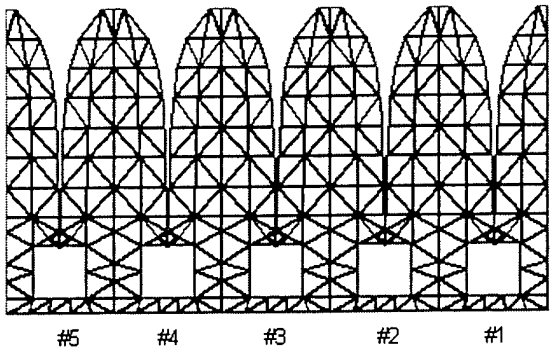

Figure 8. Geometry and triangular mesh for the 5x1 linear Vivaldi array.

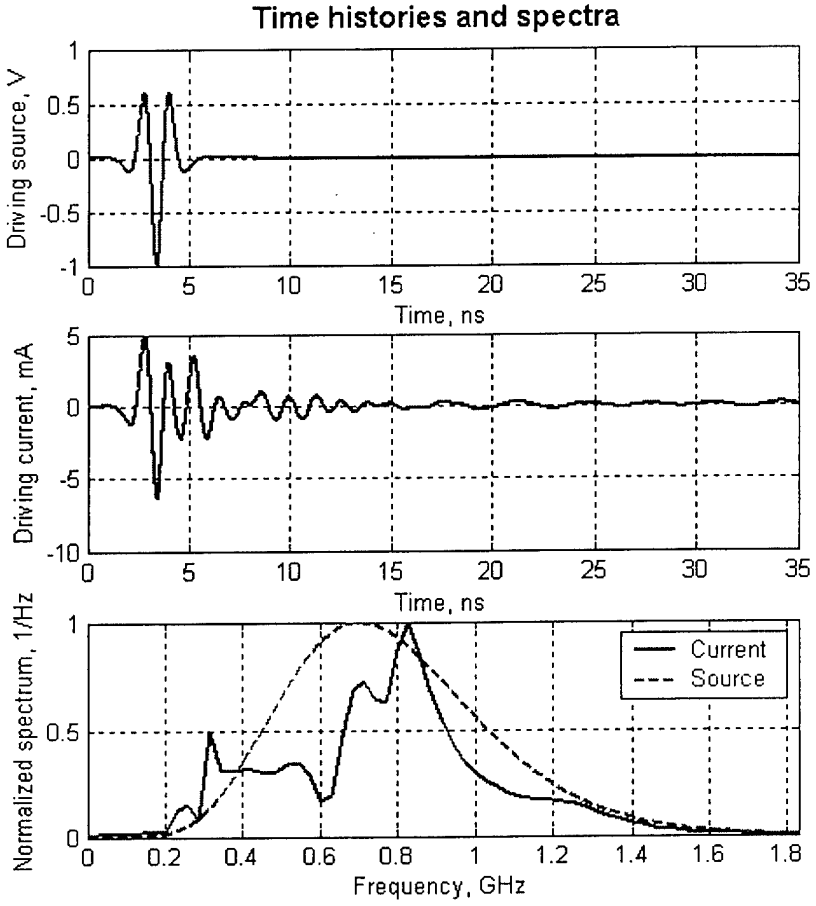

Figure 9. Transient voltage and current at the antenna feed point for the element #1 in 5x1 array, Figure 8, scanned at 45 degree in the E-plane.

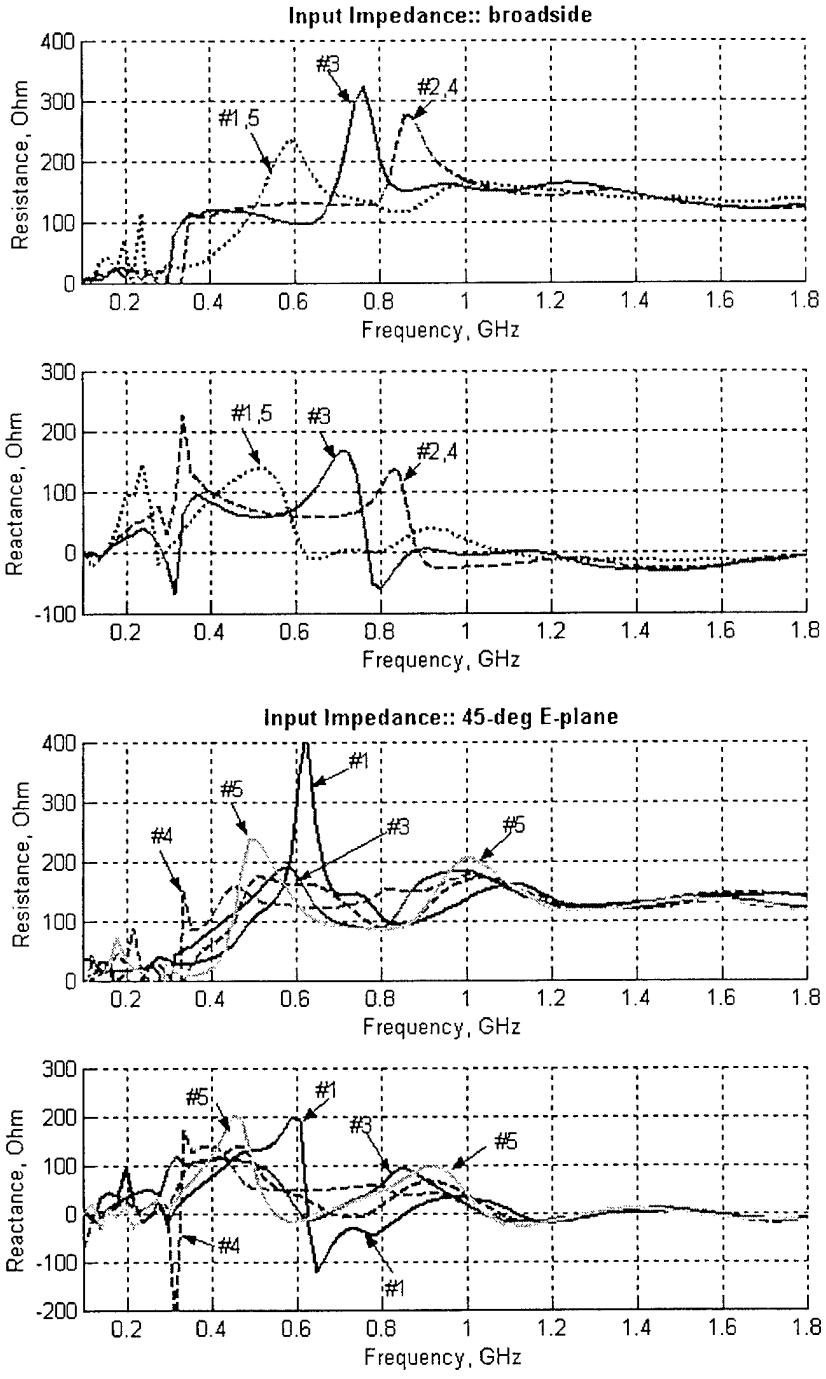

Figure 10. Input impedances for all elements in the 5x1 array for broadside radiation and 45-degree E-plane scanning.

4. The impedance of all elements is nearly constant, nearly real, and nearly equal above about 1.0 GHz.

Collectively, the data for this case indicate that all five elements are severely affected by mutual coupling and truncation effects for frequencies in the lower part of the intended operating band, which is approximately 0.3-1.4 GHz. As might be expected, the impedances of end elements (#1 and #5) resemble the isolated element more than do the interior elements.

The data for 45-degree scan illustrate several interesting features as well:

1. Element #1 has a resonance near 0.6 GHz that is closer in magnitude to that of the single element in Fig. 7 than for broadside radiation.
2. Elements 2, 3, and 4 lack any appreciable resonance.
3. The input resistances in the frequency range 0.3-0.5 GHz are larger than for the single element. The resistance of element #1 is lower than elements 2, 3 and 4 throughout this frequency range. The resistance of element #5 is very small below 0.4 GHz.
4. The impedance of all elements is approximately equal, relatively constant and nearly real above about 1.0 GHz.

These data demonstrate many similarities to the broadside case, but they also suggest that the energy sweeping across the array from right to left of Fig. 8 (to create the beam steering) causes element #1 to be less affected by mutual coupling than other elements. Linear arrays of parallel dipoles scanned in the H-plane exhibit similar behavior of the end element. The increase of radiation resistance at low frequencies is consistent with the behavior of these antennas in very large (infinite) arrays. The element width (11.25 cm) is only about 1/10 wavelength at 0.3 GHz, yet in a large array, the antenna has input resistance of the order of 100 ohms.

Additional displays of the 5x1 array data are VSWR plots in Figure 11 and current magnitude plots in Figure 12. For broadside beam position, the high VSWR of element #3 near 0.7 GHz and elements #2 and #4 near 0.8 GHz are due to the resonance peaks of the impedance. For 45-degree scan, the high VSWR of element #1 near 0.6 GHz is due to the resonance peak of the impedance.

The current distribution shows peaks at the feed points, as expected. The current distribution on each element is skewed for scanning at 45 degrees and the narrow conducting strip behind the slotline cavity has a large current for the scanned case, whereas this current is relatively low for the broadside case.

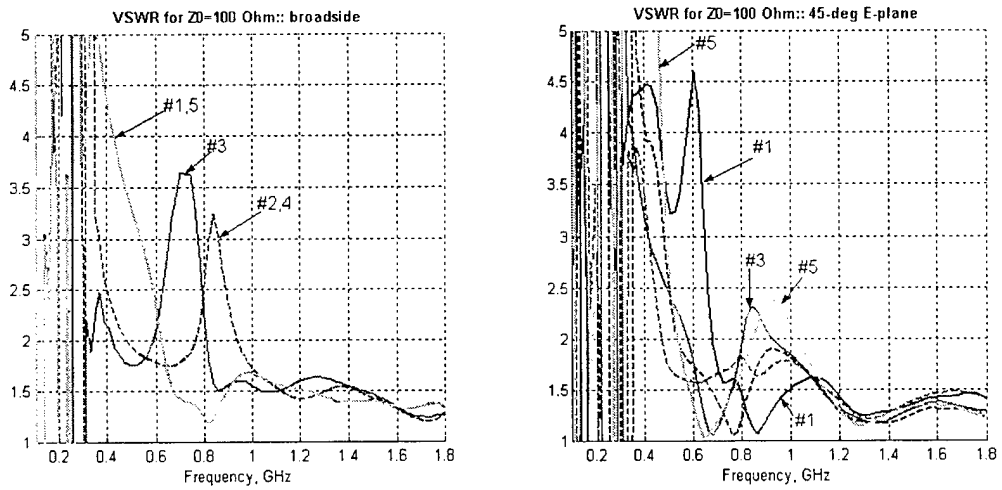

(a) (b)

Figure 11. VSWR for all elements in the 5x1 array versus frequency for: (a) broadside radiation, (b) 45-degree E-plane scanning.

A 10x1 linear array is depicted in Figure 13. The elements are identical to those of the 5x1 array. The input impedances for broadside and 45-degree E-plane scan are shown in Figure 14.

The data for broadside show:

1. The resonances for the end elements (#1 and #10) are smaller in magnitude than the single element and have split into two peaks located above and below 0.6 GHz.
2. The resonances of #2, #3, #5, #6, #8 and #9 are shifted much higher in frequency than that of the single element. The resonance of elements #4 and #7 has split into two peaks above and below 0.8 GHz.
3. The resistances and reactances of interior elements are relatively large in the range 0.3-0.5 GHz and display large variations below 0.3 GHz.
4. Above 1.0 GHz, the element impedances are nearly constant, real and equal.

These characteristics are similar to those observed for the 5x1 array. The differences between the central elements (#5 and #6) and their neighbors (#4 and #7) suggest that truncation effects are still very important 3 or 4 elements away from the edge of the array.

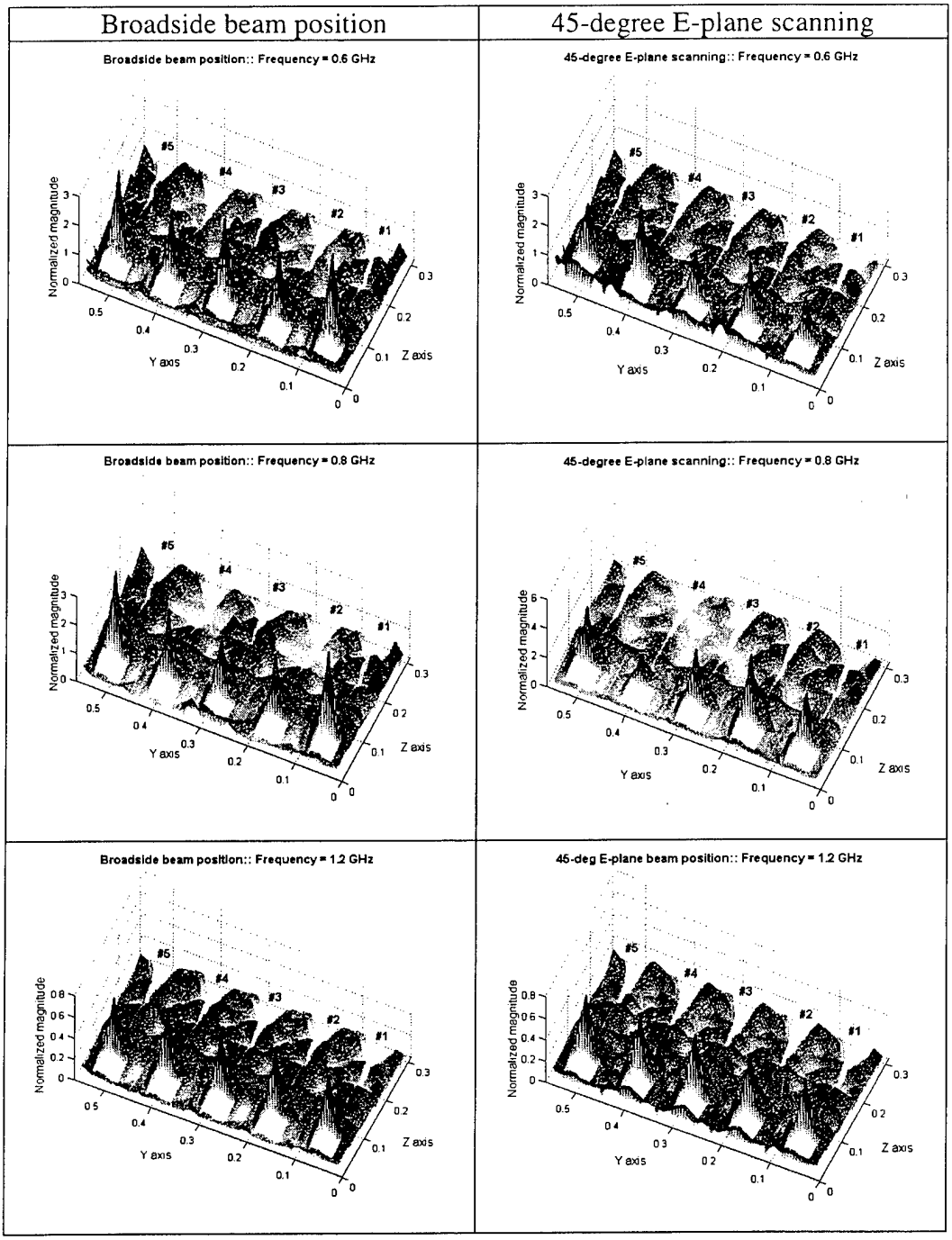

Figure 12. Surface current distribution in the 5x1 array shown in Figure 8.

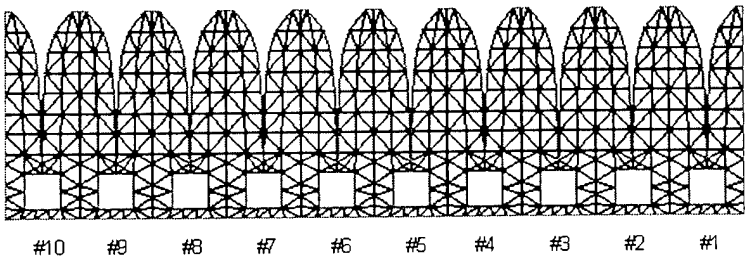

Figure 13. 10x1 linear array of TSA simulated for broadside and scanning in E-plane.

The data for 45-degree scan show similar characteristics to those observed for the 5x1 array and the 10x1 array with broadside beam. For example, element #1 looks somewhat like the single element, but with an additional weak resonance near 0.7 GHz. Above 1.0 GHz, the impedances are nearly equal, constant and real, but with more variations than for broadside. Compared to the single element, below 0.5 GHz the interior elements (#2 - #9) have much larger resistance and the reactance curves are different in shape.

Figure 15 shows the impedance versus element location in the array for several frequencies. At the higher frequencies (1.0 GHz and above), the impedance of all array elements is nearly equal, constant and real, as noted above. In the vicinity of 0.8 GHz, where several of the elements display resonances, the impedance is a strong function of location in the array. Figure 16 shows the same kind of data for 45-degree scan. The symmetry about the array center is lost when the array scans. The plots for 0.8 GHz in both Figures 15 and 16 show oscillations of the impedance as a function of location in the array. However, the 10-element array is too small to observe a significant decrease in the oscillation amplitude toward the center of the array, which should occur when the array becomes large. Also, the oscillations are not so evident at lower frequencies. Initial results of recent studies suggest that larger TSA arrays create oscillations near their edges that decay toward the center, but more study is needed to explore the nature and significance of the oscillations in wideband TSA arrays.

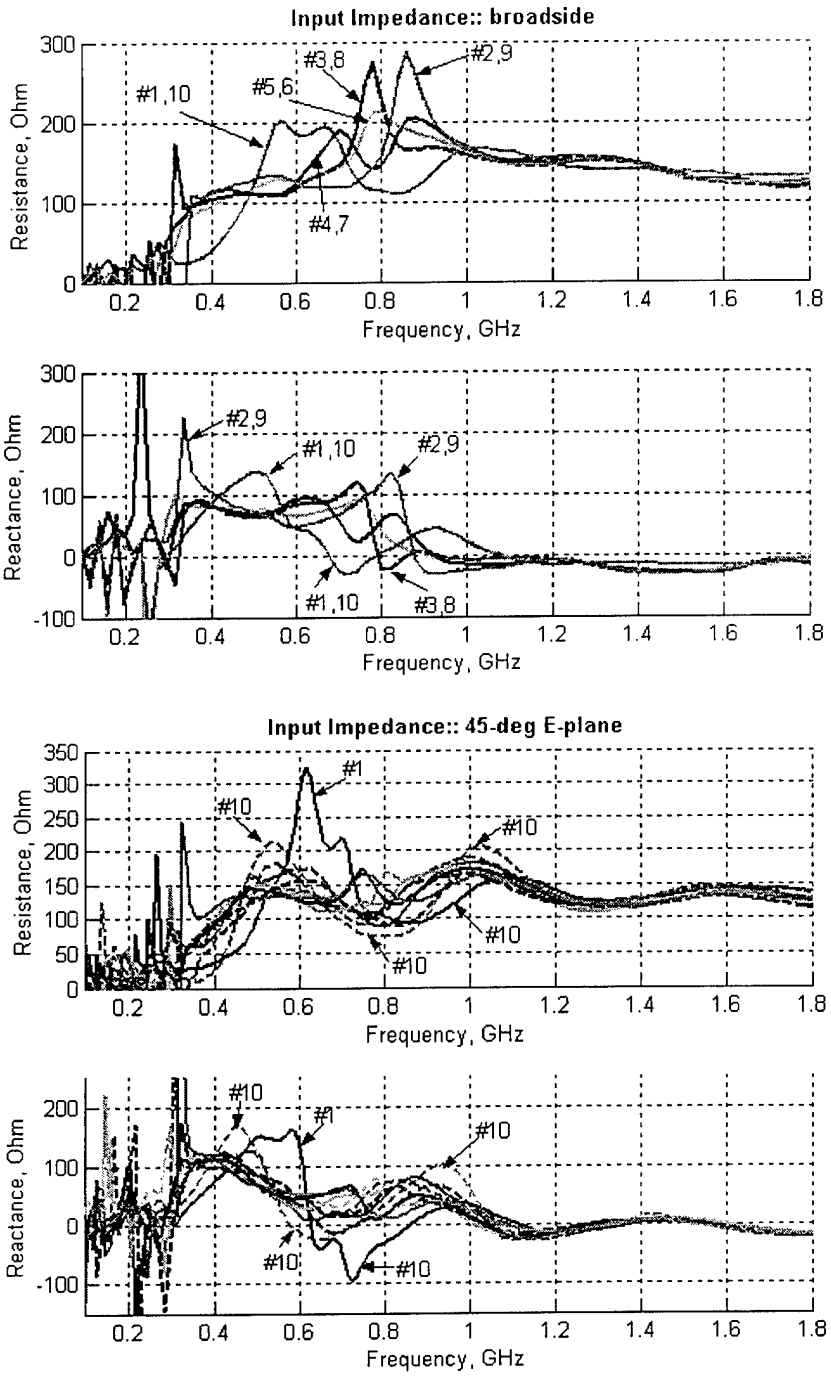

Figure 14. Input impedances of all elements in 10x1 array for broadside radiation and 45-degree E-plane scanning.

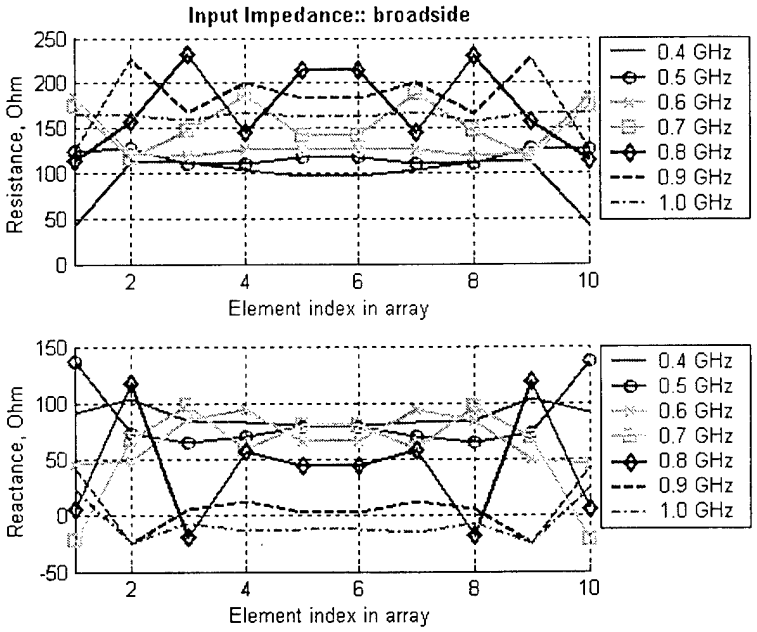

Figure 15. Input impedance versus element location at several frequencies for broadside radiation.

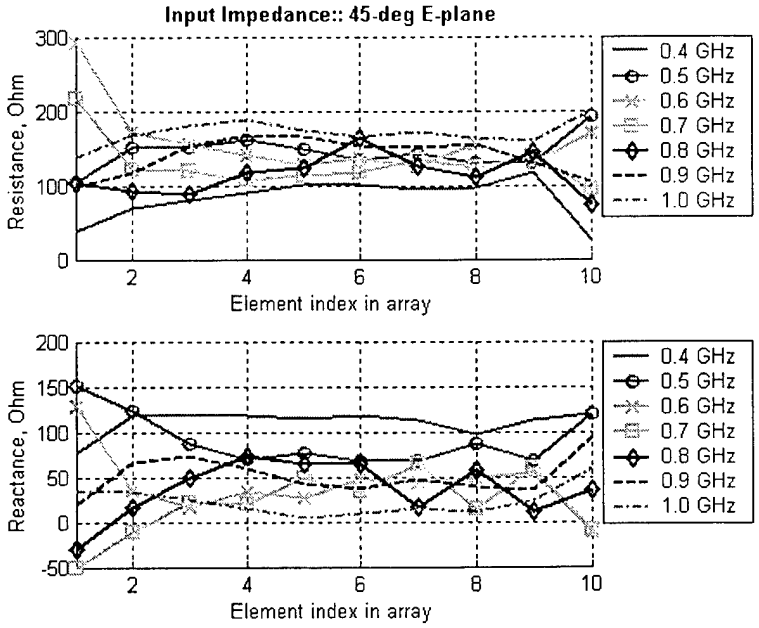

Figure 16. Input impedance versus element location at several frequencies for 45-degree E-plane scanning.

4. Simulation of planar arrays

This section contains some results on TSA arrays with planar aperture. Figure 17 depicts 3x3 and 5x5 arrays of elements like the one in Figure 1. The TDIE code has so far successfully analyzed arrays up to 8x8 in size on a modest desktop PC. However, the stacks of conducting fins, Figure 17, that comprise the planar array create a parallel plate-waveguide-like structure that has high-Q (long time) oscillations requiring careful selection of MoM-MoT parameters and stabilization filtering [12] to obtain stable results.

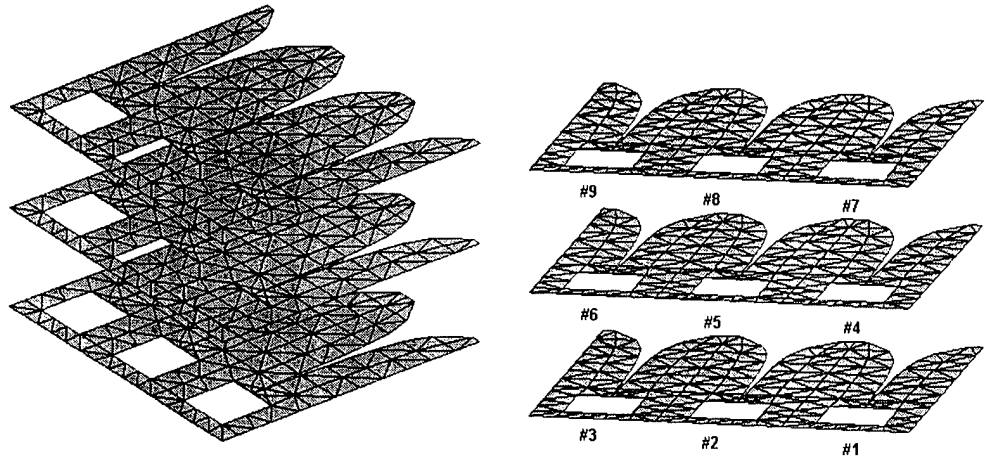

(a)

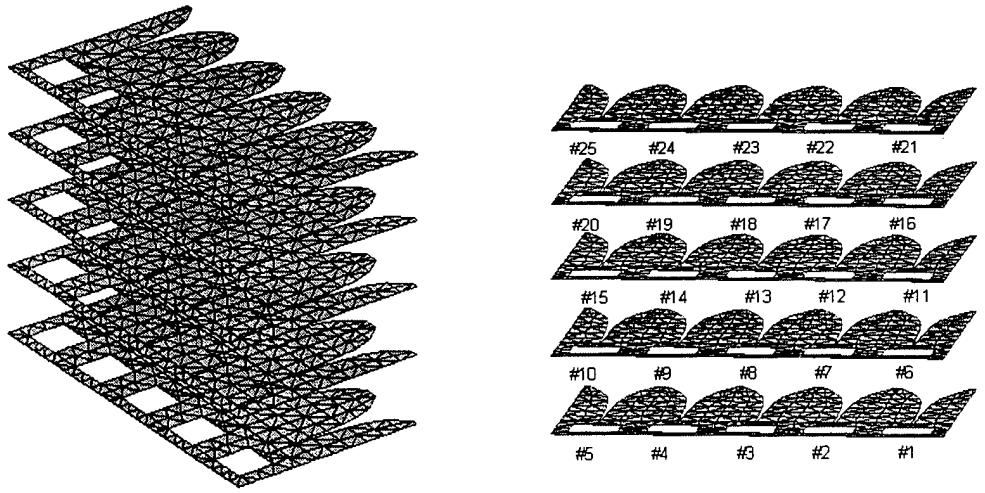

(b)

Figure 17. The 3x3 (a) and 5x5 (b) arrays of the Vivaldi dielectric-free elements.

The input impedances of all 3x3 array elements for broadside as well as 45-degree E-plane, H-plane and D-plane beam positions are plotted in Figure 18. Symmetry about the central planes of the array is evident for broadside and scanning in the E- and H- planes. The symmetry is lost when the array scans in intercardinal planes.

In contrast to single elements and linear E-plane arrays, at the higher frequencies above 0.9 GHz, the impedance of the array elements varies enough for broadside and H-plane scanning to render the VSWR of some elements greater than 2, Figure 19. Unlike the linear array where coupling is not sufficient to erase the desirable high-frequency behavior of the single element, coupling in the planar array causes the high-frequency behavior of several elements to be more like that of infinite arrays, which typically exhibit strong variations near the frequency corresponding to 0.5-wavelength element spacing.

For the linear E-plane arrays radiating a broadside beam, the central elements displayed resonances in the vicinity of 0.8 GHz. The planar array radiating broadside displays a similar characteristic for elements #2, #5 and #8. This resonance was not present in the single element, so it is apparently due to coupling from neighboring elements on the same metallic sheet. However, for scanning in the H-plane with the beam pointing toward element #8, element #2 lacks this resonance and it is weaker in #5 than in #8.

Element #1 of the linear arrays scanned in the E-plane showed a resonance near 0.6 GHz that resembles that of the single element. For the 3x3 array, elements #1 and #7 show a similar effect, and #4 shows resonance with lower peaks there. However, for scanning in the H-plane, elements #1, #2 and #3 do not show a resonance near 0.6 GHz. Although the end elements of linear arrays and planar arrays scanning in the E-plane resemble single elements, H-plane scanning creates a different effect. For D-plane scanning, element #1 has a resonance with very large resistance near 0.6 GHz. Note that although elements #6 and #8 are similar for D-plane scan, they are not truly symmetrical and, thus, are not identical.

The active VSWR of the elements in the 3x3 array is shown in Figure 19 for broadside 45-degree E-plane, 45-degree H-plane and 45-degree D-plane beam positions. Over the range of frequencies and scan angles, many elements have high VSWR. Overall, elements of this small array are not very well matched even though large arrays of this element are reasonably well matched.

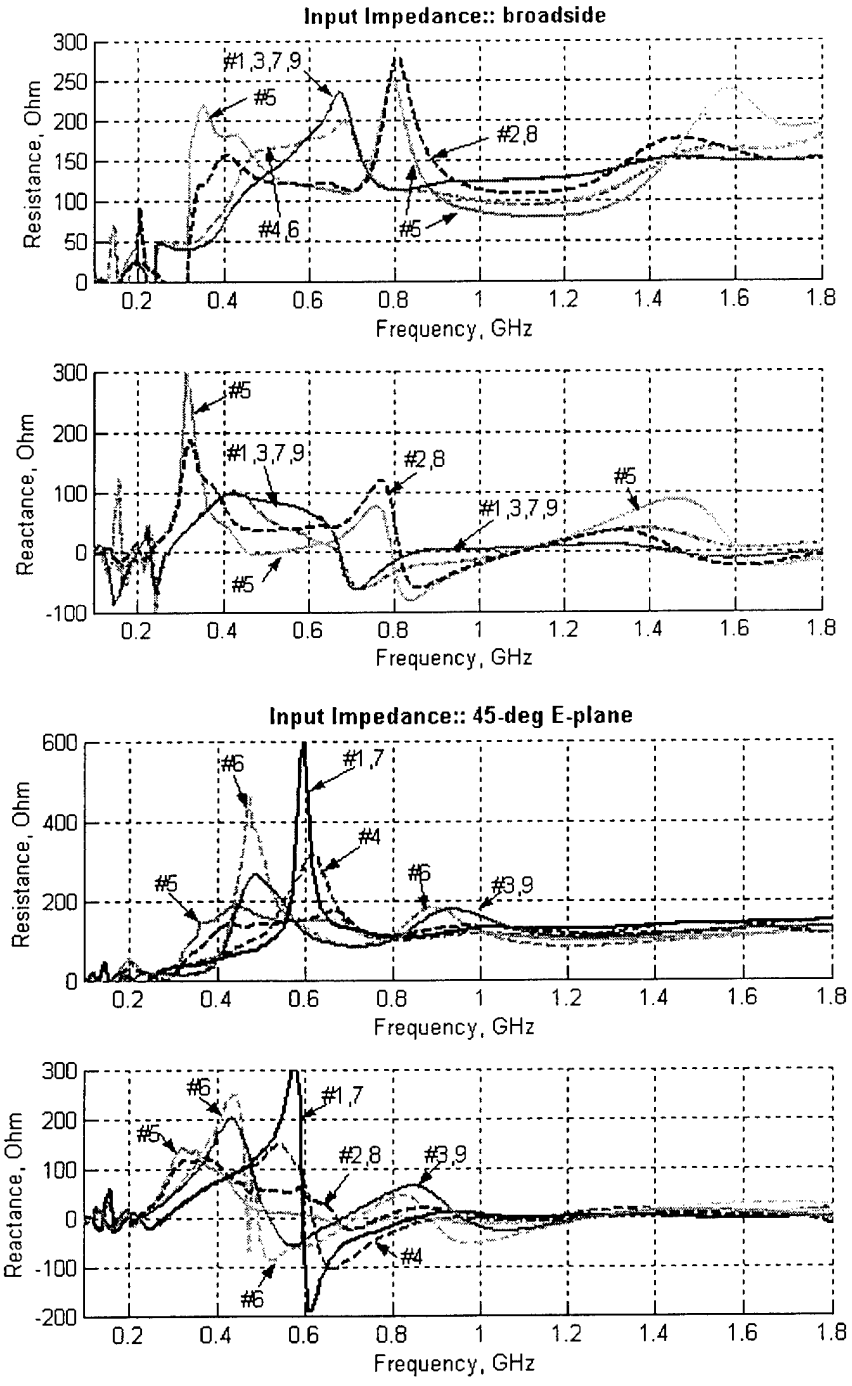

Figure 18. Input impedances of all elements in 3x3 array for broadside radiation and 45-degree E-plane scanning (continued on next page).

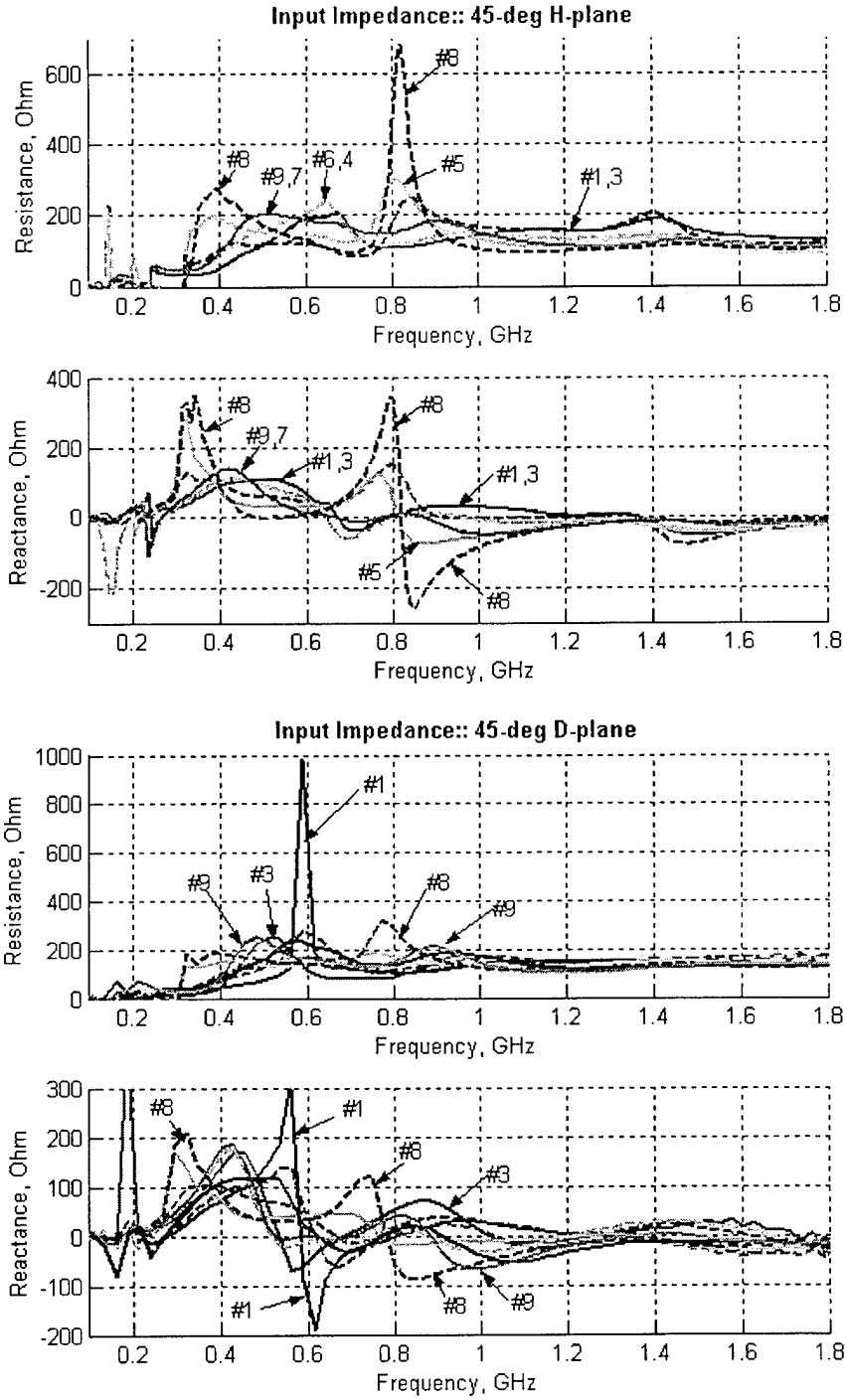

Figure 18. Input impedances of all elements in 3x3 array for 45-degree H-plane and D-plane scanning (continued from previous page).

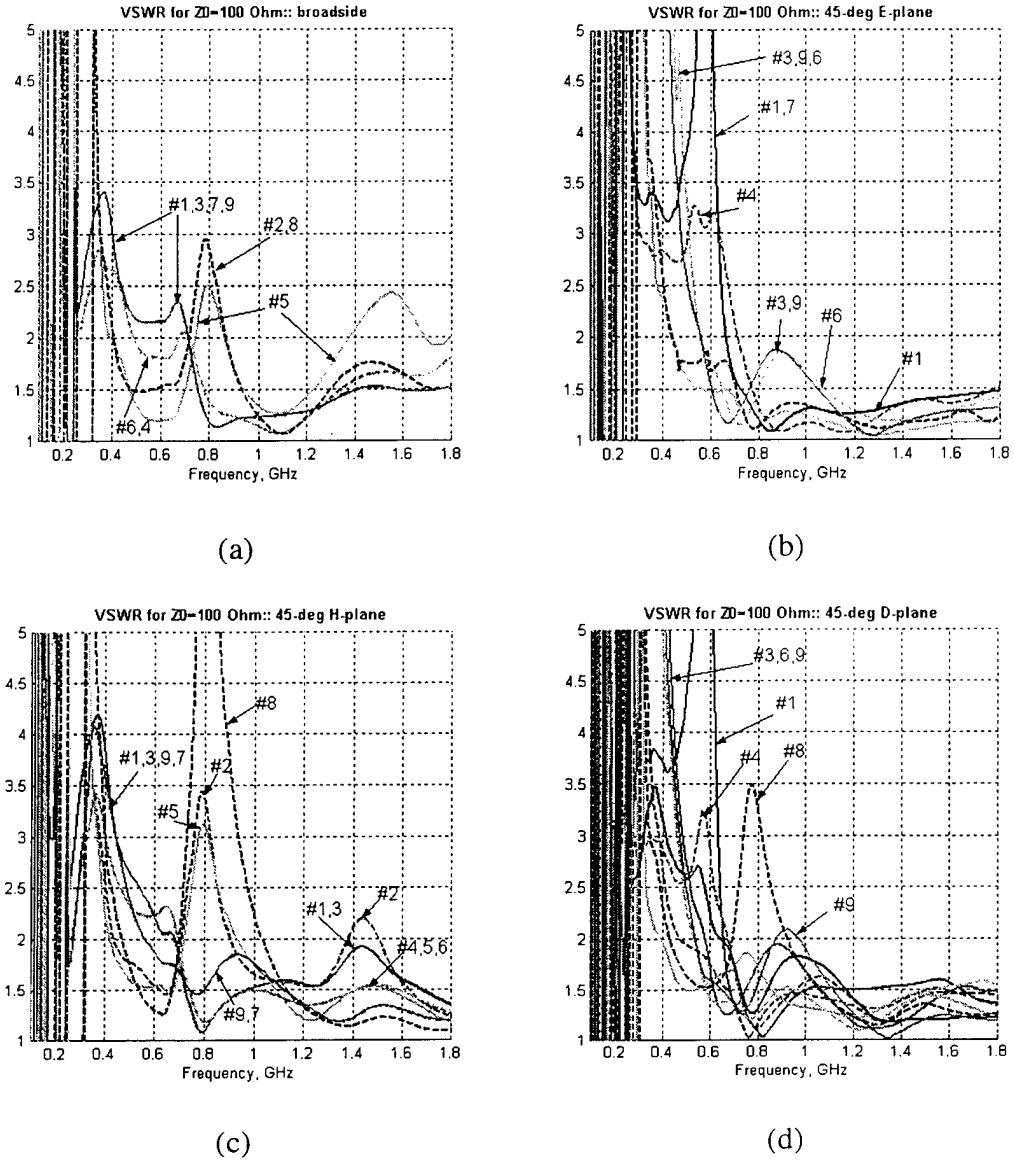

Figure 19. VSWR for the 3x3 array: (a) broadside, (b) 45-degree E-plane scanning, (c) 45-degree H-plane scanning, (d) 45-degree D-plane scanning.

The active impedance and VSWR plots for the 5x5 array are shown in Figure 20 and 21, respectively. The element impedance for an infinite array is plotted with a bold line in Fig. 20. For these computations, the numerical model has about 2000 triangles in the mesh, resulting in 2000 unknowns for the surface charge and about 3000 RWG modes for the surface current. The TDIE solution requires about 1.5 hours of CPU time and 150 MB RAM on a 933-MHz Pentium-III processor. The elements do not perform well in the 5x5 array.

Some observations from the data are:

1. The impedances for broadside, E- and H-plane vary in the higher frequency range, 1.3-1.7 GHz, more than the 3x3 array.
2. Several elements exhibit large impedance variations below about 0.4 GHz. For broadside, these resonances are clustered near 0.3 GHz, but they are spread more for E- and H-plane scan.
3. The single element resonance near 0.6 GHz is visible in several elements. The particular elements that display this resonance change with scan plane.
4. As for the 3x3 array, corner elements often differ from other elements along the side of the array for E- and H-plane scanning. For example, #1 and #21 are the same for E-plane scan and they are similar to but slightly different from #6 and #16.
5. As for the linear arrays and 3x3 array, the element resistance at low frequencies is increased in the array environment, enhancing the potential for wide bandwidth operation. However, the 5x5 array is too small to produce good low-frequency behavior of all elements. More elements are apparently needed to suppress the low-frequency resonances appearing near 0.3 GHz in Fig. 20, *cf.*, infinite array impedance.

The results obtained so far with the TDIE simulation agree with the findings of [1], which showed that a dual-polarized, stripline-fed array comprised of 9x8 elements in each polarization is too small to avoid truncation effects even at the array's center. Holter and Steyskal [4] concluded that the array should be much larger, perhaps 40x40. So far, the studies using TDIE simulation suggest evolutionary trends of array performance as the number elements increases. However, we cannot yet specify a minimum size to achieve certain performance nor can we say how edge elements will behave in very large arrays. Among the questions to be answered by future work is the value of "dummy" elements around the active array.

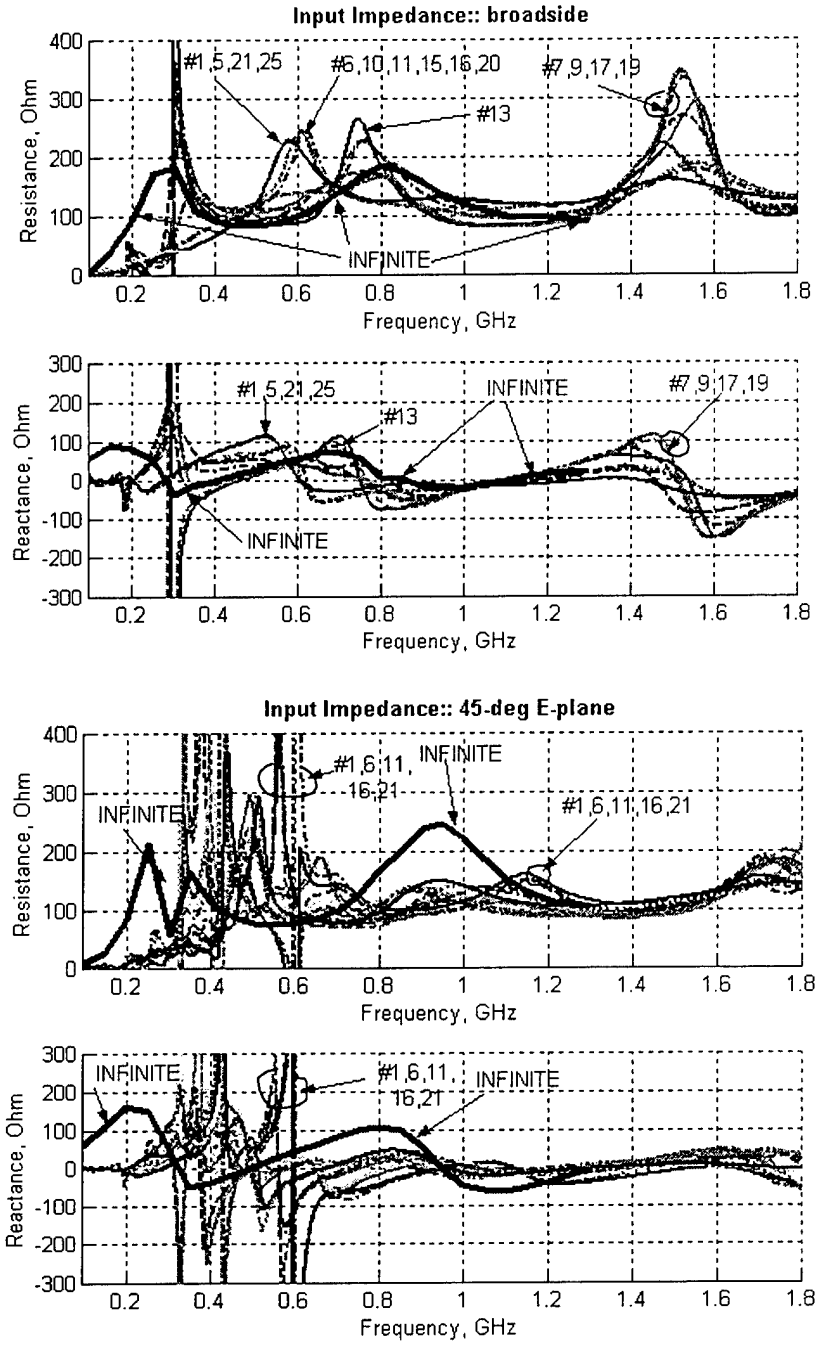

Figure 20. Input impedances of all elements in 5x5 array and infinite array for broadside radiation and 45-degree E-plane scanning (continued on next page).

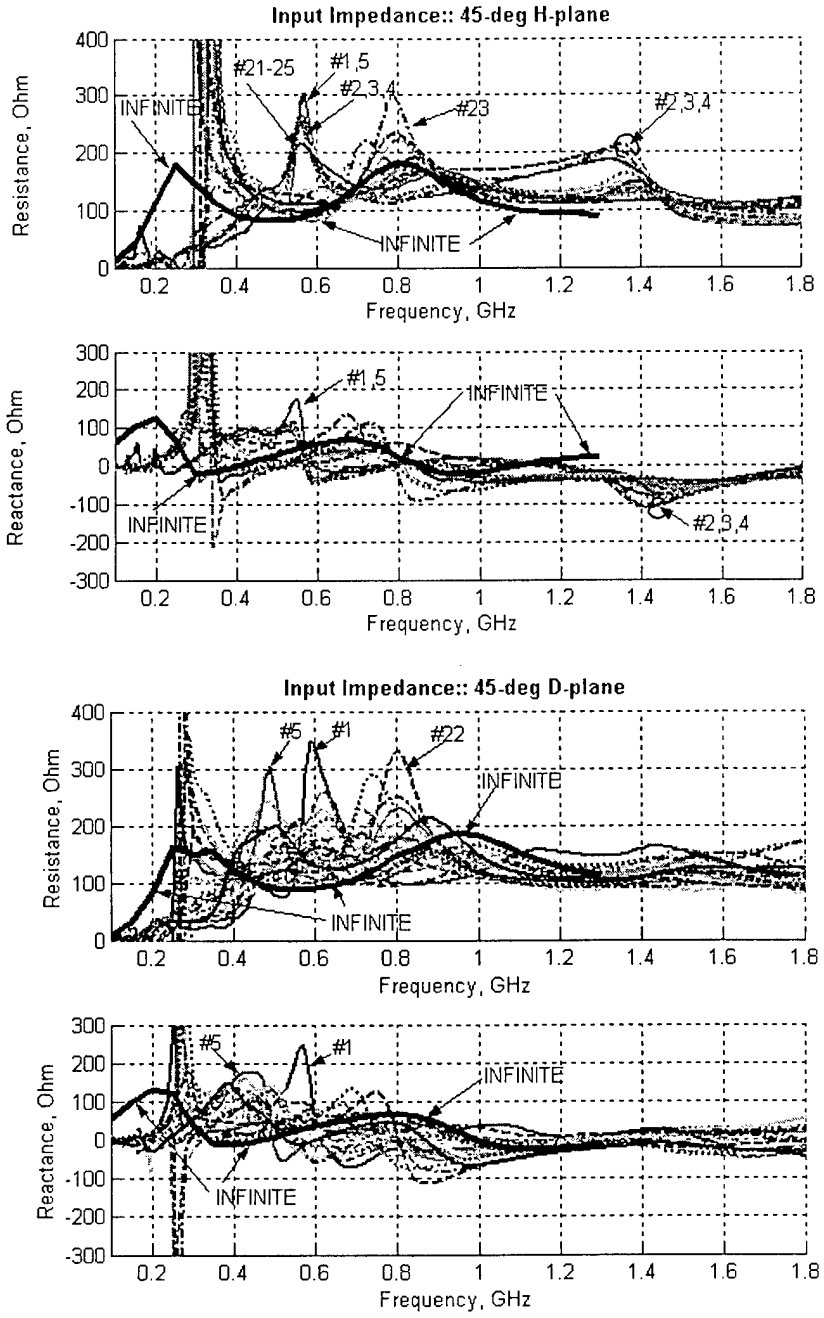

Figure 20. Input impedances of all elements in 5x5 array and infinite array for 45-degree H-plane and 45-degree D-plane scanning (continued from previous page).

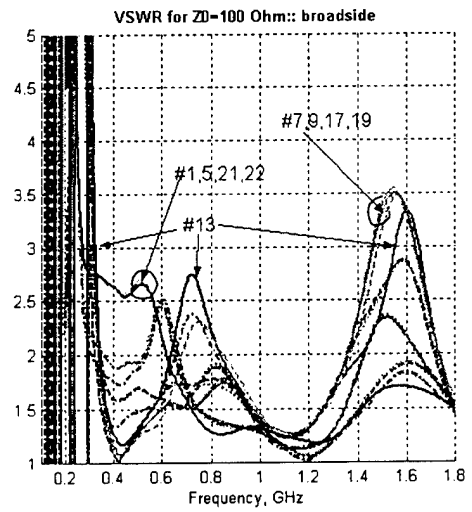

(a)

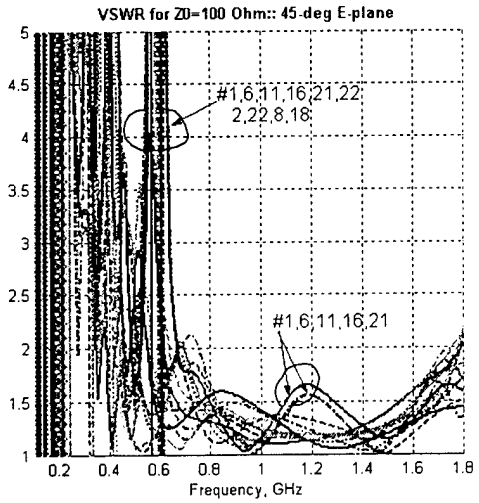

(b)

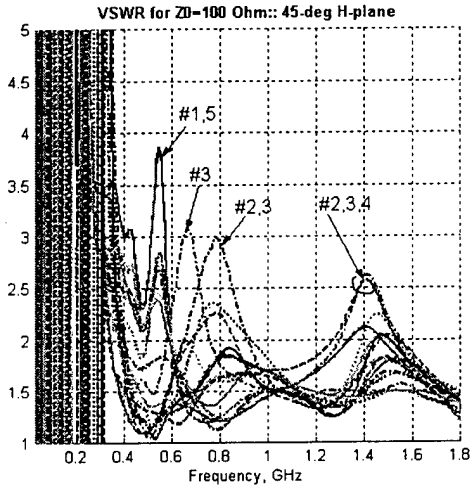

(c)

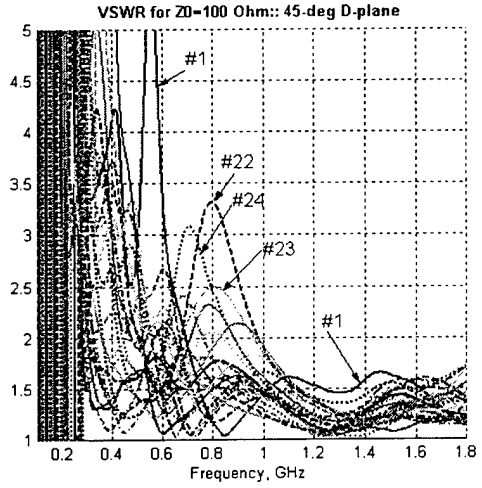

(d)

Figure 21. VSWR for the 5x5 array: (a) broadside, (b) 45-degree E-plane scanning, (c) 45-degree H-plane scanning, (d) 45-degree D-plane scanning.

6. Summary

A new time-domain integral equation simulation tool has been developed to analyze small arrays of dielectric-free TSA antennas. The TDIE simulation displays excellent late-time stability and has begun to yield insight into the performance of small arrays of TSA's. Computed impedances for linear and planar aperture arrays display some of the expected behavior, but the wideband capability of TSA arrays results in some performance features that are not yet adequately understood.

For the element configuration explored in this study, a single element exhibits a resonance near 0.6 GHz. This resonance is observed for some elements in linear and planar arrays, but often the peak values of resistance and reactance differ from the single element values. Also, many elements display a resonance at a different frequency, *i.e.*, about 0.8 GHz. Planar arrays seem to behave somewhat differently than linear arrays at the higher frequencies. Linear arrays preserve the desirable high-frequency performance of the single element, but the additional coupling from neighboring elements in the planar array creates more impedance variations with frequency and from element to element in these arrays.

The data obtained so far with the TDIE simulation support the conclusion of [1] and [4] that planar arrays of TSA must be quite large to avoid severe effects from truncation. That is, array edges affect elements that are several unit cells away from the edge. Further development of the TDIE simulation will allow extensive study of finite arrays of dielectric-free TSA's. These studies should reveal more of the phenomenology existing in these arrays and, hopefully, permit the design of high-performance arrays of moderate size. This capability together with the lower cost of dielectric-free antennas should expand the range of applications for these antennas.

7. References

[1] T-H Chio, D. H. Schaubert and H. Holter, "Experimental Radiation and Mutual Coupling Characteristics of Dual-Polarized Tapered Slot Antenna (TSA) Arrays," *Proc. 1999 Ant. Applications Symposium*, pp. 280-309, Monticello, IL.

[2] H. Holter, T-H Chio and D. H. Schaubert, "Elimination of Impedance Anomalies in Single- and Dual-Polarized Endfire Tapered Slot Phased Arrays," *IEEE Trans. Ant. Propagat.*, Vol. AP-48, pp. 122-124, January 2000.

[3] A. O. Boryssenko, D. H. Schaubert, "Single-Polarized, Dielectric-Free, Vivaldi Tapered Slot Phased Array: Performance Prediction", *Proc. IEEE Ant. Propagat. Symp.*, Boston, pp. 436-439, 2001.

[4] H. Holter and H. Steyskal, "Some Experiences form FDTD Analysis of Broadband Phased Arrays," *Proc. 2000 IEEE Int'l Conf. On Phased Array Systems and Technology*, pp. 387-390, Dana Point, CA.

[5] A. Ishimaru, R. J. Coe, G. E. Miller and W. P. Geren, "Finite Periodic Structure Approach to Large Scanning Array Problems," *IEEE Trans. Ant. Propagat.*, Vol. AP-33, pp. 1213-1220, November 1985.

[6] W. K. Kahn and W. Kurss, "Minimum Scattering Antennas," *IEEE Trans. Ant. Propagat.*, Vol. AP-13, pp. 671-675, September 1965.

[7] R. C. Hansen, "A Gibbsian Model for Finite Scanned Arrays", *IEEE Trans. Ant. Propagat.*, Vol. AP-44, pp. 243-248, February 1996.

[8] A. J. Roscoe, R. A. Perott, "Large Finite Array Analysis Using Infinite Array Data", *IEEE Trans. Ant. Propagat.*, Vol. AP-42, pp. 983-992, July 1994.

[9] E. Thiele, A. Taflove, "FD-TD Analysis of Vivaldi Flared Horn Antennas and Arrays", *IEEE Trans. Ant. Propagat.*, Vol. AP-42, pp. 633-641, May 1994.

[10] H. Holter and H. Steyskal, "Infinite Phased-Array Analysis Using FDTD Periodic Boundary Conditions – Pulse Scanning in Oblique Directions," *IEEE Trans. Ant. Propagat.*, Vol. AP-47, pp. 1508-1514, October 1999.

[11] S. M. Rao, D. R. Witon, "Transient Scattering Surfaces of Arbitrary Shape", *IEEE Trans. Ant. Propagat.*, Vol. AP-39, pp. 56-61, May 1994.

[12] B. P. Rynne, P. D. Smith, "Stability of Time Marching Algorithms of the Electric Field Integral Equation", *Journ. Electromagn. Waves Applicat.* ,Vol. 4, No. 12, pp. 1181-205, 1990.

[13] S. M. Rao, *Ed.*, *Time Domain Electromagnetics*, Academic Press, 1999.

[14] R. D. Richtmyer, K.W. Morton, *Difference Methods for Initial-Value Problems*, Kreiger Publishing Company, 1994.

[15] B. P. Rynne, "Time Domain Scattering from Arbitrary Surfaces Using the Electric Field Integral Equation", *Journ. Electromagn. Waves Applicat.*Vol. 5, No. 1, pp. 93-112, 1991.

[16] S. M. Rao, D. R. Wilton and A. W. Glisson, "Electromagnetic Scattering by Surfaces of Arbitrary Shape," *IEEE Trans. Ant. Propagat.*, Vol. AP-30, pp. 409-418, May 1982.

[17] A. Sadigh, E. Arvas, "Treating the Instabilities in Marching-on-in-Time Method from a Different Perspective", *IEEE Trans. Ant. Propagat.*, Vol. AP-41, pp. 1695-1702, December 1993.

[18] D. R. Wilton, S. M. Rao, A. W. Glisson, D. H. Schaubert, O. M. Al-Bundak, C. M. Butler, "Potential Integrals for Uniform and Linear Source Distributions on Polygonal and Polyhedral Domains", *IEEE Trans. Ant. Propagat.*, Vol. AP-32, pp. 276-281, March 1984.

[19] J. F. Callejon, A., R. Bretones, R. G. Martin, "On Application of Parametric Models to the Transient Analysis of Resonant and Multiband Antennas", *IEEE Trans. Ant. Propagat.*, Vol. AP-46, pp. 312-317, March 1998.

DECADE BANDWIDTH TAPERED NOTCH ANTENNA ARRAY ELEMENT

Nick Schuneman, James Irion and Richard Hodges
Antennas/Nonmetallics Product Center
Raytheon, McKinney, TX

Abstract: This paper describes the design of a decade (10:1) bandwidth flared notch array element, capable of ±60° E-plane and ±50° H-plane scan volume. Previous researchers have demonstrated flared notch arrays with approximately 5:1 bandwidth over a roughly ±50° scan volume [1-5]. A new design procedure is presented that allows one to optimize the combined performance of the balun and the flared notch taper transition. The new design technique, developed under the DARPA RECAP program, combines full-wave analysis methods with computationally efficient equivalent circuit models. The use of circuit models reduces the time needed to compute notch element performance, and therefore enables numerical optimization of the radiator. An innovative balun design, in combination with the notch optimization technique, enables one to achieve a conjugate impedance match between the balun and radiator that yields decade bandwidth performance. Experimental test data, measured in waveguide simulator, is in excellent agreement with theoretical predictions based on finite element method (FEM) models and confirms the decade bandwidth performance.

1. Introduction

Tapered notch antennas are useful as array elements due to their ease of fabrication using printed circuit board techniques and compact size that allows integration into a half-wavelength array lattice spacing. These antenna elements have been shown to exhibit large bandwidths despite their small aperture area [1,2]. This paper presents a new decade bandwidth tapered notch array (DTNA) with less than –10 dB return loss for a 10:1 bandwidth over a wide scan volume. Decade band operation has been verified in waveguide simulator tests, and the measured data agree well with computed results.

Prior to this work, printed circuit tapered notches have been designed for bandwidths of approximately 5:1 by adjusting taper and balun parameters [3,4]. Previous efforts at the Raytheon Antenna/Nonmetallics Product Center have yielded elements with bandwidths in the 3:1 range [5]. The strategy for this

approach was to use an analytical taper design, such as the Klopfenstein taper [6,7], to present a matched load impedance to the balun. When the taper impedance is well matched, the bandwidth of the antenna element is primarily limited by balun performance at the low end of the frequency band. However, it is possible to design an unconventional taper that does not present a matched load to the balun yet optimizes the element performance.

As part of the DARPA Reconfigurable Aperture (RECAP) program, the authors have developed a new design procedure that allows substantial increases in the bandwidth of tapered notch elements. An improved open-circuit balun design is used that, when feeding a matched load, provides nearly 10:1 bandwidth. Numerical optimization techniques are used to synthesize a tapered notch profile that provides a conjugate impedance match to the balun. This approach extends the low end of the frequency band, resulting in an antenna element for which the bandwidth is wider than that of its constituent parts.

2. DTNA Design Method

The basic tapered notch element and a dual-polarized array of tapered notch elements are shown in Figure 1. A tapered notch element is composed of two major components – the balun and the notch – as illustrated in Figure 1(a). The primary function of the balun is to provide a broadband transition from stripline to the tapered notch slotline. The notch is essentially a broadband impedance transformer from the stripline impedance (usually 50 Ω) to free space (377 Ω for a square lattice). In Figure 2, it is shown that the DTNA element includes an "endpiece" section composed of a dielectric transition and a radome. The dielectric transition provides further impedance transformation from the mouth of the notch to free space, and the radome protects the array from the environment.

Numerical optimization of tapered notch elements requires separate analysis of the components, as shown in Figure 3. A full-wave solution of the entire radiating element is costly in terms of solve time. However, it is possible to solve for the scattering matrices of the balun, tapered notch and endpiece individually, and to combine the models through a cascaded network solution. This significantly reduces the solve time for the system, and allows for independent design of the components. Also, additional element components can be included in an optimization routine simply by inserting the S-matrices associated with these components into the cascade.

A new design method, illustrated in Figure 4, has been developed to achieve optimal element performance utilizing tapered notch network separation. First,

the balun and endpiece are designed using a full-wave solver such as Ansoft HFSS. The balun is designed to have optimal stand-alone performance feeding a matched load at the slotline output port. Although the general concept is well understood, endpiece design is a trial-and-error process and several different endpieces may be utilized before an optimal design is determined. Once a satisfactory balun and endpiece are obtained, the notch profile is adjusted to provide minimal element return loss over the specified band.

In addition to the network model, it is useful to view the tapered notch element in terms of an equivalent circuit as shown in Figure 5. At the stripline-to-slotline junction, the balun and notch appear as a parallel impedance combination. At low frequencies, the DTNA balun is inductive while the tapered notch appears capacitive. This suggests the possibility that notch response can be tailored to provide low frequency tuning of the balun, similar to the behavior of an RLC circuit. It is this property that enables the design method described above to achieve 10:1 element bandwidth.

3. Balun Design

Design of a DTNA element begins with the stripline-to-slotline balun. To achieve decade bandwidth element performance, a balun with approximately 8:1 stand-alone bandwidth is required. Marchand baluns [8,9] can achieve 10:1 bandwidth, but will not fit within the available space of a half-wavelength lattice. Other broadband baluns, such as the Double-Y and stripline stub, have been successfully applied to tapered notch elements with bandwidths of approximately 5:1 [2-4]. We have investigated improvements to the simple open-circuit balun design shown in Figure 6(a) and developed several patentable features to facilitate the decade bandwidth element performance.

The balun behavior is best understood in terms of an equivalent circuit model (see Figure 6(b)). The cavity length L_{cavity} and the small length of slotline d are key parameters that determine the performance of the balun. The parameter d must be minimized to prevent impedance inversion of the cavity stub at high frequencies – essentially, it is desired to place the junction as close to the cavity as possible. At the low frequencies, L_{cavity} is electrically small and the balun impedance is inductive; at high frequencies, the balun impedance is capacitive and will appear as a short where $L_{cavity} = \lambda/2$. To maximize transmission into the notch, the balun cavity should approximate an open-circuit condition at the mid- and high-band frequencies (a cavity impedance of 120 Ω is necessary for –14 dB balun return loss). At the low frequencies, the balun impedance will generally not be large enough to provide an open circuit, but its inductive behavior can be tuned out by

the notch capacitance. Thus, the balun design strategy is to place the mid-band frequency – at which the cavity appears as a open-circuit quarter-wave stub – such that the high frequency balun return loss is slightly better than the low frequency performance.

In the mid-band, the transmission efficiency of the balun is determined by the impedance mismatch at the cavity. The impedance looking into the cavity is $Z_{in,cav} = jZ_{cavity}\tan(\beta L_{cavity})$ where $Z_{cavity} \propto w_{cavity}$. Ideally, the cavity should provide an open circuit; in practice the goal is to make $Z_{in,cav} / Z_{slotline}$ very large. Therefore, the cavity is made as wide as possible to increase its impedance at mid-band frequencies. The cavity width, however, is limited by the array spacing and the requirement to suppress cavity resonance at the high frequency end of the band.

4. Element Endpiece

The design of tapered notch elements can be treated as an impedance transformer problem. With that in mind, it is generally best to avoid abrupt impedance discontinuities in the notch. Printed circuit card notches have an inherent impedance discontinuity at the end of the notch due to the dielectric constant of the substrate. In order to reduce this discontinuity, dielectric material is removed to create an exponential taper that transforms the impedance from the end of the notch to free space. An illustration of a typical DTNA dielectric transition can be found in Figure 2.

It is also worthwhile to note that a protective radome may be included in the DTNA design. In fact, radome layer widths and dielectric materials may be optimized in conjunction with the element performance at broadside. However, the dielectric taper and radome are generally modeled as a single unit in HFSS.

5. Notch Optimization

Once the best stand-alone balun and endpiece performance is obtained, a tapered notch must be designed to yield the minimum element return loss over the desired bandwidth. True numerical optimization of a tapered notch requires calculation of the scattering matrix for hundreds of different taper designs. A full-wave solution of the tapered notch, such as the infinite array FEM model, is too slow for numerical optimization. Thus, a faster approximation of the tapered notch S-matrix must be found to serve as the computational engine.

The notch is fundamentally a tapered slotline, with a typical cross-section shown in Figure 7. For a given unit cell size, substrate thickness and conductor thickness, the slotline mode impedance is solely a function of the width w and frequency. At broadside, the tapered notch may be characterized as a cascade of discrete slotline segments of length δx, impedance Z, and propagation constant β as shown in Figure 8. The tapered notch S-matrix is very accurately approximated by cascading individual S-matrices of the discrete slotline segments, provided the segments are electrically small. Since the transmission line cascade is calculated for each frequency of interest, this technique inherently accounts for transmission line dispersion. This transmission line model provides a much faster solution method for the tapered notch and may be used for numerical optimization.

As described above, accurate notch solution using a transmission line model requires knowledge of the dependence of line Z and β on both slotline width and frequency. Thus, the impedance and propagation constant of the notch slotline were solved in Ansoft HFSS for a range of widths (w_i, $i = 1...N$) and frequencies (f_j, $j = 1...M$) and the values were tabulated for use in an optimization routine. The HFSS slotline models represent the specific mechanical environment of the notch – including details such as substrate materials, via placement and infinite array boundary conditions – and therefore yield highly accurate values for impedance and propagation constant at a given slotline width and frequency.

Optimization of the notch begins by calculating the discrete slotline segment S-matrices using the impedance and propagation constant values interpolated from the $Z(f,w)$ and $\beta(f,w)$ HFSS-generated slotline tables. The segment S-matrices are cascaded to form an approximation of the tapered notch S-matrix. Once calculated, the taper S-matrix can be cascaded with those of the balun and a fixed end-matching piece to yield the total element S-matrix. A Nelder-Mead simplex method [10,11] is employed to optimize the geometry of the taper by adjusting the widths of the discrete transmission line segments w_i and the length of the segments δx. The optimizer seeks a solution for the tapered notch width profile that provides the minimum element return loss over the specified bandwidth.

6. Calculated & Measured Results

The method described above has been used to design a tapered notch element with broadside return loss below –13 dB over a 10:1 bandwidth (1.8 – 18 GHz) in a 325 mil square lattice infinite array ($\lambda/2 \sim 328$ mil). It is worthwhile to note that both the balun and taper separately perform poorly at the low frequency end, but the entire element is well within return loss specifications due to the conjugate

matching at low frequencies. The calculated broadside return loss is shown in Figure 9. In this case, the balun has less than –10 dB return loss for a bandwidth of 10:1 (1.8 – 18 GHz) in the stand-alone state. The addition of the optimized taper reduces the low frequency element return loss and provides a broadside element bandwidth of 12:1 (1.5 – 18 GHz). The DTNA scan performance is plotted in Figure 10. The element is capable of 10:1 bandwidth for a ±60° scan volume in E-plane and a ~±40° scan volume in H-plane. Decade bandwidth performance at wide scan angles is difficult to achieve with boresight optimization alone. However, preliminary scan-optimization techniques have shown that DTNA designs are capable of 10:1 bandwidth at ±50° in the H-plane.

Figure 11 is an illustration of the optimized tapered notch element. The element is built on a 40 mil Rogers 3003 substrate ($\varepsilon \sim 3$) and has an overall length of ~2.45". The "wavy" shape of the notch profile can be seen very clearly in Figure 12, which is a plot of slotline width along the length of the taper. It is interesting to note that the length of a –10 dB Chebyshev taper is ~0.29 λ_L, while the optimized taper shown in Figure 12 has a length of ~0.27 λ_L and provides a return loss below –13 dB.

A prototype of an earlier element was fabricated and tested in a waveguide simulator to verify the infinite array calculations [12,13]. The comparison of waveguide simulator measurements to calculated results from HFSS is shown in Figure 13. The measured and calculated results match well, and most of the discrepancy can be attributed to fabrication error as well as inaccuracies introduced by the calibration technique. Also, it is important to note that waveguide simulator data is frequency-scanned in the H-plane (see Table 1). At the band edges, the H-plane scan angle is discontinuous which accounts for the abrupt "jumps" in return loss data.

7. Conclusion

A practical decade bandwidth tapered notch array element has been designed. The element maintains a return loss below –13 dB at boresight and below –10 dB over a wide scan volume from 1.8 – 18 GHz. Experimental results of similar elements in a waveguide simulator verify the accuracy of the numerical models.

Several improvements to previous designs were necessary to obtain decade bandwidth performance. Numerical optimization was employed to design tapered notches that provide conjugate tuning for an improved stripline-to-slotline balun. In addition, a dielectric-routed taper was used to decrease the impedance discontinuity at the radiating end of the notch. The end result was a tapered notch

element with an unusual profile, relatively short overall length and twice the bandwidth of non-optimized designs.

The design procedure described in this paper is applicable to a wide range of array environments and element types. Currently, this technique is proving useful in the design of TEM type elements such as tapered thick metal slotline and tapered parallel plate arrays. Several high-performance array programs at Raytheon are employing taper optimization to maximize element efficiency while meeting other specifications such as array depth, weight and cost. For some element types, performance over a range of scan angles has been added to the optimization routine.

8. Acknowledgement

This work was supported by DARPA, Arlington, VA., under Contract MDA972-99-C-0025, under program management of Dr. John Smith, Mr. Vince Sieracki and Dr. Larry Corey and Tom Dover of Raytheon. Approved for Public Release, Distribution Unlimited.

9. References

[1] D. A. Burrell and J. T. Aberle, "Characterization of Vivaldi antennas utilizing a microstrip-to-slotline transition," *Antennas and Propagation Society International Symposium*, vol. 3, pp. 1212 –1215, 1993.

[2] M. Kragalott, W. R. Pickles and M. S. Kluskens, "Design of a 5:1 bandwidth stripline notch array from FDTD analysis," *IEEE Trans. Ant. Propagat.*, vol. 48, pp. 1733-1741, Nov. 2000.

[3] J. Shin and D. H. Schaubert, "A parameter study of stripline-fed Vivaldi notch-antenna arrays," *IEEE Trans. Ant. Propagat.*, vol. 47, pp. 879-886, May 1999.

[4] T. H. Chio and D. H. Schaubert, "Parameter study and design of wide-band widescan dual-polarized tapered slot antenna arrays," *IEEE Trans. Ant. Propagat.*, vol. 48, pp.879-886, June 2000.

[5] C. Hemmi, R. T. Dover, F. German and A. Vespa, "Multifunction wide-band array design," *IEEE Trans. Ant. Propagat.*, vol. 47, pp.425-431, March 1999.

[6] R. W. Klopfenstein, "A transmission line taper of improved design," *Proc. IRE*, vol. 44, pp. 31-35, Jan. 1956.

[7] D. M. Pozar, *Microwave Engineering*. New York: Addison-Wesley, 1990.

[8] N. Marchand, "Transmission line conversion transformers," *Electronics*, vol. 17, pp. 142-145, Dec. 1944.

[9] V. Trifunovic and B. Jokanovic, "Review of printed Marchand and Double Y baluns: characteristics and application," *IEEE Trans. Microwave Theory Tech.*, vol. 42, pp. 1454-1462, Aug. 1994.

[10] J. A. Nelder and R. Mead, "A simplex method for function minimisation," *Computer Journal*, vol. 7, pp. 308-313, 1965.

[11] W. H. Press, S. A. Teukolsky, W. T. Vetterling and B. P. Flannery, *Numerical Recipes in Fortran*. New York: Cambridge University Press, 1992.

[12] P. W. Hannon and M. A. Balfour, "Simulation of a phased array antenna in waveguide," *IEEE Trans.*, vol. AP-13, May 1965, pp. 342-353.

[13] R. J. Mailloux, *Phased Array Antenna Handbook*. Boston: Artech House, 1994.

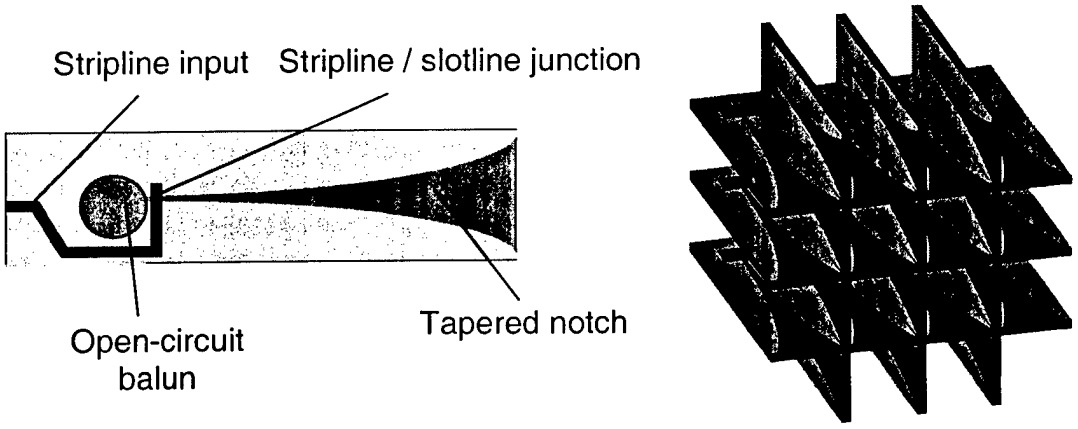

Figure 1. (a) Basic tapered notch element and (b) dual-polarized array of tapered notch elements

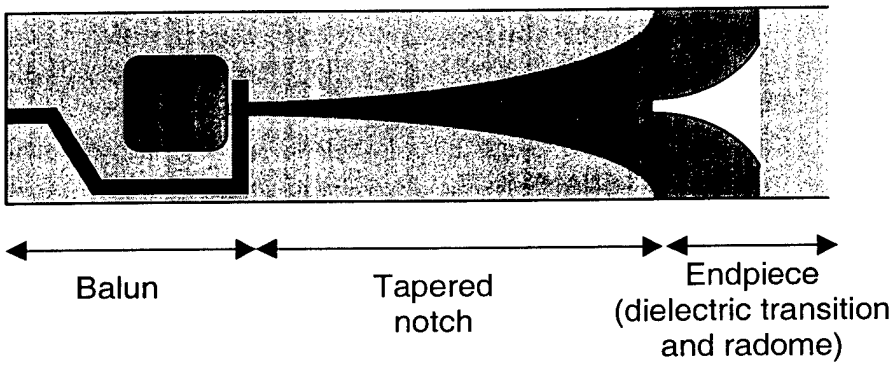

Figure 2. Typical DTNA element

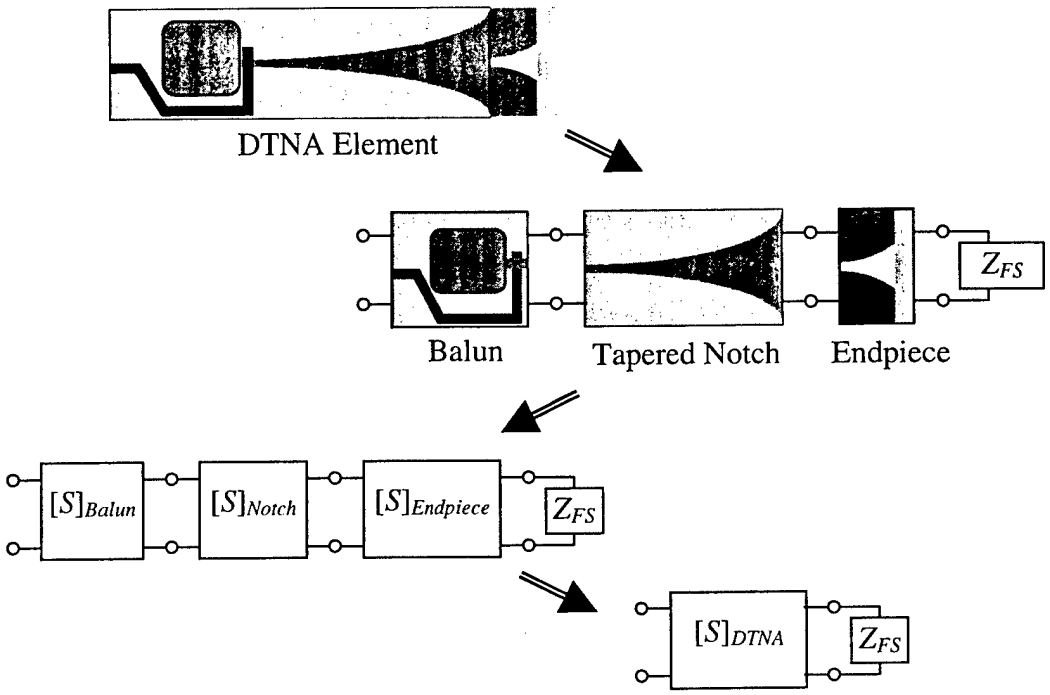

Figure 3. DTNA network separation

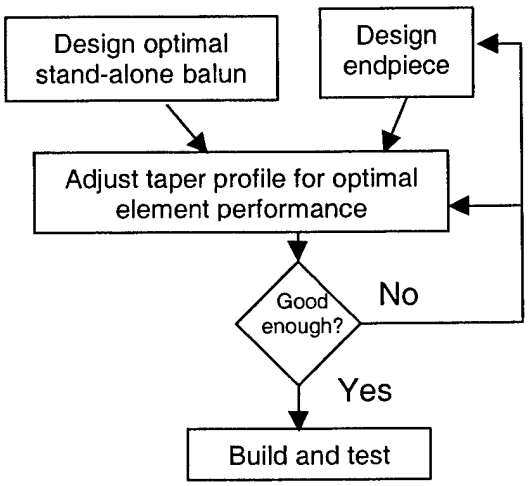

Figure 4. DTNA design method

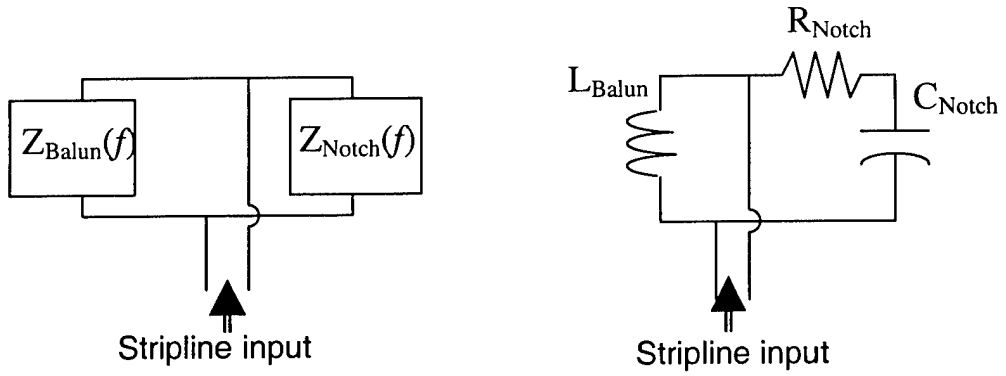

(a) (b)

Figure 5. (a) General and (b) Low-frequency DTNA equivalent circuits

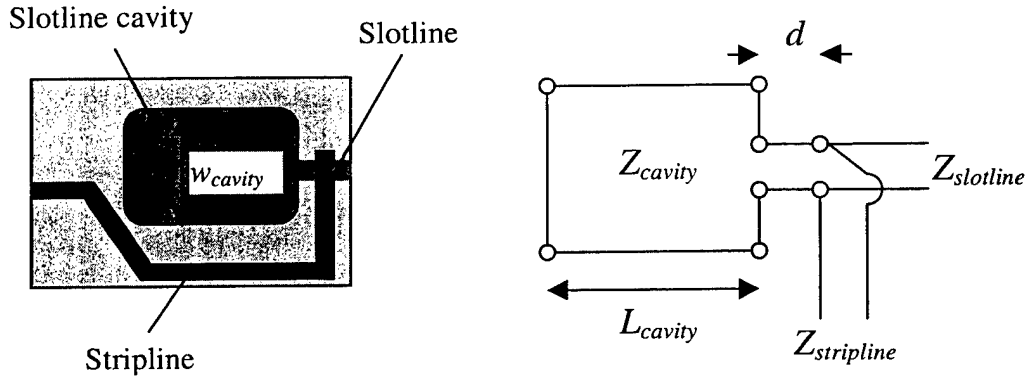

(a) (b)

Figure 6. (a) DTNA stripline-to-slotline open-circuit balun and (b) balun equivalent circuit

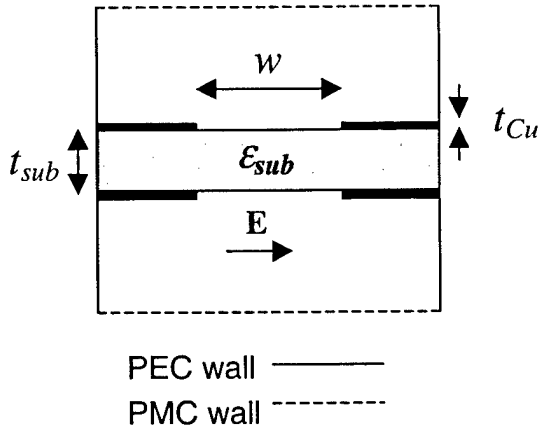

Figure 7. Cross-section of typical bilateral slotline in array lattice boresight unit cell

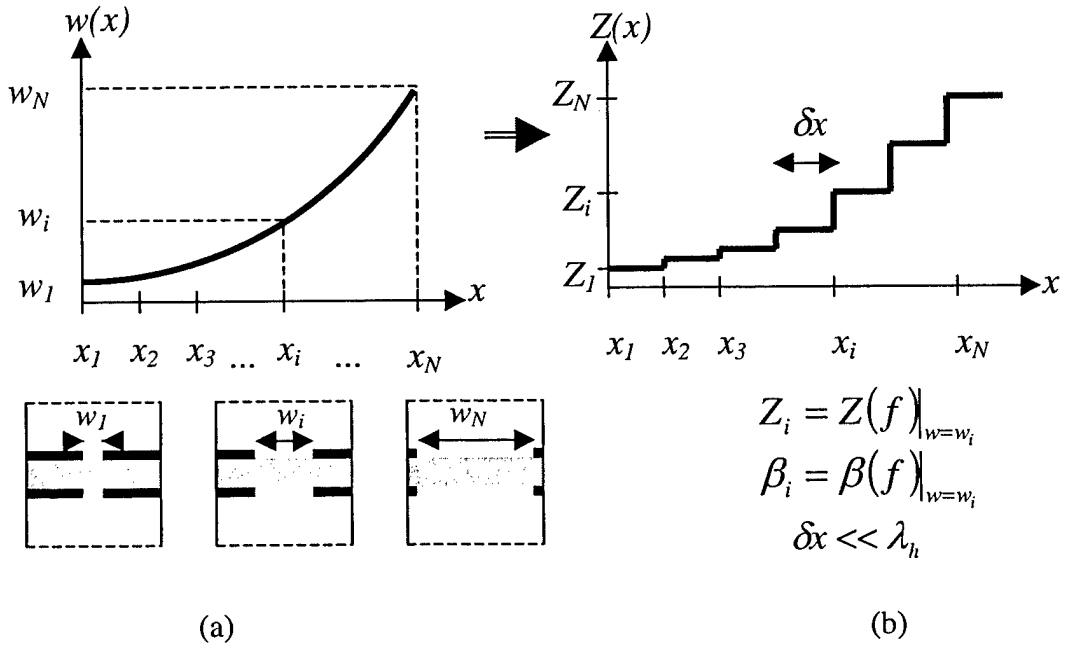

Figure 8. (a) Tapered slotline width profile and (b) cascaded discrete transmission line approximation

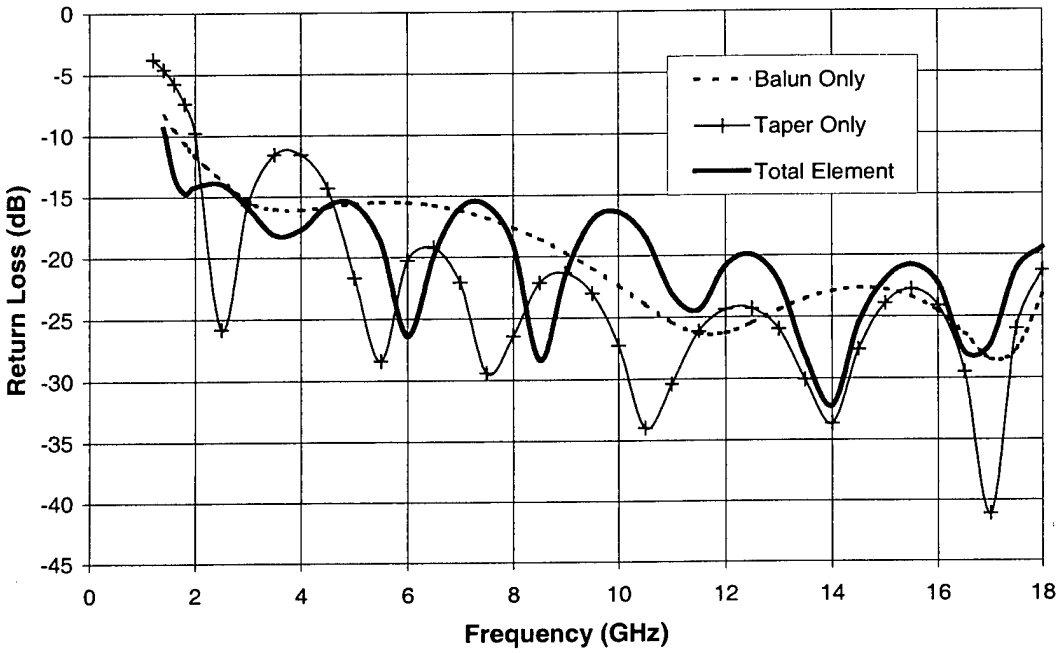

Figure 9. Broadside return loss of DTNA element in infinite array

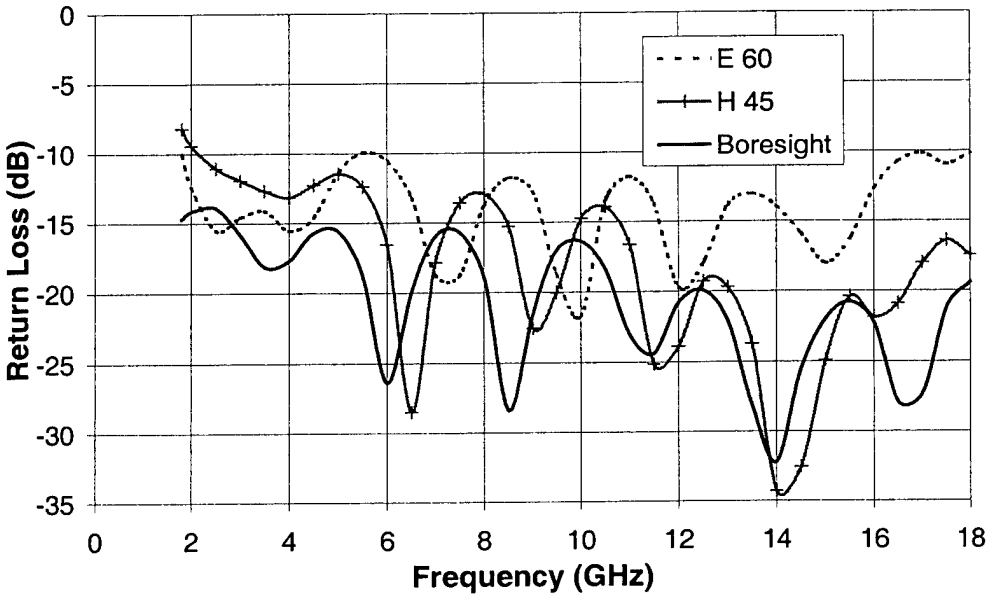

Figure 10. Infinite array TNA scan performance

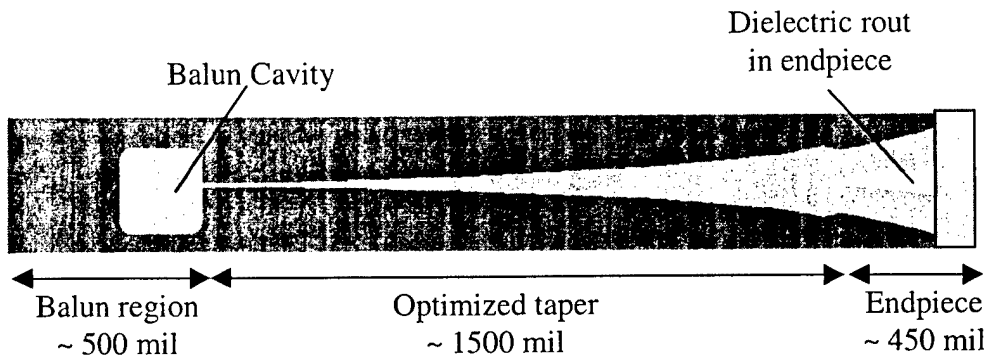

Figure 11. Optimized DTNA element

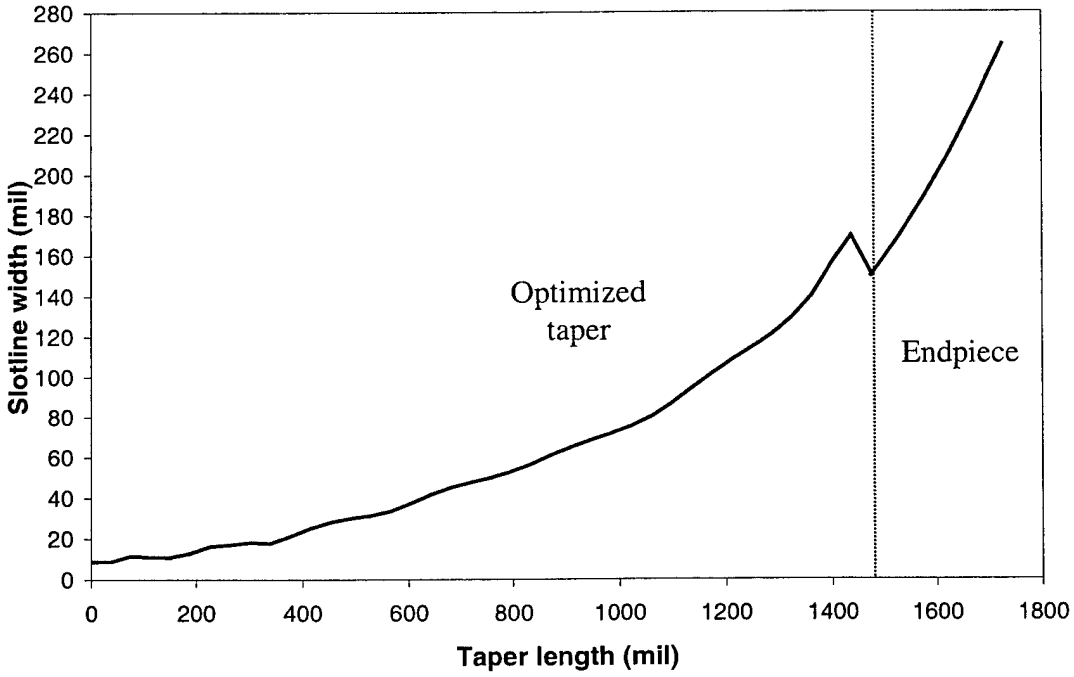

Figure 12. DTNA optimized taper width profile

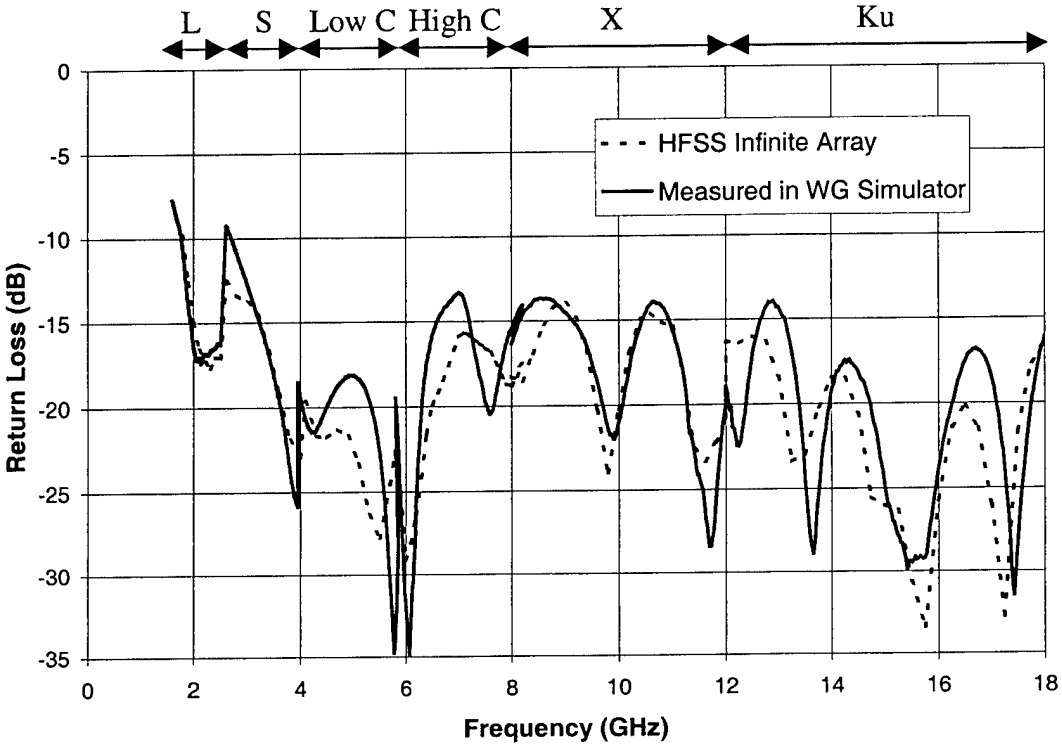

Figure 13. Comparison of HFSS infinite array and waveguide simulator results for early DTNA element

Band	f_{low} (GHz)	f_{high} (GHz)	$\theta(f_{low})$	$\theta(f_{high})$
L	1.8	2.5	46°	31.25°
S	2.6	4	51°	30.3°
Low C	4.1	5.8	47.6°	31.5°
High C	5.8	8.2	51.4°	33.6°
X	8	12	49.6°	30.3°
Ku	12	18	49.2°	30.3°

Table 1. Waveguide simulator frequency bands and range of scan angles

Radio Direction-finding for Wildlife Research

William W. Cochran*, George W. Swenson, Jr.* and Larry L. Pater#

*Dept. of Electrical and Computer Engineering, University of Illinois
1308 W. Main St., Urbana, IL 61801
#U. S. Army Construction Engineering Research Laboratory
2902 Newmark Dr. Champaign, IL 61821

Location of radio-tagged animals by triangulation is a widely applied research technique, the accuracy of which is often a major concern. Knowledge of the approximate accuracy and detection range of various types of automatic systems is a logical prerequisite to purchase or construction of the relatively expensive equipment required. The direction-finding performances of a fixed (non rotated) switched array of six 3-element Yagi antennas and of a rotated array of two 6-element Yagis, each in computer-controlled automated mode, were compared for the same distances and transmitter power in open surroundings free of reflecting objects. The rotated system yielded 50% greater precision and 9 times more coverage area than the fixed system. Human operators, using the rotated antenna connected for a null, determined bearings about 4 and 16 times more precisely than did the rotated and fixed automatic systems, respectively. Bias of the mean error of the fixed system was a function of direction to a transmitter, varying from nil to about 3° at typical signal levels and exceeding 10° for weak signals in some directions. Biases of the manually and automatically rotated systems were << 1° for all directions and signal levels.

Key words: Direction-finding accuracy, Radio direction-finding, Yagi antenna, Antenna array, Bio-telemetry, Automated Direction-finding

1. Introduction

In 1960 very small radio transmitters were attached to a cottontail rabbit and a mallard duck, which were then tracked by direction-finding in Allerton Park, Piatt County, and about the prairie of Champaign County, Illinois [1]. This was the genesis of radio telemetry for wildlife research and management, now a widely-practiced technique. Later, automatic direction finding was employed using now-obsolete continuously rotated antennas [2,3]. Now, automatic direction-finding equipment has been developed, involving fixed antenna arrays and microprocessor based control and recording systems. The system must be able to direction-find and record signal strength on a pulse as short as 15 ms repeating once per second. The design of this system will be described, with emphasis on the direction finding array and on the antenna arrangement on the target animal, typically a small bird. This system has been tested for proof-of-principle and for accuracy in operational contexts in forests and open country in Illinois, Georgia and Panama.

Location of radio-tagged animals by triangulation is a widely applied research technique, the accuracy of which is often a major concern. Knowledge of the expected range and accuracy of various types of automatic systems is a logical prerequisite to purchase or construction of the relatively expensive equipment required. The accuracy of locations depends on the accuracy of bearings obtained with direction finding (DF) antennas. Pointer calibration, mapping and map errors, the effects of and tactics for mitigating signal scattering, movement bias, and statistical methods for making and evaluating triangulated location estimates are well covered in the literature (see Samuel and Fuller, [4]). No references were found that dealt quantitatively with the bearing precision of different types of antennas at various signal-to-noise ratios.

In this study, we evaluate the effects of noise and detector non linearity on the angular precision of two automatic systems and one manual system. Comparisons among systems were made at a number of different signal levels (thus signal-to-noise ratios) representing various distances to radio-tagged animals. Vertical polarization and 302 MHz were used for all tests.

2. Methods

A "fixed" automatic system employed an array of six stationary 3-element Yagi-Uda antennas (Yagis) pointed at 60° intervals to cover 360°. A "rotated" automatic system employed two 6-element Yagis mounted at the ends of a 1.35-wavelength boom and pointed in the same direction. The antenna rotator consisted

of a computer-controlled stepper motor driving a backlash-free gear train driving a support mast in 0.09° steps.

A "manual" system used the antennas of the rotated system. The Yagis used in the arrays (Lawson, [5], Table 1.4) have the directional patterns shown in Figures 1a and 1c.

All measurements were made over flat grassland with no reflection-producing obstructions in any direction within 800 m. A test transmitter 300 m from the system under test produced a field intensity similar to that of a typical animal transmitter at close distance, i.e., about 0.7 uV into a 50-ohm (-110 dBm) receiver input from a vertical half-wave dipole at the location and height used for the systems tests. Greater distances were simulated by reducing the signal with a switched attenuator. All tests were for a 16-milliscond transmitter pulse width.

The computer controlled the antenna rotation and logged the signal strength and antenna position. The receiver employed a voltage detector, i.e., the receiver functioned as a voltmeter. The detector output was digitized by an 8-bit A-D converter. Hereafter, voltage levels are referred to by their digital step (A-D) value. Over most of its range, the detector produced an average voltage proportional to the voltage delivered by the antennas at the receiver input. At low signal voltages, however, non-linearity was apparent as the curve flattened out instead of passing through zero (Fig. 2). This non linearity caused biased mean error in fixed systems. In addition, the random noise inherent in all receiver systems produced random fluctuations of detector output voltage that for any instantaneous reading added to or subtracted from the voltage due to the signal. These fluctuations accounted for an increasing proportion of the measured voltage as the signal voltage decreased, as it would with increased distance to a transmitter or for less powerful transmitters. This random noise caused errors in both automatic systems.

3. System Descriptions

The manual system used two 6-element Yagis spaced 1.35 wavelengths and connected 180° out of phase for a boresight null (Fig. 1e). When provided with a manual switch to allow selection of an in-phase connection, a pair of such Yagis constitutes the "null-peak" antenna in common use for tracking wildlife (peak shown in Fig. 1d).

In the tests the operator judged the null position by ear while rotating the antennas using the arrow keys on the computer. The computer was programmed to rotate the antenna to a randomly chosen azimuth and then to display azimuths with a fixed randomly selected offset. This arrangement allowed the operator to view relative azimuth as he/she rotated the antenna but hid the true azimuth. When the operator stopped rotation at the azimuth of the perceived null, he/she pressed the spacebar to store the difference between measured and true azimuths in an error file; this was repeated until a set of 25 error samples was obtained for a particular attenuator setting. Sample sets were obtained for various attenuator settings.

The rotated system consisted of the same pair of 6-element Yagis as the manual system. Instead of the 180° out of phase (null) connection, a computer controlled switch connected the Yagis so that one was phased ± 90° different from the other. This provided a peak that was shifted approximately 10° CW or CCW from the equal-signal boresight, depending on switch position (Fig. 1f). Unlike peak-null switching, which provides no directional cue, the beam that produces the strongest signal indicates the direction in which the antennas must be rotated in order to bring the transmitter in line with the boresight, a key feature for automatic operation.

At transmitter azimuths less than 10° off-boresight, the ratio (R) of the stronger (Vs) to the weaker (Vw) of the voltages from each beam defines an offset angle (A) from the boresight direction according to the A(R) formula:

$$A(\text{degrees}) = 4.7 \left[\tan^{-1} (R-1) \right]^{0.98} \qquad (1)$$

This empirical formula was determined from field measurements on strong signals. The pair of 6-element Yagis was rotated under computer control plus and minus 5.6° from the true direction to the transmitter in 0.09° steps and stopped after each step while 2 sets of 16 detector voltage readings at 0.5-millisecond intervals were taken by the receiver (one set for each position of the switched beam). The 16 readings for each beam were averaged and their ratio (R) sent to the computer where R was converted to an angle (A) using the formula given above. An error file (n = 124) was created from the difference between A and the true offset angle as taken from the rotator position. The above sequence was repeated for various signal levels set by the attenuator.

The fixed system used the antennas and automated receiver described and tested by Larkin et al. [6]. Two 3-element Yagi antennas were mounted with their directions of maximum response 60° apart (Fig. 1b). We refer to the direction midway between the maximum response directions of the pair as the boresight direction. For sources in the boresight direction, the two antennas provided equal voltage. For any transmitter azimuth the ratio (R) of the stronger (Vs) to the weaker (Vw) of the voltages from two the Yagis defines an offset angle (A) from their boresight direction according to the A(R) formula:

$$A(\text{degrees}) = 27.6\,(\tan^{-1}(\,(.877 \times (R-1))\,))^{0.851}, \qquad (2)$$

determined in the same way as for the rotated system described above. This formula and the A(R) equation for the rotated system fit the relationships between R and A to an accuracy better than 0.1°. These A(R) formulas are specific to receivers with linear voltage detectors and to the particular Yagi designs, spacings, and polarization tested. Different equations would be required for other Yagi designs.

In a full fixed array, six Yagis would be used to cover 360°. Only two adjacent Yagis are needed to test performance because the pattern repeats every 60°. Moreover, because the patterns overlap symmetrically, the system could be evaluated by measurements over the CCW 30° arc from the boresight direction to the maximum of the CCW Yagi (left half of Fig. 1b).

Instead of moving the test transmitter to various azimuths, the computer rotated the Yagis through the 30° arc in 0.09° steps. At each step the receiver stored a set of 16 detector voltage readings for each Yagis at 0.5-millisecond intervals during a pulse. The 16 readings for each Yagi were averaged and their ratio (R) sent to the computer where R was converted to an angle (A) using the equation given above. An error file (n = 330) was created from the difference between A and the true azimuth to the transmitter. The above sequence was repeated for various signal levels set by the attenuator. We calculated standard deviation and mean error for the error files in 5° sectors. Analysis of 5° sectors was appropriate because the error in this type of system is dependent on azimuth, especially for weak signals.

4. Results

Standard deviations of the error distributions, summarized in Table 1, show that near the detection limit of the fixed system (-18 dB and -21 dB), SD of error is approximately 7 times that of the rotated system. Similarly, near the detection limits of the rotated system (-24 to -30 dBm), SD is approximately 4 times that for the manual system. Compared in another way, the rotated system yielded 50% better precision at 3 times the distance to a transmitter (9 times area coverage) than the fixed system, based on the following interpretation of the data. The SD of error for the fixed system at the -6 dB field level is 0.80°; that of the rotated system at the -21 dB level is 0.52°. The 15 dB difference in field levels represents a factor of about 3 in transmitter distance.

Beam-switched and human-operated peak-null systems use equal-signal azimuths symmetrical about a boresight to determine bearing and are therefore immune to receiver detector non linearity and can function without bias down to the limit of detection. Along a boresight, fixed systems are also immune to such bias, accounting for the observation by Larkin et. al. [6] (p. 66) that "DF during range tests was unexpectedly accurate: over all distances right out to the 3.8-km maximum distance of detection, each of the transmitters was localized with little bias....." Although range tests along a boresight are necessary to evaluate the maximum range of reliable detection for fixed systems, such tests are a poor choice for testing typical DF performance as we show below.

Off-boresight, fixed systems are subject to errors that increase with weaker signals and greater off-boresight angles. Ideally, measured ratio R is independent of signal level, i.e., doubling the field from the source results in doubling both Vs and Vw, thus keeping Vs/Vw (R) unchanged. Linearity of the envelope detector of the receiver degrades for levels below about 20 (Fig. 2) where Vw will be increasingly overestimated, thereby causing a bias that results in increasing mean error as the field strength decreases and off-boresight angle increases. Finally, when Vs approaches the noise level, R will tend toward 1 for any source angle and bias toward the boresight becomes very large (lower right portion of Table 2). This error is always toward the boresight and in our tests had positive sign because the sectors tested were CCW (negative angle offsets) relative to the boresight. Larkin et al. [6] (p. 67) report "angular bias away from the antenna with the stronger signal" that was probably due to the factors we described above.

The firmware used in the automatic receiver measured noise Vn (about 9, Fig. 2) for short periods prior to and after the period during which a pulse was

detected. For the tests, Vw was required to exceed a threshold of 2 above Vn to be accepted as a pulse. Data likely to have large bias due to detector non-linearity can be eliminated by using a larger threshold. A value of 5 was empirically found to be practical during operation of the fixed system for monitoring animals. This value precludes full use of the system in the lower-right portions of Table 2 where, however, the detection of a valid Vs and no Vw would at least indicate the presence of a transmitter in the general direction of the peak of a particular Yagi in a 6-Yagi array, i.e., would provide direction-finding to an accuracy of $\pm 30^{\circ}$.

5. Discussion

Our accuracy and distance (coverage area) comparisons among manual, rotated, and fixed systems are for systems of similar per-unit cost, complexity, and portability and having antenna arrays of similar size, wind resistance, and support requirements. Although accuracy and per-unit coverage will never be unimportant in wildlife radio-location systems, other factors that we do not include may be important in some applications.

For instance, the fixed systems is faster at acquiring bearings, an important factor when many animals must be located frequently; for the 1-to-70 duty cycle typical for wildlife transmitters, the fixed system can be up to 5 times faster than a rotated system of similar power consumption. Thus, where a speed of more than about 3 bearings per minute is required, a compromise must be sought among number of units (cost), per-unit coverage area, accuracy, antenna support requirements, and power consumption. Also, a fixed antenna would probably require less maintenance, an important consideration where units are used in difficult to access locations such as mountain tops. Also, the accuracy advantage of a rotated system will be less in situations with multipath propagation, such as animals and equipment both under a forest canopy. In densely wooded habitat, the attenuation versus distance can become high, reducing the per-unit coverage area advantage of the rotated system.

Our comparison of the automatic systems with a manually operated antenna is biased by two factors. First, the receiver -3dB bandwidth was 2 KHz, but for detection of coherent tone pulses > c. 15 ms, the human ear-brain operates at a bandwidth of c. 100 Hz, irrespective of equipment bandwidth. This c. 13 dB human S/N advantage in our tests explains the better accuracy of the manual system down to about -27 dB (Table 1). In fact, the measured advantage was a few dB less than 13 dB because the human ear cannot compare signals as accurately as the computer algorithm. The second bias was against the human operator, reducing his accuracy advantage to a few dB for levels below -27 dB

(Table 1). This result stems from the fact that the antenna had to be rotated to equal signal positions straddling the band gap (no-signal region around the null) and the maximum rotation speed (c. 30°/s) was so slow that comparisons became difficult as the band gap (time between comparisons) increased with weaker signals. Manually controlled beam switching, or provision of a handle for rapidly skewing the antenna, either of which would have improved human performance at low signal levels, were not tested.

Frequency drift of animal transmitters with temperature and posture places a limit on mimimum practical bandwidth for automatic systems, but for many wildlife transmitters and environments, a 500 to 250 Hz bandwidth could be used with a 6-to-9 dB improvement over the results we report. A frequency search and correction algorithm could handle the occasional drift encountered, with some reduction in system speed.

The relative precision of DF systems at medium to low S/N may be estimated from the patterns of the antennas they employ. The patterns for the fixed system we tested (Fig. 1b) show equal voltages at 0° and Vw = 0.13 and Vs = 0.5 at -30°. The difference between 0.13 and 0.5 is 0.37. Thus, as the azimuth goes from 0° to -30°, the voltage difference increases from zero to 0.37, a rate of 0.0123 volts per degree. A similar calculation from the patterns of the rotated system (Fig. 1f) over the 8° arc bracketing the boresight yields 0.1 volt per degree (also see Table 3). The ratio of these rates (8.1 = 0.1 / 0.0123) provides an estimate of the relative precision obtainable from the two antenna arrays. Our empirical results show differences in standard deviation of error by a factor we conservatively typify as 7 (range 6.6 to 9.9, Table 1), not much different from the 8.1 calculated above.

A comparison of the distances at which DFing can be done regardless of azimuth may be gleaned from the ratio of the relative minimum voltages (Vw) over the arcs that must be covered. In the example above, this voltage ratio (4.6 = 0.6 / 0.13) represents a 13 dB difference favoring the rotated 6-element antenna. Values for other antennas are given in Table 3; their differences may be approximated in terms of range from Table 1.

For the sake of simplicity we used volts in the above examples, but the vertical scale of a pattern need only be proportional to volts because all comparisons are of ratios. Engineers, however, customarily normalize antenna patterns to 1.0, regardless of gain, and sometimes plot signal in dB or power rather than voltage. Therefore, in estimating performance from published patterns, it will undoubtedly be necessary to convert to volts and normalize all patterns to the one taken as the

benchmark for comparison. Relative precision of a number of antenna arrays (using patterns in Lawson [5], pp. 1-18 to 1-21) is given in Table 3. We emphasize that the DF comparisons relate to error as expressed by SD and not to bias of the mean error. The latter, affecting only fixed systems, depends on signal level, detector linearity, and azimuth. When comparing systems, the only simple thing we can say regarding bias of mean error is that rotated systems are essentially immune to bias and fixed systems will always be subject to it, increasingly so for weaker signals and larger off-boresight azimuths.

Burchard [7] described a Doppler DF system that employed a circular array of 8 vertical dipoles and reported (his figure 19.7) "fluctuations of readings" that go from $\pm 0.4^{\circ}$ degrees to $\pm 10^{\circ}$ as receiver input drops from -120 dBm to -130 dBm. These input levels correspond approximately to the -9 dBm to -21 dB field levels of Table 1 where performance of the fixed system is roughly the same as that of the Doppler DF system.

Accuracy and per-unit coverage area, because they impact the quality and cost of data, are important factors in choosing data collection systems that are optimal for particular biological objectives. Samuel and Fuller [4], in their design section, provide the broad perspective from which the implications of these findings may be viewed. The present results are consistent with engineering experience and with well-established theory [8].

ACKNOWLEDGMENTS

R. M. Anderson, J. Knight, R. P. Larkin, T. Osborn, and A. Raim provided valuable comments on the manuscript. R. Lindsey built the rotator and wrote the control software. The project received support under U.S. Army CERL contract DACA 88-97-M-0245.

REFERENCES

[1] Cochran, W.W. and R.D. Lord. 1963. A radio tracking system for wild animals. J. Wildlife Management 27(1):9-24.

[2] Cochran, W.W., D.W. Warner, J.R.Tester, and V.B. Kuechle. 1965. Automatic radio-tracking system for monitoring animal movements. BioScience 2:98-100

[3] Deat A.R., C.Mauget, R. Maugot, D. Maurel, and A. Sempere. 1980. The automatic, continuous and fixed radio tracking system of the Chize Forest: theoretical and practical analysis. Pages 439-451 in C. J. Amlaner, Jr. and E. W. McDonald, editors. A handbook on biotelemetry and radio tracking. Pergamon Press, Oxford, U.K.

[4] Samuel, M.D. and M.R. Fuller. 1994 Wildlife radiotelemetry. Pages 370-418 in Bookhout, T.A., editor. Research and management techniques for wildlife and habitats. The Wildlife Society, Bethesda, MD.

[5] Lawson, J.L. 1986. Yagi antenna design. Publication no. 72. American Radio Relay League. Newington, CT. 198pp.

[6] Larkin, R.P, Raim, A., and R.P. Diehl. 1996. Performance of a non-rotating direction-finder for automatic radio tracking. J. Field Ornithol. 67(1):59-71.

[7] Burchard, D. 1989. Direction finding in wildlife research by Doppler effect. Pages 169-177 in C. J. Amlaner, Jr. ed. Biotelemetry X. Univ. of Arkansas Press, Fayetteville, AR.

[8] Swerling, P. 1956. Maximum angular accuracy of a pulsed search radar. Proc.IRE **44**: 1146-1155.

Table 1. Standard deviation (SD), degrees, and mean of error distributions, degrees, of n samples for three DF systems at different field strength levels.

Field dB * (distance **)	Null-connected 6-element Yagi, manually-operated	Rotated, beam-switched, 6-element Yagi, computer-controlled	Fixed switched 3-element Yagi, computer-controlled^
	SD (mean) [n]	SD (mean) [n]	SD (mean) [n]
0 (300)			.41 (+0.13) [330]
-3 (375)	.02 (0.00) [25]		.60 (+0.21) [330]
-6 (470)		.12 (-0.11) [124]	.80 (+0.19) [330]
-9 (590)	.02 (0.00) [25]		1.12 (+0.47) [330]
-12 (730)		.20 (+0.20) [124]	1.43 (+1.36) [330]
-15 (920)	.10 (0.00) [25]	.25 (-.09) [124]	2.13 (+2.49) [330]
-18 (1150)	.15 (0.00) [25]	.30 (+.08) [124]	2.97 (+2.88) [220]
-21 (1425)		.52 (+06) [124]	3.58 (+1.80) [110]
-24 (1750)	.20 (+0.01) [25]	.81 (+.03) [124]	4.05 (+1.77) [55]
-27 (2100)	.28 (0.00) [25]	1.26 (-0.22) [124]	signal unreliable
-30 (2500)	.80 (+0.01) [25]	1.65 (+.01) [124]	signal undetectable
-33 (3000)	2.32 (+0.06) [25]	signal unreliable	
-36	null unreliable	signal undetectable	

* 0 dB = the field strength that provided 0.7 uV (-110 dBm) from a vertical half-wave dipole at the location and height of the receiving antennas used for the systems tests.

** Approximate distance in meters to a 1-stage transmitter near the ground

^ Data for the switched 3-element system are the average of the useful data in Table 2.

Table 2. Standard deviation (SD), degrees and mean error distributions, degrees, of n= 55** samples for off-boresight 5° degree sectors of a 30° arc of a switched 3-element fixed array.

Field	sector 0 to –5		sector –5 to –10		sector –10 to –15	–15 to –20	sector –20 to –25		sector –25 to –30		sector	
dB	S.D.	(mean)	S.D.	(mean)	S.D.	(mean)	S.D.	(mean)	S.D.	(mean)	S.D.	(mean)
0	0.38	(0.02)	0.40	(0.17)	0.41	(0.06)	0.45	(0.15)	0.42	(0.18)	0.41	(0.21)
-3	0.60	(0.04)	0.57	(0.40)	0.59	(0.23)	0.62	(0.21)	0.63	(0.23)	0.58	(0.17)
-6	0.82	(0.11)	0.86	(0.14)	0.88	(0.21)	0.74	(0.19)	0.85	(0.01)	0.64	(0.45)
-9	1.13	(0.13)	1.11	(0.16)	1.24	(0.37)	1.24	(0.33)	1.03	(0.52)	0.95	(1.32)
-12	1.38	(0.14)	1.58	(0.94)	1.51	(1.17)	1.31	(1.88)	1.41	(1.80)	1.40	(2.14)
-15	2.29	(0.22)	2.38	(1.48)	1.89	(2.44)	2.23	(2.97)	2.24	(3.53)	1.75	(4.03)
-18	2.88	(0.50)	3.12	(2.56)	2.93	(3.65)	2.97	(4.81)	2.89	(5.16)///	2.79	(7.97)///
-21	3.52	(1.12)	3.63	(2.48)	3.00	(5.36)///	2.88	(7.58)///	3.71	(9.80)///	3.45	(11.48)///
-24	4.05	(1.77)	3.66	(5.22)///	4.08	(8.13)///	4.31	(11.77)///	4.04	(15.19)///	4.01	(17.80)///

**For the -24 dB field level, n varies between 39 and 49.

/// A threshold value of 5 excludes data taken at these field levels as not useful for DF purposes.

Table 3. Calculated comparison of automatic systems by gain, precision, dimensions, and weight/wind area.

Type system	Yagi type, (number used)	Spacing	Relative DF gain, dB ^	Precision, degrees ^^	Largest dimensions, wavelengths	Relative weight or wind area
rotated	2-element (2)	0.50*	8	0.027	0.2 x 0.5	1.5
rotated	3-element (2)	0.67*	11	0.035	0.4 x 0.67	2.4
rotated	6-element (2)	1.35*	13	0.100	1.2 x 1.35	5.7
fixed	3-element (6)	60**	0	0.012	1.2 x 1.2	7.3
fixed	6-element (10)	36**	5	0.027	3.6 x 3.6	26.1
fixed	15-element (15)	24**	11	0.055	10 x 10	143.2

* spacing, wavelengths
** arc between adjacent antennas, degrees
^ for full 360° coverage
^^ Volts per degree as a measure of relative precision is proportional to 1/ SD of error

COMPUTER MODEL FOR THE DESIGN OF A VHF ANTENNA TEST RANGE

Scott Santarelli and Hans Steyskal
US Air Force Research Laboratory
Sensors Directorate
Antenna Technology Branch
AFRL/SNHA, 80 Scott Drive
Hanscom AFB, MA 01731

Abstract

In practice, accurate measurement of VHF antenna radiation patterns can be difficult to achieve due to the presence of large multi-path reflections in the test range. Special range geometries and source arrangements have been devised over the years to mitigate the measurement errors produced by test range multi-path. In this paper, we describe a computer model designed to accurately control the influence of ground path illumination and, in turn, reduce quiet-zone amplitude and phase variation. We use an array of dipoles as our transmit source. Using an electromagnetic image-method approach, we fully characterize the test range by calculating the transfer function between the element excitations and the quiet-zone electric field. We then use this transfer function to solve for the element excitations that produce minimal amplitude and phase variation in the quiet zone. Our simulated results show that when the number and locations of the array elements are varied, reduced quiet-zone amplitude and phase variation is achievable for several range geometries.

1 Introduction

Detecting tanks and other military targets concealed by foliage remains a problem for both airborne and ground-based radar. One strategy for detecting such targets concealed by the tree canopy is the use of low radar frequencies (i.e., VHF), since leaves, branches, and trunks become electromagnetically transparent at long enough wavelengths. In other words, low frequency radar signals have the potential to penetrate the tree canopy and detect large military targets. In support of this research effort, we are in the process of designing and building a VHF antenna test range in Ipswich, Massachusetts. Once completed, this range will be used to test new antenna designs aimed at solving the above problem.

In practice, accurate measurement of VHF antenna radiation patterns can be difficult to achieve due to the presence of large multi-path reflections in the *quiet zone*. In this paper, we define the quiet zone as the planar spatial region for which the amplitude and phase variation of the incoming wave front meets a specified requirement. The quiet zone is ultimately where the antenna under test (AUT) resides. Special range geometries and source arrangements have been devised over the years to mitigate the measurement errors produced by test range multi-path [1] – [3]. These approaches are all similar in that the authors are primarily concerned with identifying the *locations* of scatterers in the test range in order to eliminate or diminish the *effects* of these scatterers. For most outdoor ranges, the ground between the source and the AUT is the primary scatterer. In

this paper, we propose a method for achieving minimal quiet-zone amplitude and phase variation that doesn't require knowledge of the locations and properties of individual scatterers. In fact, we fully characterize the test range by calculating (or in real life, by measuring) the transfer function between the element excitations and the quiet-zone electric field. In other words, all the pertinent details of the test range (i.e., scatterers, constitutive parameters of ground, *etc.*) are contained within the transfer function. We then use this transfer function to solve for the element excitations that produce desired levels of amplitude and phase variation in the quiet zone.

Figure 1 shows our current Ipswich range geometry. The transmit array consists of $\mathcal{N}$ half-wave dipoles operating at a frequency of 100 MHz (λ = 3 m). The dipoles are vertically polarized to reduce the effects of mutual coupling. The array resides on the front side of a 40-ft. (12.2-m) metal tower. (The front base of the tower is the origin of the Cartesian coordinate system depicted in the figure.) The separation between the transmit and receive towers is approximately 343 ft. (104.5 m). The surface between the towers is grass and shows a slight decline (i.e., $\alpha \cong 1°$). A 30-ft. (9.1-m) fiberglass tower separates the receiving antenna from the mount in an attempt to minimize multi-path in the quiet zone caused by scattering from the Round Building and the mount. The combined height of the Round Building and mount is about 12 m, and thus, the center of the quiet zone is initially assumed to lie roughly 20 m above the ground. It is desired that the quiet zone extend 10 – 20 ft. along both the y and z dimensions (the positive z-axis points out of the figure) with a maximum amplitude and phase variation of 0.25 dB and 5°, respectively. In this paper, we neglected the effects of the transmit and receive towers and focused on the scattering properties of the ground. In doing so, we were able to restrict our analysis to the xy-plane, realizing that a flat amplitude and phase response along the y-dimension translates to an equally flat response along the z-dimension due to the symmetric properties of the transmit array (provided the distance between the array and the quiet zone is large enough).

The remainder of this paper is outlined as follows. In Sec. 2, we first present an analysis in which we show that a transmit source consisting of a single element is inadequate to obtain desired levels of quiet-zone amplitude and phase variation for our range geometry. We then describe our approach for calculating the quiet-zone electric field from an $\mathcal{N}$-element transmit array and our method for computing the element excitations that give rise to desired levels of quiet-zone amplitude and phase variation. In Sec. 3, we demonstrate the applicability of our approach by achieving desired levels of quiet-zone amplitude and phase variation for several range geometries. Finally, Sec. 4 contains a summary of our findings.

2 Method

2.1 Single Element Analysis

Consider the simplified range geometry shown in Figure 2. The x-axis represents the boundary between medium 1 (air) and medium 2 (i.e., $\alpha = 0°$). A single, vertically-polarized, half-wave dipole transmitter is placed along the y-axis at point $(0, \eta)$. The diameter of the quiet zone along the y dimension is $\mathcal{D}_q$, and the center of the quiet zone is located at point $Q_c = (x_c, y_c)$.

We use the Ipswich range specifications and let $\mathcal{D}_q = 10$ ft. (3.05 m), $Q_c = (104.5, 20.0)$ m, and $\lambda = 3$ m. Furthermore, the maximum acceptable quiet-zone amplitude and phase variation are 0.25 dB and 5°, respectively. Figure 3 plots the quiet-zone amplitude and phase variation as a function of transmitter height η for the simple case of $\varepsilon_2 = \varepsilon_0$ (i.e., no multi-path). The darkly shaded area in each subplot represents the vertical extent of the quiet zone, whereas the lightly shaded area represents the limited values of η that are realizable for a transmit-tower height of only 12.2 m.

As expected, the point $\eta = y_c$ represents the minimum of both variation functions (amplitude and phase). The variation functions are also symmetrical about the value $\eta = y_c$. Although the amplitude variation falls within the specified limit for all values of η, the phase variation is only acceptable for values of η in the immediate vicinity of y_C (i.e., the dotted line represents the phase variation limit). In fact, if the transmit location were restricted to the height of our transmit tower, the smallest attainable phase variation would be close to 30°. Thus, even for the ideal case in which multi-path is nonexistent, a single element is inadequate to meet the specified quiet-zone amplitude and phase variation criteria for our range geometry.

The plots in Figure 4 are based on the identical range geometry described above, except $\varepsilon_2 = 88\varepsilon_0$ (a relative permittivity consistent with water). The dotted line in each subplot represents the appropriate variation limit. In this example, the amplitude variation meets the requirement for several values of η in the lightly shaded area. In contrast, the phase variation is larger than 5° for *all* simulated values of η. Thus, even if the transmit tower were tripled in size, there exists no element location for which the quiet-zone phase variation meets our specification.

These two cases clearly illustrate that a transmit source consisting of a single element is inadequate to obtain desired levels of quiet-zone amplitude and phase variation for our range geometry. The following section describes a method in which an array of elements is used to control amplitude and phase variation in the quiet zone.

The first part of this subsection describes the method we used to compute the quiet-zone electric field for a generalized range geometry containing an N-element transmit array. The latter part presents our method for achieving desired levels of quiet-zone amplitude and phase variation.

Consider the range geometry shown in Figure 5. The transmit array consists of N half-wavelength dipoles located along the y-axis and vertically polarized in the y direction. The boundary between medium 1 and medium 2 (the x'-axis) makes angle α with the x-axis. The electric field $E(x,y)$ at point (x, y) is the sum of the contributions $E_n(x,y)$ from each of the array elements:

$$E(x, y) = \sum_{n=1}^{N} E_n(x, y) \tag{1}$$

Furthermore, the electric field contribution from each element consists of a *direct* and a *reflected* component:

$$E_n(x, y) = E_{Dn}(x, y) + E_{Rn}(x, y) \tag{2}$$

where the subscripts D and R denote direct and reflected, respectively.

In general, the field at point (x, y) due to a single radiating dipole in free space can be expressed as:

$$E(x, y) = I\, f(\theta) \frac{e^{-jkR}}{R} \tag{3}$$

where I is the complex element excitation, $f(\theta)$ represents the element pattern, θ is the angle from the dipole axis, k is the wave number ($\lambda/2\pi$), and R is the distance from the element to point (x, y). Thus, the electric field due to the direct path signal from element n is simply:

$$E_{Dn}(x,y) = I_n\, f(\theta_n)\frac{e^{-jkR_n}}{R_n} \tag{4}$$

where θ_n and $\mathcal{R}_n$ are as shown in Figure 5, and

$$f(\theta_n) = \cos(\theta_n) \tag{5}$$

for a vertically-polarized, half-wavelength dipole. For element n, which is located at point (ζ_n, η_n), it is easily shown that:

$$R_n = \sqrt{(x-\zeta_n)^2 + (y-\eta_n)^2} \tag{6}$$

$$\theta_n = \tan^{-1}\left[\frac{y-\eta_n}{x-\zeta_n}\right] \tag{7}$$

In order to compute the reflected wave, the method of images is applied as shown in Figure 5. Thus, the *reflected* wave from element n to point (x, y) is equivalent to the *direct* wave from the image of element n at point (ζ_n', η_n') to point (x, y). The reflected field, therefore, can be expressed as the following:

$$E_{Rn}(x,y) = I_n\, f(\theta_n')\frac{e^{-jkR_n'}}{R_n'}\ \Gamma(\theta_n') \tag{8}$$

where θ_n' and $\mathcal{R}_n'$ are as shown in Figure 5, and Γ is the reflection coefficient, which depends on angle θ_n' and the constitutive parameters of mediums 1 and 2. From the geometry in Figure 5, it can be shown that:

$$R_n' = \sqrt{(x-\zeta_n')^2 + (y-\eta_n')^2} \tag{9}$$

$$\theta_n' = 2\alpha + \tan^{-1}\left[\frac{y-\eta_n'}{x-\zeta_n'}\right] \tag{10}$$

where

$$\zeta_n' = \zeta_n \cos^2\alpha - \eta_n[\tan\alpha + \sin\alpha\cos\alpha] \tag{11}$$

$$\eta_n' = -\cos\alpha[\zeta_n \sin\alpha + \eta_n \cos\alpha] \tag{12}$$

If the relative permittivity of medium 1 is unity and the magnetic permeabilities of the two mediums are equal, then the reflection coefficient for a vertically-polarized wave incident on medium 2 from medium 1 can be expressed as the following:

$$\Gamma_V = \frac{\sqrt{1-\frac{\sin^2\gamma}{\varepsilon_{r2}}} - \cos\gamma\sqrt{\varepsilon_{r2}}}{\sqrt{1-\frac{\sin^2\gamma}{\varepsilon_{r2}}} + \cos\gamma\sqrt{\varepsilon_{r2}}} \tag{13}$$

where the subscript V denotes vertical polarization, ε_{2r} is the relative permittivity of medium 2, and γ is the angle of incidence shown in Figure 5 and is expressed as:

$$\gamma = \frac{\pi}{2} - \tan^{-1}\left[\frac{(x+\zeta_n)\tan\alpha + y + \eta_n}{x+\zeta_n - (y-\eta_n)\tan\alpha}\right] \tag{14}$$

Using the Ipswich range geometry of Figure 1 (with a frequency of 100 MHz), we calculate the far zone field for a three-element transmit array consisting of vertically-polarized, half-wavelength dipoles. The elements are equally excited and are spaced a half wavelength apart along the y-axis at 1, 2.5, and 4 m. The relative permittivity of the ground is $\varepsilon_{2r} = 9 - 3i$, which is representative of soil

having a volumetric moisture content of 15.1% [4]. Figure 6 shows the normalized field along the y-dimension from 0 to approximately 21.5 m at x = 104.5 m (i.e., the distance between the transmit and receive towers). Over a desired quiet-zone diameter $\mathcal{D}_q$ = 3 m centered 20 m above the ground, the amplitude/phase variation is 0.55 dB/57.7° (e.g., the shaded area in each subplot represents the quiet zone). Clearly, equal excitations do not produce acceptable amplitude and phase variation (i.e., 0.25 dB and 5°, respectively).

However, there is a different approach based on synthesis rather than analysis. Given a desired set of uniform field values over a set of sampling points in the quiet zone, we can attempt to determine a corresponding transmit array. The available degrees of freedom include the number of elements, the element excitations, and the vertical locations of the elements. The synthesis can be accomplished with the aid of the transfer function of the test range as illustrated below.

Consider the set of excitations for an $\mathcal{N}$-element array:

$$\mathbf{I} = \begin{bmatrix} I_1 \\ I_2 \\ \vdots \\ I_j \\ \vdots \\ I_N \end{bmatrix} \tag{15}$$

where I_j is the complex excitation corresponding to element j. Given **I**, consider the complex field at a set of $\mathcal{N}$ arbitrary spatial locations:

$$\mathbf{E} = \begin{bmatrix} E_1 \\ E_2 \\ \vdots \\ E_i \\ \vdots \\ E_N \end{bmatrix} \tag{16}$$

where $\mathcal{E}_i$ is the complex electric field at location i. Thus, one can relate **E** to **I** via the following matrix equation:

$$\mathrm{E} = \mathrm{I}\,\mathrm{T} \tag{17}$$

where **T** is the $\mathcal{N} \times \mathcal{N}$ *transfer function matrix*:

$$\mathrm{T} = \begin{bmatrix} T_{11} & T_{12} & \cdots & T_{1N} \\ T_{21} & T_{22} & \cdots & T_{2N} \\ \vdots & \vdots & \ddots & \vdots \\ T_{N1} & T_{N2} & \cdots & T_{NN} \end{bmatrix} \tag{18}$$

where $\mathcal{T}_{ij}$ represents the electric field component at spatial location i due to complex excitation j, for $I_j = 1$. In other words, **T** represents the transfer function between the element excitations and the electric field at $\mathcal{N}$ spatial coordinates. Once **T** is available, one can solve for the complex element excitations given **E** via the following:

$$\mathrm{I} = \mathrm{E}\mathrm{T}^{-1} \tag{19}$$

where $\mathbf{T}^{-1}$ represents the inverse of matrix **T**.

Applying this method to our particular problem, we can specify a uniform electric field at $\mathcal{N}$ equally spaced points within the quiet zone and compute the corresponding excitations. Using these excitations, we then compute the electric field at *all* points within the quiet zone to determine if the amplitude and phase variation are acceptable.

The major benefit of this approach is that the transfer function characterizes the entire test range, including the distance between the transmit and receive towers, the inter-element spacing of the source array, and the reflective properties of the ground medium. In other words, the entire test range geometry can be treated as a black box. Furthermore, the transfer matrix is easily calculated or measured in practice, and the computation of the element excitations involves a simple matrix inversion (for relatively small values of $\mathcal{N}$).

The above method was applied to the same range geometry as for Figure 6. The open circles in each subplot of Figure 7 denote the spatial locations within the quiet zone for which the electric field was specified to be uniform. These points are equally spaced and include the lower and upper boundaries of the quiet zone. The desired phase of the field at each point was set equal to 0°, and the desired amplitude was set equal to $\mathcal{N} \times \mathcal{E}_0$, where E_0 is the field magnitude produced by a unit magnitude transmit current, i.e.

$$E_0 = |T_{11}| \cdot 1 \tag{20}$$

Under normal conditions, this "normalized" field value should lead to synthesized element currents of roughly unit magnitude on the transmit array.

Figure 7 shows that the resulting quiet-zone amplitude and phase variation (0.0948 dB and 1.39°, respectively) are well within the specified limits, demonstrating the validity of this synthesis approach. However, they are achieved at the expense of *very* large excitations, since $|I_1| = 78$, $|I_2| = 188$, and $|I_3| = 127$. This concern is addressed in the next section.

3 Results and Discussion

Using the above synthesis method, we computed the achievable quiet-zone amplitude and phase variation as a function of $\mathcal{N}$ and the inter-element spacing of the transmit array (see Figure 8 a and b). Figure 8c represents the corresponding maximum array element excitation magnitude. The transmit array is located along the y-axis, and the first element is fixed at $y = 1$ m. The location(s) of the remaining element(s) depend(s) on $\mathcal{N}$ and the inter-element spacing. Since the transmit tower is of finite height, the maximum allowable inter-element spacing decreases with increasing $\mathcal{N}$. $\mathcal{R} = 104.5$ m, and $\varepsilon_{2r} = 9 - 3i$. The shaded region in the top subplot represents acceptable values of amplitude variation (i.e., < 0.25 dB). All computed phase variation values fall within the specified limit (i.e., < 5°).

It is clear from the figure that both the amplitude and phase variation decrease with increasing $\mathcal{N}$, whereas the maximum array element excitation magnitude increases with $\mathcal{N}$. Slightly less obvious is a tendency for all three quantities to decrease with increasing inter-element spacing. According to the figure, the minimum number of elements that will meet the quiet-zone amplitude variation criterion is $\mathcal{N} = 3$. For such an array, the maximum, array excitation magnitude is always greater than 30. Thus, again, acceptable quiet-zone

amplitude and phase variation are achieved at the expense of large excitations. Considering that the quiet-zone field is normalized, these large excitations imply the cancellation of very large fields from the individual elements in order to meet variation requirements.

Figure 9 offers an explanation for these large excitations. In the far zone, the transmit array can be modeled as a point source positioned at the origin of a coordinate system, and the dotted circles represent the resulting far-field spherical wave front. Two possible locations for the quiet zone are denoted by A and B (A and B have the same x-coordinate, but different y-coordinates). As seen, location A inherently leads to a phase variation, which is very difficult to suppress and requires large currents. Location B inherently yields a relatively flat phase, since the direction of propagation is perpendicular to the quiet-zone.

In general, one can relate the process of trying to achieve minimal quiet-zone amplitude and phase variation as being analogous to "flattening" the spherical wave front for a particular region of space. For the current Ipswich range, the quiet zone is defined at a higher y-coordinate than the transmit array (corresponding to Figure 9, case A). The analysis presented in Sec. 2A (Figure 3) also demonstrated that minimum quiet-zone amplitude and phase variation occurs when the height of the transmitter and the quiet-zone center (Q_c) are equal (corresponding to Figure 9, case B).

Figure 10 shows the same data as Figure 8, except that now the quiet-zone location varies as a function of inter-element spacing such that the y-coordinates of the transmit array center and Q_c are always equal. By aligning the quiet zone with the array center, all three quantities (amplitude variation, phase variation, and maximum array element excitation magnitude) decrease. Note that the minimum number of elements necessary to achieve acceptable quiet-zone amplitude and phase variation has decreased from 3 to 2. The corresponding excitation magnitudes for a two-element array are only slightly greater than unity for large inter-element spacings.

Thus, the results of this analysis suggests that, although it is possible to design a transmit array that will produce acceptable quiet-zone amplitude and phase variation for the geometry of Figure 1 (where the transmit array and the quiet zone are not aligned), the corresponding array excitation may not be practically realizable. By aligning the array and quiet-zone centers, we are able to reduce the number of array elements and the excitation becomes much more realistic.

Finally, we computed the quiet-zone amplitude and phase variation and the maximum array element excitation as a function of $\mathcal{N}$ and inter-element spacing for some additional ground permittivities and quiet-zone sizes. Considering the results of the previous section, we aligned the transmit array center with Q_c for each computation in order to achieve minimal quiet-zone amplitude and phase variation. In each of the following cases, we started with the

range geometry of Figure 10. We then varied one parameter at a time (i.e., either ε_{2r} or $\mathcal{D}_q$) to determine its effect on the quiet-zone amplitude and phase variation and the maximum array element excitation.

The first analysis varied the relative permittivity of the ground, ε_{2r} (Figures 11a – 11d). These plots cover a wide spectrum of ground reflective properties. Figure 11a represents a range geometry for which there is no multi-path ($\varepsilon_{2r} = 1$). Figures 11b and 11c represent ranges for which the ground medium is lossy. These particular values of ε_{2r} (3 – j0.5 and 16 – j7.7) correspond to soil mediums that have volumetric moisture contents of 4% and 28%, respectively [5, Mid-range values of permittivity are chosen from scatter plots of data]. Figure 11d represents a range for which the ground is highly reflective. A relative permittivity of 88 corresponds to water.

Note that all computed values of quiet-zone amplitude and phase variation are acceptable in this analysis, except for the case in which $\varepsilon_{2r} = 88$ (i.e., the shaded region in the top subplot of 11d represents acceptable values of amplitude variation). And even for this case, there are only a few points at which the amplitude variation is unacceptable (i.e., for a 2-element array with relatively large inter-element spacing). For all values of ε_{2r}, the quiet-zone amplitude and phase variation decrease with increasing $\mathcal{N}$. The maximum array excitation magnitude increases with $\mathcal{N}$ in all plots, except for the case where $\varepsilon_r = 1$. It seems that the absence of multi-path has had the effect of switching the order of the $\mathcal{N}$= 3 and $\mathcal{N}$ = 4 curves. There is a general trend across ε_{2r} and $\mathcal{N}$ for excitation magnitudes to decrease with increasing inter-element spacing. The shapes of the amplitude and phase variation curves vary as a function of ε_{2r}, but not with any discernable pattern. This implies that the constitutive parameters of the ground medium have an unpredictable effect on the quiet-zone amplitude and phase variation as a function of $\mathcal{N}$ and inter-element spacing; however, our method is able to find several acceptable array configurations for each value of ε_{2r}.

The second analysis varied $\mathcal{D}_q$. Figures 12a – 12d represent $\mathcal{D}_q$ values of 10, 20, 25, and 30 ft. (3.05, 6.10, 7.63 and 9.15 m), respectively. As in the previous analysis, the quiet-zone amplitude and phase variation decrease with increasing $\mathcal{N}$, and the maximum array element excitation magnitude increases with $\mathcal{N}$ for all values of $\mathcal{D}_q$. And there is a general trend across $\mathcal{D}_q$ and $\mathcal{N}$ for excitation magnitudes to decrease with increasing inter-element spacing. Note that the quiet-zone amplitude and phase variation get progressively worse for increasing $\mathcal{D}_q$, but the general shapes of these variation functions do not change as a function of $\mathcal{D}_q$. This is not surprising, since the results of the previous analysis suggest that the shapes of these curves depend on the constitutive parameters of the ground. Also note that while several array configurations will yield acceptable quiet-zone amplitude and phase variation for $\mathcal{D}_q$ = 10 or 20 ft., there are limited array configurations available for $\mathcal{D}_q$ = 25 or 30 ft. In fact, the

minimum number of required array elements for the larger values of $\mathcal{D}_q$ is three, and the corresponding excitation magnitudes are relatively high.

Altogether, these results suggest that $\mathcal{D}_q$ should be less than or equal to 20 feet. In addition, one should choose an array configuration for which $\mathcal{N} = 2$ and the inter-element spacing lies somewhere between 2 and 2.5λ. Such a configuration ensures acceptable levels of quiet-zone amplitude and phase variation, as well as excitation magnitudes that are close to unity for a wide spectrum of range geometries.

4 Summary/Conclusion

In this paper, we developed a computer model for a VHF antenna test range with an array of antennas as the illuminator. Ground reflections are modeled by simple image theory. We described a synthesis approach that utilizes the degrees of freedom inherent in an array of antennas to achieve the desired flat amplitude and phase variation in the quiet zone. Our simulations verify the applicability of our computer model for several range geometries and array configurations. The following is a summary of our findings:

- A transmitter consisting of a single element is inadequate to obtain desired levels of quiet-zone amplitude and phase variation for our range geometry.
- The *transfer function matrix* characterizes the entire test range, including the distance between the transmit and receive towers, the inter-element spacing of the source array, and the reflective properties of the ground medium. Furthermore, the transfer matrix is easily calculated or measured in practice, and the computation of the element excitations involves a simple matrix inversion.
- The range geometry of Figure 1, where the transmit array "looks up" at the quiet zone is non-optimal and requires exceedingly large array excitation currents. The optimal configuration is when the array center is aligned with the quiet-zone center, which greatly reduces the required number of array elements and current magnitudes.
- Array configuration properties:
  - The quiet-zone amplitude and phase variation decrease with increasing $\mathcal{N}$(number of array elements).
  - Element excitations increase with increasing $\mathcal{N}$.
  - Element excitations decrease with increased element spacing.

- Altogether, the results presented in this paper suggest that the quiet-zone diameter should be less than or equal to 20 ft. (with quiet zone and array center aligned). In addition, we should choose an array configuration for which $\mathcal{N} = 2$ and the inter-element spacing lies somewhere between 2 and 2.5λ. Such a configuration ensures acceptable levels of quiet-zone amplitude and phase variation, as well as excitation magnitudes that are close to unity for a wide spectrum of range geometries.

5 Acknowledgements

We would like to express our thanks to Bill Stevens and Dr. Peter Franchi for providing references [4] and [5], to David Curtis for enlightening discussions on the benefits of VHF, and Richard Wing, Edward Martin, James Kenney, and Erhard Wisniewski for providing the test range dimensions.

6 References

[1] W. D. Burnside and I. J. Gupta, "A Method to Reduce Stray Signal Errors in Antenna Pattern Measurements", *IEEE Transactions on Antennas and Propagation*, vol. 42, no. 3, pp. 399 – 405, March 1994.

[2] J. W. Odendaal and J. Joubert, "Using hardware gating to improve antenna gain measurements in compact antenna range", *Electronics Letters*, vol. 35, no. 22, pp. 1894 – 1896, October 1999.

[3] L. H. Hemming and R. A. Heaton, "Antenna Gain Calibration on a Ground Reflection Range", *IEEE Transactions on Antennas and Propagation*, vol. AP-21, no. 4, pp. 532 – 538, July 1973.

[4] Waymond R. Scott, Glenn S. Smith, "Measured Electrical Constitutive Param.s of Soil as Functions of Frequency and Moisture Content", *IEEE Transactions on Geoscience and Remote Sensing*, Vol. 30 (3), May 1992, pp 621 – 623.

[5] John O. Curtis, "Moisture Effects on the Dielectric Properties of Soils", *IEEE Transactions on Geoscience and Remote Sensing*, Vol. 39 (1), January 2001, pp. 125 – 128.

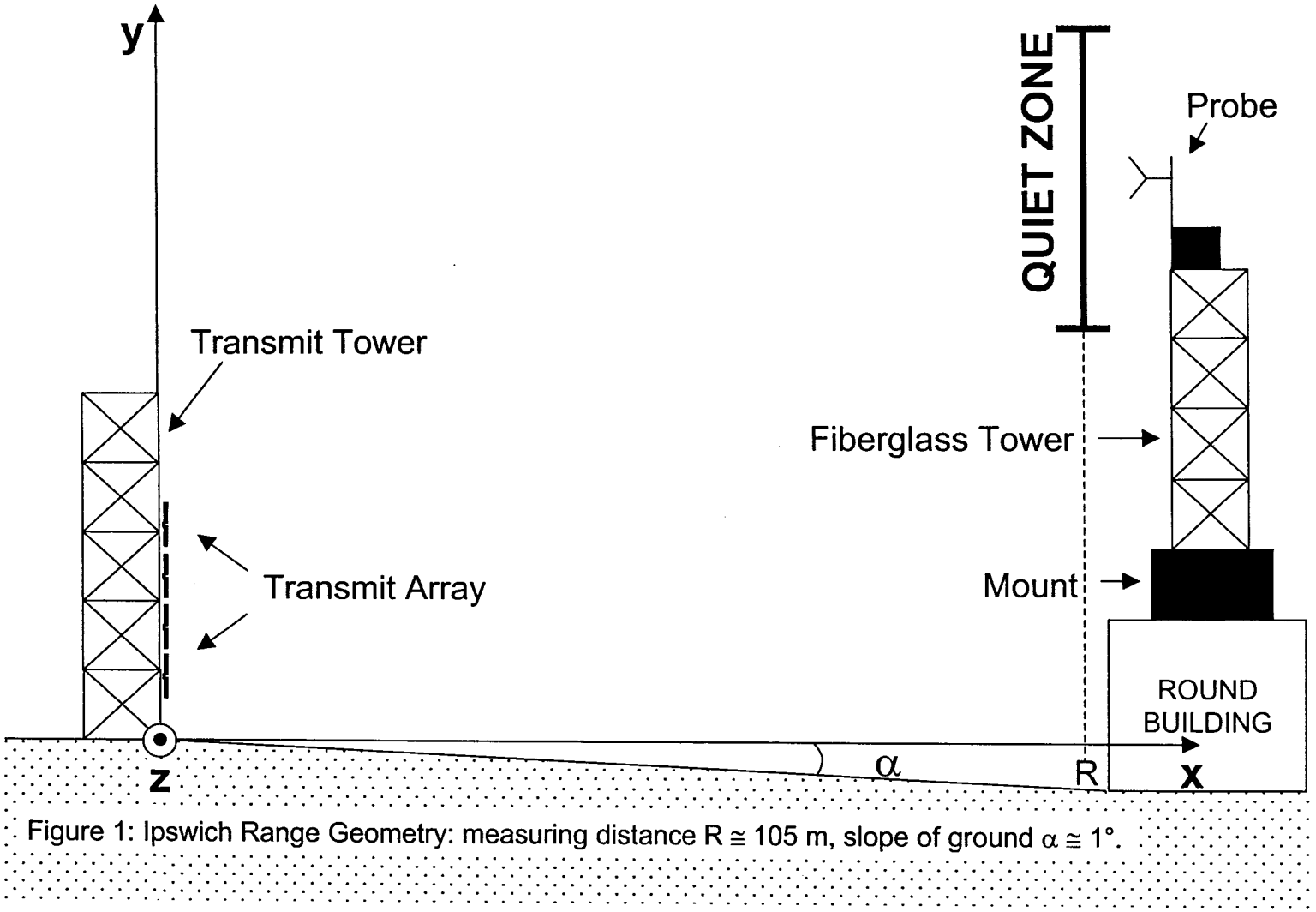

Figure 1: Ipswich Range Geometry: measuring distance R ≅ 105 m, slope of ground α ≅ 1°.

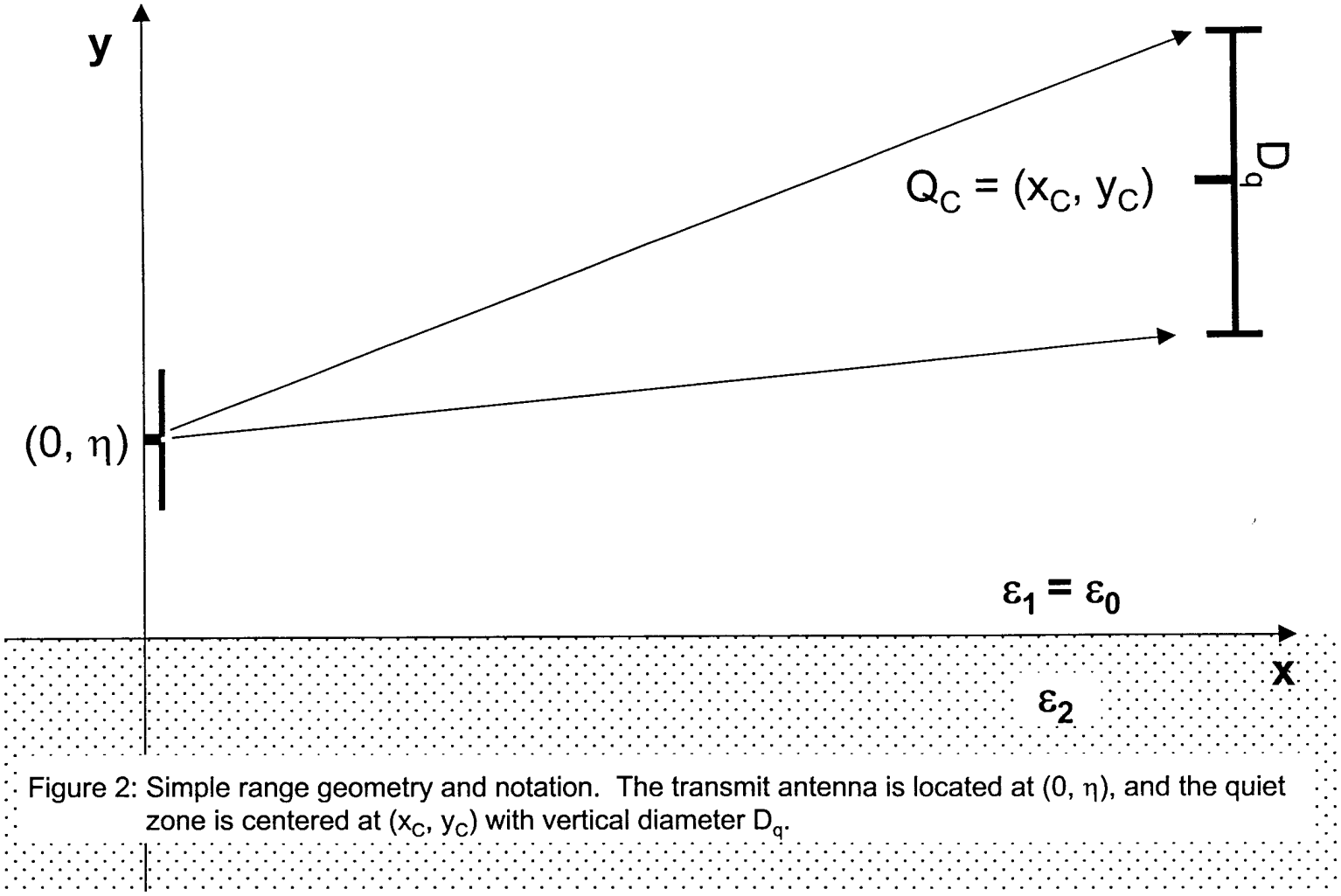

Figure 2: Simple range geometry and notation. The transmit antenna is located at $(0, \eta)$, and the quiet zone is centered at (x_C, y_C) with vertical diameter D_q.

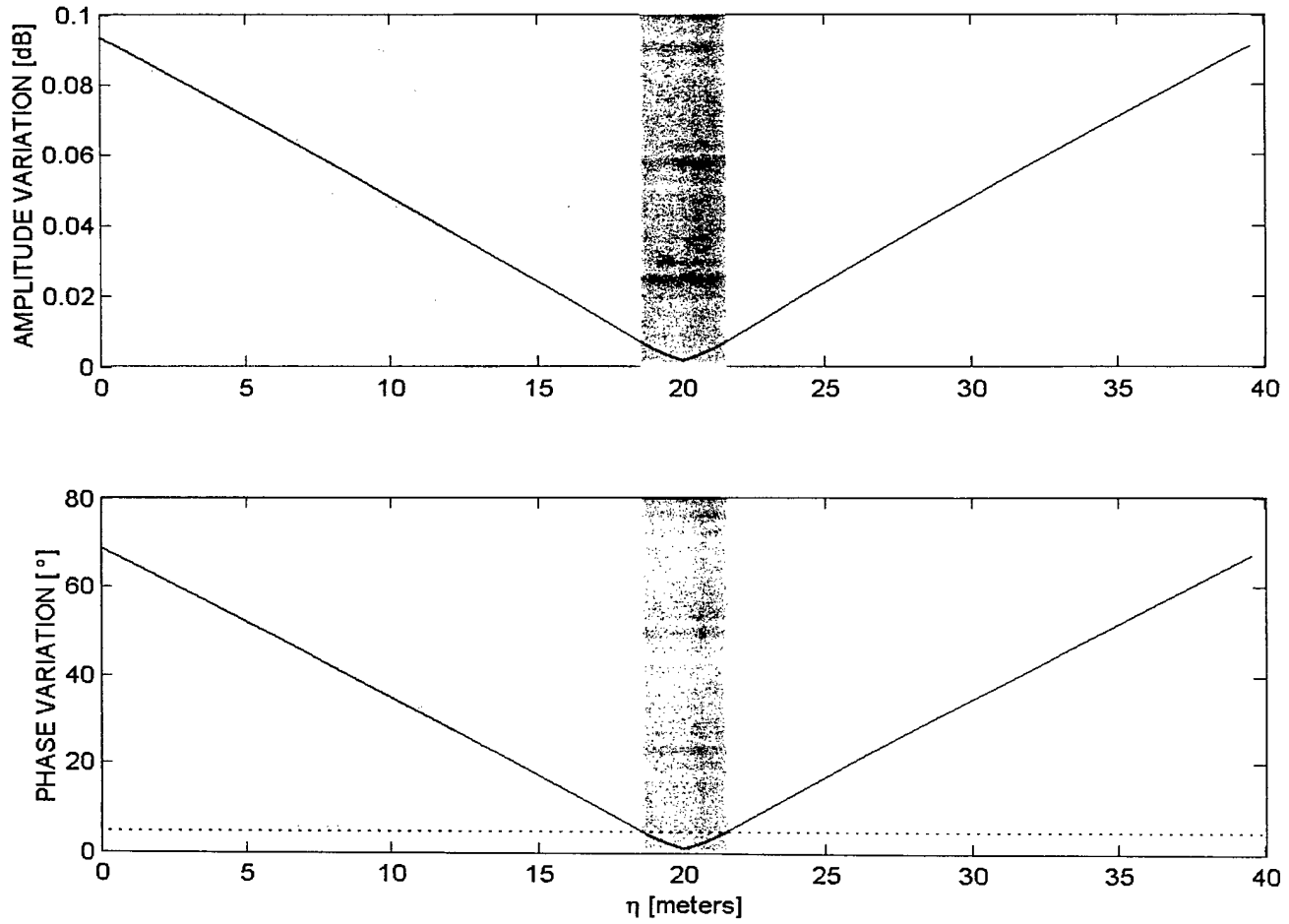

Figure 3: Quiet-zone amplitude and phase variation vs. transmit antenna height η. Quiet-zone center Q_c = (104.5, 20) and diameter D_q = 3 m. No ground reflection (i.e., $\varepsilon_2 = \varepsilon_0$).

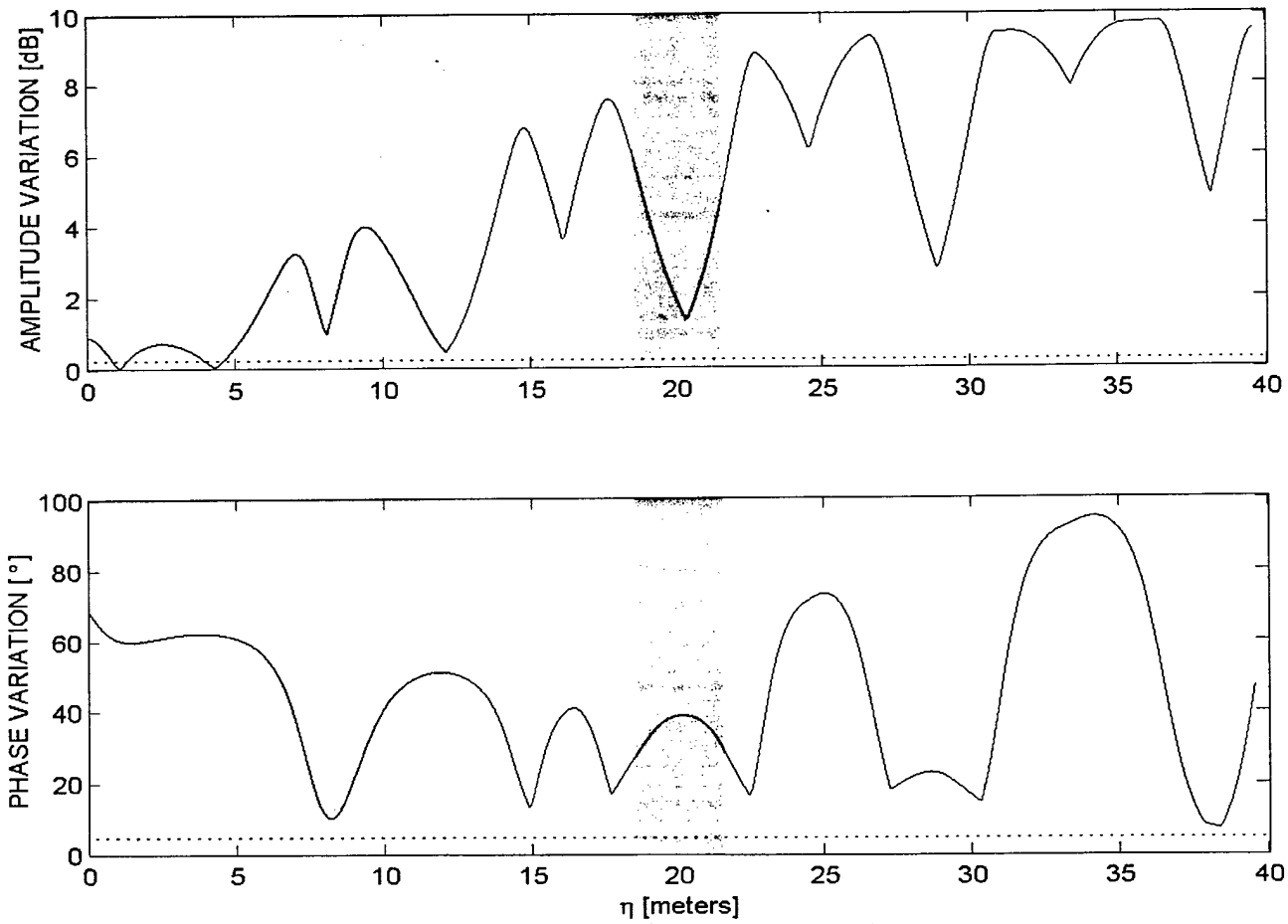

Figure 4: Quiet-zone amplitude and phase variation vs. transmit antenna height η. Quiet-zone center Q_c = (104.5, 20) and diameter D_q = 3 m. Ground reflection corresponding to water (i.e., $\varepsilon_2 = 88\varepsilon_0$).

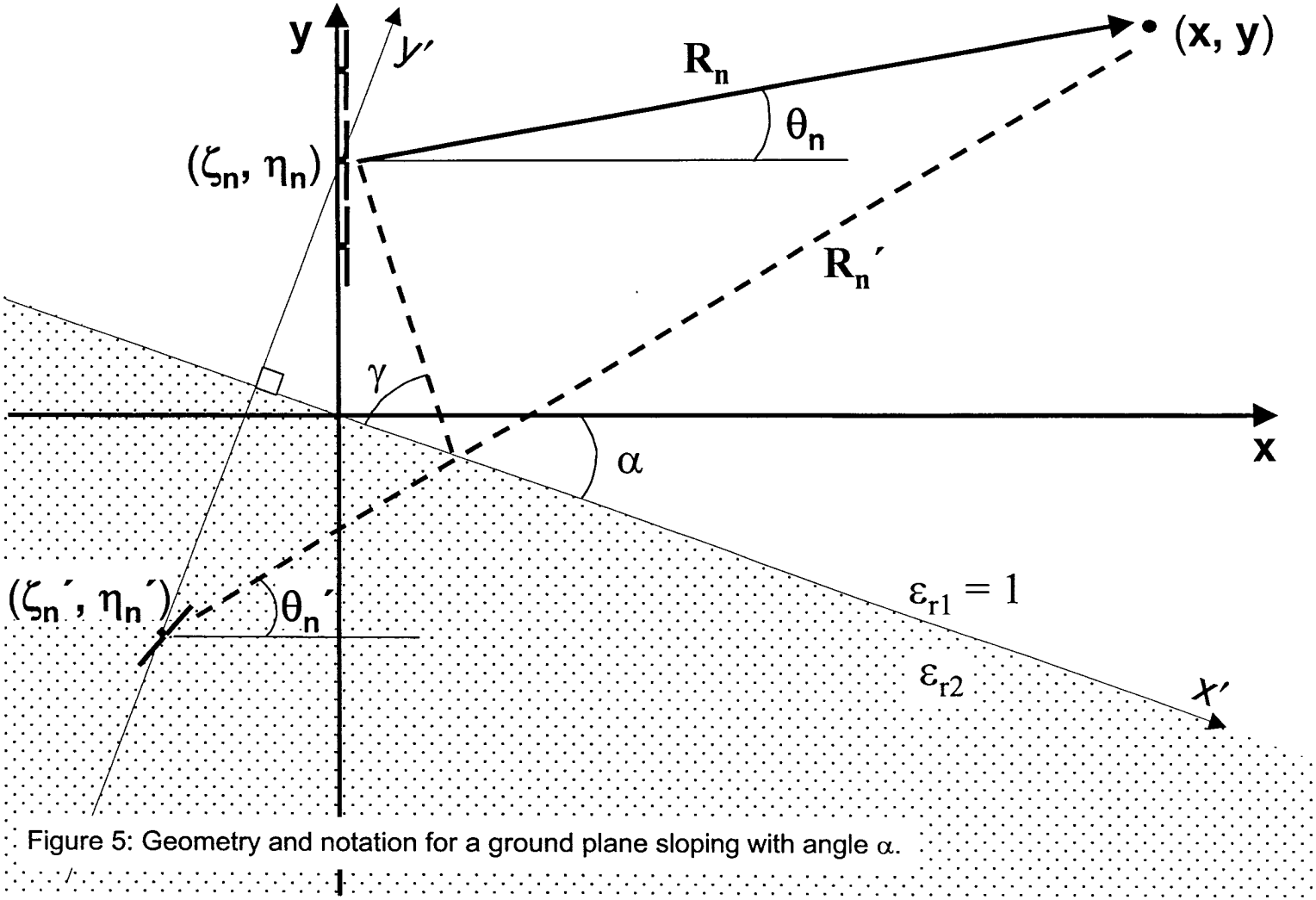

Figure 5: Geometry and notation for a ground plane sloping with angle α.

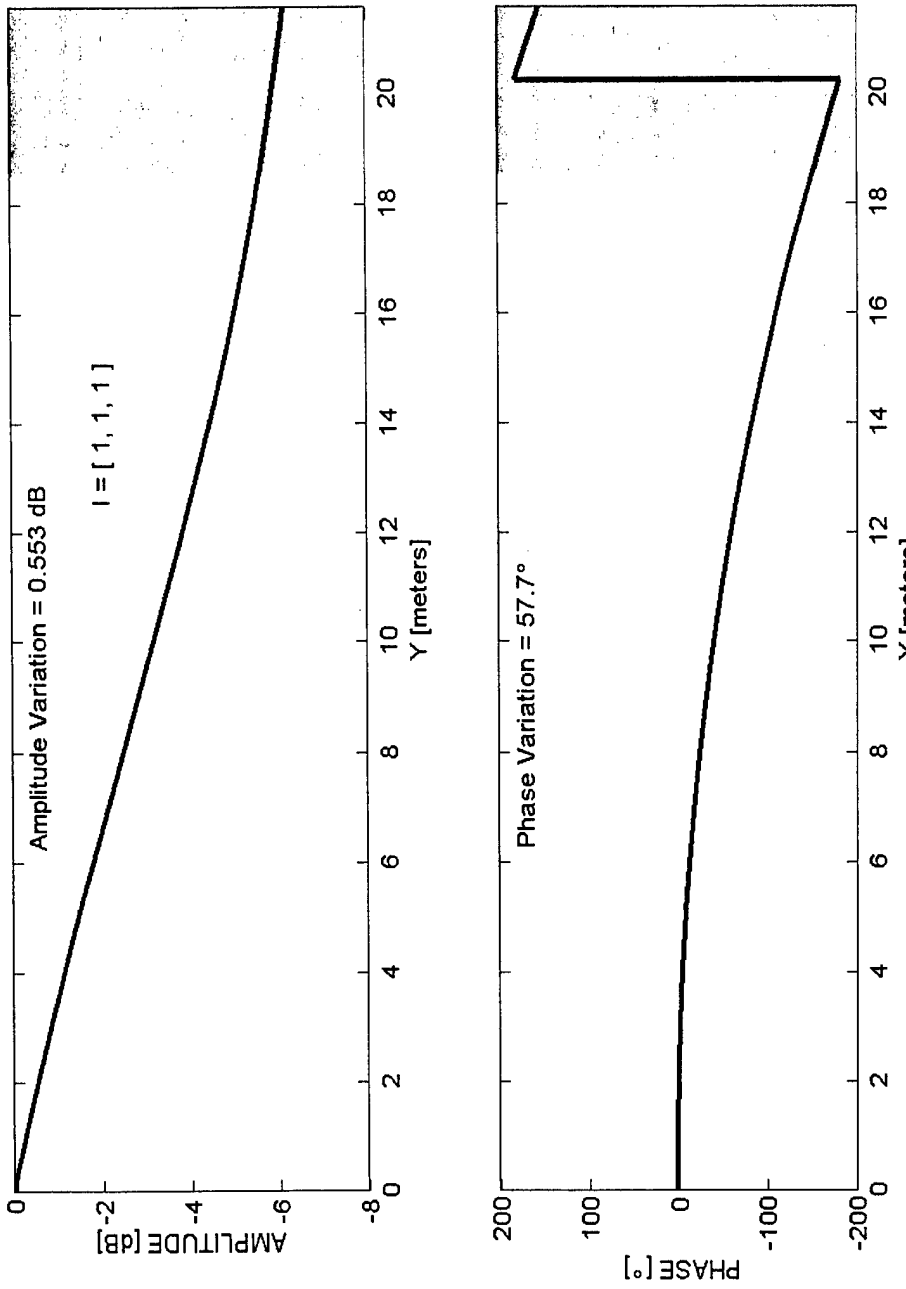

Figure 6: Normalized field vs. the height over the ground of a uniform 3-element transmit array (R = 104.5 m, ε_{2r} = 9 – 3i).

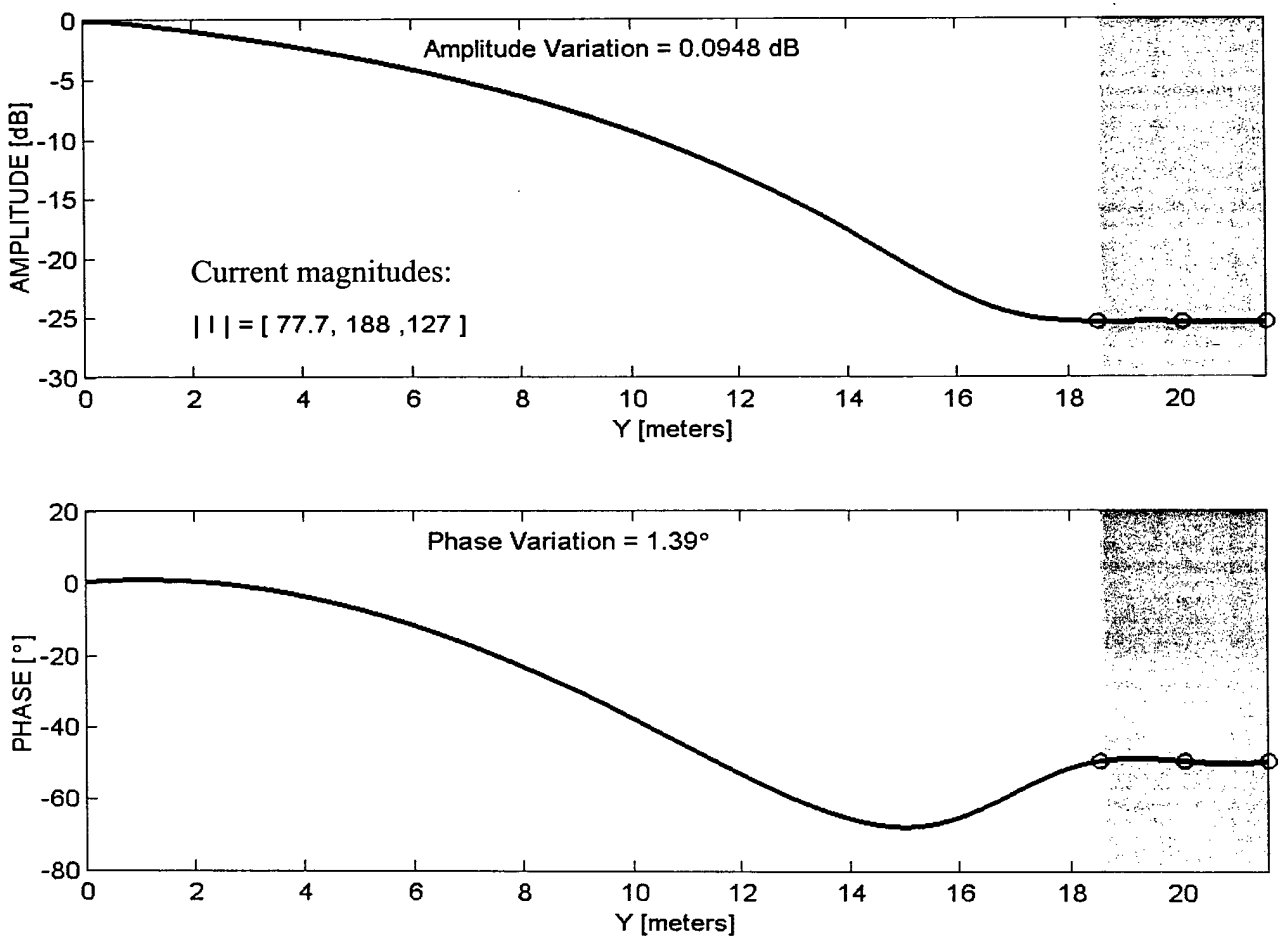

Figure 7: Normalized field vs. the height over the ground of a 3-element transmit array with synthesized excitations (R = 104.5 m, ε_{2r} = 9 –3i).

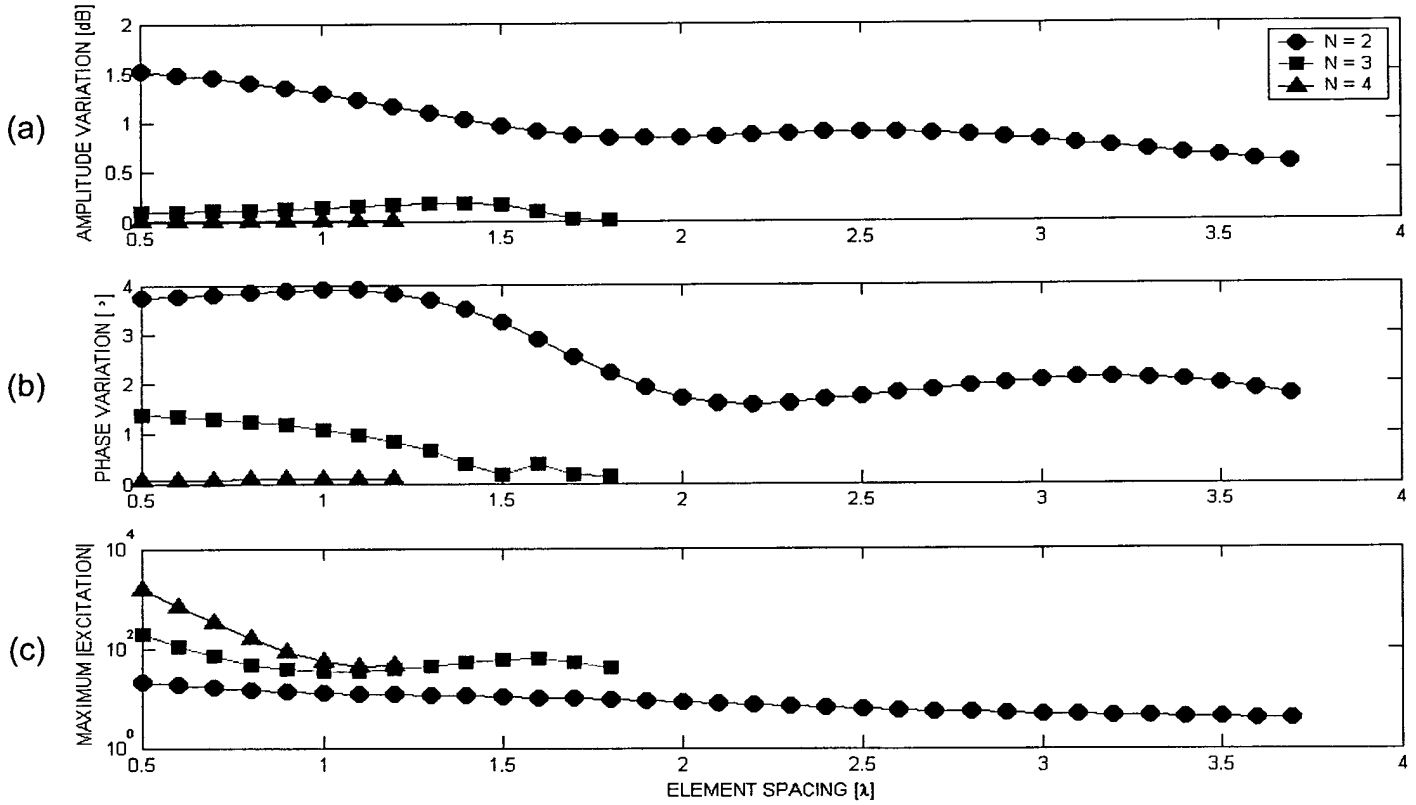

Figure 8: Quiet-zone center is at a greater height than transmit array center ($R = 104.5$ m, $\varepsilon_{2r} = 9 - 3i$, $D_q = 3$ m, $Q_C = 20$ m).
(a & b): Quiet-zone amplitude and phase variation as a function of transmit array element spacing and number of array elements, N.
(c): Maximum magnitude of synthesized array element excitations.

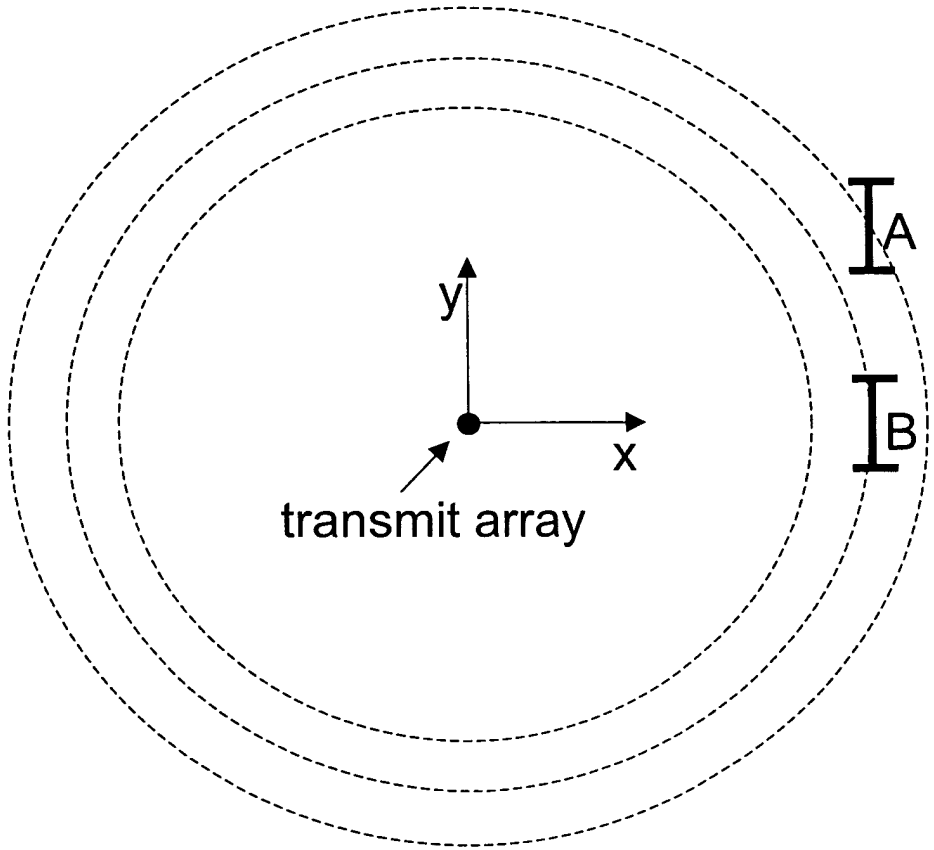

Figure 9: Quiet-zone location A inherently leads to a phase variation that is difficult to suppress. Location B naturally leads to a relatively flat phase.

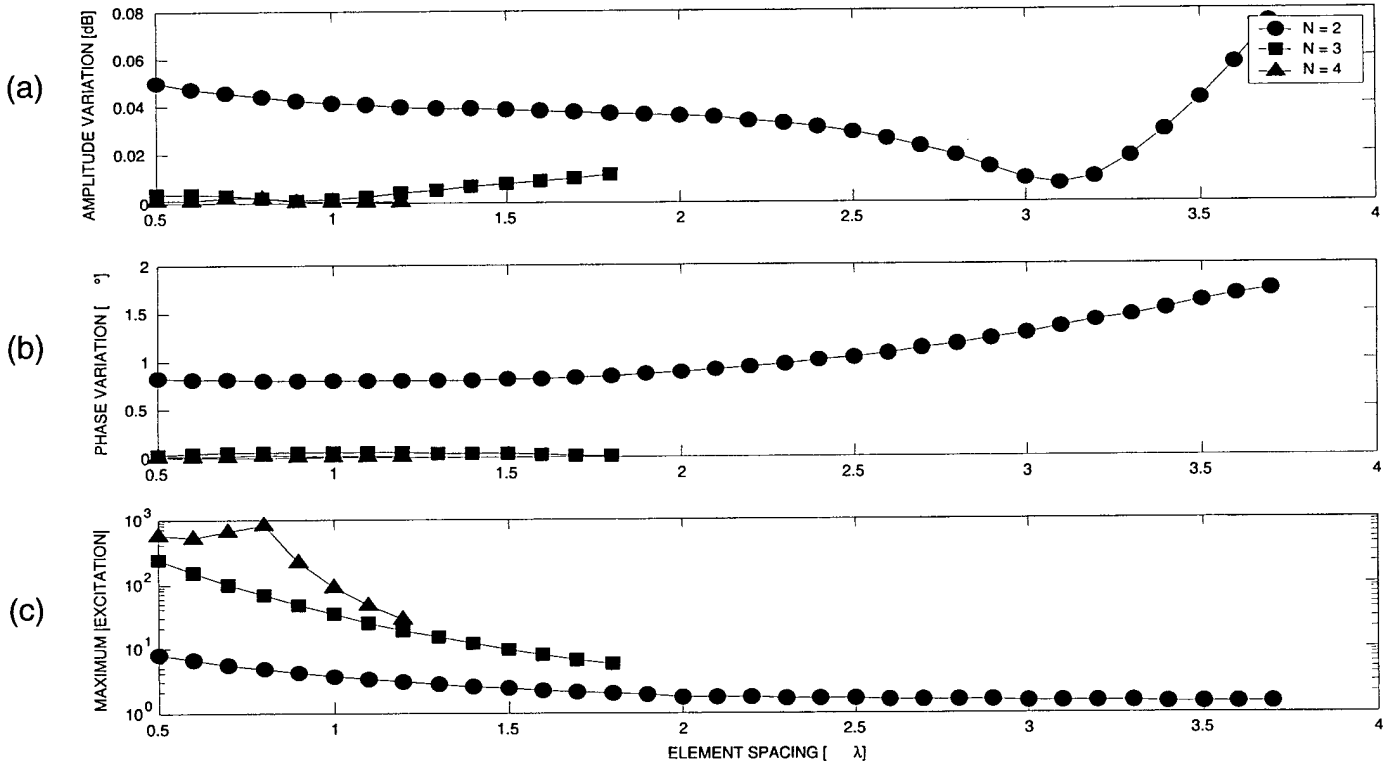

Figure 10: Quiet-zone center aligned with transmit array center
($R = 104.5$ m, $\varepsilon_{2r} = 9 - 3i$, $D_q = 3$ m).
(a & b): Quiet-zone amplitude and phase variation as a function of transmit array element spacing and number of array elements, N.
(c): Maximum magnitude of synthesized array element excitations.

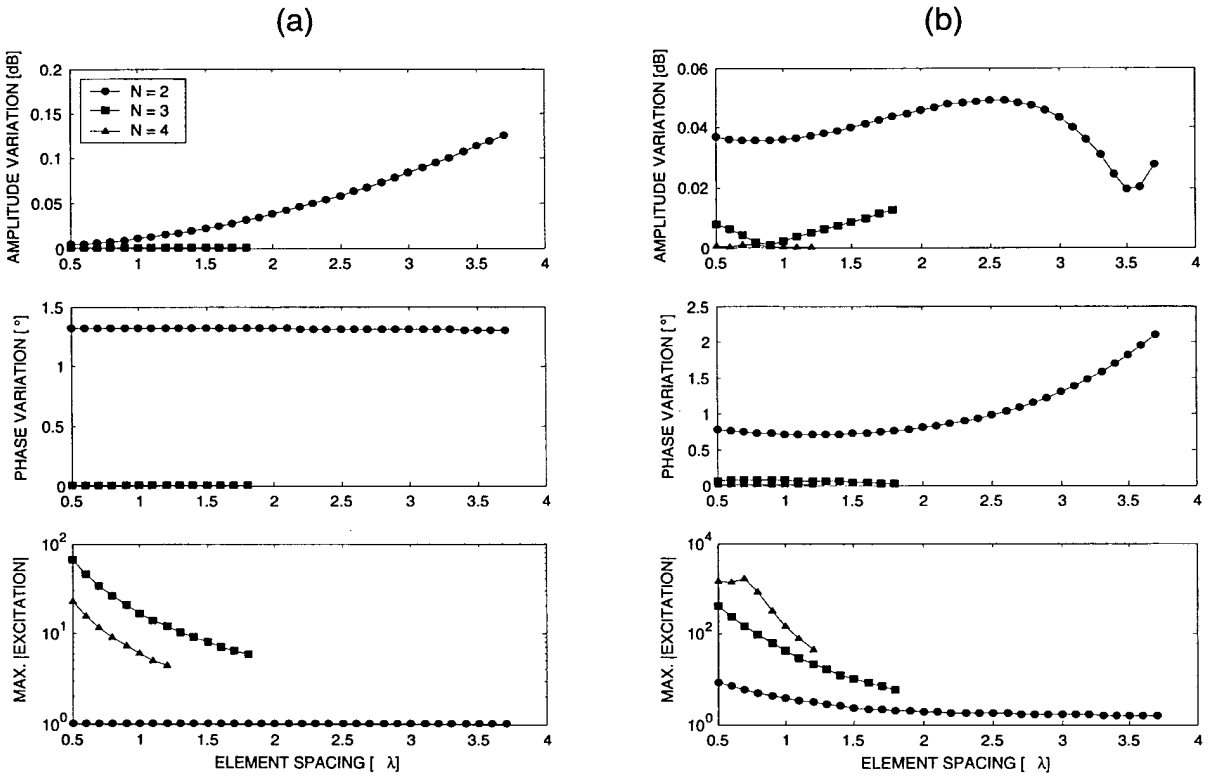

Figure 11 (a & b): Quiet-zone amplitude/phase variation and maximum magnitude of synthesized array element excitations as a function of number of array elements, N, and element spacing.
Quiet-zone center aligned with transmit array center (R = 104.5 m, D_q = 3 m).

(a): $\varepsilon_{2r} = 1$

(b): $\varepsilon_{2r} = 3 - 0.5i$

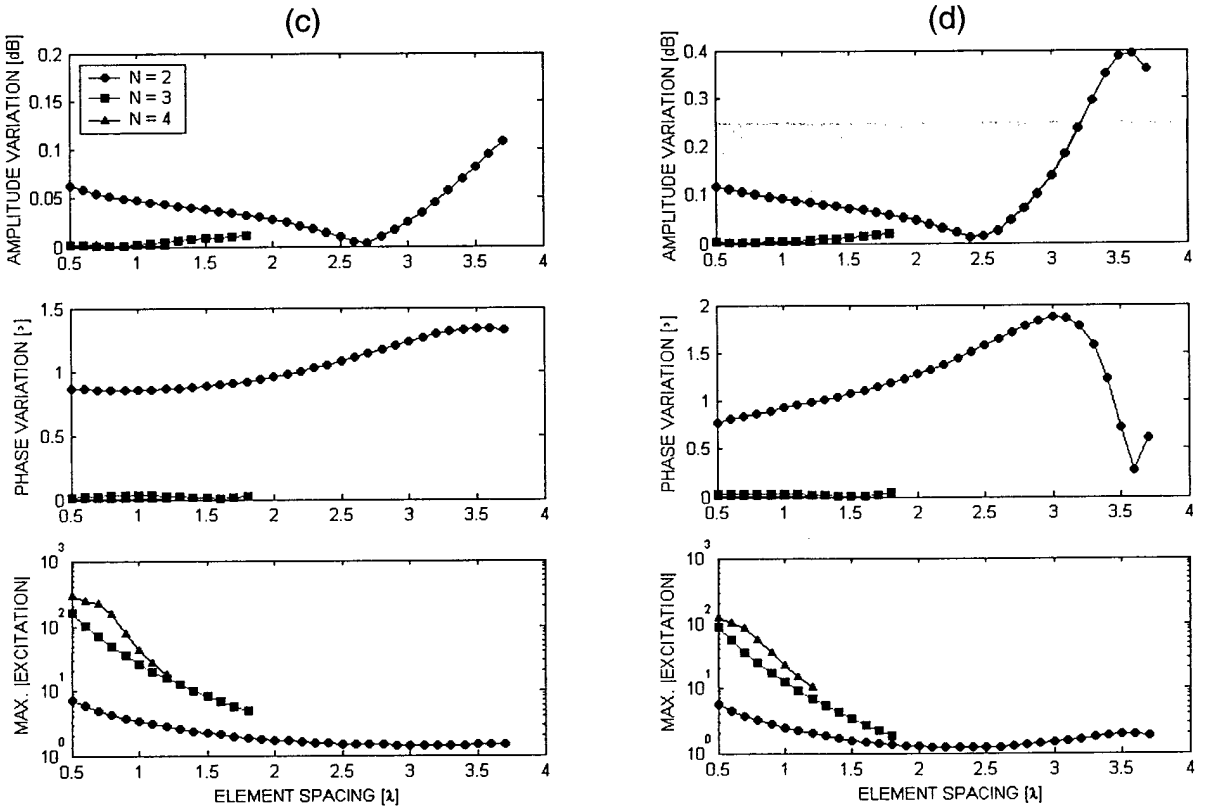

Figure 11 (c & d): Quiet-zone amplitude/phase variation and maximum magnitude of synthesized array element excitations as a function of number of array elements, N, and element spacing.
Quiet-zone center aligned with transmit array center (R = 104.5 m, D_q = 3 m).

(c): $\varepsilon_{2r} = 16 - 7.7i$

(d): $\varepsilon_{2r} = 88$

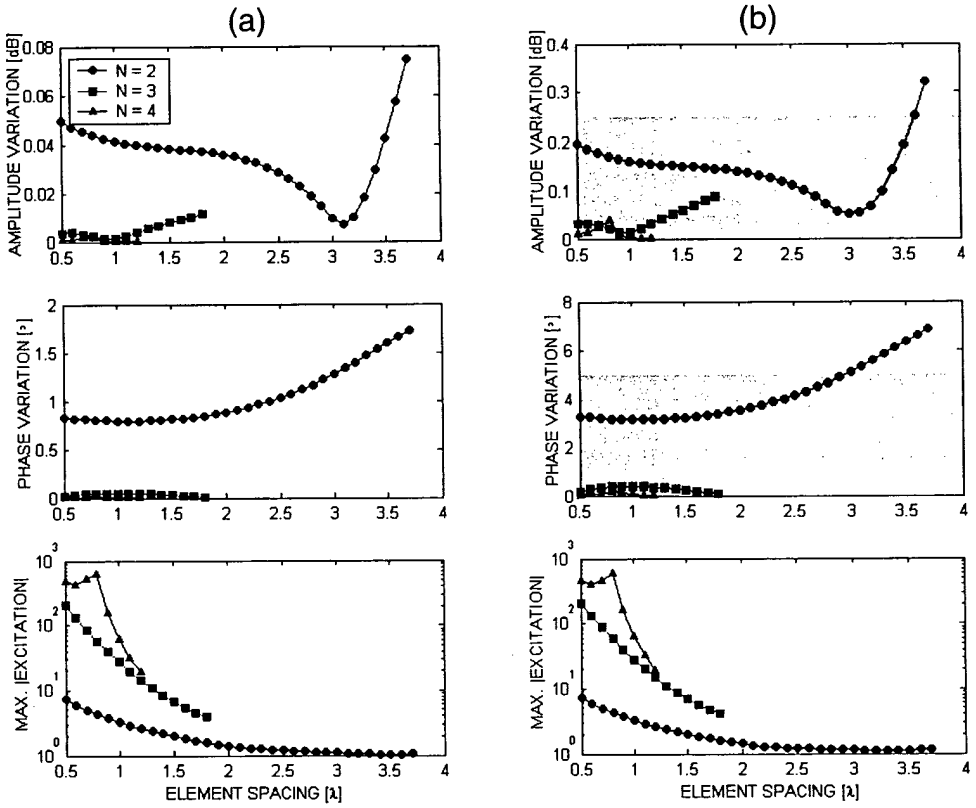

Figure 12 (a & b): Quiet-zone amplitude/phase variation and maximum magnitude of synthesized array element excitations as a function of number of array elements, N, and element spacing.
Quiet-zone center aligned with transmit array center (R = 104.5 m, $\varepsilon_{2r} = 9 - 3i$).

(a): $D_q = 10$ ft.

(b): $D_q = 20$ ft.

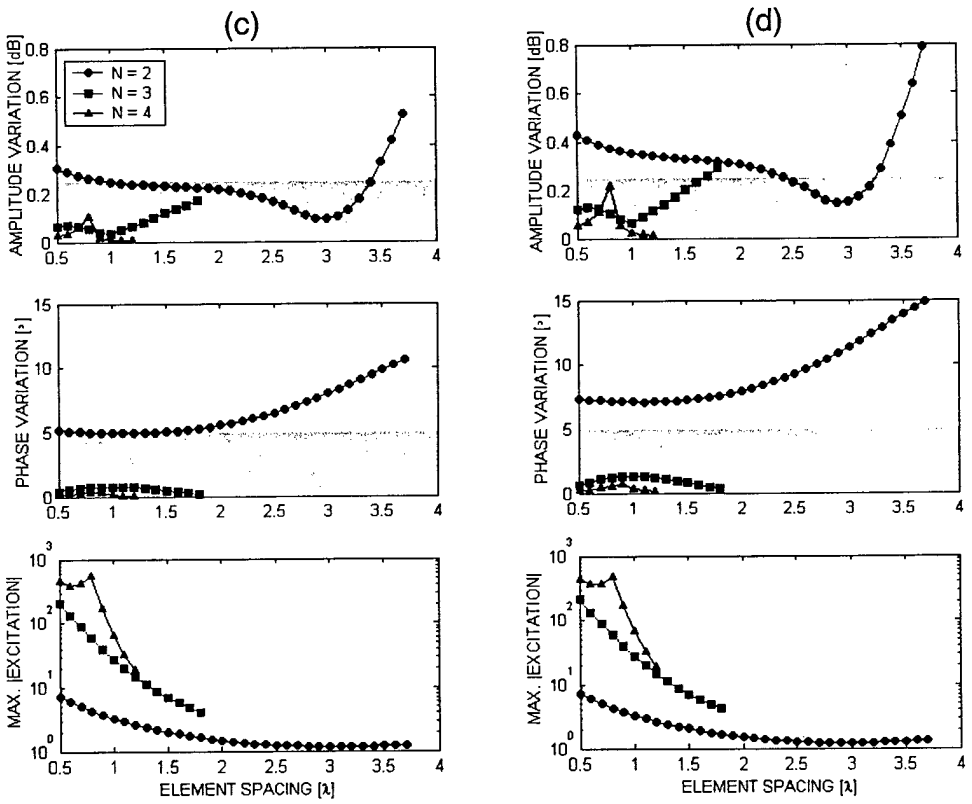

Figure 12 (c & d): Quiet-zone amplitude/phase variation and maximum magnitude of synthesized array element excitations as a function of number of array elements, N, and element spacing.
Quiet-zone center aligned with transmit array center (R = 104.5 m, $\varepsilon_{2r} = 9 - 3i$).

(c): $D_q = 25$ ft.

(d): $D_q = 30$ ft.

CONFORMAL ARRAY CONTROL USING DIGITAL BEAMFORMING

David Curtis, Michelle Champion, Boris Tomasic, Harvey Tobin, Ryan Thomas,
Scott Santarelli, Hans Steyskal, Jim Kenney, Ed Martin, Joe Tenbarge

Air Force Research Laboratory
Sensors Directorate
Antenna Technology Branch, AFRL/SNHA
80 Scott Circle, Hanscom AFB
01731-2909

Abstract

Conformal phased array antennas present unique control challenges due to their curvature. In this paper, we present methods used to control the array radiation patterns of a conformal belt-like array that wraps completely around the cross-section of an aircraft wing from leading edge to trailing edge, and back. The cross-sectional shape of this wing is significant to ongoing programs within the Air Force because it has been designated as the representative airfoil for the Air Force Research Laboratory's *SensorCraft* air vehicle concept. The conformal array designed for this airfoil contains 116 C-band microstrip patch elements, it is receive-only, and it is capable of scanning 360° in elevation. While scanning is currently accomplished in only one plane, the array is canonical in the sense that it represents the single plane scanning case of a wing completely covered with array elements. Digital beamforming is used to control the array patterns because conventional constrained feed networks do not satisfy path length equivalence conditions for this unusually shaped array, and because multiple beams and adaptive nulling will eventually be implemented in this prototype array. Measurement of the resulting array patterns is a three step process involving the measurement of each element antenna pattern, in situ, followed by the application of a new multi-sector calibration technique to remove channel mismatches around the wing, and finally, the array patterns are formed using array pattern synthesis techniques based on the method of alternating projections.

1.0 Introduction

In this paper, we present methods used to design a conformal belt-like array that wraps completely around the cross-section of an aircraft wing. The array is a single ring, comprised of 116 linearly-polarized microstrip patch antenna elements, which wraps above the wing from the leading edge to the trailing edge, and below the wing, from the trailing edge to the leading edge. Methods and results are presented for the design and first-order theoretical analysis of this array and its elements. An experimental prototype of this array has been fabricated at C-band. At the time this paper was written, out team was in the process of measuring the radiation patterns for each of the elements in the array, but that phase of the experiment had not yet been completed.

Conformal arrays of this type are of considerable interest for military applications, and therefore, they must operate in hostile electromagnetic environments. Simultaneous multiple

beams and adaptive nulling are functional requirements that will eventually be demonstrated with this experimental conformal array. We have implemented digital beamforming (DBF) [1], [2] in hardware, as a means to generate and control the array's radiation patterns. In this paper, we describe the performance of the DBF hardware channels, the data acquisition process, and the benefit of using DBF to selectively activate only portions of the array to achieve improved array performance. Also presented, are methods for conformal array calibration and conformal array pattern synthesis. Once the complex-valued element patterns have been measured for every element in the array, the element pattern data will be processed using the conformal calibration and array pattern synthesis methods, described herein, to produce far field array patterns, which we plan to present in a future paper.

2.0 Overview of the Experiment

The objectives of this experiment are three-fold. First, we set out to characterize the electromagnetic behavior of a 2-D conformal array with significantly variable rates of curvature. It was expected that this would result in the theoretical prediction and experimental observation of a number of conformal array effects, such as non-uniform array gain due to variable projected aperture, endfire behavior from the edges of selectively activated portions of the array, and significantly dissimilar element patterns due to variations in mutual coupling as a function of array curvature. Second, we sought to develop suitable methods to calibrate the conformal array to remove the effects of mutual coupling and to minimize channel-to-channel mismatches in the DBF receivers and digital hardware. Third, we aimed to develop DBF algorithms for conformal array pattern control which optimize the array pattern characteristics as a function of selective element activation and scan angle.

2.1 Antenna Design Process

As described in detail in Section 3, the microstrip patch antenna elements used in this experiment are narrowband, linearly polarized (E-plane) elements, designed to have peak radiation performance at about 5.45 GHz. The elements were designed using a commercial method-of-moments electromagnetic solver code that computes the impedances and mutual coupling of curved patch elements arranged in an array on a circular cylindrical. The use of this code was an improvement over previous techniques, but it is still an approximation, albeit a better one than earlier planar-element approximation approaches. After an iterative design process that was based on certain performance assumptions and design trade-offs, the elements were designed to have identical dimensions and periodic spacing along the surface of curvature. Once the element locations were determined, the array design was considered complete and the antenna analysis was initiated. At the same time, the prototype wing went into production at our local machine shop, and other members of the team initiated their work on developing methods and algorithms for conformal array calibration and conformal array pattern synthesis.

2.2 Wing Section Fabrication Process

The airfoil studied in this work is significant to ongoing programs within the Air Force. It has been selected as the representative airfoil for the Air Force Research Laboratory's (AFRL) *SensorCraft* air vehicle concept. *SensorCraft* is a "concept car" for high altitude, multi-mission

intelligence, surveillance, and reconnaissance systems of the future. *SensorCraft* serves as a point design for a wide variety of technology development programs conducted by four of AFRL's technical Directorates, including the Sensors, Air Vehicles, Propulsion, and Materials Directorates. The airfoil is designated FX72-MS-150B, and its design data was generously provided by the Air Vehicles Directorate at Wright-Patterson AFB.

In an effort to accurately fabricate a scaled section of the wing, the FX72-MS-150B airfoil geometry data was imported into Autocad-2000, where it was scaled, and spline curves were generated to smoothly fill in the curvature between the known design data points. This was the first step that introduced a degree of approximation to the design effort, because the actual shape of the wing was locally approximated using small arcs with derivative matching at the endpoints of consecutive arcs. The spline data was then transferred to our machine shop at Hanscom AFB, which is operated by AFRL's Space Vehicles Directorate. There, machinists imported the spline data into a large "Hurco" numerically controlled milling machine. Four identical wings ribs were produced on the milling machine from 0.5 inch thick aluminum plate stock. These were welded to 1 x 1 inch square tubular aluminum crossbars, which formed the framework of the wing. A machine-rolled aluminum skin, 0.032 inch thick, was tightly wrapped around the wing framework and riveted into place, forming the completed wing section, which is shown in Fig 1.

2.3 Antenna Analytical Processes

Two distinctly different analytical approaches were adopted in our attempt to develop an accurate 2-D electromagnetic model of the radiation characteristics of the conformal wing array, and to control and optimize its array radiation patterns. The first method, which is briefly described in Section 4, relies on a sound electromagnetic theoretical development that uses the mutual coupling and active impedances of the elements to form a scattering matrix relation. This is used to compute a set of element excitations that include mutual coupling effects. The excitations are then applied to either calculated or measured element patterns to compute the far array field pattern. Using this method, predicted far field array patterns were calculated for a few representative cases using only the first 10 to 15 elements above the leading edge of the wing.

The second analytical method, described in Section 7, is an iterative approach based on the method of alternating projections. This technique uses complex-valued element patterns to iteratively compute a set of element excitations and synthesize a far field pattern that satisfies a set of spatial constraints in the shape of the desired far field pattern. In this paper, far field array patterns were computed using this method for a few representative cases where only the first 10 to 15 elements above the leading edge of the wing were active.

By virtue of its far field constraints, the second technique is shown to generate excitations that defeat some of the undesired end-fire effects that appear to result from the endmost elements of selectively activated groups of elements in the conformal array. Such effects were observed using both analytical techniques. Complete detailed discussions of these two methods would require separate papers for each, and therefore, will not be given here. It is anticipated that papers describing these methods will be written in the near future.

2.4 Antenna Measurement Process

Experimental measurement of the far field array patterns is a three step process involving the measurement of each complex-valued element pattern in the full array environment, followed by the application of a new conformal array calibration, and finally, application of an appropriate far field analytical method, such as the two described above. The conformal calibration method is designed to remove RF and digital channel mismatches that vary slowly over time. Although the method of alternating projections is shown to compute reasonable array patterns without any prior array calibration, other digital beamforming algorithms will be implemented and tested on this conformal DBF array testbed which may require calibrated channels. The process of taking accurate complex-valued element patterns for 116 elements is a challenging task. In section 5, we describe the RF and digital hardware, and briefly, the impact of channel-to-channel mismatch on the array patterns.

3.0 Antenna Element and Array Design

The design of a microstrip antenna array conformal to the wing of an aircraft presents new and interesting design challenges. The size and complex geometry of the wing does not lend itself to conventional microstrip design, analysis and fabrication techniques, which are generally restricted to small, planar microwave circuits or larger, periodic structures. Since the development of new analysis and fabrication techniques was beyond the scope of this project, new methods of applying conventional techniques, typically used to design and build large conformal arrays, had to be found and applied to this conformal wing array.

3.1 Geometric Considerations

While there are many commercially available CAD programs that can be used for antenna design and analysis, most of these are method-of-moments techniques that apply only to "2.5-D" multi-layer planar geometries. Finite element codes can be used to analyze small 3-D antennas or larger periodic arrays, but computational requirements restrict their use in analyzing large, irregular structures such as the wing array. A newly developed method-of-moments code can be used to analyze microstrip patch arrays on cylindrically curved structures, but methods do not yet exist for analyzing large arrays on large, arbitrarily curved surfaces. Without developing new techniques, the wing shape must be approximated by geometries that can be analyzed with existing codes. Since the wing was fabricated by approximating the wing spline with small arcs, a cylindrical method-of-moments approach was selected for the design of the array.

The large size and irregular shape of the wing also presents problems for the array fabrication process, with a resulting impact on antenna design. Typical microstrip arrays are etched onto planar substrates using printed circuit techniques. Thicker substrates are desirable for both ease in processing and, more importantly, for antenna performance. The bandwidth of microstrip patch antennas is inherently narrow and decreases rapidly with a reduction in substrate thickness. Ideally, a conformal array would be constructed by molding a thicker microwave substrate into the shape of the wing and depositing the copper circuitry onto the substrate's surface. Unfortunately, techniques for processing microwave circuits on large, irregularly shaped surfaces do not yet exist. Therefore, the array had to be fabricated on thin,

planar substrates that could be folded around the sheet metal structure of the wing after the circuit was etched. In order to wrap around the tight curvature at the leading edge of the wing, thin substrates must be used, thus limiting the bandwidth of the antenna. Although a multi-layer antenna could be used to enhance the bandwidth, we determined that a single layer design was acceptable for our initial prototype demonstration.

3.2 Conformal Microstrip Patch Design

In this experiment, the primary design requirement for the radiating element was that it must maintain a low profile, conformal to the wing contour. The microstrip patch was a logical choice for such an antenna element. A single layer, microstrip-fed patch element was selected for the initial demonstration to simplify the modeling and fabrication of the array. A multi-layer, aperture-coupled patch would be a good candidate for improved performance in future designs.

The conventional approach to designing a patch radiator on a curved surface is to use a planar method-of-moments technique for an initial design and then do an iterative "build and test" process until the radiator has the desired properties. For highly curved surfaces, the antenna characteristics can be significantly different from the planar case and many iterations may be required to get a good design. Although not ideal, this works reasonably well for small antennas on a surface with constant curvature, such as a circular cylinder. However, for the wing antenna, the radius of curvature varies considerably across its surface, from less than half a wavelength at the leading edge of the wing to more than 1000 wavelengths on the flattest portions of the wing. Since each patch has a different local radius of curvature, they will each have different radiation and impedance properties. Clearly, an iterative process for each of the 116 radiating elements on the wing is not feasible, so improved analytical techniques are required.

A newly developed electromagnetic simulation computer code, CyMPA (Cylindrical Microstrip Patch Analysis), can be used to rigorously analyze microstrip patch arrays that reside on circularly cylindrical structures. The CyMPA program was developed by the University of Zagreb under the Window-on-Science program, [3]. The code has been tested by SNH on a variety of cylindrical antenna arrays. As shown in Fig. 2, the program predicts the variation of antenna input impedance as a function of changing radius of curvature. This variation in input impedance is a critical factor in the design of the radiating element for the wing array. For best performance of the array, the radius of curvature at each patch along the array should be individually calculated and the patch should be matched to the impedance for that radius of curvature. However, this complicates the fabrication process, since each patch would have different dimensions and a different feed line impedance. For simplicity in fabrication, it is better to use a single patch and a single feed design for all elements in the array. However, given the narrow bandwidth of the elements (~1%), variations in the input impedance could have a negative impact on overall array performance, so a careful design was needed. The element was designed and optimized for a single moderate radius of curvature and CyMPA was used to calculate the performance of the element design at the lowest and highest radii of curvature on the wing. The final element design was selected to ensure that element performance remained acceptable for all locations on the wing. The element design and return loss measurements are depicted in Fig. 3.

3.3 Array Design and Simulation

Although a single patch design is a reasonable starting point for the array design, the final design must be done with the patch in the array environment, so the effects of mutual coupling between elements are included. This aspect of the design is considerably more complicated that the individual element design. While the local curvature at an individual element location can be considered a reasonably close approximation to the curvature of a circular cylinder, the relationship to neighboring elements varies considerably from the cylindrical shape, particularly in areas where the curvature is rapidly changing. Even where the nearest neighboring elements maintain a reasonably close approximation to the cylinder, the farther out elements generally do not approximate as well. This makes it difficult to accurately model the effects of mutual coupling in the array.

Since polarization was not a critical parameter in the array design, the array configuration was chosen to minimize mutual coupling between the elements. Although an H-plane configuration typically gives lower mutual coupling, in this case the patch dimensions and array spacing were such that the E-plane configuration gave better performance. Since an "exact" solution for the mutual coupling could not be obtained, the CyMPA program was run for different radii of curvature and with different numbers of neighboring elements on the cylinder. These results were used to determine a final element design that would give acceptable performance across the wing surface. The layout of a single panel in the array is shown in Fig. 3.

There are several limitations to the CyMPA program which may have an impact on the final array performance. One limitation is related to the size of the cylinder that can be analyzed. As the cylinder radius increases, the number of modes required in the analysis increases, and this increases the computational effort required to run the program. For cylinder radii greater than 20 wavelengths, the computational load is significant and the results become a close approximation to the planar case, with little variation as the radius increases. Therefore, for the wing analysis, any elements with a radius of curvature greater than ~18 wavelengths were considered to be essentially identical, with a maximum radius of curvature of 100 cm used in the final array analysis. A potentially more significant limitation to the CyMPA analysis occurs on the rear, bottom surface of the wing. Here the surface curves slightly inward, so that the radiating elements appear to be on the inside surface of the cylinder, a configuration which cannot be analyzed by the CyMPA program. However, since the surface in these locations is very close to planar, these surfaces were treated as a large radius cylindrical surface with the maximum radius of 100 cm. The effect of these limitations to the CyMPA program will only be known when the complete array is measured.

4.0 Array Pattern Prediction

In this section, an electromagnetic analysis is developed, to first-order approximation, for the far field pattern performance of the conformal wing array. It is based on the use of predicted element patterns which were calculated using the CyMPA method-of-moments code that treats conformal microstrip patch antenna elements as if they reside on a circular cylinder. The code calculates mutual coupling between an array of elements on the cylinder. The mutual coupling results are used here to approximate the mutual coupling that exists between the curved patch

elements that reside on the wing surface. The approximation lies in the fact that the wing surface is not a circular cylinder, but is a surface of variable curvature.

4.1 Theory

As previously described, a conformal ring array of 116 microstrip patches was wrapped around the wing , as shown in Fig. 4. We define a global coordinate system (x, y, z) with the origin of the coordinate system located at the center of mass of the wing. We then define a local coordinate system (X_n, Y_n, Z_n), whose origin is centered at the phase center of the n^{th} element. With respect to the global coordinates, the elements are located at $\mathbf{r}'_n$. The observation point is defined by $\mathbf{r} = \mathbf{r}_o r$, where $\mathbf{r}_o$ is the unit vector in observation direction. Because the wing geometry can cause creeping waves, and since many of the elements may face away from a particular scan angle of interest, we choose to selectively activate, only a sector of N elements at any time to form the far field array pattern. The excitation coefficients, c_n , which represent the total voltages at the element ports are

$$c_n = a_n + b_n = | c_n | e^{j\delta_n} \tag{1}$$

where a_n and b_n are the voltages of the incident and reflected signals at the array element terminals, and n = 1, ... , N denotes the element index. Each element is characterized by its complex element field pattern

$$e_n(\theta, \phi) = | e_n(\theta,\phi) | e^{j\psi_n(\theta,\phi)} \tag{2}$$

where the angles θ and ϕ define the far field observation point in spherical coordinates.

The gain patterns of the conformal array with variable curvature were computed taking into account, in the first order, the array curvature and mutual coupling effects. This is done by approximating the local array geometry with a corresponding uniform circularly cylindrical array. The conformal wing array gain is computed from

$$G(\theta,\phi) = 4\pi \frac{Z_c}{\zeta_o} \frac{\left|\sum_{n=1}^{N} c(\theta_o,\phi_o)\mathbf{e}_n(\theta,\phi)e^{jk\mathbf{r}'_n \bullet \mathbf{r}_o}\right|}{\sum_{n=1}^{N}|a_n|^2} \tag{3}$$

where $\mathbf{e}_n$ are the field element patterns of the uniform circularly cylindrical array with both radius and array parameters chosen to correspond to the local geometry of the conformal wing array at element n. In (3), Z_c is the characteristic impedance of the element feed lines, and ζ_0 = 376.7 Ω. To produce a beam in the ($\theta_0 = \pi/2$, ϕ_0) direction, the phase of c_n must equal

$$\delta_n = -k\mathbf{r}'_n \cdot \mathbf{r}_o - \psi_n(\theta_o,\phi_o) \tag{4}$$

The magnitudes of the excitation coefficients | c_n | are variables that depend on the requirements for the far field array patterns. For example, if all | c_n | are chosen to equal unity, then for large radii of curvature, the results are similar to the planar array case, where the peak sidelobe level is

approximately 13 dB below the peak of the main beam. If a specific radiation pattern is desired, then the $|c_n|$ coefficients may be determined using any array pattern synthesis techniques for curved arrays. One method that we investigated is the method of alternative projections, which we discuss for the case of this conformal wing array in Section 7.

There is, however, one special set of $|c_n|$ coefficients which gives maximum gain. Namely, it is well known that in the planar arrays, maximum gain is achieved when the array elements are fed with signals of equal amplitude and uniform phase progression. By analogy, the maximum gain of a non-uniform conformal array can be obtained if the array excitation coefficients are proportional to the complex element (field) pattern values in the main beam direction, and have a phase factor that accounts for the different element propagation paths to a common phase front [4].

With a known desired voltage excitation column vector $[c] = [c_1, c_2, \ldots, c_n, \ldots c_N]$, we can determine the required incident signal voltage column vector $[a] = [a_1, a_2, \ldots, a_n, \ldots a_N]$, that includes mutual coupling effects, using the following matrix equation,

$$[a] = ([\mathbf{I}] + [\mathbf{S}])^{-1}[c] \tag{5}$$

where [I] is the identity matrix, and [S] is the scattering matrix of the wing array. The scattering matrix was obtained by approximation using the CyMPA code for a circularly cylindrical array of microstrip patches. Thus, in the computation of the wing array's far-field, mutual coupling effects are taken into account, in an approximate sense, by inserting the theoretically predicted active element patterns of a circularly cylindrical array into the conformal wing array environment. The same is true for the calculations of the required excitations, which are performed using the scattering matrix of the selectively activated sector of the wing array. Note that once the complete set of 116 complex-valued element patterns has been measured, this analysis will be used with the measured data, and the accuracy of this analysis should improve since the element patterns would no longer be approximate.

4.2 Results

As an illustrative example, we consider the case when only the first ten array elements are active, while all other array elements are terminated with 50 Ω matched loads. The selective activation of elements 1 - 10, which are located on the top of the wing near the leading edge, is illustrated by the darker dots in Fig. 5. The elements are periodic along the arc-length of the wing surface, and they are excited with unity amplitude and phased according to (4) to produce a beam in the forward direction ($\phi_0 = 180°$). Thus, $|c_n| = 1$, and $n = 1, 2, \ldots, N = 10$, where $n = 1$ corresponds to the leading edge element.

Active VSWR is shown in Fig. 6, where it may be seen that half of the array elements near the leading edge are very well matched while the elements further from the leading edge are not matched as well, but still have VSWR below 2:1. Fig. 8 is an enlarged scale version of Fig. 7, which show the magnitudes of the required incident voltages $|a_n|$. It can be seen from Fig. 8, that $|a_n|$ are not equal, and this is because of mutual coupling. Furthermore, note that even if a few of the elements in the passive region $(11 \le n \le 15)$ are not selected to be active radiators, they

too must be fed with proper a_n in order to maintain $| c_n | = 1$ for n = 1 to n = 10, and $| c_n | = 0$ for the rest of the array elements in the wing array. In a practical array design, where an amplitude taper is usually imposed across the aperture, the edge elements are weakly excited, and for all practical purposes, the requirement just described may be neglected.

Fig. 9 and Fig. 10 show the element magnitude and phase patterns, respectively, for the leading edge element, $n = 1$, and for the $n = 7$ and $n = 10$ elements. Their respective local radii of curvature are: $R_1 = 0.05$ m, $R_7 = 0.62$ m and $R_{10} = 0.93$ m. The significant differences in the element magnitude patterns, as well as the difference in the element phase patterns, is attributed to the different local radii of curvature. In planar array designs, it is desirable to have minimum variation in element pattern magnitude, but the element phase pattern variation is irrelevant as a function of angle, as long as they are the variation is the same for all elements. In a practical conformal array design, even though the smooth and wide element magnitude pattern is desirable, it is crucial to know the element phase pattern $\psi_n(\theta_o,\phi_o)$ for every array element. The reason is that unlike in planar array case, each element in a conformal array sees the observation point from a different angle with respect to its local normal, and consequently the element phase values in direction of the main beam must be known. This is required in order to define the phase of the excitation coefficients δ_n, given by (4), so that all element field contributions constructively add in the same direction. Any element phase pattern error directly translates into an excitation error which results in higher sidelobes.

The array radiation pattern is shown in Fig. 11, where ten leading edge elements are phased to produce a beam in the forward direction ($\theta_0 = \pi/2$, $\phi_0 = \pi$). The peak array gain is 14.89 dB, and the first sidelobe is about 13 below the main beam, as expected. The wide back-lobe in Fig. 11 is typical for conformal arrays and points in the direction tangent to the edge elements which are phased close to the end-fire condition. It can be reduced by tapering the aperture illumination or by simply removing several edge elements. In both cases the array gain will be reduced by one or two dB. Thus, the edges of the selectively activated region of the aperture tend to produce end-fire lobing effects that must be corrected.

Fig. 12 shows the same case, except the element excitations are computed according to maximum gain theorem, i.e., $| c_n | = [g_n(\theta_o = \pi/2, \phi_o)]^{1/2}$, where the g_n are element gain patterns. Note that indeed, the array gain is 0.1 dB higher than in the case of uniform excitation, and the sidelobes are slightly lower. Although such a slight increase in gain is insignificant for practical applications, to observe its occurrence in an array with so few active elements proves that such an excitation can be used to squeeze a fraction of a dB more gain from the conformal array, as well as reduce the sidelobes and produce deeper, more well-defined nulls. Most importantly, these small optimizations of the array pattern were achieved using considerably less input RF power than if a uniform excitation had been applied, and this is especially important in large conformal arrays for airborne and space applications where prime power is at premium.

5.0 DBF System Description

The "DBF System" is an AFRL testbed located in a 40' x 40' x 120' anechoic antenna test chamber at Hanscom AFB. The DBF System, illustrated in Fig 13, consists of the array-under-test, a large multi-axis rotational antenna mount (not shown in the figure), a programmable

antenna mount controller, and microwave frequency sources that supply the DBF receiver local oscillator tones and the anechoic chamber far-field source. The DBF System has 32 independent RF channels. Each channel contains a C-band microwave receiver, a digitizer module, and a 4 GB SCSI hard drive. The 32 pairs of digitizers and SCSI drives are housed in four C-sized VXI plug 'n' play equipment chassis. The SCSI drives have a combined data storage capacity of 128 GB. Each digitizer contains a 23 bit analog-to-digital converter (ADC) that has 16 effective bits of linear digital sensitivity, plus an internal 4 MB RAM data buffer and programmable filtering and sampling control circuits. A Windows NT workstation serves as the DBF System host computer. It controls all of the testbed equipment and the data acquisition and display processes using a custom C++ graphical user interface (GUI) Windows NT software application that was developed in-house using Visual C++ 6.0. The software also displays measured array patterns and both time and frequency domain plots of the digitized channel data, in quasi-real-time, or from stored data files that may be retrieved for post-processing. In the following section, the RF and digital hardware and the data acquisition process are described.

5.1 RF Channel Receiver Hardware

A block diagram of the C-band receiver is shown in Fig. 14. It is a triple-down-conversion design, characterized by three stages of amplification, mixing, and filtering. The receivers have a 500 MHz input tunable bandwidth that ranges from 5.2 to 5.7 GHz, with a center frequency of 5.45 GHz. The output of the receiver has a 2.0 MHz instantaneous signal bandwidth, centered at 2.5 MHz. Inside the receiver, the first stage contains a frequency-agile local oscillator (LO) that can be tuned over a 500 MHz range from 2.975 to 3.475 GHz. This agility is used to selectively demodulate any frequency within the input tunable bandwidth to a fixed first-stage intermediate frequency, $IF_1 = 2.225$ GHz. The second LO operates at a fixed frequency of 2.18 GHz, and produces a fixed second stage $IF_2 = 45$ MHz. The third LO operates at a fixed frequency of 42.5 MHz, and produces the final $IF_3 = 2.5$ MHz. The gains of the amplifiers in the receiver chain are shown in Fig. 14.

5.2 Receiver Dynamic Range

Dynamic range measurements were conducted on each of the 32 receivers to determine the average receiver performance and the range of variation across the 32 receivers. The 1 dB compression point definition of dynamic range was used in our measurements. It is typically defined as the ratio of the maximum input signal power, S_{1dB}, for which the receiver produces a linear input-to-output gain, to within 1 dB of compression, versus the minimum detectable signal, which is set by the receiver noise floor, N, as given below by

$$DR_{1\,\mathrm{dB}} = 10 \log \frac{S_{1dB}}{N} \tag{6}$$

A microwave spectrum analyzer was used to measure the dynamic range of the receivers, according to the following measurement procedure:

1. Set the far field source to a power level which produces a noticeable receiver output
2. Decrease the far field source until the receiver output just drops to the receiver noise floor

3. Increase the far field source in 10 dB steps until the receiver output compresses
4. Once compression is reached, decrease the far field source power by 10 dB
5. Repeat step 3 using 1 dB stepped increases in the far field source

Once compression is reached using 1 dB steps, the 1 dB compression point dynamic range is obtained from Eq. 6. This is an estimate because nonlinearities that may occur in the far field source can be mistaken as compression of the receiver response. Table 1 shows data measured for receivers 1 and 16, and the data indicates an average 1 dB compression point dynamic range equal to 62 dB for these two receivers, which is typical of the others as well.

Source	Receiver 1	Receiver 16
-50 dBm	-85 dBm	-85 dBm
-40 dBm	-75 dBm	-74 dBm
-30 dBm	-66 dBm	-64 dBm
-20 dBm	-56 dBm	-54.1 dBm
-10 dBm	-46 dBm	-44 dBm
0 dBm	-35 dBm	-33.8 dBm
10 dBm	-25 dBm	-23.4 dBm
11 dBm	-24 dBm	-22 dBm
12 dBm	-23 dBm	-21.4 dBm
13 dBm	-22.5 dBm	-20.5 dBm

Table 1. Dynamic Range test results for channels 1 and 16

5.3 RF Channel Match

RF channel match is a very important characteristic in DBF arrays because it is a measure of the decorrelation, or the dissimilarity, between two supposedly identical receiver channels. If two receivers could be made perfectly identical, their outputs could be added 180° out of phase to produce an infinitely deep null. However, realistic channels have mismatch, and may only produce a null that bottoms out at 10^{-5}, for example, which is only a -50 dB. Therefore, in a DBF array, it is important to attempt to match all individual channels as closely as possible, in both amplitude and phase. The ability to do directly impacts the system's ability to achieve low sidelobe levels, proper amplitude tapers and deep nulls. Array calibration techniques are used to keep amplitude and phase errors at a minimum, as described in Section 6.

The experimental test apparatus, shown in Fig. 15, was constructed for the purpose of measuring the Cancellation Ratio (CR), a parameter that quantifies channel match. The measurement procedure is comprised of two steps as follows. First, the receivers are inserted into the test apparatus and the phase shifter and amplitude trimmer are adjusted so the outputs of both receivers are in phase, which produces a sum at the output center frequency of the receiver. While holding the phase shifter and amplitude trimmer settings constant, the input frequency is swept across the receiver bandwidth, which produces the arched upper trace in Fig 16. Next, the phase shifter and amplitude trimmer are adjusted so the outputs of the two receivers are 180° out of phase at the output center frequency of the receiver, which produces a null. The phase shifter and amplitude trimmer settings are again held constant while the input frequency is swept across the receiver bandwidth, which produces the lower trace in Fig 16. At any frequency in the band, CR (in dB) is the difference between the upper and lower traces at that frequency. The null in

the center of the band is the maximum CR that was achieved when the two receiver channels were nearly 180° out of phase. CR gets worse toward the edges of the band, where a 180° phase difference was not maintained. Constant CR can be achieved across the receiver bandwidth by using a taped delay line FIR filter in each channel to equalize the channel frequency responses.

The DBF System was upgraded through a contract sponsored by AFRL. The contractor discussed the impact of CR on antenna sidelobe levels and null depths in their final report, which included the analytical development of the following four equations [5]. Channel decorrelation, or mismatch, can be quantified in terms of CR, which is defined as follows

$$CR(n) = 10\log_{10}\left|\frac{V_1(n)-V_2(n)}{V_1(n)+V_2(n)}\right|^2 \tag{7}$$

where V_1(n) and V_2(n) are voltages measured at the outputs of the two receivers, as shown in Fig. 15, and n is the index of the discrete frequency points in the 2.0 MHz receiver output bandwidth where V_1(n) and V_2(n) were measured. In Eq. 7, the numerator represents the difference between the two channels when they are adjusted to be 180° out of phase, and the denominator is the sum of the channels when they are in-phase. The cancellation ration can be related to the rms amplitude and phase errors in an array, according to the following equation, where σ_a, and σ_ϕ are the mean-square amplitude and phase errors, and N is the number of elements in the array,

$$CR = \frac{\sigma_a^2 + \sigma_\phi^2}{N} \tag{8}$$

For small, normally distributed errors, array sidelobe levels can be predicted using the following

$$S_a = S_d + \frac{\sigma_a^2 + \sigma_\phi^2}{D} \tag{9}$$

where,

S_a = actual sidelobe level.
S_d = the design sidelobe level.
D = directivity of array.

Combining equations 8and 9 yields the following relationship between cancellation ratio and sidelobe level, which clearly shows that poor cancellation ratios, expressed linearly, contribute additively to elevated sidelobe levels in an array

$$S_a = S_d + \frac{CR * N}{D} \tag{10}$$

5.4 Data Acquisition and Control

The DBF System testbed, illustrated in Fig 13, employs a Hewlett Packard HP8672A microwave signal generator as the far field source which feeds a C-band standard gain horn that is used in the anechoic chamber as the transmit antenna. At any one time, 32 of the 116 elements

in the conformal wing array may be connected to the 32 receivers. The receivers' IF_3 output signals are transmitted over separate coaxial cables to the inputs of the 32 Hewlett Packard HP E1430A digitizers that reside in the VXI equipment rack. The digitized output data is then stored either on the 32 separate SCSI hard drives, or, if the data set is small enough, directly on the 30 GB hard drive within the host computer.

The wing array is mounted on a large multi-axis rotational antenna mount that is remotely controlled using a Flam and Russell FR8502A antenna mount controller. Controlling the rotation of the antenna mount is accomplished by setting the scan range, scan resolution, and rotation speed settings of the FR8502A, via the C++ GUI control software that runs on the DBF System host computer. The host is connected via a GPIB interface to the FR8502A, and to two other Hewlett Packard microwave sources which feed the receiver local oscillators. The host is connected to the HPE1430A digitizers and the HPE1562B SCSI drive controllers through a VXI bus interface. Through the VXI bus, the host controls the ADC sampling of the 32 RF channels and the storage and retrieval of sampled data. Data is stored in raw 2s complement 16 bit integer I-Q format as it is received from the ADCs. By storing the data in a binary format, file space is conserved. The raw data is then organized in a file format which separates the ADC output data according to channel and angular position of the antenna mount. The position of the antenna mount is stored in double precision format at the first entry in every set of channel data.

In a traditional non-DBF antenna measurement, where the antenna-under-test has only one output signal, antenna measurements are made by rotating the antenna mount continuously and the single channel of received data is digitized and recorded. However, because the DBF conformal wing array has 32 channels of data, which is obtained at a bandpass sampling rate of 10 MSamples/s, the amount of data generated by the digitizers is so large that it is often desirable to sample the array pattern at discrete angular locations, rather than in a continuous sweep. The use of different equipment busses, that is, GPIB for the antenna mount controller versus VXI for the digitizers, combined with the fact that Windows NT is a message-based operating system, not a real-time operating system, makes it difficult to accurately correlate digitized channel data with the exact antenna mount rotation angle at which that data was taken. To solve this problem, a discrete measurement technique was implemented. By incrementally stepping the rotation of the antenna mount to distinct angular positions approximately 0.5 degrees apart, we can use software control to record the angular read-out from the antenna mount controller's angle sensor, which enables precise correlation of the digitized DBF channel data with the antenna mount rotation angle. This approach also has the added benefit that it greatly decreases the amount of data that is recorded. While some loss of resolution will occur, compared to the continuous mode of operation, interpolation between the discrete data acquisition angles can reduce or eliminate many of these problems. Thus, data is acquired by first moving the mount controller in a single discrete step with 0.5 degree resolution, then we stop the rotation of the antenna mount, record the angular position of the mount, and then trigger the digitizers to take a burst of samples. This process is repeated at each of the 720 positions needed to complete a full 360° measurement. At these positions complex valued data can be measured for any 2^N samples, where N may range between 0 and 11. This is the procedure currently used in our measurements of the 116 element patterns of the array.

6.0 Conformal Array Calibration

This section describes the calibration method used to obtain uniform complex gain across the receiver channels. Note that this approach includes calibration of the hardware only. We assume that any mismatch among the passive array elements will be addressed by the pattern synthesis algorithm described in Section 7. We use an external calibration method in which we illuminate the array with a far field source (as opposed to an internal calibration approach, i.e., probe injection). Since the antenna elements wrap around the entire wing, as seen in Figs. 4 and 5, and there is no single direction from which all elements are simultaneously illuminated, it is necessary to perform a "multi-directional" calibration. In other words, we must calibrate the array one section at a time and then normalize each section with respect to the others. The following paragraphs describe the method used to determine the calibration angles and the approach used to match the calibration weights across the array-section boundaries.

As a first step, the element patterns are measured using a single digitized receiver channel. Let the complex gain of the passive element i be represented by $v_i(\phi)$, where ϕ is the global angular coordinate. Also, let the complex gain of the chosen receiver be represented by G_1, as depicted in Fig. 17. Then, the set of measured element patterns can be represented by vector V:

$$\begin{aligned} V &= [v_1(\phi)G_1 \quad v_2(\phi)G_1 \quad \cdots \quad v_i(\phi)G_1 \quad \cdots \quad v_N(\phi)G_1] \\ &= G_1[v_1(\phi) \quad v_2(\phi) \quad \cdots \quad v_i(\phi) \quad \cdots \quad v_N(\phi)] \end{aligned} \tag{11}$$

where N is the total number of array elements. From Eq. 11, it is obvious that when the element patterns are measured using a single receiver, gain differences across channels are due strictly to properties of the passive elements.

Next, the element pattern amplitudes are plotted as a function of ϕ, as shown in Fig. 18. For an ideal linear array, the patterns should superimpose. However, for a conformal array, the element normal vectors are oriented in different directions with respect to the incoming wave front for any given rotational angle ϕ, shown in Fig 17. Thus, the element patterns are shifted along the ordinate with respect to one another, where these shifts are proportional to the differences in orientation directions. In addition, the shapes of the patterns may vary among elements due to individual element properties and mutual coupling.

A threshold is established 3dB below the maximum peak, as seen in Fig. 18. When dividing the array into calibration sectors, the element patterns corresponding to a particular sector must intersect the calibration angle, ϕ_C, above the threshold. This ensures that ϕ_C intersects each element pattern in a region containing a high signal-to-noise ratio. When the element patterns are plotted as shown in Fig. 18, it allows one to judiciously choose the number and locations of calibration angles and, hence, define the calibration sectors. For this example, angles ϕ_{C1} and ϕ_{C2} each intersect three element patterns above the threshold. Note that one of the element patterns is common to both sectors. It will be shown below that it is necessary to have some overlap in calibration sectors in order to normalize the calibration weights across sectors.

Consider the elements that comprise the first calibration sector of an arbitrary conformal array, as in Fig. 17. The complex gain measured at the output of channel i, $G_i v_i(\phi_C)$, contains components due to both the passive element and the receiver. As mentioned above, we wish to determine the set of complex weights that will normalize the receiver gains. In general, this is accomplished by recognizing the following relationship:

$$w_i G_i = w_j G_j \tag{12}$$

where w_k is the complex calibration weight applied to channel k. Eq. 12 can be rewritten as:

$$w_j = w_i \frac{G_i}{G_j} = w_i \frac{G_i v_i(\phi_C)}{G_j v_j(\phi_C)} \frac{v_j(\phi_C) G_1}{v_i(\phi_C) G_1} \tag{13}$$

Note that all of the quantities comprising the two fractional terms on the right side of Eq. 13 can be obtained easily through direct measurement. Thus, by letting $w_i = 1$, every complex receiver weight can be computed for the first calibration sector.

Subsequent calibration sectors must contain at least one element in common with a previous sector in order to normalize the calibration weights across sectors using Eq. 13. Now consider the example in Fig. 18. The second sector has one element in common with the first sector. Therefore, since the complex receiver weight for this common element has already been computed, w_i in Eq. 13 is known, and the remaining calibration weights in sector 2 can be computed. As a final note, this calibration method is only valid at a single frequency. Both the element patterns and receiver channels will vary as a function of frequency. Therefore, we are in the process of extending our calibration approach to accommodate a band of frequencies using channel equalization in conjunction with this calibration approach.

7.0 Conformal Array Pattern Synthesis

The maximum gain patterns described in the previous Section 4 are preferred for many applications. However, there is no sidelobe control and in some cases the pattern sidelobes may be undesirably high. In order to provide sidelobe control, therefore, we have developed a pattern synthesis method based on alternating projections [6]. This is a numerical approach which offers great flexibility and handles both shaped beam and pencil beam synthesis and arbitrary sidelobe envelopes. We use this method to synthesize power patterns, i.e. no constraints on the far field phase.

Denoting by $g_n(\phi)$ the far field pattern of array element n in its array environment, the *set of realizable patterns* is represented by $F_r(\phi) = \sum a_n g_n(\phi)$, where a_n are arbitrary complex excitation coefficients. The *set of desirable patterns* $F_d(\phi)$ may be represented by upper and lower bounds on the pattern magnitude, $M_u(\phi)$ and $M_l(\phi)$, respectively. The synthesis procedure is iterative and entails finding alternating projections on these two sets until a common point (or the particular point of the realizable set which is closest to the desirable set in the LMS sense) is found. In order to include mutual coupling effects we use array element patterns $g_n(\phi)$, which

correspond to a locally oscillating circular array. These patterns have been computed using the CyMPA code. Measured array element patterns will be used when they become available.

Fig. 19 shows an example of a synthesized pattern for a 135 degree look direction assuming elements 1-10 active. The normalized maximum gain pattern, as shown by the dashed line, has close in sidelobes of about -13 dB. In order to obtain a pattern with lower sidelobes, say –30 dB, we impose the upper and lower desired pattern bounds $M_u(\phi)$ and $M_l(\phi)$, as shown by the dotted lines, and obtain via alternating projections the best realizable pattern, shown by the solid line. In this case the desired sidelobe level is physically realizable. Also the synthesized array distribution seems very reasonable, as shown in Fig. 20. The high sidelobe of –28 dB at about 260 degrees is similar to a 'smeared out' grating lobe for our curved array and cannot be suppressed much further by lowering the desired sidelobe level or broadening the desired main beam. However, increasing the active array to include elements 1-15 is effective and allows this sidelobe to be reduced by roughly 9dB, down to –37.5 dB, as shown in Fig. 21.

Finally we attempt to synthesize a beam in the forward direction ($\phi \approx 180$ degrees), which is a difficult direction since the projected area of the array is small, and very few elements radiate efficiently in that direction. Employing the 8 elements (No. 1-7 and 116), whose normals are within 60 degrees of the desired look direction, we find that the projected aperture is only 13.5 cm $\approx$ 2.5 wavelengths, which corresponds to an expected null-to-null beam width of about 48 degrees. Setting the desired beam width equal to this estimate and gradually reducing the desired sidelobe level we find that we can realize patterns with a uniform sidelobe level of about -23 dB, as shown as a solid line in Fig. 22. At this look direction it appears difficult to realize uniform sidelobe levels which are significantly lower, although more elements allow for a considerably narrower main beam. Convergence of the method is fast, usually a few hundred iterations were adequate, which only took seconds on a 1.5 GHz PC. An uncertainty of the method of alternating projections is that it may get hung in local minima. However, preliminary results indicate that this is not a serious problem in our case, and that low sidelobe patterns are indeed achievable at all look directions.

8.0 Conclusion

In this paper, we introduced a prototype conformal array antenna that wraps completely around the cross-section of a realistic aircraft wing. The variable rate of curvature of the wing presented many challenges to the design and analysis tasks of this project. A new conformal antenna design and analysis software package was used to help us make reasonable design choices, analytical approximations, and engineering trade offs. Suitable antenna element and conformal array designs were obtained for this first of its kind "wing-wrap-around" array. A prototype wing structure was built and populated with an array of narrowand, linearly polarized, microstrip patch elements at C-band. Digital beamforming hardware was implemented in the laboratory, which will be used to produce and control multiple beams from this conformal array. A new conformal array calibration method was reported, along with two analytical methods that addressed 2-D electromagnetic modeling of the array and conformal array pattern synthesis. The element patterns of this array were being measured at the time this paper was written. Once obtained, the measured element pattern data may be calibrated and used in conjunction with the conformal array pattern synthesis and the 2-D electromagnetic analysis, described herein. This work represents an initial experimental investigation of 2-D conformal arrays on surfaces of

variable curvature. We plan to extend the work introduced here to include an extensive phase of array measurements, pattern synthesis, and analyses of conformal array phenomena. Based on our findings, we plan to investigate new methods to cancel or reduce various types of undesired pattern effects in conformal arrays, and report such results in future papers.

Acknowledgements

The authors gratefully acknowledge and thank Mr. Tom Cord, who graciously provided the *Sensorcraft* FX72-MS-150B airfoil design data to our team. Mr. Cord is employed with the AFRL Air Vehicles Directorate, AFRL/VAAA, located at Wright-Patterson AFB, OH.

The authors gratefully acknowledge and thank Mr. Howard Underwood, Mr. Tim Terry, and Mr. John Redwood, for their exceptional craftsmanship and cooperative spirit, which they exhibited throughout their fabrication of the wing section. We also gratefully acknowledge and thank Mr. Dan Godin, for his role in managing the wing fabrication effort. These gentlemen are employed by the AFRL Space Vehicles Directorate, AFRL/VSOF, located at Hanscom AFB, MA.

The authors greatly acknowledge and thank Mr. Bill Weedon and Mr. Matt Anderson for their role in fabricating the microstrip patch antenna element panels which comprise the array. These gentlemen are with Applied Radar, Inc., of Warwick, RI.

References

[1] H. Steyskal, "Digital Beamforming at Rome Laboratory", Microwave Journal, Feb. 1996

[2] P. Barton, "Digital Beamforming for Radar", IEE Proc., Vol 127, Pt. F, No. 4, Aug 1980.

[3] Z. Sipus: "CyMPA - Program for Analyzing Microstrip Patch Array on Circular-Cylindrical Structures," AFRL Final Technical Report, AFRL/EOARD Contract No. F61775-99-4040, Apr. 2000.

[4] J.C Sureau and A. Hessel:"On the Realized Gain of Arrays," IEEE Trans. on Antennas and Prop., Jan. 1971.

[5] "Advanced Development for Digital Beamforming Test Bed", Quadrant Engineering Final Technical Report, Contract Number F19628-95-C-0214.

[6] O. Bucci, G. Franceschetti, G. Mazzarella, G. Panariello: "Intersection approach to array pattern synthesis", IEE Proc. Vol. 137, Pt. H, No. 6, Dec. 1990.

Figures

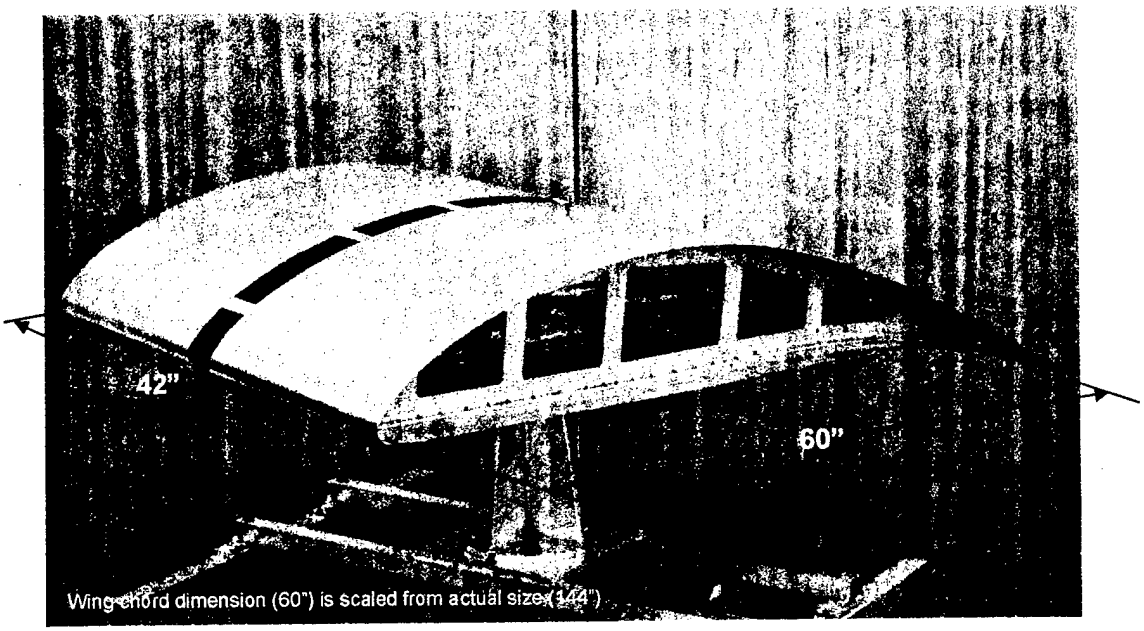

Fig 1: Scale model of the *Sensorcraft* FX72-MS-150B airfoil, fabricated in aluminum.

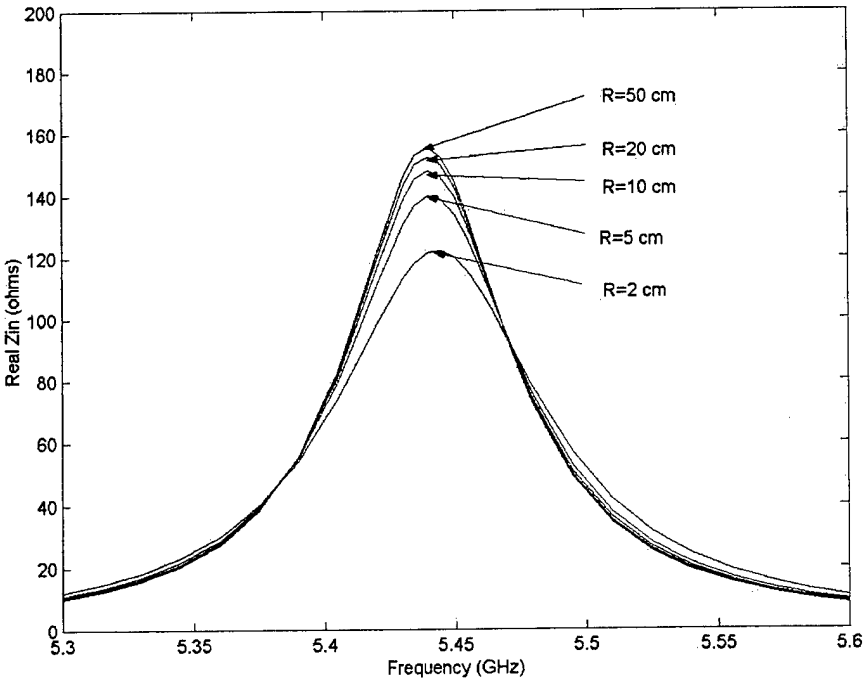

Fig. 2: Antenna input impedance versus radius of curvature, calculated using CyMPA.

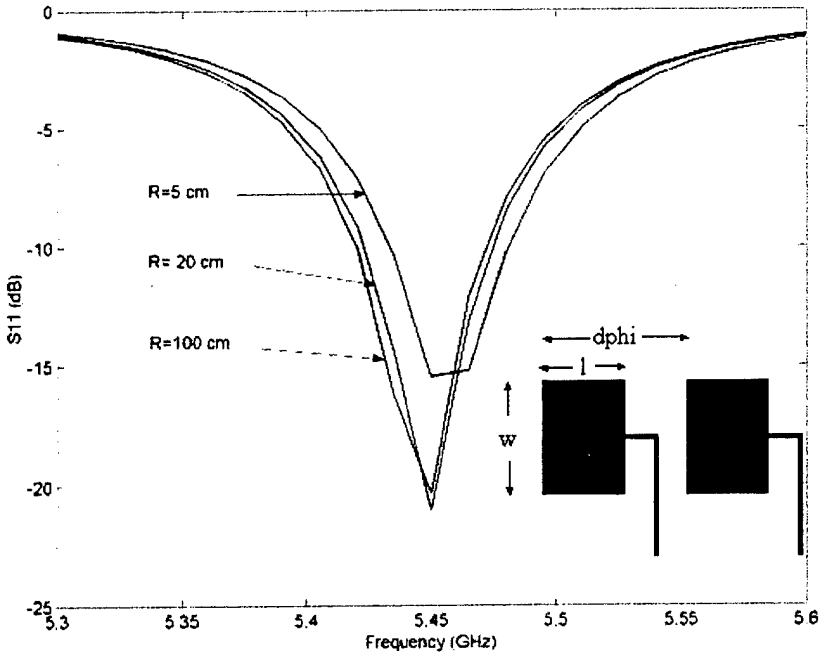

Fig. 3: Element design geometry and $|S_{11}|$ return loss versus radius of curvature.

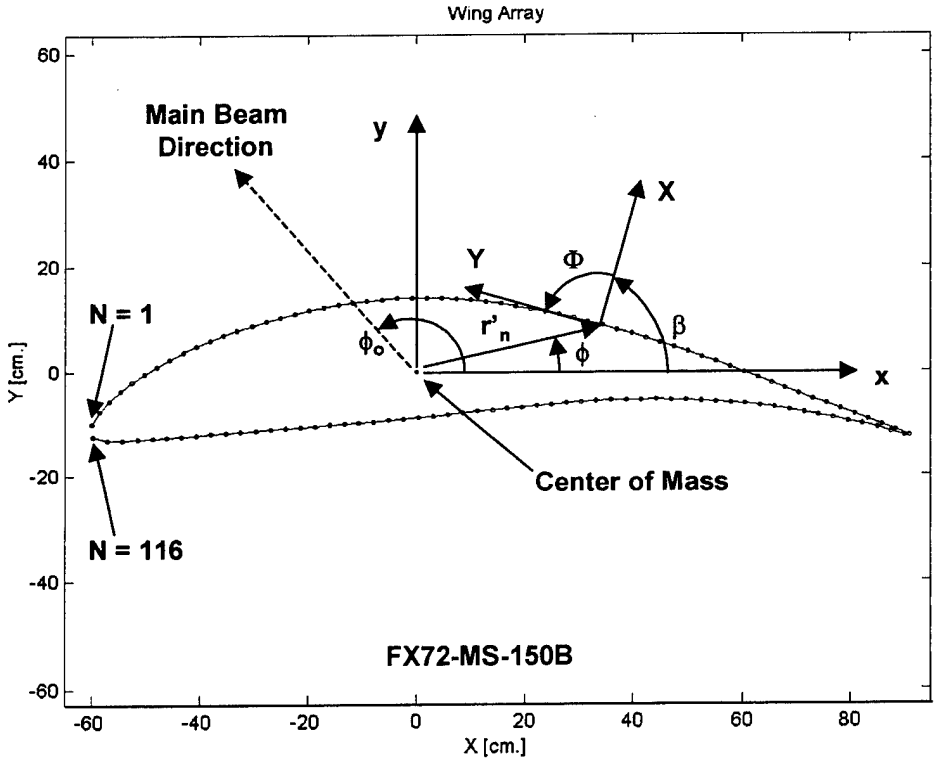

Fig. 4: Element indices, global and local coordinate systems, and angles used in Section 4.

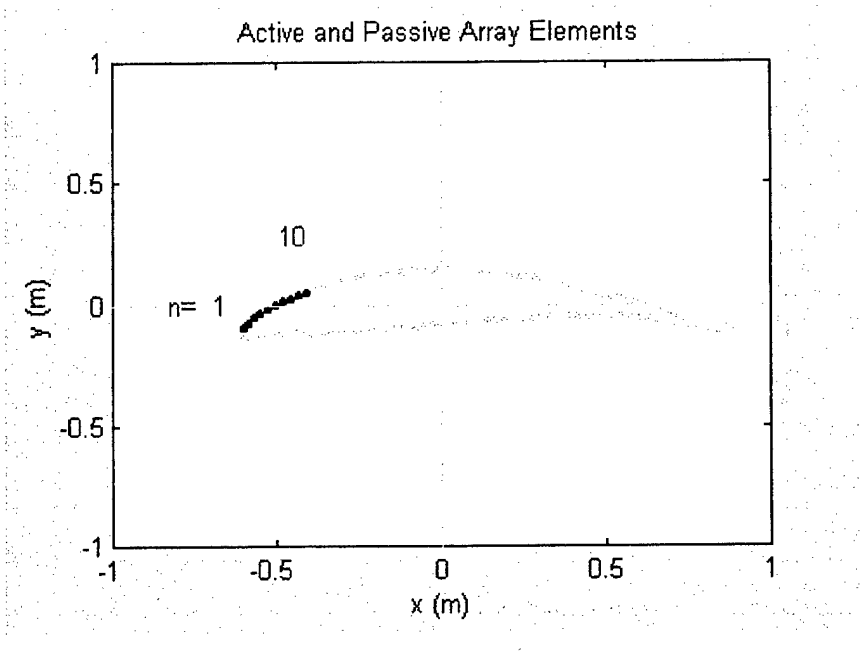

Fig. 5: The selectively activated region includes elements n = 1-10, shown as darker dots.

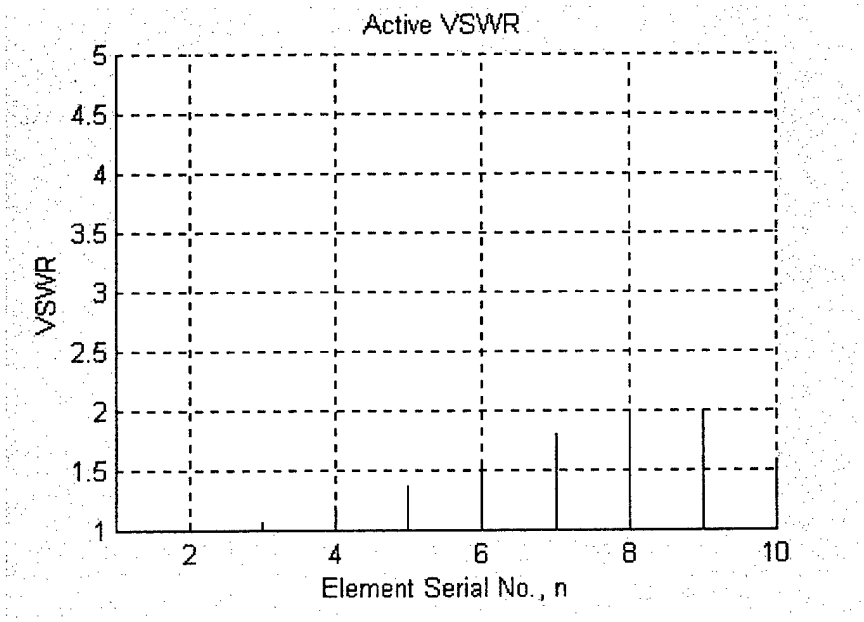

Fig. 6: Active VSWRs are below 2:1 for all active elements, n = 1-10.

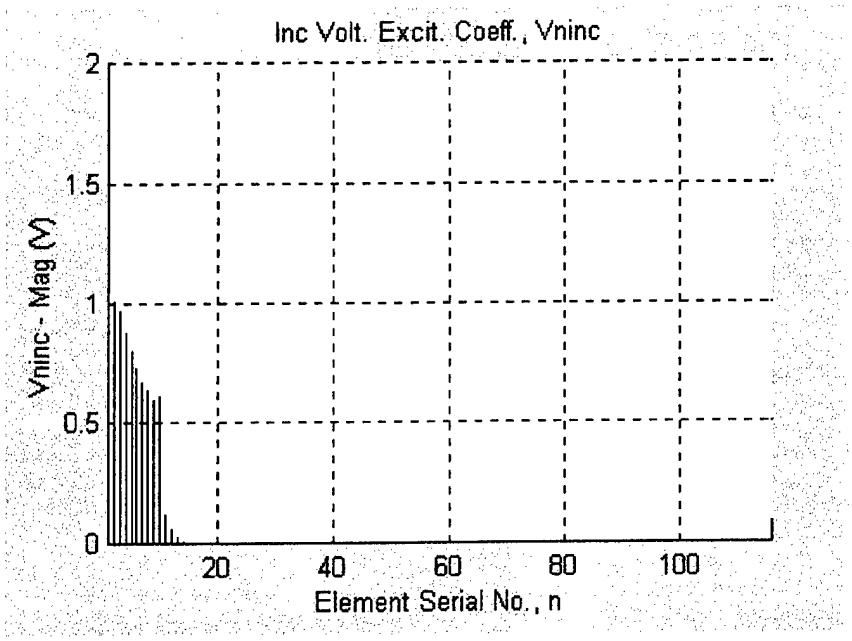

Fig .7: Magnitudes of the required incident voltages $|a_n|$, for elements 1-15.

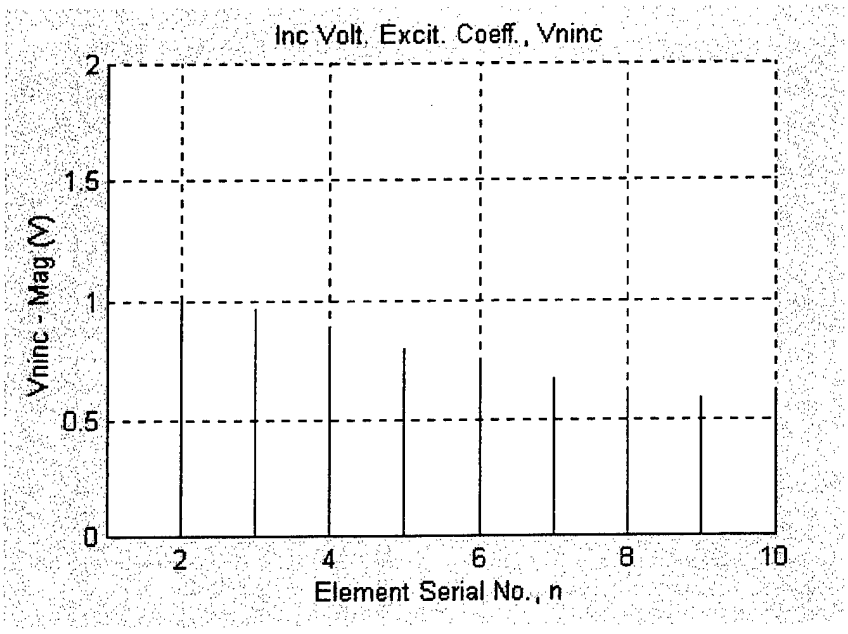

Fig. 8: Magnitudes of the required incident voltages $|a_n|$, for elements 1-10, shown enlarged.

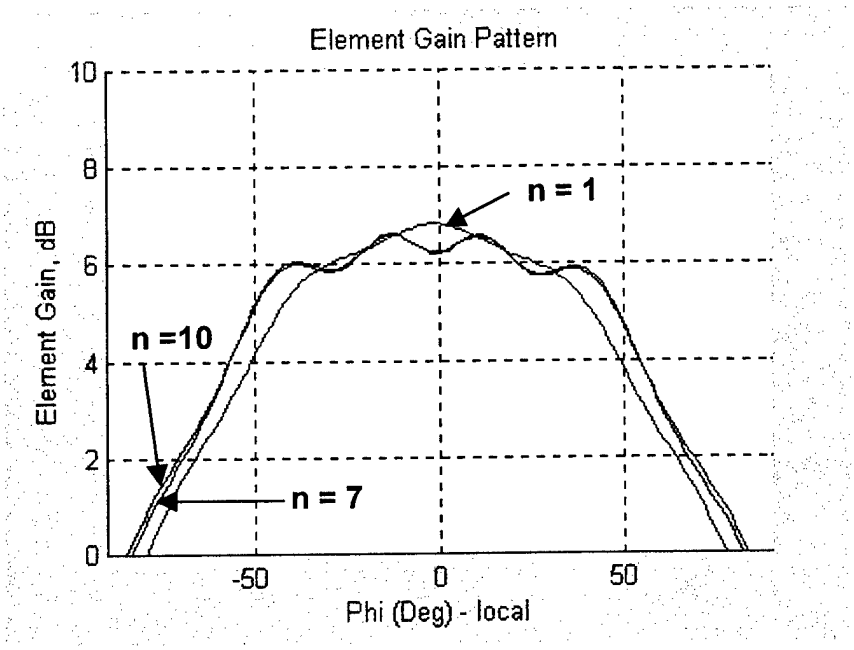

Fig. 9: Computed far field element patterns (magnitude) for elements n = 1, 7, 10

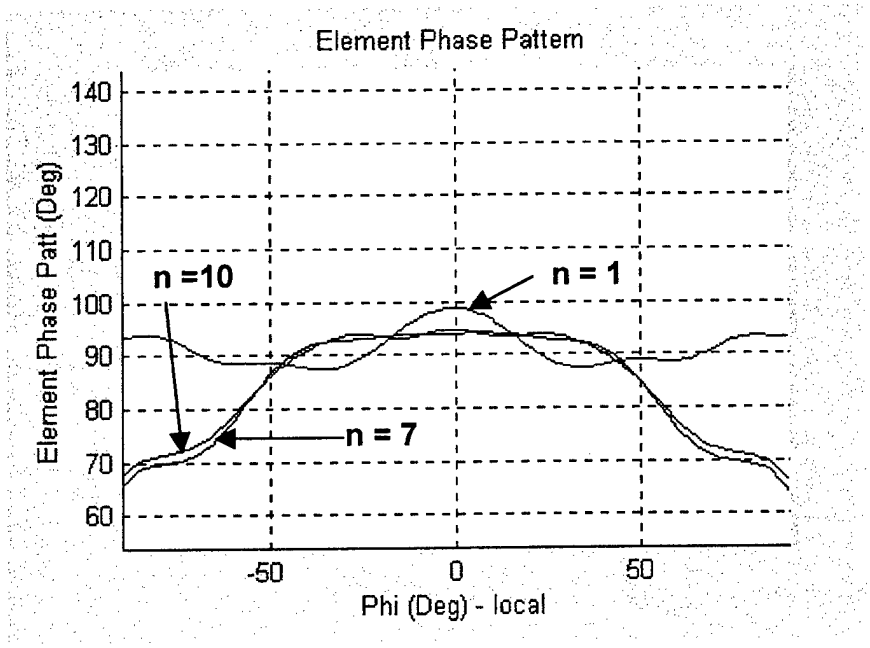

Fig. 9: Computed far field element patterns (phase) for elements n = 1, 7, 10

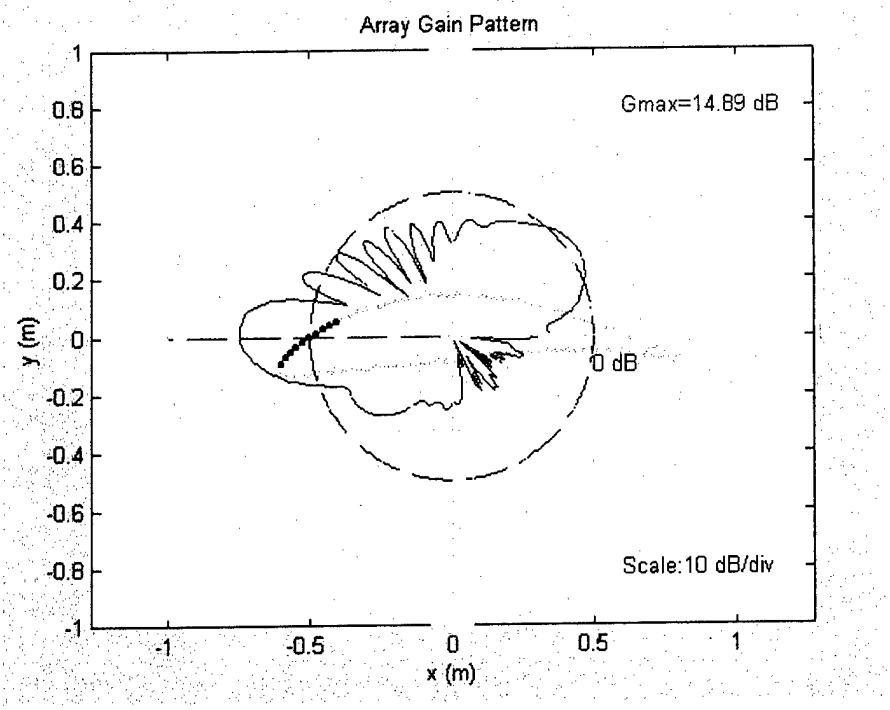

Fig. 11: Computed far field array pattern for elements 1-10, using uniform excitation

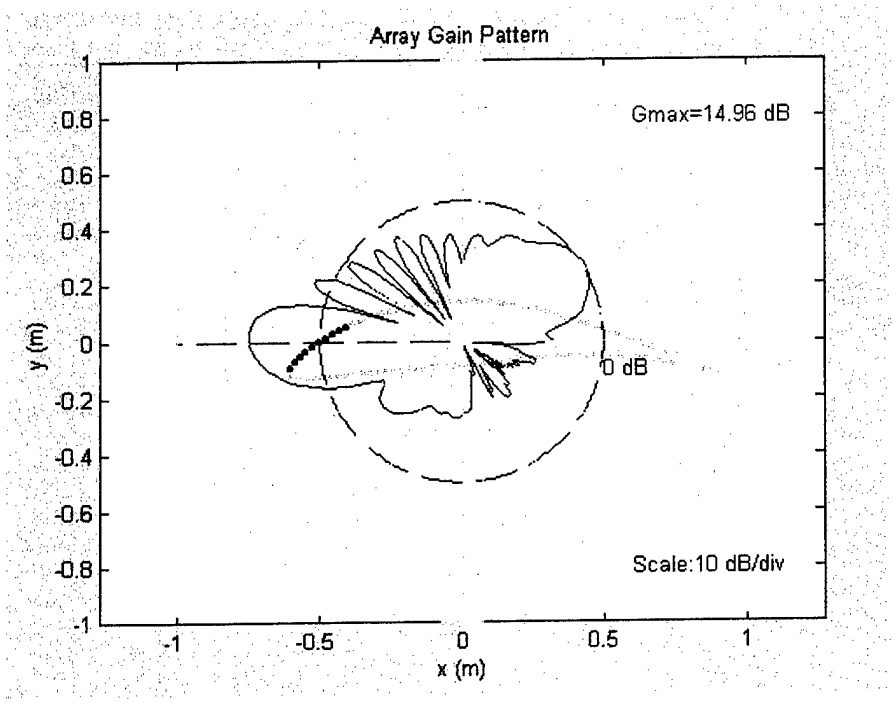

Fig. 12: Computed far field array pattern for elements 1-10, using the maximum gain theorem

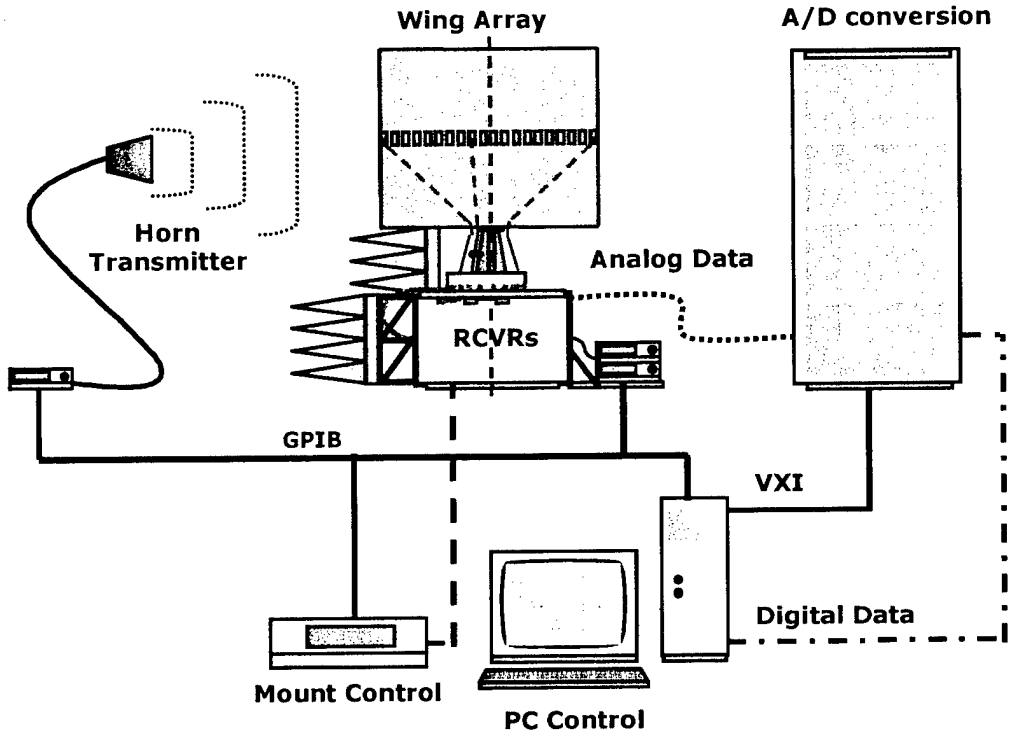

Fig. 13: Block diagram of the DBF System configuration

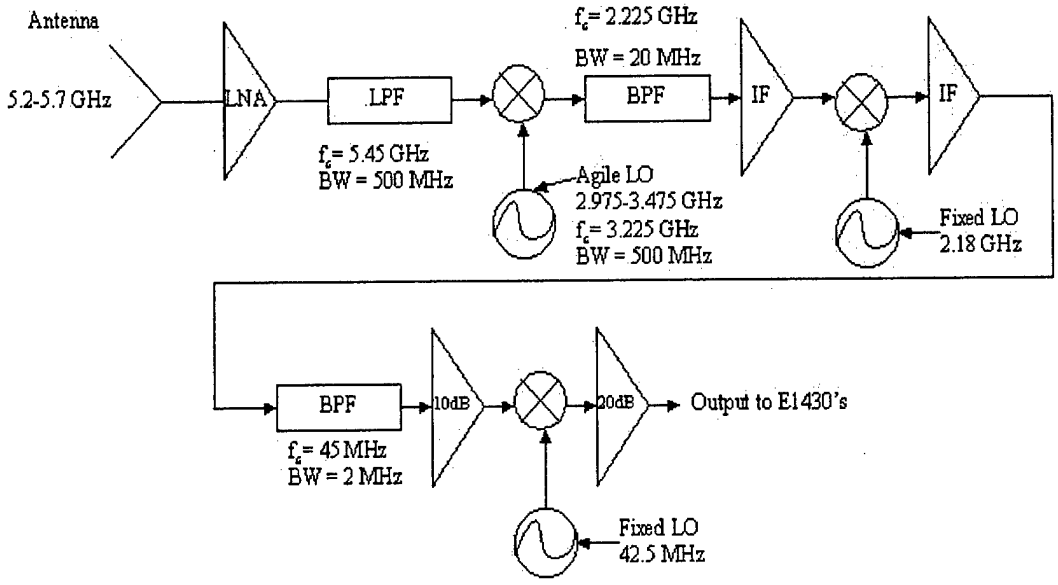

Fig. 14: Block diagram of the C-band receivers used in the DBF System

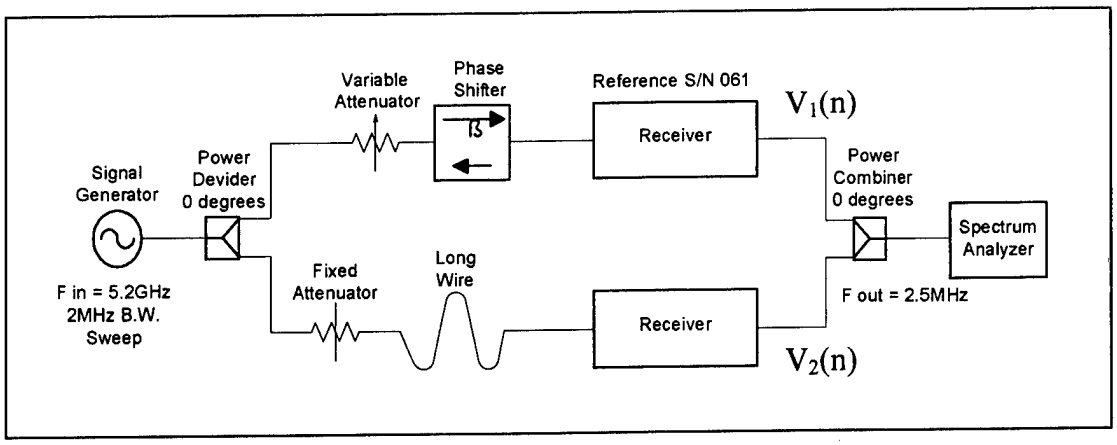

Fig. 15: Block diagram of the Cancellation Ratio experimental test apparatus.

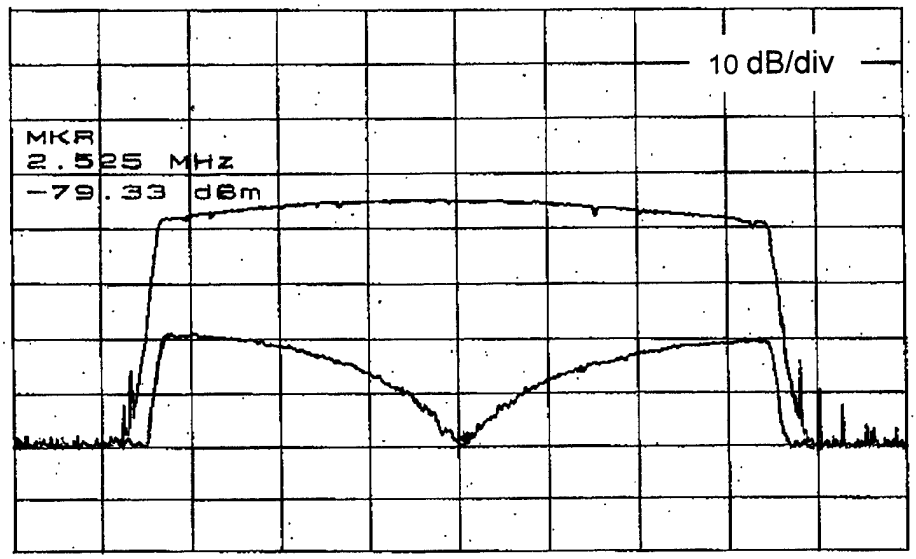

Fig. 16: Sum and difference outputs measured at the output of the CR test apparatus.

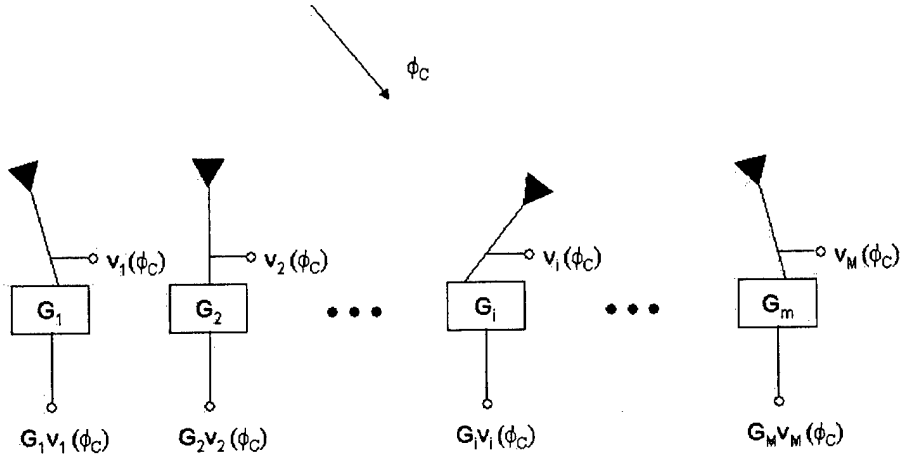

Fig. 17: Illustration of elements and receivers in arbitrary angular orientations.

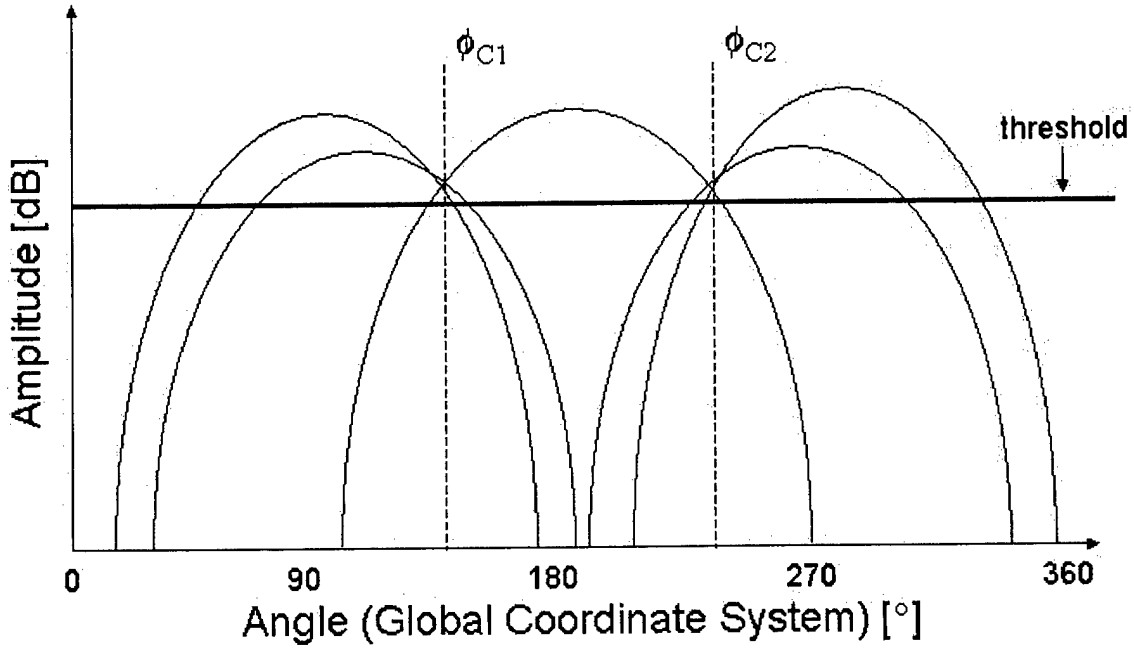

Fig. 18: Idealized cosine element pattern magnitudes overlaid as function of ϕ.

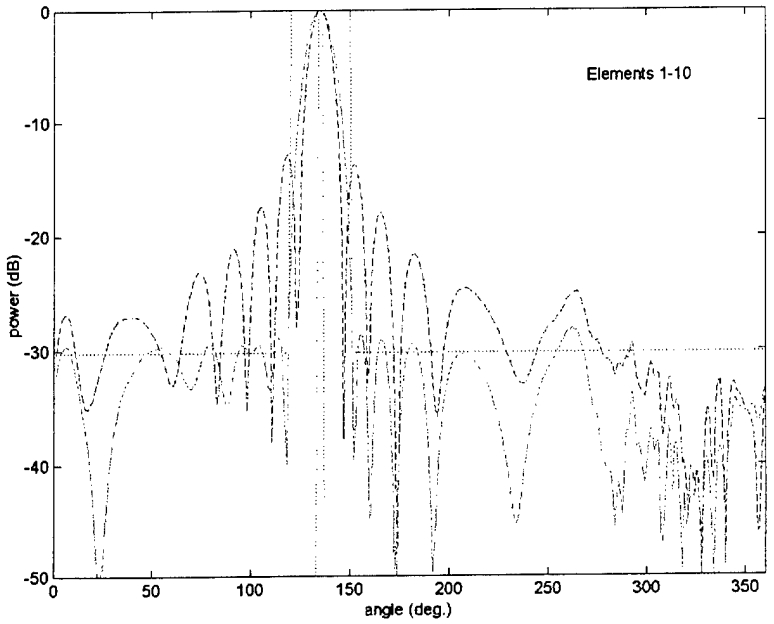

Fig. 19: Desired –30 dB sidelobe pattern (dotted) and realized pattern (solid). Maximum gain pattern (dashed) has –13 dB sidelobes. 10 elements are active. The look direction is forward, 45 degrees above the horizon.

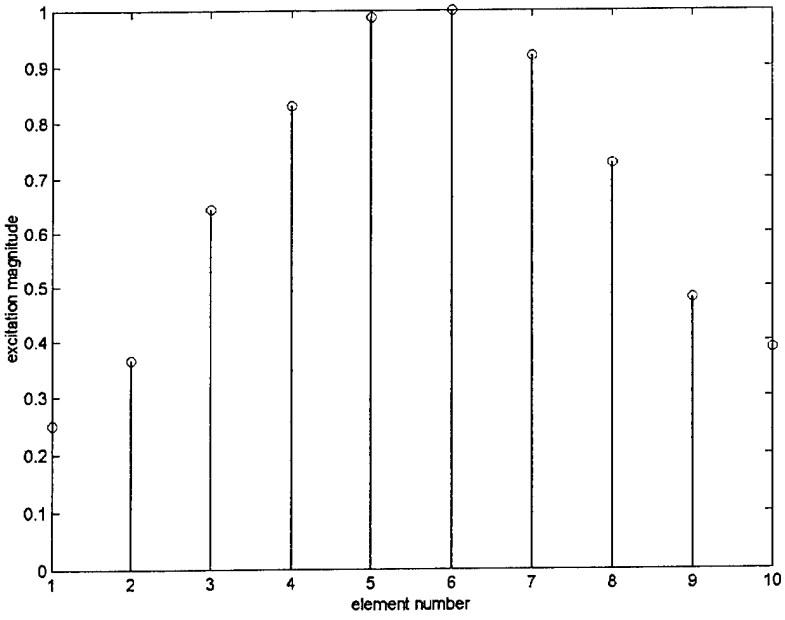

Fig. 20: Array excitation corresponding to the realized pattern.

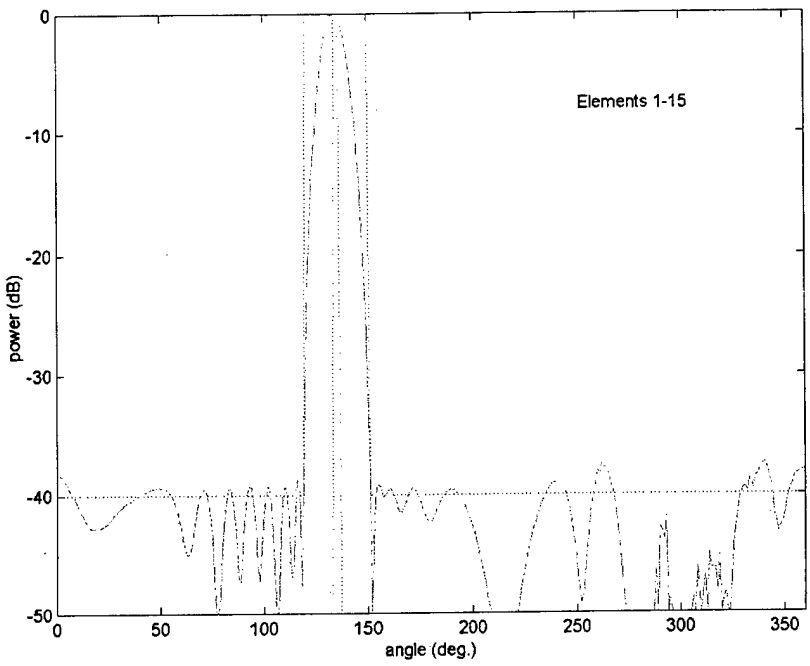

Fig. 21: With 15 elements active, a pattern with close to –40 dB sidelobes is realizable.

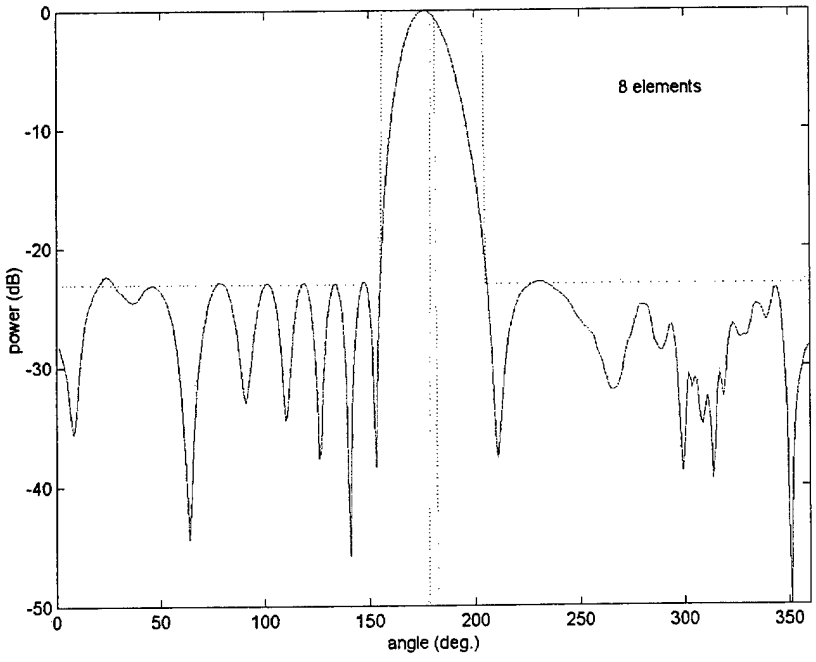

Fig. 22: With the main beam in the forward direction, where the projected aperture is minimum, a uniform sidelobe level of roughly –23 dB appears to be realizable, but not much more. Elements 1-7 and 116 are active.

USE OF SCAN IMPEDANCE AND SCAN ELEMENT PATTERN

R. C. Hansen
Consulting Engineer
Tarzana, CA 91357
818-345-0770

Abstract: Scan Impedance usually controls the bandwidth and matching capabilities of wideband arrays. But it is difficult to measure, as all elements must be properly excited. Scan Element Pattern, whether measured on transmit with one element excited, or on receive, always yields relative scan performance, and frequency squared behavior. On transmit the driven element impedance is benign, but it is not Scan Impedance. On receive the impedance is Scan Impedance, but it is difficult to measure. Computer simulations are used to elucidate these characteristics.

1. Scan Impedance and Wideband Arrays

Scan Impedance , SI, (formerly active impedance) is critical for wideband arrays, as it usually determines the useful bandwidth of the array. To measure SI requires a large array (to minimize edge effects) and the feed network must be interrupted to allow measurement of the center element impedance. This procedure is clearly difficult, and is seldom performed. What is common is to calculate SI for an infinite array using the Floquet unit cell technique. Then since all computer models need a hardware validation, several waveguide simulators are built and measured. Each simulator gives data for one scan plane, scan angle, and frequency; several simulators are usually sufficient to validate the infinite array code for narrow band arrays. See [1] for waveguide simulator data. SI can be recovered from the scattering matrix, but errors in measuring small couplings are magnified by the matrix inversion process. Thus this procedure is seldom employed.

It will be shown next that Scan Impedance is not available from transmit Scan Element Pattern measurements, and that although received SEP has Scan

Impedance inherent in the measurement, it is difficult to extract SI.

2. Scan Element Pattern Background

Scan Element Pattern, SEP, (formerly active element pattern) was developed circa 1960 by Allen [2], Oliner [3], Stark [4], and others, to provide phased array gain behavior versus scan angles. It's utility for decades has been to give insight and results on the scan performance of various elements and lattices. A common measurement procedure terminates all elements in the array, with the excited center element connected to a gain measurement setup. As early as the Lincoln Lab reports [2] it was recognized that the impedance seen in the measurement procedure was not the Scan Impedance, (impedance seen when all elements are excited with the proper amplitude and phase). Further the SEP gain did not include the Scan Impedance mis-match, following the textbook definition of gain. When the array is receiving with all elements terminated, the center element experiences the Scan Impedance. But recovering this impedance requires sampling the element voltage and current, a difficult and seldom attempted task. For example vector network analyzers and most pattern ranges will not measure impedance of a receiving antenna.

Recently wideband arrays have become of increasing interest, and the above transmit measurement procedure has been used to evaluate them, sometimes with results that seem unrealistic. The array literature contains very little information on the detailed characteristics of SEP, so it is the purpose of this paper to show: 1) that SEP does include frequency squared factors, so that array directivity is simply the number of elements times SEP; and 2) that SEP does not include array impedance mis-match. Bandwidth of a phased array is usually limited by these impedance mis-matches. A typical example using a planar dipole array will be shown.

3. Modelling the SEP Measurement

To determine exactly how the transmit SEP measurement process behaves with frequency, and whether Scan Impedance mis-match is included, a planar array code using thin dipoles on a square lattice, was

employed. This code treats a finite array, up to 100 elements each axis, thereby replicating the measurement procedure. As the dipoles are thin, and the maximum length is half-wave, the current distributions are very closely sinusoidal, so Moment Methods are unnecessary. All elements are terminated in a resistance, and the center element is excited. Solution of the mutual impedance matrix equation gives the complex currents for all the array elements. Mutual impedances were calculated in double precision [5]. Far field pattern was calculated by summing the element currents times the appropriate steering phases. Power was calculated from Real (VI) for the driven element. Gain is then simply 120 E^2/P. For a single element the simulation gives a half-wave SEP of 2.15 dB, and 1.76 dB for a short dipole.

Fig. 1 shows transmit SEP versus scan angle θ for a 20×20 element array of half-wave dipoles with half-wave spacing. As expected the E-plane result is more sensitive to edge effects; the H-plane curve matches exactly the infinite array result of Fig. 7.17 of [1], after normalization. This then is a validation of the measurement procedure for SEP, against the infinite array formulas summarized in [1].

Of more interest is behavior with frequency. Fig. 2 shows transmit SEP at broadside for the 20×20 case, versus dipole length in wavelengths. In all cases lattice spacing equals dipole length, and the terminating resistance is that of an element in an infinite driven array of half-wave dipoles at broadside. Note that SEP is proportional to frequency squared over the lower part of the dipole length range, as expected. Oscillations due to edge effects may be noted. It will be shown in the next section that this behavior arises from the array pattern versus frequency.

To show that Scan Impedance mis-match is different, an array code where every element is excited was used, and the mis-match factor $(1 - |\Gamma|^2)$ was calculated from the Scan Impedance. Fig. 3 shows mis-match gain factor for 10×10 and 20×20 dipole arrays, over a 5:1 frequency range. Note the oscillations due to edge effects, and the artifact around a spacing of $.4\lambda$. These data support the well-known fact that wideband array bandwidth is usually limited by Scan

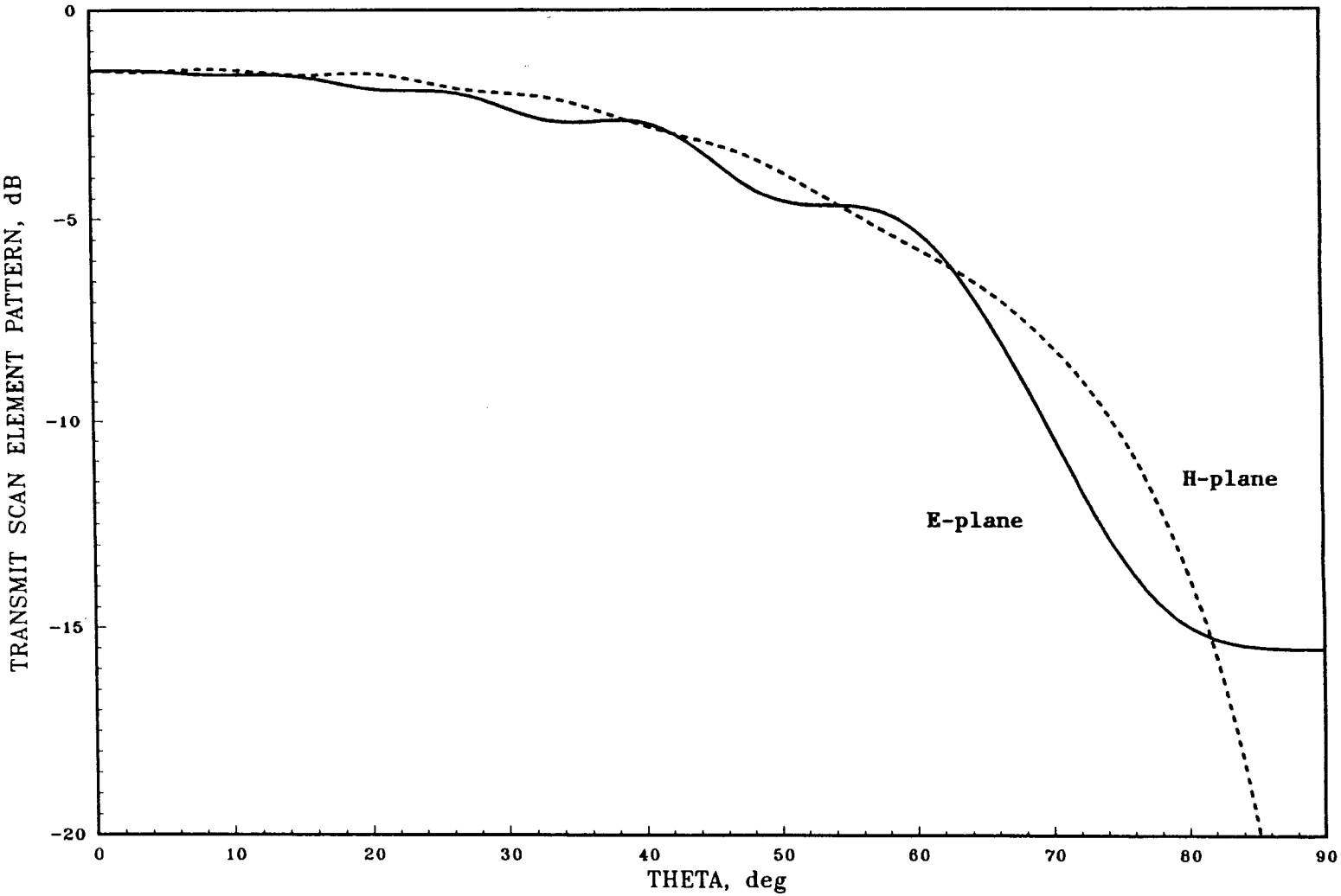

20 x 20 DIPOLE ARRAY, L=Dx=Dy=.5 wv

Fig. 1

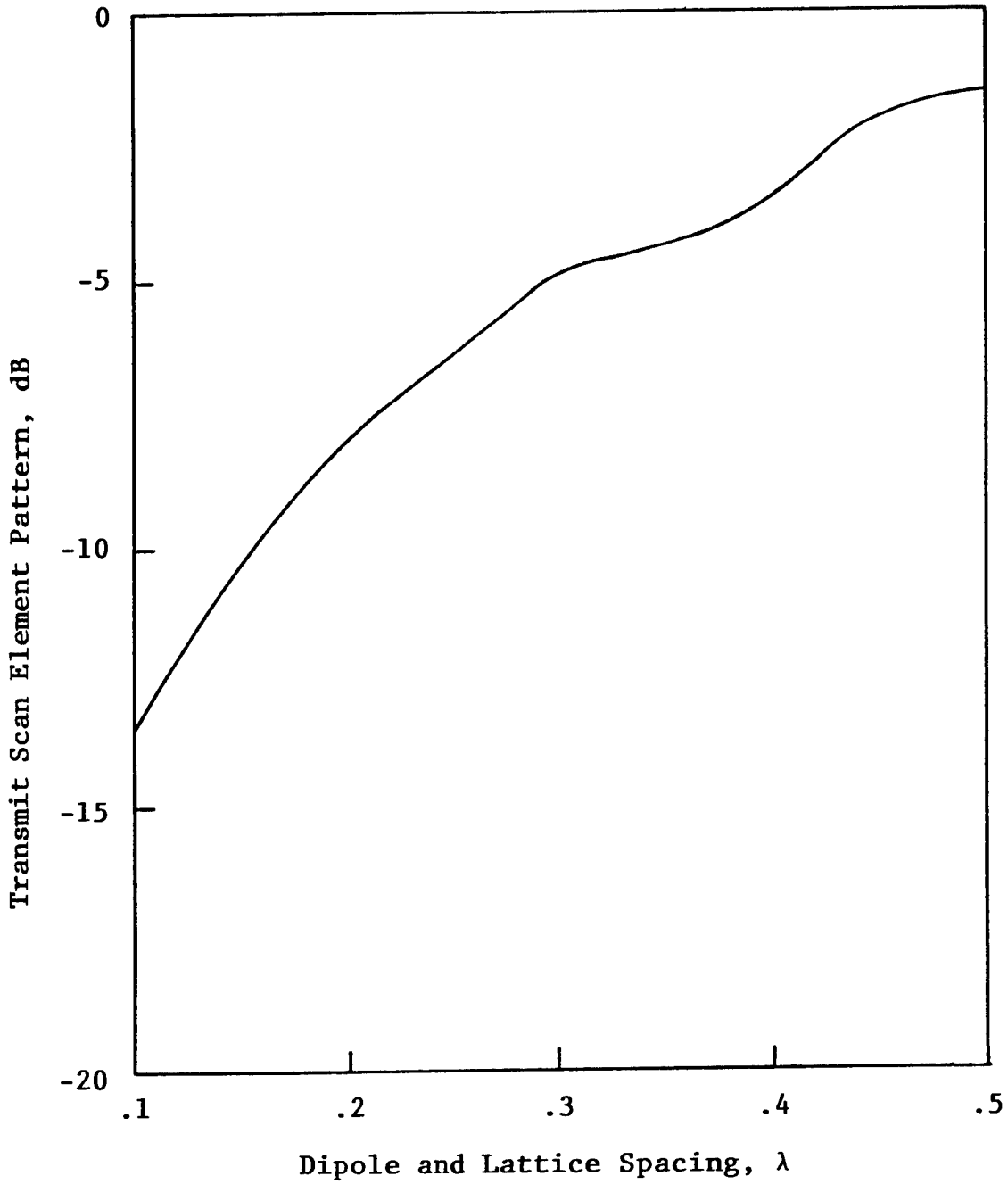

20 x 20 Dipole Array Over 5:1 Bandwidth

Fig. 2

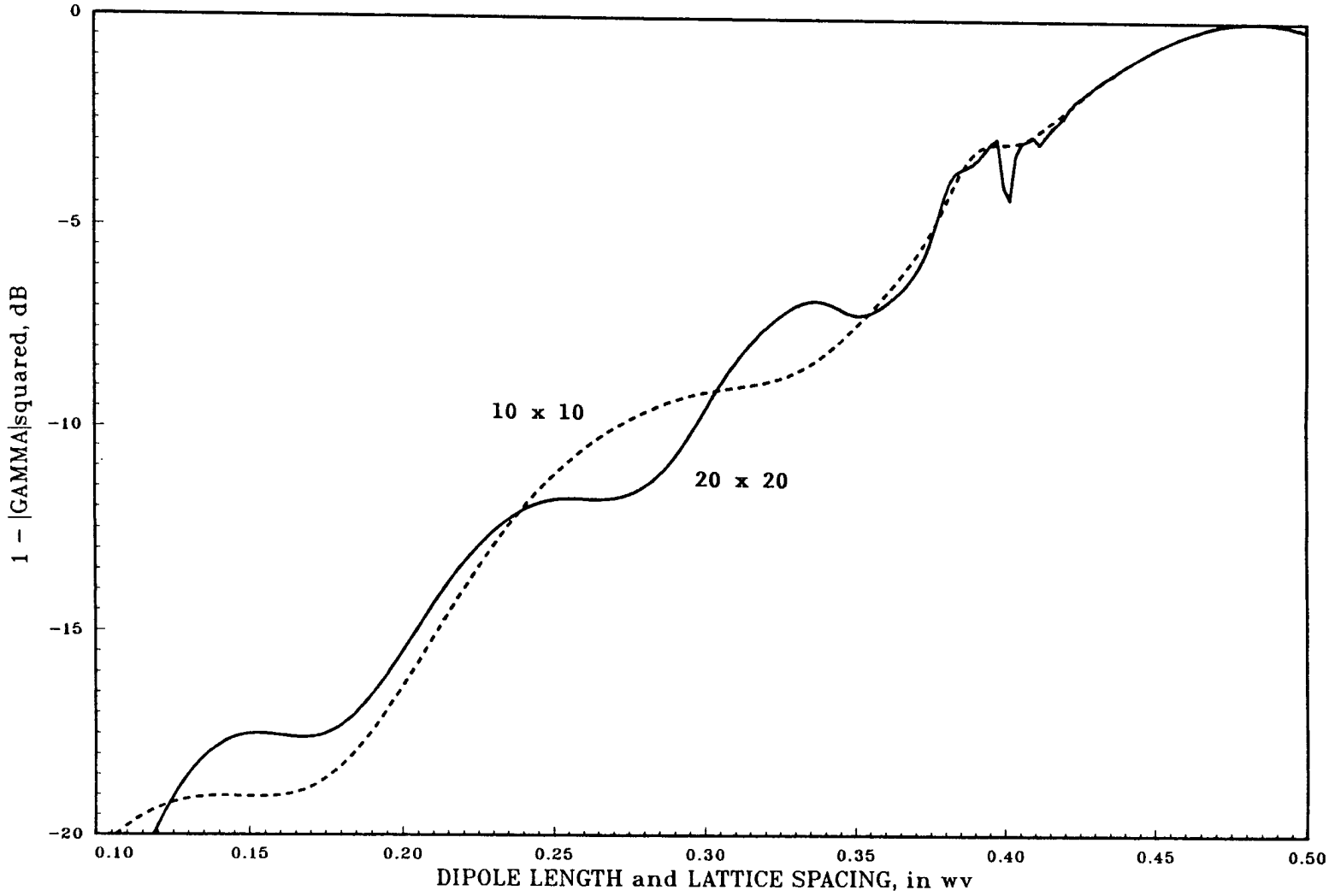

MIS-MATCH LOSS OF SQUARE DIPOLE ARRAYS

Fig. 3

Impedance mis-match losses. Array behavior over a bandwidth, then, is the sum of Figs. 2 and 3. For a 1/5 frequency, the mis-match loss is approximately 22 dB, in addition to the 14 dB array area (in wavelengths) loss.

4. SEP of an Array of Isotropes

Because short dipoles exhibit large negative reactance, it is of interest to determine the role of reactance in producing the frequency squared dependence of SEP. An isotropic array possesses virtual mutual resistances, but no reactances. The virtual mutual resistance is 120 sinc kd, where $k = 2\pi/\lambda$ and d is the separation between the elements. This virtual mutual resistance is derived from directivity equations for arrays. When the expression above is substituted in eq'n 2.64 of [1],
eq'n 2.49, the exact directivity of an array of isotropes results. Similarly for planar arrays [1].

This isotrope virtual mutual resistance replaced the mutual impedance in the SEP simulation code, and the element pattern became unity. Many computer runs disclosed that virtual impedance and power were stable, but that the array pattern, now not modulated by the element pattern, gave low values for some array sizes. Use of an amplitude taper over the array would probably stabilize the results. When the highest value is used for each dipole length/λ, the results closely match those of Fig. 2! Thus it may be concluded that the frequency squared factor is not produced by mutual impedance reactance, but by the array pattern (electric field at broadside) versus frequency.

5. Conclusions

Knowledge of Scan Impedance, where all array elements are terminated and one excited, is essential for the evaluation of wideband arrays, but it is very difficult to measure directly. Transmit Scan Element Pattern is almost useless for the determination of array performance over a wideband, as it essentially shows only frequency squared dependence and a benign impedance. Receive Scan Element Pattern measurements are useful for wideband arrays, but do not yield Scan Impedance directly. Calculations of Scan Impedance are essential, as are waveguide simulator measurements.

The equations for calculating SEP given in [5] accurately express SEP at all angles, but the Scan Resistance must be known.

6. References

[1] R. C. Hansen, Phased Array Antennas, John Wiley & Sons, 1998

[2] J. L. Allen, Phased Array Radar Studies, TR-228, Aug. 1960; TR-236, Nov. 1961; TR-299, Feb. 1963; MIT Lincoln Lab.

[3] A. A. Oliner and R. G. Malech, "Mutual Coupling," Chapters 2-4 in Microwave Scanning Antennas - Volume 2, R. C. Hansen, Ed., Academic Press, 1966; Peninsula Publ., 1985

[4] L. Stark, "Radiation Impedance of a Dipole in an Infinite Planar Phased Array," Radio Science, Vol. 3, pp. 361-375, March 1966

[5] R. C. Hansen, "Formulation of Echelon Dipole Mutual Impedance for Computer," Trans. IEEE, Vol. AP-20, pp. 780-781, Nov. 1972

Phased Array Technology and Allerton

Robert J. Mailloux
Air Force Research Laboratory
Sensors Directorate
80 Scott Drive
Hanscom AFB, Massachusetts, 01731-2909
Email: robert.mailloux@hanscom.af.mil

Abstract: For the past fifty years the Antenna Applications Symposium at Allerton has provided a podium for engineers to discuss all aspects of antenna engineering . This paper addresses the subject of phased array development, and catalogs some of the papers presented at Allerton that have contributed to this development.

The Antenna Applications Symposium at Allerton has played a significant role in phased array development. From the time of its beginnings as the Air Force Antenna Symposium, Allerton has always offered two venues for communication, one is from the podium, and a second one takes place throughout the grounds and in the hallways and the dining area. To some this second venue may be the more valuable, but it has gone unrecorded. There is a fairly complete record of the presented papers and I have tried to highlight some of those that seem more relevant to phased array developments. This paper looks at the role played by the symposium in fostering those developments in array technology.

Table 1 gives a chronology of some representative array systems or major test-beds, along with component developments that support these systems. The various items of technology highlighted are array elements, control devices and array architectures. These major topics and subtopics are referenced against specific Allerton paper references in the Appendix, which lists the principle author and a few words to describe the subject.

There are some interesting trends revealed in the system applications and the items of technology. Throughout the 60's and 70's all array system applications used dipole and waveguide elements. Ferrite phase shifters controlled radars at S-band and above. Included are AWACS and AEGIS at S-band and the Patriot ground radar at C-band, the TPN-25 PAR antenna and GPN-22 at x-band.

Array Elements

During the 60's and 70's most of the basic new array elements now in use were

discussed, and sometimes introduced at Allerton. In 1972 when Robert Munson introduced the microstrip patch antenna, it was two years before the AP-S paper by Munson was published. After that there have been numerous patch and printed circuit varieties, all tending toward wider band, better polarization and simpler excitation.
The first papers on notch and Vivaldi elements weren't presented at Allerton, but in 1977 George Monsor discussed new notch elements with 6:1 bandwidth. Since that time a number of papers, including several by our Chairman Dan Schaubert, attest to the durability of that research area and to the desirability of such wideband elements.

Array Control

There were very few ferrite or diode papers or T/R module papers presented during the early years at Allerton. There was an early paper by Adcock '54 that described a phase shifter using mechanically rotating crossed dipoles for UHF arrays. In '55 Von Aulock discussed geometries for ferrite phase shifter application. In '83 Hancic et.al. presented some very compact, lightweight diode phase shifters that represented the state of the art before MMIC.

In 1972 Collins and Hayes presented TI work on the RASSR modules, and later Harold Weber of AFRL presented a review of both MERA and RASSR modules. T/R module control of arrays grew from these first MERA and RASSR x-band test-bed demonstrations, and from the module developments from S-band to C-band that were summarized in 1980 by H. Chilton of Rome Laboratory. These included the first solid-state T/R module based system, the TPS-59, which consisted of slot arrays scanned in one plane. PAVE PAWS was the first all solid state phase-phase scanned radar.

Later, the MMIC program led to a number of integrated circuit MMIC arrays, now with multi-element modules or "trays" of MMIC modules directly integrated into the array aperture. These sorts of papers have continued to be presented at Allerton, and reflect a major change in array design, and a major change in this symposium, which now regularly accepts papers on all kinds of array control technologies. (See. For example '80 Chilton, '83 Edward, '85 Smetana et al, '87 Pepe et.al., '94 Edward, '95 Raquet).

New means of Control

Certainly ferrite phase shifters and diode phase controls, whether in active modules or passive phase shifter circuits, have been the mainstay for array control

in developed systems, but in the 1990's there were a large number of papers that addressed alternative means of beam control. These technologies are digital beam-forming, optical beam-forming and signal distribution, and MEMS phase control. The papers on digital beam-forming have not dealt with devices (A/D converters, filters etc.), but with array architecture using digital beam-forming ('92,'93 papers by Brandow and Humbert), error analysis of DBF systems, the use of neural networks for control in the presence of failures ("92 O'Donnell, '93 Simmers, '94-'96 Southall) and failure correction ('94 Mailloux).

Optical control of arrays became a topic at Allerton during the '90's, with major presentations in '92 by Herczfeld and Newberg, special sessions in'96 and '98 organized by Mike VanBlaricum, and the growth of the Navy program in photonic control (see '95 Parent, '97 Frankel et.al, and Bobowicz et.al.). A special session in '99 featured a number of papers on MEMS phase shifters and time delay devices.

Allerton has not seen many papers on adaptive array control. Probably because these went to the Air Force sponsored Adaptive Array Symposium, but there were several important early presentations b y Compton ('69) and others. Other papers ('81 Fenn and '81 Steyskal) have dealt with the array aspects of adaptive control (degrees of freedom consumed), and the formation of wide-band nulls ('95 Mailloux). In this regard one interesting presentation was the paper in '83 by Schmitt, who presented the MUSIC algorithm well in advance of the AP-S March '86 publication that described this important work on direction-finding. A special session in '00 convened by Wicks presented much current work on STAP (space-time adaptive processing).

Array Architectures

This category is interpreted broadly here, and at one extreme it includes waveguide slot arrays for low sidelobes (Evans/Hoofer '80), an early presentation of Joint Stars array technology by Harold Schnitkin in '89, and monopole synthesis with edge slot arrays by Kinsey in '95. Space fed lens ('97 Tripp and '97 Diaz) and reflectarrays ('62 Malech, '78 Montgomery, '93 Litva et.al). The '62 Malech paper is one of the earliest reflectarray references cited.

Several UHF rotodome antenna geometries ('56 Kinega, '58 Lockheed staff) were presented at Allerton, and though these were not conformal arrays, the subject of platform interaction was considered.

Members of the Hughes Corporation staff treated the topic of antennas conformal

to structures like cones and cylinders in 1952, at one of the very first Allerton symposia. Since then, various conformal array structures have been discussed at Allerton presentations, including the Navy work (Gladman et.al.'71) and a group of air Force programs ('73 Balzano, '89 Herper et al., '89 Hanfling) and including the low sidelobe circular array work of Herper and Stangel in 1980.

Multiple beam antennas have been a popular topic at Allerton throughout the years; beginning with the octave band MBA presented Mehron in 1963. A number of these are listed in the Appendix. In 1997 Jack Schuss presented an important paper on the IRIDIUM antenna, which, upon revision, was submitted to the AP-S transactions, where it won the "2000 Wheeler Applications Prize Paper Award".

Subarray technology and limited field of view antennas are related technologies, and have been a special subject of Air Force research since the late 1970's. Of particular interest are the papers of Southall and McGrath ('80 and "85) which later led to their receipt of the AP-S "1987 Wheeler Applications Prize Paper Award", the 1983 paper by Sinnott that described the Australian Ginda Lee OTH Radar, and new work by Kinsey in '98 describing subarray choices for limited field of view.

In 1972 Blakely, Burke end Cohn presented one of the first papers on meanderline circular polarizers.

Although primarily a podium for "Applications" papers, theoretical work has been welcomed throughout the 50 year history of the symposium. The theoretical papers referenced in the Appendix however, highlight the growth of numerical methods since the late 1960's. In 1969 Strait and Adams presented some of the early wire antenna theory developed at Syracuse University during and since the famous 1967 paper by Harrington. These methods were used in presentations by many authors during the 1070's and 1980's, but in the late 1980's and throughout the '90's there were a number of publications based on new classes and numerical methods, from finite element to finite difference time domain methods now viable because of the speed and storage of modern PCs, work stations and supercomputers. In '96 Professor Chew of the University of Illinois presented a special session on a variety of these powerful methods.

Mutual coupling phenomena have been described in many Allerton papers over the years, but in a recent coincidence in 1999, a paper by Hansen and one by Chio and Schaubert both revealed the dominant edge effects in the closely spaced

arrays used in wideband systems. This phenomenon may present an ultimate limitation to possible sidelobe control in modest size wideband systems.

Conclusion

The Antenna Applications Symposium and its predecessor the Air Force Antenna Symposium has been an important venue for the presentation of array research and development papers. Allerton papers have most often emphasized the practical engineering aspects of the technology, but ground breaking theoretical work has been presented too. The symposium has become important for the early publication of papers that have later received professional society "Best Paper" awards or have been shown to be the seedlings of new technologies that have gone on to advance phased array technology in major ways.

From the phased array perspective, the symposium has done its job well, and continues to play an important role in the development of phased array technology.

The Technology

	Elements	Array System or Test-bed	Control: Devices	Control: Modules	Control: Architectures
1960	Dipoles, waveguides	HIPSAF E-2C ('64) FPS-85 ('61 and '67) MUBIS De-spun Sat. Ants.	Ferrites Diodes	MERA '64	Mixer steering (triode tubes)
1970	Microstrip '70 and printed circuit Flared notch '74) Vivaldi ('79)	TPS-59 ('75) TPN-25('75) Aegis(AN-SPY-1)('75) SAM-D/ Patriot (76) E-3A/AWACS ('77) TPQ-37 ('76) PAVE PAWS ('78)		RASR '72	Digital Beamforming
1980	Wideband micristrip elements	Star wars FPS-70 (ULSA) FPS-117 (SEEK FROST) RADANT Joint Stars		MMIC packages	
1990		20/44 GHz arrays Photonic test-bed THAAD/GBR IRIDIUM	Ferroelectrics MEMS	Multilayer packages	Photonic beamforming

Appendix: A Partial List of Relevant Array Technology Papers Presented at Allerton

Major Topics and Sub-topics: Elements

Elements:

- Microstrip and Printed Circuit Antennas

'72 Munson	Microstrip ants. (AP paper '74)
'78 Kerr	Microstrip polarization techniques
'78 Lo et al..	Microstrip element cavity theory
'78 Montgomery	Microstrip reflectarray
'83 Sedivec/Hubin	44 ghz printed circuit array
'83 Paschen	Broadband microstrip matching techniques
'84 Lo et al..	Circularly polarized microstrip
'85 Lee et al..	Dual frequency microstrip
'85 Schaubert et al..	Elements for integrated phased arrays
'86 Schaubert/Pozar	Aperture coupled patches
'86 Tanner/Mayes	Wideband double tuned patches
'86 Paschen	Broadband tuning of patches
'86 Rees/Edward	Printed dipole elements for mm-freqs.
'88 Mullinix et al.	Printed circuit antennas
'91 Chen/Ingerson/Wong	Slot coupled microstrip patches
'94 Herscovici et al.	New feed network for microstrip

Major Topics and Sub-topics: Elements

Elements:

- Wide Band Elements

'73 Lopez	Wideband Dual Polarized Array Element
'77 Monser	Notch elements--6:1 band
'88 Povinelli	Notch antennas reviewed (planar too)
'92 Pickles/Rao	Broadband array (notches)
'93 Schaubert	Stripline fed tapered slot
'93 R.Q.Lee	Linearly tapered slots
'95 Shin/Schaubert	Wideband Vivaldi antennas
'99 Kishk et al.	Broadband dielectric resonator antennas
'99 Chio et al.	Tapered slot

Major Topics and Sub-topics: Control

Control:

- Phase Shifters

– Diodes	'83 Hancic et al..	Low loss, lightweight diode phase shifters
– Ferroelectrics		
– MEMS	'98 Barker/Rebeiz	MEMS time delay device
	'99 Special MEMS session	J. Smith, Overview of applications
		Reid, MEMS phase shifters
		Weeden/Rebeiz, Time delay
		Muldavin/Rebeiz

Major Topics and Sub-topics: Control

Control:

- Modules
  - MERA '64----
  - RASR '72
- Other solid state modules and MMIC arrays

'83 Weber	MERA, RASSR
'72 Collins/Hayes	RASSR array modules
'80 Chilton	T/R modules
'83 Edward	MMIC in Phased Array
'85 Smetana/Acosta	MMIC array performance
'87 Pepe / Povinelli / Komiak	Wideband (6.5-16.5) Active phased array (GaAs mod., stripline notch)
'94 Edward	94 GHz MMIC array
'95 Raquet	ACTS satellite EHF MMIC arrays

Major Topics and Sub-topics: Control Architectures

Control Architectures:

• Digital Beamforming	'92, 93 Brandow/ Humbert	Digital beamforming
	'92 O'Donnell	Neural beamforming, target resolution with errors
	'93 Filho et al.	High performance Neural net array control
	'93 Simmers et al.	Advances in Neural net beamforming
	'94 Mailloux	Failure correction with DBF
	'94 Frazier et al. (McIntosh)	DBF for X-band imaging (FOPAIR)
	'94, 95, 96 Southall et al.	Neural beamforming
	'95 Santorelli et al.	Neural nets for array synthesis

Major Topics and Sub-topics: Control Architectures

Control Architectures:

• Optical Control / Microwave Signal Distribution	'92 Kunarth et al.	Ka MMIC with fiber control
	'92 Herczfeld	Optically fed and controlled arrays
	'92 Newberg	Time delay beamsteering with optics
	'95 Parent	Optical beamforming techniques
	'96 Anderson et al.	Optical time delay device for arrays
	'96 Fetterman et al.	Optical control of arrays
	'96 Wu	Optical time delays
	'97 Collier et al.	Photonics steered wideband shipboard array
	'97 Frankel et al.	Fiber optic beamformer network
	'98 Webb et al..	Optically controlled 2-d array
	'98 Larry/Van Blaricum	Photonic reconfigurability

Major Topics and Sub-topics: Control Architectures

Control Architectures:

• Alternative Scanning Approaches	'83 Sureau	RADANT lens technology
	'85 Lam et al..	Diode grids for scanning
	'94 Harakiewicz	Array on ferrite
	'94 Manasson et al.	Light induced grating for scanning
	'99 Rao et al.	RADANT lens for low cost array
	'98 Webb	Optically controlled (photoconducting) diffraction grid array
• Adaptive control	'69 Benning	Adaptive array beamforming and steering
	'69 Compton	Adaptive arrays
	'81 Steyskal	Null constraints
	'81 Fenn	Degrees of freedom
	'83 Schmitt	MUSIC algorithm (AP paper March '86)
	'95 Mailloux	Augmented covariance matrix--wideband nulls
	'00 Wicks	Space-Time adaptive processing
	'00 Ricks/Goldstein	Architectures for implementing adaptive algorithms

Major Topics and Sub-topics: Array Architectures

Array Architectures:

• Linear and Planar Slot and Dipole Arrays	'80 Evans/Hoofer	Low sidelobe line source arrays
	'83 Sedivic/Hubin	44 GHz printed slot antennas
	'88 J. Pedersen	EHF dual-band corporate fed slot arrays with 1-D scanning
	'89 Schnitkin	Joint stars array
	'91 and 98 W. Milroy	CTS array
	'92 Lamberty et al.	Waveguide dist. Network for EHF arrays
	'92 Lamberty et al.	WAIM for circular WG array (70°scan)
	"93 Karlsson	Applications of WG arrays (Ericsson radar)
	'95 Kinsey	Monopulse synthesis with edge slot arrays
• Linear and Planar Printed Circuit Arrays	'83 Rao/Shafai	Phase error in space fed planar arrays
	'93 Westfeldt/Kenrad	Airlink L-band passive array
	'93 Litva et al.	Mcirostrip reflectarrays
	'93 Poles et al.	Superconducting array
	'97 Tripp	Light weight lens array
	'97 Diaz	Light weight lens array

Major Topics and Sub-topics: Array Architectures

Array Architectures:

• Circular arrays	'69 Boynes et al.	Step-scanned circular array
	'72 Balzano	Circular arrays
	'72 Munson	Microstrip phased arrays
	'80 Wolfson	Commutating feed for cyl. Array
• Cylindrical Arrays/ Conformal Arrays	'71 Gladman/Munger/ Boyns	Cylindrical and conical arrays.
	'73 Balzano	Cylindrical array
	'80 Herper/Stangel	Low sidelobe agile cylindrical array
	'83 Cummings/Kudrna	SHF conformal aircraft array
	'89 Herper et al.	Octave band cylindrical array
	'89 Hanfling	Conformal active array / S-band T/R modules

Major Topics and Sub-topics: Array Architectures

Array Architectures:

- Multiple Beam Antennas

'63 Mehron	Octave bandwidth MBA
'81 Chadwik et al..	Synthesis of RN2 MBAs
'82 Ewen/Bruner	Airborne Rotman lens
'83 Cramer	Geodesic Cone antennas
'83 Blaisdell	Multibeam, multiband satcom
'83 Clapp	Mobius R-2R lens
'85 Ingerson/Chen	Highly efficient MBA
'86 McGrath	Lightweight wide angle lens
'87 McGrath	Lightweight wide angle lens
'88 Montgomery et al..	Large MBA for EHF satcom
'89 Carillo	Multibeam torus
'89 Tropchak/Simon	Rotman lens fed array with 4.5:1 bandwidth
'89 White/Davis	ARSR-4 antenna
'91 Carillo	Dual reflector mulltibeam torus
'95 Rausch/Peterson	Ka band Rotman Lens
'97 Schuss	Irridium antenna

Major Topics and Sub-topics: Array Architectures

Array Architectures:

• Subarray Technology	'80 Southall	Overlapped subarray antenna
	'83 Valentino	'Optical' overlap subarray
	'83 Sinnott	Overlapped subbarrays for OTH radar
	'85 McGrath	Transform feed experiment for time delayed subarray
	'99 Mailloux	Low sidelobe, partial overlap for time delayed subs
• LFOV Antennas	'70 Tang	AGILTRACK-16 antenna
	'97 Franchi et al.	Constrained feed or overlapped subs (Dufort vs Skobelev)
	'98 Kinsey	Limited scan phased array
• Polarizers	'72 Blakely /Burke/Cohn	Meanderline circular polarizers
• Multi-frequency Arrays	'70 Boyns/Provencher	C.L, S Multifrequency/multifunction
	'92 Edward et al.	Dual band (L,X) array (and optical feed)
	'92 Evans/Vemar	Dual band (L,X)
	'93 Zimmerman et al..	Dual band (20, 30 GHz) array

Major Topics and Sub-topics: Enabling Technology

Enabling Technology:

• Theory	'69 Strait/Adams	Wire antenna theory (67 was Harrington's paper)
	'89 Povinelli/D'Angelo	FEBE analysis of tapered notch
	'92 and 98 Chew	Fast algorithms for scattering
	'94 McGrath	FEM code for infinite arrays
	'94 Chebolu et al.	FDTD for microstrip
	'96 Chen/Chu	FDTD + PML for microstrip antennas
	'96 Greenwood et al.	Hybrid FEM/SBR method for microstrip patches (shooting-bouncing ray)
• Coupling Phenomena	'85 Campbel et al.	Reduced coupling between cosited antennas
	'99 Hansen	Finite wideband arrays (edge effects)
	'99 Chio/Schaubert	Tapered slot wideband arrays (edge effects)
• Synthesis	'72 Perini	Conformal array synthesis
	'78 Hansen	Average sidelobe of one parameter sources
	'91 Lawrence et al.	Beamspace low sidelobe synthesis

Major Topics and Sub-topics: Enabling Technology

Enabling Technology:

• Measurements	'71 Woody	Determining corp. Feed errors from pattern meas.
	'81 Patton	Near field for array calibration.
	'81 Brad Hiben	6-port networks
	'90 Aumann/Willwerth	Array calib. By adaptive nulling
	'95 Evens	Phase alignment for low sidelobes
• Materials		
– Photonic or Electromagnetic Bandgap	'99 Gonzalo et al.	Patches on photonic crystal structures
– Chiral materials		
– Left handed materials		
– Flex	'96 Noll et al. (Foster Miller)	Array packaging with liquid crystal polymer (Flex)

A Study of Phased Array Antennas for NASA's Deep Space Network

V. Jamnejad, J. Huang, R. J. Cesarone
Jet Propulsion Laboratory, California Institute of Technology
4800 Oak Grove Drive
Pasadena, CA 91107

Abstract: Recently, the Jet Propulsion Laboratory (JPL) has begun an assessment of the long-term capability of the antennas of the Deep Space Network (DSN). Various alternative plans for upgrading or replacing the present 70-meter antennas have been considered. Several options have been studied which include modifying the present antennas for extended life and reliability, new 70-meter single aperture antennas with offset or symmetric feeds, 100-meter spherical antennas, an array of a few smaller 34-meter antennas, a much larger array (hundreds) of much smaller (5-10 meter) reflector antennas, and finally active planar phased arrays with millions of elements. In this paper we briefly discuss various options but focus on the feasibility of the phased arrays as a viable option for this application. Of particular concern and consideration will be the cost, reliability, and performance compared to the present 70-meter antenna system, particularly the gain/noise temperature levels in the receive mode. Many alternative phased arrays including planar horizontal arrays, hybrid mechanically/electronically steered arrays, phased array of mechanically steered reflectors, multi-faceted planar arrays, phased array-fed lens antennas, and planar reflect-arrays are compared and their viability is assessed. Although they have many advantages including higher reliability, near-instantaneous beam switching or steering capability, the cost of such arrays is presently prohibitive and it is concluded that the only viable array options at the present are the arrays of a few or many small reflectors. The active planar phased arrays, however, may become feasible options in the next decade and can be considered for deployment in smaller configurations as supplementary options.

1. Introduction

The foreseeable future of Solar System exploration includes a number of trends that are expected to place strong customer demands on the facilities of NASA's

Deep Space Network. These trends comprise the following: a migration of the exploratory spacecraft fleet further out into space; a consequent growing reliance on large aperture ground antennas; a rapid growth in the data rate capabilities of science instruments and public media formats, and; a need for long-haul trunk lines resulting from the emplacement of planetary local area networks, especially at Mars. Though these trends emerge primarily from analysis of NASA's Space Science Enterprise robotic mission model, they also apply to the future missions of the Agency's Human Exploration and Development of Space Enterprise.

Recently, JPL was tasked by NASA, to examine the potential future need for large aperture radio frequency antennas. Motivation for the task was not only the normal process of long-range (strategic) planning, but also the aging of the large, 70m diameter antennas of the DSN. Specifically, answers to two questions were sought. Will the level of capability, currently afforded by the 70 m antennas, still expected to be needed in the future? And if so, what is the best way to provide such a capability? The answer to the first question was an unequivocal "Yes," as evidenced by the mission set trends described above. In particular, two of the four themes of the Space Science Enterprise were seen as the strongest drivers. The final answer to the second question is still pending and does not in fact need to be decided until such time as implementation commitments are required. However, work to date has examined seven alternatives, described briefly as Options A - G.

Option A entails modifications to the existing 70m antennas to assure extended life and reliability. These assets were originally constructed as 64m antennas in the late-1960s and early-1970s, and were designed for a 10-year lifetime, running at ~ 25% duty cycle. The antennas are currently on the order of 30 years old, and for much of their lifetime have run at ~ 80% duty cycle. For the benefit of the Voyager Mission, they were upgraded to 70m diameter in the late-1980s, which added significant mass to the load-bearing elements. So it is not surprising that wear-and-tear and future reliability are matters for concern. The option identified a number of structural and mechanical modifications to these antennas that will be needed to assure reliable operations for the future. Also, to minimize costs, no new capabilities were assumed.

Option B is essentially the same as Option A but with the addition of a Ka-band receive capability. Though X-band (8 GHz) has been the nominal frequency band for deep space communications for 20 years, and S-band (32 GHz) before that, there is a strong push to move up to higher frequencies. Rationales include the enhanced directivity and gain (~ 6 dB, after accounting for all losses) afforded by the higher frequency plus the factor of 10 increase in allocated bandwidth.

Option C entails implementation of new ~ 70m single aperture antennas, nominally one per DSN complex. As single aperture, monolithic antennas, these would follow in the tradition of the existing 70m antennas. However, they would use the latest technology to enable high-performance operations at Ka-band frequencies. Antennas would be expected to utilize wheel & track for azimuth motion and actuated panels to maintain surface precision. Traditional designs with Cassegrain feeds and beam wave guide optics were investigated, as well as ones with a clear-aperture, offset feed, as in the recently commissioned 100m Green Bank Radio Telescope. For the purposes of the study, a 70m diameter was used as the baseline for comparison. However, there is no reason why larger diameter single aperture antennas could not be built should that choice be taken by the Agency.

Option D involves an array of four 34m diameter antennas to equate to the aperture of a single 70m antenna. 34m antennas are the current workhorses of the DSN, most often used in the configuration of a single antenna per spacecraft. There is however, significant experience in arraying 34m antennas together, or with 70m antennas, to track especially weak signals. Thus it is logical to consider such an option. However, all previous arraying experience within the DSN has been in the downlink configuration only. Uplink arraying, at this point, is still considered to be a technology development activity. As such, feasibility of this option, as a full function replacement for current 70m capability, is not yet demonstrated.

Option E proposes use of an array of ~ 5m aperture antennas to synthesize the equivalent aperture of a 70m antenna. In essence, it is a large array of small antennas rather than a small array of large antennas, as in the previous option. This option has much in common with recent trends in the radio astronomy community, where arrays are quite popular, not only for their signal sensitivity, but also for their angular resolution. In fact, proposers of this option are working closely with the Square Kilometer Array (SKA) initiative that has been recommended as a high priority in the Astronomy & Astrophysics Decadal Report. It is envisioned that the many small parabolas needed can be manufactured, and outfitted with electronics, relatively inexpensively. Side benefits include the prospect of multi-beaming, at least within the field-of view (FOV) of any given dish. Issues include, as for the previous option, the need to provide for an arrayed uplink.

Option F carries the arrayed concept one step further still by postulating the creation of electronically-steered, phased-array, flat plate antennas. For this option, the individual antenna elements are quite small and there can be many millions of them. Although such antennas have been constructed for various applications over the years, they have never been used for long-haul deep space communications, at the frequencies of interest, and with all the attendant requirements. Significant benefits may include instantaneous and simultaneous beam-forming that can lead to new modes of deep space operations – in effect a demand, rather than scheduled, DSN. Also elimination of the need for many moving parts can yield significant reductions in long-term operating costs. But there are many challenges as well, both technical and economic, that would have to be overcome to successfully implement such a concept. These will be discussed at some length in this paper.

Option G is an innovative idea called the SPHERE (Spherical Pair of High Efficiency Reflecting Elements) concept. Here the idea is to construct an antenna pair, where each element rotates only in azimuth, never in elevation. Because elevation is fixed, gravity-induced surface deformations will not be a concern. One of the pair would cover low elevation angles whereas the other would provide the complementary high elevation coverage. Elevation pointing would be effected by motion of the prime focus feed assembly, as in the Arecibo Radio Telescope. This option has shown promise and will be considered as a candidate for technology development.

Given the lead time required for government budget planning and construction of facilities processes, plus actual implementation, it is reasonable to expect that another 10 years, minimum, of age will accumulate on the existing 70m antennas before an actual replacement capability could be on line. Thus it became evident that some part of Option A will be needed regardless of which option is finally selected. Consequently the recent budget submission reflected this need and is expected to be viewed favorably.

In this paper we will focus on a number of array options (including E, F, and G) and outline some of the issues associated with these options and provide recommendations for further study.

2. Phase Arrays

Phased array antennas composed of a number of smaller antenna elements provide an attractive alternative to the conventional single reflector systems for

hemispherical (near horizon-to-horizon) coverage. These arrays can be divided into two general categories.

Arrays of Low and High Gain elements

The 'filled-aperture' array composed of small radiating elements (with a theoretical hemispherical coverage and a maximum gain of about 3 dB) which will be spaced approximately half a wavelength apart to prevent grating lobes, can provide purely electronic scanning over the hemisphere, by the proper phasing of the individual elements to provide a uniform phase front in any desired direction. However, there will be a scan loss associated with the array, which increases as the beam is steered toward the horizon. Thus the effective aperture area of the array reduces approximately by the sine of elevation angle as shown in Figure 1.

The second type of the array is composed of high gain directional elements which are themselves mechanically scanned toward the desired direction in addition to the proper phasing among the elements. An array of relatively small reflectors (5-10 meters in diameter) is such an array. The array element spacing must be such that there is no blockage between individual reflectors. However, the total effective area of the aperture remains constant and equal to the sum of the aperture areas of the individual elements.

Passive and Active Arrays

From another point of view, the phased arrays can be divided into two different categories: passive and active arrays.

In the passive arrays, in the receive mode, the input signals from the each element is phased by a phase shifter or a delay line and combined via a collection of power combiners. The loss associated with this beam-forming network (BFN), which can be in excess of several dB is directly translated into unacceptable levels of noise figure, which is not acceptable for our applications. Similarly, in the transmit mode, the high power signal is divided via a beam forming network (collection of power dividers and phase shifters) and fed to individual elements. Again the power loss associated with this BFN is completely unacceptable for this application.

In the active array, in the receive mode, there is a low-noise amplifier (LNA) immediately behind each individual element or a small sub-array of elements, which effectively and substantially reduces the noise in the following BFM

composed of phase shifters and power dividers. Similarly, in the transmit mode, the low power signal is divided by the BFN composed of power dividers and phase shifter and then fed to the individual elements (or sub-array of elements) via a High Power Amplifier (HPA). Thus only a minimal amount of power is lost at the power dividers and phase shifters. Furthermore, instead of requiring a very high power generator/amplifier, the power amplification is distributed over the entire array. In a combined transmit/receive array, the HPA and LNA behind the elements are combined to form a T/R module which also includes a diplexer to isolate the transmit and receive paths.

3. Advantages and Disadvantages of Phased Arrays

Phased array antennas provide certain advantages over conventional reflector systems. There are, of course, certain disadvantages as well, which should be taken into consideration in deciding a technically feasible and economically viable solution in the context of a near future or a longer-term (10-20 yrs) antenna system for the Deep Space Network (DSN).

Some of the advantages of a phased array are:

- **Beam agility:** The antenna beam can be moved almost instantaneously to any desired direction, a feat that cannot be accomplished by a mechanically steered reflector antenna system.

- **Reliability and graceful degradation:** A phased array, composed of a large number of radiating elements, is a more reliable system in the sense that in the event of the failure of some or many of its elements, it can still operate with various degrees of capability, namely, with a graceful degradation. While any malfunction in a single reflector antenna system, brings the operation of the whole system to a halt. This could have major implication in critical usage scenarios.

- **Maintainability:** A related issue is the question of maintainability. In a phased array failure of certain element can be addressed, and fixes and routine maintenance can be applied, while the overall system is operating. By contrast, in a single reflector antenna system, the operation of the system must be stopped in order to provide for the necessary fixes and refurbishments of the system.
Lack of mechanical motion: This applies only to the filled aperture phased arrays in which there are no moving parts and all beam steering is provided strictly electronically. This eliminates the possibility of mechanical breakdown and reduces maintenance costs.

- **Multiple beam operation capability:** The phased array provides the ability to provide simultaneous multiple beam operations which can be useful in certain situations involving multiple spacecraft at different positions. This is achieved at the expense of a complicated beam-forming network.

- **Lower long term maintenance cost:** Due to the lack of any complicated moving mechanical parts as in reflector antennas of the DSN, which require constant maintenance and repair, the long term cost of a fully electronic phased array system is expected to be substantially lower than its mechanical counterpart.

Some of the disadvantages of the phased array are:

- **Beam-forming network complexity:** This is perhaps the most significant drawback of a conventional phased array system. The implementation of dividing and /or combining signals from thousands or millions of elements is a daunting task with major architectural and layout complications. This becomes an even harder task to accomplish in a multiple beam implementation. A digital beam-forming and processing scheme may reduce some of these complications but is nonetheless far more complicated than a relatively simple reflector antenna system.

- **Limited multi-frequency operation capability:** The phased array systems are inherently narrow–band. The situation can be somewhat mitigated by appropriate beam-forming architecture and the use of true time-delay elements. The array operation can be extended to multiple frequencies by stacking or interleaving array elements at two or more frequencies (for example at X and Ka bands).

- **Lack of flexibility in adding new capabilities (additional frequencies, etc.):** Any change in operational frequency band would require a change in all the array elements in contrast to a reflector system where only a single feed for the entire system needs to be modified or replaced.

- **Poor performance of single planar array at low elevation angles**
As previously mentioned, in a single horizontal planar aperture array, as the beam scans from zenith, the effective aperture area of the array reduces approximately by the sine of elevation angle as shown in Figure 1.

- **Pattern anomalies** With phased arrays there are possibilities for generating spurious grating lobes and blind spots due to inter-element mutual coupling, existence of surface waves, etc.

- **Very High Up-front Cost:** Due to presence of a myriad of elements and the required complicated beam-forming network, the upfront implementation cost of a fully functional phased array system can be prohibitive.

4. Alternative phased array configurations

There are a number of phased array configurations or variations of the phased array that can be considered for future DSN applications. Only some of the more attractive options are outlined below. All are compared with a single 70-meter aperture reflector system with a scan capability down to 10° elevation.

4.1. Planar horizontal phased array

For a horizontal planar array, the peak is toward zenith. Such an array will be composed of small low gain elements (with a theoretical hemispherical coverage and a maximum gain of 3 dB) which will be spaced approximately half a wavelength apart to prevent grating lobes. This array can provide purely electronic scanning over the hemisphere, by the proper phasing of the individual elements to provide a uniform phase front in any desired direction as shown in Figure 2.

However, there will be a scan loss which will vary as the sine of the elevation angle (projected aperture in the boresight direction), namely, from 0 dB at zenith to as much as 3.0 dB at 30° and 7.6 dB at 10° elevation, as shown in Figure 1. The actual loss in elevation is even higher due to the additional element gain loss at lower elevations. We have also ignored the effects of the surface waves and diffraction from the edges of the finite array that prevent the radiation at the 0° elevation from going to zero according to the simple projected aperture theory.

In order to provide the same gain as a 70-meter reflector at 10° elevation, The aperture size of the array S, compared to that of the reflector, S0, need be approximately

$S = S0 / \sin(10) \approx 5.8\ S0$, or, in terms of diameter, $D = 2.4\ D0 \approx 168$ m

The imposition of the coverage down to the 10° elevation may be a rather stringent requirement. Scanning down to such low elevations may cause many problems in the performance of the array such as blind spots, surface waves, etc. A better solution would either to reduce the scan angel. For example, if scanning only down to the 30° is set as an acceptable requirement, then the array size will

be only double that of the reflector, or a diameter of about 99 meters. Notice that this or a variation of it can be a viable option, since the array can still operate below the 30° elevation but with a lower gain (down by 4.6 dB at 10°). The array can be used for high data reception at or above the 30° elevation and with a reduced capacity but still acceptable performance below that elevation. A somewhat more detailed analysis of such a planar array in provided in Appendix I.

4.2. Hybrid mechanically/electronically steered array

An alternative would be the use of a planar array pointed at 50° elevation angle (the array plane at a 40° angle from the ground) as shown in Figure 3. This array can provide coverage from 10° to 90° elevation angles with a maximum loss of only 1.16 dB for a maximum scan from peak to ±40°. Or, to provide the same gain as the reflector at 10 elevation will require the array area to be

$S = S0 / \sin(50) \approx 1.3\ S0$, or, in terms of diameter, $D = 1.15\ D0 \approx 80$ m

In this arrangement the electronic scanning is only in one dimension, namely elevation. The azimuth coverage will then be provided by mechanical rotation. Therefore the array in azimuth direction will not require phase shifters at the element or small sub-array of elements, but perhaps in each row only two large linear sub-arrays will be required with a phase shift between them to provide vernier electronic beam steering if needed. Also the beam-forming loss in each row can be reduced by the use of serial feeding arrangements as opposed to corporate feeding. All in all such an arrangement will require much smaller number of active components and electronics cost will be substantially lower, at the cost of mechanical azimuth steering and associated complexity and cost.

4.3. Multiple-face phased arrays

Another solution without any mechanical steering is the pyramidal arrangement of several planar phased array faces [1,2].

For example, Figure 4 shows a four-face array. Each face makes a 45 angle with the ground and needs to electronically scan to ±45° from normal to provide full hemispherical coverage. This arrangement requires four planar faces each with

$S = S0 / \sin(45) \approx 1.41\ S0$, or, in terms of diameter, $D = 1.19\ D0 \approx 83$ m

in order to provide the same gain as the reflector at 10° elevation. Or, alternatively, each face can be the same size as the reflector but with a scan loss of about 1.5 dB at the edge of its coverage.

Figure 5 shows a seven-face array. Top face is planar and each side face makes a 60 angle with the ground and needs to electronically scan to ±30° from normal to provide full hemispherical coverage. This arrangement requires seven planar faces each with

$S = S0 / \sin(60) \approx 1.155\ S0$, or, in terms of diameter, $D = 1.075\ D0 \approx 75$ m,

in order to provide the same gain as the reflector at 10° elevation. Or, alternatively, each face can be the same size as the reflector but with a scan loss of about 0.6 dB at the edge of its coverage.

In such multi-face arrays, only one of the faces need be operational at any given time and the face is switched as required. However, an added advantage is that more than one array can be operating simultaneously for communication with different spacecrafts, etc., thus providing a multiple beam coverage.

4.4 Phased-array fed lens antenna (dome antenna)

The dome antenna is another solution for providing hemispherical scan coverage with strictly electronic scanning. This antenna as shown in Figure 6, consists of a single planar phased array and a passive hemispherical microwave lens[3,4]. The planar array is horizontal. However, it scans only to a small angle, for example 30° from boresight). However, in radiating through the passive hemispherical dome lens which is composed of receive and transmit antenna elements, the wavefront is tilted to provide scanning down to a much lower elevation angle. Although this arrangement has some merit, the losses associated with the passive lens, and the quality of the wavefront transformation are rather problematic and make this option not a very viable one. It is possible to make the lens active by introducing T/R modules between the transmit and receive elements of the lens but then the cost and complications could become problematic.

4.5 Geodesic sphere phased array antenna

In yet another variation on the phased array concept, the array elements can be arranged on a spherical surface as shown in Figure 7. In the array, each triangular subarray panel constitutes a module. In each module antenna elements themselves

are arranged in a triangular grid [5]. The beam scanning is provided by a combination of switching the appropriate modules on or off, and by providing phase shift in elements of each module. This conecept is at an exploratory stage and further work is needed to flesh out the details and make it a viable alternative.

4.6 Phased array of mechanically steered reflectors

As already mentioned this array is composed of high gain directional elements which are themselves mechanically scanned toward the desired direction in addition to the proper phasing among the elements. Naturally this array does not provide the beam agility of a fully electronically steered array and is in that sense similar to a single mechanically steered array, although, the smaller reflector elements can be steered substantially faster than a very large reflector. In essence, this arrangement is a compromise between the phased array and the reflector concepts, combining many of the advantages and disadvantages of the two systems. The array element spacing must be such that there is no blockage between individual reflectors. However the total effective area of the aperture remains constant and equal to the sum of the aperture area of the individual elements. As a guide to the number and arrangement of such a scheme we provide the following. Total number of reflectors with a given diameter, D, equivalent to a single aperture reflector diameter $D_0 = 70$m, is

$$N= (D_0/D)^2$$

These reflectors can be compactly arranged in a triangular grid configuration. The minimum spacing between adjacent elements should be greater than

$$s = t\, D / \sin(a),$$

in which, a, is the minimum elevation angle and t factor is a number between 1.1 to 1.2 to account for diffraction effects. As shown in Figure 8, the total number of elements N, is arranged in a regular grid circumscribed within a circle of diameter S. The values of N and S are related to the number of elements along the diameter of this circle, n, by

$$N=(3\, n2 + 1)/4,\ n=1,3,5,\ \ldots$$

$$S = (n-1)\, s + D, \text{ or}$$

$$S / D = t\, \{[(4(D_0/D)2-1)/3]1/2 -1\}/\sin(a) +1$$

For 10° elevation angle limit, this is approximately

$S / D \approx 6.4 (D_0 / D)$, or $S \approx 6.4 D_0$

The following table gives some approximate number of elements and required ground area for various aperture diameters

Reflector diameter, m	2.5	5	7.5	10	12.5	15
Number of elements	760	196	87	49	32	22
Area diameter, m with t=1	454	442	430	417	405	391
Area diameter, m with t=1.1	499	442	430	417	405	391
Area diameter, m with t=1.1	499	485	472	458	444	429
Area diameter, m with t=1.2	544	529	514	498	483	467

In a previous study a detailed look at the architecture, configuration, subsystem costs, as well as performance reliability and other matters of such array of reflectors was undertaken [6,7]. In light of the recent technology improvements and cost reductions, many of these issues have been revisited by Sander Weinreb of JPL and are presently under a separate study.

4.7 Planar Reflect-array

The planar printed reflectarray with phase shifting capability is illustrated in Figures 9 and 10. The printed microstrip reflectarray antenna (see e.g., [8]) consists of a very thin (e.g., 1-mm at X-band), flat reflecting surface coupled with an illuminating feed. The reflecting surface contains many isolated microstrip patch elements without the need for an accompanying power-division transmission line network. As in a space-fed system, the feed antenna illuminates these microstrip elements, which are designed to re-radiate the incident field with appropriate phase shifts in order to form a planar phase front; this operation is similar in concept to the use of a parabolic reflector. Thus the term "flat reflector" is sometimes used to describe the printed microstrip reflectarray, which combines some of the best features of a traditional parabolic reflector antenna and a printed array.

Similar to a parabolic reflector, a reflectarray can achieve relatively high efficiency (e.g., > 50%) with very large apertures since it does not require a transmission-line type power divider/combiner as in the case of a conventional array, but does it spatially, and therefore incurs very little circuit insertion loss. On the other hand, the mainlobe of a reflectarray can be scanned quickly to relatively large angles (e.g., > 50°) from its broadside direction just as an array antenna can, thereby achieving remarkable beam agility. As a benchmark, a circular 100-meter reflectarray would require 24 million and 350 million elements at X- and Ka-band respectively.

There are several methods for reflectarray elements to achieve the desired planar phase front. The first uses identical microstrip patches with different length phase delay lines attached so that they can compensate for the unequal phase delays due to the differing path lengths from the illuminating feed. Low-loss electronic phase shifters employing micro-electro-mechanical switches (MEMS) can be inserted into these phase-delay lines to achieve electronic beam scanning. Since the antenna contains a very large number of elements, 2- or 3-bit phase shifters with low insertion loss are sufficient to achieve good overall beam scan resolution. The parallel-fed reflection-type phase shifters generally yield lower insertion loss than the conventional series-fed transmission-type phase shifters. The second method, which only works with circular polarization, employs identical circularly polarized elements with different angular rotations to compensate for the feed path length differences. Micro-machined motors can be placed underneath each patch to mechanically rotate the element and effect fast beam scanning. With this approach, there is nearly no insertion loss associated with the elements and beam-scanning speeds of the order of milliseconds can be readily achieved.

By using either the electronic phase shifters or the miniature motors, the complicated beamforming network and high-cost transmit/receive (T/R) modules of a conventional phased array with millions of elements will be avoided.

A major drawback of the reflect-array is its narrow bandwidth behavior, which is directly attributable to the array element spacing and the phase delay lines. A given combination of array element spacing and phase delay lines will achieve peak performance only at a single frequency band. Multiple frequency bands could be achieved by using multiple vertically stacked patches, however this would increase the system complexity.

5. Digital beam-forming and other advanced technologies

Some of the more recent and novel technologies include optical beam-forming, digital beam-forming, which contribute significantly to viability of a fully electronically steered arrays. In a fully digitized system, there is no need for any phase shifters, the received signal is amplified and down converted either to an intermediate frequency or to the baseband, digitally sampled and then combined with all the other signals in a digital processing center. This provides total freedom in manipulating the signals and implementing any number of single or multiple bema-forming arrangements.

The complication is, however, in real time processing, particularly of broadband signal. Nonetheless, it is expected that by ever-increasing speed of digital computers and novel parallel processing techniques, such a scheme could become feasible in the next few years. There are a number of technology advances in the phased array area explored and implemented by DOD and the communications industry in recent years [9]. These issues need to be explored in some detail and more realistic cost figures should be obtained in order to be able to ascertain the feasibility of such systems for DSN applications in the next 10 to 20 years.

6. Summary and conclusions

In this paper we presented a review of the various phased array options for DSN applications. The following preliminary conclusions can be reached.

The technology for design and development of a large phased array is presently available. However, it has not reached the maturity and low cost levels needed to make it competitive with a reflector antenna system at the present time. We believe that in the next 10-15 years the breakthroughs in mass production techniques at the components, modules and integrated circuit board level will be achieved that will make it an attractive option.

There are many advantages to a phased array system as compared to the current 70m DSN antenna network. These include, high beam agility, multi-beam multi-target applications, high reliability and easy maintainability. The disadvantages include much higher cost at the present, complexity of multi-frequency operations, inflexibility in adding new frequencies, and lower gain at lower elevations for a flat horizontal array.

The technology risks and the cost drivers include, primarily, the T/R modules and the beam-forming network architecture and implementation.

We propose that, as a proof of concept demonstration, a small scalable flat panel array be built and tested, in order to prove the maturity of the concept and to work out the potential problems at the T/R module and the beam-forming levels, for achieving a DSN-level performance. This could be a 1m-square array at X/Ka bands. This panel could become an element of a much bigger array composed of such modular elements. The architecture of the connectivity and integration of this panel into a larger system would also be part of the proposed work.

7. Acknowledgements

The research described in this paper was carried out by the Jet Propulsion Laboratory, California Institute of Technology, under a contract with the National Aeronautics and Space Administration. The authors would like to acknowledge the efforts of Ed Burns, Jim Costrell, Barry Geldzahler, Paul Hertz, John Huang, Barry Levitt, Jeff Osman, Tim Pham, Sanders Weinreb, Christoper Yung, William Imbriale and others in the various activities leading to the preparation of this manuscript.

8. References

[1] G. H. Knittel, "Choosing the Number of Faces of a Phased-Array Antenna for Hemispherical Scan Coverage," IEEE Trans. Ant. Propagat., Vol. 13, No. 6, pp. 878-882, November 1965.

[2] J.L. Kmentzo, "An Analytical Approach to the Coverage of a Hemisphere by N Planar Phased Arrays," IEEE Trans. Ant. Propagat., Vol. 15, No. 3, pp. 367-371, May 1967.

[3] J.J. Stangel and P.A. Valentine, "Phased Array Fed Lens Antenna," US Patent No. 3,755,815, August 28, 1973.

[4] P. M. Liebman, et al, "Dome Radar – A New Phased Array System," Digest of IEEE International Radar Conference, Washington, D.C., April 1975.

[5] P. K. Bondyopadhyay, "The Cellular Scanning Concept and its applications," Proceedings of 2000 Antenna Applications Conference, Allerton Park, Il, pp. 134-141, Sep. 2000.

[6] V. Jamnejad, "Cost and Reliability Study for Large Array of Small Reflector Antennas for Deep Space Network Applications," 1993 IEEE Aerospace Applications conference Digest, pp. 121-132, Ja. 31, Feb. 5, 1993.

[7] G. Resch, et al, "Synthesis of a Large Communications Aperture Using Small Antennas," JPL Publication 94-15, July 1, 1994.

[8] J. Huang and R. J. Pogorzelski, "A Ka-band microstrip reflectarray with elements having variable rotation angles", IEEE Transactions on Antennas and Propagation, Vol. 46, May 1998, pp. 650-656.

[9] M. G. Parent, et al, "Wideband Digital Subarray Beamforming Using True Time Delay Steering at the element level," Proceedings of 2000 Antenna Applications Conference, Allerton Park, Il, pp. 134-141, Sep. 2000.

Appendix I.

As an example of a phased array, in an optimum triangular-grid configuration, with half-wavelength inter-element spacing, the number of elements equivalent to a 70-meter diameter aperture at 32 GHz (λ=0.93 cm) is about 170x106.

The array perhaps will have a tapered illumination to reduce the sidelobes and thus the received noise. This could reduce the array efficiency to 80-90% or less. Furthermore, even if each array element is active (with LNA's, etc.), there is still the efficiency associated with the elements themselves that, depending on the type of element, can be 90-95% or less. Overall, the efficiency of the array may be only somewhat better than the reflector.

Assuming 85% efficiency for the array as compared with approximately 60% for the reflector, for an equivalent performance we will need a total of about 120x106 elements for the array. However, in a realistic scenario not every element will have separate LNA's, etc. Depending on the performance requirements of the array, it will be divided into sub-arrays of elements and each sub-array will be fed by a separate LNA. Depending on the size of the sub-arrays (perhaps anywhere from 16 to 256 elements, e.g., 100), the number of active components can be accordingly reduced by one or two orders of magnitude. This will be accomplished at the cost of some additional losses inside the sub-array network (and hence reduced efficiency) and other performance hits.

Also, assuming that the cost per unit of active components can be reduced from the $100 quoted by Sandy to about $10-$20 due to the economies of scale and improvements in the technology in the next few years, the total cost of the array can be estimated anywhere from $12 M to $120M.

In the above only the Ka-band frequency operations was considered. An X-band frequency operation (at about 8 GHz) by itself would require (32/8)2=16 times fewer elements and will be much less costly. However, an additional complication in all of these phased array approaches will be the shared-aperture multi-frequency operations. If both X- as well as Ka-band and perhaps even higher frequencies, such as 40 GHz for Human Exploration of Deep Space (HEDS) program, are required within the same aperture area, the questions of element overlapping or interleaving and associated complications regarding mutual coupling, grating lobes, beam-forming networks, etc., become paramount and complicated to solve. A more straightforward and much simpler solution will perhaps be the use of separate arrays for each frequency band.

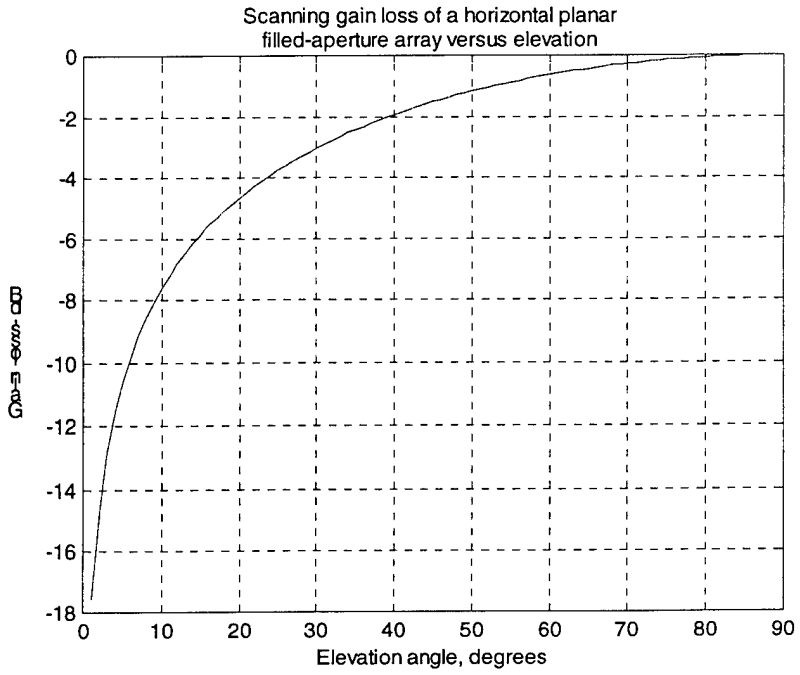

Figure 1. Scanning gain loss of a horizontal planar phased array versus elevation angle

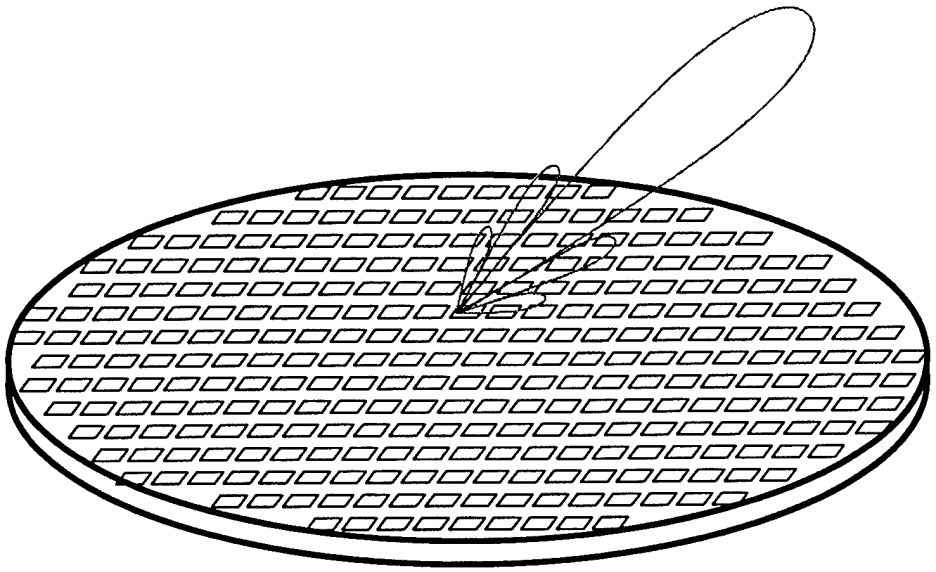

Figure 2. Schematic of a planar horizontal phased array with scanning range: ±80°

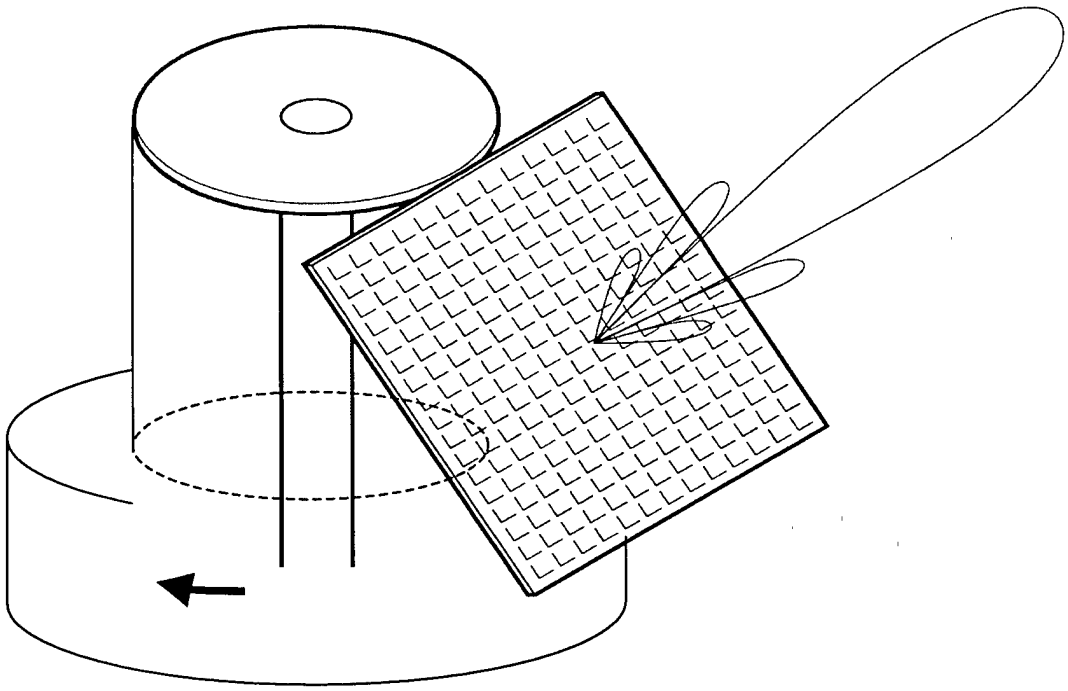

Figure 3. Schematic of a mechanically rotated 50°-tilted planar phased array with electronic scanning in elevation: ±40°.

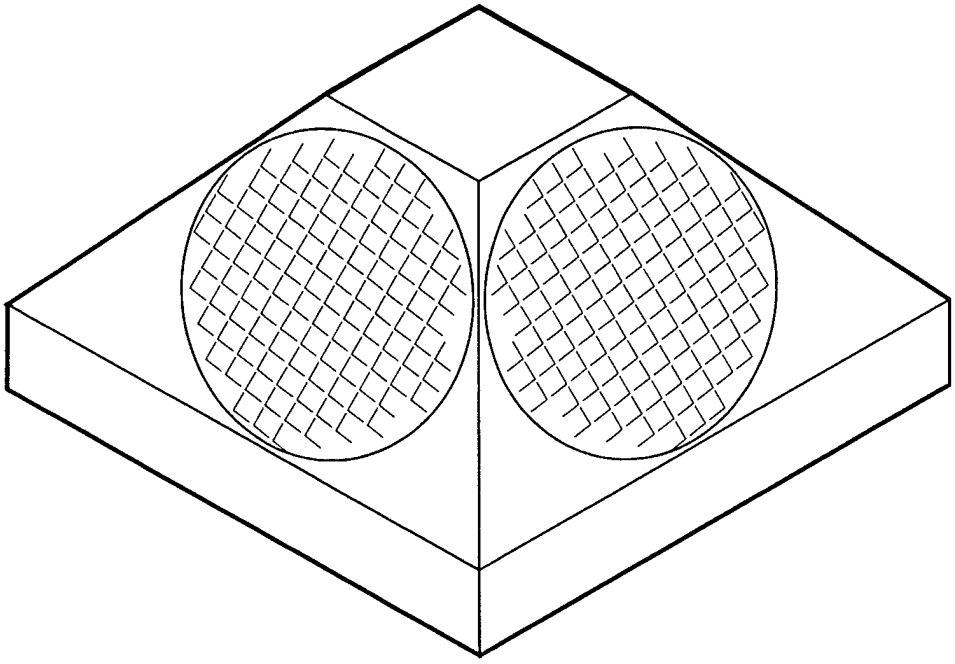

Figure 4. A four-face phased array arrangement: individual array scan: ±45°

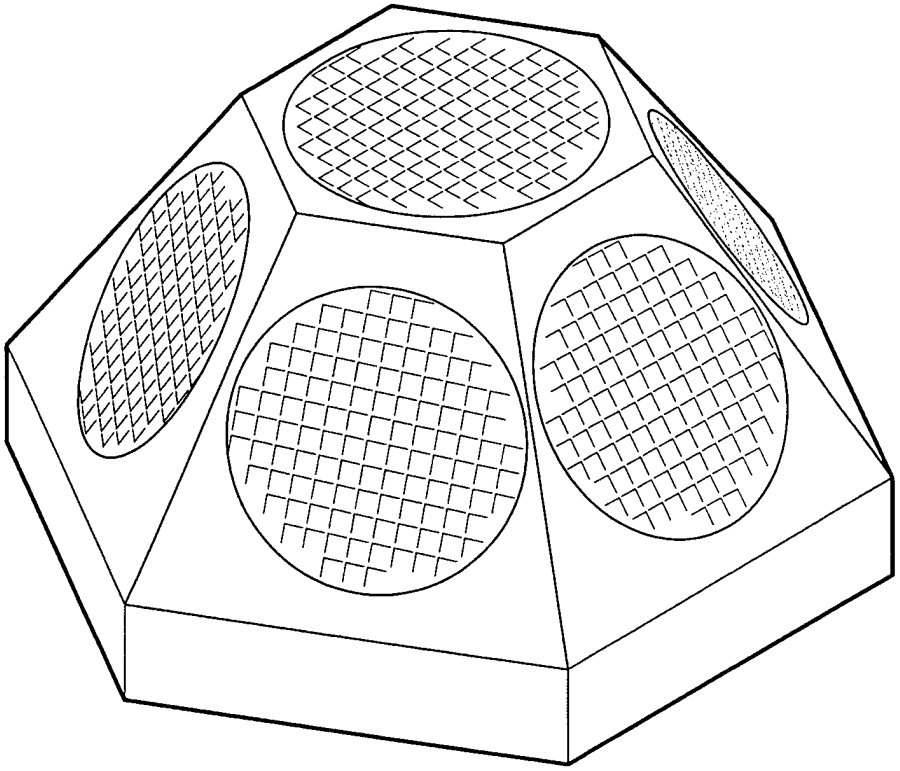

Figure 5. A four-face phased array arrangement: individual array scan: ±30°

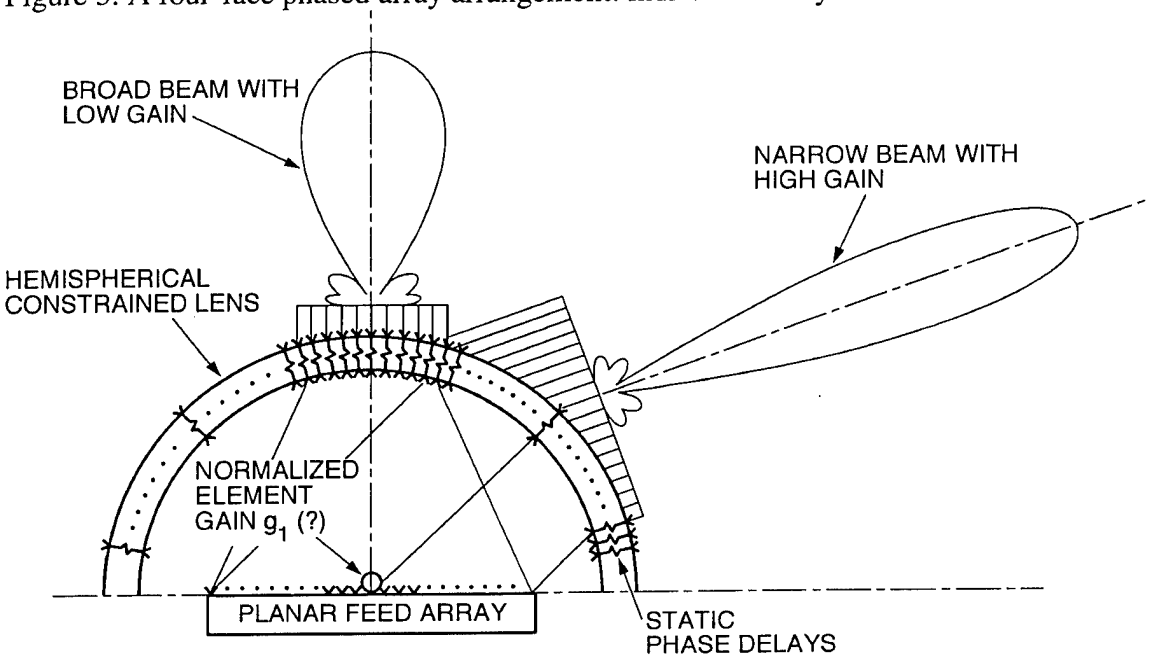

Figure 6. Schematic of a phased array fed lens antenna (Dome Antenna [3])

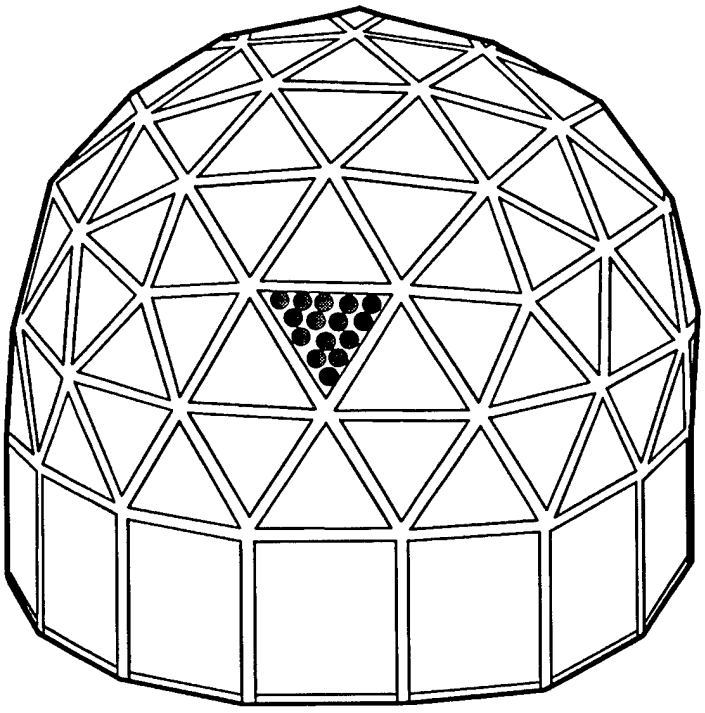

Figure 7. Schematic of a Geodesic sphere phased array antenna. Each face is a subarray. (Based on [5])

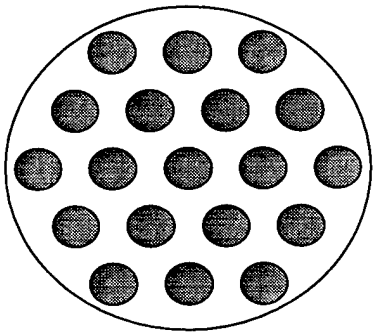

Figure 8. A triangular lattice of reflector elements,
N = (3n2+1)/4 n = 1, 3, 5, ... N=1,7,19, 37,...

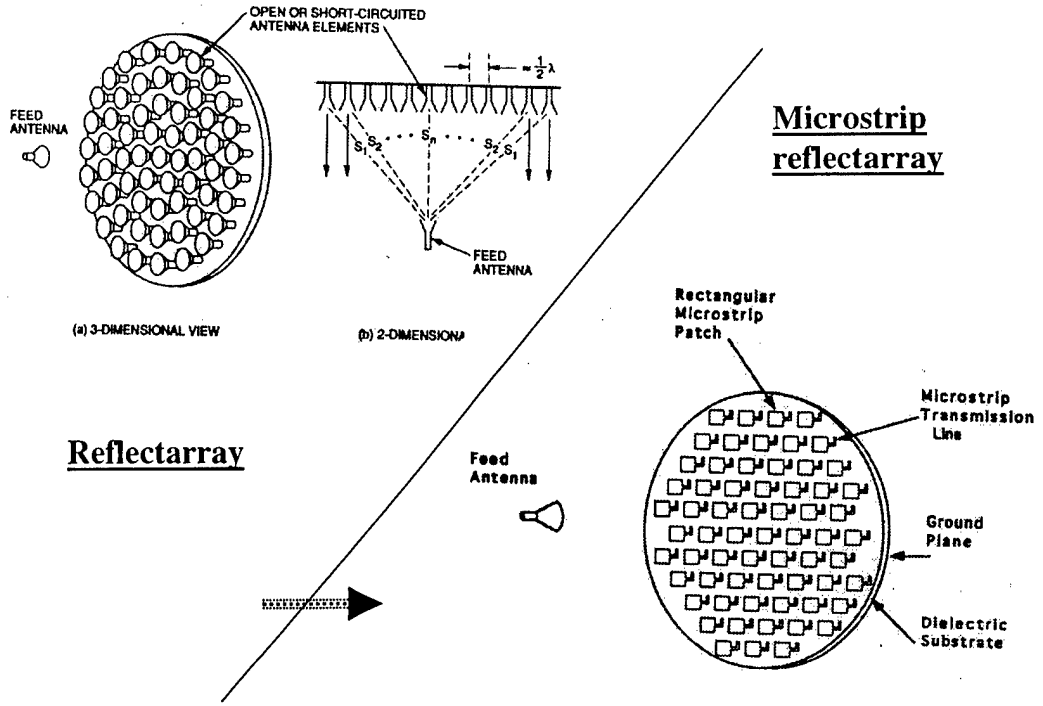

Figure 9. Concept of printed reflect-array antennas.

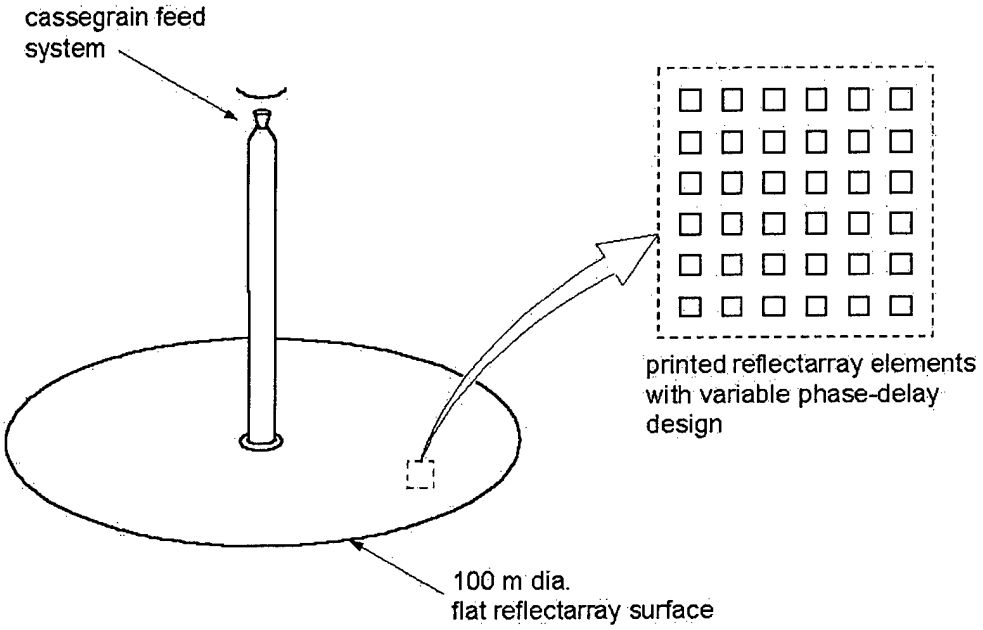

Figure 10. Beam scanning can be achieved by using electronic phase shifters or micro-machined motors located underneath each patch element.

RF Isolation of Separate Transmit and Receive Phased Array Antennas in a Multifunction Environment

Mark G Parent
Doug Taylor
Greg Tavik
Mike Kluskens
John A Valenzi

Naval Research Laboratory
Radar Division
4555 Overlook Avenue, SW
Washington, DC 20375

ABSTRACT

The ability to use Phased Arrays in a multifunctional role requires a high degree of isolation between transmit and receive apertures. Conventional arrays achieve this isolation by using time division multiplexing, pulsed operation, or fixed multi-pole filtering after each element. With the development of multifunction array systems, like the Advanced Multifunction RF Concept (AMRFC), that has multiple capabilities (radar, electronic warfare, and communication), the ability to use these conventional isolation methods can be severely limited due to the multifunction requirements imposed by each of these functions. The use of materials and blended surfaces helps mitigate the effects of scattering and surface wave coupling which tend to decrease the isolation between arrays. Near-field measurement techniques and computer simulations have helped isolate the various modes of coupling between two arrays and have led to a better understanding of array-to-array coupling. Isolation measurements have been performed on two 44-element dipole arrays with and without various isolation treatments. This paper presents these measurements and the solutions required to achieve the high degree of isolation needed between two multifunctional arrays.

1.0 INTRODUCTION

With the current development of stealthy ship designs, the use of multiple embedded arrays is required to maintain a stealthy advantage. Previous ship design typically incorporated separate antenna systems for each functional requirement, which distributed a multitude of antenna structures over the ship's superstructure, which increased the ship's RCS. The Navy is currently undertaking a program named AMRFC [1-3], which will reduce the number of antennas present on a ship. This is achieved by incorporating several functions into a single aperture. In order to accomplish this task, separate transmit and receive apertures are required. One issue that is currently being addressed is the ability to reduce coupling between arrays when embedded into a structure.

The design and implementation of embedded multifunctional array systems require new techniques to improve receiver-to-transmitter isolation as compared to separate stand-alone systems. Since stand-alone systems are optimized based on a single functional requirement, the ability to isolate the receiver from the transmitter can be achieved by physical separation, filtering, or (time, frequency, polarization) multiplexing. A typical communication system can incorporate filtering and frequency or polarization multiplexing to achieve the high degree of isolation required for optimum performance. With an advanced EW system, electrical performance is directly related to the isolation achievable between the transmit and receive antennas. This isolation is typically accomplished by physical separation and use of absorbing structures to minimize antenna coupling. Since the majority of radar systems utilize pulsed signals, isolation between the receiver and transmitter can be accomplished through circulators, limiters, or switches. All of these conventional systems are able to operate at peak performance by applying various isolation techniques that are tailored to each individual system; however, most conventional isolation techniques cannot be directly applied when a single aperture performs multiple functions.

This paper discusses the various coupling mechanisms and their measurement. The first section discusses the impact on receiver performance as viewed from an isolation standpoint. The second section discusses the computational aspect of array-array isolation, and the final section deals with the various isolation configurations and measurement results.

2.0 ISOLATION OVERVIEW

To discuss what various techniques can be utilized to improve the isolation between receive and transmit antennas, it is first necessary to define what determines the degree of isolation required in a typical receive array. The impact of isolation is broken down into two cases: noise and signal isolation.

2.1 Noise Isolation Requirements

In this case, the degree of isolation is solely based upon the increase in the receiver noise figure due to the coupling with noise from the transmit antenna. Figure 1 shows a typical array configuration with transmit and receive apertures imbedded in a structure. Let N_T be the total noise generated by the transmit aperture. This noise induces a corresponding noise N_R at each element of the receive array. The noise isolation I_n is the ratio

$$I_n = N_T / N_R. \tag{1}$$

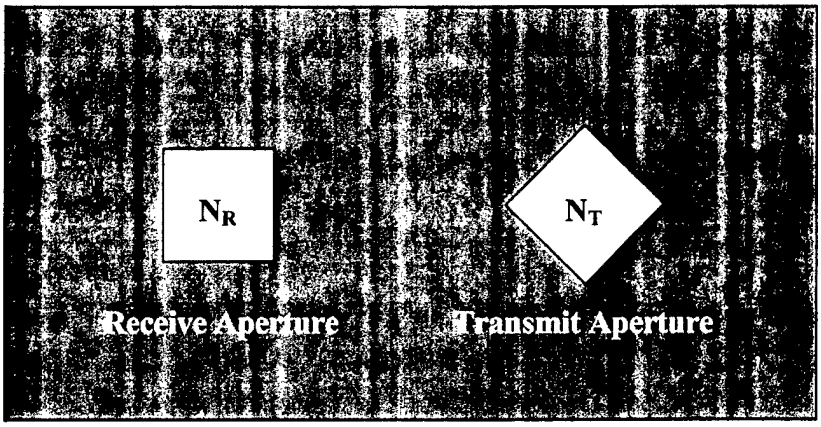

Figure 1. Generic Transmit-Receive Antenna Configuration.

Figure 2 shows a typical receiver front end that consists of a low noise amplifier (LNA), amplitude and phase control, and a K-way power combiner. The effective noise power density present at an antenna element port just prior to the LNA is given by

$$N_{eff}\,(\text{dBm}) = -174(\text{dBm}) + F\,(\text{dB}) + N_T\,(\text{dB}) - I_n\,(\text{dB}), \tag{2}$$

where –174 dBm is the thermal noise in a 1 Hz bandwidth, and F is the receiver noise figure. The maximum allowable coupled noise power density, N_{max}, at the element port depends on how well this noise is coupled from element to element. If it is highly correlated, the noise power density at the output of the K-way power combiner will be very high. On the other hand, if this noise is statistically

independent from element to element, then its contribution at the output of the power combiner will be small. One can define the maximum allowable noise power density, N_{max}, at the antenna port as

$$N_{max}\,(\text{dBm}) = -174\,(\text{dBm}) + F\,(\text{dB}) - C\,(\text{dB}) - M\,(\text{dB}), \qquad (3)$$

where C is the correlation factor, and M is the margin.

The correlation factor defines how well the noise is correlated across the array aperture. If all noise sources corresponding to the K elements are perfectly correlated across the receive array, C is given as

$$C(\text{dB}) = 10 \log (K). \qquad (4)$$

Typically, some of the noise across the aperture will be somewhat correlated and can be approximated by C/2.

As an example, consider an external signal (–190 dBm) that is incident on each element of a 1000-element array (K=1000). The LNA has a noise figure of 4 dB with a gain of 20 dB and is summed, as shown in Figure 2, with a K-way power combiner (PC). The resulting noise figures are given in Table 1 for various correlation factors (all components are assumed lossless).

Correlation Factor	Internal Noise @ output of PC	External Noise @ output of PC	Resulting Noise Figure
30	-150 (dBm)	-139 (dBm)	23 dB
15	-150 (dBm)	-155 (dBm)	5.2 dB
0	-150 (dBm)	-170 (dBm)	4.0 dB

Table 1. Receiver Noise Figures vs Correlation Factor.

Since each transmit-chain design will incorporate numerous noise sources, the total noise associated with a transmit array is the sum of all noise sources in the transmitter chain and is based upon array configurations. A typical multifunction transmit array signal chain may include (1) a waveform generator, (2) an up-converter, (3) subarray amplifiers, and (4) module electronics and power amplifiers. All of these components contribute to the total noise power radiated from an antenna element. To calculate the total radiated noise power from the array in a one hertz bandwidth, one computes

$$N_T\,(\text{dBm}) = K_T\,(\text{dB}) + N_{mod}\,(\text{dBm}), \qquad (5)$$

where N_{mod} is the total radiated noise power density from a single radiating element and K_T is the number of antenna elements in the transmit array. As an example, assume after summing all noise contributors that $N_{mod} = -110$ dBm, $K_T = 1000$. Then by equation (5), $N_T = -80$ dBm.

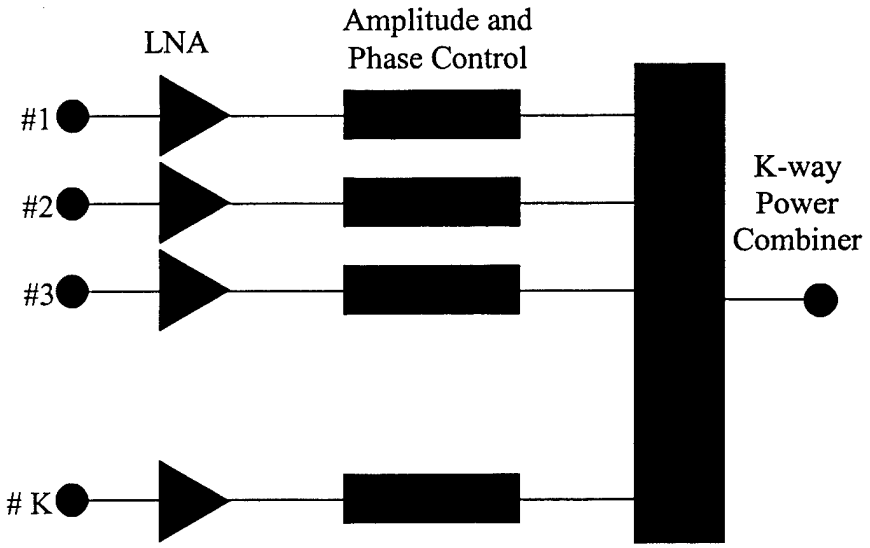

Figure 2. Typical Receiver Front End.

To determine the minimum isolation required for a given noise figure, the noise isolation I_{min} is given by

$$I_{min}\,(\text{dB}) = N_T\,(\text{dBm}) - N_{max}\,(\text{dBm}), \qquad (6)$$

$$I_{min}(\text{dB}) = N_T\,(\text{dBm}) + 174\,(\text{dBm}) - F\,(\text{dB}) + C\,(\text{dB}) + M\,(\text{dB}), \qquad (7)$$

where M is the margin, usually assumed to be 10 dB. Table 2 shows the required minimum isolation I_{min} for different values of C, when the numbers of receive elements K is 1000.

	Best Case	Worst Case	Typical Case
C	0 dB	30 dB	15 dB
I_{min}	98 dB	128 dB	113 dB

Table 2. Minimum isolation values for various correlation factors.

The worst-case correlation factor (C = 30 dB) represents the unlikely event where all of the coupled noise signals, at every receive element, add in-phase in the power combiner. The best-case correlation factor (C = 0 dB) represents an equally unlikely case where all coupled noise signals are statistically independent from element to element. The most likely case, termed the "Typical Case", where C = 15 dB, is simply midway between the two extreme cases. As Table 2 shows, even the typical required I_{min} may be difficult to achieve.

2.2 Signal Isolation Requirements

The second isolation requirement is based on array-element signal coupling that will put various stages of a receiver system into 1dB compression (P1dB). The signal isolation is given by

$$I_s = T / R, \tag{8}$$

where T is the total signal power that is being transmitted and R is the signal power measured at a single element in the receive array. Figure 3 presents a typical multifunctional (utilizing subarrays) receiver front-end consisting of a receiver module, subarray power combiner and driver, aperture power combiner, and communication and digital downconverters. The parameters in Figure 3 are the module noise gain G_M, the subarray noise gain G_{SA}, the subarray correlation factor C_{SA}, the aperture noise gain G_{AP}, and the aperture correlation factor C_{AP}.

In order to predict the required isolation needed for the above generic receiver configuration, it is necessary to determine the input power levels that will cause the system to go into compression at various stages in the receiver chain. For the receiver shown in Figure 3, the stages are defined by equations in Table 3.

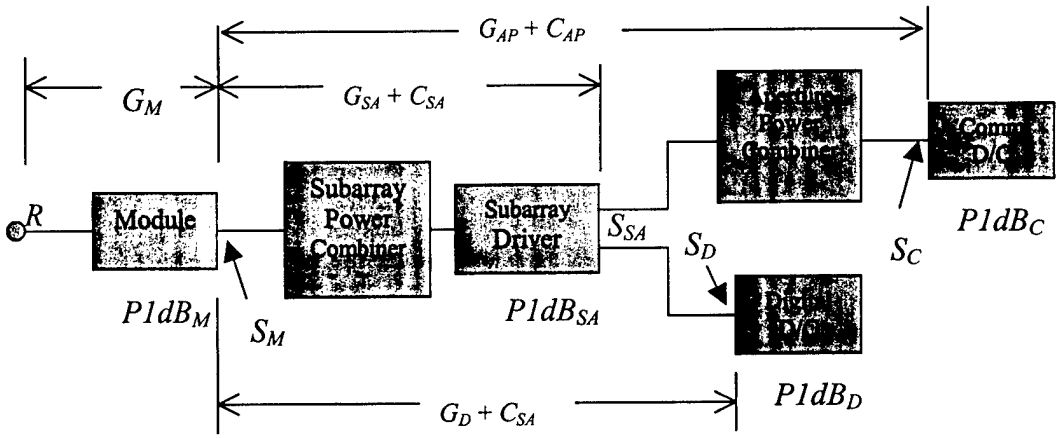

Figure 3. Receive array gain and power definitions.

Stage	Output 1 dB Compression Point	Output Power Levels
Module	$P1dB_M$	$S_M = R + G_M$
Subarray	$P1dB_{SA}$	$S_{SA} = R + G_M + G_{SA} + C_{SA}$
Communication Down Converter	$P1dB_C$	$S_C = R + G_M + G_{AP} + C_{AP}$
Digital Down Converter	$P1dB_D$	$S_D = R + G_M + G_D + C_{SA}$

Table 3. Output power levels for various receive stages.

By replacing S with P1dB and rearranging the expressions in Table 3, one can calculate the power level at each element that forces a particular part of the receive chain into 1 dB compression:

$$R_M = P1dB_M - G_M, \quad (9)$$

$$R_{SA} = P1dB_{SA} - G_M - G_{SA} - C_{SA}, \quad (10)$$

$$R_C = P1dB_C - G_M - G_{AP} - C_{AP}, \quad (11)$$

$$R_D = P1dB_D - G_M - G_D - C_{SA}. \quad (12)$$

Substituting (9) – (12) into (8) and adding the margin term M yield

$$I_M\,(dB) = T(dBm) - P1dB_M + G_M + M, \tag{13}$$

$$I_{SA}\,(dB) = T(dBm) - P1dB_{SA} + G_M + G_M + C_{SA} + M, \tag{14}$$

$$I_C\,(dB) = T(dBm) - P1dB_C + G_M + G_{AP} + C_{AP} + M, \tag{15}$$

$$I_D\,(dB) = T(dBm) - P1dB_D + G_M + G_D + C_{SA} + M, \tag{16}$$

where each subscript indicates the isolation required to prevent that part of the receive chain from entering compression.

As in the case of noise isolation, the correlation factors depend on the number of elements or subarrays. Table 4 shows the level of the correlation factors for the various cases based on a 1000-element array with ten 100-element subarrays.

Correlation Factor	**Best Case**	**Worst Case**	**Typical Case**
C_{SA}	0 dB	20 dB	10 dB
C_{AP}	0 dB	30 dB	15 dB

Table 4. Receiver correlation factors.

For example, compute I_C for T = 1000 watts, $P1dB_C$ = –20 dBm, G_M = 30 dB, G_{AP} = –10dB, and M = 3 dB. Then the required isolation that keeps the communication receiver out of 1dB compression by 3 dB is shown in Table 5 for different values of the aperture correlation factor C_{AP}.

	Best Case	**Worst Case**	**Typical Case**
C_{AP}	0 dB	30 dB	15 dB
I_C	103 dB	133 dB	118 dB

Table 5. Communication stage minimum isolation requirements.

In summary, the multifunction array designed must consider two types of isolation. Noise isolation is required in order not to raise the effective noise figure of the receive chain, and signal isolation is required to prevent signal compression in the receiver chain. Both impose very stringent requirements on isolation (> 100 dB).

3.0 SIMULATIONS

3.1 ANTENNA COUPLING

Simulating antenna isolation and coupling is viewed as an integral part of the engineering process to control coupling through design. Detailed simulations of complex antennas require high-accuracy solutions to capture the complete coupling physics that occur between near or distant apertures. The computer simulations discussed here are based on two purely numerical solutions to Maxwell's equations, a method of moments (MoM) integral-equation solution called Carlos3D and a finite-difference time-domain (FDTD) method called FDTD3D. Carlos3D was written by the Boeing Company [4] while the FDTD code is unique to NRL [5].

The antenna considered here consists of a dipole antenna element that is driven by a 50-Ω coaxial line and is impedance matched with a split-tube balun. The results of simulations for a single dipole and small arrays of dipoles are compared to measured data.

3.2 BALUN-MATCHED DIPOLE ELEMENT

The dipole element that is modeled with Carlos3D and FDTD3D is shown in Figure 4. This element is designed to be driven by a standard 50-Ω coaxial cable and mounted perpendicular to a ground plane. The numerical model of this antenna shown in Figure 5 was created using the CAD package GiD (details can be found at http://gid.cimne.upc.es), with the help of an NRL Fortran postprocessor to divide the mesh into parts based on facet type and boundary conditions.

In total, the numerical model of the dipole element was broken down into 11 separate surface pieces. The division of the model into this many sections was required to keep triangular and quadrilateral mesh elements separated, to insure that the correct boundary conditions were applied to particular sections and to allow the formation of physically correct electrical junctions between intersecting

surfaces. An exploded view of the mesh is shown in Figure 6 that lists the boundary condition and the mesh element for each section of the separated model.

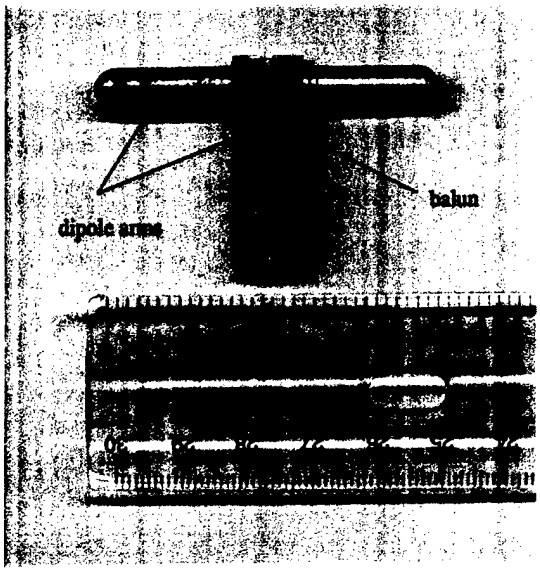

Figure 4. NRL dipole with slotted tube impedance matching balun. The resonant frequency of the dipole is approximately 3 GHz.

Each shade represents a separate part containing a piece of the finished model. The bottom section is a length of coaxial waveguide that is below the ground plane. The model contains both triangle and quadrilateral surface patch elements. The walls of the balun are modeled as infinitely thin surfaces.

The complex S-parameter S_{11} for the balun-matched half-wave (@ 3 GHz) dipole was calculated over the frequency range of 2 to 4 GHz. This range was chosen so that the midpoint (3 GHz) corresponds both to the resonance of the dipole and to the quarter-wavelength of the slot. After calculating S_{11} with Carlos3D and FDTD3D, its value was converted into a voltage standing wave ratio (VSWR) and is plotted in Figure 7, along with the measured VSWR of a single dipole.

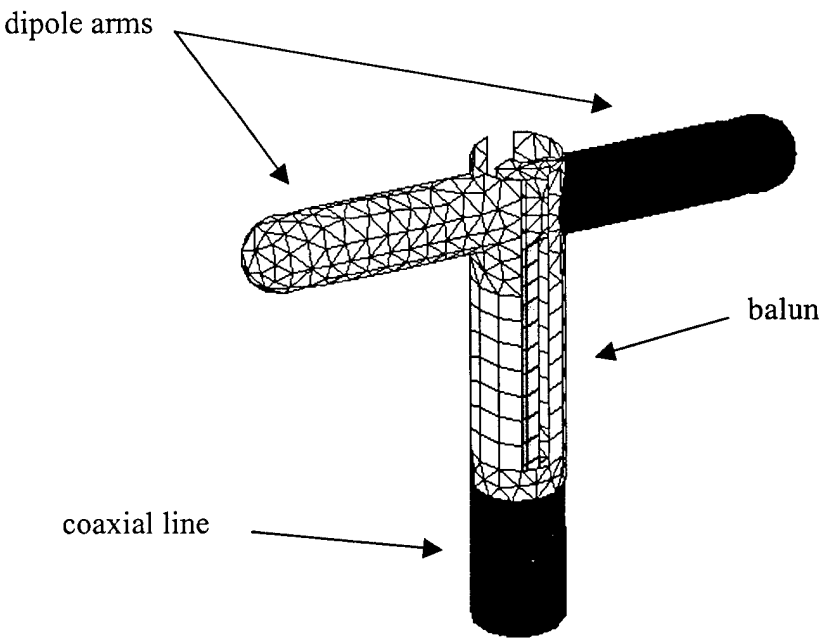

Figure 5. Numerical model of the balun-matched dipole.

The prediction of the VSWR of the dipole using the FDTD method captures the structure in the VSWR over the frequency band much better than the MoM method in this case. In particular, Carlos3D provides an overly optimistic estimate of the VSWR from 2.75 GHz to 4.00 GHz; whereas the FTDT3D estimate is cautious (lies above the measured curve). Note the small dip in the VSWR around 2.25 GHz that the FDTD method reproduces but the MoM method fails to capture. The authors believe that the discrepancy between Carlos3D and FTDT3D curves is attributable to the fact that the Carlos3D assumes zero thickness for the balun wall of the dipole while FDTD3D models the wall thickness. The cross sectional slice through the balun center in Figure 8 illustrates how the FTDT3D model incorporates the balun thickness, thereby providing a more accurate geometrical representation. Apparently, the VSWR is sensitive to the thickness of the balun wall.

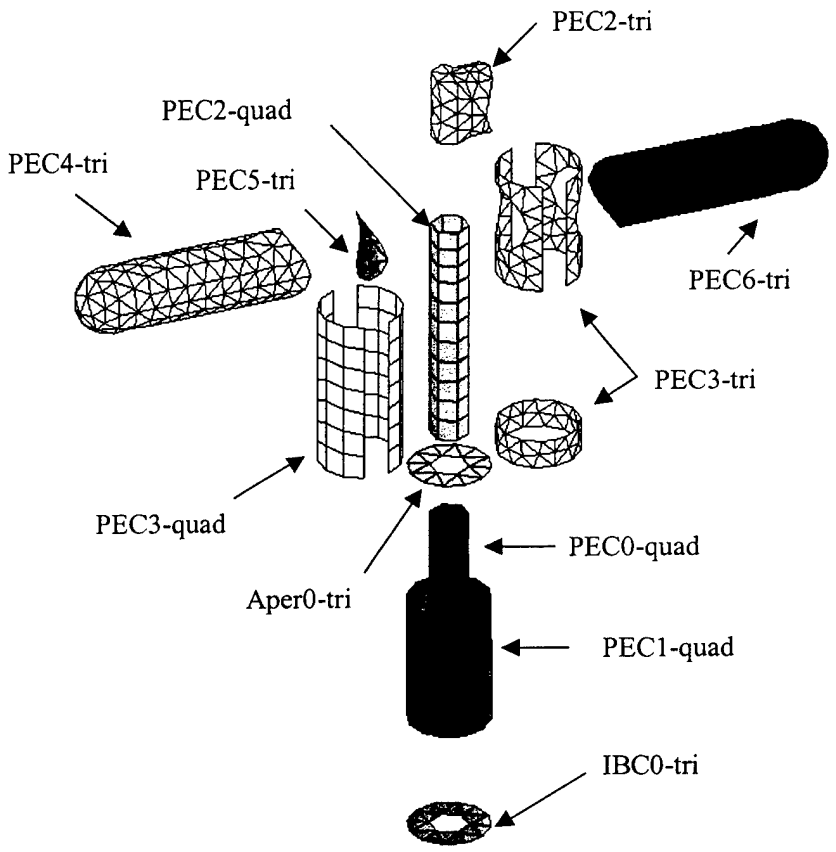

Figure 6. Exploded view of the dipole geometry used with Carlos3D. Each piece is labeled with its boundary condition, numerical order, and element type. The boundary conditions are perfect electrical conductor (PEC), impedance boundary condition (IBC), and aperture in the ground plane (Aper). The mesh elements are triangular patch (tri) and quadrilateral patch (quad).

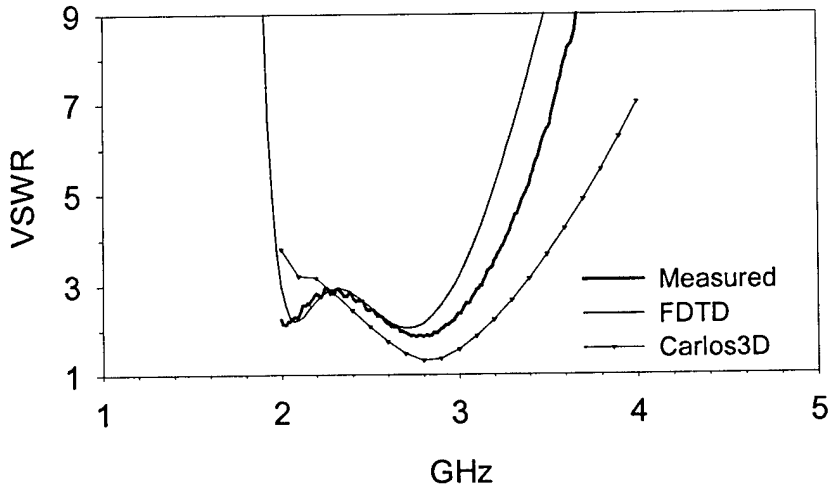

Figure 7. Calculated and measured VSWR of a single balun-matched dipole in an infinite ground plane driven by a 50-Ω coaxial feed line.

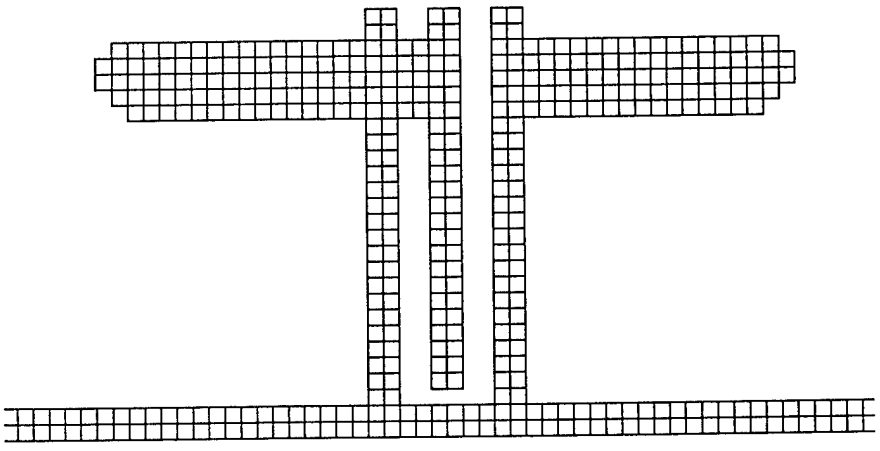

Figure 8. Cross-sectional slice through center of the dipole.

3.3 ARRAY OF DIPOLE ELEMENTS

An array of antenna elements was constructed for Carlos3D by exercising an option in the input file to use the same set of geometry files repeatedly and to translate each geometry to a new position. This approach is efficient for constructing antenna arrays since the numerical mesh for a single element is all that is required. This method was used to construct the 7-element array of the balun-matched dipole elements in Figure 9. The spacing was set so that the distances in the x-direction and the y-direction are one wavelength and one half wavelength, respectively, at 3 GHz.

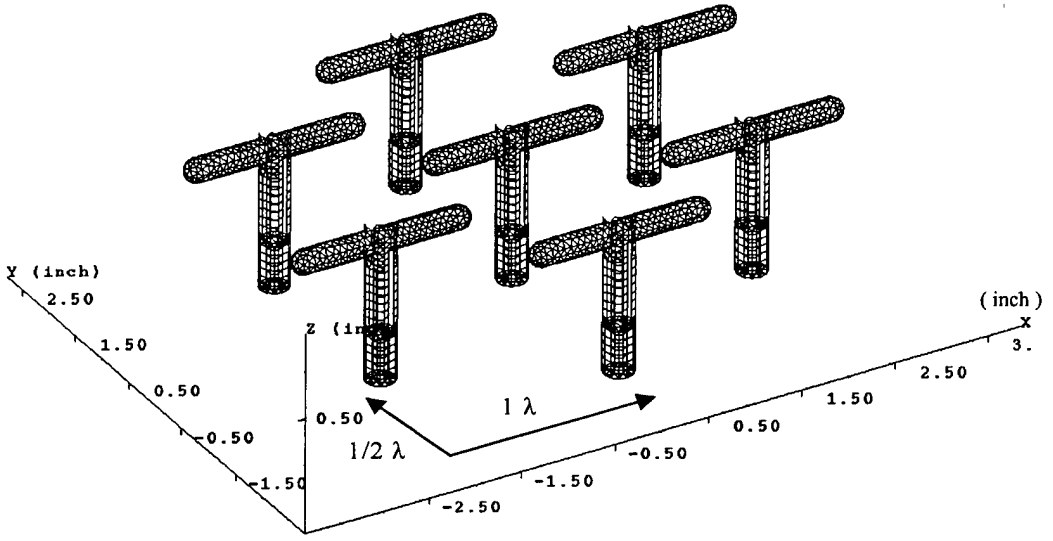

Figure 9. Array of seven balun-matched dipole elements. The wire frame image was generated with the Boeing program, MrPatches, using diagnostic output from Carlos3D. The spacing of the elements is 1 λ along the x-axis and ½ λ along the y-direction based on a frequency of 3 GHz.

The S-parameters for the 7-element array were computed using a configuration where six of the element ports were terminated with a matching load and the center element was energized. The termination was implemented by setting the surface impedance of the source aperture to unity; this impedance boundary condition effectively absorbs any energy propagating down the coaxial

line toward the source port. The energized port was given a voltage of 1 volt. The calculated VSWR for the small array is shown in Figure 10. The VSWR of the array is for the center element, and the edge elements are terminated with a 50-Ω load resistance. In this simulation the mutual coupling of the array elements has the effect of producing a better impedance match at 3 GHz.

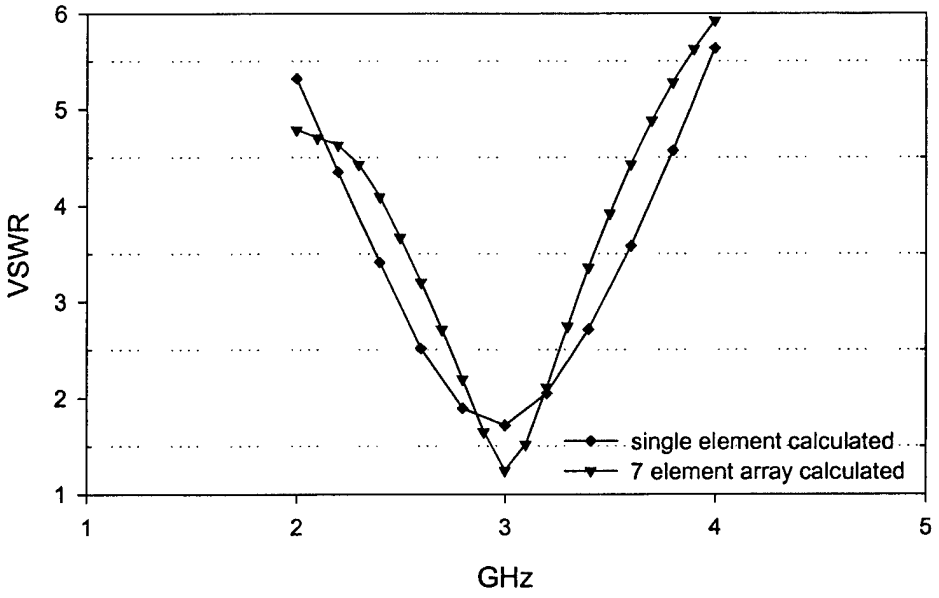

Figure 10. Calculated VSWR of a single dipole and a 7-element dipole array.

In Figure 10 only one port of the array was energized so the S-parameter set consisted of a single number. In the Carlos3D modeling it is possible to energize all the ports in the array and compute intra-array antenna mutual coupling. A calculation of this type was performed by rearranging the elements into a linear array with half-wavelength spacing and by adding a duplicate array at a fixed distance from the first array. The two energized ports were the center elements of each linear array. The other antennas were connected to coaxial ports but were terminated with matching loads. This configuration is shown in Figure 11 for two, identical, 7-element, balun-matched dipole arrays. The center elements of the arrays are separated by 34 inches, and inter-element spacing for each array is 1.7 inches. For the S-parameter simulations, the center elements are energized, and the remaining dipoles are terminated into matched loads.

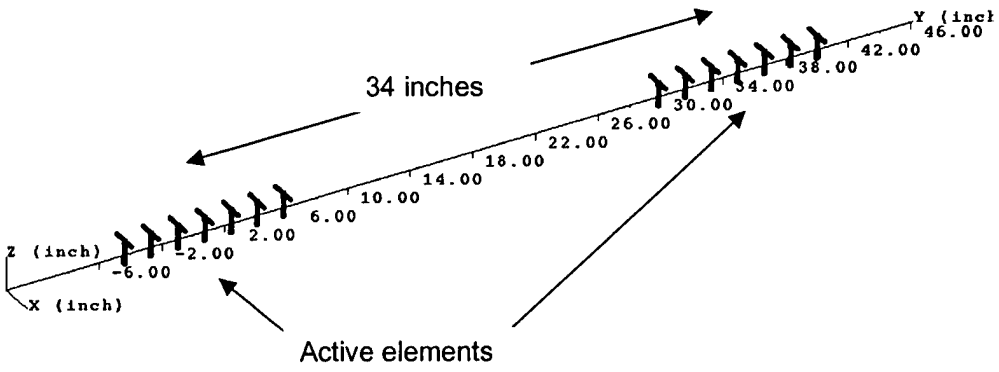

Figure 11. Geometry of an inter-array coupling simulation for two, identical, 7-element, balun-matched, dipole arrays with center elements 34 inches apart.

The results of the coupling calculation are plotted in Figure 12. Note that the S-parameter matrix is symmetric as required by reciprocity. Comparison of the measured and simulated antenna coupling indicates that the coupling is greatest near 3 GHz, where the best impedance match occurs. The smallest coupling value is seen to occur at the highest frequency, where the impedance match is poor and the number of wavelengths between the two elements is a maximum.

The measured data show a dipole-to-dipole coupling less than that produced by the simulation above 3 GHz. The measured and simulated coupling is between coaxial ports so that the dipole impedance mismatch is included. The dipole VSWR, Figure 7, shows that the simulated impedance match is better than the measured impedance match above 3 GHz. This could account for the offset between measured and simulated dipole coupling shown in Figure 12 above 3 GHz. However the shape of the curves are quite similar which indicates that the MoM method is capturing the physics of the antenna coupling interaction correctly.

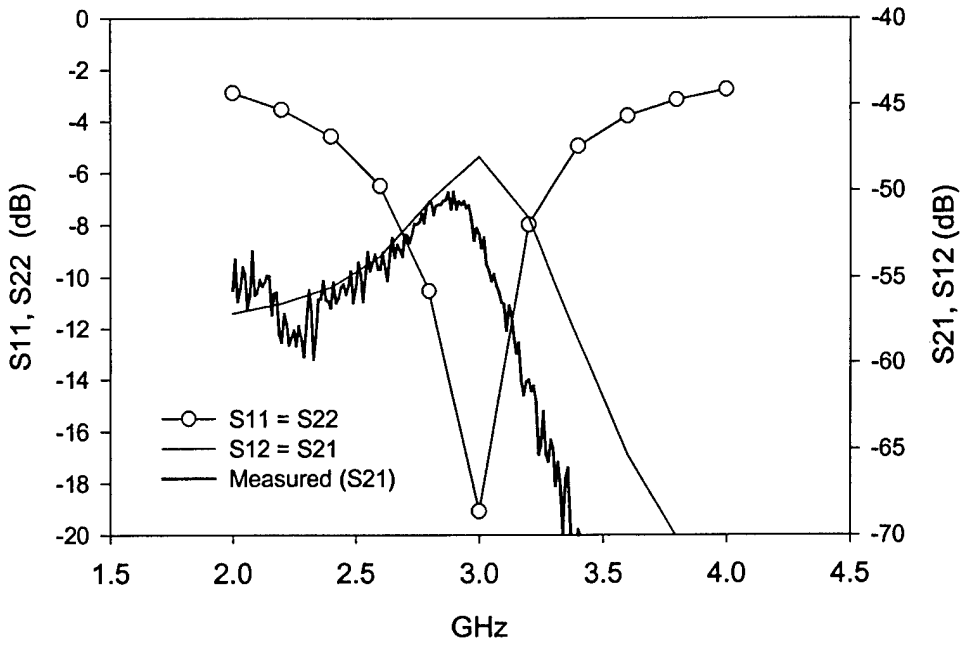

Figure 12. Measured and computed coupling between the center elements of identical, 7-element, balun-matched dipole arrays with 1.7-in inter-element spacing and the active center elements are separated by 34 in.

4.0 COUPLING TRANSFER MECHANISMS

For two proximate arrays or apertures, coupling can occur via five modes: direct coupling, diffraction, waveguide, surface wave, and leakage. Figure 13 shows the five coupling paths, all of which are highly dependent on the array environment and structure.

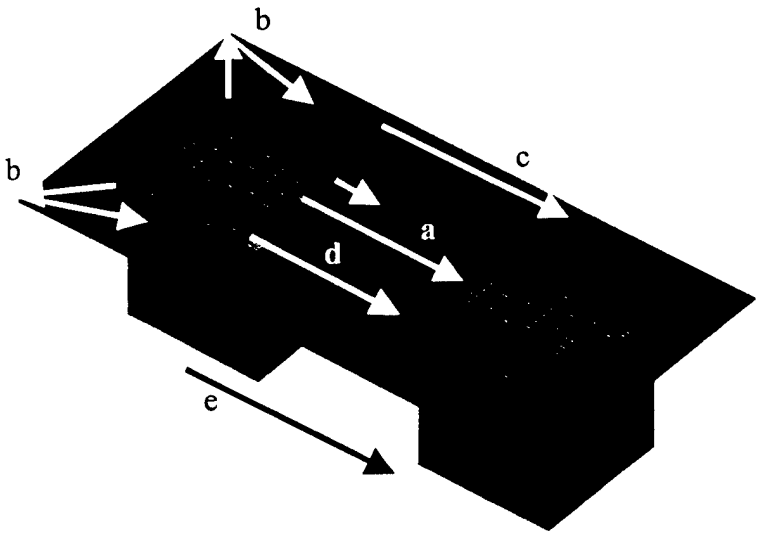

Figure 13. Coupling paths: (a) direct coupling, (b) diffraction, (c) waveguide effects, (d) surface waves, (e) leakage.

The largest amount of coupling between the two arrays occurs through the direct coupling between the arrays as aggregates, designated by path a. This coupling path is present whether the arrays are imbedded in some structure or occur in free space. This coupling mechanism is completely dependent upon the sidelobe level at or near 90 degrees (that is, in the endfire direction to the arrays). For arrays that are imbedded in some structure, additional modes of transfer will occur. In particular, coupling from diffraction (path b) of the surrounding structure may dominate the direct coupling.

The next effect that can influence the coupling between the arrays is due to the physical make-up of the surrounding structure. If a radar absorbing structure is used, care must be taken so that a waveguide mode (path c) is not excited in the structure. This is also true for thick ballistic type radomes that are placed over the arrays. At certain scan angles, it may be possible to "trap" energy inside the radome that can then leak out in an endfire direction that will also tend to increase the coupling between the arrays. Other types of materials (composites, metals) may also induce surface wave coupling (path d).

Finally, the leakage (path e) between transmitter and receiver must be properly controlled to minimize the RF coupling between arrays. Standard shielding practices must be employed to ensure that any leakage effects are removed or minimized.

5.0 EXPERIMENTAL INVESTIGATIONS

To measure isolation or coupling between separate antennas or arrays, an experimental apparatus was designed and built to allow for various antennas to be configured and tested in a controlled environment. The measurement apparatus, shown in Figure 14, consists of two computer-controlled turntables that are separately mounted on a 16-foot, twin-rail assembly. To make RF coupling measurements, an HP 8722ES network analyzer and an HP 8349B broadband amplifier are used as the transmitter-receiver system. By placing this equipment inside an anechoic chamber, isolation levels approaching 100 dB can be achieved.

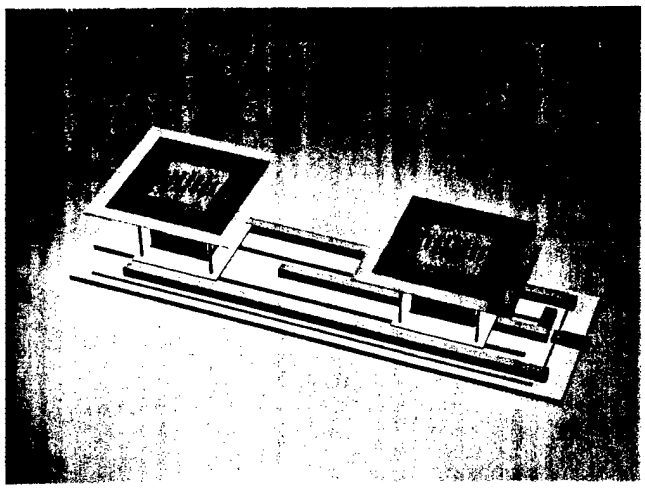

Figure 14. Isolation Measurement Apparatus

Initial isolation measurements were performed on the 44-element dipole array, shown in Figures 15-16, which was designed and built to look at the various coupling mechanisms. The array has a low sidelobe level in the H-plane, while the element spacing in the E-plane produces grating lobes starting in the middle of the operating frequency band. By changing the frequency of the array, a grating lobe is formed in the endfire direction and is a simple mechanism for increasing the coupling between the two arrays. The measured and calculated free-space E-plane and H-plane patterns are shown in Figure 17.

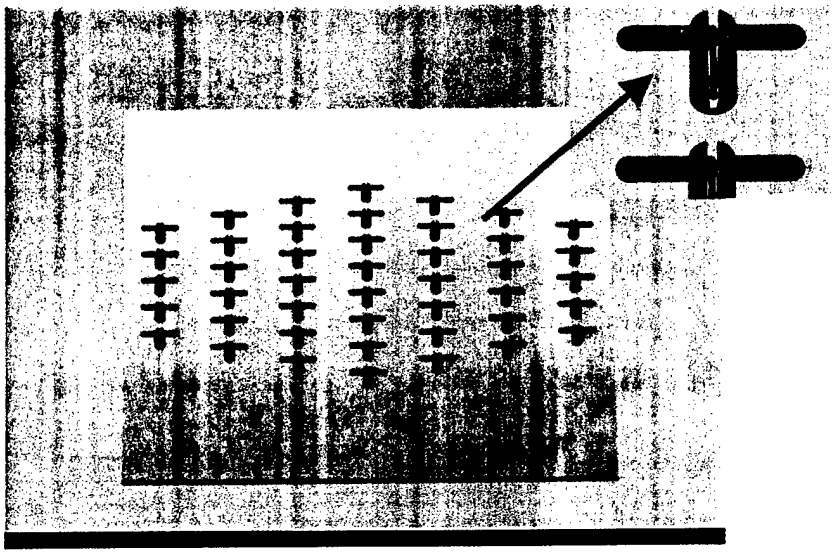

Figure 15. 44-element dipole array with $\lambda/2$ spacing in the H-plane and λ spacing in the E-plane.

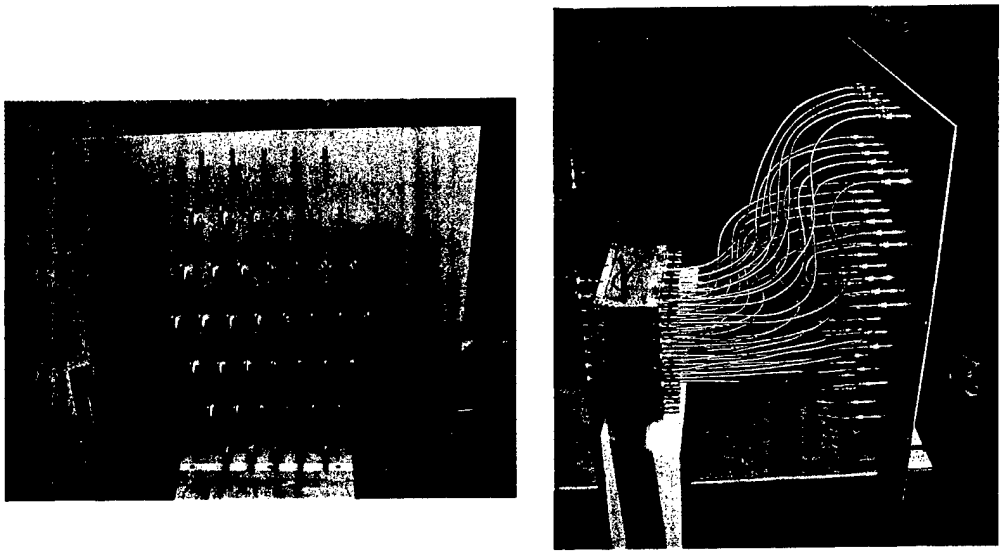

Figure 16. Front and side views of a 44-element dipole array shown with a beamformer attached.

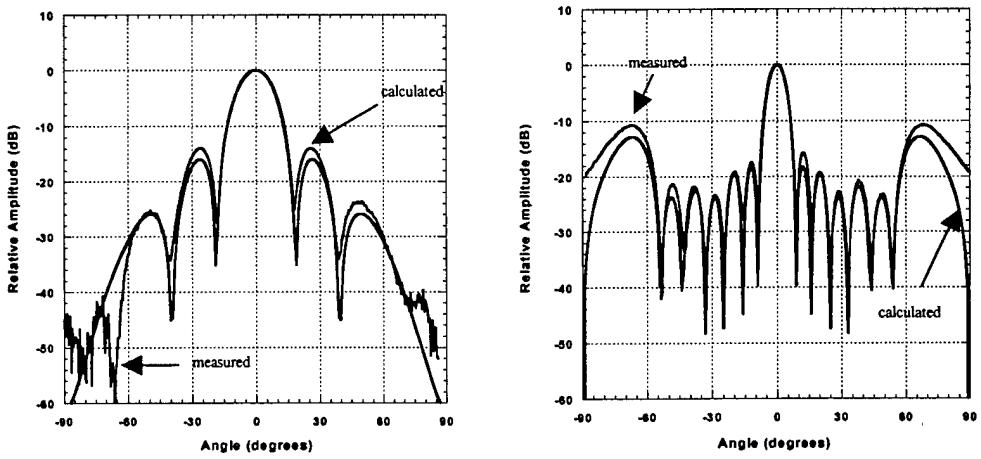

Figure 17. Measured and calculated H-plane and E-plane array patterns at 3.2 GHz.

The shape of the array produces the low sidelobe levels in the H-plane, while the element spacing in the array produces the grating lobes which show up in the E-plane cuts. The grating lobes are generated when the array is operated above 3 GHz.

6.0 EXPERIMENTAL RESULTS

To validate various electromagnetic codes and to investigate the various coupling mechanisms, a series of measurements were performed using simple absorbing structures and artificial surfaces [6-7]. Absorbing material is used to reduce the direct and diffraction coupling, while the artificial surface was used to measure the effect on surface-wave coupling as well as the direct coupling.

Selected initial measurements that were made with the two 44-element arrays using the isolation apparatus are shown in Figures 18 –20. For the first set of measurements, standard microwave foam absorber was placed between the two arrays in various configurations to measure the effect it had on direct coupling. The two arrays were positioned 4 feet apart with a metal ground plane placed between them with the absorber orientated vertically. The absorber typically reduced the mid-band coupling by 15 dB but had little effect on the low-level

diffraction coupling. This is seen as the rapid variation in signal levels across the operating band due to the diffraction signal interfering with the reduced direct coupling signal. When the absorber is oriented horizontal to the ground plane, the direct coupling is reduced by only 10 dB, but the effect of diffraction coupling is reduced by noticing the rapid variation signal is reduced. When the absorber is raised above the ground plane, the direct coupling is reduced to the levels produced when the absorber is oriented vertically. The direct coupling energy appears to be located approximately 2 inches off the surface of the metal ground plane. Further investigations are planned to map the fields over the surface to have a better insight on how the energy is transferred between arrays.

The second set of measurements investigated an artificial surface placed between the arrays. The artificial surface is made from a corrugated surface with $\lambda/4$ grooves cut to 3 GHz. Figures 21-22 show two different configurations with corresponding data. The corrugated surface works well with correlated sidelobe (large levels due to element-element phasing) but has little effect on coupling in the far out sidelobes which are due mainly to diffraction and scattering effects. The corrugated surface reduces the direct-couple E-plane signal by approximately 15 dB, as shown in Figure 22. The coupling in the H-plane is due mainly to the diffraction effect and is not affected by the corrugated surface as seen in Figure 21.

The last data set, shown in Figure 23, displays the effect of decoupling the array-element pair by physical separation [8]. It is very interesting to note that the top curve is calculated using the far-field approximation [9], including the measured gain of the transmit array and receive element. The measured data shows the monotonically decreasing amplitude as a function of distance that is representative of power measurements in the far-field. This data set shows that in the endfire direction, the far-field condition exists very close to the array. As the observation point moves towards the boresight direction, the far-field moves out to the typical $2D^2 / \lambda$ distance.

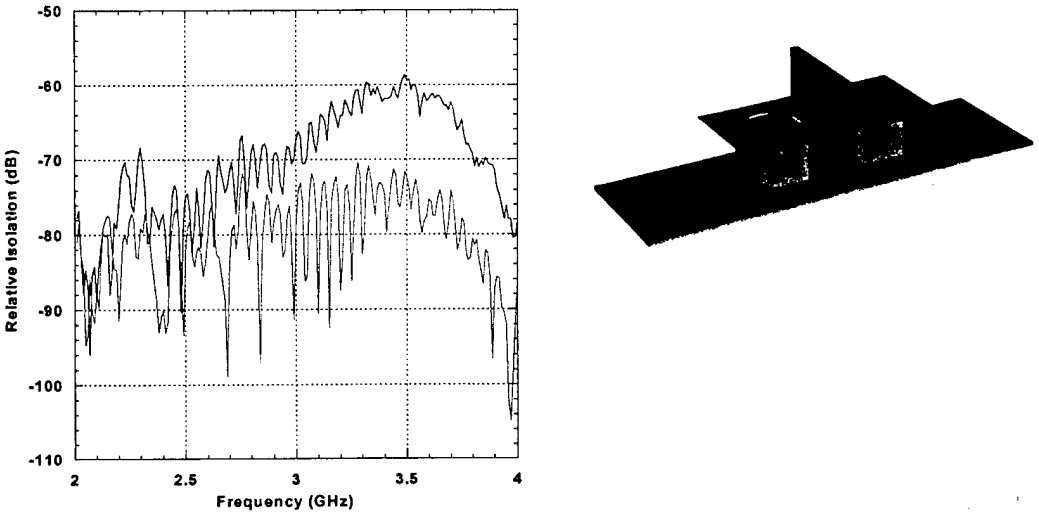

Figure 18. The upper curve displays direct coupling without the absorber, while the bottom curve displays the coupling with a 4-inch vertical absorber midway between the arrays.

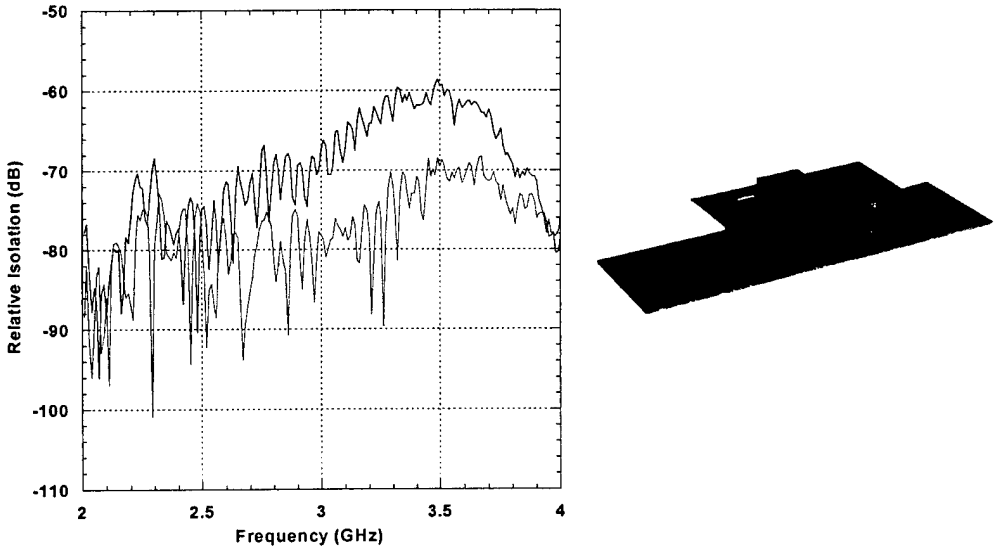

Figure 19. The upper curve displays direct coupling without the absorber, while the bottom curve displays the coupling with the 4-inch vertical absorber midway between the arrays.

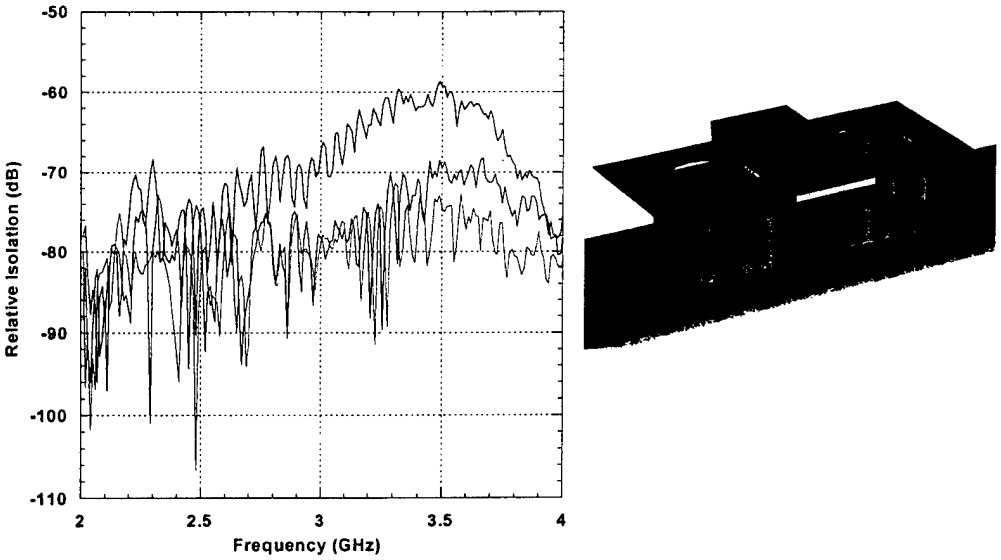

Figure 20. The upper curve displays direct coupling without the absorber; the middle curve displays the coupling with the 4-inch horizontal absorber on the surface; and the bottom curve represents the absorber raised 2 inches above the surface.

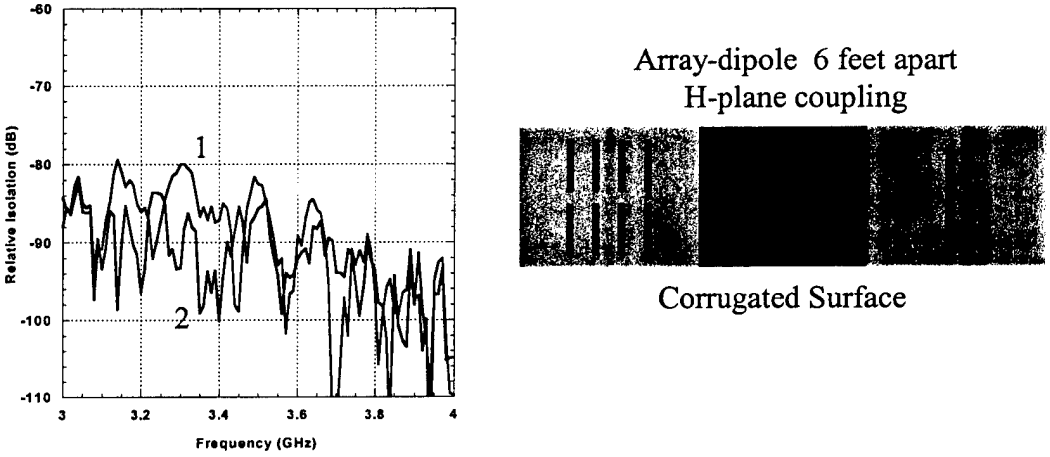

Figure 21. The upper curve (1) displays the coupling between the array (low sidelobe direction) and the element without the corrugated surface; while the second curve (2) displays the coupling with the corrugated surface placed midway between them.

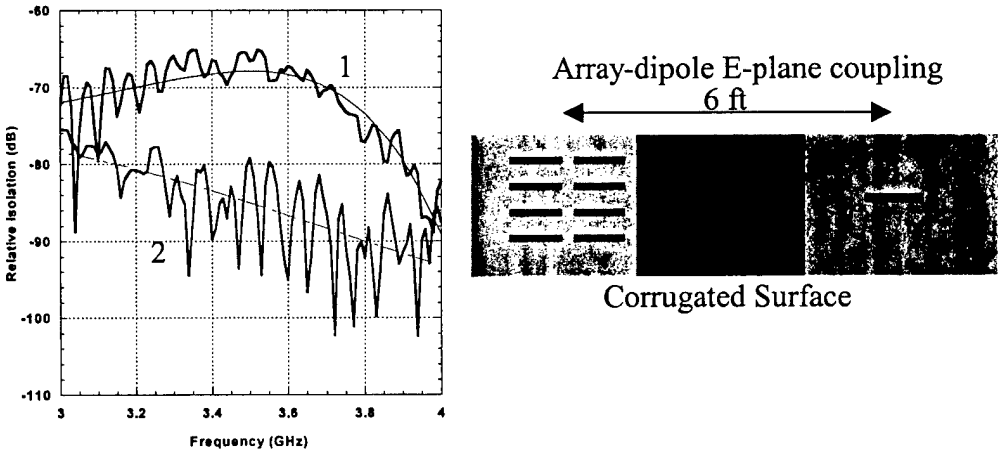

Figure 22. The upper curve (1) displays the coupling between the array (grating lobe direction) and the element without the corrugated surface while the second curve (2) displays the coupling with the corrugated surface placed midway between them.

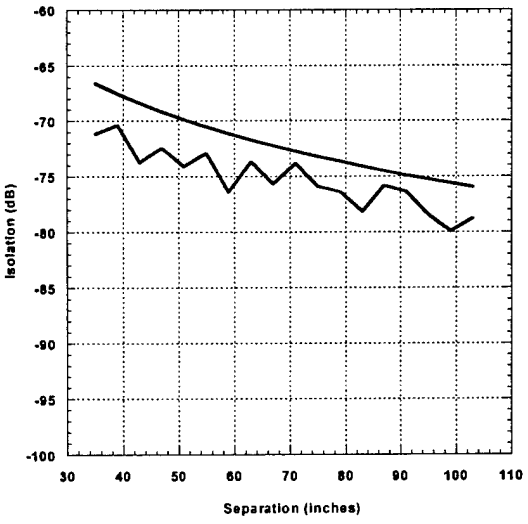

Figure 23. The upper curve displays the calculated coupling vs distance when the element is moved relative to the array (E-plane). The lower curve is the measured coupling data from the isolation apparatus for the same conditions.

7.0 SEA-SURFACE INTERACTION

Besides the array-to-array isolation, another isolation concern arises from signals being reflected off the sea surface, as well as from nearby objects. Most decoupling techniques developed for embedded arrays don't directly isolate these arrays from any environmental effects. To bound the coupling levels from sea-surface interactions, a series of sea-surface models [10] were investigated using a 10 x 10 element array located 50 feet above the sea surface. The data shown in the following figures are calculated for vertically polarized signals at 10 GHz and sea state 3. The received signals were summed (RMS) to represent the worst-case scenario; actual data would typically be lower than what was calculated.

Figure 24 shows a typical antenna pattern for a uniformly illuminated rectangular 10 x 10 array and the corresponding relative return from the sea surface as the array is scanned over a ± 60 degree azimuth/elevation sector. The large amount of backscatter seen at high elevation angles is due to the increase in sidelobe levels pointing towards the sea surface. The scalloping seen in the backscatter data is due to nulls of the antenna pattern being placed on the sea surface as the array is scanned. Figure 25 shows the backscatter levels from the same array but with the array tilted back 15 degrees. By tilting the array, the higher level far-out sidelobes that are normally produced are moved out over the sea-surface to a lower backscatter angle. This effectively decreases the overall backscatter from the surface. As a result of this effect, a 15-degree tilt improves the backscatter isolation by over 20 dB.

Another technique to improve the backscatter is by orienting the array in a diamond configuration, as shown in Figure 26. The backscatter improves by another 20 dB over the rectangular case. In this case, the sidelobes in the 45-degree plane are very low due to the geometry of the array. This places very low sidelobes on the sea-surface, which in turn reduces the coupling from the sea-surface. An extension to this is to use the rectangular array with amplitude weighting applied. Figure 27 shows the results of placing a 40 dB Taylor (N_{bar} = 5) weight across a rectangularly orientated transmit array. With this level of amplitude taper and array orientation, the effect of sea scatter can be greatly reduced. The total amount of signal reduced due to the 40 dB Taylor weight is around 2.5 dB, but the isolation improvement is over 40 dB.

Improvements in isolation due to sea-surface interactions can be achieved through the use of various physical arrangements, including array tilt and/or orientation. If the optimum array orientation can't be achieved, the use of amplitude tapering across the array can used to produce the same effect. The loss in gain due to amplitude tapering is typically outweighed by the improvement in isolation.

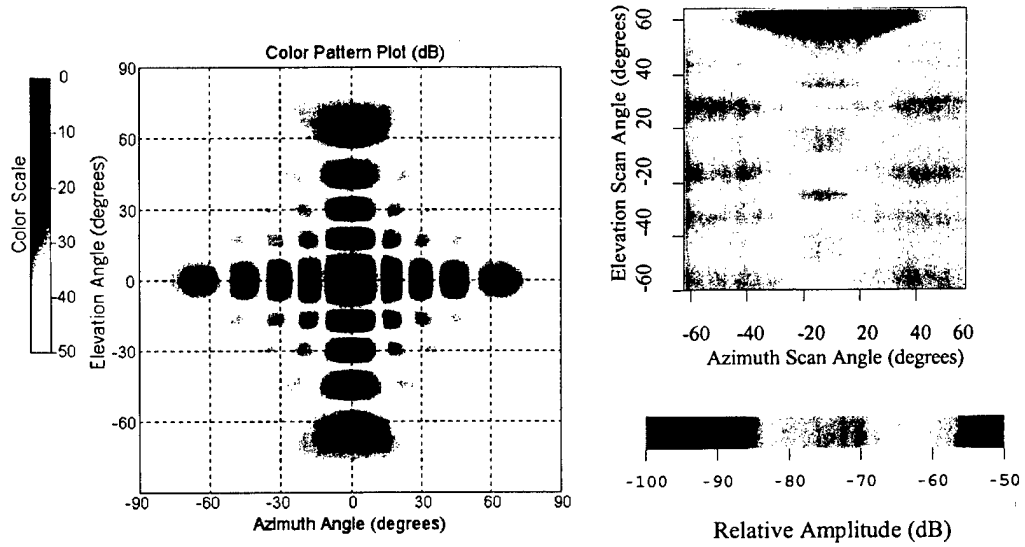

Figure 24. The left pattern displays the array pattern of a 10 x 10 element with a uniform distribution, 0-degree tilt, and operating frequency of 10 GHz. The right pattern displays the backscatter from the sea surface, measured at the receive array element as a function of scan angle for the same array geometry.

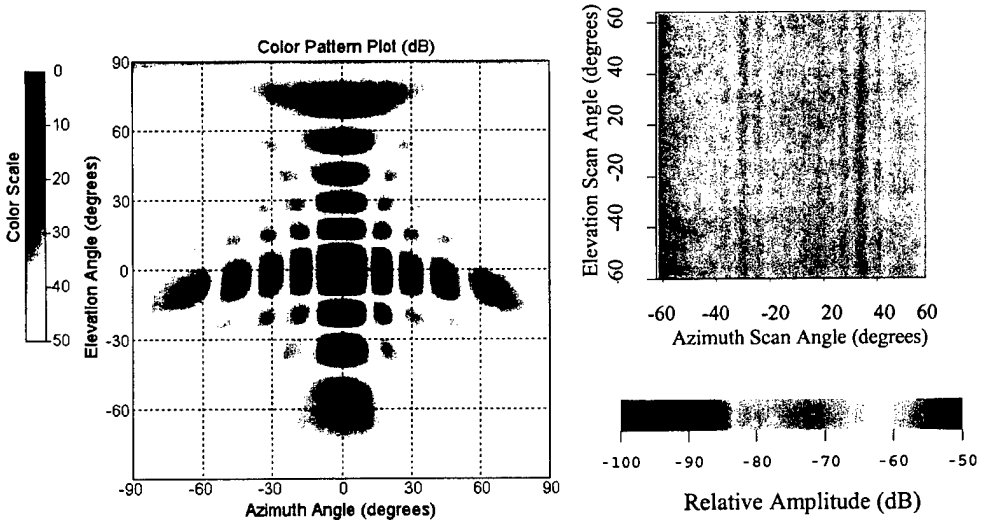

Figure 25. The left pattern displays the array pattern of a 10 x 10 element with a uniform distribution, 15-degree tilt, and operating frequency of 10 GHz. The right pattern displays the backscatter from the sea surface, measured at the receive array element as a function of scan angle for the same array geometry.

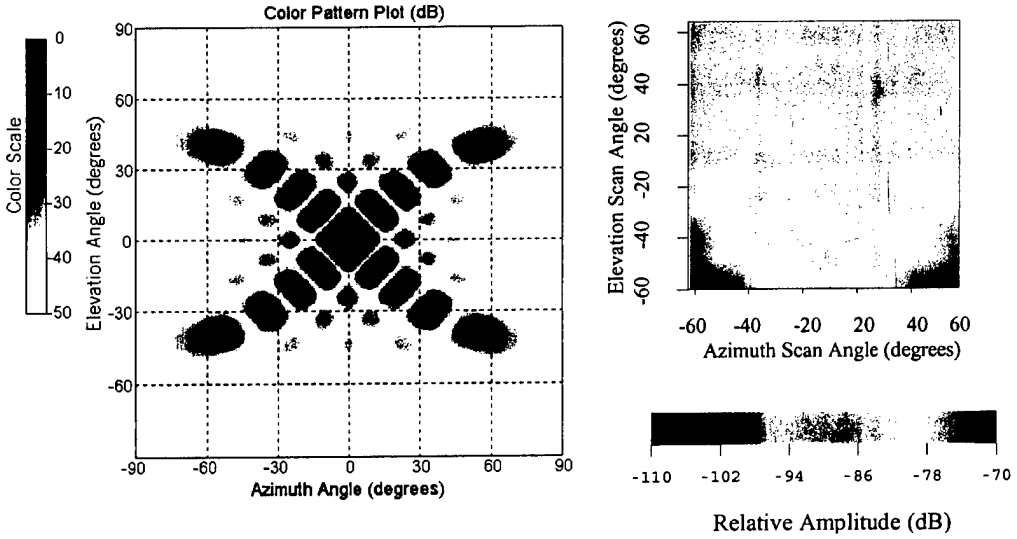

Figure 26. The left pattern displays the diamond array pattern of a 10 x 10 element with a uniform distribution, 0-degree tilt, and operating frequency of 10 GHz. The right pattern displays the backscatter from the sea surface, measured at the receive array element as a function of scan angle for the same array geometry.

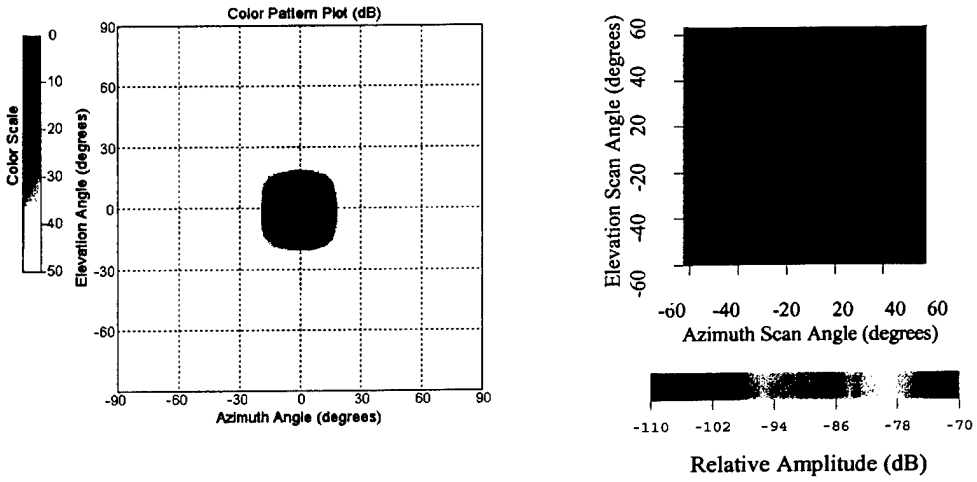

Figure 27. The left pattern displays the rectangular array pattern of a 10 x 10 element with a 40 dB Taylor distribution, 15-degree tilt, and operating frequency of 10 GHz. The right pattern displays the backscatter from the sea surface, measured at the receive array element as a function of scan angle for the same array geometry.

8.0 SUMMARY

The ability to minimize the coupling between embedded arrays requires a full and complete understanding of the receiver, the transmitter, and the isolation coupling mechanisms between them. Once the basic isolation levels are determined, each path of coupling must be identified and addressed. Using artificial surfaces or absorbing surfaces can minimize the effect of direct coupling (correlated sidelobes). To reduce the effects of scattering or diffraction (uncorrelated sidelobes), close attention must be paid to the array-surface interface. All surfaces must be blended, and all sharp edges must be eliminated. The introduction of any thick (ballistic) radome must also be carefully investigated for any possible trapped energy vs scan angle. The development of new exotic materials may help with reducing surface-wave coupling [11-12]. These types of materials are based on Photonic Band-Gap technologies and show promise for suppression of unwanted surface waves using very thin materials.

A thorough understanding of an array's external environment must also be investigated. In particular, various sea-surface interactions must be understood in terms of an array's height above the surface. The use of array tilt, orientation, and amplitude tapering on transmit must be utilized to improve the backscattering introduced from the sea surface.

Finally, the use of standard decoupling procedures between the transmitter and receiver system isolation must be implemented for the power supplies and RF subsystems.

Acknowledgment

The authors wish to thank the Office of Naval Research (ONR) for providing funds for the continuation of this program, Eric Mokole for his help in the review of this paper, and Fred Posner for his help with the sea-scattering calculations.

References

[1] G.C. Tavik, J.Y. Choe, and P.K. Hughes II, "Advanced Multifunction Radio Frequency (AMRF) Concept Test-Bed Overview," *2001 Digest of Papers for the Government Microcircuit Applications Conference (GOMAC 2001)*, pp. 100-102, March 2001.

[2] P.K. Hughes II, J.Y. Choe, and J. Zolper, "Advanced Multifunction RF System (AMRFS)," *2000 Digest of Papers for the Government Microcircuit Applications Conference (GOMAC 2000)*, pp. 194-197, March 2000.

[3] P.K. Hughes II, "Advanced Multifunction RF System (AMRFS) Technology Review," *Proceedings of the National Military Sensing Symposia (MSS)*, vol. 44, no. 2, pp.161-168, Feburary 2000.

[4] D. Taylor, "Evaluation of Carlos3D for Antenna Applications," Naval Research Laboratory Memorandum Report, Washington, DC, to be released 2001.

[5] *Private communications,* Mike Kluskens, 10 April 2001.

[6] P-S. Kildal, "Artificially Soft and Hard Surfaces in Electromagnetics," *IEEE Trans. Antennas Propagat.*, vol. AP-30 , pp. 1537-1543, October 1990.

[7] A.G. Kyurkchan, "Coupling Between Antennas in a Presence of Corrugated Structures," *Radiotekhnika I Electronika*, vol. 22, no. 7, pp. 1362-1373, 1977.

[8] X-Y. Cao, G.-X. Dai, S.-C. Zhen, and J. Gao, " The Mutual Coupling between Horns in the Near-Field," *Microwave and Millimeter Wave Technology Proceedings*, ICMMT 1998 International Conference, pp. 357-359.

[9] C.A. Balanis, Antenna Theory, pp. 64-65, New York: John Wiley & Sons, 1982.

[10] J.P. Reilly, R.L. McDonald, G.D. Dockery, and J. Stapleton, "RF-Environment Models for the ADSAM Program," Applied Physics Laboratory, Report No. A1A97U-070, August 22, 1997.

[11] D. Sievenpiper, L. Zhang, R. Broas, N.G. Alexópoulos, and E. Yablonovitch, "High-Impedance Electromagnetic Surfaces with a Forbidden Frequency Band," *IEEE Trans. Microwave Theory and Techniques*, vol. MTT-47, pp. 2059-2074, November 1999.

[12] R. Coccioli and T. Itoh, "Design of Photonic Band-Gap Substrates for Surface Wave Suppression," *IEEE MTT-S Intl. Microwave Symp. Dig.*, vol. TH1D-3, pp. 1259-1262, 1998.

Analysis of a Thick Dichroic Plate with Arbitrarily Shaped Holes

W. A. Imbriale[1]
Jet Propulsion Laboratory
California Institute of Technology
Pasadena, CA 91109
imbriale@jpl.nasa.gov

A thick dichroic plate acts as a frequency selective surface (FSS) in that it is transparent at one frequency while at the same time reflective to other frequencies. It is used in the DSN to enable simultaneous multiple-frequency operation. Most of the plates currently in use were designed with programs that analyzed only the simple geometries, such as circular or rectangular holes. Since it is too expensive to experimentally determine the FSS parameters, only designs that could be accurately analyzed were chosen, and it is the primary reason why the recent FSS designs use rectangular holes. To achieve the sharp corners of the rectangular holes, it was necessary to use an electrical discharge machining (EDM) manufacturing technique. This manufacturing technique is expensive, and an important use of the arbitrary-shaped analysis is to enable designs that use rounded corners that are able to be manufactured by less expensive techniques.

The analysis is accomplished by combining the finite-element method (FEM) for determining the waveguide modes of arbitrarily shaped guides with the method of moments and Floquet mode theory for periodic structures. The software was verified by comparison with previously measured and computed dichroic plates.

I. Introduction

The ability to transmit and receive simultaneously at multiple frequency bands is an important requirement for the DSN. This is usually accomplished either by using a dual-band feed or by using separate feeds and a frequency-selective surface (FSS), typically referred to as a dichroic plate.

The first use of a dichroic plate was as part of the reflex-dichroic feed system used on the 64-meter antenna [1]. This first dichroic plate consisted of circular holes in a half-wavelength-thick metallic plate. All subsequent dichroic plates used in the DSN were also thick plates with holes. The discussion that follows treats the most general case of the analysis of a thick dichroic plate with arbitrarily shaped holes at arbitrary angles of incidence. However, most of the plates currently in use in the DSN were designed with programs that analyzed only the simple geometries, such as circular [2] or rectangular [3] holes. This analysis limitation also impacted the choice of FSS designs. Since it is too expensive to experimentally determine the FSS parameters, only designs that could be accurately analyzed were chosen, and this is

[1] Communications Ground Systems Section.

The research described in this publication was carried out by the Jet Propulsion Laboratory, California Institute of Technology, under a contract with the National Aeronautics and Space Administration.

the primary reason why the recent FSS designs use rectangular holes. To achieve the sharp corners of the rectangular holes, it was necessary to use an electrical discharge machining (EDM) manufacturing technique. This manufacturing technique is expensive, and an important use of the arbitrarily shaped analysis is to enable designs that use rounded corners that are able to be manufactured by less expensive techniques.

The analysis parallels the development for the rectangular-hole case except that the waveguide modes are generated using the finite-element method instead of using the closed-form expressions available for the rectangular waveguide.

The relationship between the holes, the array lattice of an infinite dichroic plate, and the incident wave is shown in Fig. 1. The design variables are the hole size and shape, lattice size and shape, thickness of the plate, dielectric constant in the hole, and angle of incidence of the linearly polarized wave. The program calculates the amplitude and phase of both the transmission and reflection coefficients of the two orthogonal linear polarizations—the transverse electric (TE) and transverse magnetic (TM).

The analysis of a thick dichroic plate with arbitrarily shaped holes is carried out in a series of steps very similar to the technique described in [3]. First, a model of a half-space infinite array is constructed. A complete set of basis functions with unknown coefficients is developed for the waveguide region (waveguide modes) and for the free-space region (Floquet modes) [4] in order to represent the electromagnetic fields. Next the boundary conditions are applied at the interface between these two regions. The method of moments is used to compute the unknown mode coefficients [2,5]. The scattering matrix of the half-space infinite array is then calculated. The reference plane of the scattering matrix is moved half-a-plate thickness in the negative z-direction. Finally, a dichroic plate of finite thickness is synthesized by positioning two plates of half thickness back to back. The total scattering matrix is obtained by cascading the scattering matrices of the two half-space infinite arrays.

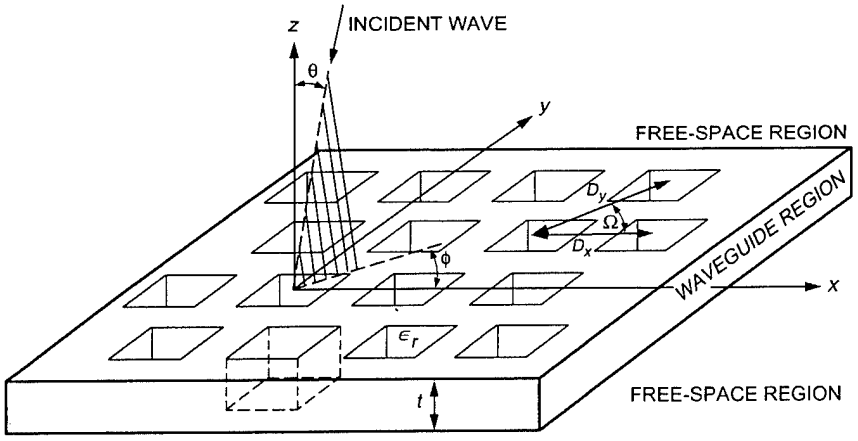

Fig. 1. Geometry of a thick dichroic plate with holes.

II. Finite-Element Formulation of the Waveguide Problem

The analysis starts with an infinite array in half space (Fig. 2) consisting of a free-space region ($z < 0$) and a waveguide region ($z > 0$). The electromagnetic fields in each region are represented by a set of orthonormal basis functions, Floquet and waveguide modes, respectively, that satisfy Maxwell's equations.

The finite-element method is used to compute the waveguide modes. The development is given in several references, including [6], but will be repeated here for completeness and notational conformance.

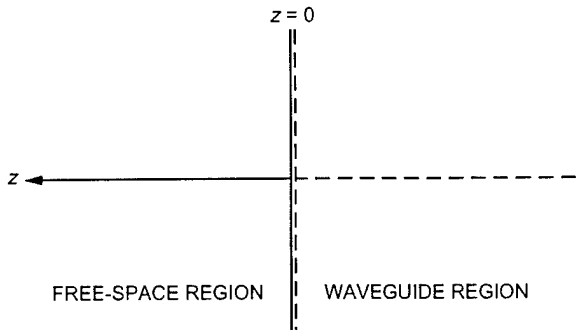

Fig. 2. Half-space infinite array with reference at $z = 0$.

As is well known, the propagating mode of a hollow, uniform waveguide may be determined by solving the two-dimensional scalar Helmholtz equation,

$$\left(\nabla^2 + k^2\right) \Psi = 0 \tag{1}$$

Here Ψ represents the magnitude of an axially directed electric or magnetic Hertz vector. If the transverse electric (TE) modes of the guide are desired, Ψ is the electric Hertz vector, and must satisfy the homogeneous Neumann boundary condition

$$\frac{\partial \Psi}{\partial n} = 0 \tag{2}$$

while the transverse magnetic (TM) modes are obtained if Ψ is taken to be the magnetic Hertz vector, subject to the boundary condition

$$\Psi = 0 \tag{3}$$

everywhere along the guide walls.

Rather than attempting to solve this eigenvalue problem directly, the finite-element method reframes it in variational terms. It is shown in books on mathematical physics [7] that the solution of the Helmholtz equation with homogeneous boundary conditions is equivalent to minimizing the functional $\mathcal{F}$ defined by

$$\mathcal{F} = \iint_R \left(- |\mathrm{grad}\varphi|^2 + k^2 \varphi^2 \right) dxdy \tag{4}$$

The region of integration is, of course, the waveguide cross-section. If a trial solution $\varphi(x, y)$ is represented geometrically as a surface spanning the region R over the x–y plane, the correct surface $\Psi(x, y)$ is that which yields the smallest possible value of $\mathcal{F}$.

In the finite-element method, the correct solution will be approximated by a surface $\varphi(x, y)$ made up of finite surface elements of a simple kind. For simplicity, all the elementary regions are taken to be triangles. Corresponding to each elementary region, a surface element will be defined by requiring $\varphi(x, y)$ to be a linear function of its values at the vertices; thus φ is then defined by

$$\varphi(x,y) = \sum_{i=1}^{N} \alpha_i(x,y)\varphi_i \tag{5}$$

$\mathcal{F}$ is now an ordinary function of the parameters that define φ, in this case the vertex values φ_i:

$$\mathcal{F}(\varphi) = F(\varphi_1, \varphi_2, \cdots, \varphi_N) \tag{6}$$

The solution is found by minimizing F with respect to all the parameters. That is, it will be required that

$$\frac{\partial F}{\partial \varphi_m} = 0 \tag{7}$$

for all m. If the region R contains altogether N vertices, this minimization requirement changes Eq. (4) into a matrix eigenvalue problem of order N, as will be shown next.

A. The Matrix Eigenvalue Problem

In view of Eq. (6), the minimization requirement, Eq. (7), is equivalent to

$$\iint_R \frac{\partial}{\partial \varphi_m} |\text{grad}\varphi|^2 \, dxdy = k^2 \iint_R \frac{\partial}{\partial \varphi_m} \varphi^2 dxdy \tag{8}$$

Differentiating repeatedly, one finds from Eq. (5) that

$$\frac{\partial}{\partial \varphi_m} |\text{grad}\varphi|^2 = 2\sum_{k=1}^{N} \left(\frac{\partial \alpha_m}{\partial x}\frac{\partial \alpha_k}{\partial x} + \frac{\partial \alpha_m}{\partial y}\frac{\partial \alpha_k}{\partial y} \right) \varphi_k \tag{9}$$

everywhere within an elementary region that abuts on vertex m. Elsewhere, α_m is zero, so that the right-hand side vanishes. By carrying out a similar differentiation, one next finds that

$$\frac{\partial}{\partial \varphi_m} (\varphi^2) = 2\sum_{k=1}^{N} \alpha_m \alpha_k \varphi_k \tag{10}$$

where again nonzero terms arise on the right-hand side only if both vertices m and k are vertices of the triangle in question.

It will be convenient to define the purely geometric quantities

$$S_{mk} = \iint_R \left(\frac{\partial \alpha_m}{\partial x}\frac{\partial \alpha_k}{\partial x} + \frac{\partial \alpha_m}{\partial y}\frac{\partial \alpha_k}{\partial y} \right) dxdy \tag{11}$$

and

$$T_{mk} = \iint_R \alpha_m \alpha_k dxdy \tag{12}$$

which express the nature of the region R and the manner of its subdivision into elementary regions. In terms of these integral quantities, Eq. (8) reads

$$S\Phi = k^2 T\Phi \tag{13}$$

where Φ is the column matrix of vertex values φ_i, and S and T are square matrices of order N, whose elements are S_{mk} and T_{mk}, as defined above. Minimization of $\mathcal{F}$ is thus equivalent to the eigenvalue problem, Eq. (13), and solution of the latter will provide approximate eigenvalues and eigenfunctions for the boundary-value problem. It will be noted that S and T are always symmetric, and the eigenvalues therefore always real.

B. Matrices *S* and *T* for Triangle Elements

If linear triangular elements are used, the unknown function ϕ within each element is approximated as

$$\phi^e(x,y) = a^e + b^e x + c^e y \tag{14}$$

where a^e, b^e, and c^e are constant coefficients to be determined and e is the element number. For a linear triangular element, there are three nodes located at the vertices of the triangle (Fig. 3). Assume that the nodes are numbered counterclockwise by numerals 1, 2, and 3, with the corresponding values of ϕ denoted by ϕ_1^e, ϕ_2^e, and ϕ_3^e, respectively. Enforcing Eq. (14) at the three nodes, we obtain

$$\phi_1^e = a^e + b^e x_1^e + c^e y_1^e$$

$$\phi_2^e = a^e + b^e x_2^e + c^e y_2^e$$

$$\phi_3^e = a^e + b^e x_3^e + c^e y_3^e$$

Solving for the constant coefficients a^e, b^e, and c^e in terms of ϕ_1^e, and substituting them back into Eq. (14) yields

$$\phi^e(x,y) = \sum_{j=1}^{3} N_j^e(x,y)\phi_j^e \tag{15}$$

where $N_j^e(x,y)$ is the interpolation or expansion functions given by

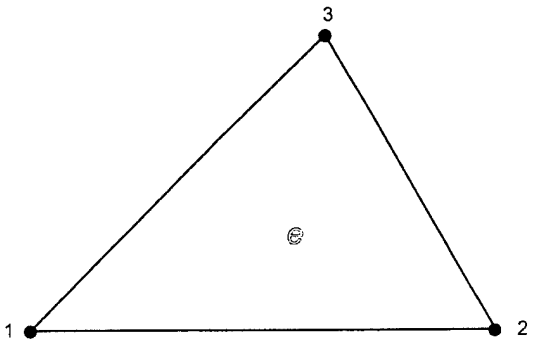

Fig. 3. Linear triangular element.

$$N_j^e(x,y) = \frac{1}{2A}\left(a_j^e + b_j^e x + c_j^e y\right), \quad j = 1,2,3 \tag{16}$$

in which

$$\left.\begin{array}{lll} a_1^e = x_2^e y_3^e - y_2^e x_3^e; & b_1^e = y_2^e - y_3^e; & c_1^e = x_3^e - x_2^e \\ a_2^e = x_3^e y_1^e - y_3^e x_1^e; & b_2^e = y_3^e - y_1^e; & c_2^e = x_1^e - x_3^e \\ a_3^e = x_1^e y_2^e - y_1^e x_2^e; & b_3^e = y_1^e - y_2^e; & c_3^e = x_2^e - x_1^e \end{array}\right\} \tag{17}$$

and

$$A = \frac{1}{2}\begin{vmatrix} 1 & x_1^e & y_1^e \\ 1 & x_2^e & y_2^e \\ 1 & x_3^e & y_3^e \end{vmatrix} = \frac{1}{2}\left(b_1^e c_2^e - b_2^e c_1^e\right)$$

$$= \text{area of the } e\text{th element} \tag{18}$$

In the above, x_j^e and $y_j^e (j = 1,2,3)$ denote the coordinate values of the jth node in the eth element. It can be easily shown that the interpolation functions have the property

$$N_i^e\left(x_j^e, y_j^e\right) = \delta_{ij} = \begin{cases} 1 & i = j \\ 0 & i \neq j \end{cases} \tag{19}$$

and, as a result, at node i, ϕ^e in Eq. (15) reduces to its nodal value, ϕ_i^e.

For ease in both analysis and computer programming, it is useful to regard the matrices S and T as being composed of sums of sparse matrices of order N, typically $s^{(i)}$ and $t^{(i)}$, made up of the contributions to the S and T matrices that are attributable to only one elementary region, say the ith. That is to say, one may write

$$S_{mk} = \sum_i s_{mk}^{(i)} \tag{20}$$

$$T_{mk} = \sum_i t_{mk}^{(i)} \tag{21}$$

Clearly, $s_{mk}^{(i)} = t_{mk}^{(i)} = 0$ whenever n equals neither m nor k, i.e., for all elements that touch neither vertex m nor k. Explicit expressions for the element matrix components are

$$s_{mk}^{(i)} = \int_i \int \left(\frac{\partial \alpha_m}{\partial x}\frac{\partial \alpha_k}{\partial x} + \frac{\partial \alpha_m}{\partial y}\frac{\partial \alpha_k}{\partial y}\right) dxdy \tag{22}$$

$$t_{mk}^{(i)} = \int_i \int \alpha_m \alpha_k dxdy \tag{23}$$

the integrations being carried out over the ith elementary region. For triangular elementary regions, $s^{(i)}$ and $t^{(i)}$ in general possess nine nonzero components and are symmetric. These component values are found by substituting Eq. (15) into Eq. (22):

$$s_{mk}^{(i)} = \frac{1}{4A^2} \int_i \int (b_m b_k + c_m c_k)\, dxdy \tag{24}$$

On carrying out the necessary integration,

$$s_{mk}^{(i)} = \frac{-1}{4A} \left[(x_m^e - x_i^e)(x_k^e - x_i^e) + (y_m^e - y_i^e)(y_k^e - y_i^e) \right] \tag{25}$$

Similarly, substitution into Eq. (23) yields the surprisingly simple result

$$t_{mk}^{(i)} = \begin{cases} \frac{1}{12} A, & m \neq k \\ \frac{1}{6} A, & m = k \end{cases} \tag{26}$$

Leaving out all rows and columns composed of zeros only, a single triangular element is thus described by the matrix contributions

$$\begin{bmatrix} s_{11} & s_{12} & s_{13} \\ s_{21} & s_{22} & s_{23} \\ s_{31} & s_{32} & s_{33} \end{bmatrix} \begin{bmatrix} \varphi_1 \\ \varphi_2 \\ \varphi_3 \end{bmatrix} = k^2 \frac{A}{12} \begin{bmatrix} 2 & 1 & 1 \\ 1 & 2 & 1 \\ 1 & 1 & 2 \end{bmatrix} \begin{bmatrix} \varphi_1 \\ \varphi_2 \\ \varphi_3 \end{bmatrix} \tag{27}$$

where the s_{mk} are calculated from Eq. (25), and the area A is given by Eq. (18).

III. Boundary Conditions and Method of Moments

The electromagnetic field in the waveguide is expressed as a sum of incident and reflected waveguide modes, while in the free-space region it is expressed as a sum of incident and reflected Floquet modes. Boundary conditions are applied at the interface between two regions, i.e., the transverse electric and magnetic fields must be continuous across the junction at $z = 0$. This leads to an integral equation for the unknown transverse electric field at the boundary. The infinite-array scattering problem then becomes similar to a two-region waveguide problem.

The method of moments is used to transform the integral equation into a matrix equation suitable for evaluation on a digital computer. Solving the set of linear equations gives the unknown mode coefficients in both regions.

A. Integral Equation Formulation

In the waveguide region, the total transverse electric field and magnetic field (see Fig. 2) at $z = 0^+$ is given by

$$\left.\begin{aligned} E_T^w(x,y) &= \sum_{i=1}^{\infty} \bar{e}_i^w(x,y)\left(a_i^w + b_i^w\right) \\ H_T^w(x,y) &= \sum_{i=1}^{\infty} y_i\, \hat{z} \times e_i^w(x,y)\left(a_i^w - b_i^w\right) \end{aligned}\right\} \tag{28}$$

where $\bar{e}_i^w(x,y)$ represents the modal fields in the waveguide and, for TE modes,

$$\left.\begin{aligned} \bar{e}_i^w(x,y) &= \hat{z} \times \nabla \Psi^{TE} \\ y_{TE} &= \frac{\gamma_i}{j\omega\mu} \end{aligned}\right\} \tag{29}$$

and, for TM modes,

$$\left.\begin{aligned} \bar{e}_i^w(x,y) &= -\nabla \Psi^{TM} \\ y_{TM} &= \frac{j\omega\varepsilon}{\gamma_i} \end{aligned}\right\} \tag{30}$$

with Ψ^{TE} and Ψ^{TM} given by the finite-element method (FEM) solution of the waveguide.

It should be noted that Ψ and $\nabla\Psi$ are real functions and the Ψ vectors are normalized so that

$$\int_{wg} \nabla\Psi_i \nabla\Psi_j ds = \int_{wg} \bar{e}_i \cdot \bar{e}_j ds = \delta_{ij} \tag{31}$$

Forming the inner product of the ith waveguide mode with the total transverse electric field, Eq. (28), we obtain an expression for the unknown modal coefficients,

$$\iint_{wg} \bar{e}_i^w \cdot E_T^w dx dy = a_i^w + b_i^w \tag{32}$$

Note that it is also possible to extend the integral over the entire Floquet cell since $\bar{E}_T = 0$ outside the waveguide. Using Eq. (32) in the $\bar{H}_T$ field expression, it is possible to write

$$H_T = 2\sum_{i=1}^{\infty} y_i a_i^w \left(\hat{z} \times \bar{e}_i^w\right) - \sum_{i=1}^{\infty} y_i \left(\hat{z} \times \bar{e}_i^w\right) \iint_{wg} e_i^w \times E_T^w dx' dy' \tag{33}$$

In a very similar manner, the total electric and magnetic fields at $z = 0^-$ are given by

$$\left.\begin{aligned} E_T^-(x,y) &= \sum_{j=1}^{\infty} \bar{e}_j^F \left(a_j^F + b_j^F\right) \\ H_T^-(x,y) &= -\sum_{j=1}^{\infty} Y_j \left(\hat{z} \times \bar{e}_j^F\right)\left(a_j^F - b_j^F\right) \end{aligned}\right\} \tag{34}$$

where, for TE modes,

$$\left.\begin{aligned} \bar{e}_j^F &= \hat{z} \times \nabla \phi_i^{TE} \\ Y_{TE} &= \frac{\gamma_i}{j\omega\mu} \end{aligned}\right\} \tag{35}$$

and, for TM modes,

$$\left.\begin{aligned} \bar{e}_j^F &= -\nabla \phi_i^{TM} \\ Y_{TM} &= \frac{j\omega\varepsilon}{\gamma_i} \end{aligned}\right\} \tag{36}$$

However, ϕ_j and $\nabla\phi_j$ are complex functions that are normalized so that

$$\int_{\substack{\text{Floquet} \\ \text{cell}}} \nabla\phi_i \cdot \nabla\phi_j^* ds = \int \bar{e}_i \cdot \bar{e}_j^* ds = \delta_{ij} \tag{37}$$

The Floquet modes on the skewed grid (skew angle Ω) and grid spacing D_x, D_y (Fig. 1) are given by [4]

$$\phi_{mn} = \frac{e^{j(\alpha_m x + \beta_n y)}}{\sqrt{D_x D_y \sin\Omega}\sqrt{\alpha_m^2 + \beta_n^2}} \tag{38}$$

for either TE or TM waves (same boundary conditions!):

$$\alpha_m = \frac{2\pi m}{D_x} - k_0 \sin\theta\cos\phi \tag{39}$$

and

$$\beta_n = \frac{2\pi n}{D_y \sin\Omega} - \frac{2\pi m}{D_x}\cot\Omega - k_0 \sin\theta\sin\phi \tag{40}$$

where k_0 is the wave number in free space.

In much the same way as with the waveguide modes, we can show

$$\iint_A e_j^* \cdot \bar{E}_T^- dx'dy' = a_j^F + b_j^F \tag{41}$$

$$H_T^- = -2\sum_{j=1}^{\infty} a_j^F \left(\hat{z} \times \bar{e}_j^F\right) Y_j + \sum_{j=1}^{\infty} Y_j \left(\bar{z} \times \bar{e}_j^F\right) \iint_A e_j^* \cdot E_T^- dx'dy' \tag{42}$$

The transverse electric and magnetic fields must be continuous across the junction at $z = 0$. Thus, equating the magnetic fields yields

$$2\sum_{i=1}^{\infty} y_i a_i^w \bar{e}_i^w + 2\sum_{j=1}^{\infty} a_j^F Y_j e_j^F = \sum_{j=1}^{\infty} y_i \bar{e}_i^w \iint_A \bar{e}_i^w \cdot E_T\left(x', y'\right) dx'dy'$$

$$+ \sum_{j=1}^{\infty} Y_j \bar{e}_j^F \iint_A \bar{e}_j^{F^*} \cdot E_T\left(x', y'\right) dx'dy' \tag{43}$$

B. Moment Method Solution

To solve the integral equation, it is necessary to expand the unknown electric field in terms of a set of basis functions. The obvious choice for this is the waveguide modes $\bar{e}_k^w(x, y)$. Thus,

$$\bar{E}_T\left(x', y'\right) = \sum_{k=1}^{\infty} c_k \bar{e}_k^w\left(x', y'\right) \tag{44}$$

Substituting this expression into the integral equation and interchanging the order of summation and integration yields

$$2\sum_{i=1}^{\infty} y_i a_i^w \bar{e}_i^w + 2\sum_{j=1}^{\infty} a_j^F Y_j \bar{e}_j^F = \sum_{k=1}^{\infty}\sum_{i=1}^{\infty} c_k y_i \bar{e}_i^w + \sum_{k=1}^{\infty}\sum_{i=1}^{\infty} c_k Y_j \bar{e}_j^F \iint_A e_j^F \cdot \bar{e}_k^w dx'dy' \tag{45}$$

To simplify the notation, define the inner product known as the intermodal coupling coefficient:

$$I_{kj} = \iint \bar{e}_k^w\left(x', y'\right) \cdot \bar{e}_j^F\left(x', y'\right) dx'dy' \tag{46}$$

Using this notation, the equation simplifies to

$$2\sum_{i=1}^{\infty} y_i a_i^w e_i^w + 2\sum_{j=1}^{\infty} a_j^F Y_j e_j^F = \sum_k c_k \left[\sum_i y_i e_i^w + \sum_j Y_j e_j^F I_{ky}\right] \tag{47}$$

To apply the moment method, we must take the inner product with the weighting. In this analysis, we use the same basis functions (Galerkin). Thus, multiply Eq. (47) by $e_\ell^w(x, y)$ and integrate over the waveguide. This yields the matrix equation

$$2\sum_i a_i^w y_i + 2\sum_j a_j^F Y_j I_{ej} = \sum_k \left[\sum_i y_i + \sum_j Y_j I_{\ell j} I_{kj}\right] c_k \tag{48}$$

Using the following definitions,

$$M_{\ell k} = \sum_i y_i + \sum_j Y_j I_{\ell j} I_{kj} \tag{49}$$

and

$$G_\ell = 2\sum_i a_i^w y_i + 2\sum_j a_j^F Y_j I_{\ell j} \tag{50}$$

Thus, Eq. (48) can be expressed as

$$G_\ell = \sum_k M_{\ell k} C_k \tag{51a}$$

or

$$[G] = [M]\,[C] \tag{51b}$$

The solution for the unknown mode coefficients is then given by

$$[C] = [M]^{-1}\,[G] \tag{52}$$

Generally, the scattered fields are the primary quantities of interest and can be derived from the mode coefficients. Recalling

$$b_i^w = \iint e_i^w \cdot E_T^w dxdy - a_i^w \tag{53}$$

then

$$\left.\begin{aligned} b_i^w &= \iint e_i^w \cdot \sum_k c_K e_k^w dxdy - a_i^w \\ b_i^w &= c_i - a_i^w \end{aligned}\right\} \tag{54}$$

Similarly,

$$b_j^F = \sum_k c_k I_{kj} - a_j^F \tag{55}$$

IV. Scattering Matrix and Reference Plane

The characteristics of the infinite array referenced to $z = 0$ are represented by a scattering matrix S that contains the transmission and reflection information for the free-space/waveguide junction:

$$S = \begin{bmatrix} S_{11} & S_{12} \\ S_{21} & S_{22} \end{bmatrix} \tag{56}$$

where S_{11}, S_{12}, S_{21}, and S_{22} are matrices with 1 representing the free-space region and 2 the waveguide region. The size of matrix S_{11} is 2 by 2; S_{22} is n by n; S_{12} is 2 by n; S_{21} is n by 2; and n is the number of waveguide modes used. For an arbitrary set of incident waveguide modes contained in vector a_1 and incident TE_{00} and TM_{00} Floquet modes contained in vector a_2, the reflected mode vectors b_1 and b_2 are determined by the following set of equations:

$$\left.\begin{aligned} b_1 &= S_{11}a_1 + S_{12}a_2 \\ b_2 &= S_{21}a_1 + S_{22}a_2 \end{aligned}\right\} \tag{57}$$

Moving the reference plane in the waveguide region from $z = 0$ to $z = -t/2$ (Fig. 4), where t is the thickness of the plate, the elements of the new scattering matrix S' become

$$S'_{11}(u,v) = S_{11}(u,v) \tag{58}$$

$$S'_{12}(u,v) = S_{12}(u,v)\exp\left(-j\gamma_v\frac{t}{2}\right) \tag{59}$$

$$S'_{21}(u,v) = S_{21}(u,v)\exp\left(-j\gamma_u\frac{t}{2}\right) \tag{60}$$

$$S'_{22}(u,v) = S_{22}(u,v)\exp\left[\left(-j\gamma_u\frac{t}{2}\right)\left(-j\gamma_v\frac{t}{2}\right)\right] \tag{61}$$

where γ_u and γ_v are the propagation constants of modes u and v.

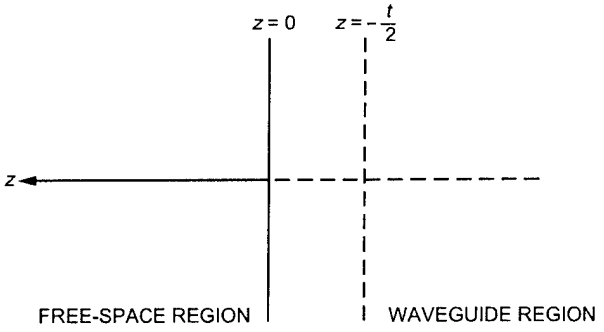

Fig. 4. Half-space infinite array with reference at $z = -t/2$.

V. Cascading the Finite Thickness

Scattering by a dichroic plate with finite thickness can be analyzed by considering two infinite-array problems. The space is divided into four regions: a free-space region (region I), two waveguide regions (regions II and III), and another free-space region (region IV), as shown in Fig. 5. The scattering matrix with reference to $z = -t/2$ for regions I and II is S', and the scattering matrix with reference to $z = -t/2$ for regions III and IV isS'', which is the transpose matrix of S':

$$S''_{11} = S'_{22} \tag{62}$$

$$S''_{12} = S'_{21} \tag{63}$$

$$S''_{21} = S'_{12} \tag{64}$$

$$S''_{22} = S'_{11} \tag{65}$$

The scattering matrix S^T for the finite-thickness plate is determined by cascading these two matrices:

$$S^T_{11} = S'_{12}\left(I - S''_{11}S'_{22}\right)^{-1} S''_{11}S'_{21} + S'_{11} \tag{66}$$

$$S^T_{12} = S'_{12}\left(I - S''_{11}S'_{22}\right)^{-1} S''_{12} \tag{67}$$

$$S^T_{21} = S'_{21}\left(I - S''_{22}S'_{11}\right)^{-1} S''_{21} \tag{68}$$

$$S^T_{22} = S''_{21}\left(I - S'_{22}S''_{11}\right)^{-1} S'_{22}S''_{12} + S''_{22} \tag{69}$$

where I is a unitary matrix.

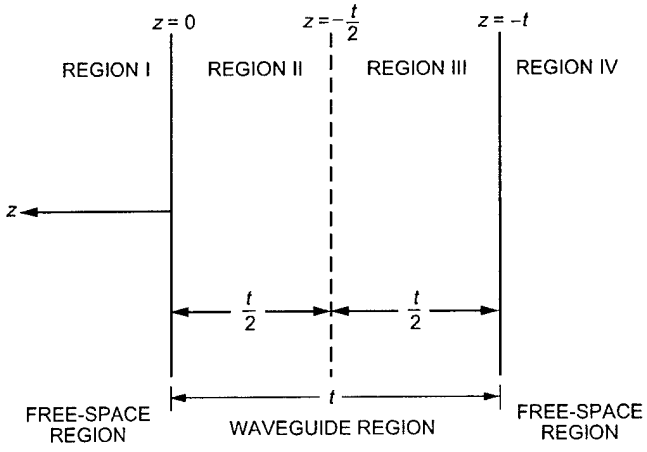

Fig. 5. The finite-thickness (t) plate is analyzed by considering two infinite-array problems.

VI. Computing the Intermodal Coupling Coefficients

The intermodal coupling coefficients are given as

$$I_{kj} = \iint_A \bar{e}_k^w (x', y') \cdot \bar{e}_j^F (x', y') \, dx' dy' \tag{70}$$

Using Eq. (38),

$$\phi_{mn} = \frac{e^{j(\alpha_m x + \beta_n y)}}{\sqrt{D_x D_y \sin\Omega} \sqrt{\alpha_m^2 + \beta_m^2}}$$

then, for TE modes,

$$\bar{e}_i^F = \hat{z} \times \nabla \phi_{mn} \tag{71}$$

and, for TM modes,

$$\bar{e}_i^F = -\nabla \phi_{mn} \tag{72}$$

where i represents the mn mode.

Also, for the waveguide modes, let

$$\Psi_i^{\mathrm{TE,TM}} = \sum_{t=1}^{NT} \sum_{j=1}^{3} N_{jt}(x, y) \phi_{jt}^{\mathrm{TE,TM}} \tag{73}$$

where $\phi_{jt}^{\mathrm{TM,TE}}$ is the solution for the ith mode of the finite-element waveguide eigenmode problem described in Section II. Also, recall that, for TE modes,

$$e_i^\omega = \hat{z} \times \nabla \Psi_i^{\mathrm{TE}} \tag{74}$$

and, for TM modes,

$$e_i^\omega = -\nabla \Psi_i^{\mathrm{TM}} \tag{75}$$

There are then four expressions for the intermodal coupling coefficients formed by combining TE and TM waveguide modes with TE and TM Floquet modes.

To develop the expression for the TE waveguide, TE Floquet mode, substitute the expressions for $\bar{e}_i^F$ and $\bar{e}_i^\omega$ into Eq. (70) and integrate. Defining

$$S_e(\alpha, \beta) = \int_{i\text{th triangle}} e^{j(\alpha x + \beta y)} dx dy$$

which is the Fourier transform of the triangular shape function for the ith triangle of the finite-element grid (see [8] for the closed-form expression to evaluate the integral), then we can write for the TE waveguide, TE Floquet mode

$$I_{kj} = -\sum_{e=1}^{NT}\sum_{i=1}^{3} \frac{(c_i^e \phi_i^e \beta_j + b_i^e \phi_i^e \alpha_j) * S_e}{\left(\sqrt{\alpha_j^2 + \beta_j^2}\right)\left(\sqrt{D_x D_y \sin\Omega}\, 2A_e\right)}$$

where c_i^e and b_i^e are given by Eq. (17) for each triangle, and the ϕ_i^{ek} are the values for the kth eigenmode on the eth triangle. There are very similar-looking expressions for the other TE,TM combinations.

VII. The Frequency-Selective Surface Finite-Element (FSSFE) Computer Program

There are a number of steps required to compute the reflection and transmission coefficients of arbitrarily shaped holes in a thick plate:

(1) The hole is defined by a sequence of x, y boundary points. There are also various subroutines that generate the required set of boundary points for specific shapes, i.e., rectangular, cross-shaped, circular, Pyle, etc.

(2) The next step is to generate the finite-element grid. This is done using a Delaunay triangularization with a public domain computer program, delaundo, based on a Ph.D. thesis by Jans-Dominik Müller [9]. Delaundo creates triangular grids based on the frontal Delaunay method (Frod) [10]. First the set of discretized curves that describes the boundary is triangulated. This initial mesh is suitable for interpolation of a local mesh size throughout the domain after a few modifications in the connections are made by the algorithm. New internal vertices are then created on frontal edges between well-shaped and ill-shaped triangles such that a new triangle with the desired size and a good shape will result.

Thus, the algorithm is similar to the various Delaunay methods in that the resulting triangulation observes a circum-circle criterion. It is also akin to advancing front methods in that new vertices are introduced in layers on the boundaries in a very regular fashion. The regularity of the point distribution and, thus, the element quality are enhanced by an averaging process that tends to choose an equilibrium position between competing edges when the front is refined or coarsened.

(3) After the grid has been generated, the finite-element method of Section II is utilized to generate the waveguide eigenvectors and eigenvalues. The S and T matrices are filled, and the corresponding eigenvalue problem is solved using ARPACK [11], a collection of FORTRAN77 subroutines designed to solve large-scale eigenvalue problems. ARPACK is designed to compute a few eigenvalues and corresponding eigenvectors of a general n-by-n matrix A. It is most appropriate for large sparse or structured matrices A, where structured means that a matrix–vector product $w \leq Av$ requires order n rather than the usual order $n^{**}2$ floating-point operations. This software is based upon an algorithmic variant of the Arnoldi process called the implicitly restarted Arnoldi method (IRAM). When the matrix A is symmetric, it reduces to a variant of the Lanczos process called the implicitly restarted Lanczos method (IRLM). These variants may be viewed as a synthesis of the Arnoldi/Lanczos process with the implicitly shifted QR algorithm that is suitable for large-scale problems. For many standard problems, a matrix factorization is not required. Only the action of the matrix on a vector is needed. However, for the generalized case that exists for the finite-element problem $Sx = k^2Tx$, it is necessary to factor the matrix T. Since T is sparse, the sparse matrix solver given in [12] is used.

(4) The solution then proceeds as shown in Sections III through VI. The intermodal coupling coefficients are computed and the matrix M is formed and inverted. Next the terms of the scattering matrix for the free-space/waveguide junction are computed. The scattering matrices are then shifted and cascaded to compute the scattering coefficients for the finite-thickness plate.

VIII. Verification of the Computer Code

The first test of the arbitrarily shaped hole computer code was to see if it could duplicate the results from the earlier code [3] that could only do rectangular-shaped holes. The case analyzed is the same test dichroic plate fabricated to verify the rectangular-hole computer code. The dimensions of the plate are $H_x = 1.850$ cm, $H_y = 1.923$ cm, $D_x = 2.388$ cm, $D_y = 2.388$ cm, and $\Omega = 60.0$ deg. And, $t = 3.584$ cm, with a tolerance of 0.0025 cm. Figure 6 plots the TE and TM reflection coefficients for the two codes and demonstrates that the new code accurately computes the reflection coefficients of the rectangular geometry. Satisfactory convergence is achieved by using 40 waveguide modes and gridding the hole with 1683 triangles. Figures 7 and 8, reproduced from [3], show that the analysis also agrees with the measured data.

The first dichroic plate used in the DSN is described in [1] and consisted of an array of hexagonally packed 2.237-cm-diameter holes drilled normal to the plate surfaces. The plate is 3.576-cm thick, and the center-to-center hole spacing is 2.388 cm. It was designed using the Chen Holey Plate computer program [2], and the computer program shows that the plate E- and H-plane resonant frequencies (30-deg incident wave tilt from normal) are 8.481 and 8.363 GHz, respectively. The FSSFE program gives 8.497 and 8.350 GHz, respectively. The small difference is probably because the Chen program does not use a sufficient number of waveguide modes. At the operational frequency, a differential phase shift of 11.3 deg (11.6 deg with the FSSFE program) and an ellipticity of 1.75 dB was predicted. This dichroic plate depolarization was cured by making the holes slightly non-circular in cross section, thus introducing a different E- and H-plane phase shift to counteract the 11.3-deg phase shift. The particular hole cross section selected was "Pyle guide" [13]. The dichroic design was approximate in that the design procedure was to adjust the guide geometry (using a program developed by Knud Pontoppidan for computing

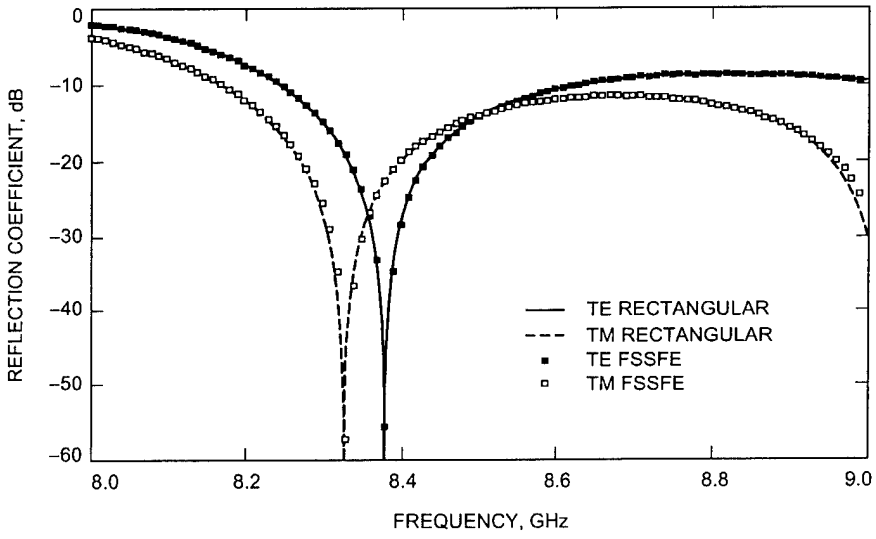

Fig. 6. Rectangular versus FSSFE code.

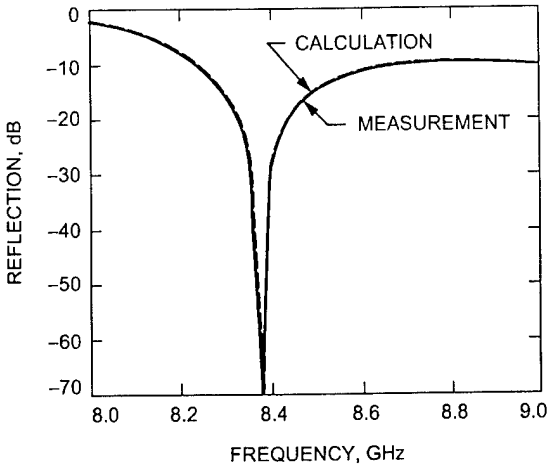

Fig. 7. Measured and calculated reflection versus frequency for the test dichroic plate for TE polarization.

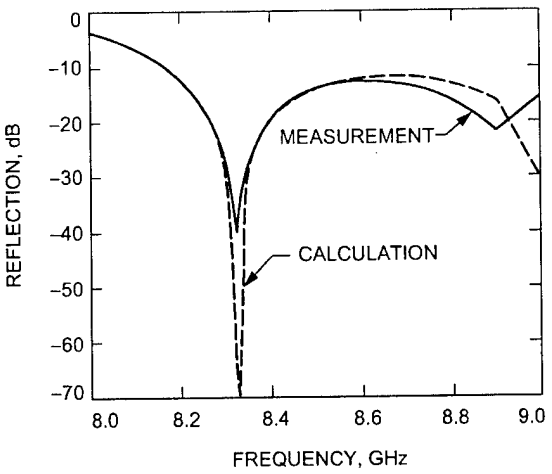

Fig. 8. Measured and calculated reflection versus frequency for the test dichroic plate for TM polarization.

the guide wavelength numbers [14]) until the plate electrical thickness at 8.415 GHz corresponded to those in the original circular-hole plate at 8.481 and 8.363 GHz, respectively. There was no FSS program at that time that could compute the reflection and transmission coefficients for the actual Pyle plate. A comparison of a measured Pyle plate [15] and the FSSFE program is shown in Fig. 9. For reference, a gridding of the guide is shown in Fig. 10.

Another plate built for the DSN that was only approximately analyzed was the cross-shaped plate [16] designed to pass both the transmit (7.145–7.235 GHz) and receive (8.4–8.5 GHz) X-band frequencies while reflecting the S-band frequencies (2.090–2.320 GHz). The analytic technique used to design the plate was to assume infinitely thin walls and then to build a plate with as thin a wall as possible. The FSSFE program can analyze the exact cross geometry, including the thickness of the walls. A plot of the measured data versus frequency compared to the calculated data from FSSFE is shown in Fig. 11, demonstrating the accuracy of the FSSFE program. The hole geometry is shown in Fig. 12, and the plate was 3.167-cm thick.

IX. Conclusions

A computer code that can accurately compute the reflection and transmission coefficients from a thick dichroic plate with arbitrarily shaped holes has been described. The code was verified by comparisons both to earlier but more restrictive computer programs (circular and rectangular holes) and to measured data for plates built with rectangular, Pyle, and cross-shaped holes.

Both the rectangular-hole and cross-shaped-hole plates were manufactured using a very accurate but very expensive electrical discharge machining (EDM) process. The EDM process produces very accurate holes with sharp (square) corners. With the new analysis tool, it is now possible to design dichroics with rounded corners that may be manufactured by a less expensive water jet or machining process. Work is currently under way to design and fabricate dichroic plates using the less expensive manufacturing processes and will be the subject of a follow-on article.

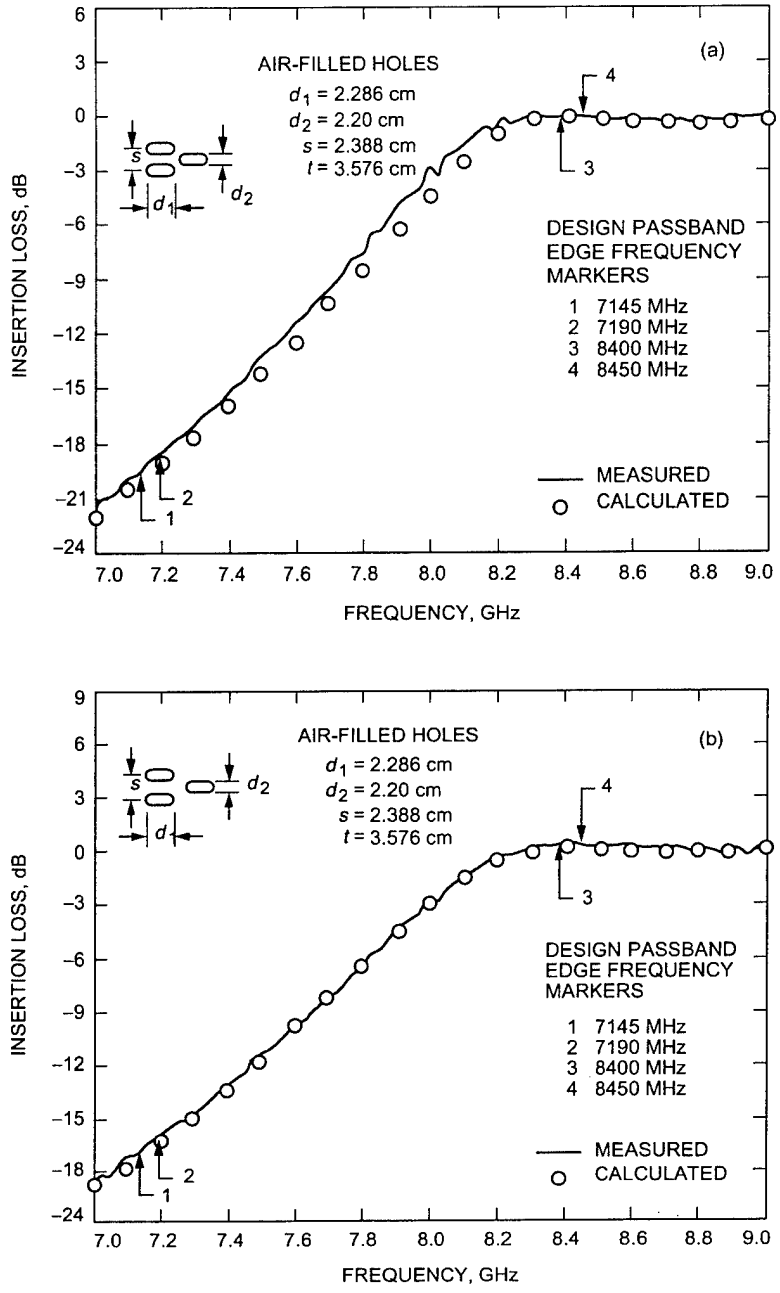

Fig. 9. Measured and calculated transmission loss versus frequency for DSN Pyle plate: (a) TE polarization and (b) TM polarization.

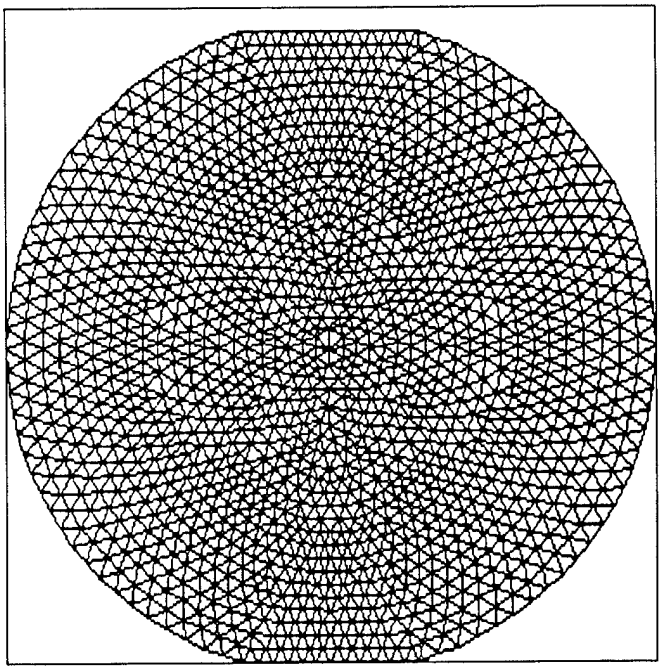

Fig. 10. Finite-element gridding for a Pyle plate.

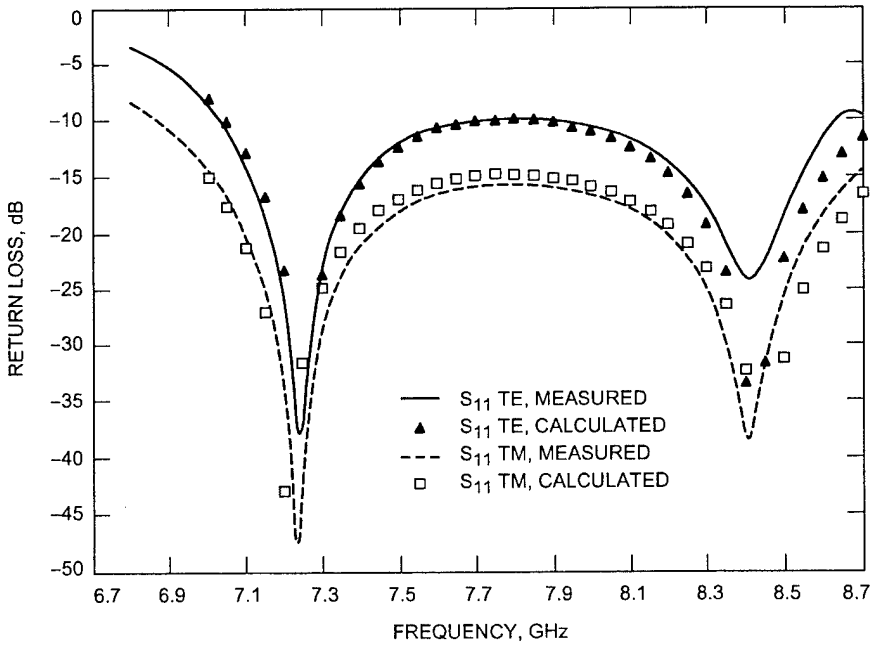

Fig. 11. Measured and calculated reflection coefficient for cross-shaped plate.

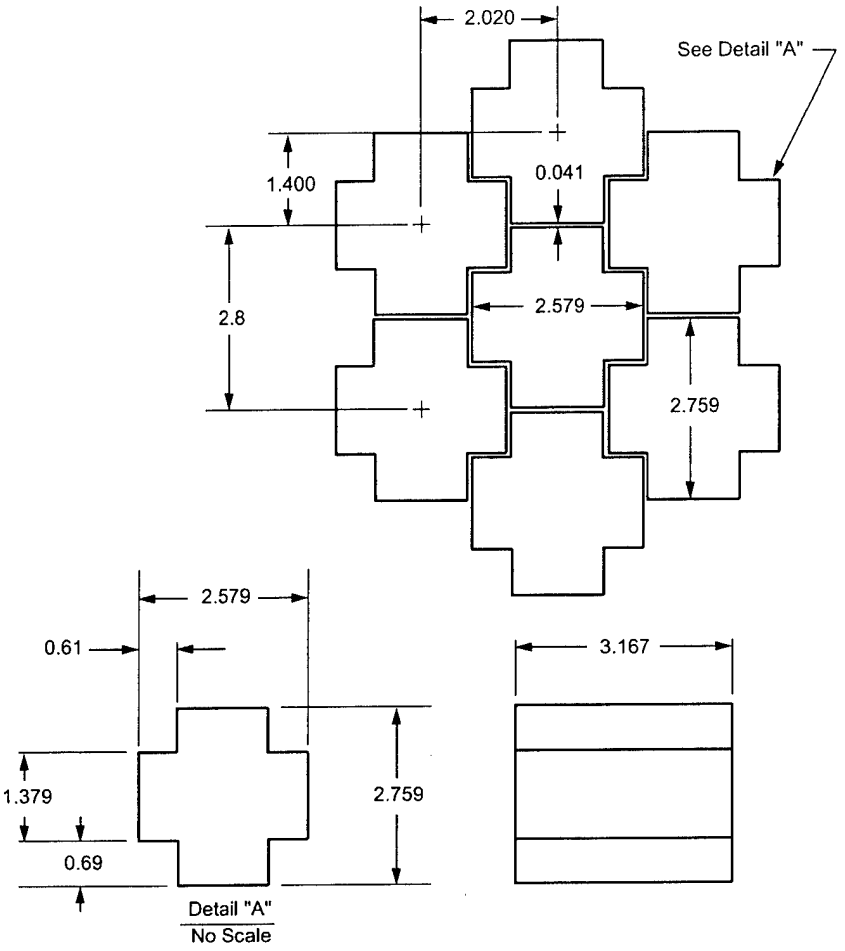

Fig. 12. Cross-shaped plate geometry (all units in cm).

Acknowledgments

As it is with many scientific/engineering endeavors, this work is built upon the shoulders of many other people. I want to thank Dan Hoppe for his many helpful technical discussions, as Dan had developed a similar program for Hughes. A significant amount of code was used from the rectangular-hole program of Jackie Chen. Glen Welsh and Dan Hoppe modified the delaundo code to make it useful for meshing waveguides. Tom Cwik supplied the code that was used to factor and solve the sparse matrix.

References

[1] P. D. Potter, "S- and X-Band Feed System," *The Deep Space Network Progress Report 32-1526*, vol. XV, Jet Propulsion Laboratory, Pasadena, California, pp. 54–62, June 15, 1973.
http://tmo.jpl.nasa.gov/tmo/progress_report/XV/XVI.PDF

[2] C. C. Chen, "Transmission of Microwave Through Perforated Flat Plates of Finite Thickness," *IEEE Transactions on Microwave Theory and Techniques*, vol. MTT-21, no. 1, pp. 1–6, January 1973.

[3] J. C. Chen, "Analysis of a Thick Dichroic Plate with Rectangular Holes at Arbitrary Angles of Incidence," *The Telecommunications and Data Acquisition Progress Report 42-104, October–December 1990*, Jet Propulsion Laboratory, Pasadena, California, pp. 9–16, February 15, 1991.
http://tmo.jpl.nasa.gov/tmo/progress_report/42-104/104B.PDF

[4] N. Amitay, V. Galindo, and C. P. Wu, *Theory and Analysis of Phased Array Antennas*, New York: Wiley-Interscience, 1972.

[5] C. C. Chen, "Transmission Through a Conducting Screen Perforated Periodically with Apertures," *IEEE Trans. Microwave Theory Tech.*, vol. MTT-18, no. 9, pp. 627–632, September 1970.

[6] R. Silvester, "Finite-Element Solution of Homogeneous Waveguide Problems," *Alta Frequenza*, vol. 38, pp. 313–317, 1969.

[7] P. M. Morse and H. Fishbach, *Methods of Theoretical Physics (Part I)*, New York: Macmillan, 1968.

[8] W. A. Imbriale and R. E. Hodges, "The Linear Phase Triangular Facet Approximation in Physical Optics Analysis of Reflector Antennas," *Applied Computational Electromagnetic Society*, vol. 6, no. 2, pp. 74–85, Winter 1991.

[9] J.-D. Müller, *On Triangles and Flow*, Ph.D. Thesis, The University of Michigan, Ann Arbor, 1996.

[10] J.-D. Müller, "The Advancing Front Method and the Delaunay Triangulation," 24th von Karman Institute Lecture Series on Computational Fluid Dynamics, vol. 2, 1994.

[11] R. Lehoucq, K. Maschhoff, D. Sorensen, and C. Yang, ARPACK SOFTWARE.
http://www.caam.rice.edu/software/ARPACK/

[12] T. Cwik, D. S. Katz, and J. Patterson, "Scalable Solutions to Integral-Equation and Finite-Element Simulations," Advanced Numerical Techniques in Electromagnetics, *IEEE Trans. Antennas Propagation*, vol. 45, pp. 544–555, 1997.

[13] J. R. Pyle, "Cutoff Wavelengths of Waveguides with Unusual Cross Sections," *IEEE Transactions on Microwave Theory and Techniques*, Correspondence, vol. MTT-12, no. 5, pp. 556–557, September 1964.

[14] K. Pontoppidan, "Finite-Element Techniques Applied to Waveguides of Arbitrary Cross Sections, Parts I and II," Ph.D. Thesis, The Technical University of Denmark, Lyngby, Denmark, September 1971.

[15] T. Y. Otoshi and M. M. Franco, "Dual Passband Dichroic Plate for X-Band," *The Telecommunications and Data Acquisition Progress Report 42-94, April–June 1988*, Jet Propulsion Laboratory, Pasadena, California, pp. 110–134, August 15, 1988.
http://tmo.jpl.nasa.gov/tmo/progress_report/42-94/94J.PDF

[16] L. W. Epp, P. H. Stanton, R. E. Jorgenson, and R. Mittra, "Experimental Verification of an Integral Equation Solution for a Thin-Walled Dichroic Plate with Cross-shaped Holes," *T-AP*, vol. 42, no. 6, pp. 878–882, June 1994.

Ranking and Selection Applied to Eigen-Analysis of Array

Michael C. Wicks Pinyuen Chen
Radar Signal Processing Branch
Air Force Research Laboratory
Rome, NY 13441

Abstract: In this paper, statistical ranking and selection theory is applied to the eigenvalue problem. Of concern is the development of a procedure for computing the number of signals in a measurement data vector. In our approach, the multiplicity of the noise eigenvalue is computed, and used in calculating the number of non-noise (signal) eigenvalues. We propose a selection procedure to estimate the multiplicity of the common smallest eigenvalue, which is significantly smaller than the other eigenvalues. We derive the probability of a correct selection, P(CS), and the least favorable configuration (LFC) for our procedures. Under the LFC, the P(CS) attains its minimum over the preference zone of all eigenvalues. Therefore a minimum sample size can be determined from the P(CS) under the LFC, P(CS|LFC), in order to implement our new procedure with a guaranteed probability requirement. Numerical examples are presented in order to illustrate our proposed procedure. The procedure parameters can be found from P(CS|LFC) and be used to perform simulation studies and for data analysis. Simulation results and numerical analysis using the US Air Force Multi-Channel Airborne Radar Measurement data collected by Westinghouse (now Northrop Grumman) will be presented to illustrate our theory.

1. Introduction

In the analysis of measured data, an approach that is often used involves modeling observations as the superposition of a finite number of signals embedded in additive Gaussian noise. This is especially true in phased array signal processing, time-harmonic analysis, computing the natural response of a system by estimating the number of poles from measurement data, and in detecting overlapping target echoes from radar backscatter. Practical adaptive array processing for airborne radar requires effective

utilization of available degrees of freedom. The question therefore arises how many degrees of freedom are required in a given interference scenario. A fundamental issue in solving these problems is correct estimation of the number of signals present.

One approach to solving this problem is based on the observation that the number of signals present can be determined via eigen-analysis of measured data. To do so, an accurate estimate of the covariance matrix of the observed data vector is essential. Once this estimate is formulated, many different techniques are available for eigen decomposition. Bartlett [1] and Lawley [2] developed a multiple hypothesis test for multiplicity of the smallest eigenvalue (latent root) and applied this approach to the analysis of measured agriculture data. Schmidt [3] applied the Multiple Signal Classification (MUSIC) algorithm to estimate the number of incident wavefronts present in an electromagnetic signal based upon the eigenstructure of the covariance matrix of received data. Other hypothesis testing and estimation methods based on eigenstructure analysis have been proposed by Wax and Kailath [4] and Zhao, Krishnaiah, and Bai [5].

This paper uses statistical selection theory to detect the multiplicity of the smallest eigenvalue of the covariance matrix, computed using measured multi-channel multi-pulse radar data. A unique aspect of the proposed methodology is that it predicts a confidence level in the estimated number of signals. As described in the a fore mentioned articles, the number of signals present is the difference between the total number of components in the observed data vector and the multiplicity of the smallest eigenvalue. In the analysis of measured data, the smallest eigenvalues may in fact be grouped about some nominal value, as opposed to being identically equal. We propose a selection procedure to estimate the multiplicity and value of the smallest eigenvalue(s), which are significantly smaller than the other eigenvalues. We derive the probability of a correct selection, P(CS), and the least favorable configuration (LFC) for our procedures. Under the LFC, the P(CS) attains its minimum over the vector space of all eigenstructures. Therefore a minimum sample size can be determined from the probability of CS under the LFC, P(CS|LFC), in order to implement our new procedure with a guaranteed probability requirement. Numerical examples are presented in order to illustrate our proposed procedure.

The techniques described above can be applied to the analysis of measured data collected from any multi-channel and/or multi-pulse radar. As such, a

new solution to the adaptive beam-forming problem arises out of the application of ranking and selection theory to the radar problem. First, the number of interfering signals present in a data vector is estimated using our new procedure. Then, optimal rank reduction can be achieved given this knowledge. And finally, adaptive processing for interference rejection and target detection can be performed using any of the standard techniques published in the literature (Reed, Kelly). This technique for estimating the number of signals in noise using statistical selection theory has applications to many other areas where eigen-analysis is useful. Note that in this paper, correct selection includes overestimating the number of signals. This is of particular importance in the radar signal processing problem (Hale and Welsh [6]). The techniques discussed in this paper, presented within the context of the radar problem, may be generalized. Targeted approaches include multiple discriminant analysis, simultaneous inferencing, principal component analysis, and canonical correlation analysis and multivariate analysis of variance. As such, the analysis of economic, educational, industrial, population, psychological, and scientific data may all benefit from this new technique.

The paper is organized as follows. In Section 2, we formally define the problem. In Section 3, we introduce ranking and selection formulation and our proposed procedure. In Section 4, we give examples to illustrate the estimation of the procedure parameter. An example using measured radar data is given in Section 5.

2. Statement of The Problem

As described in Wax and Kailath [4] and Zhao, Krishnaiah, and Bai [5], the observed vector of certain signal processing problems, denoted by the $p \times 1$ vector $\boldsymbol{x}(t)$, can be written as

$$\boldsymbol{x}(t) = \sum_{1}^{q} \boldsymbol{A}(\Phi_i) s_i(t) + \boldsymbol{n}(t) = \boldsymbol{A}\boldsymbol{s}(t) + \boldsymbol{n}(t) \tag{2.1}$$

where

$\boldsymbol{A} = [\boldsymbol{A}(\Phi_1), \ldots, \boldsymbol{A}(\Phi_q)]$, $\boldsymbol{s}(t) = (s_1(t) \ldots s_q(t))'$, $\boldsymbol{n}(t) = (n_1(t), \ldots, n_p(t))'$

and $q < p$. It can be seen in (1) of Wax and Kailath [4] and in (2.1) of Zhao, Krishnaiah, and Bai [5], that the extreme case where $q = p$ is not realistic and therefore not addressed.

In the above model, $n(t)$ is a $p \times 1$ complex vector referred to as the additive noise distributed independently of $s(t)$ as complex multivariate normal with mean vector 0 and covariance matrix $\sigma^2 I_p$ where σ^2 is unknown; $s(t)$ is distributed as complex multivariate normal with mean vector 0 and nonsingular covariance matrix ψ where $s_i(t)$ is a scalar complex waveform associated with the i^{th} signal; and $A(\Phi_i)$ is a $p \times 1$ complex vector, characterized by an unknown parameter vector Φ_i associated with the i^{th} signal. A crucial problem associated with the model described in (2.1) and considered by all the articles mentioned in Section 1 is that of determining the number of signals q from a sample $x(t_1), x(t_2), \ldots, x(t_n)$. The goal of this paper is to study formulations in statistical ranking and selection theory to determine the value q.

The covariance matrix Σ of $x(t)$ is given by

$$\Sigma = A\Psi\overline{A}' + \sigma^2 I_p \tag{2.2}$$

where $\overline{A}'$ denotes the conjugate transpose of A.
Let $\lambda_1 \geq \lambda_2 \geq \ldots \geq \lambda_p$ denote the positive eigenvalues of the covariance matrix Σ and let the hypothesis H_q: $\lambda_i = \sigma^2 + \alpha_i$ $(i = 1,2,\ldots, q)$; $\lambda_{q+j} = \alpha_i$ $(j = 1,2,\ldots, p\text{-}q)$. Therefore H_q is equivalent to the hypothesis that q signals are transmitted. Wax and Kailath [4] used Akaike's Information Criterion (AIC) and Schwart Rissanen's MDL criterion for model selection, while Zhao, Krishnaiah, and Bai [5] used a information theoretic criterion to estimate the value q. Haimovich [7] used asymptotic theory to estimate the covariance matrix Σ in (2.2) under H_q. In Section 3 below, we define a selection formulation and propose selection procedures to determine the value q.

3. Ranking and Selection Formulation and the Proposed Procedure

Ranking and selection procedures are generally developed using either an indifference zone or a subset selection approach. The literature on ranking and selection theory is dominated by these two methods. Wicks [8] first proposed applying statistical ranking and selection theory to radar signal processing for covariance matrix estimation. Chen, Melvin, and Wicks [9] used a variation of the subset selection approach in developing a screening procedure for choosing secondary data in radar signal processing. Their

results showed dramatically improved performance over conventional techniques.

Consider k populations $\pi_1,\pi_2,...,\pi_k$ where the underlying distribution of π_i is F_{θ_i}, i = 1, 2, k. In most ranking and selection studies, the k populations are independent. They could also be k-correlated components of a multivariate population, which possesses a multivariate distribution with parameters of interest. As will become clear later in this paper, we are dealing with p correlated sample eigenvalues and our parameters are the population eigenvalues. In general, the unknown real parameter, θ_i, i = 1, 2, k, represents the value of a quantity of interest for the i^{th} population. By definition, we select population π_i over π_j if θ_i is greater than θ_j. The ordered values of θ_i for all i are denoted by $\theta_{[1]} \leq \theta_{[2]} \leq \ldots \leq \theta_{[k]}$. In general, $\theta_{[i]} \neq \theta_i$. One approach to solving the basic problem of selecting the *best* population, called the indifference zone formulation, was developed in Bechhofer [10]. In Bechhofer's paper, the selection of the population associated with the ranked parameter $\theta_{[k]}$ results in a correct selection (CS). For the indifference zone approach to be of value, the procedure R must establish a lower bound on the probability of a correct selection P(CS). The minimum value of P(CS) is P*, with $1/k < P^* < 1$ whenever the separation between $\theta_{[k]}$ and $\theta_{[k-1]}$ exceeds some minimum specified value. Let $\delta(\theta_i,\theta_j)$ denote an appropriate non-negative measure of the separation between the population associated with θ_i and θ_j. For the minimum probability of correct selection, P*, δ^* is the minimum separation distance. For any specified $\delta^* > 0$, the preference zone, Ω_{δ^*} is the subset of the parameter space $\Omega = \{\tilde{\theta}|\tilde{\theta} = (\theta_1,...,\theta_k)\}$ defined by $\Omega_{\delta^*} = \{\tilde{\theta}|\delta(\theta_{[k]},\theta_{[k-1]}) \geq \delta^*\}$. Let P(CS|R) denote the probability of a correct selection under the procedure R. In order for this procedure to be valid, it should satisfy $P(CS|R) \geq P^*$ for all $\tilde{\theta} \in \Omega_{\delta^*}$. The complement of the preference zone Ω_{δ^*} is called the indifference zone, a subset of the parameter space where no requirement on P(CS) is made.

For the analysis of measured data, δ^* and P* are specified in advance. Suppose that the procedure R is based on samples of fixed size n from each population. One problem of practical interest in radar signal processing is to determine the smallest sample size n for which the

probability requirement P* holds. In the subset selection approach of Gupta [11], a procedure was developed to guarantee a non-empty subset of the k given populations which include the desired (or best) population with a minimum probability P*. Any subset, which includes the desired population, results in a correct selection. In case of a tie, any contender may be tagged best. Any valid procedure R should satisfy $P(CS|R) \geq P^*$ for all $\tilde{\theta} \in \Omega$. In the subset selection approach, the size of the selected subset S is not decided in advance, but is determined based on the analysis of data. The procedures developed in ranking and selection theory are designed to satisfy the requirement for a minimum probability of a correct selection P*. Any parameter configuration $\tilde{\theta}$ which yields the infimum of the P(CS) over Ω_{δ^*} in the indifference zone approach, or Ω in the subset selection approach, is called the least favorable configuration (LFC).

Many variations and generalizations of these two basic approaches have been studied. For example, one problem involves procedures for selecting the most appropriate sample populations better than a control population π_0. These sample populations may then be used to estimate other parameters of interest such as the covariance matrix. In our study of selection procedures for analyzing the eigenvalues of the covariance matrix in radar data, the control population can be taken as the smallest eigenvalue. The observations are taken and their covariance matrix is estimated. Eigenvalues are selected from those populations (eigenvalues in our study) $\pi_1, \pi_2, \ldots, \pi_p$ (instead of using k in traditional selection theory, we use p here to represent the total number of components in a random vector) having the same or similar values as the control population.

We define two disjoint and exhaustive sets Ω_G and Ω_B of the set $\Omega = \{\lambda_1, \ldots, \lambda_p\}$ by using ratio as the distance function d. That is, we define

(3.1) $$d(\lambda_i, \lambda_j) = \lambda_i / \lambda_j;$$

$\Omega_G = \{\lambda_i, i = 2, 3, \ldots, p | d(\lambda_i, \lambda_p) \geq \delta^*\}$ and $\Omega_B = \Omega - \Omega_G$.

where $\delta^* > 1$ is a preassigned real number used to differentiate between good and bad eigenvalues. Our goal is to separate the set of eigenvalues into two disjoint subsets, S_G and S_B. The separation is correct (CS) if $S_G \supseteq \Omega_G$, meaning that all eigenvalues with values significantly larger than the smallest eigenvalue will be classified into Ω_G. Our conclusion for the value of q is the number of elements in S_G. We require a

procedure R that will satisfy a predetermined probability requirement $P(CS|R) \geq P^*$.

Procedure R: Compute the covariance matrix $S = \frac{1}{n}\sum_{i=1}^{n} x(t_i)x'(t_i)$ using the samples $x(t_1), x(t_2), ..., x(t_n)$. Let $\ell_1 > \ell_2 > ... > \ell_p$ be the ordered eigenvalues of S. Let r be the largest integer in $\{1, 2, ..., p - 1\}$ such that $\ell_r / \ell_p > c$, where $c > 1$ is a real number chosen to satisfy the probability requirement $P(CS) \geq P^*$. Claim that $S_G = \{\lambda_1, \lambda_2, ..., \lambda_r\}$ and the number of signals is $q = r$. When $\ell_r / \ell_p \leq c$ for all integer in $\{1, 2,..., p - 1\}$, we claim that $q = 0$. We will explain how to obtain a conservative approximation for c, the procedure parameter, in next section. We make the following two assumptions about the model:

Assumption 1:

H_q: $\lambda_i = \sigma^2 + \theta_i$ $(i = 1, 2, ..., q)$; $\lambda_{q+j} = \sigma^2$ $(j = 1, 2, ..., p-q)$.

That is, the multiplicity of the smallest eigenvalue is p - q, where p is known and q is unknown. Moreover, we assume that $\theta_1 > \theta_2 ... > \theta_q$. This is a reasonable assumption because $\theta_1, \theta_2 ..., \theta_q$ came from the first term of the covariance matrix in (2.2). Adding ε to an eigenvalue and then letting it go to zero will not change the form of the covariance matrix and therefore it will not change our results.

Assumption 2: When $q > 1$, the parameter configuration belongs to Ω_G, the so-called preference zone in ranking and selection theory. That is, $\lambda_q / \lambda_p \geq \delta^*$. The case $q = 0$ corresponds to the case where there is no signal. The only configuration for the parameter is the equal parameter configuration $\lambda_1 / \lambda_p = 1$.

The probability of a correct selection under H_q using Procedure R can be written as

$$(3.2) \quad P(CS|R) = P(q \leq r) = \sum_{j=q}^{p-1} P(\ell_j / \ell_p > c, \ell_{j+1}/\ell_p \leq c).$$

In the following, we will first state an important result about the least favorable configuration (LFC) of our procedure in asymptotic theory. Then we will express P(CS) under the asymptotic LFC. In Section 4, we

will describe how the results in this section can be used to determine the sample size needed for our procedure R.

Theorem 3.1: The asymptotic least favorable configuration (ALFC) for our procedure R under the preference zone defined in Assumption 2 is given by

(3.3) $\lambda_1 = \lambda_2 = \ldots = \lambda_q > \lambda_{q+1} = \ldots = \lambda_p$, where q is an integer between 1 and p and $d(\lambda_1, \lambda_p) = \lambda_1 / \lambda_p = \delta^*$.

Corollary 3.1: Under the asymptotic least favorable configuration $\lambda_1 = \lambda_2 = \ldots = \lambda_q > \lambda_{q+1} = \ldots = \lambda_p$ where $\lambda_1 / \lambda_p = \delta^* > 1$, *Asy*-P(CS) is a decreasing function of δ^*.

Theorem 3.2: Under the asymptotic least favorable configuration given in Theorem 3.1, *Asy*-P(CS) is an increasing function of n, the sample size.

From the above theorems and the corollary, we know that the probability of a correct selection for our procedure approaches 1 by either increasing δ^*, the size of our "indifference zone" or the sample size n. It is also clear that P(CS) increases as c decreases. But, the size of the selected subset of the eigenvalues will also increase. Therefore we may overestimate the number of signals by decreasing c. In next section, we will discuss the method we use to find the procedure parameter c and the role that the sample size, n, plays in the procedure.

4. Illustrative Examples for The Procedure Parameter

In this section, we explain how to approximate and obtain a conservative bound for c, the procedure parameter. From Theorem 3.1 and the fact that the distributions of the sample eigenvalues depend on the population covariance matrix only through their eigenvalues, the *Asy*-LFC that we use to calculate P(CS) can be written as

(4.1) $\Sigma = \text{diag}(a, \ldots, a, a\delta^*, \ldots, a\delta^*)$ where a is a positive real number.

It is clear that we can take a = 1 in (4.1) since our procedure R is defined by the selection statistic ℓ_r / ℓ_p (r = 1, ..., p - 1) whose distribution is invariant under a scalar multiplication.

In the first example, we show how to obtain the procedure parameter, c, by simulation.

Example 1: Finding the procedure parameter c for the case p = 10, n=200, $\delta^* = 2$, simulation repetition = 10000:
The following table shows the 5 percentiles for the given statistic ℓ_q / ℓ_{10}, q = 0, ..., 9.

q	ℓ_9/ℓ_{10}	ℓ_8/ℓ_{10}	ℓ_7/ℓ_{10}	ℓ_6/ℓ_{10}	ℓ_5/ℓ_{10}	ℓ_4/ℓ_{10}	ℓ_3/ℓ_{10}	ℓ_2/ℓ_{10}	ℓ_1/ℓ_{10}
0	1.0308	1.1111	1.1906	1.2911	1.3791	1.4858	1.5950	1.7149	1.8697
1	1.0316	1.1099	1.2034	1.2867	1.3896	1.4910	1.6109	1.7766	2.5615
2	1.0272	1.1160	1.2061	1.3073	1.4037	1.5359	1.6788	2.3528	2.8001
3	1.0326	1.1137	1.2120	1.3180	1.4280	1.5790	2.1617	2.5029	2.8332
4	1.0329	1.1229	1.2193	1.3362	1.4794	1.9973	2.2989	2.5880	2.9165
5	1.0326	1.1280	1.2246	1.3739	1.8496	2.1157	2.3559	2.6030	2.9110
6	1.0335	1.1438	1.2717	1.7160	1.9542	2.1660	2.3603	2.5998	2.8688
7	1.0428	1.1627	1.5655	1.7828	1.9586	2.1677	2.3500	2.5700	2.8488
8	1.0539	1.4332	1.6123	1.7798	1.9533	2.1125	2.3034	2.4767	2.7523
9	1.2478	1.4225	1.5650	1.6958	1.8530	1.9999	2.1509	2.3423	2.5538

The underlined diagonal entries are the 5 percentiles of ℓ_q / ℓ_{10} when q value is the correct number of signals. We choose c = 1.24, the 5th percentile of ℓ_9 / ℓ_{10} rounded to the second decimal place. By doing so, more than ninety-five percent of the time our estimated q values are 9, 8, 7, 6, 6, 6, 6, 6, 6, 6 when the true q = 9, 8, 7, 6, 5, 4, 3, 2, 1, 0, respectively. As a matter of fact, $P(\ell_9 / \ell_{10} > c, \ell_8 / \ell_{10} \le c) \approx .95$ which is only the first term in the sum of P(CS|R) given in (3.2). Therefore, c is clearly a conservative procedure parameter for our method and we over-estimate the true number of signals, especially when q is small when c is chosen in this manner.

Next we present an example to demonstrate the performance of our method. The example adopts the same sensor array processing model assumed in all the three simulation results given in Wax and Kailath [4], Section VI. For comparison purpose, we use exactly the same model configuration as in Wax and Kailath [4].

Example 2: The vector of the received signal at the array is given by

(4.2) $x(t) = \sum_{k=1}^{q} A(\phi_k)e^{-jh(t)} + n(t)$ where $A(\phi_k)$ is the p × 1 "direction vector" of the kth wavefront; $A(\phi_k)^T = [1\ e^{-j\tau_k} \ldots e^{-j(q-1)\tau_k}]$ with $\tau_k = \pi\sin\phi_k$; $\eta(\cdot)$ = random phase uniformaly distributed on $(0, 2\pi)$; $n(\cdot)$ = vector of white noise with mean 0 and covariance $\sigma^2 I$. The signal-to-noise ratio, defined as $10\log(1/2\sigma^2)$, is 10 dB. From (5.1) (formula (24) in Wax and Kailath [4]), the signals have variance 1. Therefore, we assume that $\delta^* = 10$ in our study. We first consider seven sensors (p = 7) and two sources (q = 2). Using n = 100 samples, we simulate radar data according to (2.1) and the resulting eigenvalues of the sample covariance matrix are 1.0722, 0.9623, 1.1965, 0.7105, 0.5800, 7.3697, 10.3601. We next consider p = 7 and q = 3. Using n =100 samples, the eigenvalues of the sample covariance matrix of simulated radar data are 1.0688, 1.1311, 0.7159, 1.5023, 8.2028, 8.5212. 10.6351. The simulated 5 percentiles of ℓ_q / ℓ_7 for q = 0, 1, ..., 6 are in the following table.

q	ℓ_6/ℓ_7	ℓ_5/ℓ_7	ℓ_4/ℓ_7	ℓ_3/ℓ_7	ℓ_2/ℓ_7	ℓ_1/ℓ_7
0	1.0454	1.1709	1.3180	1.4908	1.6664	1.9125
1	1.0476	1.1834	1.3447	1.5262	1.7566	11.6115
2	1.0491	1.1900	1.3595	1.5759	9.8242	12.8793
3	1.0522	1.2059	1.4207	8.5851	10.9399	13.3350
4	1.0570	1.2364	7.4859	9.3746	11.1370	13.2385
5	1.0649	6.4364	7.9776	9.4016	10.9034	12.7948
6	5.2116	6.4327	7.5204	8.6702	9.9161	11.5024

Following the method in Example 1, we choose c = 5.21. Therefore by our procedure, we correctly declare that there are 2 signals in the first case and that there are 3 signals in the second case. In fact, at least 95% of the time, our method will detect correctly the number of signals in this model no matter what the true q is. Moreover, for any sample size n great than or equal to 35, we have more than 95% probability of correctly detecting the number of signals no matter what the true number q is. The value n = 35 is obtained by running a search algorithm based on the method used to produce the table above.

5. A Measured Radar Data Example

One of the prime motivations for this research is the application to radar signal processing. This example uses data from the Multi-Channel

Airborne Radar Measurements (MCARM) program, a vast collection of airborne radar measurements over many flights with multiple acquisitions during flight. The radar antenna is a 22 (2x11) rectangular array (p=22). In several acquisitions, the transmitter was off resulting in no clutter to mask signals generated by a Moving Target Simulator (MTS) at preset Doppler frequencies.

In this example, the data cube comprising 1408 pulses with the transmitter off were analyzed. The MTS transmits 10 signals overall. Figure 1 shows the MTS signal strength as a function of Doppler frequency. As can be seen, there are 9 signals in a pattern centered at -500Hz and a strong signal at zero Doppler. Within the MCARM database, this data set matches the model of Eqn. (2.1) with q=10. All 1408 pulses (n=1408) were used to estimate the covariance matrix S. As noted before, p=22. The ratio of the eigenvalues to the smallest estimated eigenvalue is shown in Table 1. The ratio of the first eigenvalue is 520 times that of the smallest eigenvalue. In this case the value of c for $\delta^* = 2.0$ (3dB) is found to be $c = 1.577$. From Table 1, this sets the minimum number of signals with signal-to-noise ratios greater than δ^* at 11.

Table 1 : Statistics for determining number of signals in noise. MCARM Data

Number	Eigenvalue	Ratio	AIC Value	MDL Value
0	4423.7	507.97	148733.9	74366.96
1	123.95	14.233	15253.19	7739.47
2	37.448	4.3002	3458.01	1949.50
3	21.403	2.4577	1636.28	1141.01
4	18.363	2.1086	1337.59	1088.79
5	16.847	1.9345	1214.14	1118.94
6	16.081	1.8466	1154.17	1175.57
7	15.859	1.8211	1113.94	1236.84
8	15.341	1.7616	1064.70	1288.34
9	14.196	1.6301	1021.56	1337.64
10	14.061	1.6147	1015.42	1400.20
11	13.543	1.5552	999.94	1452.83
12	13.199	1.5156	991.36	1503.67
13	12.621	1.4493	982.07	1548.89
14	12.263	1.4082	981.34	1593.16
15	11.944	1.3715	980.55	1632.13
16	11.705	1.4410	977.69	1664.83
17	11.030	1.2666	968.50	1689.11
18	10.708	1.2296	967.66	1712.31
19	9.9416	1.1416	962.57	1728.14
20	9.4735	1.0879	964.99	1742.48
21	8.7084	1	966.00	1750.86

Table 1 also lists the AIC and MDL values, used to determine the number of signals in this case, as suggested by Wax and Kailath [4]. This approach used is to determine the AIC or MDL values and the number of signals is the number where the AIC and MDL values are the lowest. As can be seen from the table, the AIC criterion sets the number of signals to be 19, while the MDL criterion determines the number of signals to be 4. Both values are clearly erroneous since the true number of signals is 10. In the AIC case, even though it is better to overestimate the number of signals rather than underestimate (the MDL case), the overestimation here is extremely large. In a practical situation, this would imply a significant waste of energy and other resources. This example clearly indicates the superiority of the proposed approach over the earlier approaches.

6. REFERENCES

[1] Bartlett, M. S. (1954) A note on the multiplying factors for various Chi-square approximations, Journal of Royal Statistical Society, ser. B, 16, 296-298.

[2] Lawley, D. N. (1956) Tests of significance of the latent roots of the covariance and correlation matrices, Biometrica, 43, 128-136.

[3] Schmidt, R. O. (1979) Multiple emitter location and signal parameter estimation, Proceedings of the RADC Spectrum Estimation Workshop, Rome, NY, 243-258.

[4] Wax, M. and Kailath, T. (1985) Detection of signals by information theoretic criteria, IEEE Transcations on Acoustics, Speech, and Signal Processing, vol. ASSP-33, no. 2, 387-392.

[5] Zhao, L. C., P. R. Krishnaiah, and Bai, Z. D. (1986) On detection of the number of signals in presence of white noise, Journal of Multivariate Analysis, 20, 1, 1-25.

[6] Hale, T. and B. Welsh (1998) Secondary data support in Space Time Adaptive Processing, Proceedings of the 1998 IEEE Radar Conference, pp. 183-188, Dallas, TX.

[7] Haimovich, A. M. (1997) Asymptotic Distribution of the conditional aignal-to noise ratio in an eigenanalysis-based adaptive array, *IEEE Transactions on Aerospace and Electronic Systems*, vol. 33, 3, 988-997.

[8] Wicks, C. M. "Applications of ranking and selection theory to radar signal processing", Technical Report.

[9] Chen, P, Melvin, W. L., and Wicks, M. C. (1999) Screening among multivariate normal data, *Journal of Multivariate Analysis*, 69, 10-29.

[10] Bechhofer, R. E. (1954). A single-sample multiple decision procedure for ranking means of normal populations with known variances. *The Annals of Mathematical Statistics*, 25, 16-39.

[11] Gupta, S. S. (1956). On a decision rule for a problem of ranking means. *Mimeograph Series.*

VERTICAL DIVERSITY IN ARRAY OF COLLOCATED HF LOOP ANTENNAS

G. Le Bouter*, L. Bertel, D. Lemur** and Y. Erhel*****

* : CRESAT,
35042 RENNES-Cedex France

** : ART Laboratory, University of Rennes 1
35042 RENNES-Cedex France

*** : CREC, 56381 GUER-Cedex France

Abstract : The aim of this paper is to propose a new single site direction finding system operating in the HF band. After a presentation of a signal model including both propagation and antenna effects, the paper describes the technique used to choose simultaneously the geometry of the array and the different types of antenna for each sub array. Then the height of setting up two sub arrays on the same mast is determined by correlation between the antenna complex responses. Finally, some theoretical and experimental results of direction finding related to this new type of vertical array of collocated antennas are given.

1. Introduction

In HF band and for sky wave, the ionosphere serves to be the propagation channel : several ionospheric layers may act as reflectors for waves propagating in one or more hops. The non-isotropic nature of the ionosphere imposes a multipath propagation to the transmitted signal. When a channel generates multipaths, radio direction finding must resort to hight resolution algorithms such as MUSIC to discriminate angle of arrival (AOA) of the incident signal on an antenna array. In such method of signal processing, the contribution of antenna effects on the incoming signal must be known. Depending on the type of antenna array, AOA estimation accuracy can be affected..

This article shows how the vertical space diversity could be set on collocated antenna array. The height mastered permit to control the radiation pattern. This control is very important for the

2. Antenna part in direction finding techniques : a short review

Different kinds of antenna elements could be used for direction finding (DF). The choice of the antenna type is explained at paragraph 3.2. . Array which is composed of same antennas (same antenna pattern) is call homogeneous otherwise is heterogeneous.

The DF technique depends on antenna array types and geometry :

- methods using space diversity in homogeneous array, as interferometry, Doppler, beamforming, high resolution method, frequentiel analysis, or TDOA....
- methods using space diversity in heterogeneous array, which applies usually a high resolution method as MUSIC,
- methods without space diversity in heterogeneous array, in this case only collocated array can be employed. The laboratory of Rennes University uses in this case a high resolution algorithm to determine the angle of arrival [].

2.1. Bi-vectorial model of received signals in the case of multipath propagation

This paragraph remains a narrow band model of H. F. (3-30 MHz) signals after propagation via the ionosphere. The originality of this model published previously [1] is that it includes both the propagation effects and the antenna effects. Moreover this mathematical model can be simulated using a propagation software.

The general model of propagation for HF links (3-30 MHz) is based on optical geometry. If the transmitted signal is assumed to be written as $e(t) = m(t) \cdot e^{j \cdot \omega_0 t}$ where $m(t)$ represents the modulation of the signal and ω_0 is the carrier angular frequency, the received signal, for narrow band and for the k^{th} mode ($1F_2O$ for example) of propagation, can be expressed as [1, 2] :

$$s_{rk}(t) = A_k . m(t - \tau_{gk}) . e^{j\omega_{rk}\left(t - \tau_{pk}\right)} \qquad (1)$$

where A_k is the attenuation related to the k^{th} mode, τ_{gk} is the group delay corresponding to the k^{th} mode, ω_{rk} is the received angular frequency including the Doppler shift, τ_{pk} represents the phase delay for the considered mode. The modeling of all these parameters can be deduced from ionospheric propagation and prediction softwares (attenuation, group delay or angle of arrival) such as LOCAPI [2] or from physical considerations and measurements (Doppler shift).

A narrow band model is then defined as a model for which the parameters A_k, τ_{gk}, ω_{rk}, and τ_{pk} can be considered as constant in the band.

Maxwell equations induce a dispersion equation from which the phase indexes (for the O and X modes) and the polarization relations can be defined. At the exit of the ionosphere (at an altitude of about 90 km) the polarization relations are given by the limit conditions of Budden [4], wave behavior is not affected by the troposphere.

Let us consider a receiving antenna. In a general form, the electric field related to an incoming wave is expressed as a three component vector $\boldsymbol{E(t)}$; hence the signal $s(t)$ at the output of an antenna can be expressed as a vectorial product

$$s(t) = \boldsymbol{M} . \boldsymbol{E(t)}$$

where $\boldsymbol{M}$ is a matrix which characterizes the antenna response. Since the components $E_1(t)$, $E_2(t)$ and $E_3(t)$ of the electric field can be written in the following form according to the polarization relations

$$E_1(t), \qquad E_2(t) = a\,E_1(t), \qquad E_3(t) = bE_1(t)$$

the signal can be expressed as :

$$s(t) = (M_1 + aM_2 + bM_3) \cdot E_1(t) \qquad (2)$$

The scalar term $E_1(t)$ contains all the propagation effects as developed at equation 1.

Generally the coefficients of $\boldsymbol{M}$ are a complex function of the directions of arrival (azimuth and elevation) as well as a and b. This dependence will be noted $\boldsymbol{M(\theta)}$, $a(\theta)$ and $b(\theta)$. In the HF band, these two forms of diversity (antenna and polarization) must be considered : the coefficients of $\boldsymbol{M}$ are related to the type of antenna and the a and b terms depend on the angle between the geomagnetic field and the direction of propagation of the wave [4, 5].

This expression is then written in a compressed form as :

$$s(t) = F(\theta) \cdot E_1(t) \qquad (3)$$

The $F(\theta)$ complex function is named the antenna response function. It can be obtained with some approximations from physical laws [5, 6] or more rigorously with the help of simulations [8]. The ground effect in the area of the sensor can be included in the computation of the $F(\theta)$ function [5]. In the HF band this function is also related (via the polarization linked to the geomagnetic field, the frequency

and the wave vector) to the geographic characteristics of the considered link [5, 6, 8].

The inhomogeneous and the anisotropy of the ionosphere induce multipath and multimode propagation. The formula mentioned above for a receiving antenna can also be applied for a transmitting antenna ; thus, a general expression for the received signal can be written as :

$$x_{rli}(t) = \sum_{k=1}^{ns} A_k . G_{lk} . F_{ik} . m\left(t - \tau_{gk}\right) . e^{j\omega_{rk}\left(t - \tau_{pk}\right)} + n_i(t) \qquad (4)$$

where k identifies the O or X propagation paths and ns the number of paths, G_{lk} and F_{ik} are the complex functions of the transmitting antenna l and the receiving antenna i ; these functions are determined for the O and X propagation modes and depend upon the angles of arrival. A_k characterizes the attenuation of the wave corresponding to the k^{th} mode and $n_i(t)$ is additive noise.
For an array of NC collocated antennas, omitting the transmitting antenna effect, the vectorial expression of the received signal becomes [14] :

$$x_{ri}(t) = \sum_{k=1}^{ns} F_{ik} . s_{rk}(t) + n_i(t) \quad i = 1,..., NC \qquad (5)$$

For a receiving antenna of type i at the position p in an array using antenna and space diversity the general expression of the received signal is :

$$x_{rlip}(t) = \sum_{k} A_k . G_{lk} . F_{ik} . m\left(t - \tau_{gk}\right) . e^{j\omega_{rk}\left(t - \tau_{pk}\right)} e^{j\delta_{pik}} + n_i(t) \qquad (6)$$

where δ_{pik} indicates the phase shift regarding a reference for the wave k.
In the relations [7, 8, 9] the complex functions G_{lk} and F_{ik} act as weights for the signals corresponding to the different incoming waves. So the signals at the output of the antennas appear with uncorrelated envelopes.

If the transmitting antenna is unknown, the G_{lk} function cannot be determined and the determination of absolute amplitude and phase corresponding to a path and a polarization is impossible. In direction finding techniques, only differential amplitude and phase are used, so the knowledge of the transmitting antenna is not necessary. In this case, the model can be simplified and the phase term for a given mode is:

$$F_{ik} . e^{j\omega_{rk}(t - \tau_{pk})} e^{j\delta_{pk}} \qquad (7)$$

If the incident wave is plan, the phase term is reduced to:

$$F_{ik}\ e^{j\delta_{P_k}} \tag{8}$$

Where F_{ik} is antenna effect and $e^{j\delta_{pk}}$ is the space effect.

2.2. MUSIC algorithm operating on an array of identical sensors

The parametric methods aim to estimate parameters which are bound by incident sources such as angles of arrival, power, and by computation of a directional function from the steering vector of the array. For a source whose direction of arrival is denoted θ (angle or couple of angles in a 3-D problem), this vector is written as:

$$a(\theta) = [F(\theta) \quad F(\theta)e^{j\delta_2(\theta)} ..... \quad F(\theta)e^{j\delta_{NC}(\theta)}] \tag{9}$$

is the common complex directional response of the NC sensor (supposed to be identical) and is the geometrical phase of sensor p (sensor 1 being chosen as a reference).

The MUSIC algorithm is based on the orthogonality of the incident steering vectors and the noise subspace of the data covariance matrix : the pseudo spectrum is computed from the norm of the projection of the normalized steering $b(\theta) = a(\theta)/|a(\theta)|$ vector in the subspace :

$$PSSP(\theta) = \frac{1}{\sum_{p=NSE+1}^{NC} \left| v_p^T . b(\theta) \right|^2} \tag{10}$$

Where the set of vectors v_p define the noise subspace. The pseudo-spectrum $PSSP(\theta)$ can be computed with out the knowledge of the sensor responses $F(\theta)$:

$$\underline{b}(\theta) = \frac{\underline{a}(\theta)}{|F(\theta)|\sqrt{NC}} \tag{11}$$

The physical meaning of this result is that the type of antenna does not occur in the determination of the angles of arrival if there is a signal at the output of the antenna.

It can be noted that $PSSP(\theta)$ is the same, whether we integrate the directional responses in the calculation or not.

2.3. MUSIC algorithm operating on a heterogeneous array

An original method operating on an array that is made up different sensors has been proposed [3] ; each antenna of the array has a different pattern what necessitates to compute the complex responses of the antennas therefore it's be considered well known. The normalized steering vector, which appears in the determination of the pseudo spectrum, is expressed as follows:

$$b(\theta) = \frac{1}{\sqrt{\sum_{p=1}^{NC} \left| F_p(\theta) \right|^2}} \begin{pmatrix} F_1(\theta) \\ F_2(\theta) e^{j\delta_2(\theta)} \\ . \\ F_{NC}(\theta) e^{j\delta_{NC}(\theta)} \end{pmatrix} \qquad (12)$$

The term $e^{j\varphi_k(\theta)}$ determines the geometrical phase of the space diversity. In collocated array, this term is removed.

If radiowaves are received with two possible types of polarization (Ordinary O and eXtraordinary X in the HF range), this method provides an identification of that information. Antennas have spatial responses that are different for each polarization type and can be identified as $F_{nT}(\theta)$, with index T for O or X in the HF.

$$b_T(\theta) = \frac{1}{\sqrt{\sum_{p=1}^{NC} \left| F_p(\theta) \right|^2}} \begin{pmatrix} F_{1T}(\theta) \\ F_{2T}(\theta) e^{j\delta_2(\theta)} \\ . \\ F_{NCT}(\theta) e^{j\delta_{NC}(\theta)} \end{pmatrix} \qquad (13)$$

Therefore, the two sets of steering vectors (T=O or X) provide two pseudo-spectra $PSSP_O(\theta)$ and $PSSP_X(\theta)$.

3. Array of collocated antennas

3.1. Existing collocated antenna array

The term "collocated" appears toward the years 1980 and it specifies a array composed of antennas with the same phase center or antennas with a distance between them, small regarding the wavelength.
In 1981, Compton [4] proposed in the UHF band, a tripole antenna which is made up of three orthogonal dipoles. In 1983, Ferrara and al [5] proposed an circular array, each sub array used two cross loop. In 1987, Flam and al [6] designed a collocated array with three small antennas : two vertical cross loops and a vertical dipole. In 1990, Bull and Burgess [7] simulated an array of six collocated antennas. In 1997, Brandwood and al [8] proposed a sensor with three small loop antennas.
In 1998, Marie and al [9] realized in the HF band an array of seven collocated antennas, (two vertical cross loop, a horizontal loop, two inverted V 45°, a vertical dipole and XYZ loop) and they used this array in a single site direction finding system.

All these arrays are set up with collocated antennas and they do not introduced space diversity. The definition says that an array is collocated if antennas have the same phase center or a distance less than a wavelength. In the proposed array, the both antenna and space diversities are introduced in the geometry definition. This is the purpose of the following paragraph.

3.2. Antennas and space geometry choices

To propose a method to choose the type of antennas, the number of antennas and the number of sub array, several criteria has to be taken into account.

- **The size** of each antenna has to be small regarding to the wavelength : a good spatial sampling of the electromagnetic field requires the dimension of an antenna smaller than Lambda/10 when applying the Shannon theorem transposed to the spatial domain. In application of this hypothesis and for frequency less than 30 MHz (Lambda=10 m), the size of the antennas have to be in order of one meter. The only solution to get such size is to choose an active antenna as element of the array. In these antennas the current distribution can be considered as uniform [10].

- **The total number** of antennas is function of the local experimental possibilities : in the Rennes university system 8 channels are available, so 8 antennas can be used. In the work presented in this paper two sub array were set up, this means that 4 antennas maximum have to be employed for each sub

array. The results presented in this paper are relative to a space array of two sub arrays of three antennas each set on the same mast.

The type of antenna is related to :

–their directivity diagrams : the total space has to be «seen» by the antennas [ ],
– their phase responses which must be variable versus the angle of arrival and the propagation modes : for HF ionospheric propagation two complementary modes may be present for each path [11],
–the fact that the coupling between the different antennas in the same sub array must be low (brevet) to avoid a correlation between the output signals. The quality and accuracy of the direction finding results are generally related to this uncorrelation.

- The geometry of the array is imposed by the expected applications such as direction finding from a single geographical point (boat, track...). So an implementation on a single mast is a possible solution : this implies that only vertical diversity will be introduced in the system.

For this study the antennas response determination were done using a moment method : a NEC algorithm modified to determine the phase and amplitude response was implemented on a computer. So the simulation of the antenna responses take into account the following parameters :

–angle of arrival (azimuth and elevation)
–location of the received station
–frequency of the carrier
–type of antenna
–height the antenna
–characteristics of the ground (conductivity and permittivity)
–electrical characteristics of the amplifier and the cables.

The two first sets of parameters induced the polarization characteristics (function of the geomagnetic field) of the incoming waves. In the HF band and for ionospheric propagation, the polarization for the two possible modes (named O and X) is defined by the limit conditions of Budden [12] implemented by Bertel and al [13].
The type and height of antenna are two interesting parameters because the system designer can change them. The choice made in this system is to use same type of antenna, but with different heights.

4. Theoretical results

4.1. Description of the collocated array

The array uses two sets of sensors placed on a vertical mast of 18 meters high. Each sensor is composed of three active loop antennas (figure 1) oriented in the east west, north south, and horizontal directions. The first set of sensors is situated at 3 meters high ; the second can be positioned at different heights from 4 to 15 meters.

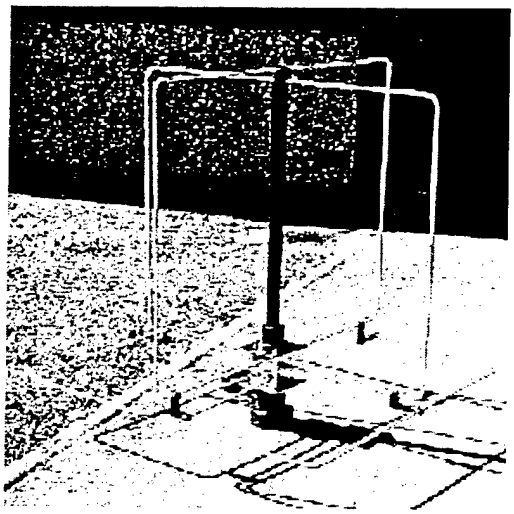

figure 1 : Sub array of three active collocated loop antennas

The interest of using the same antenna type is that they all have the same electrical characteristics and used the same type of preamplifier. This choice cuts down the error on the determination of steering vector.

The electrical responses at figure2 show that modulus responses are the same for all the preamplifiers: gain of 40 dB and bandwidth about 27 MHz (2.3 to 30 MHz). In each preamplifier, filters, located between the adaptation stage and the power stage, cut down all parasitic signals, which are outside the HF band.

4.2. Antenna complex responses

The characterization of the incoming wave is a 3D problem. Elevation (El) and azimuth (Az) are the two angles that characterize the incoming wave. The field relation (3) becomes :

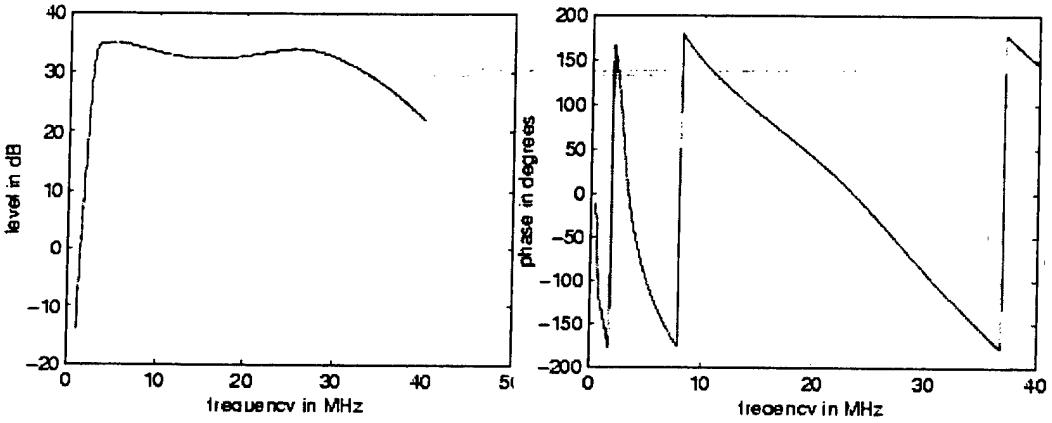

figure 2 : electrical responses (modulus and phase) of a preamplifier

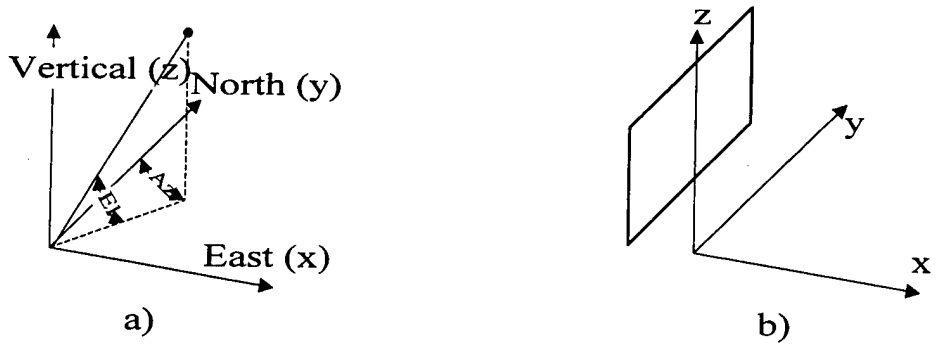

figure 3 : a) representation of the axe system, b) loop oriented north south

$$s(t) = F(Az, El).E(t) \qquad (14)$$

For example, a vertical loop antenna (figure 3-b), which is oriented north south, gives the modulus diagrams given figure 4. These diagrams depend on the

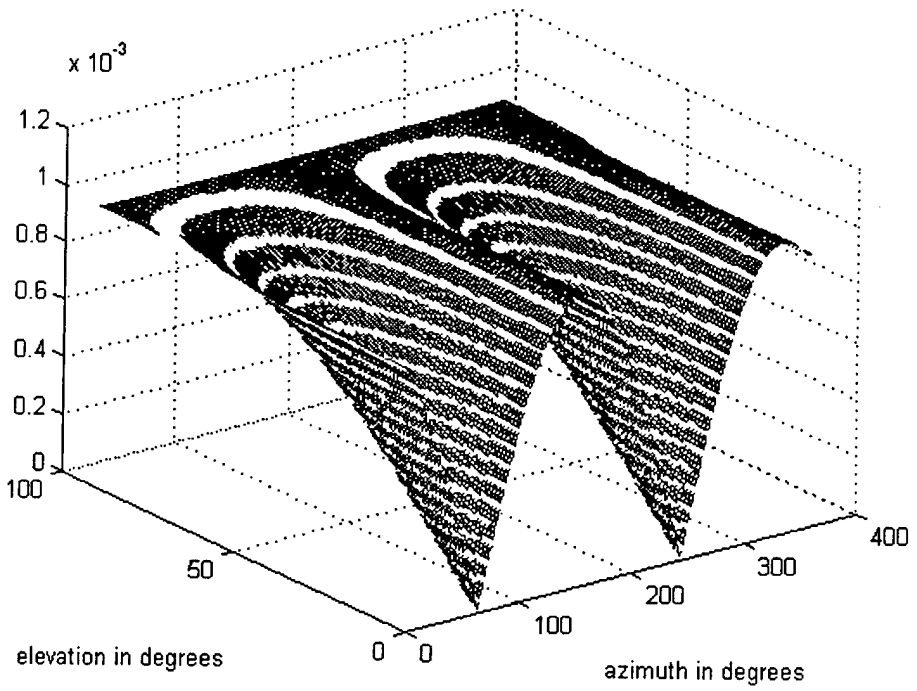

figure 4 : loop antenna oriented north south: modulus

characteristics mentioned at paragraph 3.2. . The only changing parameter is the height. The relation *F(Az,El)* is function of the antenna height : this means that the effect of the antenna on the signal *s(t)* is not the same for antennas placed at different height. This phenomena is related to the ground effect

The summary of all these considerations is

- all the incoming waves are characterized by azimuth and elevation,
- the antenna response is function of the angles of arrival,
- the MUSIC algorithm needs to imposed the use of several antennas (six in this case),

- the steering vector (modulus and phase response of each antenna) must be different for each angle of arrival,
- antennas use are active loop antennas.

The solution to find steering vectors, which cover the entire 3D dimension with the less ambiguity, is to study the intercorrelation product between them. This product could be calculated for different heights. The least value of this criteria can determinate the position of the two sub arrays.

4.3. Sub array height determination

The first step to determinate the height of sub arrays is to study intercorrelation product for a frequency carrier and for the height of the higher sub array (the lower is placed at 3 meters high).

$$SV(Az_x, El_x) = \begin{pmatrix} F_1(Az_x, El_x) \\ F_2(Az_x, El_x) \\ F_3(Az_x, El_x) \\ F_4(Az_x, El_x) \\ F_5(Az_x, El_x) \\ F_6(Az_x, El_x) \end{pmatrix} \quad (15)$$

For a angle of arrival (Az_i, El_i) :

$$\alpha_i(Az_y, El_y) = \frac{SV^T(Az_i, El_i) \bullet SV(Az_y, El_y)}{\sqrt{SV^T(Az_i, El_i) \bullet SV(Az_i, El_i)} \bullet \sqrt{SV^T(Az_y, El_y) \bullet SV(Az_y, El_y)}} \quad (16)$$

Az_y is varying from 0° to 360°, El_y from 0° to 90°.

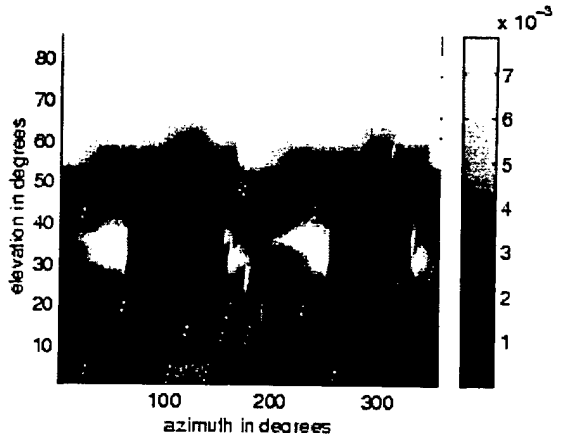

figure 5 : intercorrelation product for O mode 18 meters high and a 20MHz of frequency carrier

The intercorrelation product is determined for each angle of arrival.
The second step consists to sum up the intercorrelation values that are greater to 0,95. This level is chosen because MUSIC algorithm isn't efficient for values up to this level. The figure5 shows an example of intercorrelation between steering vectors for a frequency carrier of 20 MHz and for a height of 18 meters of the second sub array. The scale is expressing in percentage of correlated values (up to 0.95).
The third step permits to determinate the sum of value numbers, which are correlated (up to 0,95), depending on the height. (figure 6) This function is normalized by the number of points of computation point of each height (in this case 18 × 72 points).

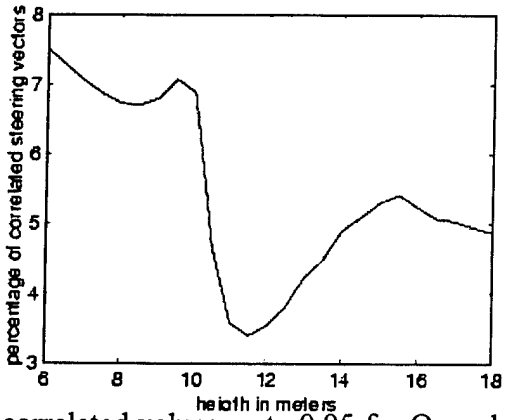

figure 6 : number of correlated values up to 0,95 for O mode versus height for a constant frequency of 20 MHz.

In the last step, the same computation as before is done, for frequency carrier varying from 6 to 20 MHz (figure 7). The frequency step is 2 MHz, so the graph introduces unrealistic discontinuities.

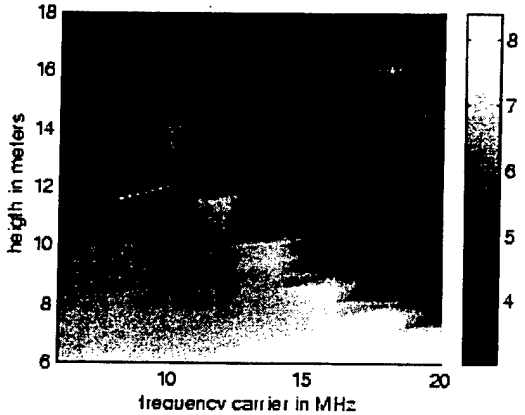

figure 7 : this graphic, for O mode, allows to determine the height of the second sub array

From these results it can be seen that the height of 12 meters for the second sub array could be a good compromise. Experimentally this value is quite acceptable.

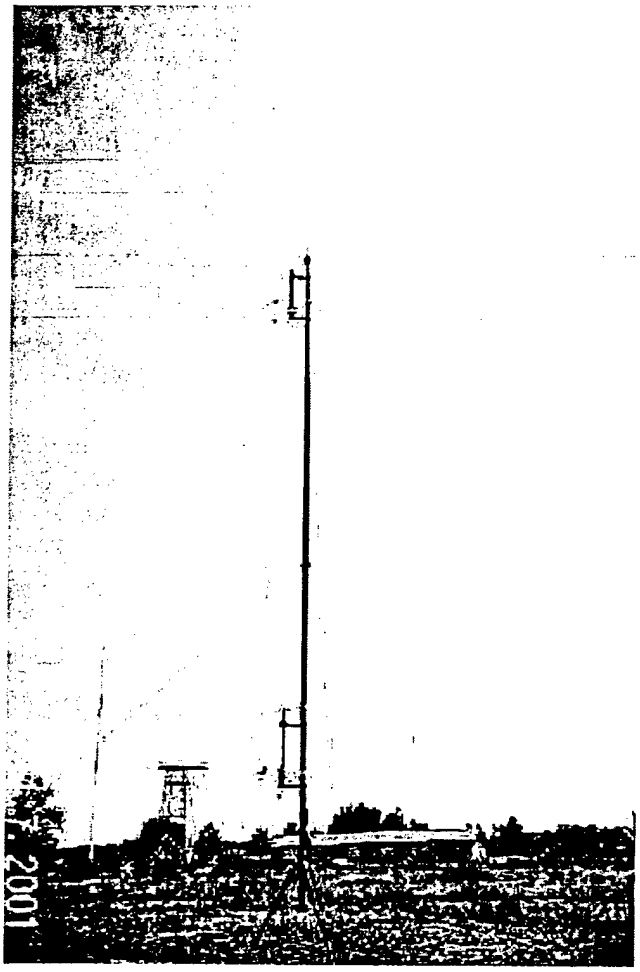

Figure 8 : 2 sub arrays set up on the same mast: first sub array at 3 meters high, the second at 12 meters.

4.4. Signals simulation with the collocated antenna array

The signal simulation is realized for the array of which the parameters are determined in the preceding paragraph.

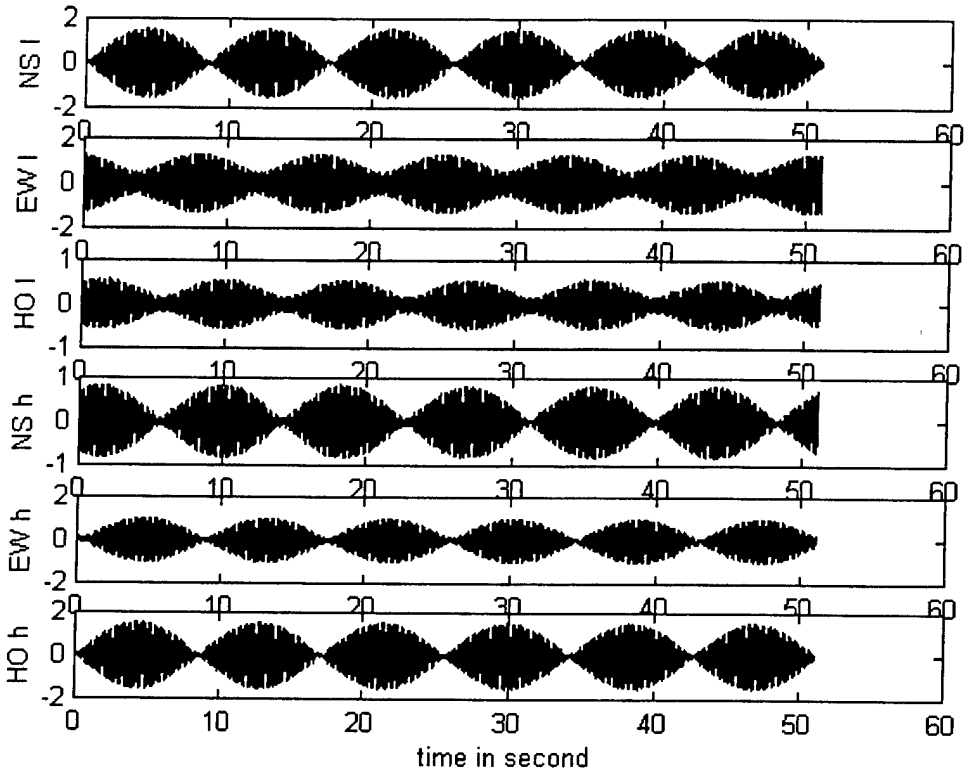

Figure 9 : Simulated signals on the collocated array

Figure 9 shows simulated signals on the six channels, two modes occur (one O and one X), they are characterized by a doppler shift of 0.1 Hz and their relative amplitude (ratio of 0.5 between O and X mode). The direction of arrival for the O mode is : Azimuth of 67 and elevation of 20 and for the X mode is : Azimuth of 67 and elevation of 60.

4.5. Direction finding simulation

From previous simulated signals, angles of arrival can be obtained using the Music algorithm in the configuration described in 2.3. The figure 10 gives a representation of the sorted eigenvalues, the two incoming modes corresponding to the eigenvalues of greatest amplitude are brought to light. Pseudo-spectra for the modes O and X are shown on figures 11 for the O mode and for the Xmode. The directions of arrival are those fixed in generated signals.

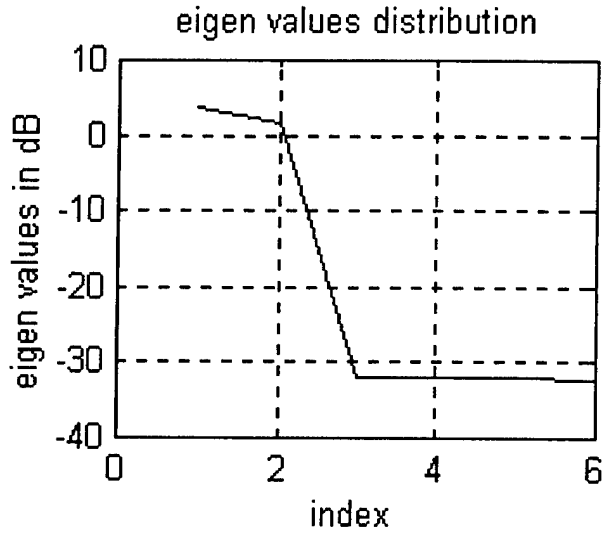

Figure 10 : eigen values distribution : two AOA are determined

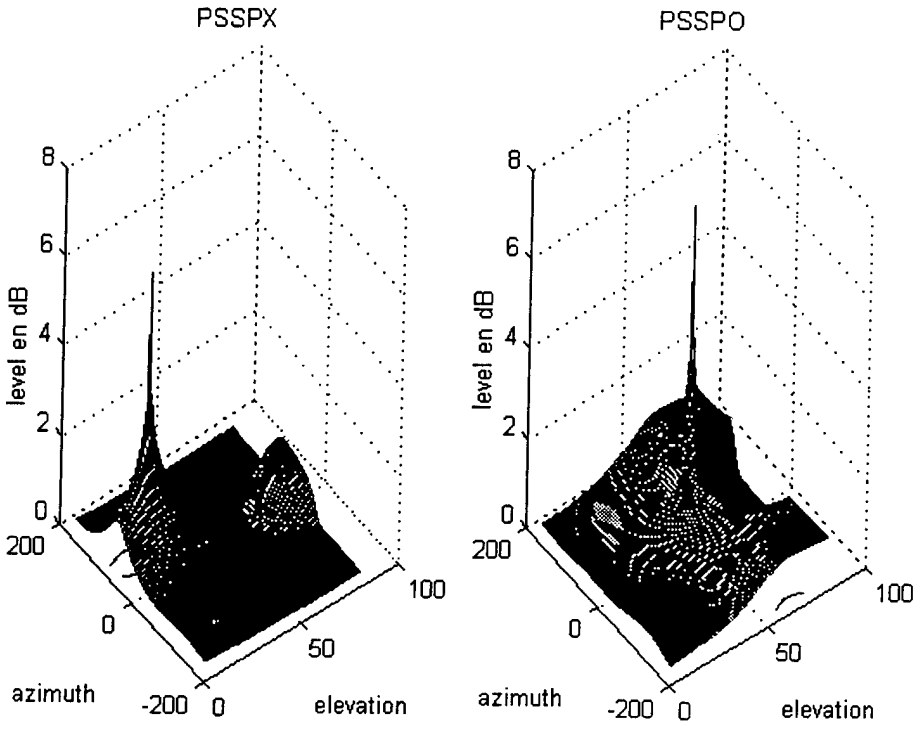

Figure 11 : pseudo spectra for X mode and O mode : the AOA is determined with a good accuracy

5. Experimental results : example

The figure 12 shows an example of the received carrier signals, plotted over 50 seconds on the array of collocated antennas. Each channel is normalized by his maximum value. The frequency carrier is 7,22 MHz. The sampling frequency is 160 Hz.

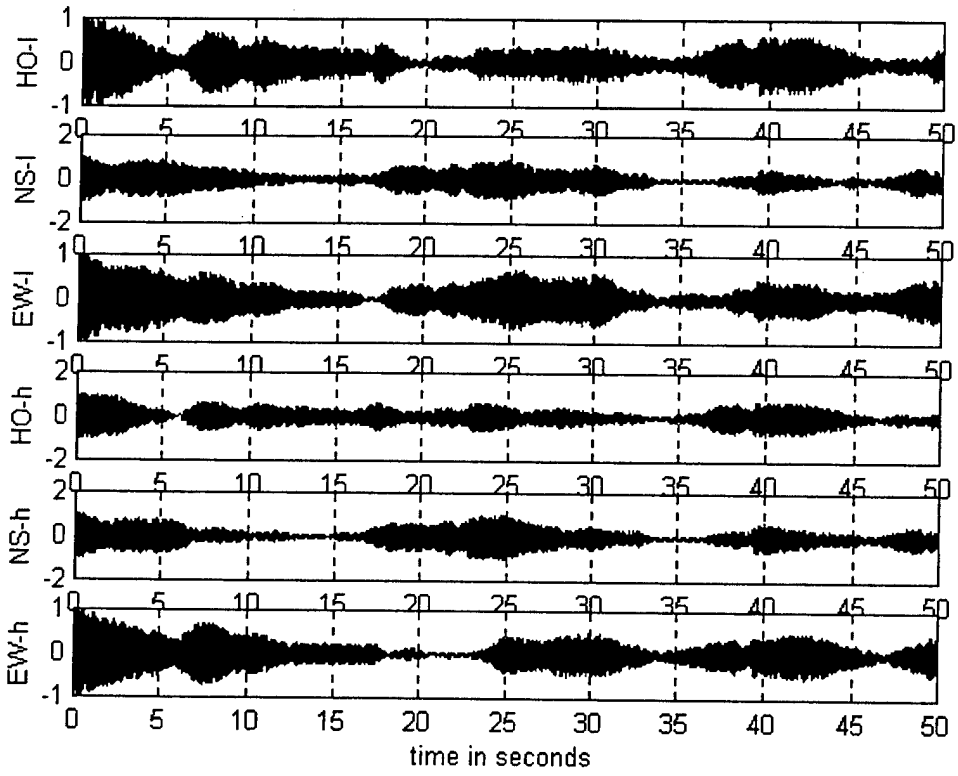

figure 12 : Measured signals on collocated antennas :
HO-l : Horizontal loop at lower height
NS-l : north-south oriented vertical loop at lower height
EW-l : east-west oriented vertical loop at lower height
HO-h : Horizontal loop at higher height
NS-h : north-south oriented vertical loop at higher height
EW-h : east-west oriented vertical loop at higher height

Figure 13 shows that the envelopes of the signals appear to be uncorrelated.

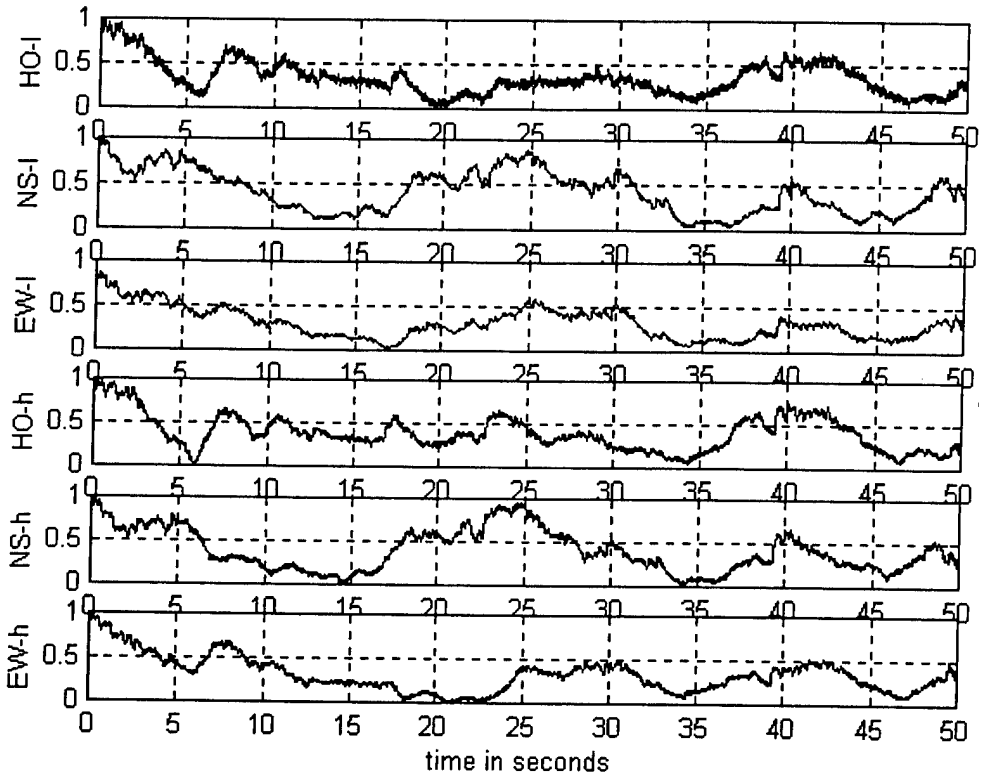

figure 13 : the signals envelopes of the carrier
HO-l : Horizontal loop at lower height
NS-l : north-south oriented vertical loop at lower height
EW-l : east-west oriented vertical loop at lower height
HO-h : Horizontal loop at higher height
NS-h : north-south oriented vertical loop at higher height
EW-h : east-west oriented vertical loop at higher height

Depending on the propagation conditions, fading on each channel do not usually occur at the same time and so, this kind of antenna diversity gives complementary information which can be used in direction finding estimation or in source separation.

Using vertical spatial diversity in addition to collocated antenna brings interesting information because the temporal behavior of same antenna placed at several heights is different.

The correlation matrix for these signals is given below :

	signal 1	signal 2	signal 3	signal 4	signal 5	signal 6
signal 1	1.0000	0.2076	0.5401	0.1895	0.8785	0.8610
signal 2	0.2076	1.0000	0.8548	0.9321	0.3240	0.3790
signal 3	0.5401	0.8548	1.0000	0.7455	0.4895	0.7452
signal 4	0.1895	0.9321	0.7455	1.0000	0.4075	0.2609
signal 5	0.8785	0.3240	0.4895	0.4075	1.0000	0.6263
signal 6	0.8610	0.3790	0.7452	0.2609	0.6263	1.0000

Most channels are relatively well uncorrelated. All signals are under the level 0,95. Generally this value give a guarantee for a good estimation of AOA with Music algorithm.

Received Signals haven't the same strength. The two lower vertical loops receive more power. The horizontal loop placed at 12 meters has the same power than the two upper vertical loops. The power differences are due to the ground effect.

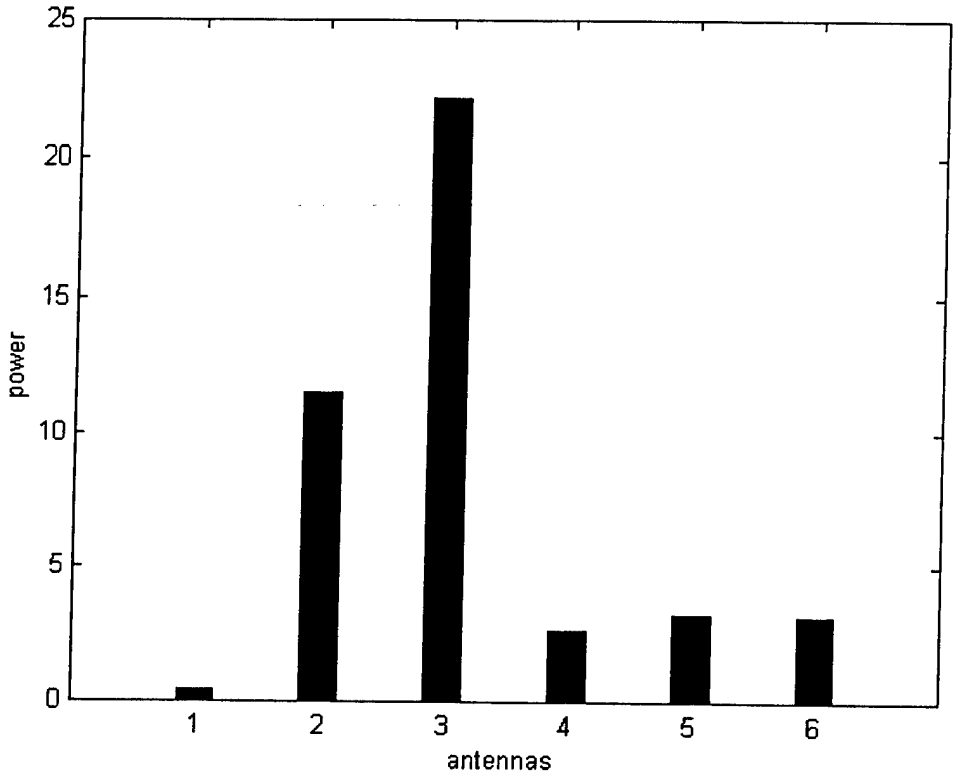

Figure 14 : relative power (power reference is channel 1) received on each antenna
1 : Horizontal loop at lower height
2 : north-south oriented vertical loop at lower height
3 : east-west oriented vertical loop at lower height
4 : Horizontal loop at higher height
5 : north-south oriented vertical loop at higher height
6 : east-west oriented vertical loop at higher height

6. Conclusion

General considerations about space and antenna diversity arrays and their implementation in the MUSIC algorithm have been discussed. Collocated sensors with three antennas of the same type associated with a vertical spatial diversity between the sensors have been presented. A method to determine their relative height has been given. Simulated and experimental results have shown the availability of the technique using uncorrelated signals.

7. Acknowledgements

The authors wish to thank the French Department of Defense for its support regarding the financing of the experimental direction finding systems through the contract n°00-42-553

8. References

[1] : **L. Bertel, F. Marie, D. Lemur**, "Model of narrow HF band ionospheric channel including both propagation and antenna effects". AP 2000- Davos- Suisse – Avril 2000.

[2] : **C. Brousseau, V. Gasse, L. Bertel**, "A new prediction program of radio-circuits in the HF band: LOCAPI" 5th Solar Terrestrial Predictions Workshop'96 – Hitachi, Japan – January 1996.

[3] : **Y. Erhel, L. Bertel, F. Marie**, "A method of direction finding operating on an array of collocated antennas", IEEE,APS/URSI/International symposium, Atlanta, 21-26 June 1998.

[4] : **R.T. Compton,** " The tripole antenna : an adaptative array with full polarization flexibility ", IEEE Transaction on Antennas and Propagation Vol. AP-29 N°6, nov 1981.

[5] : **R. Earl Ferrara, JR. Terry, M. Parks**, "Direction finding with an array of antennas having diverse polarization", IEEE Transactions on Antennas and Propagation Vol. AP-31 N°2, March 1983.

[6] : **M. Flam, J.F. Bull, R. Burgess,** "Adaptative array for frequency hopping HF communications", ICAP 87/IEEE, conf. Pub N°244,1987

[7] : **J. Bull, L. Burgess**, " A compact antenna array for direction finding in the HF band", proceedings of tactical communications conference, Fort Wayne, Indiana, Vol 1, p. 24-26 April 1990.

[8] : **D.H. Brandwood, J.A. Cornforth,** "HF polarization sensor with digital processing", Roke Manor Research Ltd., England, 10th International Conference on Antennas and Propagation, Edinburgh, 14-17 April 1997, Conference Publication N° 436 IEE 1997.

[9] : **F. Marie**, "conception, réalisation et test d'un capteur constitué d'antennes colocalisées en HF" thesis of University, 27 January 1999.

[10] : **J.D. Krauss**, "ANTENNAS", Mc Graw-Hill book Company, p.155 ,1950.

[11] : **K. Davies**, "Ionospheric Radio Propagation", US Departement of Commerce, p 63, 1965

[12] : **K.G. Budden**, "Ionospheric Radio Waves", Chap. 12, 13, 15, Cambridge University Press, 1985.

[13] : **L.Bertel, C. Brousseau and V. baltazart**, " Real time reactualizing of the ionospheric electron density profile", Onde électrique, mai-juin 1992 vol.72

ANTENNA DIVERSITY AS A MEANS OF IMPROVING HF TRANSMISSIONS

Alexis Bisiaux, Louis Bertel
Laboratoire ART, University of Rennes 1
Bat. 11C, Campus de Beaulieu
35042 Rennes, France

Abstract : many studies on communications systems include antenna arrays. Their ability to modify their radiation pattern makes them particularly adequate when source separation or interference cancellation are needed, but they usually do not take into account the polarization of the waves that they receive. This paper describes an unusual kind of array based on antenna diversity instead of space diversity that uses polarization to improve spatial filtering. The concept is illustrated by experimental results obtained in the HF band (3-30 MHz).

Introduction

HF waves extend from 3 to 30 MHz. By reflection against layers of the ionosphere, they allow to realize very long distance transmissions. On the other hand, they encounter severe propagation conditions in this multipath fading channel. Those restrictions have put a brake on the increase of HF digital communications throughputs for a long time. Among the methods put forth to combat them, one consists in using antenna arrays. They are of quite frequent use in diverse types of applications, but most of the time they are tackled from a scalar point of view : arrays are attributed a gain that varies as a function of the direction of arrival (DOA) of the received wave but that does not depend on its vectorial properties. Thus polarization is completely left aside, yet it bears some information about the electromagnetic field that could be exploited. Previous works led on this basis have shown that packets of errors appear at different moments depending on the polarization favored by the receiving antenna [1]. This paper reaches another step, as it shows how an array of particular design, made of collocated antennas and resorting to antenna diversity instead of common space diversity, can be used to include a polarization treatment in addition to the space-filtering process usually associated to classic arrays.

In order to introduce the array of collocated antennas and to bring its advantages to light, it is necessary to start with a short description of ionospheric propagation. The signal distortions caused by this fading multipath channel and the way that they affect digital transmissions are presented in a first place. Then some means involving different kinds of arrays are proposed to cope with them, and it is shown that antenna diversity can be a good solution. This idea is developed more precisely in a third part where the vectorial nature of the electromagnetic field is closely linked to the antennas' responses. Finally, experimental results are provided to illustrate the theory by a practical example.

1. Propagation of the HF waves in the ionosphere

1.1 Multipath and multimode

Two main phenomena must be considered about ionospheric propagation. The first one is that waves can follow several distinct paths by reflecting themselves against different layers of the ionosphere. Then the transmitted signal gives birth to as many replicas, that are affected in different ways by the channel : their differential time delays can be large, and their Doppler shifts, as well as their angles of arrival, can be spaced out too. The second phenomenon appears because of Earth's magnetic field that makes the medium anisotropic. Within each path, the wave splits into two complementary propagation modes called O (ordinary) and X (extraordinary). Both are very close and therefore have similar time delays, Doppler shifts and DOA's. On the other hand, their polarization properties are very different. In the plane orthogonal to the direction of propagation, their

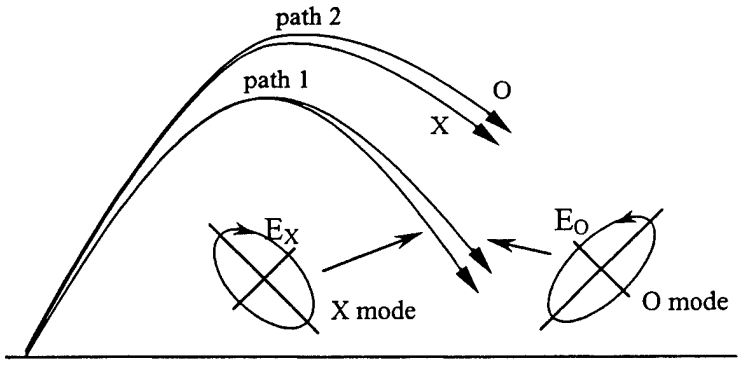

Figure 1 : multipath and multimode propagation in the ionosphere

electromagnetic fields describe orthogonal ellipses in opposite directions [2]. Multipath and multimode propagation are illustrated on Figure 1.

1.2 Effects on transmission

All the transmitted signal's replicas created by multipath and multimode propagation interfere, which degrades the transmission quality. Again, two cases can be distinguished that do not have the same consequences, although they are of same nature. If two signals are delayed by a time smaller than 1/B (where B is their bandwidth), they interfere in a way that the resultant signal fades, making the signal to noise ratio (SNR) vary in time (an example in given on Figure 2). In the opposite case, the SNR remains constant but frequency selectivity occurs.

Fading is due to multimode propagation. Only the O and X modes of a same path can be close enough to cause it. It is the most important problem for transmitting data since the signal is susceptible to completely disappear for a while. Concerning frequency selectivity, it is caused by modes coming from distinct paths. When several modes are present, both phenomena may be observed. The time-frequency analysis of the signal displayed on Figure 2 is reproduced on Figure 3. It represents the mapping of its power in the time-frequency plane, and is obtained directly through the observation of the broadband modulated signal [3]. Two sets of interference patterns are clearly visible, generating both fading and frequency selectivity. They denote the presence of at least 3 modes, among which 2 come from the same path (the line spectrum that appears every 4

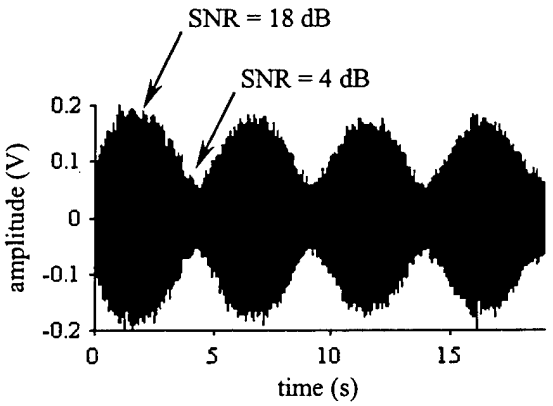

Figure 2 : example of a fading signal (16-QAM, 3 kHz bandwidth, carrier frequency of 8 MHz)

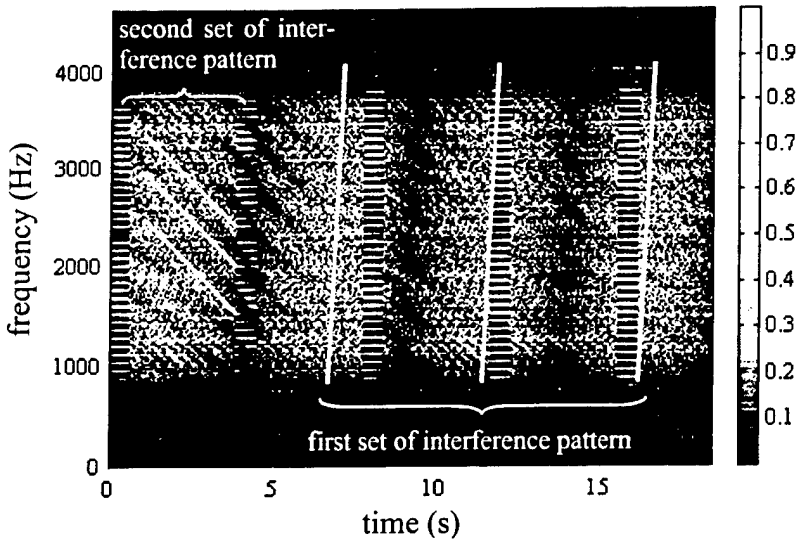

Figure 3 : time-frequency analysis of an HF signal set onto an intermediate frequency of 2250 Hz (same signal as in Figure 2)

seconds is not a computation aberration, it is due to a periodic pattern inserted into the transmitted signal).

Frequency selectivity can be compensated by using adequate equalization techniques. On the other hand, there is nothing to do against fading, except interleaving and coding the data in order to diminish the number of errors caused by the loss of SNR [4]. For these reasons, HF communications links have low throughputs (typically 2.4 kbps in 3 kHz bandwidth) and a bit error ratio (BER) of 10^{-3} is considered to be an acceptable value. Those poor performances show how hard multipath and multimode propagation is on single-antenna receiving systems.

2. How arrays can improve HF transmissions

2.1 Classic arrays

Most of the time, arrays are made of identical elements set distant from one another (they are homogeneous arrays). Space diversity allows them to steer their main lobe toward the DOA of a desired signal, or to create notches in the

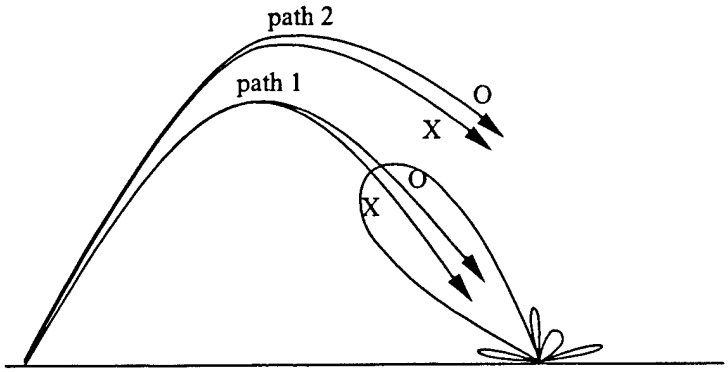

Figure 4 : source separation with a classic array

direction of unwanted ones. Such arrays would not be a very good solution for HF communications applications though. The reason for that is illustrated on Figure 4 : they would be efficient to combat multipath effects, but would not be able to separate the complementary modes of a single path because they usually leave the ionosphere at very close angles. The spatially filtered signal would then still be affected by fading. Furthermore, given that the wavelength ranges from 10 to 100 meters, such arrays would spread over a large area, making them rather unpractical. For these reasons, homogeneous arrays are rarely used for transmission purposes in the HF band. Yet it is possible to suppress fading by separating the O and X modes, but it requires to include some kind of polarization treatment in the whole process, which is not possible with homogeneous arrays.

2.2 Polarization filtering

The easiest way of introducing polarization is to use two orthogonal sensors, like crossed loops or crossed dipoles for example. This approach is quite common in HF and has been used before in industrial systems. It is based on the assumption that the two complementary modes, bearing the signals s_O and s_X, have circular polarization patterns and have almost vertical DOA's. Under these conditions, s_O and s_X can be separated by combining the received signals x_1 and x_2 in the following way :

$$s_O(t) \approx x_1(t) + j x_2(t) \quad \text{and} \quad s_X(t) \approx x_1(t) - j x_2(t) \tag{1}$$

This technique is attractive because it is easy to implement, however it is limited by a number of factors. First of all, it is based on assumptions that are not always met in reality. Indeed, HF waves may have oblique DOA's and be elliptically polarized, in which cases they do not project themselves onto the crossed antennas in the ideal way ; the two modes cannot be completely separated then. Secondly, it can work if only two complementary modes are received, but it is inefficient in a multipath environment. Therefore the method is suboptimal.

2.3 Heterogeneous arrays

With antenna diversity, it is possible to join the ability of an array to alter its radiation pattern on the one hand, and polarization filtering on the other hand. This leads to the realization of a heterogeneous array, that is, made of antennas with various shapes or orientations, as opposed to classic homogeneous arrays. Its application to HF transmissions can be illustrated in a simplified way by the drawing on Figure 5 : the radiation pattern of the array is not the same for all the waves because it depends on their polarization. Since O and X modes coming out of the ionosphere have different polarization properties, two different radiation patterns must be considered instead of one, as is usually the case. One regards O modes, and is completely unrelated to the other one that concerns X modes. For this reason it is theoretically possible to separate two complementary modes, even if they come from the same direction, and still being able to create notches in the two radiation patterns. Such a principle is ideal for combating both multipath and multimode propagation. It is however an uncommon approach that should therefore be described in more details, and that the next part is dedicated to.

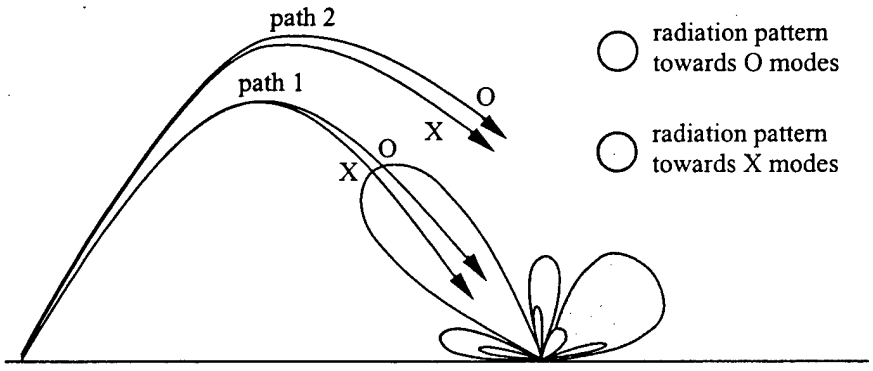

Figure 5 : source separation with a heterogeneous array

3. Antenna diversity

An antenna's response to an incoming wave depends on two main global factors : The first one is the vectorial configuration of the local electromagnetic field ; the second one is the shape of the sensor. Both are described in the following paragraphs in order to introduce the originality of the collocated-antenna array.

3.1 Electromagnetic field in the vicinity of an antenna

In general, the electric field **E** (as well as the magnetic field) describes an ellipse in the polarization plane, as shown on Figure 6. This pattern can be characterized by two parameters : the polarization ratio η and the tilt angle α. The direction of rotation (clockwise or counterclockwise) is determined by the sign of η. The three components of the field as received by a given antenna thus depend on these two parameters. They also depend on the wave's direction of arrival, as shown on Figure 7. Two other parameters intervene : the angles of arrival ϕ (azimuth) and θ (elevation). In the axes of the fixed antenna (X,Y,Z), the expression of **E** is a function of these 4 parameters :

$$\mathbf{E}_{|X,Y,Z} = f(\phi,\theta,\eta,\alpha) \tag{2}$$

This equation is displayed to insist on the fact that the local field depends on both the DOA and the polarization of the incoming wave. The purpose here is not to calculate the function *f*, which has been done elsewhere, including ground effect [5].

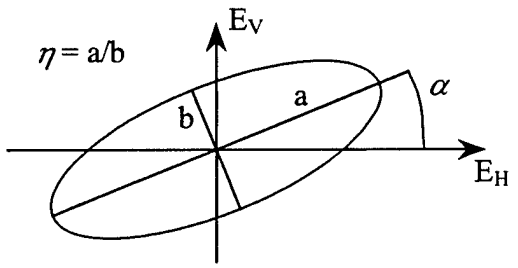

Figure 6 : ellipse in the polarization plane

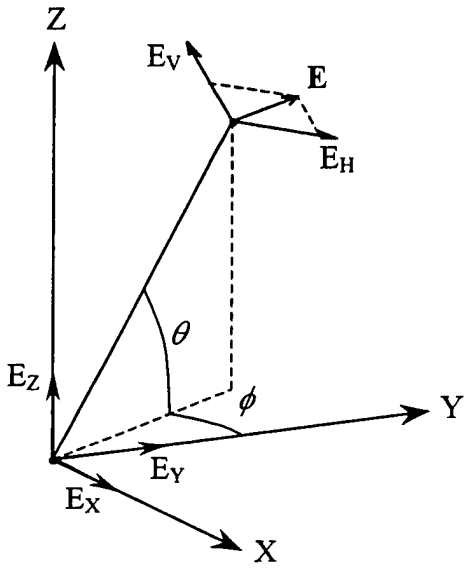

Figure 7 : electric field projected onto an antenna's axes

3.2 Antenna response

Given an antenna i, a wave bearing a signal $s(t)$ and characterized by the 4 parameters of its electric field (ϕ, θ, η and α) is transformed by the antenna into a signal $s_i(t)$ according to the following equation :

$$s_i(t) = F_i(\phi,\theta,\eta,\alpha) \times s(t) \tag{3}$$

where F_i is the antenna's response to the field. It is a complex function, reflecting the fact that the sensor influences the signal's amplitude as well as its phase. Moreover, F_i is closely linked to its shape and orientation in space, so that the responses of unlike antennas are different, which is the fundamental principle of antenna diversity.

F_i is complex-valued and depends on 4 parameters, hence it is uneasy to represent it. This problem can be simplified however in the case of HF applications. According to the limit conditions of Budden [2], a wave coming from a given

direction can only have two polarization patterns, one for each mode. Theoretical models allow to determine 2 values of η and α given a set of angles of arrival ϕ and θ. The antenna response F_i with 4 degrees of liberty is then reduced to 2 functions with 2 degrees of liberty, $F_{iO}(\phi,\theta)$ and $F_{iX}(\phi,\theta)$. They represent the antenna's response towards O and X modes and only depend on their DOA's.

Such functions are represented on Figures 8 and 9 for a vertical square loop (contained in the East-West vertical plane) and a horizontal square loop respectively. The radiation patterns reflect their modulus, but their phase is displayed too since it plays an important role in completing diversity. Three interpretations can be drawn from these diagrams :

- For a given antenna and a given mode type, the response varies as a function of the direction of arrival, not only in amplitude but also in phase, whereas the usual approach focuses on the former only (radiation pattern).

- For a given antenna and a given DOA, the response towards a wave is different whether it is of O or X type.

- For a given DOA and a given mode type, the response of an antenna depends on its shape and orientation.

These remarks show that antenna diversity by itself is enough to discriminate waves regarding to their DOA and polarization. Of course, it is still possible to add space diversity to the system in order to improve its efficiency. This concept is presented in another article in these proceedings with an application to direction finding [6]. But since antenna diversity is sufficient for an array to discriminate incoming waves in DOA and polarization, space diversity can be completely suppressed, which makes it possible to use an array of collocated antennas.

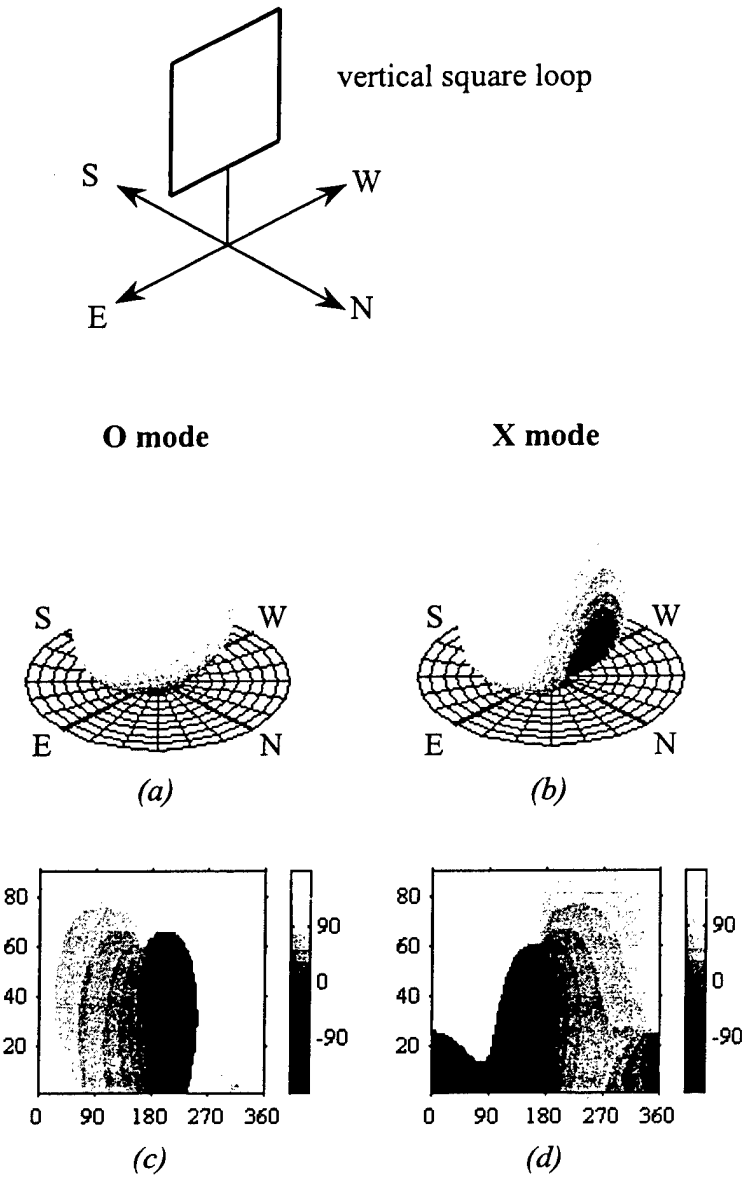

Figure 8 : complex response of a vertical loop antenna towards O modes (*(a)* and *(c)*) and X modes (*(b)* and *(d)*) ; modulus (*(a)* and *(b)*) and phase in degrees versus azimuth (from 0 to 360°) and elevation (from 0 to 90°) (*(c)* and *(d)*)

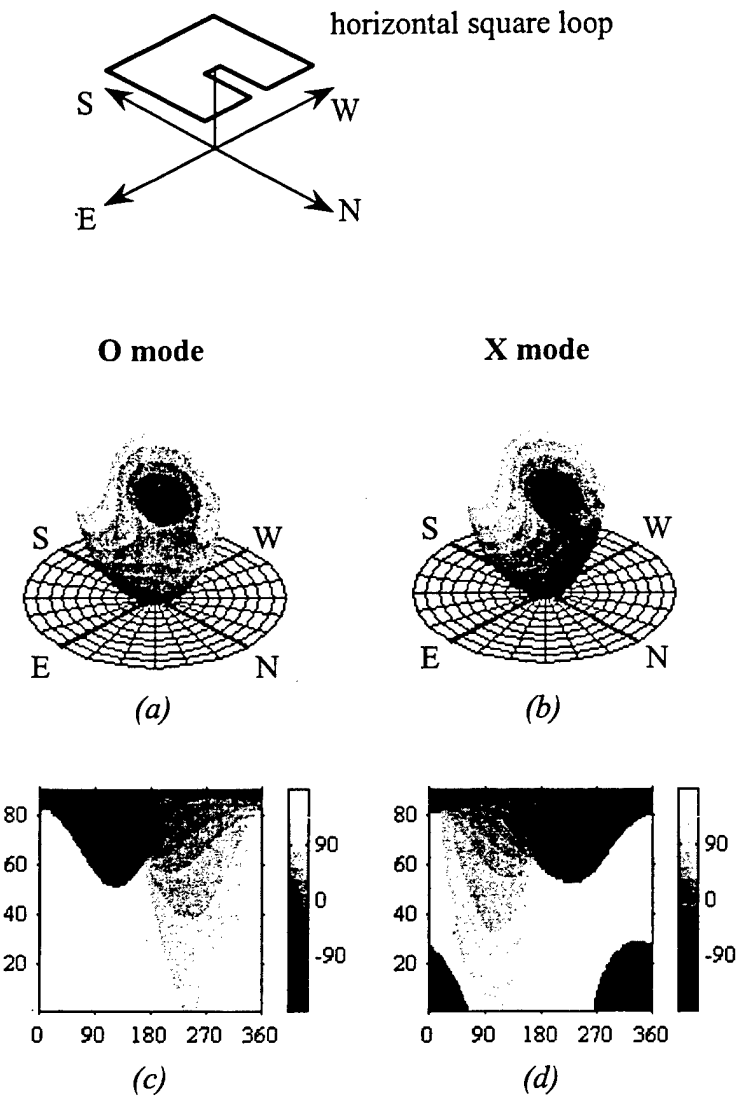

Figure 9 : complex response of a horizontal loop antenna towards O modes (*(a)* and *(c)*) and X modes (*(b)* and *(d)*) ; modulus (*(a)* and *(b)*) and phase in degrees versus azimuth (from 0 to 360°) and elevation (from 0 to 90°) (*(c)* and *(d)*)

3.3 Array of collocated antennas

An array of M elements receives N waves bearing the signals $s_i(t)$ $(1 \le i \le N)$. According to [7], the signal $x_i(t)$ observed at the output of antenna i is a combination of the signals $s_i(t)$ weighted by the complex responses of the antenna, whose value depends on their DOA's and mode types :

$$x_i(t) = \sum_{k=1}^{N} F_{ik}(\phi_k, \theta_k) s_k(t) + n_i(t) \qquad 1 \le i \le M \tag{4}$$

where $n_i(t)$ is an additive noise. F_{ik} is the response of antenna i towards signal k, characterized by its angles of arrival ϕ_k and θ_k and its mode type. The steering vector $\mathbf{a}_k$ of the array for the incoming wave k is given by :

$$\mathbf{a}_k = \left[F_{1k}(\phi_k, \theta_k) \quad \cdots \quad F_{Mk}(\phi_k, \theta_k) \right]^T \tag{5}$$

The M antennas yield a vectorial signal with M components that can be written as :

$$\mathbf{X}(t) = \mathbf{A}\mathbf{S}(t) + \mathbf{N}(t) \tag{6}$$

with :

$$\mathbf{A} = \left[\mathbf{a}_1 \quad \cdots \quad \mathbf{a}_N \right], \tag{7}$$

$$\mathbf{S}(t) = \left[s_1(t) \quad \cdots \quad s_N(t) \right]^T, \tag{8}$$

$$\mathbf{N}(t) = \left[n_1(t) \quad \cdots \quad n_M(t) \right]^T. \tag{9}$$

Equation (6) is commonly encountered in array applications. The difference with classic arrays, though, holds in the steering-vector matrix **A**. Indeed, since space diversity has disappeared, there are no phase terms due to propagation delay from one sensor to another. It must also be reminded that for a given set of angles of arrival, two distinct steering vectors exist (one for each mode type) instead of just one.

The experimental system is made of 8 collocated antennas as shown on Figure 10. As compared to classic arrays, it has two advantages : it is sensitive to polarization and it is not larger than a single aerial. Both are particularly interesting features for HF applications : a classic array would spread over a large area (the wavelength ranges from 10 to 100 meters), which is not very practical, and it would not be able to separate complementary modes anyway without some polarization treatment.

Source separation based on this array of collocated antennas has been presented before [8]. According to the least-mean-square criterion, the incoming signals can be separated by the use of a spatial filter :

$$\hat{\mathbf{S}}(t)=(\mathbf{A}^H\mathbf{A})^{-1}\mathbf{A}^H\mathbf{X}(t) \qquad (10)$$

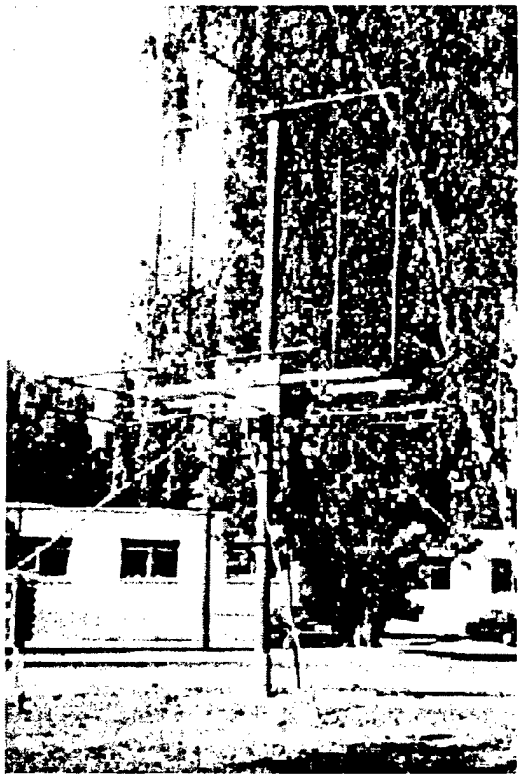

Figure 10 : experimental array of 8 active collocated antennas

Although the experimental results presented in the fourth part of this article were not obtained with this formula, it is still useful to calculate the radiation pattern of the array, in the aim of illustrating the behavior of heterogeneous arrays in general, and of collocated arrays in particular. The diagrams on Figure 11 have been obtained by simulation after having considered 3 incoming signals with the following properties :

- a first O mode to be kept (azimuth : 230°, elevation : 40°),
- one X mode to be suppressed (azimuth : 230°, elevation : 40°),
- a second O mode to be suppressed (azimuth : 80°, elevation : 60°).

There are actually two different radiation patterns, just as there were two different kinds of antenna responses, depending on the mode type of the received wave. Figure 11 *(a)* shows that the main beam of the array has been steered toward the desired signal whereas a notch has been created in the direction of the unwanted one. Yet the most interesting part is given by Figure 11 *(b)* : the X mode is completely suppressed, even though it comes from the same direction as the first O mode. This ability to separate waves with identical DOA's is specific to antenna-diversity arrays, as it had been suggested in paragraph 2.3 and in Figure 5. Also, it should be added that only two radiation patterns exist because only two polarization configurations are possible with HF waves. The principle would still be valid in a more general case, but it would then be necessary to consider an infinity of radiation patterns, which is more difficult to represent.

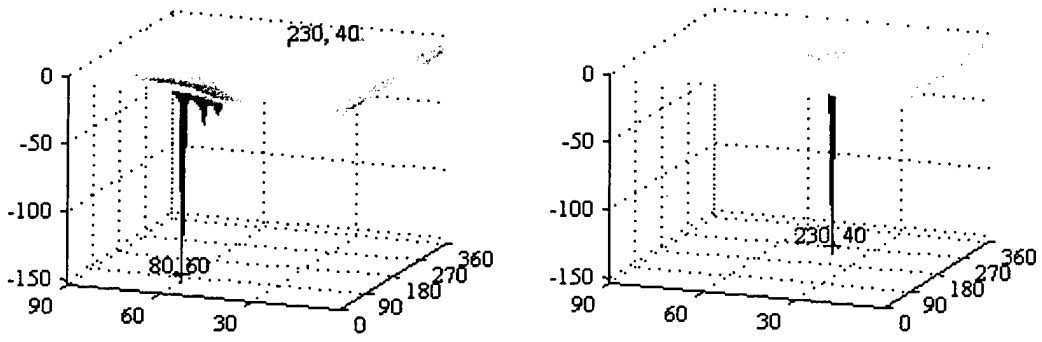

(a) *(b)*

Figure 11 : radiation pattern (gain in dB) of the array towards O modes *(a)* and X modes *(b)*, versus azimuth (from 0 to 360°) and elevation (from 0 to 90°)

4. Experimental results

4.1 Characteristics of the received signals

The results presented in this section are based on an example that reflects the behavior of the system in the majority of cases. Only 4 antennas were used out of the 8 available ones because the 4 others proved to be unnecessary : they did not help to improve the transmission performances and required more computational time. The 4 elements of the array, as pictured on Figure 12, are :

- a vertical square loop contained in the East-West plane,
- a vertical square loop contained in the North-South plane,
- a horizontal square loop,
- an XYZ dipole.

The transmitted signal has the following properties :

- 16-QAM modulation with rolloff factor of 0.2,
- 3 kHz bandwidth,
- 10 kbps (2500 baud),
- carrier frequency of 8 MHz.

The transmission is realized over a unidirectional link of 250 km in France. The transmitter stands in Poitiers (lat : 46°35' N, long : 0°25' E), the receiver is in

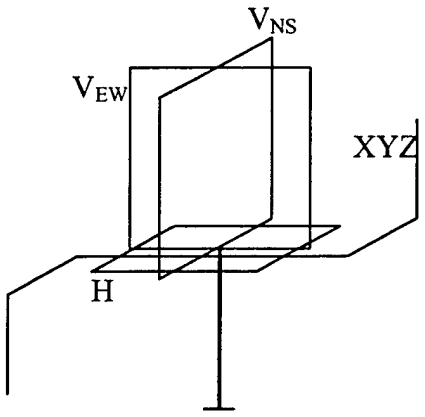

Figure 12 : view of the array actually used (4 collocated antennas)

Monterfil (lat : 48°03' N, long : 2°00' O). The 4 signals are transposed independently onto an intermediate frequency (IF) of 30 kHz and filtered with a 12 kHz bandpass filter. They are then sampled at 9250 Hz (thus shifting the IF to 2250 Hz) and saved into a file that can contain a 20-second acquisition.

The 4 received signals are plotted on Figure 13. They are all affected by fading, which denotes that propagation is mainly provided by 2 complementary modes of a principal path. In such a case, these modes come from very close directions, however the array's antenna diversity is enough to introduce a significant difference between the 4 observations. This remark is reinforced by the time-frequency representations of the first two signals (Figures 14 and 15). Two interference patterns appear (as in Figure 3) ; in addition to fading (the most visible one), some frequency selectivity shows that a second path also exists. But for these two interference patterns, the signal fades at different instants and frequencies from one antenna to the other, which shows that diversity is indeed reached.

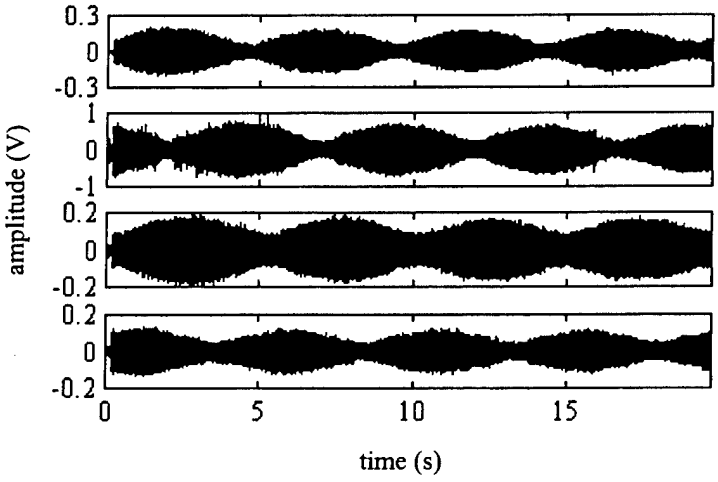

Figure 13 : signals received by the array (V_{EW}, V_{NS}, H, XYZ)

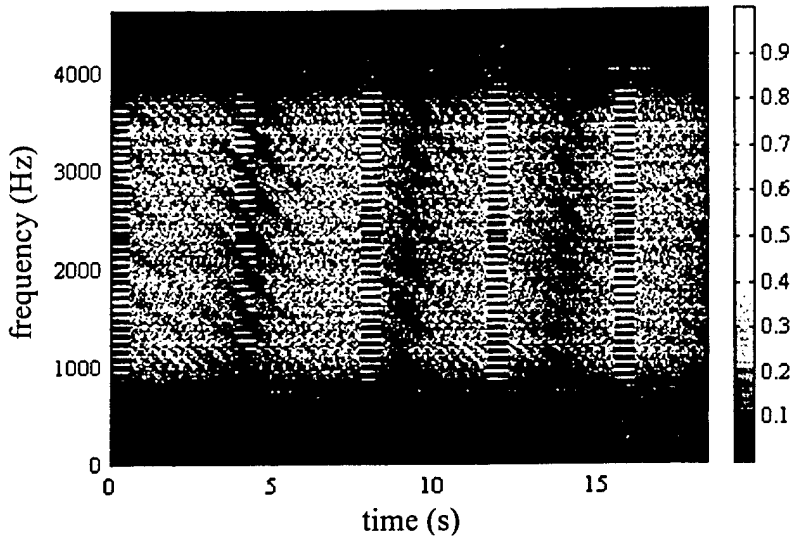

Figure 14 : time-frequency analysis of the first signal (received by V_{EW}) with IF of 2250 Hz

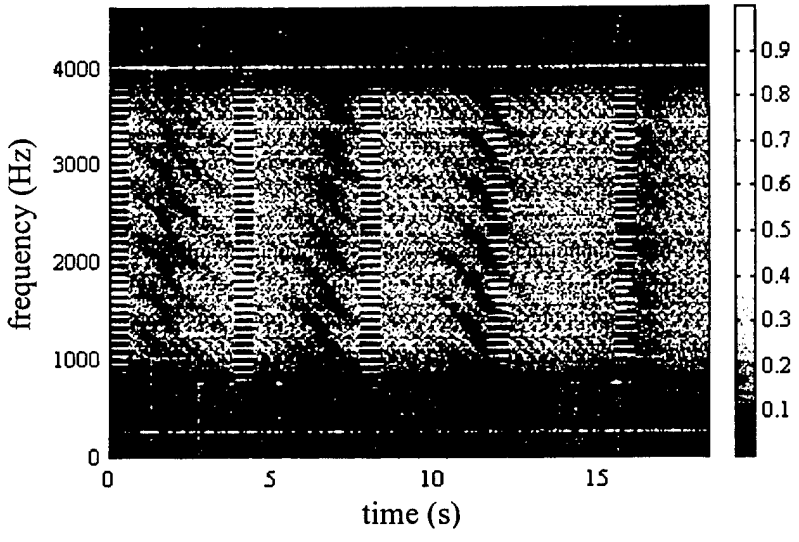

Figure 15 : time-frequency analysis of the second signal (received by V_{NS}) with IF of 2250 Hz

4.2 Description of the processing method

The method used to process the signals delivered by the array includes both space-polarization filtering (by combination of the received signals) and time treatment, as shown on Figure 16. A whole 6-tap transverse equalizer is included in each branch ; T is the symbol duration. The weights $w_{i,j}$ (where i denotes the antenna and j the delay) are determined through an adaptive method based on the LMS algorithm [9].

The deep fading experienced by the signals on each branch makes the method inefficient if only one antenna is used, therefore no results are provided for such a case. Considering the weakness of the available SNR, it would require more sophisticated processes in order the achieve a reliable transmission with a single-sensor modem, like coding, interleaving and soft decision techniques, which are not necessary when antenna diversity is used, as the results will show.

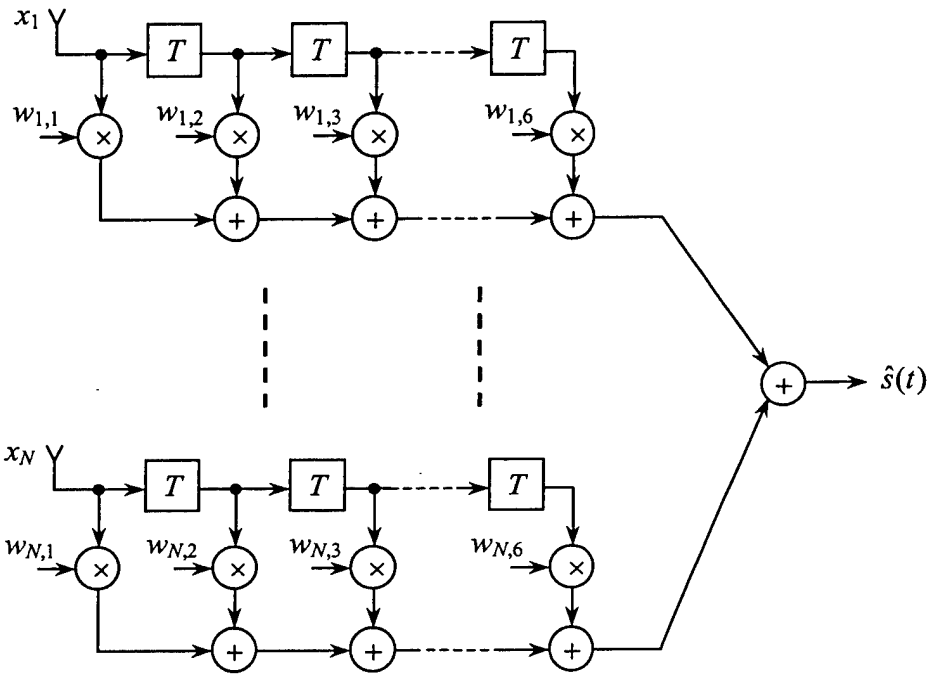

Figure 16 : diagram of the adaptive space-time filter

4.3 Results with a simple polarization filter

The receiving module of Figure 16 is fed with a single signal derived from the combination of the first two observations (as described in §2.2) : $V_{EW} - j\,V_{NS}$ and $V_{EW} + j\,V_{NS}$. Time treatment is still applied. Since the powers received by the first two antennas are quite different (11 dB between V_{NS} and V_{EW}, as can be seen on Figure 13 ; this may be due to an imbalance in the electronic system and/or to the polarization conditions), the first signal had to be multiplied by a factor of 3.65 in order to readjust their levels and make the polarization filter work correctly.

The two filtered signals are then demodulated and the results are plotted on Figures 17 and 18, in terms of BER (Bit Error Ratio), which is the more convenient way to assess the efficiency of the method in a system dedicated to transmissions.

The filtered signals are still affected by fading which has in turn repercussions on the BER. Although it seems acceptable on Figure 17 with an average of 1.6×10^{-2} over the whole transmission, the pattern on Figure 18 (with an average of 5.3×10^{-2}) tends to prove that the filter's efficiency is far from ideal. Furthermore, the polarization filter is here employed under the best conditions, since waves coming from Poitiers and received at Monterfil are supposed to have a circular polarization, as shown by the graphic on Figure 19. Hence, the results would be even worse on a link with less favorable conditions.

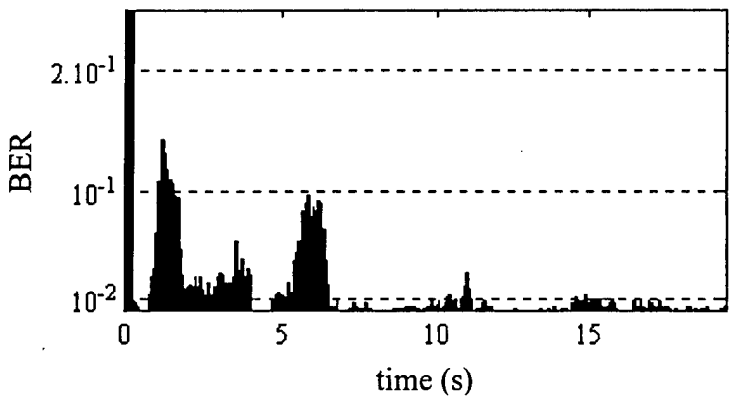

Figure 17 : BER with a simple polarization filter ($V_{EW} - j\,V_{NS}$)

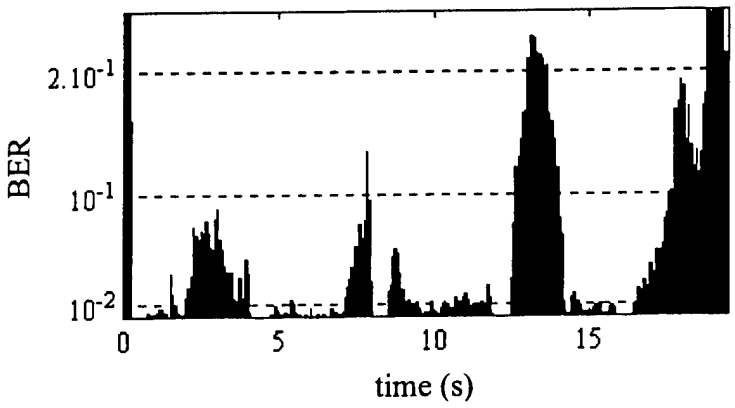

Figure 18 : BER with a simple polarization filter ($V_{EW} + j\,V_{NS}$)

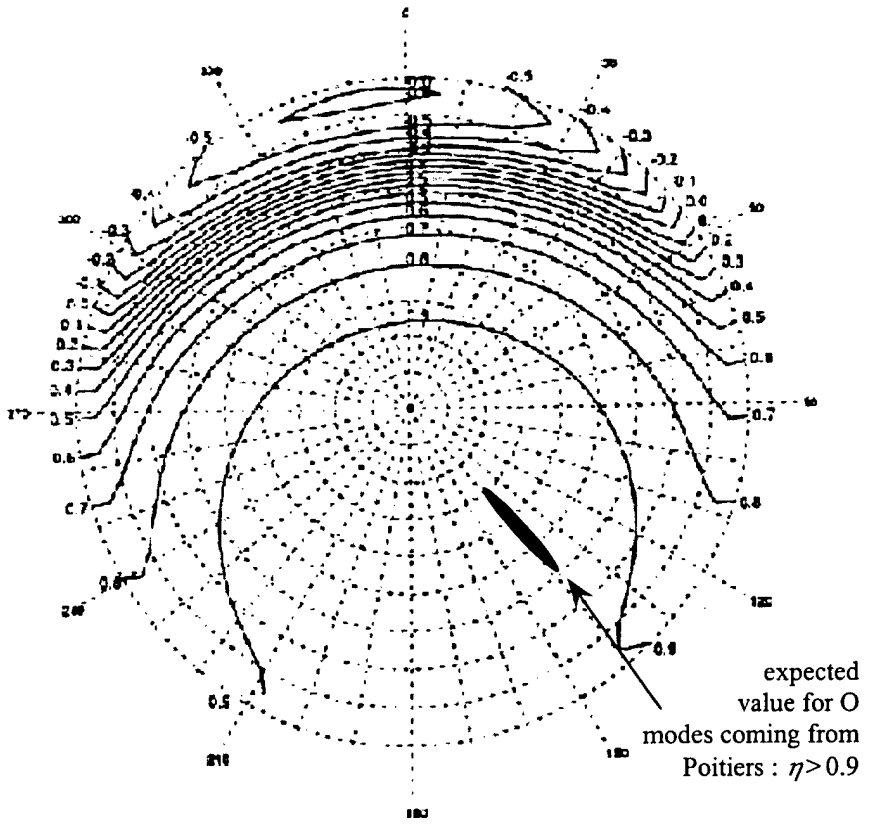

Figure 19 : expected value of η (polarization ratio) for O modes in Brittany (receiving area) according to [10] ; azimuth from 0 to 360°, elevation in concentric circles from 0° (exterior) to 90° (center)

4.4 Results obtained with the 4 antennas and the adaptive filter

The adaptive method based on the LMS algorithm has been applied successively to 2, 3 and 4 antennas in order to evaluate the influence of the array's size.

- 2 antennas (Figure 20) : the propagation conditions are too constraining during the first seconds of the transmission, and the algorithm is unable to keep track. However, it starts to converge again after 6 seconds and then the BER remains below 10^{-2} independently of the fading. The average BER in this case is 2×10^{-2}, not much higher than in the best case with a simple polarization filter. Obviously, two antennas are not enough to realize a reliable filter.

- 3 antennas (Figure 21) : this time the algorithm converges immediately and the BER always remains below 3×10^{-2} with a mean value of 3.7×10^{-3}.

- 4 antennas (Figure 22) : since the previous case led to very good results, the fourth antenna does not bring as much change as the third one, but still the BER is improved with an average of 2.8×10^{-3}.

The SNR obtained in the latter case (after adaptive filtering) is reproduced on Figure 23, along with the raw SNR received on the first antenna (the same pattern can be observed on the 3 others with fading occurring at different times). This figure shows the advantage of antenna diversity : whatever the method employed to demodulate the signal, the quality of the transmission can only be improved when the SNR remains almost constant and is not subject to deep fading.

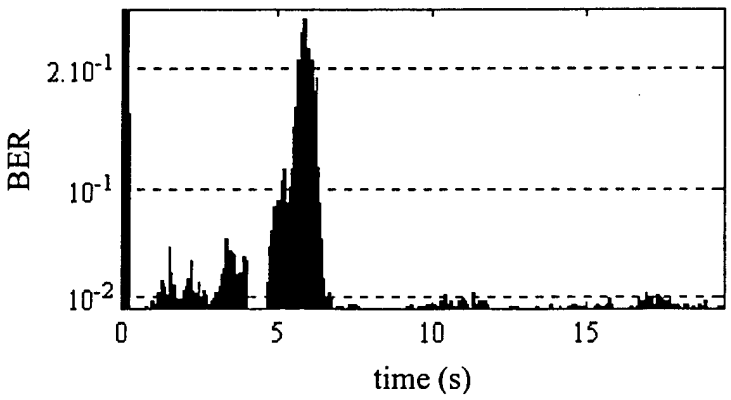

Figure 20 : BER obtained with the first 2 antennas

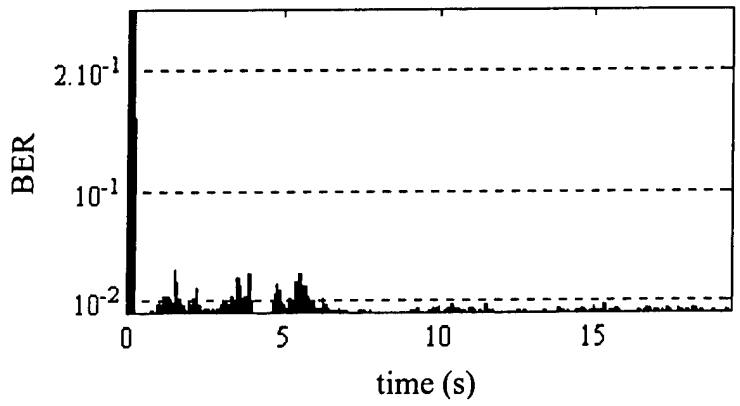

Figure 21 : BER obtained with the first 3 antennas

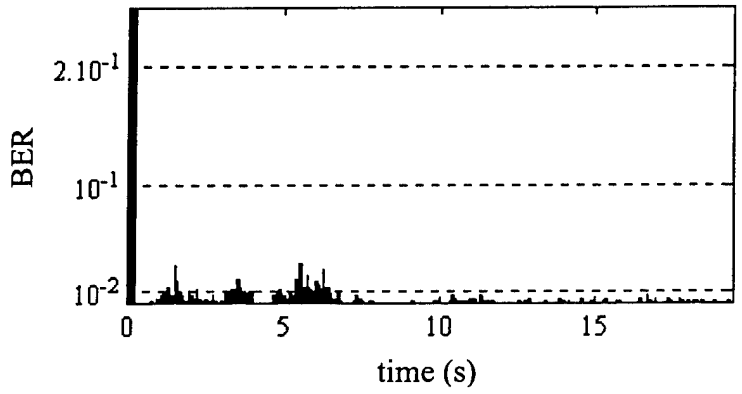

Figure 22 : BER obtained with the 4 antennas

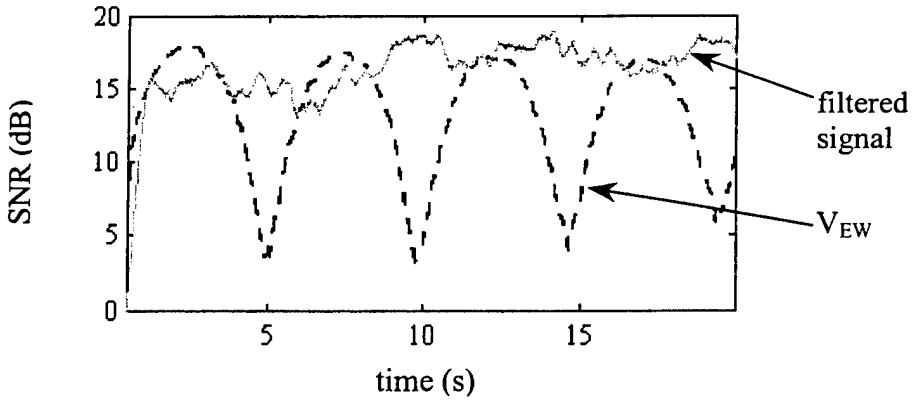

Figure 23 : comparison of SNR on antenna V_{EW} and after filtering

Conclusion

This article was meant to bring in light all the benefits that can be taken from the introduction of antenna diversity in a system devoted to digital communications. The various shapes of the array antennas make them react differently towards incident waves, depending on their directions of arrival as well as their polarization. This latter aspect is never taken into account by classic homogeneous arrays that only resort to space diversity : they are therefore unable to separate complementary modes coming from very close directions, which occurs frequently though in HF propagation. Another advantage of antenna diversity is the possibility of using a compact array made of collocated antennas, instead of spreading it over a large area as it is done when space diversity is the only solution.

The principle has been illustrated through a practical example based on experimental data. It showed that an array of at least 3 collocated antennas was sufficient to correctly separate 2 modes and make the SNR of the filtered signal almost constant and independent of the fading, whereas a single-antenna modem would have to cope with severe losses of power, while a simple polarization filter (using 2 antennas) would not perform very well, even in a favorable polarization configuration. The results obtained in terms of BER (about 3×10^{-3}) are considered to be acceptable for HF transmission, and the throughput is four times higher than in usual HF modems (10 kbps instead of 2.4 kbps). Moreover, no coding, interleaving nor soft decision techniques were employed to reach these performances. Hence the transmission quality could be a lot better still if some coding were added, with only a few throughput loss.

The application presented in this paper proves that arrays of collocated antennas can be successfully used to improve HF transmissions, but the principle could also be extended to other frequency bands : taking polarization into account increases the diversity range of a receiving system, thus increasing its ability to separate incoming signals and suppress interferences.

Acknowledgement

The authors wish to thank THALES Microelectronics for providing the financing of this project.

References

[1] L. Bertel, O. Lebaillif, Y. Le Roux, R. Fleury, "Influence des antennes et de la propagation sur le comportement d'un système de transmissions numériques en HF", *AGARD conference proceeding*, Athen, Greece, 1995

[2] K. G. Budden, *The magneto-ionic theory and its applications to the ionosphere*, Cambridge University Press, 1985

[3] A. Bisiaux, *Définition, conception et réalisation d'un modem vectoriel large bande utilisable dans la gamme Hautes Fréquences*, PhD thesis, Université de Rennes 1, September 2001

[4] "Characteristics of 1200/2400/3600 bits per second single tone modulators/ demodulators for HF radio links", NATO STANAG 4285

[5] D. Lemur, P. Parion, A. Edjéou, L. Bertel, "Propagation effects on phase and amplitude of HF antenna response", *Ionospheric Effects Symposium*, Alexandria (Virginia), USA, May 1996

[6] G. Le Bouter, L. Bertel, D. Lemur, Y. Erhel, "Vertical diversity in array of collocated HF loop antennas", *25th Antenna Applications Symposium*, Robert Allerton Park (Illinois), USA, September 2001

[7] L. Bertel, F. Marie, D. Lemur, "Model of narrow band H.F. ionospheric channel including both propagation and antenna effects", *AP2000*, Davos, Switzerland, April 2000

[8] C. Le Meins, Y. Erhel, L. Bertel, F. Marie, "Source separation operating on a set of collocated antennas : theory and application in the HF band (3-30 MHz)", *23th Antenna Applications Symposium*, Robert Allerton Park (Illinois), USA, September 1999

[9] B. Widrow, J. M. McCool, "A comparison of adaptive algorithms based on the methods of steepest descent and random search", *IEEE Trans. on Antennas and Propagation*, Vol. AP-24, pp. 615-637, September 1976

[10] L. Bertel, J. Rojas-Varela, D. Cole, P. Gourvez, "Polarisation and ground effects on H.F. receiving antenna patterns", *Annales des Télécommunications*, FRA., Vol. 44, n°7-8, pp 413-427, July-August 1989

GEODESIC SPHERE PHASED ARRAYS FOR LEO SATELLITE COMMUNICATIONS

----- Array Symmetry Issues

Dr. Probir K. Bondyopadhyay
MAHANAD COMMUNICATIONS INC.
14418 Oak Chase Drive
Houston, Texas 77062
E Mail : p.bondy@worldnet.att.net

Technology is both an end in itself and a means to other ends. When you figure something out and make it work, there is pleasure and excitement. Not just because the technology is going to do something, but because you created something with its own inherent beauty, like art, like literature, like music.

--- Andrew S. Grove, Intel.

ABSTRACT

Invention of a new phased array antenna architecture, the Geodesic Sphere Phased Array, is described [1]. Presence of symmetry in these new phased array antenna structures are examined in this paper. A comparison is made between the two antenna element arrangements in the geodesic sphere panels-- one derived from the regular icosahedron and the other derived from the truncated icosahedron. A detailed computation could then be made to quantitatively assess the performance.

1. INTRODUCTION

Structural symmetry plays an important role in the design and operation of phased array antenna systems. This paper deals with the symmetry issues associated with the element arrangements in geodesic sphere phased array antenna

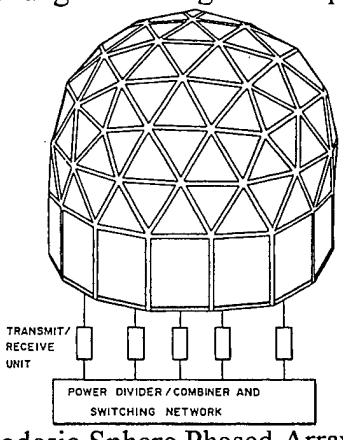

Figure 1: Schematic of a Geodesic Sphere Phased Array Antenna system. Each triangular subarray consists of circularly polarized antenna elements.

system recently invented[1, 2, 3, 4, 5] for communication with Low Earth Orbit (LEO) satellites and for ballistic missile defense applications. An outline of an antenna structure is shown in Figure 1. There are two versions of the array structures that are under consideration. One is based on regular icosahedron (Platonic solid) and the other is based on truncated icosahedron (Archimedean solid). Alternative breakdown scheme employed to construct the geodesic sphere based on the *regular* icosahedron shows that the triangular subarray panels are not all equilateral triangles. This implies that element arrangements in the array are nonuniform but the element positions are fixed according to the geometry of the array structure. The situation is more favorable with the geodesic sphere phased array based on the truncated icosahedron.

2. THE INVENTION IN HISTORICAL PERSPECTIVE

This year 2001 marks the hundredth anniversary of array antennas. Guglielmo Marconi was first to use an array of grounded monopoles arranged in the shape of a triangular fan antenna to transmit the world's first transatlantic wireless signal from Poldhu, Cornwall, England in December 1901.

In the second half of the century gone by, intermittent attention has been focused on arrays on spherical surfaces. Well-known antenna engineer Robert C. Hansen in his recent book of 486 pages, *Phased Array Antennas[6]* devoted *one page* to the subject of spherical arrays with the following introductory remarks:

"A spherical array behaves much like a cylindrical array scanned only in azimuth, but the lattice and depolarization problems are unique to the sphere."

This observation speaks for itself. However, one wonders, what lattice problems ? In relation to phased arrays, have we ever considered lattice structures that are characteristic to the spherical surface ?

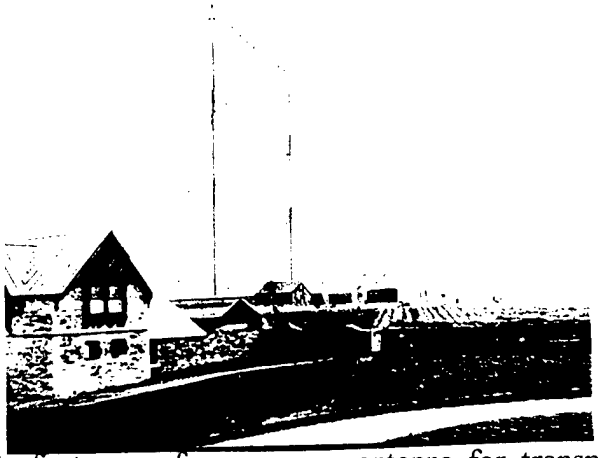

Figure 2 Marconi's first use of an array antenna for transmitting the first transatlantic wireless signal from Poldhu, Cornwall, England in December 1901.

Sixty nine years since Marconi's first use of an array antenna, Schrank in a paper [7] read at the second Phased Array Antenna Symposium in 1970 held at Polytechnic University of Brooklyn, Long Island Center, presented a preliminary performance analysis of spherical arrays where the array was constructed on the *curved* spherical surface by projecting a planar arrangement of elements on each of the twenty faces of a regular icosahedron. Decades later, Collier and Holzheimer in a patent [8] described accommodation of an all hexagonal arrangement on the spherical surface which was a inventive improvement over an all pentagonal arrangement experimented with earlier. Around the same time, Stuart[9] in a patent described an accommodation of all hexagonal planar arrangement on to a dome by making the connecting linear edges flexible. None of these arrangements are characteristic to the spherical surface. The geodesic sphere arrangement is a characteristic arrangement pertaining to the spherical surface.

3. GEODESIC SPHERE PHASED ARRAY APPLICATIONS

One of the advantages of the geodesic sphere phased array antenna architecture is that it is made up entirely of triangular flat *planar* subarray panels and *no curved surfaces or lines are involved.* Thus array construction and assembly are much easier. A geodesic phased array structure is modular and could be easily taken apart by the independent and self-sufficient triangular flat subarray panels and transported. The phased array could then be reassembled anywhere. This is a major advantage. Another advantage is in maintenance. A defective subarray panel could be easily detected, quickly removed and replaced by a new one.

As depicted in the schematic in Figure 3, a geodesic sphere phased array antenna operating in X-band could be the radar sensor of choice in a Ballistic Missile defense scenario. In the commercial arena, the geodesic sphere phased array has worldwide applications in tracking and communications with Low Earth Orbit satellites.

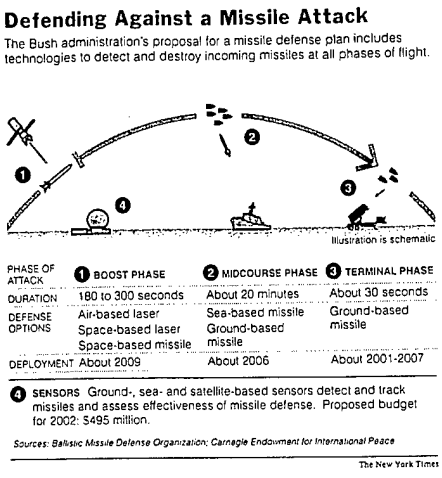

Figure 3 An application scenario for the Geodesic Sphere Phased Array Antenna

4. ARRAY CONSTRUCTION

Corresponding to each face of the regular icosahedron, the geodesic sphere phased array structure is constructed using 'alternative breakdown scheme' as explained with the schematic in Figure 4. A few of the triangular panels are equilateral, some are isosceles and a majority of them are neither. This will result in an array which will have a definite ordered arrangement but the rotational symmetry in the array around many geodesic vertices will be degraded. This degradation in rotational symmetry and their consequences in the array radiation pattern needs to be assessed quantitatively.

Whereas, for the truncated icosahedron based structure, the planar faces that are further subdivided to construct the geodesic sphere array, are equilateral triangular in shape. Consequently further subdivisions will result in a geodesic sphere array where the element arrangements are substantially uniform. A quantitative estimate of the array symmetry reflected in the array element radiation pattern around a polar axis through any one of the vertices needs to be ascertained. The first step in this direction is the determination of the coordinate points of all the elements in the array. This is done by first calculating the coordinate points in the Cartesian coordinate frame and then transforming these coordinate points in a global spherical coordinate frame. Calculation of the element positions for arrays of the two types has been carried out from analytical expressions derived first.

5. ARRAY ANALYSIS

In the geodesic sphere phased array, none of the antenna elements are on the surface of the circumscribing sphere. Only the vertices where the planar triangular subarray panels intersect are on the spherical surface. In the far field radiation pattern calculations, the phase relations amongst the antenna element excitations

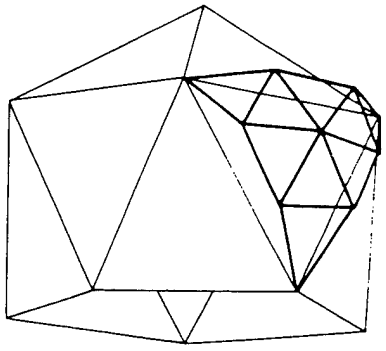

Figure 4. Construction of the geodesic sphere phased array antenna panels. Most of the triangular panels are not exactly equilateral. This results in nonuniformity in the element arrangements for the array of the Platonic type.

are most important. The antenna elements could be circular apertures or circular microstrips capable of carrying dual orthogonal circular polarizations. In the beginning, when array antenna pattern symmetry is to be studied, one ignores the mutual coupling effects and just computer the array element pattern or array radiation pattern when a portion of the array is energized, to set up a beam in a given direction.

5.1 Field representations

The electromagnetic field exterior to the array surface is represented in terms of spherical waveguide modes in a global coordinate frame [9] with polar axis through one of the original vertices of the icosahedron(regular or semi-regular). The element field are represented in terms of circular waveguide modes and expressed in terms of local spherical coordinates. The element field polarizations are resolved along global $\theta_{\square}$ and $\phi_{\square}$ directions.

5.2 Enforcement of approximate boundary conditions

Element by element approach is utilized in the array analysis. For each element, the field matching is done at the element interface and spherical transmission line relations are utilized to transform spherical transmission line modal fields from the radial position of the element to the radius of the circumscribing geodesic sphere.

5.3. Array pattern computations

Unless mutual coupling analysis is needed to be performed, it is not necessary to solve the approximate boundary value problem and one goes directly into array

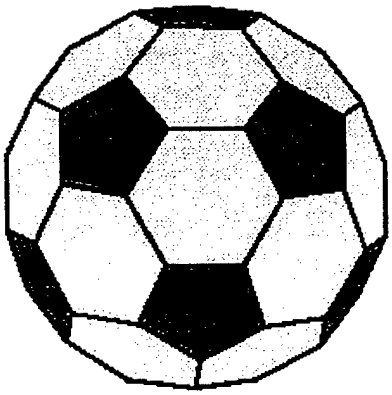

Figure 5. This geodesic sphere array layout defines the array symmetry of the truncated icosahedron based structure. Further subdivisions of the hexagonal and pentagonal panels provide triangular panels.

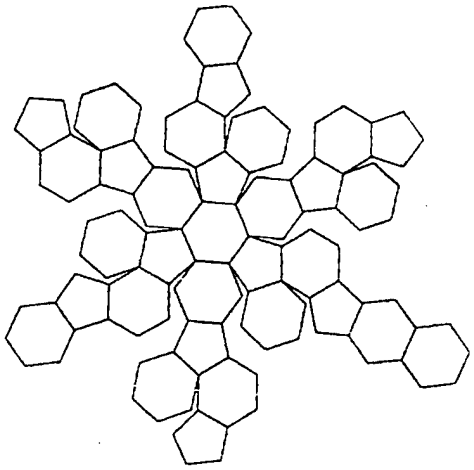

Figure 6. The subarray panel of the geodesic sphere phased array antenna laid out on a planar surface.

pattern computations. Towards this end, each element field contributions are expressed in terms of spherical waveguide mode fields on which far field approximations are made.

As outlined earlier[3,4], the array could be energized to set up a main beam in the direction of a vertex and subarray scanning techniques could then be employed to provide limited electronic scanning in the space between the vertices. This scheme has the promise of a lower cost.

6. SUB ARRAY SCANNING

The geodesic sphere phased array could be designed to have each and every element equipped with a power amplifier whose gain is variable in digital steps with required precision and a digital phase shifter of desired precision. Then a digital computer becomes capable of fully controlling the array with multiple high precision beam forming capabilities. However for the array to be affordable for commercial applications, one needs to explore the subarray scanning performance of the array in tracking and communication with a maximum of two satellites at a time. Then the requirements become simplified. A computer program is currently under development that will numerically evaluate the array performance and provide a design based on given physical performance parameters. Incremental progress made in this direction is the subject matter of this paper.

7. ARCHITECTURAL CHOICE : ARCHIMEDES VERSUS PLATO

The geodesic sphere phased array based on the truncated icosahedron is the system of choice in the present investigation. The subarray panels are more uniform, lending itself to lower cost of fabrication. Four or sixteen element triangular subarray panels are basic building blocks, each equipped with Gallium Arsenide based MMIC units to provide power amplification(or LNA) and phase shifting to the transmitted (or received) signa in digital steps.

8. REFERENCE

[1] Probir K. Bondyopadhyay, "Geodesic Sphere Phased Array Antenna for Multi-Satellite Communications", U.S. Patent Application No. 60/121,874, Filed, 26th February 1999.

[2] Probir K. Bondyopadhyay, "Geodesic Sphere Phased Array Antenna System", U.S. Patent Application No. 09/513,014, Filed, 25th February 2000.

[3] Probir K. Bondyopadhyay, "Geodesic Sphere Phased Arrays for LEO Satellite Communications, Part 1, The Architecture", 2000 IEEE Antennas and Propagation Society International Symposium, Salt Lake City, Utah, July 16- 21, 2000, pp. 206-209.

[4] Probir K. Bondyopadhyay, "Geodesic Sphere Phased Arrays for LEO Satellite Communications, Part 2, Cellular Scanning and its Advantages", 2000 IEEE Antennas and Propagation Society International Symposium, Salt Lake City, Utah, July 16- 21, 2000, pp. 210-213.

[5] Probir K. Bondyopadhyay, "The Cellular Scanning Concept and its Applications", Proceedings of the 2000 Antenna Applications Symposium, Allerton Park, Monticello, Illinois, September 20-22, 2000, pp. 134-141.

[6] Robert C. Hansen, PHASED ARRAY ANTENNAS, John Wiley & Sons Inc., New York, 1998, ISBN No. 0-471-53076-X, Chapter 11, pp. 445.

[7] H. E. Schrank, "Basic Theoretical Aspects of Spherical Phased Arrays", in Phased Array Antennas, (A. A. Oliner and G. H. Knittel Editors), Artech House, Dedham, MA, 1972, pp. 323-327.

[8] C. Collier and T. R. Holzheimer, "Conformal Switched Beam Array Antenna", U. S. Patent No. 5,457,465, filed, Sept. 1, 1987, issued Oct. 10, 1995.

[9] J. R. Stuart, "Spacecraft designs for Satellite Communication System", U. S. Patent No. 5,386,953, filed, August 18, 1992, issued Feb. 7, 1995.

[10] Probir K. Bondyopadhyay, "Analysis of rotationally Symmetric Arrays of Apertures on Conducting spherical Surfaces", IEEE Trans. On Antennas and Propagation, Vol. 40, No. 8, August 1992, pp. 857-866.

ABOUT POSSIBILITY THE VECTOR'S PARABOLIC ANTENNA DP TO IMPROVE RADAR RESOLUTION

Vera Ginzburg, Dr.Sc
SPIE member No: 00373899, IEEE member No: 40360208
3085 Brighton 13th St., Apt. 2A
Brooklyn, NY 11235
Phone: 718-891-3753; E-mail: veraginz@msn.com

Abstract

The resolution of contemporary parabolic radars as well as radars under development with various scanning patterns are defined by the width of their directionality patterns (DP). Usually these DPs are calculated by the field integration at the parabolic mirror's aperture, and only the real part of DP is taken in consideration. The simple formula $\theta \approx 70(\lambda/D)$, evaluates the width of such DP when a radiator is at the mirror's focus. But in a real situation, when the radiator is displaced from focus and the classic Gyugens-Kirchhoff approach is used for the field integration, the resulting DP becomes a complex function due to significant phase change. Therefore the directionality pattern of the scanning parabolic antenna should be described by vector function (Vector DP). Vector DP have much larger maximum scanning angle than conventional "amplitude" DP, especially for an asymmetrical parabolic antenna.

In this article several examples of results for calculated and experimental vector DPs are presented and they practically coincide.

The usage of vector DP can vastly improve the parabolic radar resolution. This is especially important for development of large range early warning radars.

Key words: Radar, Parabolic Antenna, Vector DP, and Super-Resolution.

Introduction

This article presents some DP calculation results from the *Calculation of parabolic antennas*[1] published in Russia, in particular, for DP of parabolic antennas with various beam-scanning methods when the radiator is displaced from a parabola's focus. The goal was to reach desired radar specifications, using computer simulation. To solve this problem, one has to determine the relationship between the antenna's location parameters (the scanning angle, side beam's, level

of beam dilation, decrease in amplification) and its technical parameters (the radiator displacement from the focus, the parabolic antenna size to its focus ratio, the required level of illumination of the mirror's edge area).
This article gives a brief description of the two methods for vector DP calculations. The first one is based on integration of the field at the mirror's aperture when the radiator is displaced from focus. The second one is based on the integration of the currents at the mirror surface induced also when the radiator is displaced from focus. The calculations were made for the regions of the main maximum and near side lobes for both symmetrical and asymmetrical antennas.

The first part presents the results for parabolic antennas with scanning angles of no more than 10 degrees. Within this range it is possible to calculate DP by the field integration at the reflector's aperture as is proved by the comparison of the calculation and the experimental results. Besides that, the mutual influence of DP between horizontal and vertical planes may be neglected. This means that the 3-D problem of DP calculation can be reduced to a 2-D problem. In addition, one can get both the amplitude and the phase field components, which are amplitude and phase DP. All these allow characterizing the far-field zone by the Vector DP (VDP), which can much better utilize the antenna's potential. And again, there are a few examples of calculated and experimental amplitude and phase DP and VDP. It is also shown that VDP, with the same displacement from focus, provides much larger scanning angle than conventional amplitude DP.

The second part presents the results of the induced current integration at the mirror surface for cases when the radiator is in and out of focus for both main and parasitic polarizations. For instance, when DP is presented in isolines, one can see field deformation shaped like a comma. All calculations were made in Mathematical Institute of Russian Academy of Science using the computer designed by academician C.A. Lebedev.
The calculation algorithm was elaborated by I. Belova, the coauthor of *Calculation of parabolic antennas*[1].

Part 1: The calculation of a parabolic antenna DP by integrating the field at the reflector's aperture.

The parabolic antenna beam pattern for the main maximum and nearest side lobes can be described in Kirchhoff's approximation by the following formula:

$$g(\theta) = \int_{\xi_1}^{\xi_2} F(\xi) e^{j[k\xi \sin\theta - \psi(\xi)]} d\xi \qquad (1)$$

where θ - is the angle that shows the direction to the distant point relative to the antenna axis, normal to the axis ξ; $\xi_2 - \xi_1 = D$ – the parabolic reflector diameter; $k=2\pi/\lambda$. For the symmetrical reflector $|\xi_2| = |\xi_1| = D/2 = \xi_{max}$. For asymmetrical, $\xi_{max} = \xi_2$.

The solution for this equation (1) is obtained by the numerical integration for many peculiar cases. This enables to plot the generalized DP for scanning parabolic antennas when the radiator has small offset from the mirror focus.

For these calculations two coordinate systems are used, as shown on Figure 1. Cylindrical coordinates r, α , with polar axis z, going through the focus O_1, and orthogonal coordinates ξ, z with the zero point at the parabolic reflector apex.

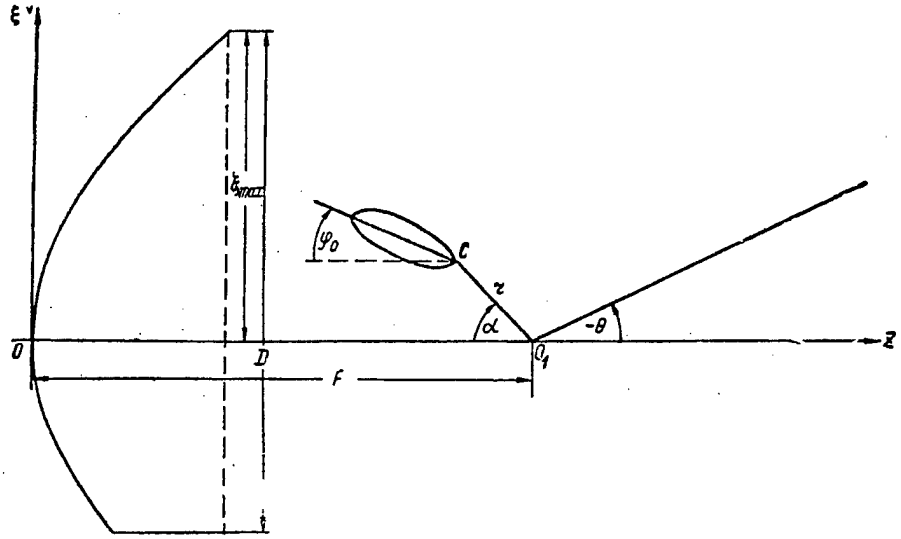

Figure 1: The coordinate systems were used in calculations

Let us put the radiator at the point C, with the beam pattern maximum direction under the angle φ_0 to the axis z. Let us put in dimensionless values: $r/F=a$; $\xi_{max}/F=b$, new variable $x=\xi/\xi_{max}$ and denote $u/\pi = (D/\lambda)\sin\theta$. Then the integral (1) can be written as:

$$g(u/\pi) = \int_{x_i=\frac{\xi_1}{\xi_{max}}}^{1} F(x)e^{j[ux-\psi(x)]}dx \qquad (2)$$

For numerical integration, the integral (2) is presented by:

$$g(u/\pi) = A(u/\pi)e^{j\Phi\left(\frac{u}{\pi}\right)}\Delta x$$

Then the far-field amplitude according *Calculation of parabolic antennas*[1] is equal to:

$$A(u/\pi) = \Delta x \sqrt{\left\{\sum_{i=1}^{n} F(x_i)\cos\left[ux_i - \psi(x_i)\right]\right\}^2 + \left\{\sum_{i=1}^{n} F(x_i)\sin\left[ux_i - \psi(x_i)\right]\right\}^2} \quad (3)$$

and the far-field phase:

$$\Phi(u/\pi) = \arctan \frac{\sum_{i=1}^{n} F(x_i)\sin\left[ux_i - \psi(x_i)\right]}{\sum_{i=1}^{n} F(x_i)\cos\left[ux_i - \psi(x_i)\right]} \quad (3a)$$

Here: $x_1 = \xi_1 / \xi_{max}$; $x_i = x_{i-1} + \Delta x$, ... $x_n = 1$; $n = D/\Delta x$ – the number of the point of summing.

It was shown that for the DP calculation at different n, at the main maximum, and at nearby side lobes for $D \approx 100\lambda$, it is sufficient to calculate $A(u/\pi)$ and $\Phi(u/\pi)$ with intervals $\Delta x \cong 2{,}5\lambda$. For smaller antenna calculation intervals Δx needs to be smaller to provide an $n \geq 40$. For the determination of $F(x)$ and $\psi(x)$ let us use the Figure 2.

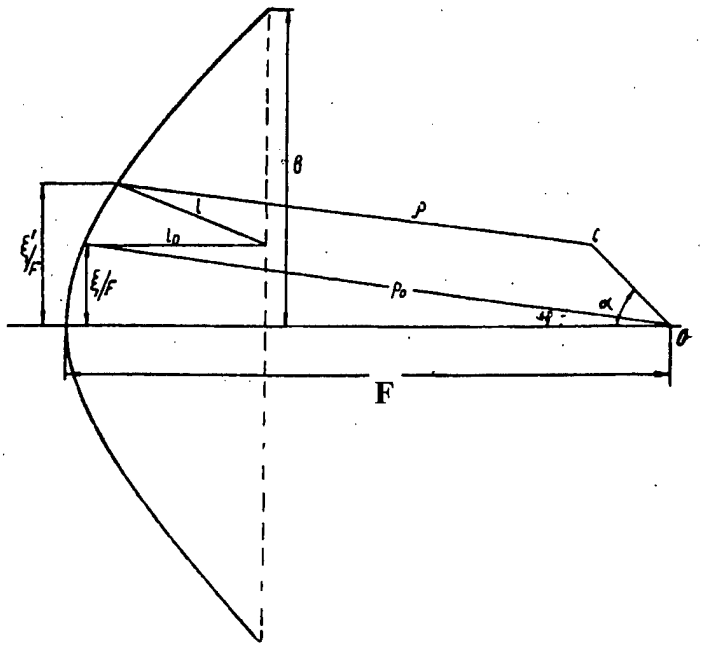

Figure 2: The process of field formation at the mirror's aperture.

Figure 2 shows the incident (ρ_o and ρ) and reflected (l and l_o) beams, which came at the same aperture point, when the radiator is in focus or at some arbitrary point C respectively. This figure was used for determination the field distribution at the antenna aperture. In the general case, the equation for the calculation of $\psi(x)$ is rather cumbersome. But in our case, with the radiator having a small displacement from the focus, it was assumed that:

$$\xi' \cong \xi \text{ and } l_o \cong l. \tag{4}$$

then, according *Calculation of parabolic antennas*[1]:

$$\psi(x) = \frac{\pi D}{b\lambda} \cdot \frac{a\left\{bx \sin\alpha + \left[1 - \left(\frac{bx}{2}\right)^2\right]\cos\alpha\right\} - \frac{a^2}{2}}{1 + \left(\frac{bx}{2}\right)^2} \tag{5}$$

where $x = \xi/F$, $a=r/F$ - is the radiator displacement from the focus, and $b=\xi_{max}/F$ Now, let us determine the expression for calculating the value $F(x)$ in the formula (3). Let us assume that the real radiator DP (for power) is described by function $f(x)$. Then, the field distribution along the aperture, with condition (4), can be described as:

$$F(x) = \frac{\sqrt{f(x)}}{\rho}$$

here ρ is convenient to write as:

$$\rho = \sqrt{(bx - a\sin\alpha)^2 + \left[1 - \left(\frac{bx}{2}\right)^2 - a\cos\alpha\right]^2} \tag{6}$$

Absolute value of $F(x)$ depends on the value ρ, i.e. on the mirror dimension and on the radiator displacement from the focus. It is more convenient in the equation (3) to use the normalizing value of the amplitude at the mirror aperture i.e. $F_n(x)=F(x)/F(x)_{max}$. If the radiator's DP is normalized, then one can determine the radiator position at the focus and the direction of its maximum to the parabola's apex, $\rho_M=1$ и $f_M(x)=1$, when the linear dimensions are presented through the focal distance. In the general case, when the radiator's DP maximum is turned from the optical axis on some angle φ_0 (as in Figure 1), or in the case of asymmetrical reflectors, when $\xi_1 \neq \xi_2$, the radiator's DP maximum has to be directed approximately to the mirror's center.

By failing to get the simple formula for the DP calculation of real horn-type antenna, the determination of $f(x)$ can be done quite well by the following approximation:

$$f(x) = e^{-[n(\varphi-\varphi_o)]^2} \tag{7}$$

Here φ - the angle between straight line ρ and the reflector optical axis z, equal to:

$$\varphi = \arcsin\frac{bx - a\sin\alpha}{\rho}$$

The relation between φ and x, for the case when the radiator is at the parabolic focus, is expressed by:

$$\varphi = 2\arctan\frac{bx}{2} \tag{8}$$

The value φ_0 in (7) is the angle of radiator's beam rotating with respect to the reflector optical axis. The function (7) is a good approximation of real radiator DP in the vicinity of reflector's aperture, as was shown by the calculation. In the limit case of the uniform field distribution in the antenna's aperture $f(x)=\rho^2$.
The formulas (5) – (7) permit the parabolic antenna DP calculation by the usage of equations (3). However, in order to investigate the influence of specific parameters on the antenna's DP such as for instance $b = \xi_{max}/F$, it is necessary to keep aperture field distribution the same, while changing F. From (8) one can see that at the same x and at different b the angles φ and φ_1 are related by the equation: $\tan(\varphi_1/2) = (b_1/b)\tan(\varphi/2)$. For this case following condition[1] provides the equal field distribution at the mirror's aperture:

$$f(x) = f_1(x)\left\{\frac{(1+\cos\varphi_1)\cdot(1+\cos\varphi_0)}{(1+\cos\varphi)\cdot(1+\cos\varphi_{01})}\right\}^2 \tag{9}$$

Here the real radiator DP is approximated by function:

$$f_1(x) = e^{[n(\varphi-\varphi_0)]^2} \tag{10}$$

The condition (9) permits one to move into the calculation the series of universal distribution $F(x)$ which, for the case of radiator's disposition in the focus, can be calculated by the formula:

$$F(x) = \frac{\sqrt{f(x)}}{\rho} \tag{11}$$

By using formula (11), such series of amplitude distributions becomes invariant for any b values.

As a rule φ_0 (at Figure 1) is chosen from the condition of symmetrical illumination at the antenna's aperture. For asymmetrical reflectors at $\xi_1 \neq \xi_2$ the maximum radiator's DP, φ_0 is directing approximately to the center of reflector, Figure 3 shows the series of amplitude distribution $F(x)$ for asymmetrical (a) and symmetrical (b) reflectors. The value γ is the field level at the reflector's corner in % and is determined by the formula (10) for different n.

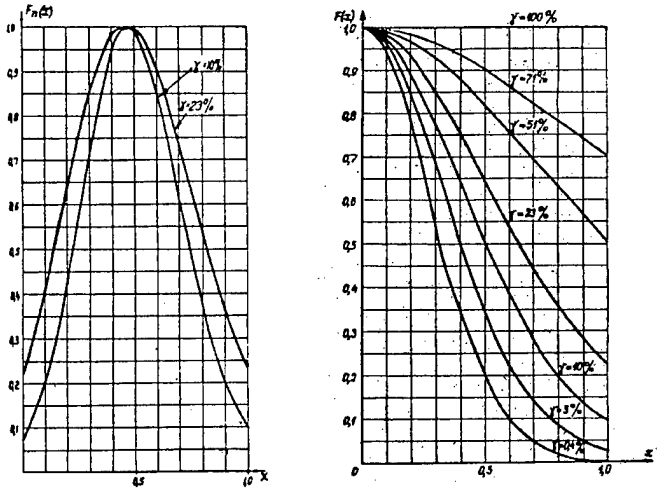

a b

Figure 3: (a) - aperture field for asymmetrical reflector,
(b) - for symmetrical reflector and various γ

In *Calculation of parabolic antennas* [1] it was shown that for the case when the radiation comes from the focus and φ is taken as an argument, the aperture field distribution is similar to the Gaussian curve described by the formula (10), but with a different index of exponent. Herewith, both indexes, for reflector and radiator, are linear to each other.

Formula (3) was used for the calculation of the DP series. To determine the range of u/π variation, i.e. the range of angle θ, one can use well-known empirical formula for determining the θ_{max}

$$(u/\pi)_{max} = D/\lambda \sin\theta_{max} \approx (D/\lambda)\,(a \sin\alpha)/(1+ b^2/8)$$

The range for u/π is determined to be 3-4 DP's width, which can be approximately calculated, by the known formula $\theta_{p/2} = \lambda/D$ in radians.

The algorithm, based on the mentioned formulas, allows us to calculate the values: $A(u/\pi$ and $\Phi(u/\pi)$ i.e. amplitude and phase DP.

For testing the proposed method, calculations of DP were provided for real antennas, with different radiator offset from the reflector focus. The real radiator DP was approximated by the formula (10).

Figure 4 shows the examples of calculated and experimental DP.

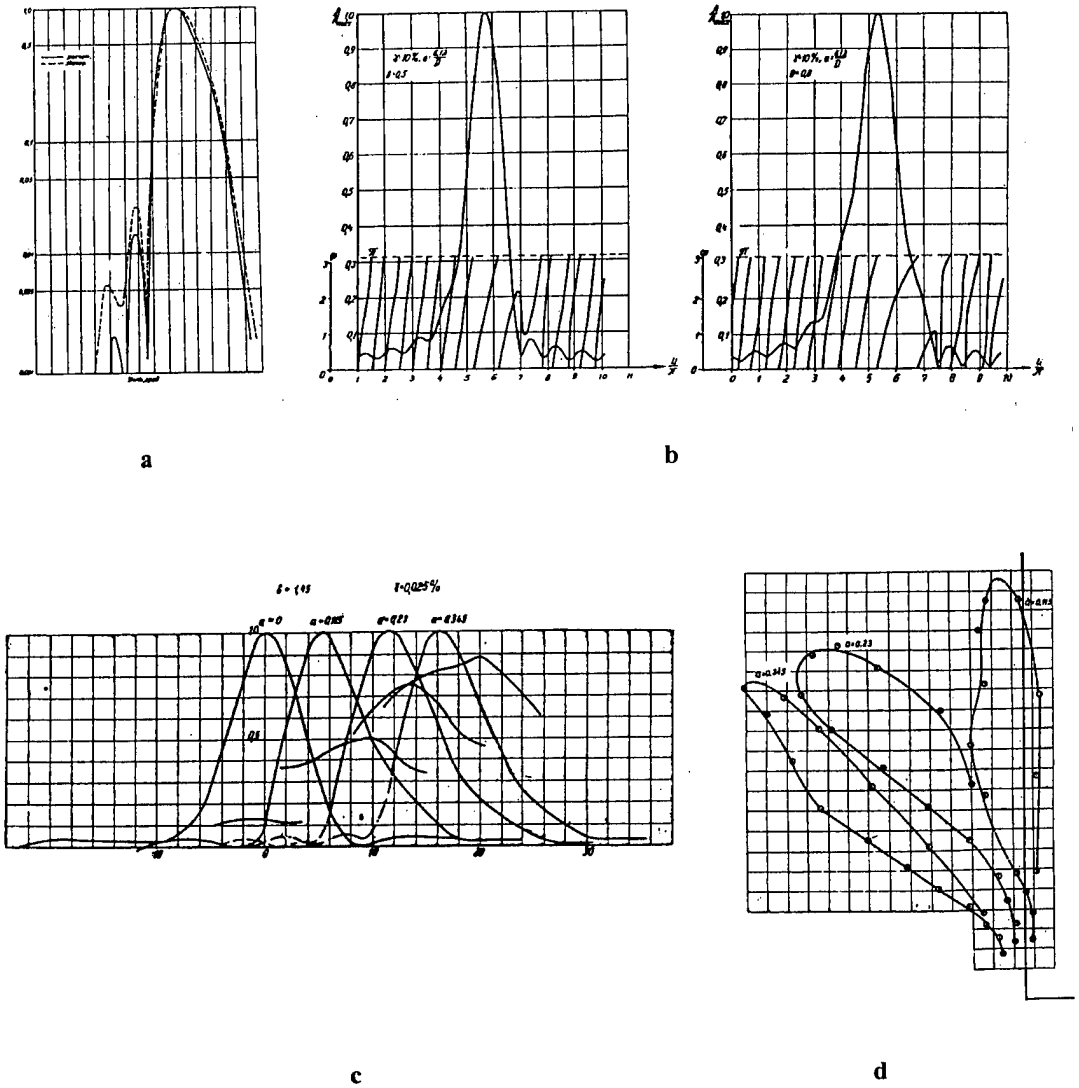

Figure 4: The examples of calculated and experimental DP:
(a) - calculated and experimental amplitude DPs;
(в) - calculated amplitudes and phase DPs;
(c) - experimental amplitude and phase DPs;
(d) - vector DPs plotted using the amplitude and phase DPs from (c).

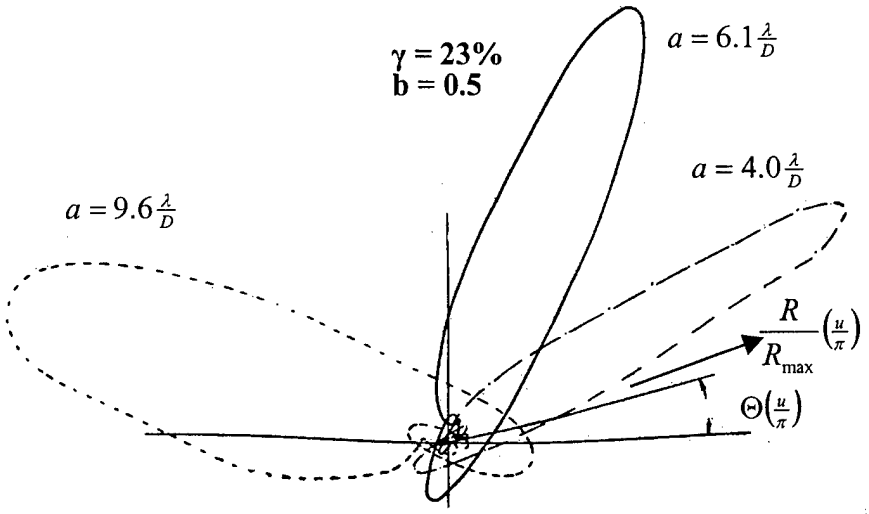

Figure 5: An example of calculated vector's DPs of the antenna with the symmetrical reflector

Figure 4 and Figure 5 show that the vector DP maximum, with the same rotation of phase front at the reflector's aperture, scan with a much greater angle than the traditional antennas, which only use the amplitude DP.

Obviously, the vector DP (VDP) can vastly improve the locator resolution, particularly for distant detection.

In *Calculation of parabolic antennas* [1] the numerous examples of amplitudes and phases DP were calculated for different generalized parameters: $a = r/F$ – relative offset radiator from reflector focus; $b = \xi_{max}/F$, where ξ_{max} (for a symmetric reflector), is equal to $D/2$, where D – reflector diameter, γ - the field level at the reflector's edge relative to maximum value in %.

Part 2: Some results of DP calculation for parabolic antennas by integration of the current on the reflector's surface.

It is known, that electrical and magnetic currents generated by arbitrary radiator at the surface S produce far-field **E** and **H** at the distance R. These fields are described by following expressions *Antennas of centimeter's and decimeter's waves* [2]:

$$\mathbf{E}=\frac{k}{4\pi j}\cdot\frac{e^{-jk|R|}}{|R|}\left[\left(\sqrt{\frac{\mu}{\varepsilon}}F_{\Theta}+F_{\mu\varphi}\right)\cdot i_{\Theta}+\left(\sqrt{\frac{\mu}{\varepsilon}}F_{\varphi}-F_{\mu\Theta}\right)\cdot i_{\varphi}\right] \qquad (12)$$

$$\mathbf{H}=\sqrt{\frac{\varepsilon}{\mu}}\,[i_R\,\mathbf{E}]$$

Calculation of parabolic antennas [1] describes the method for calculation of the spatial DP of the parabolic antenna based on the calculation of the current at the reflector surface S, excited by the radiator arranged at the reflector's focus or somewhere near it, and on the subsequent calculation of the spatial distribution of the far-field components **E** and **H**, i.e. the spatial DP.

The calculations were based on the following assumption: the reflector's conductance is infinite and, therefore, on the reflector surface there exist only the current distribution $\mathbf{k} = -2[\mathbf{n}\mathbf{H}_s]$, where $\mathbf{H}_s$ – the field vector of radiator near the reflector surface and **n** – unit vector normal to the reflector surface, directed to the radiator. Magnetic currents induced on the reflector's surface generate far-field $\mathbf{E}(R)$ and $\mathbf{H}(R)$, which can be calculated by the formula (12) with:

$$\mathbf{F} = \int_S [H_S \cdot n]\, e^{jk|r|\cos\delta} dS$$

Here H_s is the vector of radiator's field at the reflector surface S. Figure 6 shows some examples of calculations. (Note: in (12) the value $F_\mu = 0$ due to reflector's infinite conductance).

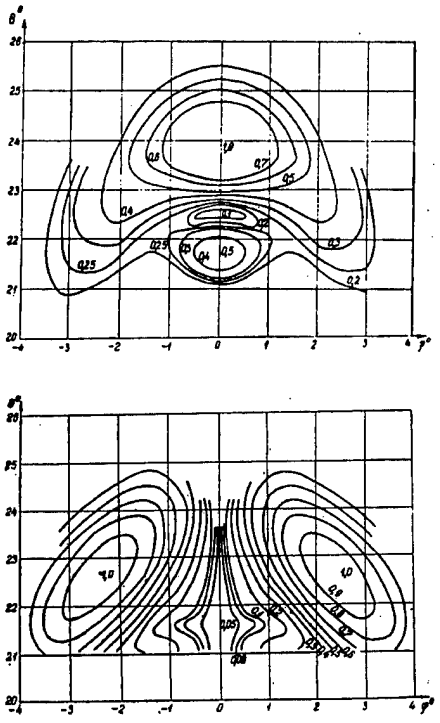

a,b

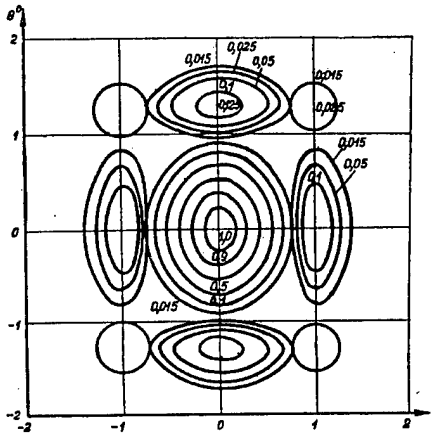

c

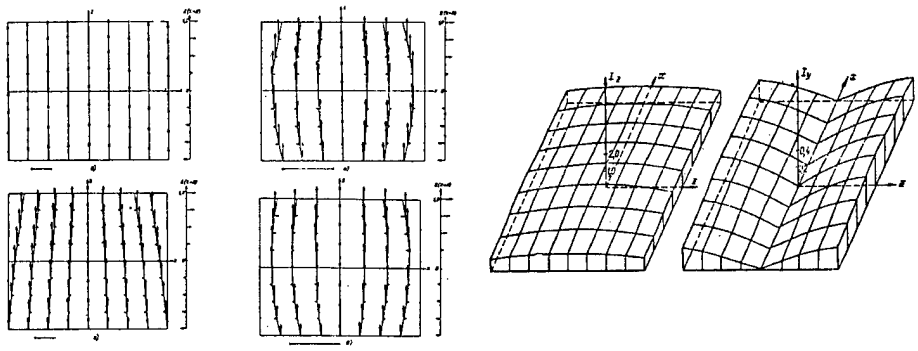

d e

Figure 6: Examples of calculated far-field zones, when the radiator is displaced from the reflector focus for $z = 18\lambda$ and $z=0$.

(a) - for primary and (b) - for parasitic polarization respectively at $z = 18\lambda$
(c) - for primary polarization at $z = 0$ and with emphasized level (up to 85%) of illumination of the reflector's outer boundary
(d) - the pattern of current directions at the reflector surface
left: up – for electrical and magnetic dipoles (the horn analog) in the reflector focus, down – dislocated from the focus
right: up - electrical dipole in the focus, down - dislocated from the focus
(e) - current distribution at the mirror surface when electrical dipole is at the focus

Conclusion

From a brief description of this research, which is described in detail in *Calculation of parabolic antennas* [1], one can make the following conclusion:
The actual DPs of parabolic antennas with the radiator displaced from reflector's focus, are described by the complex function: $g(\theta) = A\ e^{\ i\ \varphi}$ where A – is "amplitude" and φ - "phase" DPs .
With an increase of the radiator displacement from the parabola's focus, especially with asymmetrical reflectors, n phase chops multiple to π take place inside the "amplitude" DP, i.e. the resulting vector DP (VDP) contains several maximums.
Use of VDP i.e. measuring amplitude and phase of received signals, allows significant improvement in resolution of parabolic locators. From the big series[1] of amplitude and phase DP calculations, it follows that the biggest advantage of VDP occurs with an asymmetrical parabolic reflectors because of their sharper phase DP.

Literature

1. V.M. Ginzburg, I.N. Belova, *Calculation of parabolic antennas,* "Sov. Radio", Moscow, pp.250, 1959 (in Russian)
2. Ya.N.Fel'd, L.S. Benenson, *Antennas of centimeter's and decimeter's waves*. Part1, VVIA by name N.E. Jukovsky, 1955 (in Russian)

ACCURATE ANALYSIS OF REFLECTOR ANTENNAS USING FAFFA-MLFMA ALGORITHM

Tie Jun Cui and Weng Cho Chew
Electromagnetics Laboratory
Department of Electrical and Computer Engineering
University of Illinois at Urbana-Champaign
Urbana, IL 61801-2991

Jiming Song
Motorola, 2100 East Elliot Road
Tempe, AZ 85284

Abstract: The traditional methods to analyze reflector antennas are based on the physical optics (PO) and geometrical theory of diffraction (GTD), which are high-frequency approximation methods. The modern development of fast algorithms and high-speed computers makes it possible to analyze the reflector antennas accurately based on the integral equation method. In this paper, we propose an efficient algorithm to accelerate the solution of the combined field integral equation using the multilevel fast multipole algorithm (MLFMA) combined with the fast far-field approximation (FAFFA). MLFMA is a fast $N \log N$ algorithm, which has found wide applications. However, the translation between groups in MLFMA is expensive because spherical Hankel functions and Legendre polynomials are involved and the translator is defined on an Eward sphere with many $\hat{k}$ directions. When two groups are in the far-field region, however, the translation can be greatly simplified by FAFFA where only a single $\hat{k}$ direction is involved in the translator. Numerical results show that both the computational load and memory requirement can be reduced using the FAFFA-MLFMA algorithm with little loss of accuracy. For over-a-million-unknown problems, the reduction of CPU time can reach as much as 40%. Using the FAFFA-MLFMA algorithm, the reflector antennas can be accurately analyzed and the current distribution on the reflector can be obtained.

1. Introduction

The traditional methods to analyze reflector antennas are based on the physical optics (PO) [1] and geometrical theory of diffraction (GTD) [2], which are high-frequency approximation methods. PO and GTD can give good approximation for the radiation pattern, but the current distribution on the reflector surface cannot be accurately obtained. Also, PO and GTD are less accurate when the frequency is low. The modern development of fast algorithms, for example, the fast multipole method (FMM), and high-speed computers makes it possible to analyze the reflector antennas accurately based on the integral equation method.

FMM was originally proposed by Rokhlin and coworkers to evaluate particle simulations rapidly in solving the static integral equations [3]-[5]. In 1990, the FMM was extended by Rokhlin to solve two-dimensional (2D) acoustic wave scattering problems [6] and it has been extended to solve electromagnetic scattering problems by many researchers in both two and three dimensions [7]-[14]. Due to the reduced computational and memory complexities of FMM, it can greatly reduce the CPU and memory requirements in solving integral equations when large problems are considered. This is known as the cruelty of computational complexity in computer science. A regular two-level FMM reduces both the computational and memory complexities for a matrix-vector multiply from $O(N^2)$ to $O(N^{1.5})$, where N is the number of unknowns. Without nesting, the ray-propagation fast multipole algorithm and the fast far field approximation algorithm [12]-[13] can further reduce the computational complexity to $O(N^{1.33})$.

The multilevel fast multipole algorithm (MLFMA) further reduces the complexity and memory requirement to $O(N \log N)$ [15]-[20]. In the MLFMA implemented by Dembart, Epton, and Yip [20], the complexity of matrix-vector multiplication has been reduced to $O(N \log^2 N)$ using the interpolation, signature function, and filtering. In [15]-[17], Song, Lu and Chew have implemented an efficient MLFMA using the translation, interpolation, anterpolation, and grid-tree data structure, where both the computational complexity and memory requirement are reduced to $O(N \log N)$. Based on the efficient MLFMA, the Fast Illinois Solver Code (FISC) was proposed. Solutions of integral equation with an equivalent dense matrix system of up to ten million unknowns have been solved using such a method.

However, MLFMA is still expensive in solving the radiation and scattering problems of large objects because the required floating point operations (FPO) is

proportional to $AN\log N$ where the constant A is large. The exact translation between groups in the three-dimensional (3D) MLFMA involves spherical Hankel functions and Legendre polynomials, and the translator is defined on the Eward sphere with multiple $\hat{k}$ directions. Hence, the translation process is time consuming even though interpolation and anterpolation are used. The exact translation is necessary when two groups are close or in the resonant region. When they are in the far-field region, however, the translation can be greatly simplified using the fast far-field approximation (FAFFA) [13]. The FPO of FAFFA is proportional to $A_1 N^{1.33}$ where the constant A_1 is smaller due to the simplicity of the algorithm. Therefore, the combination of MLFMA with FAFFA will improve the efficiency of the algorithm. Lu and Chew have developed a two-level FAFFA method for 2D problems. Later, the FAFFA was extended to 3D case in [21]-[22]. However, the proposed FAFFA is not efficient since there are many non-far-field-region groups for an observation group, which have to be considered as near interactions and be computed using direct matrix-vector multiplication. Moreover, the computation of the group far-field patterns in FAFFA is a M^2 procedure, where M is the number of required directions.

Therefore, we propose to combine FAFFA with MLFMA to accelerate the solution of scattering problems. For an observation group, the interaction from near- and resonant-region groups, i.e., the non-far-field groups, is implemented using the conventional MLFMA, while the contribution from far-field groups is computed using FAFFA. To combine FAFFA with MLFMA [15]-[17] and FISC efficiently, new forms of radiation patterns and translator different from those in [13], [21], [22] have been derived for FAFFA, which are valid for all the EFIE, magnetic field integral equation (MFIE), and combined field integral equation (CFIE). Numerical examples are given, which show the efficiency to analyze the reflector antennas using the FAFFA-MLFMA algorithm.

2. FAFFA-MLFMA Algorithm

The basis of MLFMA is the addition theorem. We consider two points $\mathbf{r}_i$ and $\mathbf{r}_j$ in a computational domain. Suppose that $\mathbf{r}_i$ is an observation point, which is located in group m (observation group), and $\mathbf{r}_j$ is a source point which is located in group n (source group). $\mathbf{r}_m$ and $\mathbf{r}_n$ represent the centers of observation and source groups. Hence, the spatial vector from the source point to the observation point can be written as

$$\mathbf{r}_{ij} = \mathbf{r}_i - \mathbf{r}_j = \mathbf{r}_{im} + \mathbf{r}_{mn} + \mathbf{r}_{nj} \tag{1}$$

If groups m and n are not overlapping or adjacent, then

$$|\mathbf{r}_{im} + \mathbf{r}_{nj}| < |\mathbf{r}_{mn}|.$$

Therefore, the spherical wave function can be expanded using the addition theorem as:

$$\frac{e^{ik|\mathbf{r}_i - \mathbf{r}_j|}}{|\mathbf{r}_i - \mathbf{r}_j|} = \frac{ik}{4\pi} \int d^2\hat{k} e^{i\mathbf{k}\cdot(\mathbf{r}_{im}+\mathbf{r}_{nj})} \alpha_{mn}(\hat{k} \cdot \hat{r}_{mn}), \tag{2}$$

where the integral is defined on a unit sphere (Eward sphere), and α_{mn} is called a translator which is defined as

$$\alpha_{mn}(\hat{k} \cdot \hat{r}_{mn}) = \sum_{l=0}^{L} i^l (2l+1) h_l^{(1)}(kr_{mn}) P_l(\hat{k} \cdot \hat{r}_{mn}), \tag{3}$$

where L is the truncation number of an infinite series, $h_l^{(1)}(\cdot)$ is the spherical Hankel functions of the first kind, and $P_l(\cdot)$ is the Legendre polynomial. Here, r_{mn} and $\hat{r}_{mn}$ represent the distance and direction from group m to group n.

From (1) and (2), we notice that many $\hat{k}$ directions have to be used for numerical evaluation of the integral, which is expensive. Instead of using the addition theorem, the electrical distance $k|\mathbf{r}_i - \mathbf{r}_j|$ can be rewritten as

$$k|\mathbf{r}_i - \mathbf{r}_j| \doteq kr_{mn} + k\hat{r}_{mn} \cdot (\mathbf{r}_{im} + \mathbf{r}_{nj}) . \tag{4}$$

when the two groups are well separated. Hence, the spherical-wave function (2) can be approximated in the far-field as

$$\frac{e^{ik|\mathbf{r}_i - \mathbf{r}_j|}}{|\mathbf{r}_i - \mathbf{r}_j|} \doteq \frac{ik}{4\pi} e^{i\mathbf{k}_0\cdot(\mathbf{r}_{im}+\mathbf{r}_{nj})} \alpha_{mn}^{\text{far}}, \tag{5}$$

where $\mathbf{k}_0 = k\hat{k}_0$, $\hat{k}_0$ is the ray direction from group n to group m, and α_{mn}^{far} is the translator in far-field region:

$$\hat{k}_0 = \hat{r}_{mn}, \quad \alpha_{mn}^{\text{far}} = 4\pi \frac{e^{ikr_{mn}}}{ikr_{mn}}. \tag{6}$$

Clearly, Equations (5) and (2) share some similarities. However, only one direction $\hat{k}_0$ is used in (5) with a simple translator.

Using the plane-wave expansion of the spherical wave defined in (2) and (5), we develop a FAFFA-MLFMA algorithm for electromagnetic radiation and scattering by general 3D conducting objects. If the conducting objects are closed, the CFIE is used to eliminate the resonant effects; if they are open, the EFIE has to be used. Since EFIE is a special case of CFIE where the combination parameter $\alpha = 1$ [17], we apply the CFIE to formulate the problem. Choosing the Rao-Wilton-Glission (RWG) basis functions [23], the CFIE can be discretized using the method of moments (MOM) as a matrix equation

$$\sum_{j=1}^{N} Z_{ij} I_j = V_i, \quad (i = 1, 2, \cdots, N), \tag{7}$$

where the impedance matrix and voltage vector have been defined in [16], $\mathbf{I}$ is the current on the conducting surface, and N is the number of unknowns.

2.1 Two-Level Algorithm

For a two-level algorithm, the first step is the grouping of the unknowns. Usually, the relative spatial positions of two groups m and n can be classified into three types:

- the near region, where groups m and n are overlapping or adjacent;
- the resonant region, where groups m and n are not overlapping and non-adjacent, but they are not well separated;
- the far-field region, where groups m and n are well separated;

For the near-region interaction, the impedance matrix has to be evaluated using conventional MOM and direct matrix-vector multiplication. Fortunately, the number of near-region groups is very small.

For the resonant-region interaction, the impedance matrix can be efficiently computed through the fast multipole expansion (2). Using the formulations derived in [17], the impedance matrix can be expressed as

$$Z_{ij} = \frac{ik}{4\pi} \int d^2\hat{k} \mathbf{V}_{fim}(\hat{k}) \cdot \alpha_{mn}(\hat{k} \cdot \hat{r}_{mn}) \cdot \mathbf{V}_{snj}(\hat{k}), \tag{8}$$

where $\mathbf{V}_{snj}(\hat{k})$ and $\mathbf{V}_{fmi}(\hat{k})$ are the radiation pattern and receiving pattern, which are given by

$$\begin{aligned} \mathbf{V}_{fim}(\hat{k}) &= \alpha \int_S dS \left(\bar{\mathbf{I}} - \hat{k}\hat{k}\right) \cdot \mathbf{t}_i(\mathbf{r}_{im}) e^{i\mathbf{k}\cdot\mathbf{r}_{im}} \\ &- (1-\alpha)\hat{k} \times \int_S dS e^{i\mathbf{k}\cdot\mathbf{r}_{im}} \mathbf{t}_i(\mathbf{r}_{im}) \times \hat{n}, \end{aligned} \tag{9}$$

$$\mathbf{V}_{snj}(\hat{k}) = \int_S dS \left(\bar{\mathbf{I}} - \hat{k}\hat{k}\right) \cdot \mathbf{f}_j(\mathbf{r}_{nj}) e^{i\mathbf{k}\cdot\mathbf{r}_{nj}}, \tag{10}$$

where α is the combination parameter of the CFIE, $\mathbf{t}_i(\mathbf{r}_{im})$ is the testing function, $\mathbf{f}_j(\mathbf{r}_{nj})$ is the basis function, and $\hat{n}$ is the normal direction of the conducting surface.

We remark that (8) is a general formulation if the observation group is not overlapping and non-adjacent to the source group. The conventional FMM is just based on this equation. However, the multipole expansion (8) is still expensive if the two groups are well separated.

For the far-field interaction, the impedance matrix is simply computed through the far-field approximation (5). Since (5) has a similar expression to (2), the impedance matrix can be directly written from (8) as

$$Z_{ij} = \frac{ik}{4\pi} \mathbf{V}_{fim}(\hat{k}_0) \cdot \alpha_{mn}^{\text{far}} \cdot \mathbf{V}_{snj}(\hat{k}_0), \tag{11}$$

where $\mathbf{V}_{snj}(\hat{k})$ and $\mathbf{V}_{fmi}(\hat{k})$ are given by (9) and (10) when $\hat{k} = \hat{k}_0$.

Considering the above three cases, the matrix-vector multiplication in the two-level algorithm is easily written as

$$\begin{aligned}\sum_{j=1}^{N} Z_{ij} I_j &= \sum_{n \in N_m} \sum_{j \in G_n} Z_{ij} I_j \\ &+ \frac{ik}{4\pi} \int d^2\hat{k} \mathbf{V}_{fim}(\hat{k}) \cdot \sum_{n \in R_m} \alpha_{mn}(\hat{k} \cdot \hat{r}_{mn}) \cdot \sum_{j \in G_n} \mathbf{V}_{snj}(\hat{k}) I_j \\ &+ \frac{ik}{4\pi} \mathbf{V}_{fim}(\hat{k}_0) \cdot \sum_{n \in F_m} \alpha_{mn}^{\text{far}} \cdot \sum_{j \in G_n} \mathbf{V}_{snj}(\hat{k}_0) I_j, \quad (i \in G_m), \quad (12)\end{aligned}$$

where N_m, R_m, and F_m denote indices of near region, resonant region, and far-field region with respect to group m, respectively. In the resonant and far-field interactions in (12), the summation $\sum_{j \in G_n} \mathbf{V}_{snj} I_j$ represents the aggregation of all unknowns in group n to the group center, the summation $\sum_n \alpha_{mn}$ represents the translation from group n to group m, and $\mathbf{V}_{fim} \cdots$ represents the disaggregation from the center of group m to all unknowns in this group.

2.2 Multilevel Algorithm

To solve very large problems efficiently, a multilevel algorithm is required. First the 3D object **S** is immersed in the smallest box that contains **S**, which is referred to be the zeroth level box. Then this box is divided into eight subboxes to form the first level. Then each box in level 1 is divided into eight subboxes to generate the second level, and recursively continued until the finest level F, in which each box has a size of around 0.2λ □ 0.5λ. The above procedure makes an oct-tree structure. Similarly, a quad-tree structure can be made for planar objects like conducting patches. After setting up the tree structure, boxes at all levels are indexed, but only nonempty boxes are recorded. Thus, the computational cost depends only on the nonempty boxes.

In the conventional MLFMA, the coarsest level (or top level) is chosen as level 2 [15]-[17] for the best efficiency. However, FAFFA usually cannot be used at this

level because all groups at this level are usually not in the far-field region. To apply both FAFFA and MLFMA in the multilevel algorithm, we consider a general case where the coarsest level is supposed to be C, so that the groups at this level can be classified into the near region, the resonant region, and the far-field region.

For an arbitrary observation group at the coarsest level, the interaction from resonant region is implemented using MLFMA [17], where interpolation is used in the aggregation from the finest level to the coarsest level and anterpolation is used in the disaggregation from the coarsest level to the finest level because the number of multipole expansions ($\hat{k}$ directions) increases tremendously as one progresses from the finest level to the coarsest level; the interaction from far-field region groups, however, can be simply computed using FAFFA, where only one $\hat{k}_0$ direction is involved. Besides the resonant and far-field region groups, the interaction from near-region groups should be performed using a next lower-level algorithm, and this process can be continued until the finest level. At the finest level, the interaction from near region groups has to be considered by direct multiplication.

From the above analysis, it seems that two separate sets of aggregation, translation, and disaggregation are required for MLFMA and FAFFA, respectively. But this is very expensive and unnecessary. In fact, the radiation patterns at all levels in all $\hat{k}$ directions on the Eward sphere have been computed in MLFMA. Hence, the radiation patterns for FAFFA can be directly obtained using interpolation at the specified $\hat{k}_0$ direction. In the other word, only one aggregation is needed. To combine FAFFA with MLFMA efficiently, the FMM and FAFFA parts in the impedance matrix can be combined together. For example, the two parts in the two-level algorithm in (12) can be rewritten as

$$\frac{ik}{4\pi}\int d^2\hat{k}\,\mathbf{V}_{fim}(\hat{k})\cdot\left[\sum_{n\in R_m}\alpha_{mn}(\hat{k}\cdot\hat{r}_{mn})+\sum_{n\in F_m}\alpha_{mn}^{\text{far}}\delta(\hat{k}-\hat{k}_0)\right]$$
$$\cdot\sum_{j\in G_n}\mathbf{V}_{snj}(\hat{k})I_j, \tag{13}$$

where $\delta(\hat{k}-\hat{k}_0)$ is a Dirac δ function. From (13), we clearly see that only one disaggregation procedure is required after the translation in the FAFFA-MLFMA algorithm. Hence, the combination of FAFFA and MLFMA is performed only in

the translation. The Dirac δ function in (13) implies that the FAFFA translator has a weight of one when $\hat{k} = \hat{k}_0$ and zero when $\hat{k} \neq \hat{k}_0$.

In the numerical implementation of the algorithm, however, limited sampling points $\hat{k}_p (p = 1, \cdots, K)$ are used on the Eward sphere in the MLFMA. Here, K is chosen as

$$K = 2L^2 + 2, \quad L = kD + C(kD)^{\frac{1}{3}},$$

where C is a constant and D is the equivalent group diameter at the coarsest level. In this case, (13) can be used only if $\hat{k}_0$ is exactly one of $\hat{k}_p$. Otherwise, an interpolation has to be made for the FAFFA part in (12):

$$\frac{ik}{4\pi} \sum_{t=1}^{M} \mathbf{V}_{fim}(\hat{k}_{p_t}) \cdot \sum_{n \in F_m} \beta_{p_t} \alpha_{mn}^{\text{far}}(\hat{k}_{p_t} \cdot \hat{k}_0) \cdot \sum_{j \in G_n} \mathbf{V}_{snj}(\hat{k}_{p_t}) I_j, \tag{14}$$

where $p_t \in [1, 2, \cdots, K]$, $M \ll K$, $\hat{k}_{p_t}$s the direction close to $\hat{k}_0$. The above equation implies that all $\hat{k}_p$ directions are considered for the FMM groups, but only few $\hat{k}_{p_t}$ directions (or one $\hat{k}_0$ direction) are considered for the FAFFA groups. Therefore, both the CPU time and memory requirement can be reduced in the FAFFA-MLFMA algorithm.

The choice of the coarsest level C is very important in the FAFFA-MLFMA algorithm. If C=2, fewer or no groups can be treated using FAFFA; if C is too large, however, the level of the algorithm will be small which leads to the inefficiency of the algorithm. Usually, the coarsest level is chosen as 3, 4, or 5 depending on the size of the object.

3. Numerical Results

In the analysis of radiation and scattering problem using the FAFFA-MLFMA algorithm, a criterion to define the far region is required. In the conventional MLFMA [17], a concept of second near neighbors was introduced, where two

groups are not near neighbors at the current level but their parents are near neighbors. The MLFMA part is usually performed within the second near neighbors. Thus, we can define the criterion in a quantitative form as

$$r_{mn} \geq \gamma D_{2\text{nd}}, \tag{15}$$

where γ is a constant larger than or equal to one.

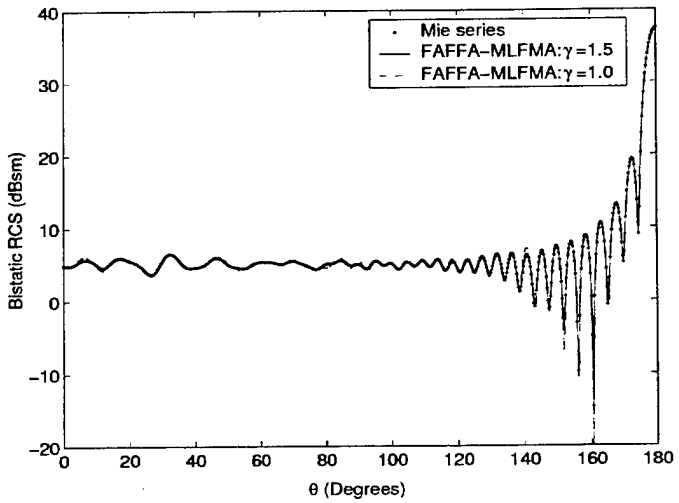

Figure 1. The bistatic RCS of a conducting sphere of radius 1 m at 2 GHz (V-V polarization). A 6-level algorithm is used. In FAFFA-MLFMA, the coarsest level is chosen as 3.

To test the validity and efficiency of the FAFFA-MLFMA algorithm, we first consider the scattering by a perfectly conducting sphere of radius 1 m at the frequency of 2 GHz, where 119,808 unknowns have been used. Figure 1 illustrate the validation of numerical results from a six-level FAFFA-MLFMA with different parameter γ against the Mie series solution of the bistatic RCS for VV polarization. In FAFFA-MLFMA, the coarsest level is chosen as 3. Clearly, the numerical results from FAFFA-MLFMA are very accurate in both cases when $\gamma = 1.5$ and $\gamma = 1.0$, as shown in Figure 1. When $\gamma = 1.0$, it implies that the interaction from second near-neighbor groups is performed by the MLFMA, and the interaction from groups outside the second near neighbor is performed by FAFFA.

The comparison of memory requirement and CPU time among the conventional MLFMA (C=2 and $\gamma = 100$), the FAFFA-MLFMA (C=3 and $\gamma = 1.5$ or $\gamma = 1.0$), and the MLFMA-only (C=3 and $\gamma = 100$) algorithms is illustrated in Table 1. From this table, we clearly see that both the memory requirement and CPU time have been noticeably reduced in FAFFA-MLFMA compared with the MLFMA-only algorithm under the same coarsest level. When the parameter γ decreases, more groups are handled using FAFFA, and hence the reduction increases; however, the accuracy of the numerical results becomes worse since FAFFA is used in some groups that are not really located in the far-field region. When $\gamma = 1.0$, both the memory requirement and CPU time used in FAFFA-MLFMA have a significant reduction comparing with the conventional MLFMA.

Table 1. Co Comparison of memory requirement and CPU time of the FAFFA-MLFMA algorithm when the coarsest level is chosen as 2 and 3

The coarsest level	Parameter γ	Memory (MB)	CPU time (s)
$C = 2$	100	249.45	1115.52
$C = 3$	100	260.89	1299.04
$C = 3$	1.5	249.26	1186.90
$C = 3$	1.0	237.47	1063.59

Next, we consider a large-scale problem: the radiation of a 60m aperture parabolic antenna. The parabolic surface is described by

$$z = 0.0125(x^2 + y^2),$$

where the aperture is 60m in diameter, and the focal point is located at (0, 0, 20m). A $\hat{x}$-directed electric dipole with unit electric current is fed at the focal point. When the working frequency is 450 MHz, 723,178 triangular facets and 1,084,135 edges are used. For such an over-one-million-unknown problem, an 8-level algorithm is used, and all computations are made on the Origin2000 machine with 10 processors.

When the coarsest level C is chosen as 2, 3, 4, and 5, the comparison of memory requirement and CPU time of FAFFA-MLFMA is shown in Table 2, where C=2 corresponds to the conventional MLFMA. From Table 2, it is evident that over 100 MBytes in memory requirement and 27,554 seconds in CPU time have been

saved using FAFFA-MLFMA when C=3 and $\gamma = 1.0$. Clearly, the reduction of CPU time is more than 28 %. Hence, FAFFA-MLFMA is very efficient in solving large-scale problems. This is because a huge amount of sampling points of $\hat{k}$ are required for large problems in the conventional MLFMA (112,340 points in this example); but only four points of $\hat{k}$ are needed in the FAFFA part of FAFFA-MLFMA if we use four-point interpolation in (14). For small problems, the number of sampling points for $\hat{k}$ is small in the conventional MLFMA. However, four points are still used in the FAFFA part for the interpolation.

Table 2. Comparison of memory requirement and CPU time for the large parabolic antenna problem.

The coarsest level	Parameter γ	Memory (MB)	CPU Time (s)
$C = 2$	100.0	3331.05	96885.17
$C = 3$	1.0	3228.84	69331.54
$C = 4$	1.5	3167.14	88796.14
$C = 4$	1.0	3113.26	66499.20
$C = 5$	1.5	3052.83	58819.16

To compare the accuracy of the numerical results, Figure 2 plots the radiation pattern of the parabolic antenna computed from the conventional MLFMA and FAFFA-MLFMA when C=3 and $\gamma = 1.0$. Clearly, the numerical results from the conventional MLFMA and FAFFA-MLFMA agree very well. Within 40 degrees centered at the main beam direction, the two results are nearly identical.

For large-scale problems, the coarsest level can be set higher to increase the efficiency of FAFFA-MLFMA. When C=4, FAFFA-MLFMA provides very accurate results if $\gamma = 1.5$ and $\gamma = 1.0$. When $\gamma = 1.0$, more than 217 MBytes in memory requirement and 30,386 seconds in CPU time have been saved using FAFFA-MLFMA. The reduction of CPU time is more than 31 %. The numerical result in this case is illustrated in Figure 3. Clearly, the computed radiation patterns from the conventional MLFMA and FAFFA-MLFMA agree very well.

When the coarsest level is set at 5 and $\gamma = 1.5$, the FAFFA-MLFMA is even more efficient. Comparing with the conventional MLFMA, more than 279 MBytes in memory requirement and 38,066 seconds in CPU time have been reduced using the FAFFA-MLFMA. The reduction of CPU time is nearly 40 %. The radiation patterns computed from the conventional MLFMA and FAFFA-MLFMA when

C=5 and $\gamma = 1.5$ are illustrated in Figure 4. Clearly, the two results are in agreement. However, FAFFA-MLFMA becomes inefficient when the coarsest level is higher than 5, due to the increased number of groups for FAFFA interactions.

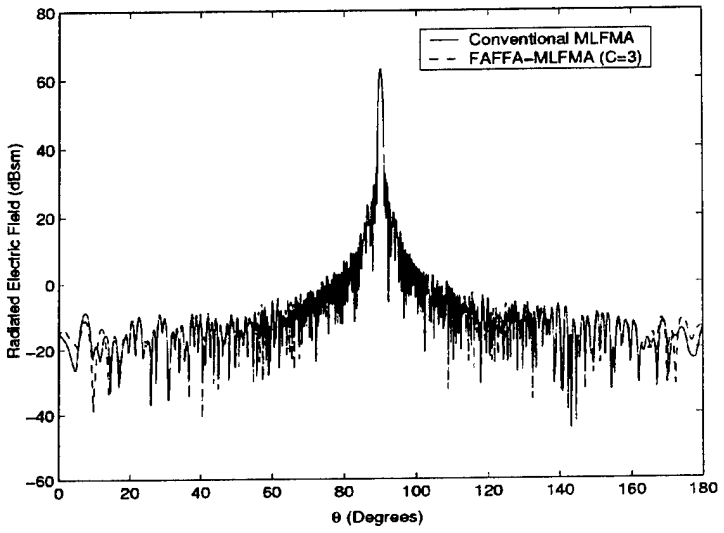

Figure 2. The radiation electric field of the parabolic antenna at 450 MHz. An 8-level algorithm is used. In FAFFA-MLFMA, the coarsest level is chosen as 3 and $\gamma = 1.0$.

4. Conclusions

An efficient FAFFA-MLFMA algorithm has been implemented to accelerate solving the combined field integral equation in the electromagnetic scattering and radiation problem. Comparing with the conventional MLFMA, both the memory requirement and CPU time can be reduced using the FAFFA-MLFMA algorithm. For very large problems, the reduction of CPU time can reach as much as 40 %.

5. Acknowledgment

This work was supported by the Department of Energy grant DOE DEFG07-97ER 14835, Air Force Office of Scientific Research under MURI Grant F49620-96-1-0025, and National Science Foundation under grant NSF ECS 99-06651. The computer time of this work was provided by the National Center for

Supercomputing Applications (NCSA) at the University of Illinois at Urbana-Champaign.

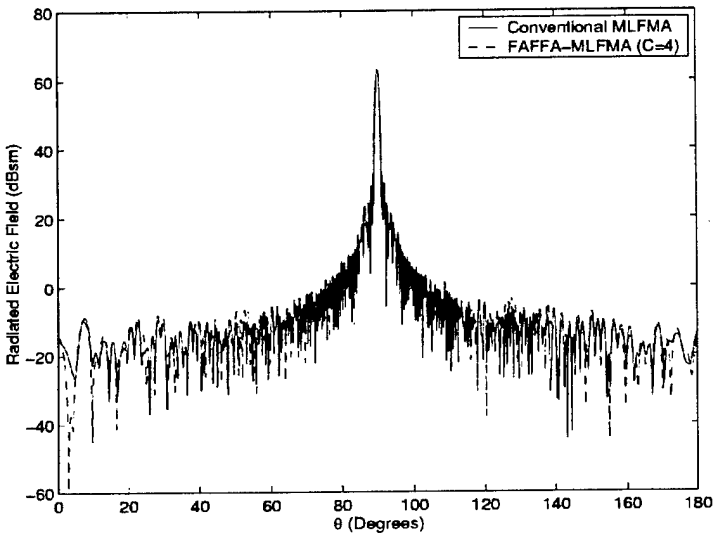

Figure 3. The radiation electric field of the parabolic antenna at 450 MHz. An 8-level algorithm is used. In FAFFA-MLFMA, the coarsest level is chosen as 4 and $\gamma = 1.0$.

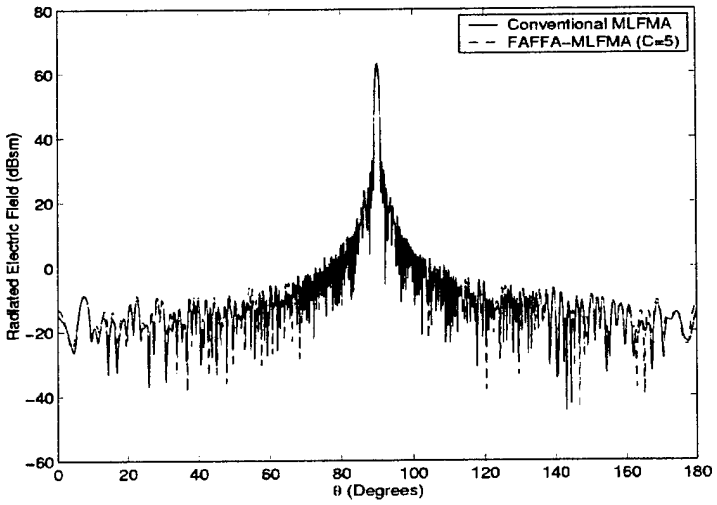

Figure 4. The radiation electric field of the parabolic antenna at 450 MHz. An 8-level algorithm is used. In FAFFA-MLFMA, the coarsest level is chosen as 5 and $\gamma = 1.5$.

6. References

[1] L. B. Felsen and N. Marcuvitz, *Radiation and Scattering of Electromagnetic Waves*, New Jersey: Prentice-Hall, 1973.

[2] S. H. Lee and R. C. Rudduck, "Aperture integration and **GTD** techniques used in the NEC reflector antenna code," *IEEE Trans. Antennas Propagat.*, vol. 33, pp. 189-194, Feb. 1985.

[3] V. Rokhlin, "Rapid solution of integral equations of classical potential theory," *J. Comput. Phys.*, vol. 60, pp. 187-207, Sept. 1985.

[4] L. Greengard and V. Rokhlin, "A fast algorithm for particle simulations," *J. Comput. Phys.*, vol. 73, pp. 325-348, Dec. 1987.

[5] J. Carrier, L. Greengard, and V. Rokhlin, "A fast adaptive multipole algorithm for particle simulations," *SIAM J. Sci. Stat. Comput.*, vol. 9, pp. 669-686, July 1988.

[6] V. Rokhlin, "Rapid solution of integral equations of scattering theory in two dimensions," *J. Comput. Phys.*, vol. 86, pp. 414-439, Feb. 1990.

[7] N. Engheta, W. D. Murphy, V. Rokhlin, and M. S. Vassiliou, "The fast multipole method (FMM) for electromagnetic scattering problems," *IEEE Trans. Antennas Propagat.*, vol. 40, pp. 634-641, Jun. 1992.

[8] L. R. Hamilton, M. A. Stalzer, R. S. Turley, J. L. Visher, and S. M. Wandzura, "Scattering computation using the fast multipole method," in *IEEE APS Int. Symp. Dig.*, Ann Arbor, MI, June 1993, pp. 852-855.

[9] C. C. Lu and W. C. Chew, "Fast algorithm for solving hybrid integral equations," *Proc. Inst. Elect. Eng.*, vol. 140, pt. H, pp. 455-460, Dec. 1993.

[10] R. Coifman, V. Rokhlin, and S. M. Wandzura, "Fast single-stage multipole method for the wave equation," in *10th Annu. Rev. Progress Appl. Computat. Electromagn.*, Monterey, CA, Mar. 1994, pp. 19-24.

[11] J. M. Song and W. C. Chew, "Fast multipole method solution using parametric geometry," *Microwave Opt. Tech. Lett.*, vol. 7, no. 16, pp. 760-765, 1994.

[12] R. L. Wagner and W. C. Chew, "A ray-propagation fast multipole algorithm," *Microwave Opt. Tech. Lett.*, vol. 7, no. 10, pp. 435-438, 1994.

[13] C. C. Lu and W. C. Chew, "Fast far-field approximation for calculating the RCS of large objects," *Microwave Opt. Tech. Lett.*, vol. 8, no. 5, pp. 238-241, 1995.

[14] R. Coifman, V. Rokhlin, and S. M. Wandzura, "The fast multipole method for the wave equation: A pedestrian prescription," *IEEE Antennas Propagat. Mag.*, vol. 35, pp. 7-12, Jun. 1993.

[15] C. C. Lu and W. C. Chew, "A multilevel algorithm for solving boundary integral equations of wave scattering," *Microwave Opt. Tech. Lett.*, vol. 7, no. 10, pp. 466-470, 1994.

[16] J. M. Song and W. C. Chew, "Multilevel fast-multipole algorithm for solving combined field integral equations of electromagnetic scattering," *Microwave Opt. Tech. Lett.*, vol. 8, no. 1, pp. 14-19, 1995.

[17] J. M. Song, C. C. Lu, and W. C. Chew, "Multilevel fast multipole algorithm for electromagnetic scattering by large complex objects," *IEEE Trans. Antennas Propagat.*, vol. 45, pp. 1488-1493, Oct. 1997.

[18] N. Geng, A. Sullivan, and L. Carin, "Multilevel fast-multipole algorithm for scattering from conducting targets above or embedded in a lossy half space," *IEEE Trans. Geosci. Remote Sensing*, vol. 38, pp. 1561-1573, Jul. 2000.

[19] B. Dembart and E. Yip, "A 3-D fast multipole method for electromagnetics with multiple levels," in *11th Annu. Rev. Progress Appl. Computat. Electromagn.*, Monterey, CA, Mar. 1995, pp. 621-628.

[20] M. A. Epton and B. Dembart, ``Multipole translation theory for the three-dimensional Laplace and Helmholtz equations," *SIAM J. Sci. Comput.*, vol. 16, pp. 865-897, July 1995.

[21] A. McCowen, "Efficient 3-D moment-method analysis for reflector antennas using a far-field approximation technique," *Proc. Inst. Elect. Eng.*, vol. 146, pt. H, pp. 7-12, Feb. 1999.

[22] L. Rossi, P. J. Cullen and C. Brennan, "Implementation of a multilevel fast far-field algorithm for solving electric-field integral equations," *Proc. Inst. Elect. Eng.*, vol. 147, pt. H, pp. 19-24, Feb. 2000.

[23] S. M. Rao, D. Wilton and A. W. Glisson, "Electromagnetic scattering by surfaces of arbitrary shape," *IEEE Trans. Antennas Propagat.*, vol. AP-30, pp. 409-418, May 1982.

[24] W. J. Wiscombe, "Improved Mie scattering algorithm," *Applied Optics*, vol. 19, no.9, May 1980.

[25] O. M. Bucci and G. Franceschetti, "On the spatial bandwidth of scattered fields," *IEEE Trans. Antennas Propagat.*, vol. AP-35, pp. 1445-1455, Dec. 1987.

[26] V. Rokhlin, "Sparse diagonal forms for translation operations for the Helmholtz equation in two dimensions," *Research Report*, YALEU/DCS/RR-1095, Dept. Comp. Sci., Yale University, Dec. 1995.

A New Class of Broadband Planar Apertures

P. Friederich, L. Pringle, L. Fountain, P. Harms,
D. Denison, E. Kuster, S. Blalock
Georgia Tech Research Institute
400 10th Street NW
Atlanta, GA 30332-0866

G. Smith
School of Electrical And Computer Engineering
Georgia Institute of Technology
Atlanta, GA 30332-

J. Maloney, M. Kesler
Photonex Corporation

GTRI has developed a novel class of antennas called fragmented apertures, comprising a matrix of conducting and dielectric regions. The antennas are typically fabricated on thin dielectric substrates using printed circuit board etching techniques. As such, they are thin, lightweight, and inexpensive to manufacture. With a pixel size of approximately $\lambda/20$ at the highest frequency, the design process uses a two-step optimization consisting of a genetic algorithm combined with a simple hill-climb. The result is near diffraction-limited gain over wide bandwidths from a single feed point. The antenna can also be matched to arbitrary feed impedance.

Arrays using fragmented elements are also presented. The individual elements are allowed to connect electrically with each other. The pixel pattern for the individual element is derived in an infinite array environment, and the effects of finite aperture size (edge effects, scan patterns) are then determined from simulations of the finite array. We present an example design with a good match over a 20:1 bandwidth, as well as measured data from test coupons with a 12:1 bandwidth (single linear polarization) and an 8:1 bandwidth (dual linear polarizations). The measurements are found to match FDTD predictions.

Application of ground planes to the fragmented apertures is also examined with a consideration of the attendant effects on bandwidth.

1. Introduction

Applications that require low profile, broadband antennas traditionally turn to candidates such as spiral or bowtie antennas. These antennas are based on geometrical constructs that maintain a constant scale across varying wavelengths. Typical instances of these antennas are presented in Figure 1 along with the predicted realized gain performance for each in a 10-inch aperture. Realized gain is defined as directive gain times mismatch (both conductor and dielectric substrate are considered lossless in these simulations).

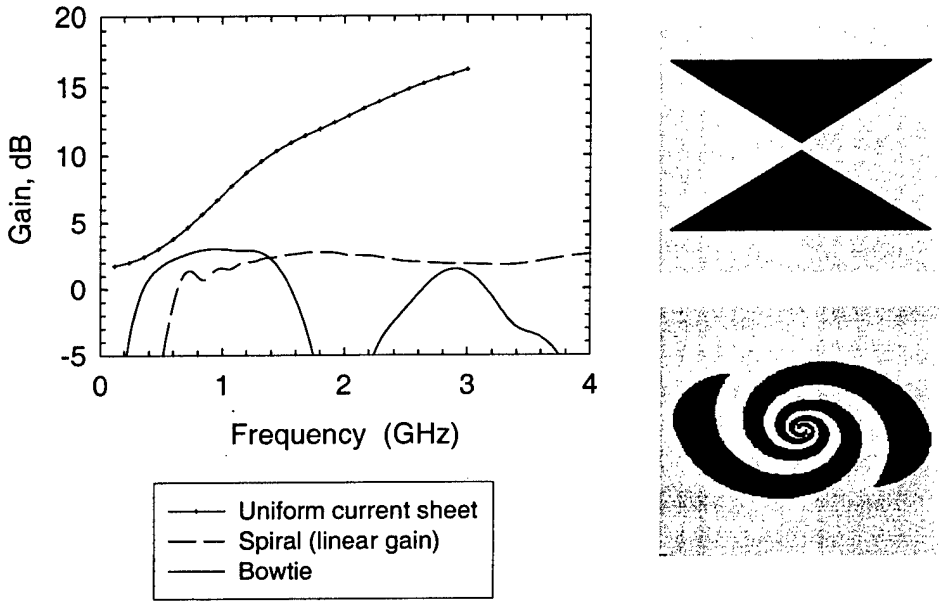

Figure 1. Traditional broadband, low profile antennas. Realized gain is compared to the gain of a uniformly illuminated aperture of equivalent size.

The directivity of a uniformly illuminated aperture, given by

$$D = 4\pi A / \lambda^2$$

represents an ideal performance level for a practical wideband aperture. The gain performance of the standard antenna designs suggested the possibility for improvement. Thus, speculation turned to the kind of distribution of conducting regions that might provide optimum performance for a given bandwidth.

2. Single Feed Designs

In order to search for such a distribution, a 25-cm aperture was gridded into a matrix of regions to be assigned either conducting or dielectric properties. The practical problem then became how best to conduct the search.

2.1 Design approach (single feed)

To simplify the problem initially, consideration was given only to broadside radiation in a single polarization. Thus, the feed point was placed in the center of the aperture. The distribution of conductor regions was constrained to be symmetric both up-down and right-left about the feed point, so only a single quadrant of the radiating element needed consideration at each step.

To meet the need for a better search strategy, we developed a multi-stage optimization approach to design the antennas. The radiating structure of the antenna is optimized with a modified genetic algorithm (GA) using a driver from Carroll [1]. An aperture of the type described above has 961 (i.e. 31 x 31) degrees of freedom ($2^{961} = 10^{289}$ possible antennas). A direct genetic optimization with 961 binary genes exhibits very poor convergence. We have developed a two-step process to improve the convergence rate. The first stage is a direct genetic optimization using a large-scale characterization of the aperture – typically 40 genes. The second stage is a stochastic hill climb optimization using the fine scale characterization – 961 degrees of freedom for a typical 31 x 31 aperture (actually one quadrant of the aperture). This two-step approach has exhibited good rates of convergence.

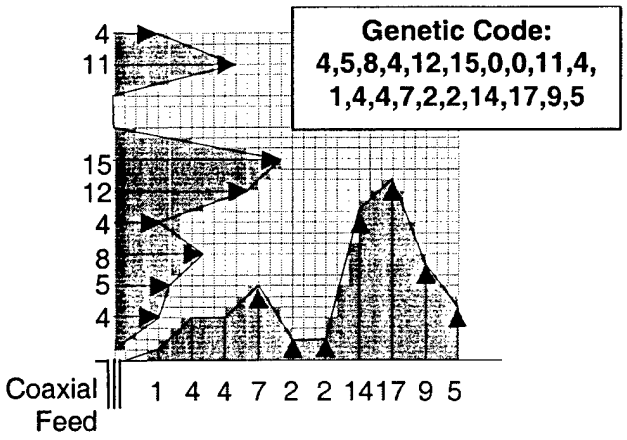

Figure 2. Representation of the first stage of the design process. The description of the antenna is reduced to 5-bit numbers or genes (32 distinct possible lengths) that describe trapezoids that make up the conductor distribution.

The key to the first stage of optimization is the description of potential antennas with a smaller number of binary digits than the full 961 bits required for the 31 by 31 aperture. Our usual approach uses a set of triangular or trapezoidal conducting strips in fixed locations in the aperture to provide a coarse description of possible antennas. Figure 2 illustrates this stage of the design process. In this typical example, the binary genes describe the length of two opposite sides of the trapezoid, so that the conducting strip can be a triangular region (one side equal to zero), a rectangular region (both sides equal), a general trapezoid (unequal but non-zero sides) or not present (both sides equal to zero). The length of a side is quantized to 32 possible lengths; thus only 5 bits are needed to prescribe a given strip. A typical antenna contains 10 to 20 strips, so a total of 50 to 100 bits describes the antenna for the first stage of the optimization process.

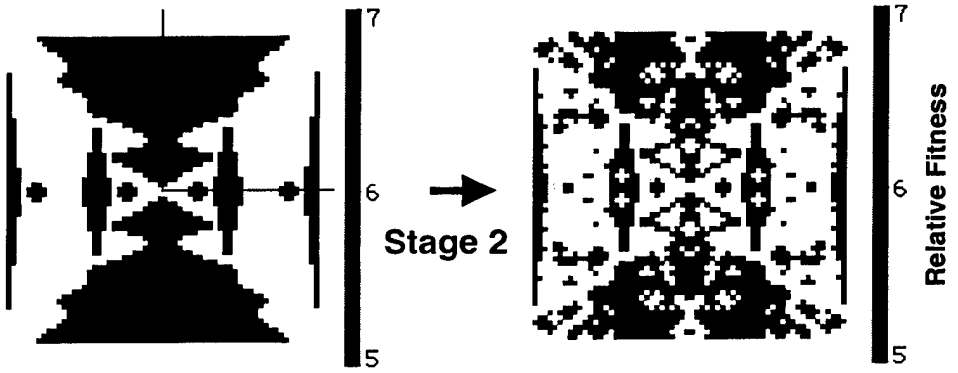

Figure 3. In the second stage of the design process, individual locations may be randomly changed from conductor to dielectric or vice versa. In this example, Dark gray indicates addition of conductor material and light gray indicates removal of material

Once the genetic optimization has been performed using the large-scale description of the aperture distribution, a fine-scale optimization process is performed. This process uses the full description of the antenna (961 bits for this 31 x 31 aperture example). The fine-scale optimization process makes a minor modification then compares the performance of the new antenna to that of the genetically optimized antenna. A random location in the antenna is selected; if the selected site contains conductor, the conductor is removed and the performance of the resulting antenna is computed. If the site did not originally contain conductor, it is added and the performance is likewise computed. If the new antenna performs better than the initial antenna, it is kept and the process is repeated as many times as desired or until no further improvements are found. This procedure, illustrated in Figure 3, can dramatically change the appearance of the conductor distribution in the aperture and typically results in a 3 dB improvement in the antenna performance.

2.2 Design results (single feed)

The radiating structure of the antenna shown in Figure 4 was optimized using this two-stage process to yield the best, uniform broadside realized gain over the frequency span of 800 MHz to 2.5 GHz. Because the optimization includes the effect of mismatch, the VSWR of the designed antennas is indirectly constrained. The measured gain (solid black line) for the antenna shown in Figure 4 is compared with the design prediction generated using a numerical code based on the finite-difference time-domain (FDTD) method (dashed line). This single feed design yields in excess of 6 dB of realized gain over the ~3:1 frequency band. The measured H-plane radiation pattern at 2.0 GHz (dotted line) is compared with the design prediction (solid line) in Figure 5. The radiation is directed in the broadside direction as designed.

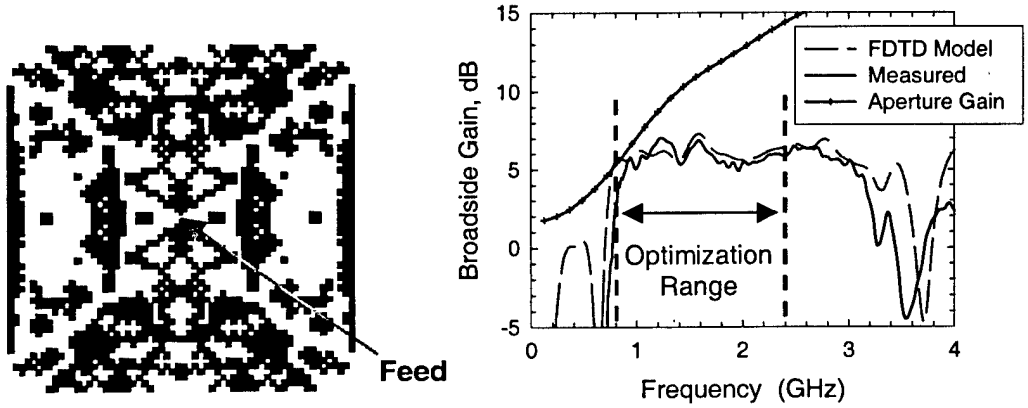

Figure 4. Fragmented aperture antenna optimized over the 0.8 – 2.5 GHz frequency range for flat system gain.

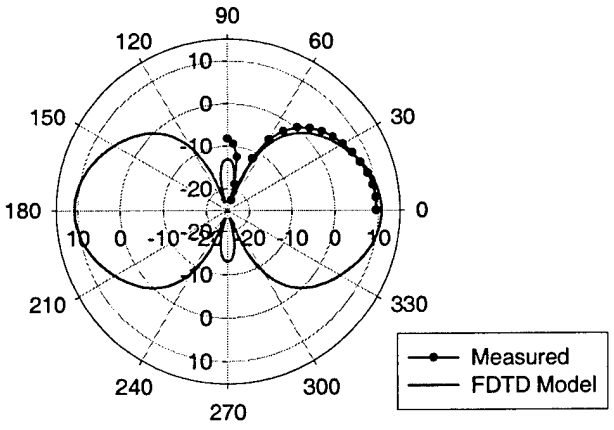

Figure 5. Pattern of the antenna shown in Figure 4.

Since the optimization process was attempting to achieve a flat gain, the result was limited by the lowest frequency in the band of operation. This observation led to a reformulation of the optimality criterion – search for designs whose gain over frequency mimics the uniformly illuminated result instead of a flat gain. Four of the resulting designs are shown in Figure 6.

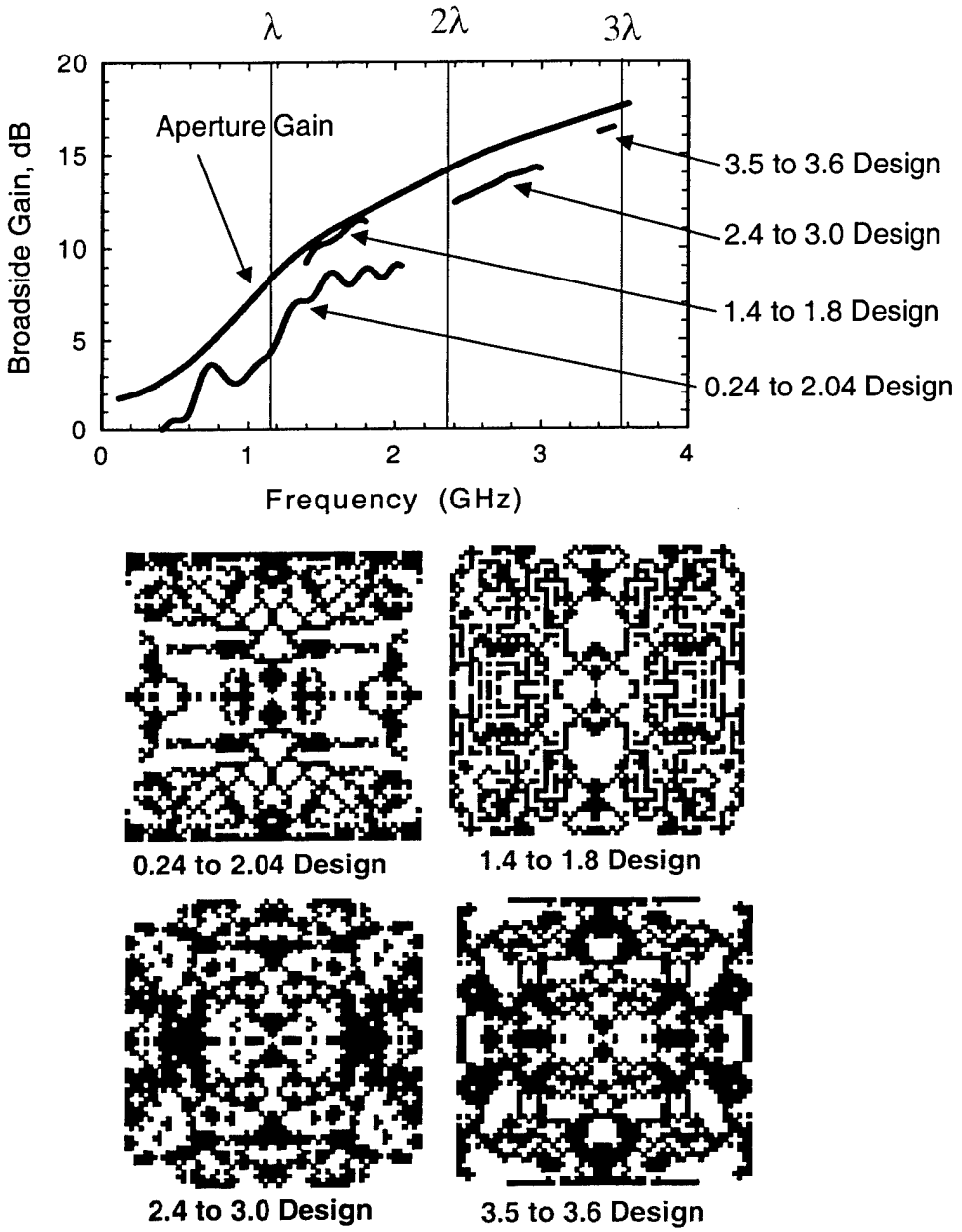

Figure 6. Four aperture designs and their predicted broadside gains.

2.3 Interpretation of single feed designs

The designs of Figure 6 are for 10-inch square apertures with a single feed point. Although these four designs do not encompass a very large population, they suggest certain trends about performance trade-offs. The design from 1.4-1.8 GHz achieved performance closer to the uniform aperture than the design from 0.24 to 2.04 GHz. This is consistent with intuition that one might have to trade some gain for broader bandwidth. Note also that the design from 3.5-3.6 GHz is farther from the diffraction limit than the 1.4-1.8 GHz aperture design, even though its operational bandwidth is narrower. This may be because the aperture is electrically larger at the higher frequencies and thus may be harder to excite from a single feed point.

2.4 Dual-pol design

The designs presented so far have all been linearly polarized. It is also possible to design a dual polarized antenna with separate feeds for the two linear polarizations. Such an antenna is shown in Figure 7. This antenna was designed to operate from 1.4-1.8 GHz for both polarizations. The predicted performance is also shown in Figure 7. The realized and directive gains at broadside both follow the uniform aperture result.

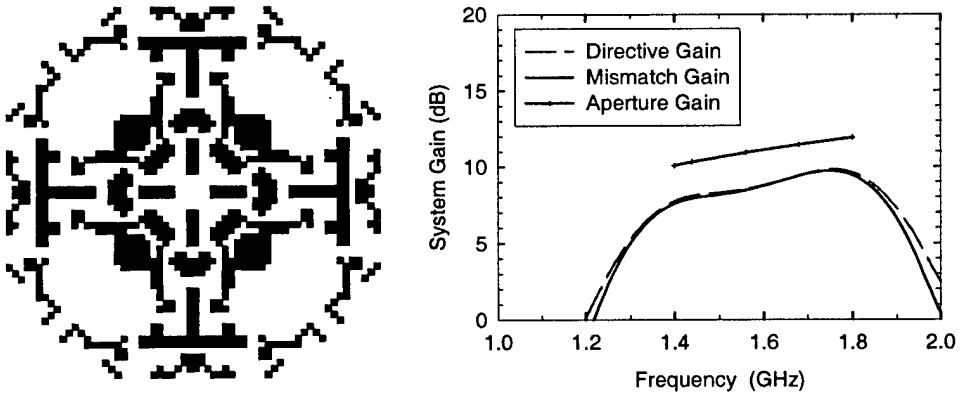

Figure 7. Fragmented aperture antenna optimized for dual polarization over the 1.4 – 1.8 GHz frequency range.

3. Fragmented Array Antennas

The fragmented aperture design approach was also applied to array antennas. With numerous elements in a finite array, however, the modeling problem becomes much more computationally intensive, and an array of any significant size slows down the optimization process to the point where it is no longer practical. As an alternative, we employ the standard approach of designing a single element in an infinite array environment, where our FDTD field solver efficiently realizes Floquet expansion through periodic boundary conditions. Such

an approximation is usually sufficient for the iterations required of an optimization algorithm. Then, when a design is obtained, the finite array may be modeled once to determine the effects of array truncation. A comparison of the two situations is illustrated in Figure 8.

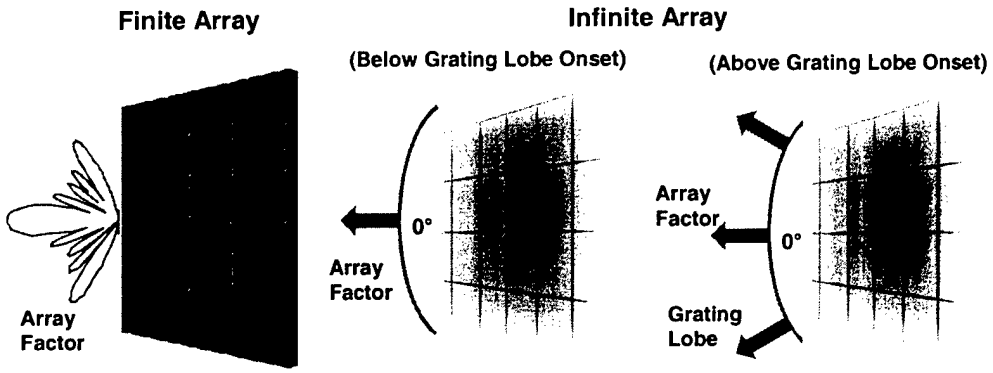

Figure 8. Notional representation of the effect of array factors in finite vs. infinite arrays.

The antenna pattern is just the element pattern times the array factor. For the finite array, this permits features of the element pattern to have a significant impact on the antenna pattern, such as when an element pattern null leads to scan blindness in a particular direction. In the infinite case, on the other hand, the array factor is a delta function (or group of delta functions in the case of grating lobes). Thus the antenna directive gain does not depend on the element pattern. The realized gain is influenced by how well matched the elements are at their feed points. Designing with an infinite array effectively means working toward the best possible match, and then evaluating the finished design in the finite array. Since the gain of an infinite array is infinite, we normalize the result to a perfectly matched array. The gain in an infinite array environment therefore will be 0dB or less (for apertures radiating equally into both forward and back hemispheres).

3.1 Connected arrays

With a traditional approach to designing arrays, one chooses the element based on requirements of bandwidth, gain, polarization, etc., and then chooses the element spacing to avoid grating lobes. In a useful design, the element is smaller than the array spacing and inter-element coupling is manageable. In our application of the fragmented aperture concept to array antennas, neighboring elements are allowed to make electrical contact with each other. This has the effect of extending the lower limit of operations to a frequency corresponding to the overall aperture size rather than being limited by the individual elements. Since the element design is performed while neither restricting the elements from touching nor requiring them to touch, the optimizer can find the best way to connect the elements and account for the resulting inter-element coupling. The longer dimensions of the connected

conducting regions in the aperture are a key reason that the array bandwidth can be extended to lower frequencies for a given aperture size.

Figure 9 illustrates the advantage of connected over unconnected arrays. Two design exercises were performed for a 6-cm element. One design was constrained so that the elements could not touch, and the other was unconstrained. Both designs were optimized for match from 250 to 2500 MHz. As can be seen from the plot, the design that resulted in a connected array exhibits much better match, including a bandwidth beyond the original design criterion. In Figure 10, a comparison of directivity only (neglecting mismatch) for each design in an 8 x 8 element array shows nearly identical performance between the connected and unconnected arrays at these two operating frequencies. The advantage of the connected design is improved match, especially at the lower frequencies.

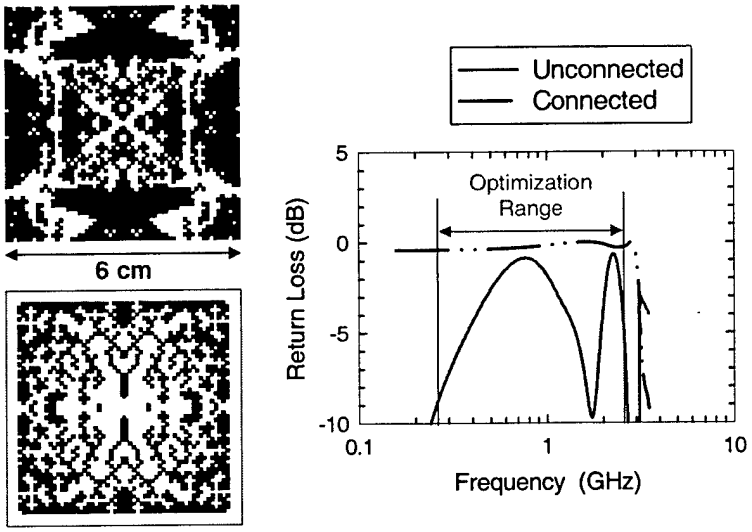

Figure 9. A comparison of bandwidth achieved with an array of 6 cm elements, with element contact permitted or restricted.

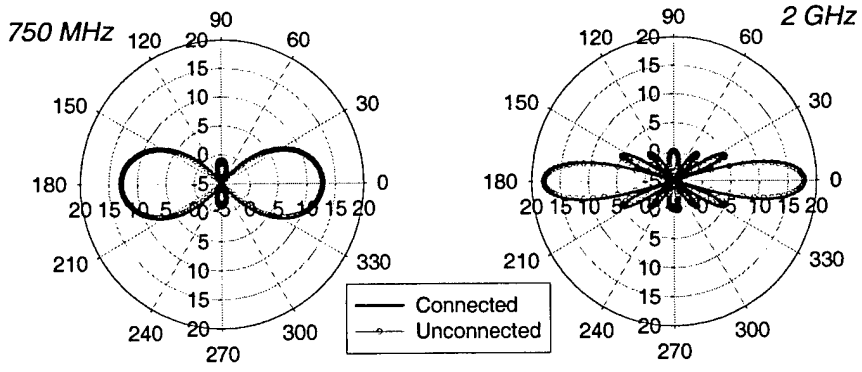

Figure 10. Comparison of directivity of connected and unconnected arrays.

3.2 Bandwidth and Aperture Size

For a given element design, the high frequency performance of an array is dominated by the embedded element characteristics and element spacing, while the low frequency performance is limited more by the physical size of the array. In Figure 11 a comparison is made of the same element design in a 2 x 2 array, a 4 x 4 array, an 8 x 8 array, and a 16 x 16 array (12 x 12 cm, 24 x 24 cm, 48 x 48 cm, and 96 x 96 cm, respectively). The low frequency cutoff occurs in each case when the aperture dimension is approximately $\lambda/3$.

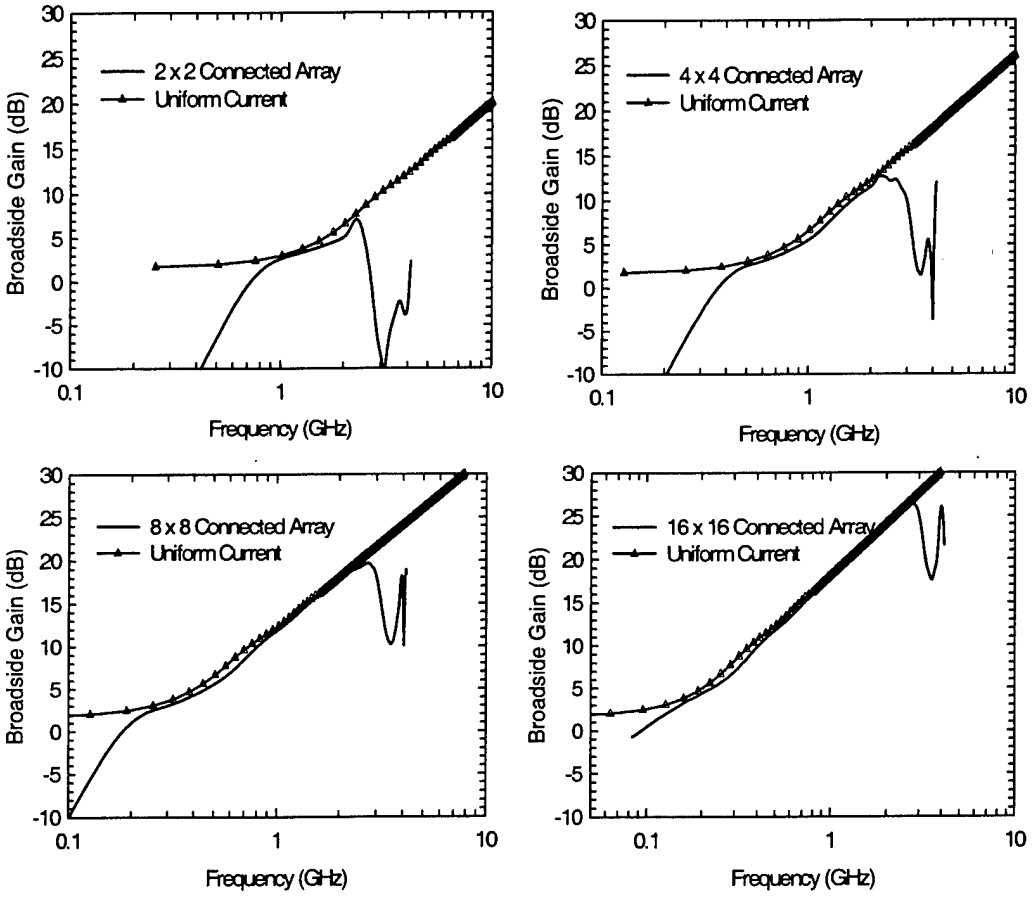

Figure 11. Predicted realized gain from arrays of the connected 6-cm element in Figure 9.

When the low frequency and high frequency cutoff points (defined as the frequencies where the realized gain of the aperture falls 1 dB below the gain of the uniformly illuminated aperture) are plotted as a function of array size, as in Figure 12, it becomes clear that the low frequency limit scales inversely with array size. The high frequency limit is relatively independent of aperture size, on

the other hand. It is determined by the individual element design (including the resolution with which the conductor distribution can be controlled) and element spacing.

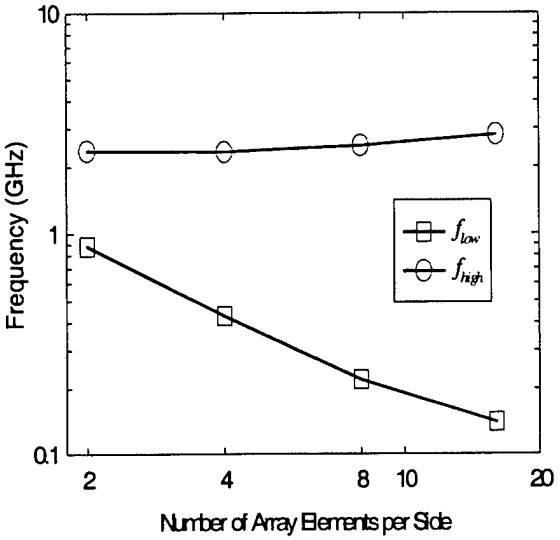

Figure 12. Variation of the high and low frequency band limits for the arrays in Figure 11 as a function of the overall aperture size.

3.3 Single Polarization Array Design

Figure 13 shows a photograph of the first array for which an actual test coupon was fabricated. The element spacing is 3 cm, so no broadside grating lobe should appear up to 10 GHz. The measurement fixture used to characterize these antennas dictated the aperture dimension of 30 x 25.5 cm. The test coupons were fabricated and mounted on brass plates 30 cm in diameter, which were rotated in an image plane 6 m on a side. Figure 13 also shows a photo of the test setup. With the test coupon imaged in the reflection plane, the array effectively measured 30 x 51 cm and consisted of 10 x 17 elements.

Figure 14 shows good agreement between prediction and measurement of the realized gain of the embedded center element at broadside (all other elements terminated with matched loads). The figure also includes the embedded element pattern at 10 GHz.

Figure 15 predicts realized gain of the finite array (10 x 17 elements, all elements driven) compared to the gain of a uniform current sheet on the same size aperture. At 1 GHz, the smallest dimension of the antenna is one wavelength and the predicted gain is still following that of the uniformly illuminated aperture. Broadside performance is good all the way to 12.5 GHz, which is beyond the

grating lobe onset (10GHz). A "notch" in the element pattern (see Figure 14) at 90 degrees serves to suppress the far out grating lobes.

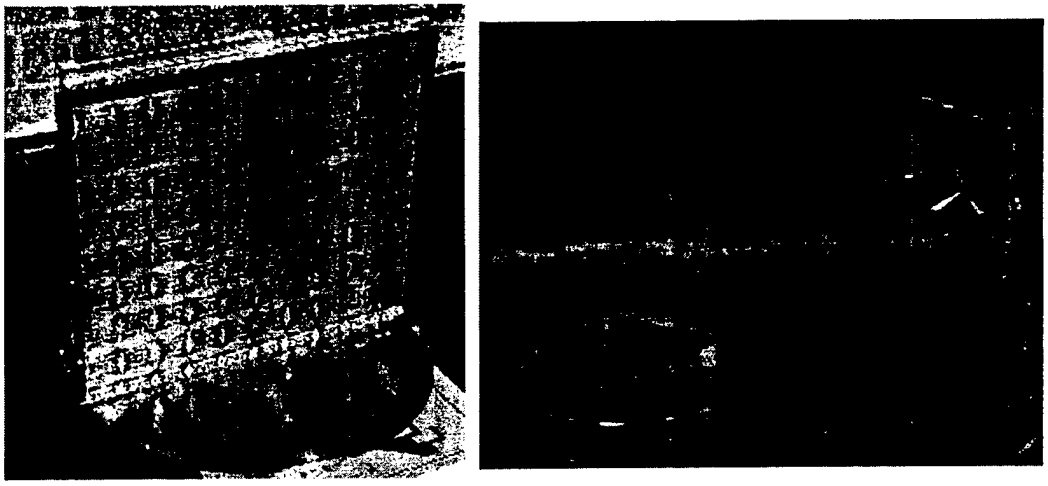

Figure 13. ***Left,*** **test coupon for a single-pol aperture designed to operate from 800 MHz to 10 GHz.** ***Right,*** **photo of the test setup used to characterize the array.**

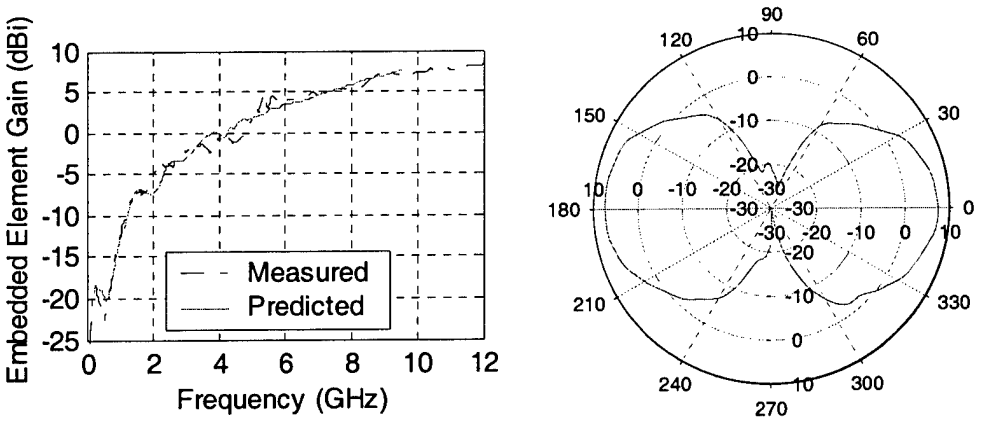

Figure 14. ***Left,*** **Realized gain (FDTD calculation and measurement) for the center element of the 10 x 17 element array with other elements terminated.** ***Right,*** **Embedded element pattern at 10 GHz.**

If one assumes every element has the same gain-mismatch (admittedly a shaky assumption for off normal scan angles and elements near the aperture edges), the total array performance can be inferred by multiplying the embedded element gain (scan element pattern) by the number of elements (170 with the imaged

elements). When this calculation is done with the measured pattern from the center element, good agreement is obtained with the numerical simulations of array performance. This approximation falls apart at low frequencies where array truncation has the most pronounced effect, but surprisingly, it does well down to about 1 GHz.

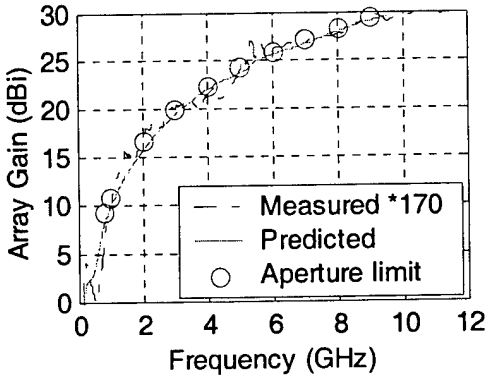

Figure 15. Realized gain (FDTD calculation) for the 10 x 17 element array compared to the aperture limit (gain of a uniform current sheet of the same size) and a projection based on the measured embedded element gain.

3.4 Dual Polarization Design

To assure good dual polarization performance for these designs, we restricted the design space to those configurations with symmetry about the 45-degree diagonal containing the element feed. For operation from 1.25-10 GHz, the element spacing was fixed at 1.5 cm ($\lambda/2$ at 10 GHz). Design goals included good scanning performance out to 60 degrees from boresight.

We used a standard design procedure for these arrays. A pixel size of 0.5 mm ($\lambda/60$ at 10 GHz) was chosen. The pixel distribution was optimized in the infinite array environment, and then a finite array of 17 x 17 elements (chosen to fit our 30 cm diameter test fixture) was modeled to verify adequate performance in the finite case. Finally the embedded element pattern was computed (17 x 17 array with only the center element driven and all other feeds terminated). The calculated embedded element pattern can be measured directly on the GTRI image plane test facility, and thus serves to validate the design. In addition, by examining the element pattern for nulls, one can anticipate frequencies and angles where scan blindness might be a problem for the full array. With this in mind, five candidate element designs were generated (optimizing only at boresight), and the most robust element pattern was selected for additional analysis, fabrication and scanning tests. Figure 16 shows a cartoon of a 2x2 element section of the

array, along with a photo of one half of the 17x17 array mounted on an image plane for measurement purposes.

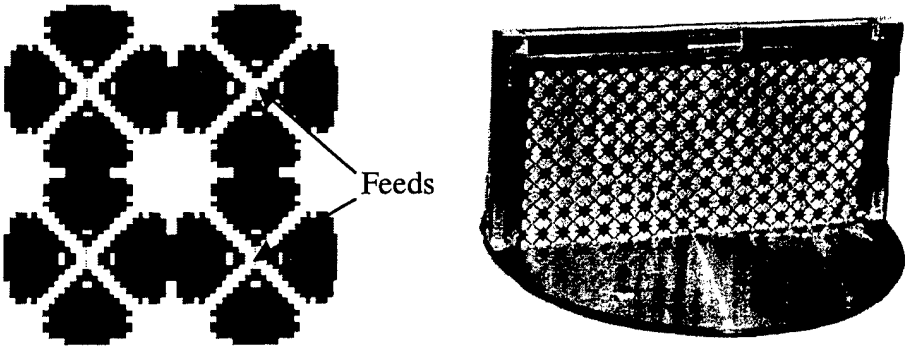

Figure 16 ***Left,*** **2 x 2 elements of the pattern optimized for 1.25 to 10 GHz.** ***Right,*** **An array test coupon mounted on a brass plate for measurement on the image plane.**

The test pieces that were fabricated consist of 17 x 8½ elements etched onto a polyimide sheet. This "half array" was mounted on a rotating brass plate embedded in the image plane, so together with its image it formed a 17 x 17 array. Fed from below the image plane, the center row of 17 elements were available for actual signals; other feed points were terminated with 100 Ω load resistors (the imaged equivalent of the 50 Ω transmission line feeds).

Two sets of measurements were performed on the test coupon after it was fabricated. In the first set, the center element was driven with all other feed points terminated. This embedded element performance can be compared directly to numerical predictions, and the measurement can be extrapolated to the performance of a 17 x 17 array with all elements driven. In the second set, the row of elements along the image plane was driven with appropriate phase offsets to evaluate scan performance of the design.

3.4.1. Embedded element results

Embedded element patterns were measured by driving only the center feed with undriven feeds terminated with 100 Ω resistors. Figure 17 shows aperture impedance plotted on a Smith chart, along with the magnitude of the corresponding reflection coefficient. Figure 18 shows a plot of the predicted and measured realized gains. The agreement between measurement and prediction is good.

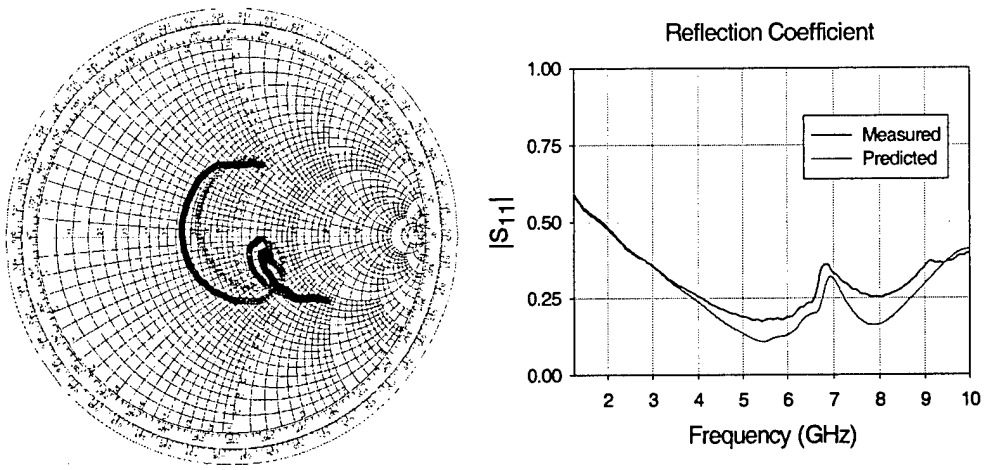

Figure 17. ***Left,*** **Smith Chart of the embedded element impedance measured at the center element with other elements terminated.** ***Right,*** **Plot of $|\Gamma|$ vs. frequency.**

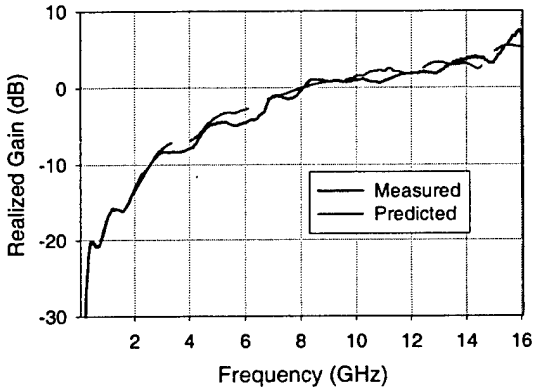

Figure 18 Comparison of measured and predicted realized gain at 0° azimuth, driving only the center element feed with other feeds terminated.

Embedded element patterns for this aperture were measured at 1.25, 1.4, 2.5, 3.7, 5.0, 7.0, and 10.0 GHz. Figure 19 shows plots of realized gain as a function of azimuth angle. In these plots, the antenna is aligned so that the 0-degree azimuth angle line is perpendicular to the face of the antenna. Because there is no ground plane behind the antenna, it radiates as much energy in the back hemisphere as in the forward hemisphere. One expects symmetry in the antenna patterns along azimuth lines at 0-180 degrees and –90-+90 degrees. The symmetry is automatic for the predicted patterns (because of the symmetry in the calculations). The symmetry is also evident in the actual measured patterns.

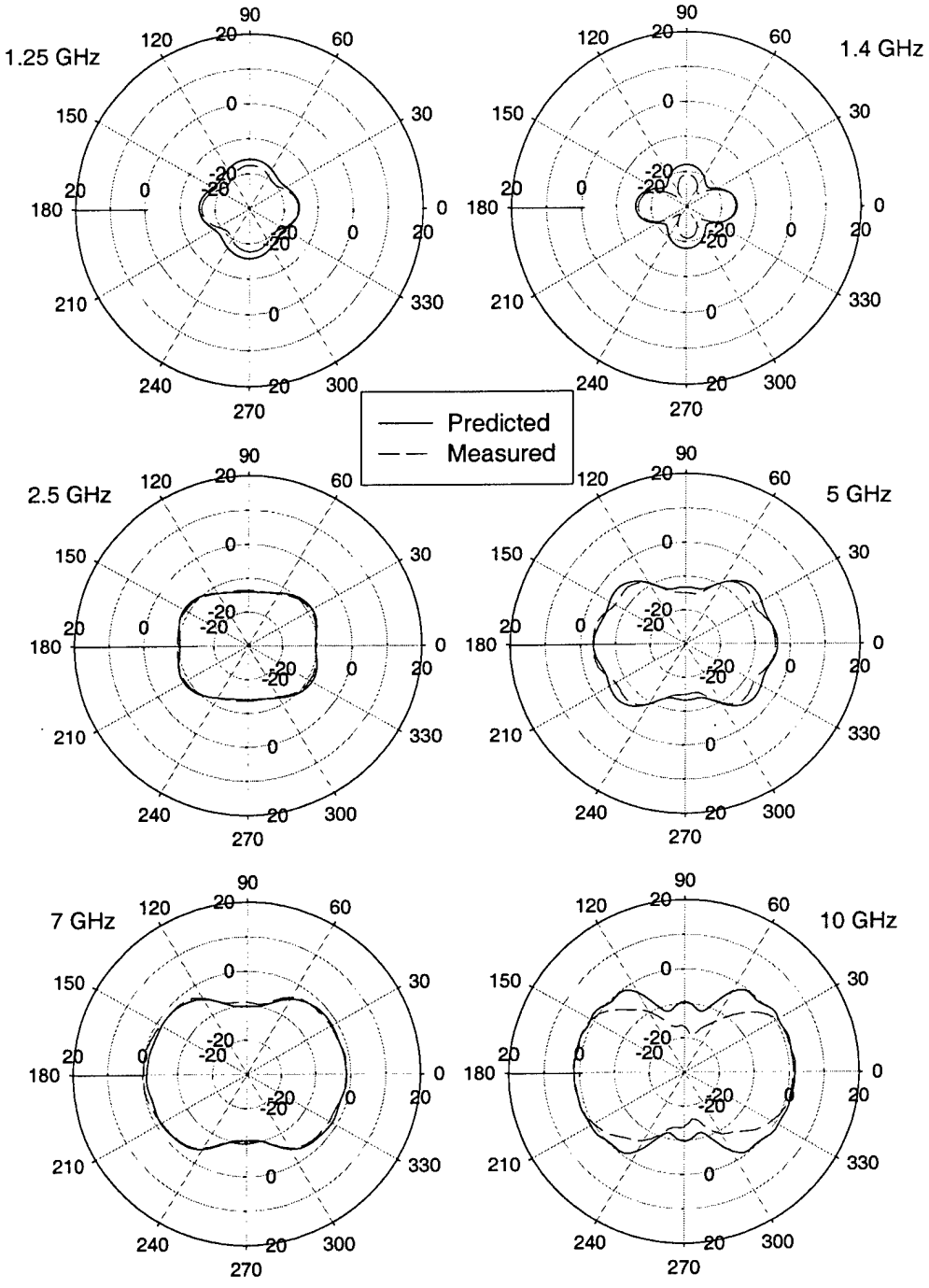

Figure 19. Embedded element patterns for 17x17 array of optimized elements.

The predicted and measured data agree well for each of the embedded element patterns from –30° to +30° about broadside. For the frequencies from 2.5-7.0 GHz, the patterns agree through the entire 360 degrees of azimuth angle. However, for angles around endfire (+90 and +270) the predictions and measurements diverge somewhat.

Within the design region, especially along the 0° azimuth line, the antenna shows a reasonable realized gain. This is consistent with the antenna optimization applied to the broadside direction. However, a deep null exists around 1.6 GHz from approximately 50 to 130 degrees. This null explains the discrepancies in the embedded element patterns at 1.25 and 1.4 GHz for angles near +/-90°. Slight shifts between the predicted and measured frequencies of the null manifest themselves as large discrepancies in plots of gain versus angle at the affected frequencies. Figure 20 illustrates this more explicitly with a comparison of measured and predicted realized gain vs. frequency at an azimuth angle of 60 degrees. For example, one would expect the most serious disagreement at 60 degrees for frequency cuts at 1.55 and 1.65 GHz.

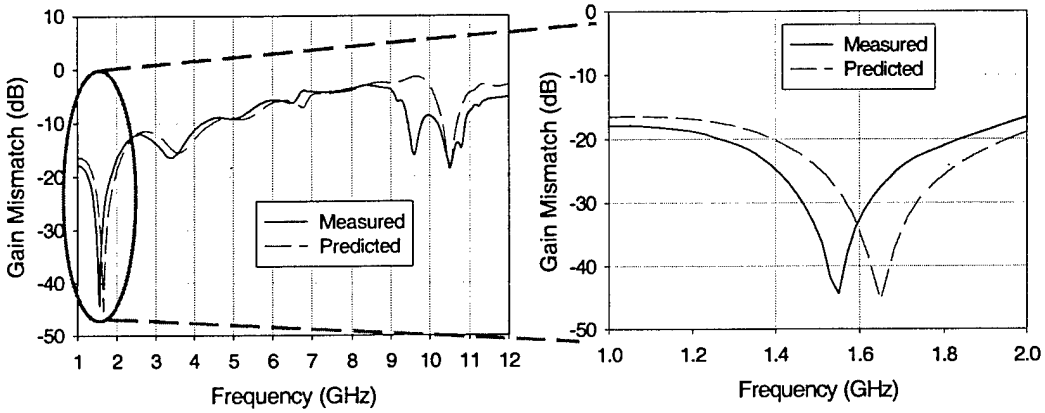

Figure 20. Frequency cut at 60-degree azimuth angle showing the slight shift in null position responsible for pattern discrepancies in the 1.25 and 1.4 GHz pattern cuts of Figure 19. The plot on the right is a blowup of the region circled in the plot on the left.

3.4.2. Scanned row array results

3.4.2.1. Scan impedance

An important measure of performance for scanning arrays is the input impedance as a function of scan angle, the so-called scan impedance. Hansen [2] points out the necessity of measuring this quantity with all active elements driven to get accurate results. Our test coupons are not configured to perform full array

scanning, but the test coupon can be configured as a row array by driving the feeds along the image plane row and treating each column as an individual element. Thus, we performed a series of measurements on the row array to determine scan impedance (of the column element) for comparison with predictions.

The row array was driven through a splitter network that produced 16 matched signal outputs. Since the row array had 17 columns, one element would not be driven. To maintain the center of rotation under the center of the array, both outside elements were terminated with matched loads and the other elements were driven with 15 of the 16 splitter outputs. Symmetry was also maintained in the measured pattern cuts (an easy verification that the measurement system is set up correctly). Appropriate phasing for scan angles of 0°, 30° and 50° was achieved by fabricating three sets of feed cables with individual length differences calculated to produce the requisite time delays. Then the row array was measured using each set of feed cables. Data sets collected at each scan angle include realized gain and gain vs. frequency and azimuth angle, and scan impedance measured at the center element.

Figure 21 shows the setup below the image plane for measuring the scan impedance. The output of the network analyzer feeds into a 4-way power divider that feeds four more 4-way power dividers. The output of one of these 16 ports is terminated, and the other 15 used to drive the center 15 feeds along the image plane. Scan impedance can be determined from the reflection coefficient (Γ), or s_{11} parameter, at the port of interest when the other elements are fed with the appropriate time delayed lines. The s_{11} parameter for the center feed is measured with a microwave network analyzer. The scan impedance (Z_{in}) then is calculated as:

$$Z_{in} = Z_0\left(\frac{1+\Gamma}{1-\Gamma}\right), \qquad \text{where } Z_0 = 50\ \Omega.$$

The scan impedance was measured vs. frequency for 0°, 30°, and 50° steering. Note that the antenna is steered through the use of true time delay (different cable lengths) rather than fixed length cables and phase shifters. Each steering angle requires a different set of cables because the time delay between feed points is a function of the steering angle.

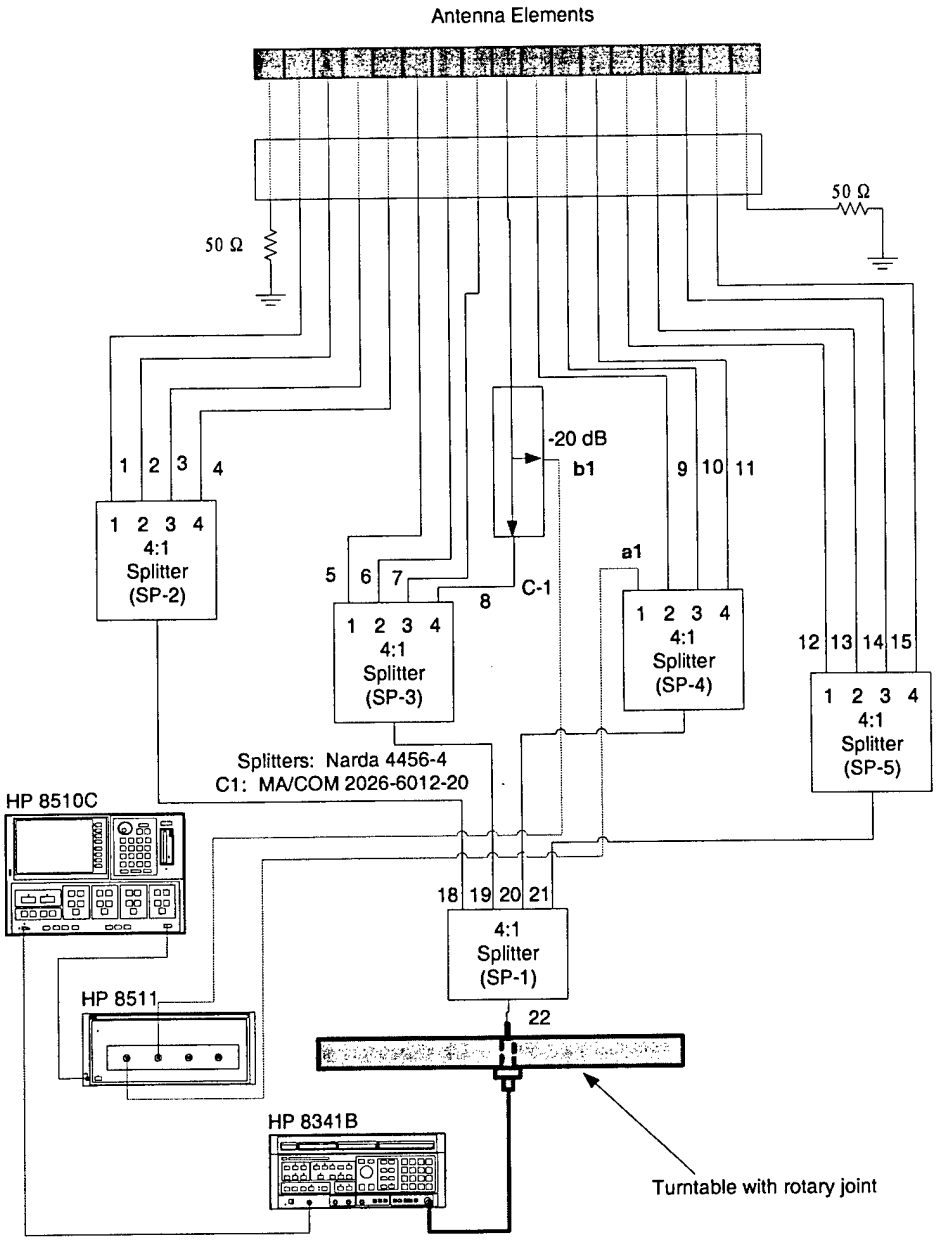

Figure 21 Schematic of the experimental setup used to measure scan impedance.

Measured and predicted data are shown in two formats: plots of the magnitude of the reflection coefficient as a function of frequency, and Smith charts. Figure 22 through Figure 24 show results for scan angles of 0, 30 and 50 degrees,

respectively. The agreement between measured and predicted values of scan impedance (and reflection coefficient) validate the model being used and give us confidence in the predicted values for arrays with all elements driven.

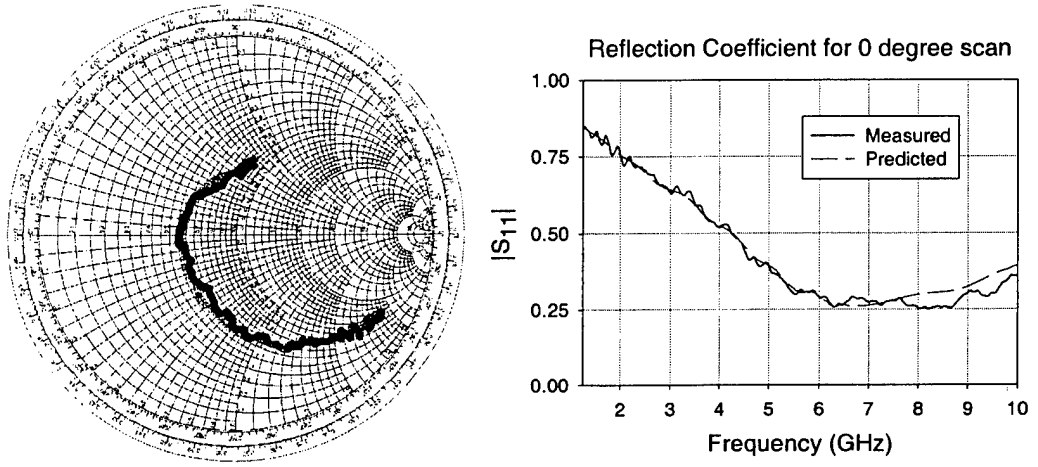

Figure 22. ***Left,*** **Smith chart of the predicted and measured scan impedance at the center element for 0 degree scan angle.** ***Right,*** **Corresponding plot of $|\Gamma|$ vs. frequency.**

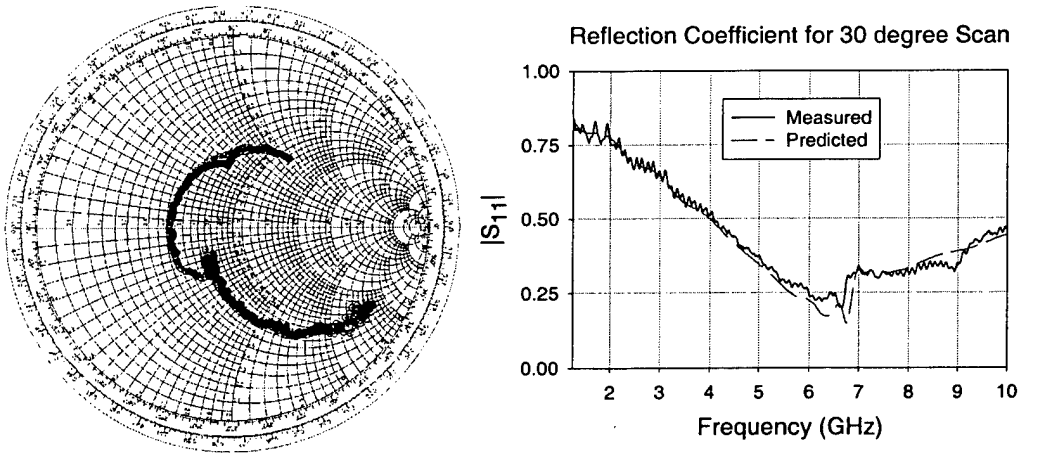

Figure 23. ***Left,*** **Smith chart of the predicted and measured scan impedance at the center element for 30 degree scan angle.** ***Right,*** **Corresponding plot of $|\Gamma|$ vs. frequency.**

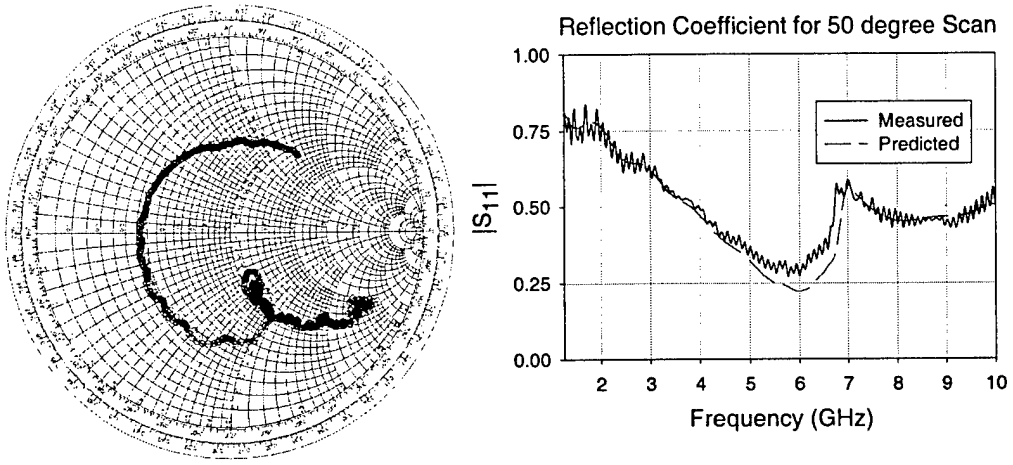

Figure 24. ***Left,*** **Smith chart of the predicted and measured scan impedance at the center element for 50 degree scan angle.** ***Right,*** **Corresponding plot of $|\Gamma|$ vs. frequency.**

3.4.2.2. Steered Antenna Gain Performance

The experimental setup for measuring pattern cuts for the row array was very similar to the scan impedance setup illustrated in Figure 21. The changes were that signal *a1* from the directional coupler and signal *b1* from splitter SP-4 were both terminated with matched loads. (The coupler remains in place because the phasing of the coaxial feeds was based on the coupler being in the signal path.) In addition, the HP8510C was replaced with a HP8720 at the feed point below the rotary joint, and s_{21} was measured instead of s_{11}. Again, the array was steered using 15 of 17 elements along the image plane. The 2-port calibration of the network analyzer includes the cable feeding the first power divider.

In order to compare measured data with predictions, the insertion loss of the feed network must be accounted for. The uniformity of the power splitters simplifies the task. Variation between ports is typically on the order of 0.01 dB, with a worst case spread of 0.3 dB. Similar ranges occur from splitter to splitter. The theoretical best-case insertion loss along one signal path through two splitters and a feed cable is approximately 12 dB for lossless devices, due to the 16-way split. An additional 1 to 4 dB is dissipated by the feed network itself. In view of the uniformity of the splitters and cables, the measured data was corrected by a factor equal to 15 times the insertion loss of a typical measured signal path.

In Figure 25 through Figure 27, antenna power pattern plots of realized gain are presented for scan angles of 0, 30, and 50 degrees, respectively. In each case,

measurement and prediction are compared at frequencies of 1.25, 2.5, 3.7, 5, 7, and 10 GHz. The agreement is good.

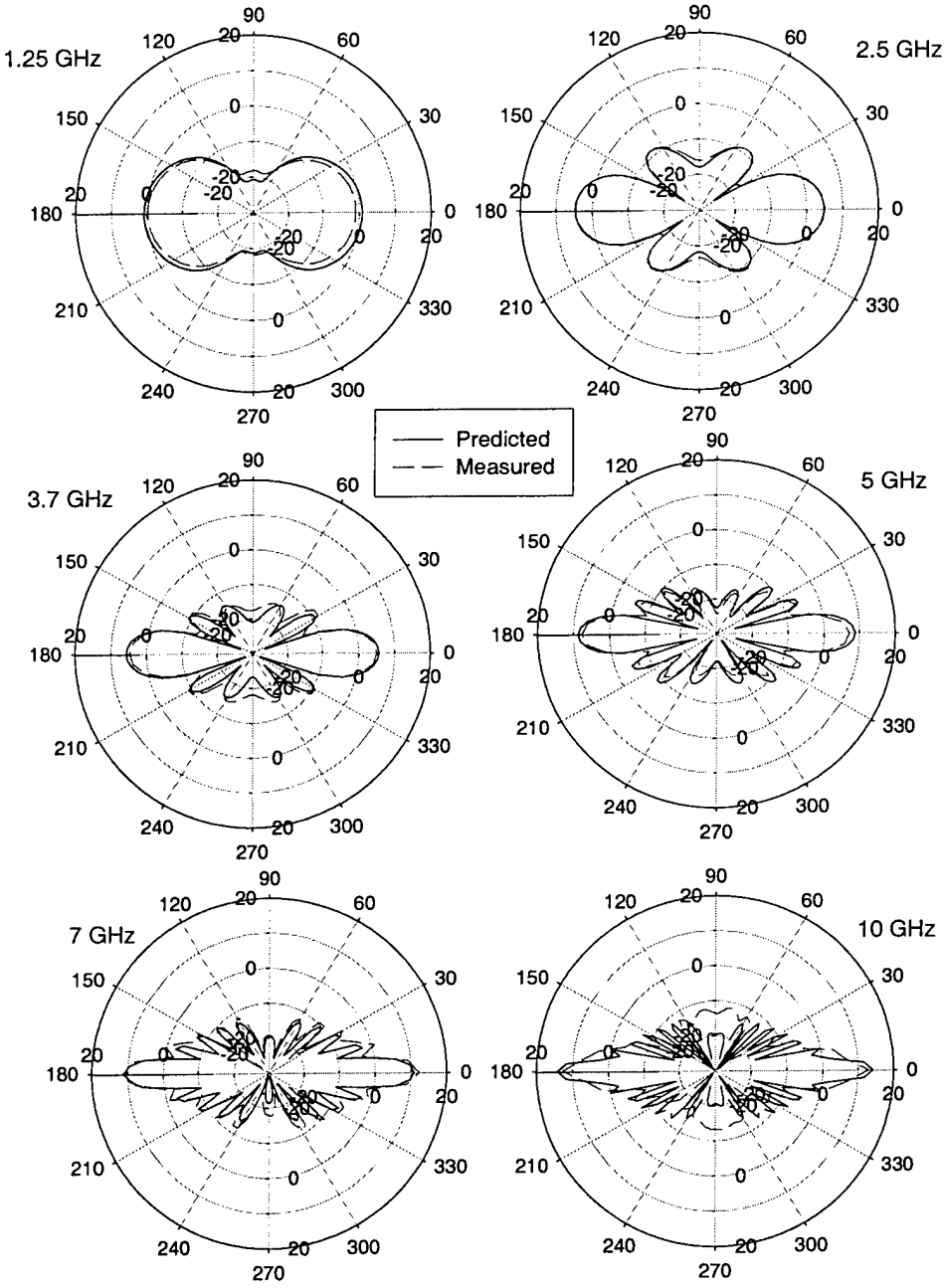

Figure 25. Comparison of measured and predicted antenna patterns for the row array steered to 0 degrees.

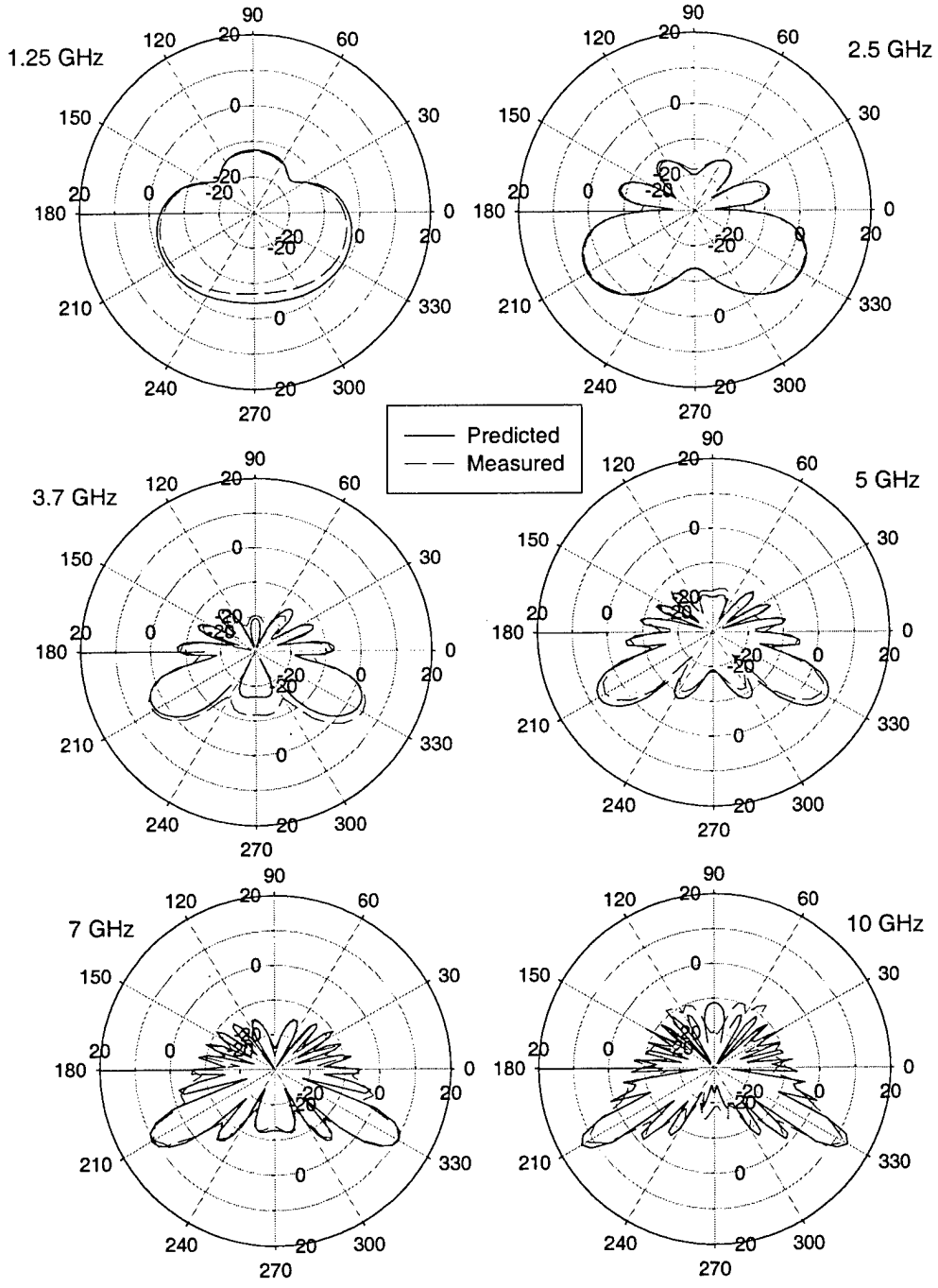

Figure 26. Comparison of measured and predicted antenna patterns for the row array steered to 30 degrees.

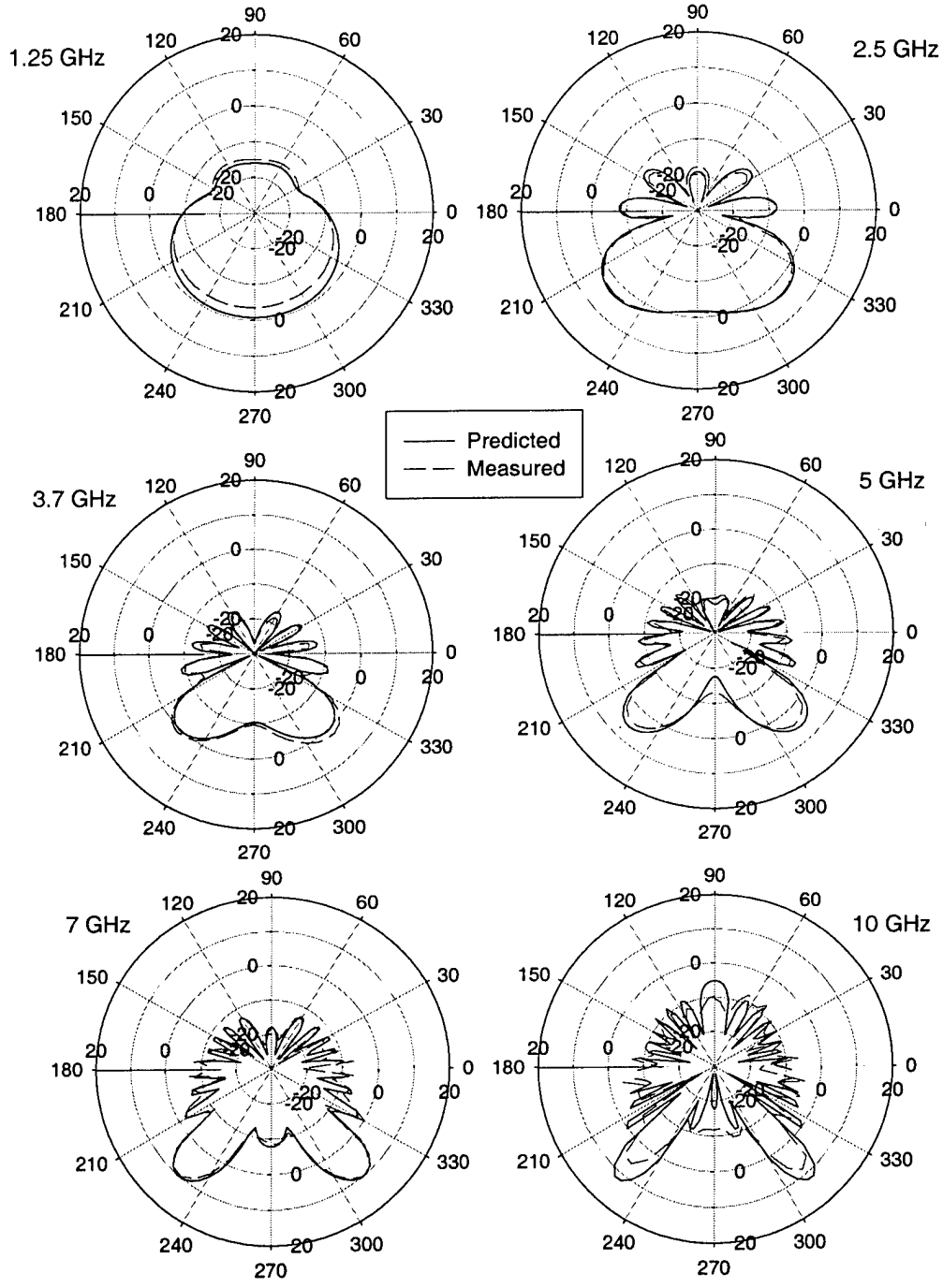

Figure 27.. Comparison of measured and predicted antenna patterns for the row array steered to 50 degrees.

4. Ground Plane Effects

The test coupons discussed in this paper so far have all been characterized with no backplane, i.e., each aperture radiated equally in both the forward and back hemispheres. In many cases, antennas will be operated with a backplane to shield feed structures and instrumentation behind the antenna and to direct more of the energy in the direction of interest in the forward hemisphere. This is particularly true for antennas conformally mounted on structures such as vehicles or walls. A solid metal backplane or ground plane will ideally be placed at $d = \lambda/4$ behind the radiating aperture for optimal performance, i.e. for the direct and reflected waves to add in phase, resulting in a 3 dB increase in gain. For apertures operating at more than one frequency, of course, the ideal spacing must be compromised, and the wider the operating bandwidth the more problems this will cause. Periodic nulls for broadside radiation will result at frequencies where the separation is a multiple of a half wavelength. For frequencies where the separation is electrically small, the ground plane produces a large mismatch and essentially shorts out the antenna.

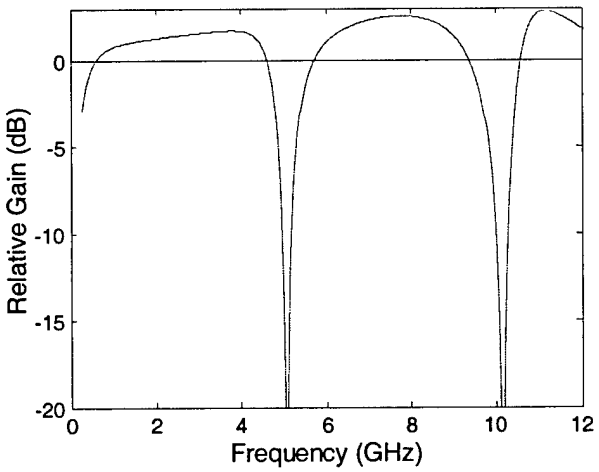

Figure 28. Predicted response of wideband array with ground plane placed 3 cm behind the aperture.

4.1 Wideband array with ground plane

Figure 28 illustrates the effect of a solid metal ground plane placed 3 cm behind an infinite array of the element design from Figure 16. The half-wave nulls occur at approximately 5 and 10 GHz. If the operating bandwidth for an aperture in front of a ground plane is defined as the region where broadside gain equals or exceeds the 0 dB baseline, i.e. the region where the ground plane contributes positively to the antenna gain, then this antenna exhibits a bandwidth from 574 MHz to 4.6 GHz, or approximately 8:1 with a solid metal ground plane. This is a

typical response for a fragmented aperture design optimized without a ground plane and then modeled with the ground plane present. Interestingly, optimizing with the ground plane present does not seem to improve performance for these wideband designs.

4.2 Single feed antenna with ground plane

Although λ/4 spacing between radiating surface and ground plane is considered optimal, some applications require a low profile antenna at frequencies where a λ/4 separation is not practical. If the fragmented aperture surface is designed in the presence of the ground plane, better than anticipated performance may be obtained at separations of as little as λ/30-λ/60 (depending on the aperture design) over a narrower bandwidth. Figure 29 plots the gain and reflection coefficient for two designs. Both are single-feed, fragmented apertures designed for optimal performance from 2-3 GHz, and both are 9.3 cm square. One design was performed with no ground plane present, and one was designed with a solid metal ground plane 2 mm (λ/60 at 2.5 GHz) behind the aperture. It can be seen that even with a solid metal sheet only λ/60 away, the realized gain is within 2 dB of the no-ground-plane case over the design band. Furthermore, it is a significant improvement over the case where a ground plane is added to the "no ground plane" design.

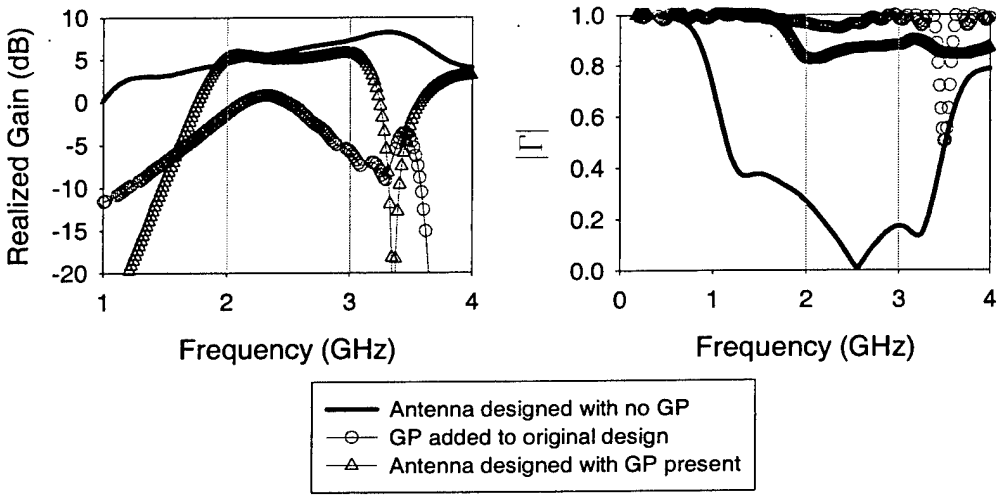

Figure 29. Gain and reflection coefficient for single feed fragmented apertures designed for operation from 2-3 GHz, with and without ultra-close ground plane.

5. Conclusion

Fragmented apertures provide antennas that are thin, lightweight, and inexpensive to manufacture. An efficient two-step optimization process consisting of a genetic algorithm combined with a simple hill-climb has been developed to make antenna design practical for both single feed and array cases. The approach allows near diffraction-limited gain over wide bandwidths from a single feed point. The antenna can also be matched to arbitrary feed impedance.

Incorporating these elements into connected arrays provides many of the same benefits (thin, light weight, inexpensive). Designs have been developed and tested with good match over a 12:1 bandwidth (single pol) and an 8:1 bandwidth (dual pol), and measurements were found to match FDTD predictions.

The fragmented arrays can be operated with a solid metal ground plane over 8:1 bandwidths. It is not known if this level of performance is unique to the fragmented design approach or is characteristic of wideband antenna designs in general. However, the fragmented design approach does permit accommodation of ultra-close spacing between aperture and ground plane ($\lambda/60$ or better) with little loss of performance over bandwidths as great as 50% from a single feed.

6. References

[1] D.L. Carroll, Program *gafortran*, Univ. of Illinois, Urbana, IL, 1997.

[2] R.C. Hansen, *Phased Array Antennas*, pp. 217-222, New York: John Wiley & Sons, 1998.